Atomic and Molecular Dynamics Probed by Intense Extreme Ultraviolet Attosecond Pulses

Peschel, Jasper

2021

Document Version:
Publisher's PDF, also known as Version of record

Atomic and Molecular Dynamics Probed by Intense Extreme Ultraviolet Attosecond Pulses

JASPER GEORG CHRISTOPHER PESCHEL
FACULTY OF ENGINEERING | LUND UNIVERSITY

Spherical Harmonic of the third order

Atomic and Molecular Dynamics Probed by Intense Extreme Ultraviolet Attosecond Pulses

Atomic and Molecular Dynamics Probed by Intense Extreme Ultraviolet Attosecond Pulses

by Jasper Georg Christopher Peschel

LUND
UNIVERSITY

A doctoral thesis at a university in Sweden takes either the form of a single, cohesive research study (monograph) or a summary of research papers (compilation thesis), which the doctoral student has written alone or together with one or several other author(s).

In the latter case the thesis consists of two parts. An introductory text puts the research work into context and summarizes the main points of the papers. Then, the research publications themselves are reproduced, together with a description of the individual contributions of the authors. The research papers may either have been already published or are manuscripts at various stages (in press, submitted, or in draft).

Cover illustration: Illustration of spherical harmonics inspired by *A Treatise on Electricity and Magnetism* by James Clerk Maxwell. Produced by Teresa Arana Aristi.

Division of Atomic Physics, Department of Physics, Lund University

ISBN: 978-91-8039-015-6 (print)
ISBN: 978-91-8039-014-9 (pdf)
ISSN: 0281-2762
Lund Reports on Atomic Physics, LRAP 576 (2021)

Printed in Sweden by Media-Tryck, Lund University, Lund 2021

Media-Tryck is a Nordic Swan Ecolabel certified provider of printed material. Read more about our environmental work at www.mediatryck.lu.se

Printed matter 3041 0903

MADE IN SWEDEN

Abstract

This thesis work was aimed to investigate dynamical processes in atoms and molecules on ultrafast time scales initiated by absorption of light in the extreme ultraviolet (XUV) regime. In particular, photoionization and photodissociation have been studied using pump-probe techniques involving ultrafast laser pulses. Such pulses are generated using either high-order harmonic generation (HHG) or free-electron lasers (FELs).

The work of this thesis consists to a large extent in the development and application of a light source, enabling intense XUV attosecond pulses using HHG. In a long focusing geometry, a high-power infrared laser is frequency up-converted so as to generate a comb of high-order harmonics. An important aspect was the study of the spatial and temporal properties of the generated light pulses in order to gain control of their influence on the experiment. Combining theoretical and experimental results, the effect of the dipole phase on properties of high-order harmonics was explored, along with a metrological series of studies on the harmonic wavefront and the properties of the focusing optics used.

Further, the HHG light source was employed to investigate photoionization. Individual angular momentum channels involved in the ionization were characterized using two-photon interferometry in combination with angle-resolved photoelectron detection. A method is applied allowing the full determination of channel-resolved amplitudes and phases of the matrix elements describing the single-photon ionization of neon.

Finally, the process of photodissociation was investigated using light pulses generated via both HHG and FELs. The dissociation dynamics induced by multiple ionization of organic molecules were studied. Correlation techniques were used to unravel the underlying fragmentation dynamics, and additionally, pump-probe experiments provided insights into the time scales of the (pre-)dissociation dynamics.

Popular Science Summary

The aim of the following work is to get a glimpse into time scales, which rarely allow insights. An electron is released from an atom. A molecule breaks into its components. A chemical reaction impacts our environment. Investigated down to the smallest detail and yet, it is often difficult for us to control such processes or to imitate them. In order to gain control, motions of the smallest of particles must be observed and understood. The challenge is to resolve the speeds such processes bring with them. In the next paragraphs, I will try to explain this in a few simple sentences.

Atomos. In Greek philosophy, considerations arose as to whether matter consists of a continuum that can be divided endlessly, or whether there is an elementary particle that cannot be split. In the 5th century BC, the word átomos (Greek for indivisible) appeared for the first time, formulated by Leucippus and his student Democritus. The existence of such particles and their structure, made up of a core and a shell, was experimentally proven at the beginning of the 20th century and described by Ernest Rutherford in his well-known atomic model. At the same time, however, the indivisibility was refuted by the discovery of ionizing radiation.

The electron in motion. The release of an electron from an atom exposed to light is called photoionization, which was first quantitatively explained by the photoelectric effect described by Albert Einstein. Energy in the form of a photon is transferred to the atom, which allows the electron to overcome the binding energy of the atomic compound. Any excess energy is converted into velocity given to the electron making it possible for it to move away from the atom. Shortly after Einstein's elucidation of the photoelectric effect, quantum theory explained that such a process only takes place in certain portions of energy, which means that the electron is released only into specific states. To date, research has largely understood which particles and fields play a role before and after photoionization. The atomic structure can to a great extent be studied using photoionization. What remains an unsolved mystery are the time scales of the process. How long does it take for an electron to leave an atom? What does the speed of the process depend on? Do all the electrons leave the atom with the same velocity?

The atom in motion. Similar questions can be asked when exploring the interactions between atoms. When several atoms are bound together, they form a compound, which is referred to as a molecule. In chemistry, many reactions involve breaking and re-creating such bonds between the atoms of a molecule. Often, it is understood which components are present at the beginning and at the end of a reaction. The exciting question is how exactly and on what time scales the reaction

takes place. Why does a molecule break apart in one place, but not another? How quickly does a molecule break apart and which fractions receive how much energy? Once again, the distribution of the electrons in the molecular compound, as well as the motion of these during (or shortly before) a reaction, play an important role.

Magnifying time. In theoretical considerations, it has been shown that such electron motions take place on time scales that are significantly faster than the human eye can see or slow-motion cameras can resolve. Electrons often move within attoseconds, which correspond to 0.00000000000000001 seconds. In order to resolve motions on these time scales, tools that operate in comparably short time scales are required. Similar to a video camera, which uses a mechanical shutter to illuminate a film at regular intervals, it is possible to generate light pulses that are no longer than a few hundred attoseconds. The generation of such pulses is achieved by overlapping light waves of different colors. This superposition leads to a cancellation of the waves at almost all points in time, and for only an ultrashort moment (a few 100 attoseconds) they all add up to one large wave forming a light pulse. The different colors are generated as overtones of a fundamental wave, which is why the process is referred to as *high-order harmonic generation*. In order to make use of these attosecond pulses for the 'filming' of electrons, the atoms or molecules are illuminated with the light pulses triggering an ionization or reaction. Shortly after, a second light pulse is used to see where the electron is located and how fast it moves. This process is repeated frequently with a varying delay between the two pulses, which gives the method its temporal resolution.

On the one hand, the focus of my work has been the technique described above, which we applied in various experiments throughout the project, both in atoms such as neon and helium, as well as in molecules such as the diamondoid adamantane or polycyclic aromatic hydrocarbons. On the other hand, the method of high-order harmonic generation itself has been part of my research. Its investigation and further developments have led to many of my publications and thus advancements in the field.

Populärvetenskaplig Sammanfattning

Målet med detta arbete är att få en inblick i tidsskalor som oftast inte låter sig observeras. En elektron frigörs från en atom. En molekyl splittras upp i sina beståndsdelar. En kemisk reaktion påverkar vår miljö. Trots att de är undersökta in i minsta detalj är det ofta svårt för oss att kontrollera sådana processer eller imitera dem. För att kunna göra det måste de minsta partiklarnas rörelser observeras och förstås. Utmaningen är att följa med i de hastigheter som sådana processer medför. Här nedan kommer jag att försöka förklara mitt arbete med hjälp av några korta stycken.

Atomos. I grekisk filosofi diskuterades huruvida materia består av ett kontinuum som kan delas i oändligt små delar eller om det finns en elementär partikel som inte kan delas. På 500-talet f.Kr. formulerade Leucippus och hans student Demokritus för första gången ordet **átomos** (grekiska för **odelbar**). Förekomsten av sådana partiklar och deras struktur, bestående av en kärna och ett skal, bevisades på experimentell väg i början av 1900-talet och beskrevs av Ernest Rutherford i hans välkända atommodell. Under samma tid motbevisades emellertid odelbarheten genom upptäckten av joniserande strålning.

Elektronen i rörelse. När en elektron frigörs från en atom med hjälp av ljus, kallas detta fotojonisation, vilket först förklarades kvantitativt med den fotoelektriska effekten som beskrevs av Albert Einstein. Energi i form av en foton överförs till atomen, vilket tillåter elektronen att övervinna dess bindningsenergi. All överskotts energi omvandlas till hastighet hos elektronen vilket gör att den rör sig bort från atomen. Strax efter Einsteins förklaring av den fotoelektriska effekten visade kvantteorin att en sådan process endast sker för vissa mängder energi, vilket innebär att elektronen släpps ut i specifika tillstånd. Hittills har forskningen till stor del förstått vilka partiklar och fält som har betydelse före och efter fotojonisation. Atomstrukturen kan i stor utsträckning studeras med hjälp av fotojonisation. Det som förblir ett olöst mysterium är processens tidsskalor. Hur lång tid tar det för en elektron att lämna en atom? Vad beror processens hastighet på? Lämnar alla elektroner atomen med samma hastighet?

Atomen i rörelse. Liknande frågor kan ställas när man tittar på interaktionen mellan atomer. När flera atomer är sammanbundna bildar de en förening som kallas för en molekyl. I kemi innebär många reaktioner att sådana bindningar mellan atomer i en molekyl bryts och återskapas. Oftast förstår man vilka komponenter som finns i början och i slutet av en reaktion. Den spännande frågan är exakt hur och på vilken tidsskala reaktionen sker. Varför bryts en molekyl på ett ställe, men inte på ett annat? Hur snabbt bryts en molekyl isär och hur mycket energi

får dess olika delar? Återigen spelar fördelningen av elektronerna i den molekylära föreningen, liksom rörelsen hos dessa under (eller strax före) en reaktion, en viktig roll.

Förstora tiden. I teoretiska överväganden har det visat sig att sådana elektronrörelser sker på tidsskalor som är betydligt snabbare än det mänskliga ögat kan se eller slowmotion-kameror kan fånga på bild. Elektroner rör sig ofta inom någon så kallade attosekunder, vilket motsvarar 0.00000000000000001 sekunder. För att kunna studera rörelser på dessa tidsskalor behövs verktyg som fungerar på lika korta tidsskalor. Likt en videokamera som använder en mekanisk slutare för att belysa en film med jämna mellanrum, kan ljuspulser genereras som inte är längre än några hundra attosekunder. Genereringen av sådana pulser uppnås genom att ljusvågor i olika färger kombineras. Denna kombination leder till att vågorna släcker ut varandra vid nästan alla tidpunkter, endast under ett ultrakort ögonblick (några hundra attosekunder) läggs vågorna samman till en enda stor våg som bildar en ljuspuls. De olika färgerna genereras som övertoner av en grundfärg, varför processen kallas generering av höga övertoner. Dessa attosekundpulser används sedan för att filma"elektroner. Det görs genom att belysa atomerna eller molekylerna med ljuspulserna, vilket utlöser en jonisation eller en reaktion. Strax därefter används en andra ljuspuls för att se var elektronen befinner sig och hur snabbt den rör sig. Denna process upprepas med varierande fördröjning mellan de två pulserna, vilket ger metoden dess tidupplösning.

Fokus för mitt arbete har dels varit tekniken som beskrivs ovan, vilken vi använde i åtskilliga experiment, både i atomer som neon och helium, och i molekyler som diamantoiden adamantan eller polycykliska aromatiska kolväten. Dessutom var även själva metoden för generering av höga övertoner en del av min forskning. Undersökningen och vidareutvecklingen av metoden har lett till många av mina publikationer och därmed framsteg inom området.

Populärwissenschaftliche Zusammenfassung

Das Ziel der folgenden Arbeit ist es, in Zeitskalen einzutauchen, in die man selten einen Einblick bekommt. Eine chemische Reaktion verändert unsere Umwelt. Ein Molekül zerfällt in seine Bestandteile. Ein Elektron löst sich aus einem Atom. Erforscht bis ins kleinste Detail und trotzdem fällt es uns häufig schwer, solche Prozesse zu kontrollieren oder sogar zu imitieren. Um diese Kontrolle zu gewinnen, müssen die Bewegungen kleinster Teilchen beobachtet und verstanden werden. In den nächsten Absätzen werde ich versuchen, dies in ein paar einfachen Sätzen zu erklären.

Atomos. Schon in der griechischen Philosophie wird die Frage gestellt, ob Materie aus einen Kontinuum besteht, welches beliebig häufig zerteilbar ist, oder ob es ein elementares Teilchen gibt, welches sich nicht spalten lässt. Im 5. Jahrhundert v. Chr. wird zum ersten Mal das Wort *átomos* (griechisch *unzerschneidbar*) erwähnt, formuliert von Leukipp und seinem Schüler Demokrit. Dass dieses Teilchen existiert und aus einem Kern und einer Hülle aufgebaut ist, wurde Anfang des 20. Jahrhunderts experimentell erwiesen und von Ernest Rutherford in seinem bekannten Atommodell beschrieben. Im gleichen Zuge wurde die angenommene Unteilbarkeit jedoch durch die Entdeckung von ionisierender Strahlung widerlegt.

Das Elektron in Bewegung. Das Auslösen eines Elektrons aus dem Atom durch Licht wird als Photoionisation bezeichnet, welche erstmalig quantitativ durch den von Einstein beschriebenen Photoeffekt erklärt wurde. Hierbei wird dem Atom Energie in Form eines Photons zugeführt, welche auf ein Elektron übertragen wird und es diesem erlaubt, die Bindungsenergie des Atomverbundes zu überwinden. Das Elektron wandelt jegliche überschüssige Energie in Geschwindigkeit um und entfernt sich so von dem Atom. Kurz nach Einsteins Erklärung des Photoeffekts wurde durch die Quantentheorie ergänzt, dass dieser Prozess nur in bestimmten Energieportionen stattfindet, was bedeutet, dass das frei gewordenen Elektron sich in ganz bestimmte Zustände begibt. Bis zum heutigen Tag hat die Forschung zu einem großen Teil verstanden, welche Teilchen und Felder vor und nach der Photoionisation eine Rolle spielen und wie sich Energien verhalten und umwandeln. Was ein ungelöstes Rätsel bleibt, ist die zeitliche Komponente dieses Prozesses. Wie lange dauert es, bis ein Elektron das Atom verlassen hat? Wovon hängt die Geschwindigkeit des Prozesses ab? Verlassen alle Elektronen das Atom mit der gleichen Geschwindigkeit?

Das Atom in Bewegung. Ähnliche Fragen können gestellt werden, wenn man die Wechselwirkung zwischen Atomen untereinander betrachtet. Binden sich mehrere Atome zu einem Verbund zusammen, spricht man von einem Molekül. In der

Chemie gehen viele Reaktionen mit dem Auflösen und Neuerschaffen von Bindungen zwischen den Atomen eines Moleküls einher. Häufig ist hierbei genau bekannt, welche Bestandteile am Anfang und am Ende einer Reaktion stehen. Spannend ist die Frage, wie genau und auf welchen Zeitskalen diese Reaktion abläuft. Warum bricht ein Molekül an einer Stelle auseinander, an einer anderen aber nicht? Wie schnell zerteilt sich ein Molekül und welches Bruchteil bekommt wieviel Energie? Auch hier spielt die Verteilung der Elektronen im Atomverbund, sowie die Bewegung dieser während (bzw. kurz vor) einer Reaktion, eine bedeutende Rolle.

Zeitlupe. In theoretischen Überlegungen konnte gezeigt werden, dass die beschriebenen Prozesse auf Zeitskalen stattfinden, welche deutlich schneller sind, als dass sie mit dem menschlichen Auge oder sogar Zeitlupenkameras aufgelöst werden könnten. Elektronen bewegen sich häufig innerhalb sogenannter Attosekunden, was 0,00000000000000001 Sekunden entspricht. Um Bewegungen auf diesen Zeitskalen auflösen zu können, benötigt man Messinstrumente, die ebenfalls in diesen Zeitskalen operieren. Ähnlich einer Videokamera, die mechanische Klappen benutzt, um in regelmäßigen Abständen einen Film zu beleuchten, können Lichtpulse erzeugt werden, die nicht länger als einige 100 Attosekunden kurz sind. Die Erzeugung dieser Pulse wird durch die Überlagerung verschiedener Lichtwellen mit unterschiedlichen Farben erreicht. Diese Überlagerung führt dazu, dass die Wellen sich zu fast allen Zeitpunkten auslöschen, nur in den genannten wenigen 100 Attosekunden addieren sich alle zu einer großen Welle auf. Die verschiedenen Farben werden hierbei als Obertöne einer Grundschwingung erzeugt, weshalb der Prozess als die Erzeugung von Höheren Harmonischen bezeichnet wird. Um nun diese Attosekundenpulse zum 'Filmen' von Elektronen nutzen zu können, werden die zu untersuchenden Atome oder Moleküle mit den Lichtpulsen beschossen und somit eine Ionisation oder Reaktion ausgelöst. Wenige Zeit später wird ein zweiter Lichtpuls benutzt, um zu schauen wo sich das Elektron befindet und wie schnell es sich bewegt. Dieser Prozess wird häufig wiederholt, wobei der zeitliche Abstand zwischen den zwei Pulsen variiert wird, um den zeitlichen Prozess aufzulösen.

Im Fokus meiner Arbeit steht zum einen die eben beschriebene Technik zur Erforschung von Atomen und Molekülen. Diese wurde während meiner Forschungszeit in verschiedenen Experimenten angewendet, sowohl in Atomen wie Neon und Helium, als auch in Molekülen wie dem Diamantoid Adamantan oder Polycyclischen aromatischen Kohlenwasserstoffen. Zum anderen war die Methode der Erzeugung Höherer Harmonischer Teil meiner Forschung. Die Untersuchung und Weiterentwicklung dieser hat zu vielen meiner Veröffentlichungen geführt.

List of publications

This thesis is based on the following publications, referred to by their Roman numerals:

I **Complete characterization of multi-channel single photon ionization**

J. Peschel, D. Busto, M. Plach, M. Bertolino, M. Hoflund, S. Maclot, H. Wikmark, F. Zapata, J. M. Dahlström, A. L'Huillier and P. Eng-Johnsson
Submitted, arXiv:2109.01581

II **Focusing properties of high-order harmonics**

M. Hoflund, **J. Peschel**, M. Plach, H. Dacasa, K. Veyrinas, E. Constant, P. Schmorenburg, C. Guo, C. Arnold, A. L'Huillier, P. Eng-Johnsson
Ultrafast Science 2021, 9797453 (2021)

III **Spatiotemporal coupling of attosecond pulses**

H. Wikmark, C. Guo, J. Vogelsang, P. W. Smorenburg, H. Coudert-Alteirac, J. Lahl, **J. Peschel**, P. Rudawski, H. Dacasa, S. Carlström, S. Maclot, M. B. Gaarde, P. Johnsson, C. L. Arnold, and A. L'Huillier
Proc. Natl. Acad. Sci. 116, 4779–4787 (2019)

IV **Dissociation dynamics of the diamondoid adamantane upon photoionization by XUV femtosecond pulses**
S. Maclot, J. Lahl, **J. Peschel**, H. Wikmark, P. Rudawski, F. Brunner, H. Coudert-Alteirac, S. Indrajith, B. A. Huber, S. Díaz-Tendero, N. F.Aguirre, P. Rousseau, and P. Johnsson
Sci. Reports 10, 2884 (2020)

V **A 10-gigawatt attosecond source for non-linear XUV optics and XUV-pump-XUV-probe studies**
I. Makos, I. Orfanos, A. Nayak, **J. Peschel**, B. Major, I. Liontos, E. Skantzakis, N. Papadakis, C. Kalpouzos, M. Dumergue, S. Kühn, K. Varju, P. Johnsson, A. L'Huillier, P. Tzallas, and D. Charalambidis
Sci. Reports 10, 3759 (2020)

VI **Time-Resolved Relaxation and Fragmentation of Polycyclic Aromatic Hydrocarbons Investigated in the Ultrafast XUV-IR Regime**
J. W. L. Lee, D. S. Tikhonov, P. Chopra, S. Maclot, A. L. Steber, S. Gruet, F. Allum, R. Boll, X. Cheng, S. Düsterer, B. Erk, D. Garg, L. He, D. Heathcote, M. Johny, M. M. Kazemi, H. Köckert, J. Lahl, A. K. Lemmens, D. Loru, R. Mason, E. Müller, T. Mullins, P. Olshin, C. Passow, **J. Peschel**, D. Ramm, D. Rompotis, N. Schirmel, S. Trippel, J. Wiese, F. Ziaee, S. Bari, M. Burt, J. Küpper, A. M. Rijs, D. Rolles, S. Techert, P. Eng-Johnsson, M. Brouard, C. Vallance, B. Manschwetus, and M. Schnell
Accepted in Nature Communications

VII **Formative period in the X-ray-induced photodissociation of organic molecules**
E. Kukk, H. Fukuzawa, J. Niskanen, K. Nagaya, K. Kooser, D. You, **J. Peschel**, S. Maclot, A. Niozu, S. Saito, Y. Luo, E. Pelimanni, E. Itälä, J. D. Bozek, T. Takanashi, M. Berholts, P. Johnsson, and K. Ueda
Phys. Rev. Res. 3, 013221 (2021)

VIII **Single-shot extreme-ultraviolet wavefront measurements of high-order harmonics**
H. Dacasa, H. Coudert-Alteirac, C. Guo, E. Kueny, F. Campi, J. Lahl, J. Peschel, H. Wikmark, B. Major, E. Malm, D. Alj, K. Varjú, C. L. Arnold,G. Dovillaire, P. Johnsson, A. L'Huillier, S. Maclot, P. Rudawski, and P. Zeitoun
Opt. Express 27, 2656–2670 (2019)

IX **Micro-focusing of broadband high-order harmonic radiation by a double toroidal mirror**
H. Coudert-Alteirac, H. Dacasa, F. Campi, E. Kueny, B. Farkas, F. Brunner, S. Maclot, B. Manschwetus, H. Wikmark, J. Lahl, L. Rading, **J. Peschel**, B. Major, K. Varjú, G. Dovillaire, P. Zeitoun, P. Johnsson, A. L'Huillier, and P. Rudawski
Appl. Sci. 7, 1159 (2017)

X **A versatile velocity map ion-electron covariance imaging spectrometer for high-intensity XUV experiments**
L. Rading, J. Lahl, S. Maclot, F. Campi, H. Coudert-Alteirac, B. Oostenrijk, **J. Peschel**, H. Wikmark, P. Rudawski, M. Gisselbrecht, and P. Johnsson
Appl. Sci. 8(6), 998, (2018)

Related publications by the author, which are not included in this thesis:

Time-resolved site-selective imaging of predissociation and charge transfer dynamics: the CH3I b-band
R. Forbes, F. Allum, S. Bari, R. Boll, K. Borne, M. Brouard, P. H.Bucksbaum, N. Ekanayake, B. Erk, A. J. Howard, P. Johnsson, J. W. L. Lee, B. Manschwetus, R. Mason, C. Passow, **J. Peschel**, D. E. Rivas, A. Rörig, A. Rouzée, C. Vallance, F. Ziaee, D. Rolles, and M. Burt
J. Phys. B: At. Mol. Opt. Phys. 53, 224001 (2020)

Time-resolved photoelectron imaging of complex resonances in molecular Nitrogen
M. Fushitani, S. T. Pratt, D. You, S. Saito, Y. Luo, K. Ueda, H. Fujise, A. Hishikawa, H. Ibrahim, F. Légaré, P. Johnsson, **J. Peschel**, E. R. Simpson, A. Olofsson, J. Mauritsson, P. A. Carpeggiani, P. K. Maroju, M. Moioli, D. Ertel, R. Shah, G. Sansone, T. Csizmadia, M. Dumergue, N. G. Harshitha, S. Kühn, C. Callegari, O. Plekan, M. Di Fraia, M. Danailov, A. Demidovich, L. Giannessi, L. Raimondi, M. Zangrando, G. De Ninno, P. R. Ribič and K. C. Prince
J. Chem. Phys. 154, 144305 (2021)

Singleshot polychromatic coherent diffractive imaging with a high-order harmonic source
E. Malm, H. Wikmark, B. Pfau, P. Villanueva-Perez, P. Rudawski, **J. Peschel**, S. Maclot, M. Schneider, S. Eisebitt, A. Mikkelsen, A. L'Huillier, and P. Johnsson
Opt. Express 28, 394–404 (2020)

Contents

Thesis

Chapter 1

Introduction

The interaction between light and matter is one of the fundamental processes behind chemical and biological transformations. Studying the basic principles behind such interactions allows us to understand and eventually control them. One of these basic interactions is *photoionization*, where the energy of a photon is transferred to an atom or a molecule allowing one or multiple electrons to be released. A common way to investigate photoionization is the detection of the outgoing electron. While making use of its charge, we are able to map out the kinetic energy of such an electron, a technique known as photoelectron spectroscopy. This allows us to draw conclusions on the internal properties of the atom or molecule, as well as the ionization process itself. Photoionization leaves the atom/molecule in an ionic state. For molecules this often leads to further dynamics ultimately breaking the chemical bonds between the atoms, which is known as *photodissociation*. In photodissociation, it is often the ion that is detected, or more precisely the ionized fragments created through the dissociating process.

An important aspect, creating immense experimental challenges, are the time scales on which such nuclear and electronic motion occur. Purely electronic motion take place on time scales in the attosecond regime (1 as = 10^{-18} s), as indicated by the $\approx$150 as orbital period of an electron bound in atomic hydrogen approximated within Bohr's model. In molecules, photoionization leads to a rearrangement of the electrons inducing a drastic change of the forces acting on the atoms. The natural time scales for the resulting motion and the eventual breakup of bonds is in the femtosecond domain (1 fs = 10^{-15} s). Generally, time-resolved studies are facilitated by correspondingly short light pulses, where one so-called *pump* pulse is used for the photo-induced initiation of the process of interest and a second *probe* pulse is utilized to characterize the state of the system after a well-defined delay.

The temporal resolution thus depends on the duration of the two pulses and the precision with which the delay can be defined. Within the last few decades, the invention of femtosecond laser pulses has led to the emergence of time-resolved spectroscopy in the femtosecond regime, better known as *femtochemistry* [1], allowing the temporally resolved observation of e.g. photodissociation. However, the pre-dissociative migration of electrons in molecules occurs too fast to be detected by femtosecond lasers its study thus remains a challenge.

Only recently, two types of light sources have provided unprecedented insights and a promising outlook towards time-resolved experiments down to the attosecond time-scale: high-order harmonic generation (HHG) and free-electron lasers (FELs). Both techniques generate radiation in the extreme ultraviolet (XUV) up to the X-ray regime. During HHG, discovered in the late 80's [2, 3], a train of attosecond pulses is generated which quickly opened up the field of attosecond science [4, 5, 6]. Up until now, experiments unraveling electron dynamics on attosecond time scales in atomic [7, 8, 9, 10, 11] and molecular [12, 13, 14] systems as well as in solid-state physics [15, 16, 17] have been performed. Whereas most of these experiments rely on a second infrared photon to serve as a probe, the nonlinear interaction with two XUV photons would provide a direct way to trace electron motion, while making use of the attosecond resolution. However, the low conversion efficiency intrinsic to the HHG, typically on the order of 10^{-5}, makes it difficult to generate pulses with pulse energies high enough to enable nonlinear interactions. Recent efforts to generate intense attosecond pulses in the µJ regime [18, 19, 20, 21], have nevertheless paved the way towards XUV-pump-XUV-probe experiments using HHG.

FELs, on the other hand, overcome this intrinsic limit of HHG and provide pulses with much higher pulse energies. With the first realization of FEL pulses in the XUV regime [22], high intensity experiments in this wavelength range were realized. Multiphoton ionization at high intensities and short wavelengths is of significant interest as emitted electrons experience a much lower ponderomotive shift compared with multiphoton ionization induced by infrared laser-based sources. This has led to numerous experiments on multiphoton nonlinear interactions in the XUV and X-ray regime [23, 24, 25, 26]. The limit to all these studies is however the temporal resolution, as FELs up until not long ago only provided pulses down to tens of femtoseconds. Only recently were the first results presented enabling temporal resolution in the attosecond regime [27, 28].

The aim of the present work was the application of intense XUV pulses in order to study dynamical processes in atoms and molecules. Ultrafast effects during photoionization and photodissociation have been investigated using both HHG based sources and FELs.

At the Intense XUV Beamline (IXB) at the Lund Laser Centre, high-order harmonics are generated with pulse energies in the µJ regime. For the duration of this thesis, the beamline was still under development and was rebuilt several times. During that process, a number of studies involving interesting physics were necessary for the generation and application of intense high-order harmonics. Especially, spatial and temporal effects, intrinsic to the process of HHG, led to a series of metrological studies and ultimately contributed to extending existing models for HHG and improving our experiments. The resulting publications are introduced in chapter 2. First, the generation of ultrashort laser pulses is discussed followed by an introduction to the fundamentals of HHG. Further, the different parts of the IXB are described, including a summary of paper X presenting the design and commissioning of the double-sided velocity map imaging spectrometer (DVMIS) as well as of paper IX describing the broadband micro-focusing system. The XUV wavefront and its dependence on the generation conditions is discussed in the following sections presenting the findings of paper VIII. Connected to these results, the influence of the dipole phase introduced during HHG and the resulting chromatic aberration between different harmonics are put forward, summarizing the studies demonstrated in papers II and III. Finally, the experimental tools for time-resolved studies at the IXB, i.e., the IR-XUV interferometer and the split-and-delay unit, are detailed. Different techniques to characterize the temporal structure of the XUV pulses are expounded along with experimental results. In addition to the work performed at the IXB, selected results from a study visit to the FORTH institute in Heraklion, Greece, are described, introducing paper V.

Chapter 3 reports on results on the photoionization of neon, introducing paper I. The experiments were conducted at the IXB using the two-color interferometric technique known as the *Reconstruction of Attosecond Beating by Interference of Two color Transitions* (RABBIT) [29]. While making use of the angular resolution of the DVMIS, we are able to disentangle the different angular momentum channels involved in the ionization process and thus completely characterize single-photon ionization from the $2p^6$-ground state of neon.

Finally, chapter 4 focuses on the investigation of photodissociation of organic molecules. Results of experiments performed both at the IXB as well as with the FELs FLASH at DESY in Hamburg, Germany, and SACLA at the Spring8 facility in Sayo, Japan, are accounted for. The dissociation dynamics induced by the double ionization of adamantane, described in paper IV, are introduced and complemented by preliminary time-resolved results. In the second part of the chapter, two similar studies, investigating the dissociation of different carbon-based molecules using FELs, are summarized based on papers VI and VII.

Chapter 2

High-order Harmonic and Attosecond Pulse Generation

In the late 1980s the discovery of an interesting phenomenon led to a promising technique, which was ultimately able to generate pulses on the attosecond time scale. The strong-field ionization of noble gases using ultrashort infrared laser pulses induces a frequency up-conversion producing a broad spectrum in the extreme ultraviolet (XUV) regime [2, 3]. Interestingly, the spectrum consists of a discrete comb of harmonic order of the fundamental infrared field, hence the name high-order harmonic generation (HHG). Shortly after, the effect was explained by the so-called *three-step model*, partly based on classical mechanics [30] as well as from a quantum mechanical point of view in the strong-field approximation (SFA) [31]. It took almost a decade to experimentally show that the process of HHG indeed generates pulses in the attosecond regime [29].

This chapter gives a brief overview of ultrashort laser pulses, including a description of the laser system used in Lund, followed by an introduction to the key principles behind HHG. The experimental setup around the IXB in Lund is shown in detail, and it should be mentioned that the IXB has been modified several times since the start of this thesis work. The beam transport system between the laser room and the HHG chamber was rebuilt twice, the second time to ensure the propagation of the ultrashort, intense pulses in vacuum. A new XUV spectrometer was constructed and relocated relative to the previous, commercial one. An XUV split-and-delay unit and an infrared-XUV interferometer have been implemented and commissioned. This dissertation describes the present setup, nevertheless the steps leading up to it were an essential part of the thesis work.

Finally, experimental and theoretical results regarding the metrology of the generated XUV pulses are presented along with an in-depth study of the chromatic aberration inherent in HHG, summarizing the results in papers II, III, X and XI. Finally, the temporal structure of the attosecond pulses is examined.

2.1 Ultrashort Laser Pulses

Light can be described either as an electromagnetic wave with angular frequency ω, or as a mass-less particle with energy $\hbar\omega$, called a photon. Whether light appears as a wave or a photon depends on the way it interacts with matter. If light is absorbed, the photon picture is intuitive, due to the quantum nature of the absorbing medium, and will play an important role in later chapters. However, when light is diffracted after passing through a slit, the wave picture is more straight forward, and will help us to understand the generation of ultrashort light pulses. To grasp spatial and temporal interactions in the wave picture, light can be described as a superposition of monochromatic waves, where each wave is described by its frequency, amplitude and phase.

2.1.1 Superposition of Waves

Where a single wave, oscillating with a single frequency, extends infinitely with a constant amplitude in space and time, the superposition of two waves with different frequencies leads to a beating effect of the amplitude in time. When the spectrum is extended to a comb of frequency peaks, the amplitude of the resulting wave can show recurring pulses in time, whose durations depend on the range of its frequency components. The condition for the forming of such pulses is a single instant in time at which the temporal phases of all components are equal.

In order to study this effect in more detail, a simple mathematical expression for waves with frequency ω, phase ϕ and amplitude $\mathcal{E}(t)$ is introduced in the temporal domain:

$$E(t) = \mathcal{E}(t)\mathrm{e}^{\mathrm{i}(\omega t - \phi(t))}, \tag{2.1}$$

which is a solution of a homogeneous wave equation derived from Maxwell's equations. This expression can be further written in the spectral domain via its Fourier transform:

$$\tilde{E}(\omega) = \mathcal{F}\{E(t)\} = \int \mathrm{d}t\, E(t)\mathrm{e}^{-\mathrm{i}\omega t} = \tilde{\mathcal{E}}(\omega)\mathrm{e}^{-\mathrm{i}\Phi(\omega)}, \tag{2.2}$$

where $\tilde{\mathcal{E}}(\omega)$ and $\Phi(\omega)$ are respectively the spectral amplitude and phase. The former describes the composition of frequencies of the wave. Due to this Fourier transform relation, the duration of a light pulse, more specifically the width of its envelope, has an intrinsic limit given by its bandwidth. The broader the range of frequencies is, the shorter the pulse can be in time, as the Fourier transform of the spectral amplitude corresponds to the envelope of the wave in the temporal domain.

However, for a short duration in time, a broad bandwidth is not sufficient in itself. The spectral phase has to be considered to obtain spectral interference for all frequencies at a single instant in time, as mentioned earlier. The spectral phase can be approximated by its Taylor expansion around a central frequency ω_0:

$$\Phi(\omega) = \Phi_0 + \Phi_0'(\omega - \omega_0) + \frac{1}{2}\Phi_0''(\omega - \omega_0)^2 + \dots . \tag{2.3}$$

Here, the first term describes the relation between the carrier and the envelope of the wave, the so-called carrier-envelope phase (CEP). The second term is the first derivative of the spectral phase and describes the temporal delay of the pulse structure. This derivative is called the group delay and does not have an effect on the overall structure of the pulse, due to the lack of a defined reference point in time. In the third term, Φ_0'' corresponds to the second derivative and is referred to as the group delay dispersion (GDD). This term, as well as the higher-order terms, give the pulse its temporal structure. If they are zero, the pulse is as short as it can be and referred to as transform limited. However, given a second-order GDD, the spectral phase carries a quadratic component and is then referred to as linearly chirped.

2.1.2 Ultrashort High-Intensity Lasers

In order to generate short pulses down to femto- or even attoseconds, a sufficiently broad spectrum needs to be generated. When using light-amplification by stimulated emission of radiation (LASER) in solid crystals, the broad landscape of energy bands in the crystal offers radiative transitions with an intrinsic broad bandwidth. In a Ti^{3+}-doped sapphire crystal (short: Ti:Sa) lasing can be achieved in the near-infrared range from 650 to 1100 nm. If the emitted waves are stabilized

in various cavity modes in an oscillator, the spectral phases of different modes can be locked to each other in order to achieve short pulses [32].

In order to further amplify the pulses, the light can be sent through externally pumped Ti:Sa crystals. However, with each amplification the intensity increases and thus to prevent damage, the frequency components are sent through the crystal individually by stretching the pulse in time. Typically, a linear chirp is introduced before the amplification in a stretcher and compensated for later in the process in a compressor. This technique is called Chirped-Pulse Amplification (CPA) and its inventors Donna Strickland and Gérard Mourou were awarded the Nobel prize in 2018 [33].

2.1.3 The Terawatt Laser System

The laser system used at the Intense XUV Beamline in Lund generates near-IR pulses with energies up to 1 J, a pulse duration of 40 fs and thus peak powers of ~25 TW. It has been the main driver for strong-field physics at the Lund Laser Centre since 1992 [34, 35] and is, in addition to for our experiments, used for the acceleration of protons [36] and electrons [37], which is not further discussed in this thesis.

The system is based on a Kerr-lens mode-locked Ti:Sa oscillator pumped by a frequency-doubled Neodymium-doped Yttrium-Aluminum Garnet (Nd:YAG) laser. The output has a bandwidth of 50 nm centered at 800 nm. The initial repetition rate of 80 MHz is reduced to 10 Hz by a pulse picker and the temporal contrast is increased in a multipass preamplifier. After stretching the pulses to about 300 ps in an Öffner triplet-type stretcher [38], the beam is subsequently amplified to ~400 mJ by a regenerative as well as a multipass amplifier, each pumped with 1 J pulses from Nd:YAG lasers. Hereby, the bandwidth reduces to ~37 nm. A spatial filter cleans the beam profile by absorbing higher spatial frequencies in the Fourier plane of the focused beam.

At this point, the beam is split using a 50/50 beam splitter, where one part is amplified further and used for the above-mentioned strong-field experiments. The other part is guided to the Intense XUV Beamline. Due to the high pulse energy, the beam creates nonlinear interactions in air while propagating, such as self-focusing [39]. In addition, after being compressed, the intensity is high enough to cause damage on optical surfaces. Hence, the beam expands in a telescope to ~38 mm at $1/e^2$ to reduce the intensity. Finally, a grating compressor re-compresses the pulses to ~40 fs with a pulse energy of 100 mJ.

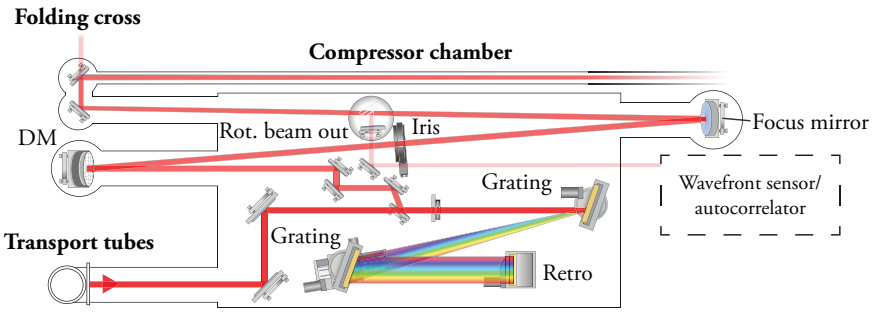

Figure 2.1: Design of the new vacuum chamber housing the in-vacuum compressor, DM, iris and the focusing mirror. The red line represents the infrared beam path, which is compressed during a round trip between two gratings (colored beams). After compression the beam is reflected on a deformable mirror and a 8.7 m focusing mirror. The entire setup is set under vacuum, pumped by a central fore-vacuum system and turbo molecular pumps.

2.1.4 In-vacuum Compressor

In a previous design of the Intense XUV Beamline, the beam had to propagate in air to reach the setup, which was placed in a neighbouring room. In addition, the grating compressor was built in air, which added up to a total propagation distance of about 15 m in atmospheric pressure. Thus, the beam suffered from distortions in the beam profile due to nonlinear interactions as well as pointing instabilities and alignment drifts due to air circulations between the rooms. As a consequence, we designed and installed a new vacuum chamber housing the compressor and other beam-shaping optics. After the telescope, the beam enters a vacuum transport system guiding it into the experimental room, where it reaches the 1500x860 mm² vacuum chamber housing the compressor setup. The compressor consists of two 120x120 mm² sinusoidal gratings with 1000 lines/mm. The beam arrives on the upper part of the grating and the first order is reflected at an angle of 6.2° towards the second grating. The dispersed beam propagates and is folded downwards on a retro reflector, introducing the required path difference between frequency components in order to compress the pulse. Finally, the different frequency components are recollimated between the lower parts of the two gratings, which are placed on rotation stages in order to adjust the linearity of the GDD correctly and compensate for pulse-front-tilts. The second grating is additionally mounted on a linear translation stage in order to vary the GDD and thus adjust the resulting pulse duration.

After exiting the compressor, the beam is guided onto a deformable mirror (DM), which, in conjunction with an infrared wavefront sensor (WF), is used to compensate for wavefront aberration and vary the focusing conditions. The beam further

propagates through a motorized iris and is focused using an 8.7 m spherical mirror. Due to space restrictions in the lab, the beam is folded ~4 m after the focusing mirror with two dielectric mirrors. A mirror on a rotation stage can be used to guide the beam through a window outside the vacuum chamber for beam diagnostics, where the wavefront sensor and an autocorrelator for pulse duration detection are placed.

In the next step, the focused beam interacts with a noble gas in order to generate high-order harmonics. The following chapters describe this process in detail and derive the framework for the experimental results.

2.2 The Single-Atom Response

High-order harmonic generation (HHG) describes a frequency up-conversion typically from the near-infrared to the XUV [3]. There are two advantages of this technique: the XUV range makes it possible to ionize many atomic and molecular systems with a single photon and the comb of generated harmonics can be synchronized such that pulses on the attosecond time scale are produced. HHG appears in an intensity regime, where the driving field is high enough to tunnel-ionize electrons from the target gas, but below the threshold for over-the-barrier ionization [40].

2.2.1 The Three-Step Model

The process of HHG was first described by Corkum [41] and Schafer *et al.* [42] in three steps using a semi-classical formulation providing qualitative insights into the relevant physics involved and even showing quantitative agreement with certain experimental aspects.

The first step details the birth of an electron from a bound to a continuum state. The near infrared laser pulse is focused, such that its electric field becomes of comparable strength to the Coulomb field binding the valence electrons to the nuclei. The superposition of the two fields creates a distorted electron potential $V(x)$, as indicated in figure 2.2. At a certain time t_i, there is a probability that the electron tunnels through the created barrier into the continuum with initially zero velocity. In the second step, the electron is accelerated by the electric field of the infrared pulse $E(t) = \mathcal{E}\cos(\omega_0 t)$. When the effect of the Coulomb potential is neglected and the electron is considered to be a point charge the following equation of motion can be written using Newton's second law:

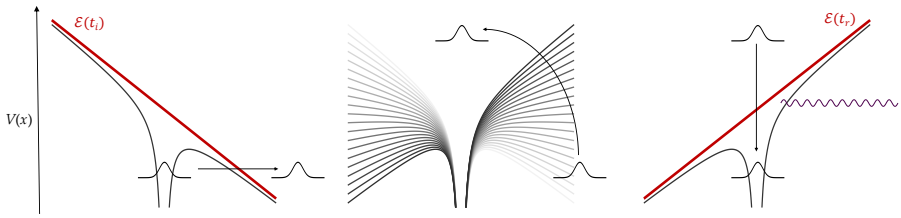

Figure 2.2: Schematic of the three step model describing the process of HHG. In the first step (left) the infrared driving field distorts the electron potential such that tunnel ionization takes place. In the second step (middle) the released electron is accelerated by the electric field of the driving pulse. The final step (right) describes the recombination, which, together with the gained energy during propagation, leads to the emission of an XUV photon.

$$\ddot{x}(t) = -\frac{e}{m_e}\,\mathcal{E}\cos(\omega_0 t), \tag{2.4}$$

where the initial conditions is chosen to be $\dot{x}(t_i) = x(t_i) = 0$. Note, that the one- dimensional equation is shown to simplify the problem, which however is applicable to the three-dimensional space in the same way. The propagation of the electron and its trajectories in the continuum can be calculated by integrating the equation of motion twice:

$$\dot{x}(t) = -\frac{e\mathcal{E}}{m_e\omega_0}\big[\sin(\omega_0 t) - \sin(\omega_0 t_i)\big] \tag{2.5}$$

$$x(t) = \frac{e\mathcal{E}}{m_e\omega_0^2}\big[\cos(\omega_0 t) - \cos(\omega_0 t_i) + \omega_0\,\sin(\omega_0 t_i)(t - t_i)\big]. \tag{2.6}$$

Equation 2.6 describes the one-dimensional trajectories of the electron, shown for different tunneling times in figure 2.3. For certain tunneling times t_i, the electron trajectory leads away from the parent ion (dotted lines). However, for $\frac{\pi}{2\omega_0} \leq t_i \leq \frac{\pi}{\omega_0}$, the trajectories reach $x = 0$ again, which means that the electron re-collides with its parent ion. Here, the re-collision time t_r depends on the tunneling time. The color-coding in figure 2.3 represents the return energy of the propagating electrons, which peaks for a tunneling time $t_i \approx \frac{2\pi}{3\omega_0}$. The trajectories can be grouped into two different families: all re-colliding pathways with tunneling times before the peak return energy are driven further away from the core and are thus referred to as *long trajectories*, whereas the ones after the peak return energy are called *short trajectories*. It is important to mention that for this consideration, linear polarized light is essential, since an additional perpendicular component introduced by an elliptically polarized field, would drive the electrons further away and render a re-collision unlikely.

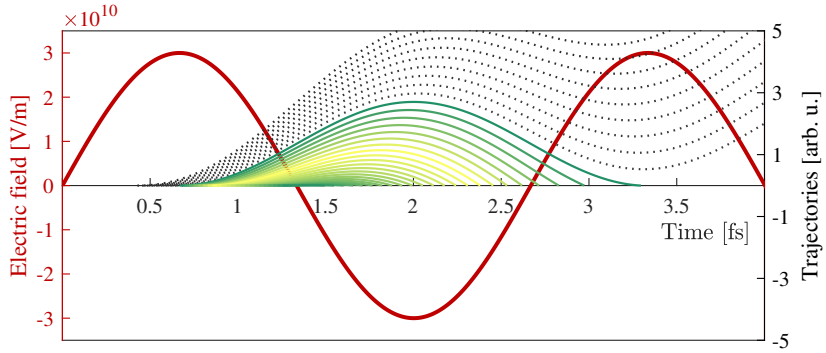

Figure 2.3: Classically calculated electron trajectories for different tunnelling times. The trajectories returning to the parent ion are color-coded according to their return energy, where green corresponds to the lowest and yellow to the highest energy. The grey dotted lines are electrons propagating further in the continuum without returning to the parent ion. The driving laser field (red curve) with a wavelength of 800 nm and an intensity of 10^{14} W/cm^2 is plotted as a reference.

Finally, the third step describes the recombination of the electron with the parent ion to its ground state. The excess energy is released in form of a photon which, due to the acceleration of the electron, has a higher photon energy than that of the driving infrared field. At this point it is useful to examine the energy balance of the process: the energy of the emitted photon is composed of the kinetic energy, acquired by the electron during propagation in the continuum, and the ionization potential of the atom: $E_{\text{ph}} = E_{\text{kin}}(t_i) + I_{\text{p}}$. For every pair (t_i, t_r), the kinetic energy is calculated according to:

$$E_{\text{kin}}(t_i) = \frac{m_e}{2}\dot{x}\big[t_{\text{r}}(t_i)\big]^2 = \frac{e^2\mathcal{E}^2}{4m_e\omega_0^2}\big[\sin(\omega_0 t) - \sin(\omega_0 t_i)\big]^2 \tag{2.7}$$

The recollision energy peaks at $t_i = \frac{2\pi}{3\omega_0}$, resulting in a maximum photon energy of:

$$E_c = I_{\text{p}} + 3.17\frac{e^2\mathcal{E}^2}{4m_e\omega_0^2} = I_{\text{p}} + 3.17U_{\text{p}} \tag{2.8}$$

This so-called 'cutoff law', defined using the ponderomotive potential $U_{\text{p}} = e^2\mathcal{E}^2/4m_e\omega_0^2$, was numerically found by Krause *et al.* [43]. In conclusion, when using a near infrared driving laser, the photon energy ranges through the visible into the extreme ultraviolet regime. Interestingly, the cutoff increases when the frequency of the driving field decreases, as seen in equation 2.8. As a result, the generation of harmonics up to the X-ray regime requires driving the laser with frequencies down to the mid-infrared range [44, 45].

Since this three-step process is a result of the interaction with the field of the infrared pulse, it is repeated every half-cycle. The field however alternates its sign with the same periodicity $T_0/2$, which leads to a phase shift of π for every other field that is generated. Through interference, the resulting superposition of emitted waves suppresses all spectral components except those corresponding to odd harmonics of the fundamental frequency ω_0.

2.2.2 The Dipole Phase

An important consequence of the three-step model is that the varying return time of different trajectories (see figure 2.3) means that different spectral components are generated at different times. This time-dependent frequency leads to a phase difference between harmonic orders, often referred to as the *attochirp*, affecting the temporal shape of the emitted burst of light and setting a limit for the achievable pulse duration [46]. This order-dependent intrinsic phase acquired during HHG is called the dipole phase. The intensity-dependent influence of the dipole phase on the spatial properties of the emitted light is further discussed in papers II and III and in section 2.5. In the following, a simple model to describe the dipole phase based on the three-step-model is derived. This model was developed during the scope of this work and is presented in paper III.

Figure 2.4 shows the return frequency Ω plotted as a function of the re-collision time for two different intensities. The peak of the curve corresponds to the return time of the cutoff harmonics emitted at time t_c. The up- and down-slopes of the curves can be approximated by straight lines which define four characteristic times: the threshold time $t_p^{s,l}$ for short and long trajectories, and the cutoff time $t_c^{s,l}$ for short and long trajectories, both indicated in figure 2.4. The respective frequencies at the threshold and cutoff are defined as Ω_p and Ω_c. The frequency-dependent return time $t_r^{s,l}(\Omega)$ for short and long trajectories can hence be approximated as:

$$t_r^{s,l}(\Omega) = t_p^{s,l} + \frac{t_c^{s,l} - t_p^{s,l}}{\Omega_c - \Omega_p}(\Omega - \Omega_p) \tag{2.9}$$

This time can be interpreted as the group delay of the emitted field, which means its integral is the spectral phase:

$$\Phi^{s,l}(\Omega) = \Phi^{s,l}(\Omega_p) + t_p^{s,l}(\Omega - \Omega_p) + \frac{t_c^{s,l} - t_p^{s,l}}{\Omega_c - \Omega_p}\frac{(\Omega - \Omega_p)^2}{2} \tag{2.10}$$

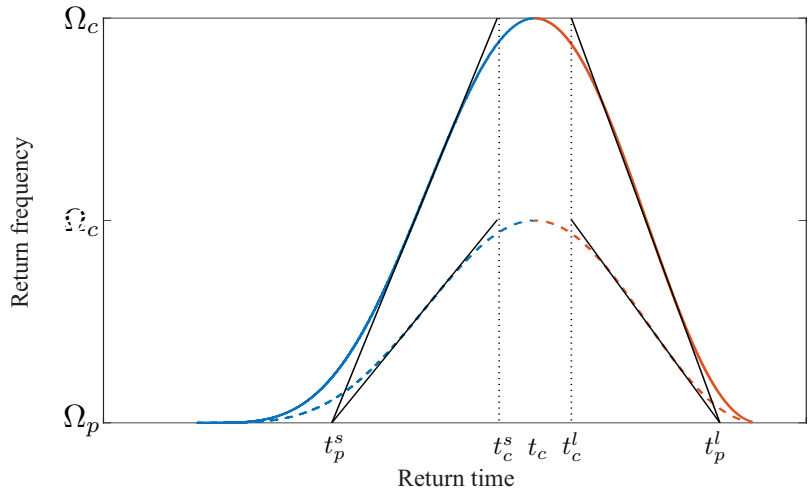

Figure 2.4: The return frequency plotted as a function of the return time for the short (blue) and long (orange) trajectories. The dotted and solid lines corresponds to two different intensities. The black lines represent the linear approximation of the model.

The tunneling frequency Ω_p, corresponding to the lowest return frequency, is equal to the ionization potential $I_p/\hbar$ and thus $\Omega_c - \Omega_p = 3.17U_p/\hbar$. The spectral phase can be rewritten as:

$$\Phi^{s,l}(\Omega) = \Phi^{s,l}(\Omega_p) + t_p^{s,l}(\Omega - \Omega_p) + \frac{\gamma^{s,l}}{I}\frac{(\Omega - \Omega_p)^2}{2}, \tag{2.11}$$

where

$$\gamma^{s,l} = \frac{(t_c^{s,l} - t_p^{s,l})\pi c^2 m_e}{3.17\alpha_{FS}\lambda^2} \tag{2.12}$$

The ponderomotive potential is defined in an alternative definition $U_p = \alpha_{FS}\hbar I\lambda^2/2\pi c^2 m_e$, where α_{FS} is the fine structure constant and λ the fundamental wavelength. The first term $\Phi^{s,l}(\Omega_p)$ can be derived using a fully quantum mechanical approach to HHG, and this is presented in the following chapter.

2.2.3 The Strong-Field Approximation

Shortly after the semi-classical description of HHG using the three-step model, a quantum mechanical approach was presented by Lewenstein *et al.* [31], known as

the strong-field approximation (SFA). In order to find an analytical solution, the following assumptions, reducing the number of possible interactions, are made:

1. Only the ground state interacts with the electric field, which is valid with a sufficiently low driving frequency.
2. The depletion of the ground state can be neglected, due to a laser intensity low enough to not fully ionize the parent atom.
3. The effect of the Coulomb potential on the continuum states is neglected and the electron is treated as a free particle, i.e., the driving field is sufficiently strong compared to the Coulomb potential.

These assumptions lead to an ansatz for the wavefunction $|\Psi\rangle$ as a superposition of a bound state, described by a hydrogen-like wavefunction in the single-active electron approximation, and a set of continuum states described as complex plane waves. The analytical expressions of such wavefunctions can be derived by inserting the ansatz into the Schrödinger equation and solving the resulting differential equation. In order to access the emitted field, the time-dependent electric dipole moment $\mathbf{d}(t) = \langle\Psi(\mathbf{r},t)|\,\mathbf{x}\,|\Psi(\mathbf{r},t)\rangle$ is calculated, while neglecting all continuum-continuum transitions, resulting in:

$$\mathbf{d}(t) = \mathrm{i}\int_{-\infty}^{t} \mathrm{d}t_i \int \mathrm{d}^3\mathbf{p}\;\; \mathbf{d}^*_{\mathbf{p}-\mathbf{A}(t_r)}\;\; \mathrm{e}^{-\mathrm{i}S(\mathbf{p},t_r,t_i)}\;\; \mathbf{E}(t_i)\cdot\;\mathbf{d}_{\mathbf{p}-\mathbf{A}(t_i)} + c.c. \quad (2.13)$$

Here, the three steps of HHG can easily be identified as the following probability amplitudes: $\mathbf{E}(t_i)\;\mathbf{d}_{\mathbf{p}-\mathbf{A}(t_i)} = \mathbf{E}(t_i)\,\langle\mathbf{v}|\,\mathbf{x}\,|0\rangle$ describes the transition of the electron from the ground state $|0\rangle$ to the continuum $|\mathbf{v}\rangle$ at tunneling time t_i. In the continuum, the electron acquires a phase given by $\mathrm{e}^{-\mathrm{i}S(\mathbf{p},t_r,t_i)}$ relative to the ground state, corresponding to the propagation described in the three-step model. The canonical momentum is here defined as $\mathbf{p} = \mathbf{v}+\mathbf{A}(t)$, where $\mathbf{A}(t)$ is the vector potential of the electric field. The so-called quasi classical action is given by:

$$S(\mathbf{p},t_r,t_i) = \int_{t_i}^{t_r} \mathrm{d}t\left(\frac{(\mathbf{p}-\mathbf{A}(t))^2}{2} + I_\mathrm{p}\right). \quad (2.14)$$

The electron recombines with the parent ion at time t_r with a probability amplitude of $\mathbf{d}^*_{\mathbf{p}-\mathbf{A}(t)}$, which concludes the three steps. The solution for the five-dimensional integral in equation 2.13 is found using a saddle-point approximation. Each electron quantum path can be associated with a semi-classical action,

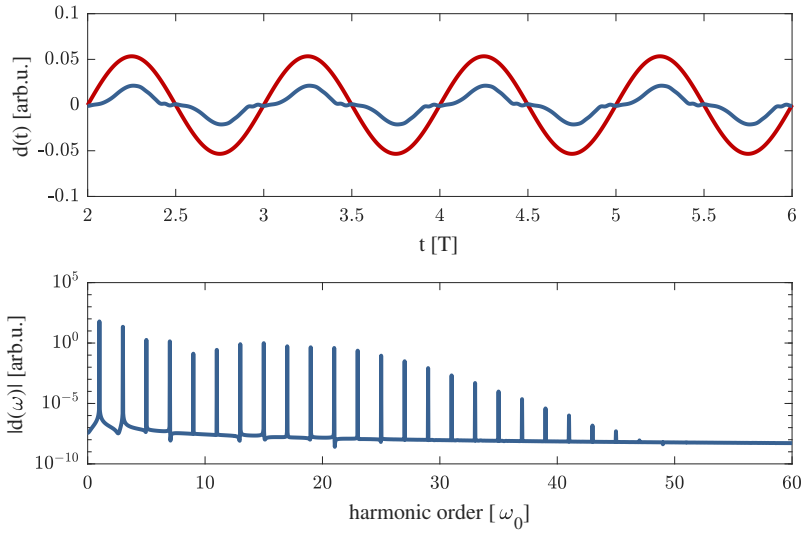

Figure 2.5: Quantum mechanical calculation of the dipole response in the strong-field approximation. The top plot shows the driving laser field (red curve) with an intensity of 10^{14} W/cm^2 and a wavelength of 800 nm, as well as the dipole moment (blue curve) for argon with an ionization potential of $I_\mathrm{p} = 15.76$ eV. The bottom plot shows the corresponding dipole spectrum on a logarithmic scale.

of which the saddle-point approximation selects a finite number, resulting in trajectories that can be identified as the short and long trajectories. For further details, the interested reader is referred to [47].

The calculated dipole is plotted in figure 2.5 (blue line) together with the driving infrared field (red line). It is clear that the linear dipole response with frequency ω_0 is the dominant contribution in the dipole oscillation. The corresponding spectrum (bottom panel) shows the predicted comb of odd harmonics with a perturbative region up to the 5$^{\text{th}}$ harmonic and a plateau region between 5$^{\text{th}}$ and 23$^{\text{rd}}$ harmonic. The cutoff region for decreasing intensities starts above the 23$^{\text{rd}}$ harmonic, which is in excellent agreement with the classically derived cutoff law (equation 2.8) which predicts the cutoff to be between harmonic 21 and 23 at E_c =34.5 eV.

If we only consider a set of classical quantum paths j, the intensity-dependent dipole phase can be derived from the SFA theory and is often approximated as [46, 48, 49]:

$$\Phi^{s,l}(q) \approx \alpha^{s,l}(q) I, \tag{2.15}$$

where $\alpha^{s,l}(q)$ depends on the trajectory and harmonic order. Using this expres-

sion, we can now define the first term in equation 2.11 as $\Phi^{s,l}(\Omega_p) = \alpha^{s,l}(\Omega_p)I$ for the long trajectories, and $\alpha^s(\Omega_p) = 0$ for the short trajectories.

2.3 The Macroscopic Response

So far, the response of only one atom has been taken into consideration when generating high-order harmonics. This, however, does not accurately describe the macroscopic field and its spatial and temporal characteristics since the field results from the coherent superposition of various emitters along and across the generation medium. In order to determine the overall yield, macroscopic effects need to be accounted for.

2.3.1 Phase Matching

The driving field propagates along the optical axis z interacting with the atoms in the medium. Each atom becomes an emitter of XUV radiation, with amplitude and phase depending on the local intensity and phase of the driving field. To ensure an efficiently high yield, the phases resulting from individual emitters have to be matched to create constructive interference between them, which is often referred to as *phase-matching*. However, due to a variation of the refractive index along and across the medium, the harmonic fields are very likely to be mismatched in phase. Consequently, for the harmonic generation to be as efficient as possible, it is important to minimize this mismatch.

The total wavevector mismatch for the qth harmonic, defined as:

$$\Delta\mathbf{k}(q) = q\mathbf{k} - \mathbf{k}_q, \tag{2.16}$$

where $\mathbf{k}$ is the fundamental wavevector, can be described using four contributions, as presented in [50]:

$$\Delta\mathbf{k}(q) = \Delta\mathbf{k}_g + \Delta\mathbf{k}_n + \Delta\mathbf{k}_p + \Delta\mathbf{k}_d. \tag{2.17}$$

The contributions correspond to the following effects:

- The beam acquires a geometrical phase due to the focusing of the infrared beam, which is referred to as the Gouy phase [51]. $\Delta\mathbf{k}_g$ denotes the Gouy phase difference and can be expressed in terms of the harmonic order q and the Rayleigh length z_R:

$$\Delta\mathbf{k}_g = -\frac{q}{z_R} \tag{2.18}$$

and is thus always negative.

- The second term, $\Delta\mathbf{k}_n$ arises from the neutral gas dispersion of the medium and the third term $\Delta\mathbf{k}_p$ from the plasma dispersion resulting from the intrinsic ionization during HHG. Both effects depend on the gas pressure, while the mismatch caused by the plasma dispersion also depends on the ionization rate and thus the intensity. The two contributions have opposite signs, meaning that the resulting mismatch ideally can be minimized by tuning the generation pressure accordingly.

- The final term is a result of the earlier introduced dipole phase, intrinsic to the process of HHG. Its contribution to the wavevector mismatch can be calculated as the derivative of the dipole phase:

$$\Delta\mathbf{k}_d = \frac{\partial\Phi^{s,l}(\Omega)}{\partial z} = \frac{\partial I}{\partial z}\Big[\alpha^{s,l} - \frac{\gamma^{s,l}}{I^2}(\Omega - \Omega_p)^2\Big]. \tag{2.19}$$

  This expression leads to a negative mismatch before the focus and a positive one after the focus. However, since the dipole phase variation as a function of the intensity is larger for the long trajectories, the mismatch differs for long and short trajectories. Hence, it is possible to tune the generation conditions, such that either the long or short trajectories are preferably created.

These four contributions are helpful approximations to achieve an efficient harmonic yield and allow us to adjust the experimental parameters, such as the pulse energy, gas pressure and focusing geometry, in order to minimize the mismatch between harmonic emitters. It is however unrealistic to achieve perfect phase matching ($\Delta\mathbf{k}(q) = 0$) for all harmonics under typical experimental conditions.

2.3.2 Generating Intense High-order Harmonics

Under typical generation conditions the conversion efficiency of HHG $\Gamma = E_{\text{out}}/E_{\text{in}}$ seems to be on the order of $\approx 10^{-5}$ in argon for photon energies between 20-50 eV [52]. Also, the output energy E_{out} does not increase after a certain input intensity is reached, since an excessive degree of ionization in the medium ruins the phase matching. However, the output energy can be optimized by scaling up the experimental setup and the input energy E_{in} accordingly [50, 53]. These scaling relations are introduced in table 2.1 and illustrated for two different experimental conditions in figure 2.6. The input energy is scaled as $E_{\text{in}} \to \eta^2 E_{\text{in}}$ with the general scaling factor η. As can be seen, the pulse energy E_{out} increases for a larger focal length f and medium length L, while the density of the medium ρ is decreased.

Table 2.1: The experimental parameters and their corresponding scaling laws in relation to the scaling factor η.

Exp. parameter	Scaling law
Pulse energy	$E \propto \eta^2$
Focal length	$f \propto \eta^2$
Medium length	$L \propto \eta^2$
Medium density	$\rho \propto 1/\eta^2$

As a consequence of these considerations, large scale HHG setups have been developed, using driving lasers in the hundreds of mJ regime and loose focusing geometries with focal lengths of several meters. Both the IXB at the Lund Laser Centre, as well as the beamline presented in paper v follow this approach.

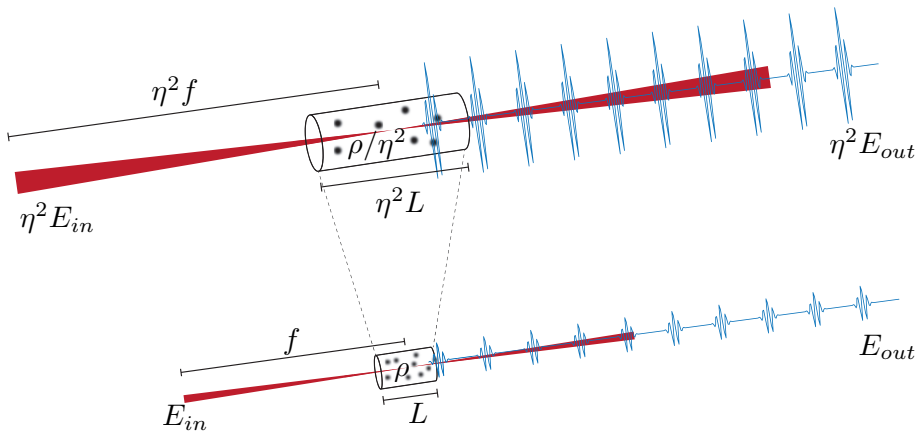

Figure 2.6: Illustration of the principle of scaling high-order harmonic generation. Two different generation conditions are shown, while the conversion efficiency is invariant and the experimental parameters scale with the general scaling factor η.

2.4 The Intense XUV Beamline

Following the concept of scaling the process of HHG, the idea of generating intense XUV high-order harmonics was born. At the LLC, this led to the development of the IXB. A high infrared pulse energy combined with a long focusing geometry provides intensities in the tunneling regime over a large volume. A comparably low gas density in a long gas cell enables the generation of high-flux high-order harmonics. Figure 2.7 provides an overview of the beamline. It can be divided into four segments:

- the *compressor chamber* described in chapter 2.1.4.
- the *generation chamber*, which houses the gas cell to generate the high-order harmonics.
- the *interferometer chamber*, which is described in detail in chapter 2.6.3.
- the *application chamber*, where the atomic and molecular experiments are performed.

All results presented in papers I-IV and VIII-X are the outcome of work performed at the IXB. Paper V uses a similar beamline design at the FORTH institute, in Heraklion, Greece.

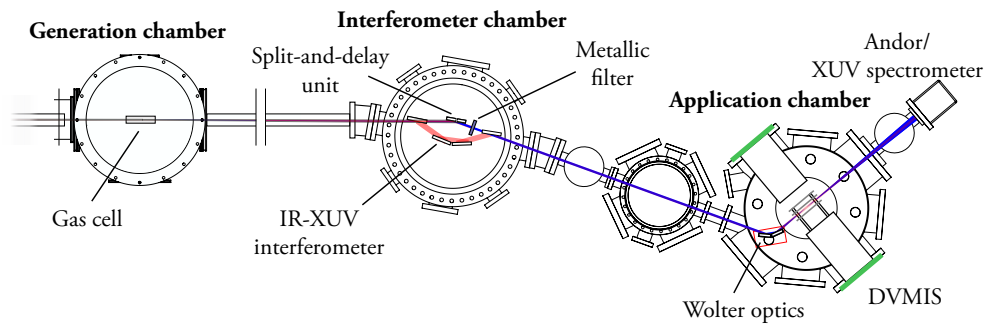

Figure 2.7: Schematic illustration of the Intense XUV Beamline. To the left, the focused beam comes from the compressor chamber and enters the generation chamber. The gas filled cell/jet enables the HHG. In the interferometer chamber a delay either between infrared (red) and XUV (blue) or between two replicas of the XUV beam is introduced. Finally, the beam is focused in the application chamber using the Wolter optics. An Andor CCD camera and a XUV spectrometer provide beam diagnostics. The ionization products are detected with the double-sided velocity map imaging spectrometer (DVMIS).

2.4.1 Harmonic Generation

The infrared pulses from the TW laser system, as described in chapter 2.1.3, are focused using a spherical mirror with a focal length of 8.7 m. In the generation chamber, this leads to a focal spot size of $\sim 300\ \mu$m and a Rayleigh range of ~ 300 mm. The exact focus position can be manipulated using the spherical actuator on the DM over a range of > 200 cm around the center of the generation chamber. A pulsed piezoelectric valve mounted on an x-y tilt and translation stage is used to inject the generating gas medium, allowing a high momentary pressure release without creating too high ambient pressure in the chamber. Throughout the scope of this work different type of media were used, including a nozzle to create a gas jet, as well as gas cells with lengths between 0.5-6 cm. For all experiments mentioned in this thesis, argon or xenon were used as the generation medium.

The generated harmonic field propagates over a distance of ~ 6 m expanding the beam width to $\sim$ 1mm before a reflection on a fused silica plate at an angle of incidence of 10°. Such a small angle provides a reflectivity of around 50% in the generated XUV spectral range. Additionally, the surface is anti-reflection coated for the remaining IR field. A set of metallic filters is used to shape the XUV spectrum and block the remaining infrared beam. Mainly, a 200 nm aluminum filter was used during the experiments presented in this thesis, suppressing all frequencies below the 11^{th} harmonic.

2.4.2 XUV Beam Diagnostics

Detecting the properties of the generated and shaped XUV field is essential for the application and interpretation of further experiments. In addition, it offers the possibility to study the intrinsic parameters of the HHG process itself, which led to a series of studies throughout this thesis.

The generated spectrum was detected using a newly developed XUV flat-field spectrometer. It was located behind the target area in the application chamber. A Hitachi 001-0639 grating was used to disperse the spectral components of the beam along the vertical axis of a set of multi-channel plates (MCPs). The grating had a concave curvature imaging the focal spot in the application chamber in the vertical direction, making it possible to record the spatial profile of the beam along the horizontal axis of the MCP. The resulting image was recorded by a charge-coupled device (CCD) camera imaging a phosphor screen coupled to the MCP. The top panel of figure 2.8 shows the resulting image for a spectrum generated in argon. The bottom panel displays the projection along the spatial axis. The grating is mounted on a linear translation stage such that the beam is able to pass the setup

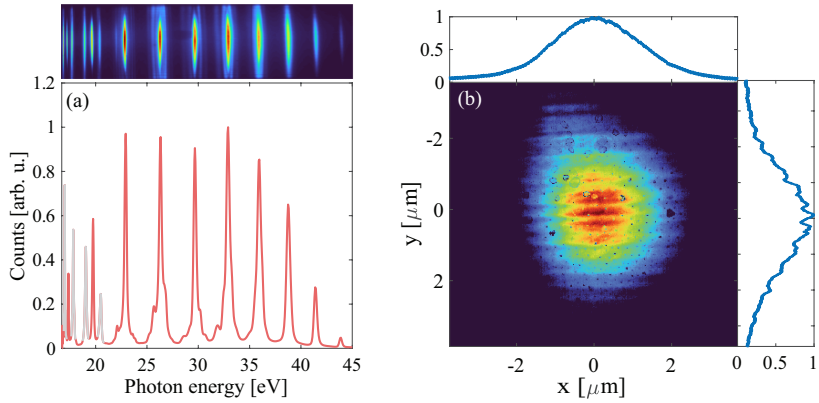

Figure 2.8: (a) XUV spectrum generated in argon and filtered by 200 nm aluminum foil. The top panel shows the recorded image on the phosphor screen and the bottom its projection along the spatial axis. (b) Typical XUV far-field beam profile together with its x- and y-projections recorded with the Andor CCD camera.

and continue towards an XUV CCD camera.

The spatial profile of the XUV beam is detected using an Andor iKon XUV CCD camera with a resolution of 2048x2048 pixel and a pixel size of 13.5 µm. The chip has an additional coating, which enables the measurement of the pulse energy of the beam. Figure 2.8 (b) portrays a typical beam profile. Additionally, a home-built XUV wavefront sensor (WFS) was developed at the IXB as part of a Master project [54]. The assembly consists of a Hartmann mask mounted 4 cm in front of the XUV camera. A set of 80 µm holes enables the detection of the local curvature of the XUV beam, making it possible to reconstruct the entire wavefront of the beam. The working principle is detailed in chapter 2.5.1.

For the experiments presented in papers VIII and IX, a commercial WFS, co-developed by the Laboratoire d'Optique Appliquée (LOA) and Imagine Optics, was used at the Intense XUV Beamline in the scope of two Laserlab Europe campaigns.

2.4.3 Application

The application chamber is designed to study ionization of atoms and molecules and detect the resulting charged particles. With the intention of maintaining the broadband XUV spectrum, the beam is focused using two gold-coated toroidal mirrors in a Wolter-like configuration, as described in paper IX. The shallow angle of the two mirrors ensures a sufficient reflection of the entire spectrum. Additionally, the geometry is chosen such that the second mirror compensates for the

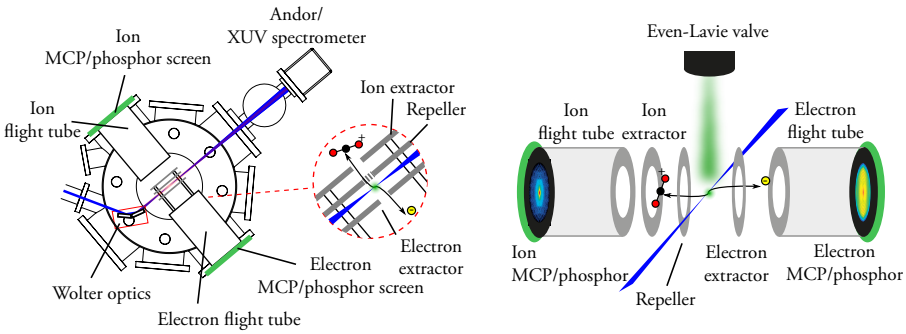

Figure 2.9: Schematic illustration of the applications chamber. The left panel shows a top view and the right panel a front view of the VMIS. The beam (blue) is focused by the Wolter optics in the center of the chamber. After expanding, the beam is detected by an Andor CCD camera or an XUV spectrometer. The VMI, consisting of an ion and electron extractor, a repeller, two flight tubes and two MCP/phospor screens, detects the ionization products. The target gas is injected from the top using an Even-Lavie pulsed valve, as indicated in the right panel.

aberrations introduced by the first one [55]. The alignment of the focusing optics can be realized in a closed-loop algorithm together with the XUV wavefront sensor, optimizing the focal spot down to a size of 3.6 x 4 μm^2. A detailed study of this interplay is described in paper IV.

The atomic or molecular target is injected using a pulsed Even-Lavie valve [56], which in combination with two skimmers creates a high-density supersonic gas jet from the top into the center of the chamber, where it meets the focus of the beam. The valve can be used for gases, as well as for liquid and solid samples in combination with a carrier gas. The sample cartridge can be heated to temperatures up to 250° C. The entire assembly was used for the experiments at the Intense XUV Beamline presented in papers I, II and X, as well as in paper VI at the Free-Electron-Laser FLASH at DESY in Hamburg, Germany.

Finally, the charged particles are detected by a double-sided velocity map imaging spectrometer (VMIS) [57], designed to simultaneously measure the angle-resolved momentum distributions of released electrons and ions, as presented in detail in paper X. The design and its operating principle are shown in figure 2.9. Using a static electric field created by a set of ring electrodes, the charged particles are forced onto a trajectory towards a set of MCPs. Depending on their initial velocity, the charged particles are distributed around the center of the MCP. As a result, the 3D momentum distribution of outgoing particles is projected as a 2D map onto the detector. A phosphor screen together with a CCD camera is used to record the resulting image. In order to reconstruct the 3D distribution of the momenta, an inverse Abel transform can be applied [58]. Two different methods were used for the results in this thesis: an iterative method [59] or a fit to a set of Legendre

polynomials, called pBaseX [60].

In addition to the momentum distribution, the time-of-flight spectrum of the detected ions can be extracted from the MCP using a decoupling circuit. Hence, the mass-over-charge ratio of the resulting ionization products can be determined.

The VMIS is designed with two extracting electrodes and two flight tubes in opposite directions to each other, such that ions and electrons are imaged simultaneously making use of their opposite charge. The correlation of the respective momentum distributions is of great interest for the understanding of the studied processes. Due to the comparably low repetition rate, a conventional coincidence analysis [61] is not practical. However, the high event rate per shot enables the investigation of correlations using a covariance scheme, further described in chapter 4 and papers IV and VI.

2.5 Spatio-Temporal Aspects

This chapter discusses the effects of the dipole phase on spatial and temporal aspects of the generated high-order harmonics. The study of the dipole phase became important for us, when trying to refocus the high-order harmonics to create high intensities, while taking advantage of the attosecond pulse duration. Combining theory and experiment, we investigated the influence of the dipole phase on the spatial and temporal properties of high-order harmonics, which led to papers II and III. In papers VIII and IX,we present metrological results of the harmonic wavefront and the quality of the XUV focusing at the IXB.

2.5.1 Harmonic Wavefront

A good wavefront quality, for both the XUV and infrared beam, is essential for the experiments conducted throughout the scope of this work. It allows focusing to small spot sizes, which is important in order to reach high intensities. The wavefront of an expanding wave is defined as the surface through all points of equal phase, e.g., the peaks or the valleys, within the sinusoidal oscillation. The wavefront of a plane wave corresponds to a flat plane, whereas a divergent beam has a curved wavefront. Aberration describes the deviation of a wavefront from that of a plane wave, which can be introduced as a result of mirror surfaces that are not perfectly flat, or by nonlinear interactions with a medium. One common way to characterize aberrations is to project the wavefront on a set of so-called Zernike polynomials of different radial and angular dependencies [62].

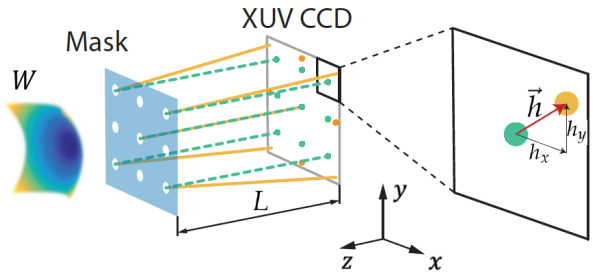

Figure 2.10: Working principle of the XUV wavefront sensor. The beam is diffracted through an array of holes, called Hartmann mask. The detected positions on the screen behind the mask depend on the wavefront when passing through the holes. The displacement, referenced to the position for a flat wavefront, is referred to as the Hartmann vector $\vec{h}$. Figure adapted from paper IX.

A well-established technique for measuring wavefronts is to use a Hartmann wavefront sensor (WFS). A sketch of the working principle is shown in figure 2.10. The beam passes through an array of diffracting optics, which guide it towards the direction orthogonal to the tangent of the local wavefront. In the infrared and visible range, such arrays usually consist of microlenses, whereas in the XUV regime a small hole is sufficient to create enough diffraction. A screen placed behind the mask is utilized to detect the displacement behind each hole/lens referenced to the position that would be obtained for a plane wave. The difference between the displaced point and the reference point is called the Hartmann vector $\vec{h}$, which length is proportional to the derivative of the local wavefront. In order to reconstruct the wavefront, two different algorithms are commonly used: following the decomposition in Zernike polynomials the *modal* reconstruction fits a gradient field of each polynomial to the vector field created by the measured Hartman vectors and thus allows the reconstruction of the wavefront [63]. The *zonal* reconstruction algorithm on the other hand calculates the wavefront by a numerical integration of all

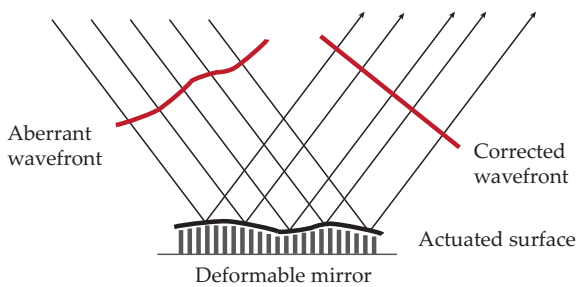

Figure 2.11: The working principle of the deformable mirror, which compensates wavefront aberration. A set of actuators adjusts the surface of a mirror such that the reflected wavefront is flat.

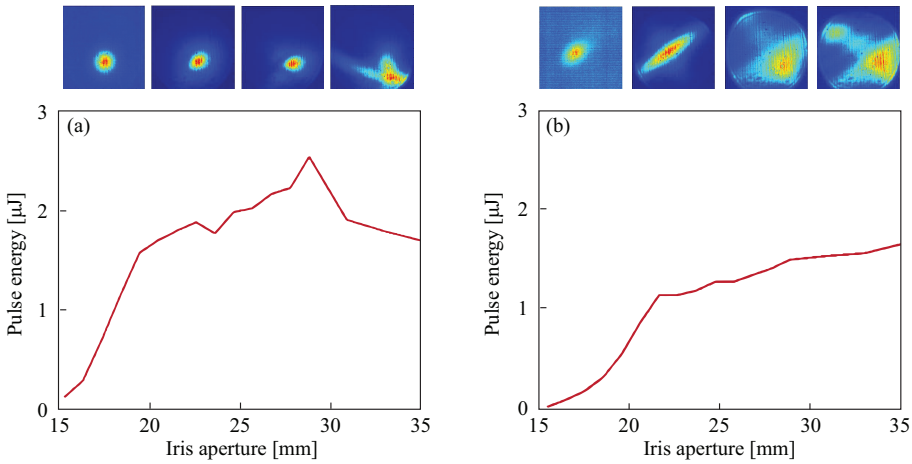

Figure 2.12: Generated XUV pulse energy as a function of the beam aperture introduced by the iris in the generation chamber. The scan was performed with and without aberration correction (a,b respectively). The insets on the top show the measured beam profile for four different apertures.

the local slopes [64].

Measuring the infrared laser wavefront allows us to compensate the aberrations acquired along its path through the beamline. A common way to do so is to use a deformable mirror (DM), consisting of an array of piezoelectric actuators individually attached to the surface of a reflective optic. Each actuator changes the local curvature of the surface, which then compensates the wavefront of the reflected beam, as illustrated in figure 2.11. In a closed-loop circuit, an optimization algorithm applies a hill-climb procedure to the actuators of the DM while monitoring the changes to the wavefront. The quality of the wavefront is hereby measured as the root mean square (RMS) of the deviation to a flat wavefront in units of the central wavelength, which typically lies around $\lambda/40$ after the aberration correction.

The implementation of the deformable mirror, correcting the aberrations of the infrared beam, led to a significant improvement of the spatial shape of the XUV beam, both in the far and the near field. Figure 2.12 shows the variation of the XUV pulse energy and the far-field beam profile as a function of the aperture of the iris, which is located before the generation medium, both with and without the aberration correction introduced by the DM. The aperture introduced by the iris affects the pulse energy of the driving infrared field and the shape of the focal spot in the generation medium. A smaller aperture creates a larger focal spot size and changes the shape of the focal spot towards a super-gaussian, which is favorable for phase-matching considerations. As can be seen in figure 2.12 (a), the

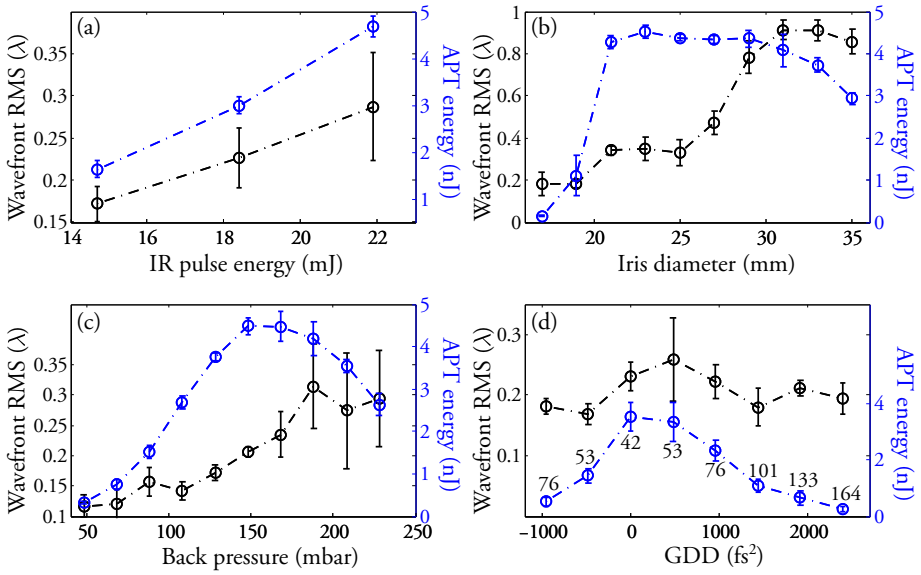

Figure 2.13: Measured wavefront error (black) and generated pulse energy (blue) as a function of four different generation parameters: (a) the fundamental IR pulse energy, (b) the iris diameter, (c) the backing pressure of the gas cell and (d) the GDD introduced by translating the distance between the two gratings in the compressor varying the pulse duration of the infrared pulses. Figure adapted from paper VIII.

generated pulse energy increases for an increasing aperture until reaching a maximum at around 29 mm. The beam profile, measured in the far field on the Andor XUV camera, remains round and of similar size until 29 mm. For higher aperture values the beam profile starts to distort, due to a too high intensity in the generation medium. The resulting ionization leads to a modified refractive index in the medium, which compromises the phase matching and introduces guiding effects to the beam. Without the aberration correction, the beam profile is elongated already for smaller apertures and breaks apart for apertures larger than around 25 mm, as shown in figure 2.12 (b). Interestingly, the generated pulse energy is in a similar range as with the aberration correction and increases with the iris aperture, even though the beam profile is of very poor quality. Nevertheless, it is certain that the intensity available for further experiments is much higher for the beam with the aberration correction, due to its superior beam profile.

Paper VIII presents an in-depth study of the effect of different generation parameters on the XUV wavefront. The wavefronts were measured on a single-shot basis to avoid averaging effects due to pointing instabilities and wavefront variations. Figure 2.13 shows the retrieved wavefront error in units of the central wavelength as a function of (a) the IR pulse energy, (b) the iris aperture, (c) the backing pressure of the gas cell and (d) the compressor GDD. The generated pulse energy is

shown in blue. The optimal XUV wavefront is not necessarily generated under the same conditions as the highest XUV pulse energy and it is hence important to take into account the wavefront, when performing experiments that require focusing the radiation on a small focal spot to reach high intensities.

Paper VIII also shows that the XUV wavefront is affected by the infrared beam in two ways: the spatial phase is equal to the phase of the infrared field multiplied by the process order, as in any regular up-conversion process, plus a contribution proportional to the laser intensity profile, due to the intensity dependence of the dipole phase. The intensity distribution across the infrared beam profile, which is approximately a two-dimensional Gaussian distribution, leads to a larger dipole phase contribution in the center compared with the outer parts of the beam. This implies the generation of harmonic orders with varying radii of curvature. Also, if the infrared beam profile is asymmetric, it leads to an astigmatic XUV wavefront. These effects play an important role when refocusing the generated harmonic beam for further experiments and led to a series of further studies presented in the following sections.

2.5.2 Focusing Properties

In a connected series of investigations, Paper IX discusses the quality of the XUV beam focusing achieved by two toroidal mirrors in a Wolter-like configuration, using wavefront measurements in the far-field. The two toroidal mirrors are designed in a geometry such that the aberrations introduced by the first one are compensated by the second one. In addition, the alignment of the entire assembly can be manipulated in order to counteract the aberration of the incoming beam, as predicted in [65]. The two mirrors are mounted with a fixed angle to each other, prealigned by the manufacturing company, on a 6-way translation stage. Two translation stages are used to align the incoming and outgoing beams, two go-

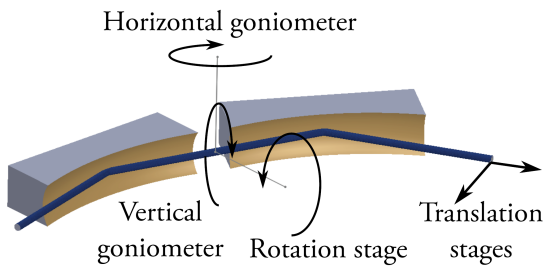

Figure 2.14: Schematic of the degrees of motion of the Wolter focusing optics. Figure adapted from paper IX.

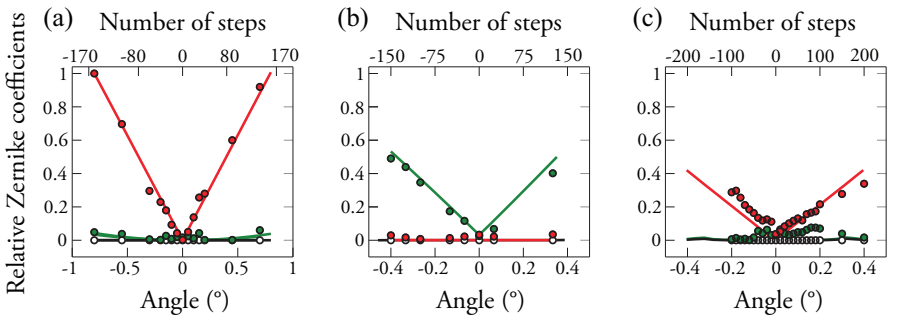

Figure 2.15: (b) Measured Zernike coefficients of 0° astigmatism (green), 45° astigmatism (red) and coma (black) plotted as a function of the motion of the rotation stage (b), the horizontal (c) and the vertical goniometer(d). Figure adapted from paper IX.

niometers to tilt and twist the mirrors and a rotation stage to rotate the entire assembly, as indicated in figure 2.14.

The wavefront was analyzed in terms of projections on Zernike polynomials, each corresponding to a certain aberration. Figure 2.15 displays the effect of the movements of the rotation stage and the two goniometers on the coefficients of the low-order Zernike-polynomials, e.g. the 0° and 45° astigmatism and coma. Each motion creates a change in the wavefront affecting the coefficient of a particular Zernike polynomial. The rotation stage, shown in (a), mainly changes the value of the 45° astigmatism (red), barely the 0° astigmatism (green) and not at all the coma (black). The horizontal goniometer (b) on the other hand only affects the 0° astigmatism (green). The vertical goniometer (c) shows a much smaller influence overall, mostly on the 45° astigmatism (red). This systematical behavior of the wavefront introduced by independent settings is of great advantage in order to not only compensate the wavefront aberrations introduced by the two toroidal mirrors, but also to compensate for any initial aberrations the XUV beam carries before being focused. As described in paper IX, we could therefore minimize the focal spot size, retrieved from the wavefront measurements, to 3.6 x 4 μm^2.

2.5.3 Chromatic Aberration

So far, only the wavefront of the entire XUV spectrum has been considered, which corresponds to an average of all harmonic contributions. Papers II and III reveal that the process of HHG creates an intrinsic variation of the harmonic wavefronts. This leads to a spread of the harmonic foci (virtual or real) around the generation medium, thus also creating a spread of the focus position along the propagation axis when the harmonics are refocused.

The variation of the wavefront curvature can be understood by studying the effect of the dipole phase on the spatial phase of the generated harmonic beam, which can be written for the q^{th} harmonic as:

$$\Phi_q(r,z) = q\phi(r,z) + \Phi^{s,l}(r,z). \tag{2.20}$$

The last term $\Phi^{s,l}(r,z)$ corresponds to the dipole phase described in equation 2.11, where the spatial dependence is introduced using $I = I(r,z)$. Further, the phase of the fundamental can be written as

$$\phi(r,z) \propto \frac{kr^2}{2R(z)}, \tag{2.21}$$

where k is the wavevector, r is the radial distance from the center of the beam and $R(z)$ is the radius of curvature. Figure 2.16 (a) illustrates the curvature due to the fundamental field $q\phi(r,z)$ in black and the contribution introduced by the dipole phase Φ_s for shot trajectories in green. As can be seen, the fundamental curvature varies through the focus from negative to positive, as expected from a Gaussian beam. The dipole phase contribution to the curvature on the other hand is constant over the propagation direction z, which means that the combined harmonic curvature is flat at a position different from the fundamental focus, as indicated by the blue dashed line. Given the fact that the dipole phase contribution is intensity and order dependent, the focus position of the harmonics therefore varies as a function of order. As a consequence, the high-order harmonics are generated with an intrinsic chromatic aberration.

Assuming a Gaussian fundamental beam profile $I(r,z) = I_0 \mathrm{e}^{-2r^2/w^2(z)}$, with the radial width $w(z)$ at $1/e^2$, the radius of curvature of the harmonic field can be approximated using a Taylor expansion around the center of the beam for the long and short trajectories:

$$\frac{1}{R^{s,l}(z)} = \frac{1}{R(z)} - \frac{4\alpha^{s,l} I_0 w_0^2 c}{w^4(z)\Omega} + \frac{4\gamma^{s,l}(\Omega - \Omega_p)^2 c}{I_0 w_0^2 \Omega} \tag{2.22}$$

The width of the harmonic beam at the generation position is approximated to be half of the fundamental width, which is confirmed by TDSE calculations and detailed in paper III. Figure 2.16 (b) plots the radii of curvature for the fundamental beam (black), the long trajectories (red) and the short trajectories (blue) for the 23rd harmonic as a function of the generation position. The focus positions (where the radius of curvature goes to infinity) are quite different for the long and short

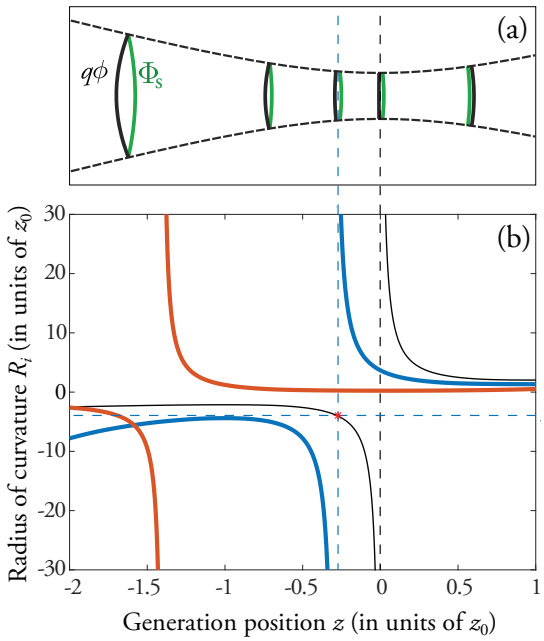

Figure 2.16: (a) Contributions to the harmonic wavefront created by the fundamental (black) and the dipole phase (green) at different generation positions z. (b) Radius of curvature for the fundamental infrared (black), the generated short (blue) and long (orange) trajectories of the 23rd harmonic as a function of the generation position z relative to the fundamental focus. The position of the infrared focus is indicated by the vertical black dashed line and the point where two wavefront contributions add up to a flat wavefront is marked by the blue dashed line. Figure adapted from paper III.

trajectories as well as for the fundamental beam. As a result, also the divergence of the generated harmonic field varies and is minimal when the total radius of curvature is infinity, i.e., when the harmonics are generated with a flat wavefront.

For the high-order harmonics generated at the IXB, these properties affect the refocusing in the application chamber. For a high intensity in the focus, all harmonics need to be located at the same position. However, the predicted chromatic aberration introduces a variation of the intensities of different spectral components along the propagation axis and modifies the temporal structure of the attosecond pulses. In paper II, the model described above was used to estimate the focus positions of the harmonic beam for the experimental parameters of the IXB. Figure 2.17 shows a comparison of the harmonic focus positions in the generation chamber (a,c) as well as after refocusing with the Wolter optics in the application chamber (b,d) for harmonic order 11 (red) to 25 (blue). The top row corresponds to the simulation run without the dipole phase, whereas in the bottom row the dipole phase is included. The x-axis is the position of the medium relative to the fundamental

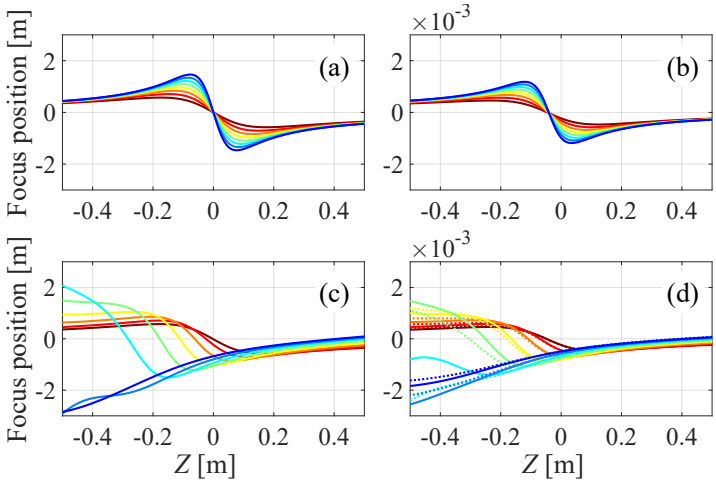

Figure 2.17: Simulated focus positions of generated harmonics as a function of the generation position Z, in the generation chamber (a,c) and the application chamber after refocusing (b,d). The simulations were performed without (left column) and with the dipole phase contribution (right column). The color code represent the different harmonic orders from 11 (red) to 25 (blue). Figure adapted from paper II.

focus. As shown in the top row, the refocused harmonics are already displaced in the application chamber when generating within the infrared focus without the dipole phase involved in the process. This is due to the Rayleigh range of the harmonics, which is longer than the distance between the generation position and the Wolter optics. It is however possible to compensate for this effect and refocus all harmonics to the same position, when generating slightly outside of the infrared focus (at $Z \approx -0.05$ m). With the dipole phase included in the simulations, the focus positions vary strongly with the harmonic order, in particular for negative generation positions, corresponding to a generation before the infrared focus.

In order to confirm the simulation presented in figure 2.17, a knife-edge scan around the focus in the application chamber was performed, as described in detail in paper II. A knife-edge was placed on a translation stage, making it possible to insert the knife horizontally into the beam for different displacements along the propagation direction, as shown in figure 2.18(a). As a first step, a scan close to the focus was performed for three positions: before, after and in the focus. While inserting the knife, the spectrum was measured by the XUV spectrometer. Figure 2.18(b) shows the spectrum without any knife insertion. When the knife is inserted before the focus, a shadow appears on the opposite side visible in all harmonic orders, as shown in (c). Inversely, when inserted after the focus (e), the shadow appears on the same side as the knife. For a knife insertion in the focus shown in (d), the shadow appears from the right side for the low-order harmonics,

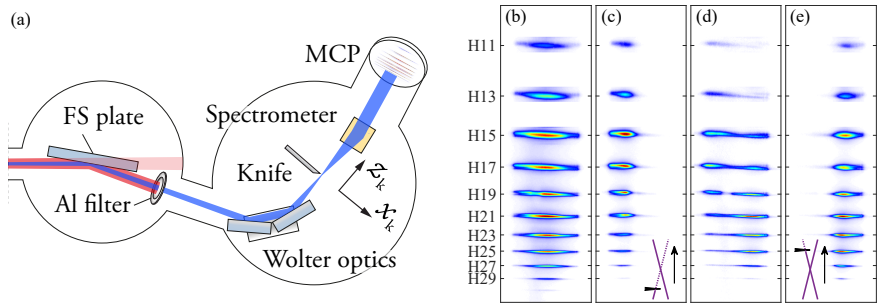

Figure 2.18: (a) Schematic of the experimental setup used for the knife-edge measurements. The knife is placed around the focus in the application chamber in a z_k-x_k translation stage. (b) Measured XUV spectra for different knife edge positions: no insertion (b), knife inserted before (c), after (e) and in the focus (d). The insets indicate the position of the knife for (c) and (e). Figure adapted from paper II.

i.e., the knife is positioned before the focus, while for the high-order harmonics the shadow is on the left side, which means that the knife is placed behind the focus. For the mid-order harmonics, the signal on the spectrometer is reduced without much change in shape, which indicates that the knife is inserted in or very close to the focus. This experimental result confirms the predictions from the above-mentioned simulations: under certain generation conditions, the generated harmonic orders are refocused at different position due to the intrinsic chromatic aberration caused by the dipole phase.

In order to quantify our findings in more detail, a slightly modified knife-edge scan was performed. The knife was now inserted at four positions outside the Rayleigh range. The beam width at each position was extracted by fitting an error function to the harmonic intensity as a function of the knife insertion. A linear fit to the four extracted beam widths as a function of the knife position in the propagation direction z_k determines the focus position as the point where the fit crosses zero. This is done for all detected harmonic orders on the spectrometer, while the position of the fundamental infrared focus is varied by changing the curvature on the deformable mirror.

The resulting focus positions of the harmonic beam are shown as functions of the harmonic order in figure 2.19. Each plot corresponds to a different position ΔZ of the generation medium with respect to the infrared focus, indicated in the insets of each figure. The solid black line shows the measured values with the corresponding errors extracted from the fitting procedure and the dashed lines are the simulated values using the model described above. As can be seen, the focus positions are much closer together when the harmonic beam is generated after the fundamental infrared focus ($\Delta Z > 0$). In (a) and (b) the XUV foci are separated by almost

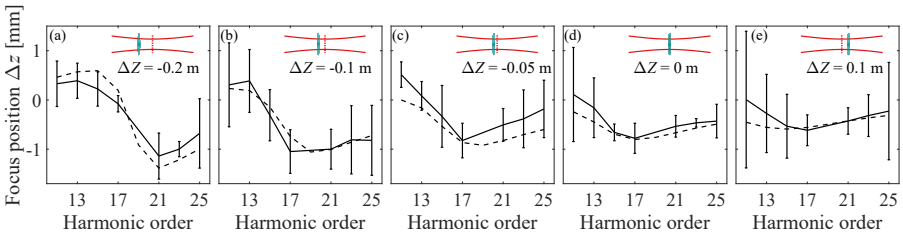

Figure 2.19: Measured (solid line) and simulated (dashed line) focus positions as a function of the harmonic order for five different generation positions. The position of the generation medium (green) in relation to the infrared focus (red dotted line) is indicated in the insets. Figure adapted from paper II.

1.5 mm, which is a large difference given the short Rayleigh range due to the tight focusing geometry in the application chamber.

Paper II gives a simple estimation of the spatio-temporal properties of the focused pulses. The peak intensity of the resulting XUV pulses is evaluated as a function of the generation position. We show that the spread of the focus position of different harmonics for $\Delta Z < 0$ leads to a drastic drop in intensity compared to the pulse energy. Additionally, due to the time-frequency coupling, the temporal structure of the attosecond pulses varies along the focal region. As a consequence, it is crucial to take the chromatic aberration of the generated harmonic fields into account, when performing experiments that require high intensity and short pulses.

2.6 Attosecond Pulse Characterization

Traditional pulse characterization methods, such as FROG [66, 67], SPIDER [68] and d-scans [69], are not suitable for XUV pulses, due to the high absorption and low reflectivity of optics in this spectral region. That is why, since the birth of attosecond science, other techniques have been proposed and realized, the most prominent being attosecond streaking [70] and the reconstruction of attosecond beating by interference of two-photon transitions (RABBIT) [71]. Both techniques use photoelectrons to measure the spectral phase in order to reconstruct the temporal characteristics of the beam. The streaking method characterizes an isolated attosecond pulse with a comparably high infrared intensity, whereas the RABBIT technique is able to determine the phase and amplitude of an attosecond pulse in a train (ATP). Both methods are based on an interferometric measurement to extract the phase separately from the spectrum. However, a more direct way to determine the temporal structure of XUV pulses is an autocorrelation measurement. As presented in paper V, the envelopes of individual pulses of an APT

can be extracted from a nonlinear ionization signal by varying the delay between the APT and a replica of itself.

This chapter describes the efforts taken to perform an autocorrelation measurement at the IXB as well as results of a RABBIT experiment. The authors contribution to the paper v was conducted during a study visit to the FORTH institute in Heraklion, Greece, and is partly summarized.

2.6.1 Split-and-Delay Unit

At the IXB, a split-and-delay unit (SDU) has been developed to create two replicas of the XUV beam [72]. Two anti-reflection coated silica plates are used to split the wavefront of the beam in equal parts, reflecting them in a grazing incidence angle to ensure a sufficient reflectivity. The second plate is hereby piezo-actuated in order to adjust the overlap as well as to introduce a path length difference between the two beams. Both the pointing and the delay are stabilized by an external optical interferometer, co-propagating with the XUV beam, which enables a temporal precision of 10-20 as over a range of 50 fs. A detailed description of the design and the commissioning of the SDU can be found in [65]. In the current setup, the SDU is integrated in the XUV-IR interferometer setup, further described in chapter 2.6.3.

In the work presented in paper v, a similar design was used, with the difference that, instead of a silica plate, the focusing mirror consists of two parts and is used to split and delay the XUV beam at a normal incidence angle. The disadvantage of this design is that the reflectivity in a normal incidence angle is much lower for higher harmonic orders.

2.6.2 Multiphoton Ionization and Autocorrelation

Within the scope of the present work, several attempts were made to use the SDU in order to record an XUV-XUV second-order autocorrelation and thereby determine the temporal structure of the attosecond pulses. The detection scheme was based on the two-photon double-ionization of neon, as presented in [20]. With a spectrum ranging from 20-50 eV, the XUV beam is intense enough to enable the double ionization of neon (62.5 eV), which requires two photons. Hence, the double-ionization rate depends quadratically on the intensity, which enables an autocorrelation measurement.

Figure 2.20 portrays an experimental ion time-of-flight spectrum, from which the

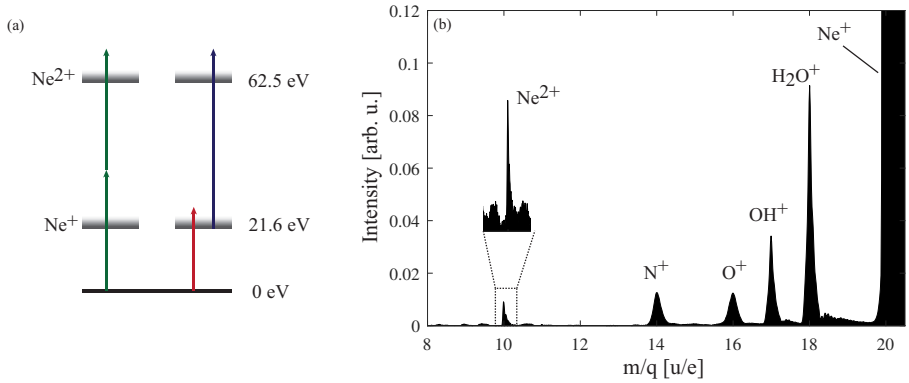

Figure 2.20: (a) Schematic of the two-photon double-ionization process in Neon. Shown are the one- and two-photon ionization thresholds and for the direct (left) and sequential (right) ionization. (b) Retrieved mass-over-charge spectrum showing all detected ions including the Ne^{2+} signal, which is shown as a zoom in the inset.

yield of individual ionization products can be extracted. The singly ionized $^{20}Ne^{+}$-signal dominates the spectrum and is accompanied by peaks created by the ambient background gases in the chamber, namely N^{+}, O^{+}, OH^{+}, H_2O^{+}. At a mass-over-charge ratio of m/q=10 u/e the peak created by double-ionized Ne can be seen.

Despite a nonlinear signal of around one count per shot on average, it was not possible to record an autocorrelation trace during the performed attempts. There are several potential explanations for this. On the one hand the pointing instabilities of the laser led to fluctuations in the splitting ratio between the two beams. Consequently, the contrast of an autocorrelation is reduced. Another reason might be the reduced flux, lost on the slit between the two mirrors. This effect may be small, but since the signal is nonlinear, the effect on the detection rate of $^{20}Ne^{+}$-ions could be significant. Finally, the wavefront dependence between harmonic orders might lead to a strong chromatic aberration in the re-focused beam, as presented in papers II and III, and drastically impact the temporal structure and intensity of the pulse. Especially for a sequential double ionization, which was predominantly produced in these experimental settings (see [20]), different harmonics are required at high intensities. However, if they are not focused at the same position, the yield of the $^{20}Ne^{+}$-ions is strongly affected. Paper V presents a successful autocorrelation measurement of the XUV pulses, where the nonlinear signal is created via a direct double ionization of argon. Here, only low-order harmonics (11^{th}-17^{th} order) were used, which reduces the effect of the chromatic aberration.

Despite the difficulties recording an XUV-XUV autocorrelation at the IXB, the SDU was tested on an above-threshold ionization (ATI) signal of argon using the

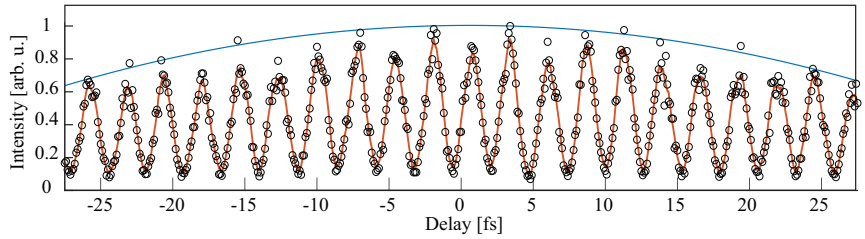

Figure 2.21: Autocorrelation measurement retrieved from a ATI signal recorded in singly ionized argon (black dots). A fit reveals an oscillation period of 2.7 fs, corresponding to a single cycle of the infrared field. Figure reproduced from [73]

fundamental infrared field. The ionization potential of argon is approximately 15.8 eV, which is more than 5 times higher than the photon energy of the infrared field. As a consequence, the signal is highly nonlinear with the intensity of the field, making it an ideal candidate for an autocorrelation measurement. Figure 2.21 displays the retrieved total ion yield as a function of the delay between the two replicas, which shows a strong oscillation. The measured period corresponds to 2.7 fs, which is in agreement with the period of a single cycle of the infrared field.

2.6.3 XUV-IR Interferometer

In addition to the SDU, an XUV-IR interferometer was developed and implemented at the IXB during this work. Due to the long beamline design, traditional interferometers add the risk of pointing instabilities and temporal jitters, while propagating over long distances. Hence, the interferometer has a compact in-line design, shown in figure 2.22, where the path difference is kept as short as possible, thus resulting in excellent temporal and spatial stability.

The XUV beam is separated from the fundamental infrared field by taking advantage of its lower divergence. A set of holey mirrors create two interferometric arms, where the hole diameter is chosen in a way that the entire XUV beam propagates through the hole, so that the reflected part only consists of fundamental infrared radiation. In the XUV arm (marked in blue in figure 2.22) the SDU is placed on a translation stage. For the operation of the XUV-IR interferometer it is displaced such that only one of the silica plates is used to reflect the beam. In the infrared arm (red path in the bottom of figure 2.22) two dielectric mirrors mounted on a translation stage guide the beam onto the second holey mirror. The translation stage is used to vary the path difference between both arms and hence to intro-

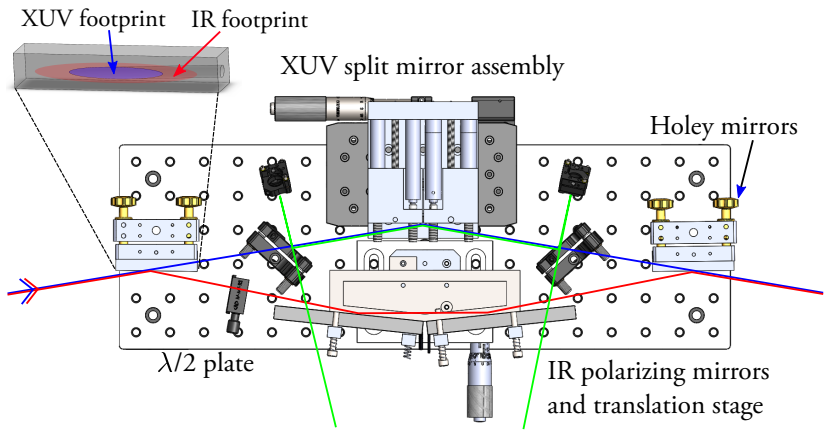

Figure 2.22: Schematic illustration of the IR-XUV interferometer. The incoming XUV (blue) and infrared (red) beams are split by the first holey mirror to the left. The infrared beam is reflected on two mirrors mounted on a translation stage introducing a delay between the two beams after being recombined by the second holey mirror to the right. In the XUV arm, the SDU is placed, which is displaced such that only one of the plates reflects the beam for the operation of the XUV-IR interferometer. An aluminium filter in XUV arm blocks the remaining infrared field and shapes the XUV spectrum. Figure reproduced from [73]

duce a time delay between APT and the infrared probe field. A 200 nm thick aluminum filter in the XUV arm blocks the remaining infrared beam and the intense low-order harmonics. The two beams are recombined on the second holey mirror, after which the XUV beam and the annular infrared beam co-propagate co-linearly towards the application chamber.

2.6.4 The RABBIT Technique

When using an XUV APT to ionize an atomic target, the resulting photoelectron spectrum shows a series of peaks due to absorption of the odd-order harmonics. Similar to the XUV spectrometer, the photoelectron spectrum only gives access to the spectral amplitude of the XUV pulses modified by the ionization cross-section. However, in order to reconstruct the pulse in the temporal domain, the spectral phase is required. The measurement of this phase can be achieved by adding a second infrared photon, which is either absorbed or emitted by the outgoing electron. In the spectrum, this leads to additional peaks, called *sidebands*, which appear in between photoelectron peaks from absorption of harmonic contributions. Each sideband can be reached by two different pathways, as indicated in figure 2.23. Consequently, an interference is created between these two quantum paths, which affects the yield of photoelectrons in the sidebands. When changing the delay between the APT and the infrared pulse, the sideband signal starts to oscillate.

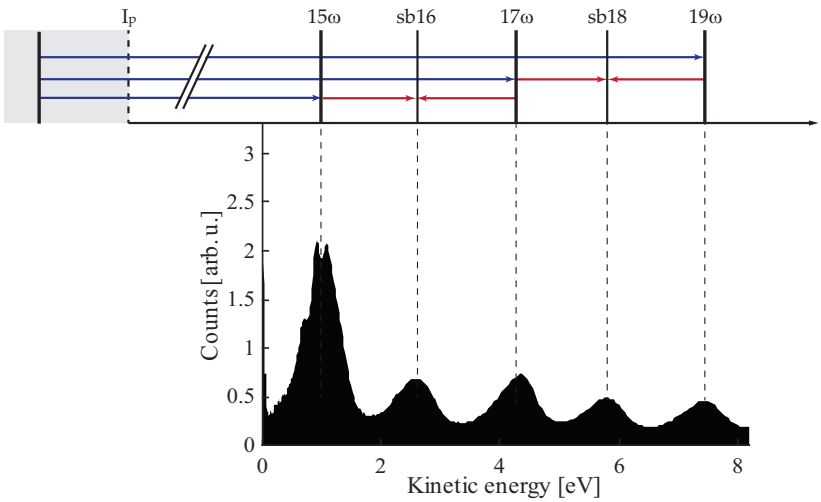

Figure 2.23: Measured angle-integrated photoelectron spectrum. The schematic above describes the photon transitions leading to electrons generated by harmonics (15ω, 17ω and 19ω) as well as the sidebands (sb16, sb18). Blue arrows represent XUV photons and red arrows the infrared photons.

This oscillation depends on the different phases acquired during the two-photon transition and thus carries information about the spectral phase of the harmonics. It can be used to reconstruct the temporal shape of the XUV pulse, as well as the two-photon ionization process, which plays an important role in paper I and is further described in chapter 3. The oscillating sideband signal can be written as [74]:

$$I_{SB}(\tau) = \alpha_q + \beta_q \cos(2\omega\tau - \Delta\Phi_{2q} - \Delta\phi_A), \tag{2.23}$$

where α_q and β_q are constants, q is an integer indicating the order of the sideband and τ is the delay between XUV and infrared pulses. $\Delta\Phi_{2q} = \phi_{2q-1} - \phi_{2q+1}$ corresponds to the phase difference between consecutive harmonics and $\Delta\phi_A$ is the phase acquired during the electronic transition. The phase of the sideband oscillation thus depends on two unknown quantities: $\Delta\Phi_{2q}$ and $\Delta\phi_A$. Some assumptions need to be made in order to extract only $\Delta\Phi_{2q}$. As proposed in [29], the atomic phase often has a minor contribution and can therefore be neglected for the extraction of the "photonic" phase $\Delta\Phi_{2q}$.

Since $\Delta\Phi_{2q}$ describes a phase difference, the harmonic phases can be calculated by arbitrarily setting the phase of the first harmonic to zero and adding the phase differences consecutively. The time-dependent intensity of the pulse train can then be reconstructed by a monochromatic approximation of each harmonic order q:

$$I(t) \approx \left| \sum_q \sqrt{I_q} \mathrm{e}^{-\mathrm{i}(q\omega t - \Phi_q)} \right|^2 \tag{2.24}$$

This technique was introduced by Paul and co-workers in 2001 [29] and named the *Reconstruction of Attosecond Beating by Interference of Two-color Transitions* (RABBIT). It provided the first evidence that the process of HHG indeed creates an attosecond pulse structure in the temporal domain.

2.6.5 Pulse Reconstruction

In order to perform a RABBIT scan at the IXB, the XUV-IR interferometer was used. The delay was scanned over a total range of 100 fs. The photoelectron spectrum was recorded with the electron side of the VMIS. Only the angle-integrated spectrum is used for the analysis, since it provides enough information to reconstruct the APT. The yield of each sideband was extracted by energy integrating the individual peaks in the spectrum. Figure 2.24(a) displays the yield of different sidebands plotted as a function of time. The oscillation period corresponds to twice the driving field frequency ω, as expected. The phase is then retrieved by a cosine fit to the oscillation signal for all sidebands, as shown in red in figure 2.24(a). Using equation 2.24 and the XUV spectrum measured at the same

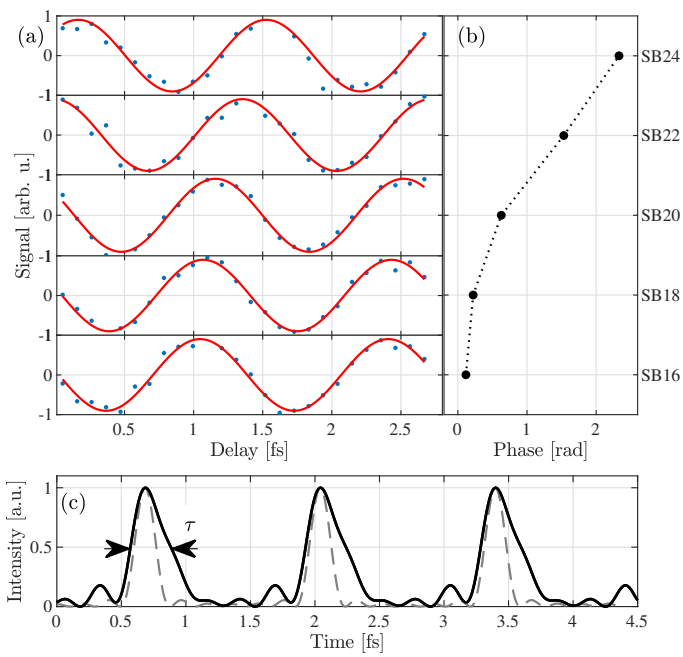

Figure 2.24: (a) Sidebands 16-21 are integrated across their spectral width and plotted as function of the delay (blue dots). A cosine fit (red line) extracts the phase of each sideband, plotted in (b). In (c) the reconstructed APT is shown using the extracted phase (black line). Also shown is the Fourier transform limited pulse using the same harmonic components (grey dashed line).

time, the APT is reconstructed and portrayed in figure 2.24(c). A pulse duration of 313 as FWHM is measured from the temporal reconstruction. As a comparison is shown the Fourier transform limited pulse train using the same spectral components, which has a pulse duration of around 180 as. Hence, the intrinsic chirp, introduced by the process of HHG, stretches the pulse duration by 133 fs.

Chapter 3

Photoionization

Photoionization describes an interaction between a photon and an atom leading to the release of one or several electrons such that the atom becomes an ion. For the bound electron to overcome the potential barrier created by the binding Coulomb force, the photon energy needs to be sufficiently high. For noble gases the ionization energy I_p lies between 12-25 eV, which requires a photon in the XUV regime.

A common approach for studying the photoionization process is to detect and characterize the outgoing electron. During photoionization, this electron undergoes a transition from a bound to a continuum state, where the final energy depends on the photon energy and the ionization energy of the atom. Generally, this transition occurs via various ionization channels corresponding to different initial or final angular momenta. For the full characterization of all ionization channels the amplitude needs to be determined and, when they add coherently, also the phase of each angular momentum channel.

It may be tempting to assume that in order to study single-photon ionization, which is the aim of this work, the interaction with one photon is enough to characterize the process. In practice however, it is in general not possible to access all involved parameters, in particular the phases of the individual angular momentum components [75, 76, 77]. Two-photon techniques, like RABBIT, provide the means to determine those phases by interferometry. Such studies combine either attosecond XUV pulses generated via HHG [29, 78] or FEL femtosecond pulses [79] with infrared pulses from optical lasers. The absorption of a second photon, which is essential for interferometry, adds complexity, making the analysis difficult. So far, studies of multi-channel ionization using two-photon interferometry have therefore been limited to the characterization of the final two-photon

wave packet [78, 79, 80].

Paper I presents a method that enabling the complete characterization of the single-photon ionization from the $2p^6$ ground state in neon. Using angle-resolved RABBIT, the amplitude and phase for different ionization channels are measured as a function of the kinetic energy of the photoelectron. In the following, the key theoretical tools essential for the method are derived. The transition between two continuum states involved in our method is shown to be independent of the atom, i.e. universal, and thus predictable. Finally, the angle-resolved photoelectron spectra for single- and two-photon transitions are analyzed and our method is applied to extract single-photon amplitudes and phases.

3.1 Theoretical Tools

Describing the process of photoionization theoretically requires some basic concepts of quantum mechanics. Starting from the time-independent Schrödinger equation, both bound and continuum states can be expressed in a central field approximation. For the coupling of the electron to the electromagnetic field, transition matrix elements are introduced in an asymptotic approximation [81].

3.1.1 Bound and Continuum States

Atomic states are usually defined as eigenstates $\phi(\mathbf{r})$ of the time-independent Schrödinger equation:

$$\Big(-\frac{\hbar^2}{2\mathrm{m}_e}\nabla^2 + V(\mathbf{r})\Big)\phi(\mathbf{r}) = E\phi(\mathbf{r}), \tag{3.1}$$

where E is the energy eigenvalue, $\hbar$ is Planck's reduced constant, m_e is the electron mass and $V(\mathbf{r})$ is the potential felt by the electron. An electron interacting with the nucleus of charge Z feels a force caused by the Coulomb potential and the interaction with other electrons, often approximated by a radially symmetric potential $V(r)$ in the central field approximation. In this case, the wave function can be written as a product of a radial and an angular part and characterized by the quantum numbers l and m:

$$\phi_{lm}(\mathbf{r}) = R_l(r)Y_{lm}(\theta,\varphi), \tag{3.2}$$

where $R_l(r)$ is the radial part and $Y_{lm}(\theta,\phi)$ are the spherical harmonics describing the angular part. Here, spherical coordinates are used, where r,θ and φ describe the radial distance, the polar angle and the azimuthal angle, respectively.

The spherical harmonics are eigenstates of the Laplace operator in spherical coordinates. Thus, inserting equation (3.2) into (3.1) and using the simplification $f_l = rR_l$, leads to the *radial Schrödinger equation*:

$$\Big(-\frac{\hbar^2}{2\mathrm{m}_e}\frac{\mathrm{d}^2}{\mathrm{d}r^2} + \frac{l(l+1)\hbar^2}{2\mathrm{m}_e r^2} + V(r)\Big) f_l(r) = E f_l(r), \tag{3.3}$$

which is effectively a one-dimensional version of equation (3.1), when defining the effective potential:

$$V_{\text{eff}}(r) = V(r) + \frac{l(l+1)\hbar^2}{2\mathrm{m}_e r^2}, \tag{3.4}$$

where the second term is referred to as the *centrifugal potential*. The solutions of equation (3.3) depend drastically on whether the eigenvalues E are positive or negative. For negative eigenvalues $E < 0$, the eigenstates are referred to as *bound states* ϕ_{nlm} and are characterized by another discrete quantum number n. Each bound state is associated to a negative energy eigenvalue $E_n \propto -Z^2/n^2$.

For positive eigenvalues $E > 0$, the solutions are referred to as *scattering states* with the radial part $R_{kl}(r)$. Here, l remains a discrete quantum number, whereas k is continuous and connected to the energy as $k = \sqrt{2\mathrm{m}_e E}/\hbar$. The radial wavefunction can then be written in its asymptotic limit as:

$$\lim_{r\to\infty} R_{kl}(r) = \sqrt{\frac{2}{\pi k}}\frac{1}{r}\sin\Big(kr + \frac{Z\ln(2kr)}{k} + \eta_l(k) - \frac{\pi l}{2}\Big). \tag{3.5}$$

The second term in the sine function is a logarithmic divergence characteristic for the Coulomb potential created by the ionic core. The scattering phase $\eta_l(k)$ consists of two contributions: $\eta_l(k) = \varsigma_l(k) + \delta_l(k)$, where $\varsigma_l(k) = \arg[\Gamma(l + 1 + \mathrm{i}Z/k)]$ is the Coulomb phase shift and $\delta_l(k)$ is a correction term for the short-range deviation of the potential compared to a pure Coulomb potential. Finally, the last term describes the effect of the centrifugal barrier. It is worth emphasizing that the scattering phase and the centrifugal barrier effect both depend on the quantum number l, which plays an important role in paper I.

The wave function describing an outgoing electron with momentum $\mathbf{k}$ can be expanded in what is known as *partial waves*, as they in practice often combine to a set of eigenfunctions forming a so-called *electron wave packet* (EWP). Such a superposition of partial waves can be written as:

$$\phi_{\mathbf{k}}(r,\theta,\varphi) = (8\pi)^{3/2}\sum_{l,m} \mathrm{i}^l \mathrm{e}^{\mathrm{i}\eta_l(k)} Y^*_{lm}(\hat{k}) R_{kl}(r) Y_{lm}(\hat{r}), \tag{3.6}$$

where $\hat{k} = \mathbf{k}/k$ and $\hat{r} = \mathbf{r}/r$. From this equation, scattering states can be identified as spherical waves with wave number k, modified by the spherical harmonics

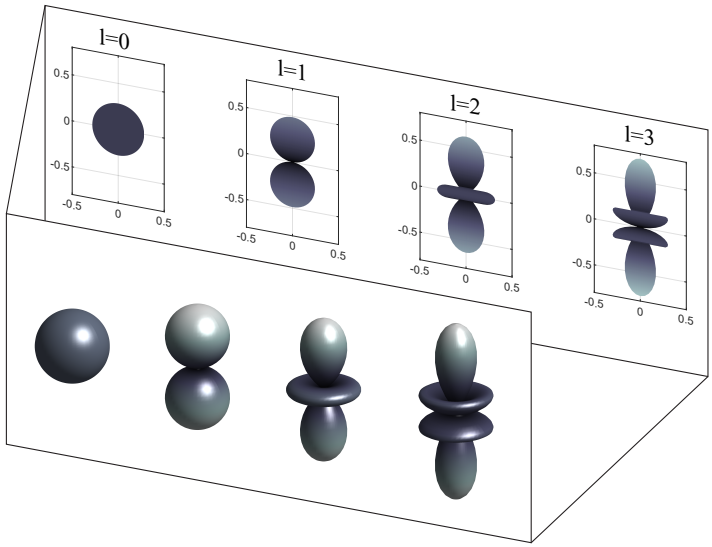

Figure 3.1: Spherical harmonics $Y_{lm}(\theta, \varphi)$ for $l = 0, 1, 2, 3$ and $m = 0$.

$Y_{lm}(\theta, \varphi)$. Figure 3.1 shows the first few orders of the spherical harmonics. The quantum number l, called the angular quantum number or short *angular momentum*, hereby imposes the number of non-centrosymmetric nodes. This dependence is a fundamental element of the method presented in paper 1.

3.1.2 Two-Photon Interferometry

The transition of an electron from the ground state to a scattering state is characterized by its transition matrix element. In the following, we focus on laser-assisted two-photon transitions, where an XUV photon with angular frequency Ω is absorbed, taking an electron from a bound state $|i\rangle$ to an intermediate scattering state $|\nu\rangle$. Subsequently, an infrared photon with angular frequency ω is either absorbed or emitted, in a continuum-continuum (cc) transition from $|\nu\rangle$ to the final scattering state $|k\rangle$. Note that for simplicity the states are written in Dirac notation, where the corresponding wave functions are calculated as: $\phi_i(r) = \langle r|i\rangle$ for the initial state with negative energy E_i and $\phi_{kLm} = \langle r|k\rangle$ for the final state with positive energy $E_k = k^2\hbar^2/2\mathrm{m}_e = E_i + \hbar\Omega \pm \hbar\omega$. Assuming linear polarization for both the XUV and the infrared field along the axis $\hat{z}$ and using second-order perturbation theory, the transition matrix element can be written as [81]:

$$M_{ki}^{(\pm)} \propto \lim_{\epsilon \to 0^+} \int_\nu \frac{\langle k|z|\nu\rangle \langle \nu|z|i\rangle}{\hbar\Omega^{(\pm)} - E_\nu + E_i + \mathrm{i}\epsilon}. \tag{3.7}$$

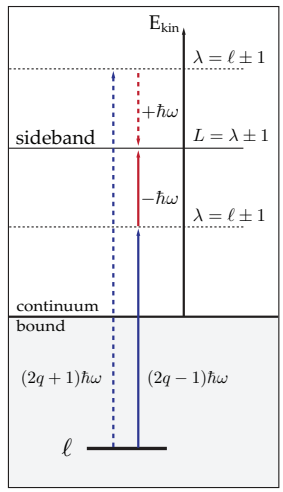

Figure 3.2: Schematic representation of the RABBIT technique. An XUV photon (blue arrow) initiates the transition from the ground state with angular momentum ℓ to the intermediate state with angular momentum λ. An additional infrared photon leads to the final state with angular momentum L. The sideband is reached via two interfering quantum path, as indicated by the solid and dashed lines.

The integral runs over an infinite number of continuum states, while the sum of all discrete states (resonances) are neglected. The $(\pm)$ refers to two different paths: the infrared photon is either absorbed $(+)$ with $\Omega^{+} = (2q-1)\omega$ or emitted $(-)$ with $\Omega^{-} = (2q+1)\omega$. As shown in figure 3.2, for two consecutive harmonics, the two paths interfere at $\Omega_q = 2q\omega + E_i/\hbar$ forming a sideband.

The final energy states can have different angular momenta and magnetic quantum numbers. In addition, the same final state can be reached via a variety of different channels following the selection rules of an electric dipole transition. The angular momentum of the intermediate state λ relates to the ground state angular momentum ℓ as $\lambda = \ell \pm 1$, and the final state angular momentum L to the intermediate state as $L = \lambda \pm 1$.

The transition amplitude is a function of the delay τ between infrared and XUV pulses and can be written as a sum of partial waves:

$$\mathcal{A}^{(\pm)}_{Lm}(\theta,\phi,\tau) = -\frac{\mathrm{i}e^2}{\hbar} E_{XUV}(\Omega) E_{IR}(\omega) \mathrm{e}^{(\pm)\mathrm{i}\omega\tau} \sum_{\lambda} M^{(\pm)}_{L\lambda\ell m} Y_{Lm}(\theta,\phi), \quad (3.8)$$

where the transition matrix element for each partial wave can be decomposed into its amplitude and its phase:

$$M^{(\pm)}_{L\lambda\ell m} = C^{m}_{L\lambda} C^{m}_{\lambda\ell}\, \sigma^{(\pm)}_{L\lambda\ell}\, \mathrm{e}^{\mathrm{i}(\phi^{(\pm)}_{L\lambda} + \varphi^{(\pm)}_{\lambda\ell} + \Phi_{2q\mp1})}. \quad (3.9)$$

Here, m is the magnetic quantum number of the initial state, $C^m_{L\lambda}$, $C^m_{\lambda\ell}$ are angular coefficients equal to $\langle Lm|Y_{10}|\lambda m\rangle$ and $\langle \lambda m|Y_{10}|\ell m\rangle$, and $\sigma^{(\pm)}_{L\lambda\ell}$ is the radial amplitude. The phase consists of three terms: $\varphi^{(\pm)}_{\lambda\ell}$ is the phase associated to one-photon ionization, $\phi^{(\pm)}_{L\lambda}$ is the continuum-continuum (cc)-phase, and $\Phi_{2q\mp1}$ is the phase of the $(2q \mp 1)^{\text{th}}$ harmonic field.

In an angle-resolved RABBIT experiment, the final states for a given magnetic quantum number m add coherently, whereas states with different m add incoherently. The resulting signal of a sideband resolved in angle and delay can be written as [82]:

$$I_{SB}(\theta,\tau) = \int_0^{2\pi} \mathrm{d}\phi \sum_m \Big| \sum_L \Big(\mathcal{A}^{(+)}_{Lm}(\theta,\phi,\tau) + \mathcal{A}^{(-)}_{Lm}(\theta,\phi,\tau) \Big) \Big|^2 \qquad (3.10)$$

The angular dependence of the sidebands is therefore given by the contributions of the individual states with different angular momenta as well as the interference between them.

The additional interaction with the second photon leads to an increase in the number of angular channels, as shown in figure 3.5, and modifies the radial amplitude and phase of the outgoing photoionization wavepacket [81, 83, 84]. Hence, the angular structure of the sidebands not only depends on the different partial waves of the angular momentum channels reached via single photon ionization, but is also strongly influenced by the cc-transition [83, 85]. In order to disentangle the two contributions, an investigation of the cc-transition is presented in the following. It is found that its universal behavior allows a characterization of the cc-phase independently of the atom and that the cc-amplitudes can be connected via Fano's propensity rule.

3.1.3 Continuum-Continuum Transitions

The cc-transition has recently attracted much attention [81, 84, 86] and it can be shown that for certain aspects it is independent of the atom, while it mostly depends on the angular momenta involved in the transition. In the following, both the amplitude $\sigma^{(\pm)}_{L\lambda\ell}$ and the phase $\phi^{(\pm)}_{L\lambda}$ are studied and the universality is demonstrated based on calculations using angular-channel-resolved many-body perturbation theory, performed in collaboration with Eva Lindroth and Jimmy Vindbladh [87].

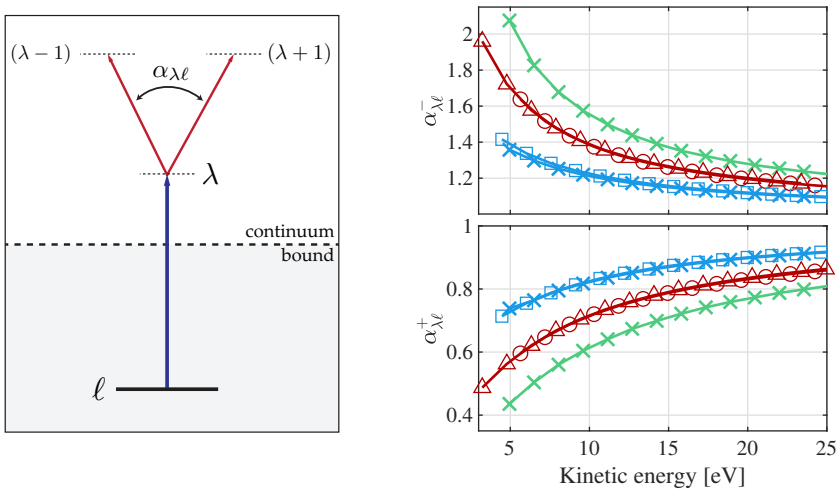

Figure 3.3: Calculated amplitude ratios for the absorption $\alpha^+_{\lambda\ell}$ and emission $\alpha^-_{\lambda\ell}$ processes. The left panel sketches how the ratio connects the two cc-transitions exemplified for $\alpha^+_{\lambda\ell}$. The right panels show the calculated curves corresponding to different intermediate states (λ=1,2,3 in blue, red, green, respectively) and different atoms/initial states (square, He, 1s initial state); (cross, Kr, 3d); (triangle, Ne, 2p); (circle, Ar, 3p).

First, the two-photon radial amplitudes $\sigma^{(\pm)}_{(\lambda\pm1)\lambda\ell}$ for a given intermediate state with angular momentum λ and, in accordance with the selection rules, the two final states $L = (\lambda \pm 1)$ are compared. Figure 3.3 presents the calculated ratio between the radial amplitudes for increasing and decreasing angular momenta, defined as:

$$\alpha^{(\pm)}_{\lambda\ell} = \frac{\sigma^{(\pm)}_{(\lambda-1)\lambda\ell}}{\sigma^{(\pm)}_{(\lambda+1)\lambda\ell}}. \tag{3.11}$$

The different curves correspond to the ionization of valence electrons from various atoms and initial states, as indicated in the figure caption. As can be seen, the ratio shows a universal behavior, independent of the atom. Only the orbital angular momentum of the intermediate state, λ, is of importance, as predicted by Fano's propensity rule for the cc-transitions [86]. This result is very promising as it allows us to connect two different ionization channels via the constant $\alpha^{(\pm)}_{\lambda\ell}$ and hence to reduce the number of unknown parameters in the process.

Further, the phases introduced by the cc-transitions are considered. Figure 3.4 shows the result of the calculated cc-phase for increasing $\phi^{(\pm)}_{(\lambda+1)\lambda}$ and decreasing

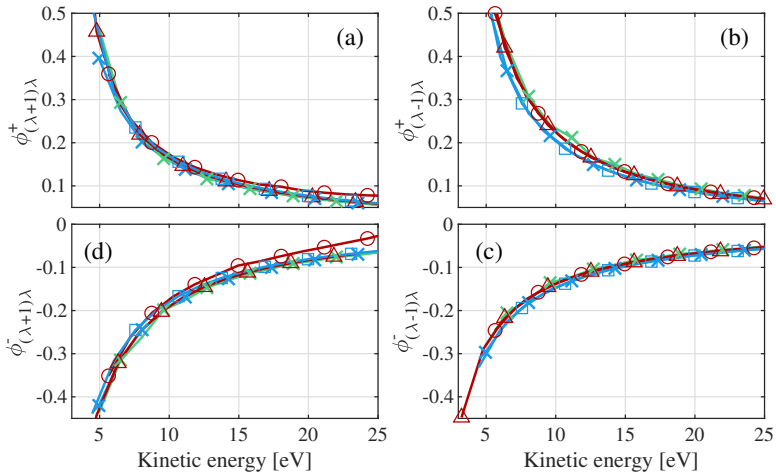

Figure 3.4: Calculated continuum-continuum phases $\phi_{L\lambda}^{(\pm)}$ for the absorption (a,b) and emission (c,d) processes. The different curves correspond to different intermediate states (λ=1,2,3 in blue, red, green, respectively) and different atoms/initial states (square, He, 1s initial state); (cross, Kr, 3d); (triangle, Ne, 2p); (circle, Ar, 3p). (a,d) refer to transitions with increasing angular momentum, $L = \lambda + 1$, while in (b,c), $L = \lambda - 1$.

angular momenta $\phi_{(\lambda-1)\lambda}^{(\pm)}$, in case of absorption (+) or emission (-). Several colors and markers, corresponding to different intermediate angular momenta and atoms respectively, are detailed in the figure caption. For both increasing and decreasing angular momenta, all curves are in good agreement with each other. Only for certain energies do the cc-phases depend slightly on the intermediate angular momentum and not at all on the atomic system. For the absorption, the cc-phase decreases as a function of kinetic energy and is positive, while for the emission, it increases and is negative. Note that the phases are not mirror images of one another, i.e. $\phi_{L\lambda}^{+} \neq -\phi_{L\lambda}^{-}$. To conclude, these results show that the variation of the continuum-continuum phase can be seen as universal, independent of the atom.

3.2 Measuring Channel-Resolved Single-Photon Ionization

As is clear from equation 3.8, the coherent superposition of different partial waves leads to an interference imprinted in the angular distribution of the emitted electrons. The detection of the angular distribution of the outgoing electron is therefore required. In addition, two-photon interferometry [29, 78, 88], enables the characterization of the phase of the EWP, which has recently gained much atten-

tion [83, 85, 89, 90]. Figure 3.5 depicts the energies and angular momenta involved in two-photon transitions starting from a p ground state for $m = 0$. In total, there are two intermediate states, s and d, and two final states, p and f, involved in the transition, enabling three ionization channels: $p \rightarrow s \rightarrow p$, $p \rightarrow d \rightarrow p$ and $p \rightarrow d \rightarrow f$. Note that for $m = \pm 1$ only the path via the d intermediate state exists. The angular distribution of the different intermediate and final states is proportional to the spherical harmonics, which is why they are shown in figure 3.5. Additionally, the superposition of the various angular momentum channels, leading to the resulting angular distribution of the sidebands, is indicated. As illustrated, the photoelectron angular distributions are probed by two interfering quantum paths based on the RABBIT technique (solid and dashed lines).

In the following, it is demonstrated that the photoelectron angular distributions, in combination with the universality of the cc-transitions, provide the needed information to further disentangle the different angular momentum channels. To fully describe the EWP nine unknown parameters need to be determined, one of them being the single-photon phases. However, only the two-photon amplitude can be extracted from this approach. Hence, a similar method is presented, where only one XUV photon is used for the ionization and, in combination with the previously extracted phases, it is possible to also access the one-photon amplitudes.

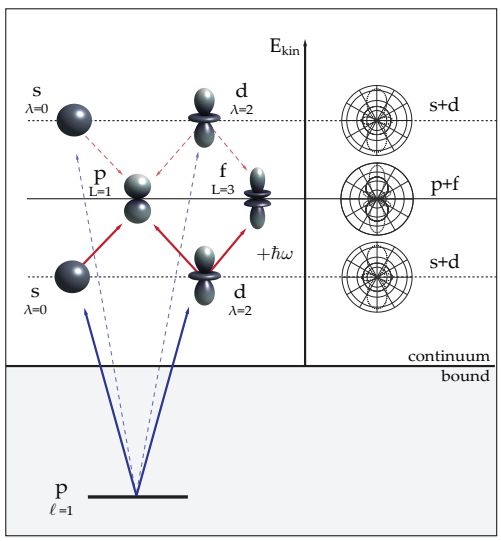

Figure 3.5: Angular channels involved in the two-photon transition. The photoionization from the p-ground state towards s- and d- continuum states (blue arrows) is followed by the interaction with an additional infrared photon (red arrows) leading to the final p- and f states. The two interfering quantum path needed for the RABBIT technique, are indicated by the solid and dashed lines.

3.2.1 Single-Photon Phase Characterization

The two-photon transition, as described in equation 3.7, starting from the $2p^6$ ground state of neon results in sidebands, of which the angle- and delay-dependent signal $I_{SB}(\theta, \tau)$ can be written as:

$$I_{SB}(\theta,\tau) \propto \int \mathrm{d}\phi \sum_{m=0,\pm1} \Big| \sum_{\substack{L=1,3 \\ \lambda=0,2}} M^{+}_{L\lambda\ell m} Y_{Lm}(\theta,\phi) \mathrm{e}^{\mathrm{i}\omega\tau} + M^{-}_{L\lambda\ell m} Y_{Lm}(\theta,\phi) \mathrm{e}^{-\mathrm{i}\omega\tau} \Big|^2, \tag{3.12}$$

When expressing the matrix elements as introduced in equation 3.9, and using the knowledge of the cc-transition, shown in figures 3.3 and 3.4, the unknown quantities in equation 3.12 are the single-photon phases $\varphi_{01}^{(\pm)}$ and $\varphi_{21}^{(\pm)}$ for the s- and the d-channel, the radial two-photon amplitudes $\sigma_{101}^{(\pm)}$ and $\sigma_{321}^{(\pm)}$, while $\sigma_{121}^{(\pm)}$ is given by $\sigma_{121}^{(\pm)} = \alpha_{21}^{\pm}\sigma_{321}^{(\pm)}$, and the phase difference $\Delta\Phi_{2q} = \Phi_{2q+1} - \Phi_{2q-1}$ between consecutive harmonic orders. The number of unknown quantities required to describe the ionization process is therefore nine.

The following chapter presents the analysis of the experimental two-photon data and demonstrates that we are able to extract nine observables from the time-dependent photoelectron angular distribution, which then enables the characterization of the nine unknown parameters in equation 3.12. We thus are able to determine the one-photon phases for both angular momentum channels.

3.2.2 Single-Photon Amplitude Characterization

As is clear from the above consideration, only the radial amplitudes of the entire two-photon transition $\sigma_{L\lambda\ell}^{(\pm)}$ can be extracted from the two-photon photoionization experiment. With the aim of measuring only the one-photon radial amplitude $\sigma_{\lambda\ell}$, we performed an experiment with a single XUV photon ionizing the atom. The resulting angle-dependent photoelectron signal is written as:

$$I_{\mathrm{H}}(\theta) \propto \int d\phi \sum_{m=0,\pm1} \Big| \sum_{\lambda=0,2} M_{\lambda\ell m} Y_{\lambda m}(\theta,\phi) \Big|^2. \tag{3.13}$$

Here, $M_{\lambda\ell m}$ is the one-photon matrix element from the ground state with angular momentum ℓ to the final continuum state with angular momentum λ, which can be written as

$$M_{\lambda\ell m} = C^{m}_{\lambda\ell}\, \sigma_{\lambda\ell}\, \mathrm{e}^{\mathrm{i}(\varphi_{\lambda\ell} + \Phi_{2q+1})}. \tag{3.14}$$

Since it is possible to extract the one-photon phases φ_{01}, φ_{21} from the two-photon data, this equation has only two unknown quantities: the radial amplitudes σ_{01} and σ_{21}. As shown in the next chapter, the experimental photoelectron angular distributions enable the assessment of two observables and hence the characterization of the radial single-photon amplitudes.

3.3 Angle-Resolved Photoelectron Spectra

In the following chapter, the experimentally achieved angle-resolved photoelectron spectra are presented for ionization with a single XUV photon, as well as one XUV and one infrared photon. The XUV pulses are produced via HHG in argon. The spectrum is shaped using an aluminum filter, which results in a spectral range from harmonic 11 at around 17 eV up to harmonic 27 at 42 eV. The DVMIS in the application chamber, as described in chapter 2.4.3, is used to detect the 2D projection of the 3D photoelectron emission distribution onto the MCP detector. In order to retrieve the electron momentum distribution, an inverse Abel inversion is performed. For the two-photon data, the IR-XUV interferometer, presented in chapter 2.6.3, introduces the delay between the two pulses in a range of 100 fs with a step size of 100 as. The inverse Abel inversion is highly sensitive to the signal-to-noise ratio of the recorded images, which is why the entire delay range was resampled to only one period of the infrared pulse ($\approx$ 2.7 fs) before the inversion was performed. In doing so, the statistics of each delay step were increased by a factor of around 38. As a result, the quality of the inverted momentum maps was sufficient enough to determine the delay dependence of the photoelectron angular distributions for sidebands up to the 24^{th} order.

3.3.1 Single-Photon Emission Spectra

Figure 3.6(a) shows the momentum distribution taken in neon ionized by a single XUV photon. The individual rings correspond to electrons released by consecutive harmonic orders. The first ring is due to ionization by absorption of the 15^{th} harmonic, which is the first one to overcome the ionization potential of neon at 21.6 eV. Figure 3.6(b) shows the photoelectron spectrum as a function of the kinetic energy.

A common way to analyze the angular distribution is by using an expansion in Legendre polynomials up to the second order. The resulting signal can be written as

$$I_{\mathrm{H}}(\theta) = h_0 + h_2 P_2(\cos\theta), \tag{3.15}$$

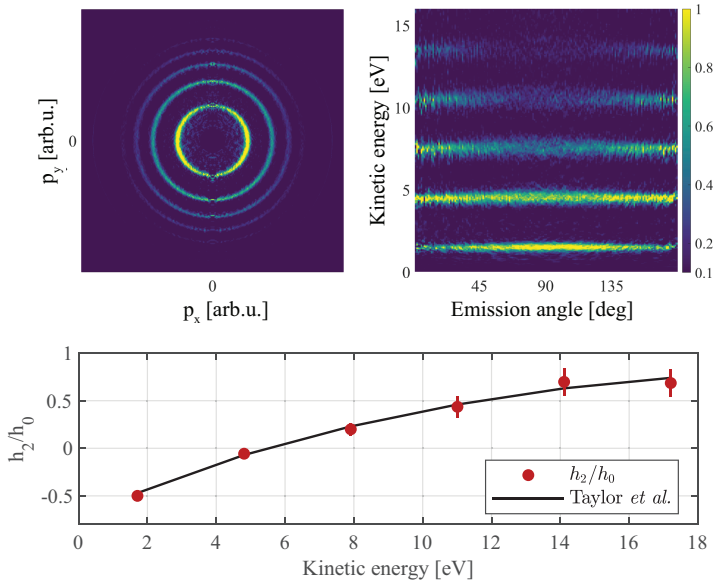

Figure 3.6: (a) Photoelectron momentum distribution retrieved by an Abel-inversion of the VMI image. (b) Angle-resolved photon photoelectron spectrum. (c) Extracted asymmetry coefficient h_2 as a function of the energy. The red dots are the extracted values with error bars returned from the fit and the black line are literature values from Taylor et al. [91].

where $P_2(x) = (3x^2 - 1)/2$. Each line in figure 3.6 (b) is therefore energy-integrated and equation 3.15 is fitted to the resulting angular distribution. Figure 3.6(c) shows the obtained asymmetry coefficients h_2/h_0 as a function of the kinetic energy of the electron. The black line corresponds to calculated values from Taylor *et al.* [91], and good agreement with the data was found. As can be seen, the emission is the strongest at 90° for contribution from the lowest harmonic, which is represented by the negative value of h_2/h_0. For photoelectrons released by higher harmonics, the yield at 0° and 180°, e.g., along the laser polarization, is the strongest.

3.3.2 Two-Photon Emission Spectra

For the case of a two-photon ionization, sidebands can be found in between contributions from electrons from the direct ionization. The delay between the XUV and the infrared τ plays an important role for the sideband yield, as already discussed in chapter 2.6.4. Figure 3.7 presents the angular-resolved delay-integrated momentum distribution in (a) and the corresponding photoelectron spectrum in (b) as well as the angular-integrated delay-dependent spectrum in (c). It shows contributions from the absorption of harmonics 15 to 25 as well as sidebands 16

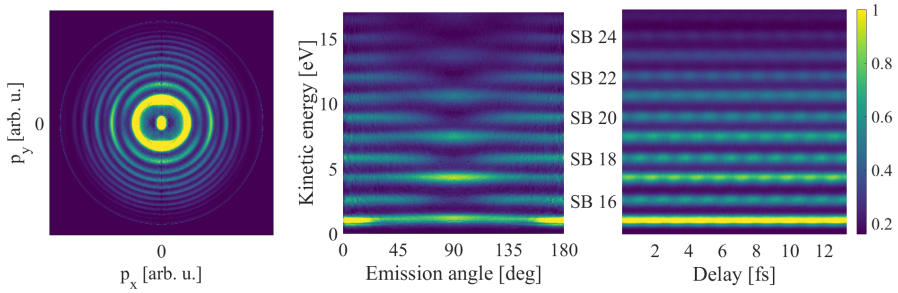

Figure 3.7: (a) Photoelectron momentum distribution retrieved by an Abel-inversion of the VMI image after integrating over all delays. (b) Angle-resolved photon photoelectron spectrum. (c) Angle-integrated photoelectrons spectrum as a function of the delay.

to 24. The sidebands in figure 2(c) oscillate at a frequency 2ω, as expected from equation 2.23. Consequently, the photoelectron peaks corresponding to the absorption of harmonics oscillate with the same frequency but the opposite phase, due to a redistribution of the electrons from the main absorption peaks to the sidebands. The sidebands are maximized at the angles of 0° and 180°, corresponding to emission along the polarization axis of the XUV and IR fields.

Finally, figure 3.8(a) shows the delay and angle dependence of the 16th sideband integrated in energy. The angle-resolved oscillation phase is extracted by fitting a cosine to the temporal evolution for all recorded angles. The red dots in figure 3.8(a) show the measured phase as a function of the emission angle. Despite the difference in signal strength, an oscillation with frequency 2ω can be seen at all angles. The phase of the oscillation depends strongly on the angle and varies by more than 2 rad between 0° and 90°. The experimentally retrieved phase is compared with simulations based on the angular-channel-resolved many-body perturbation theory (black line). In 3.8(b) the measured phases for sidebands 18-24 are shown together with the corresponding simulations. The agreement between the measurement and the simulations is overall very convincing. The values only start to deviate for sideband 24, which might be due to lower statistics as the intensity is comparably low for higher harmonic orders.

Similarly to the single-photon case, the angular distribution of the sidebands results from the superposition of partial waves, in this case with angular momenta p and f as shown in figure 3.5 The angular distribution of the sidebands can again be described by Legendre polynomials. However, since the transition involves the interaction with two photons, and there is no parity mixing, the expansion consists of three polynomials: $P_0(x) = 1$, $P_2(x) = (3x^2 - 1)/2$, and $P_4(x) = (35x^4 - 30x^2 + 3)/8$. The sideband yield can be written as a function

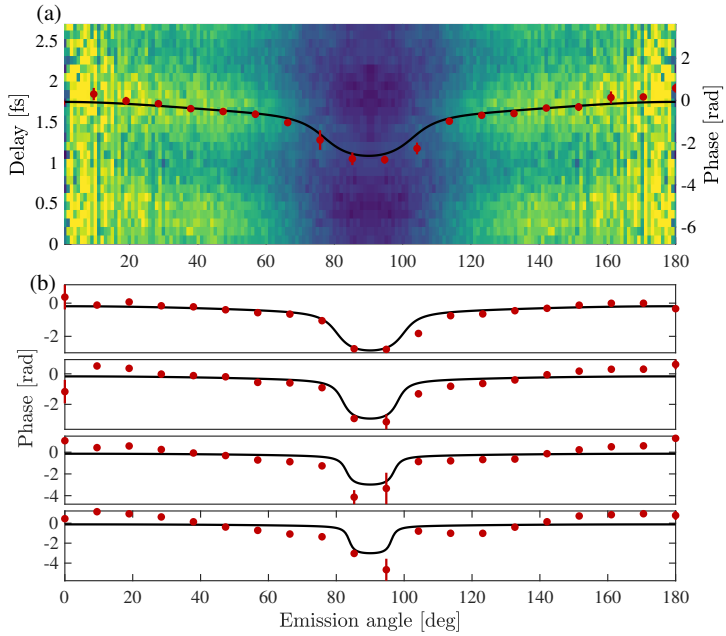

Figure 3.8: (a) shows the Energy-integrated sideband 16 as a function of angle and delay. The red dots are the extracted phase with error bars returned from the fit, and the black line shows the simulated result. In (b) the extracted phases for sideband 18-24 are shown from top to bottom respectively.

of the delay between XUV and infrared pulses τ [92, 93] according to:

$$I_{\mathrm{SB}}(\theta, \tau) = h_0(\tau)P_0(x) + h_2(\tau)P_2(\cos\theta) + h_4(\tau)P_4(\cos\theta). \tag{3.16}$$

Equation 3.16 is fitted to the experimentally retrieved angular distributions for each delay step. Figure 3.9 shows the resulting asymmetry coefficients $h_0(\tau)$, $h_2(\tau)$ and $h_4(\tau)$ of sideband 18 as a function of the delay with the corresponding error bars retrieved by the standard deviation returned by the fit. As is clear from Figure 3.9, each $h_i(\tau)$ oscillates with the delay τ at the frequency 2ω and is therefore fully determined by three observables: its mean value, its amplitude and its phase. Thus, a total of nine parameters are required to describe the angle and delay dependence of the sideband signal $I_{\mathrm{SB}}(\theta, \tau)$. This implies that the nine unknown quantities in equation 3.12 can be determined through these nine observables.

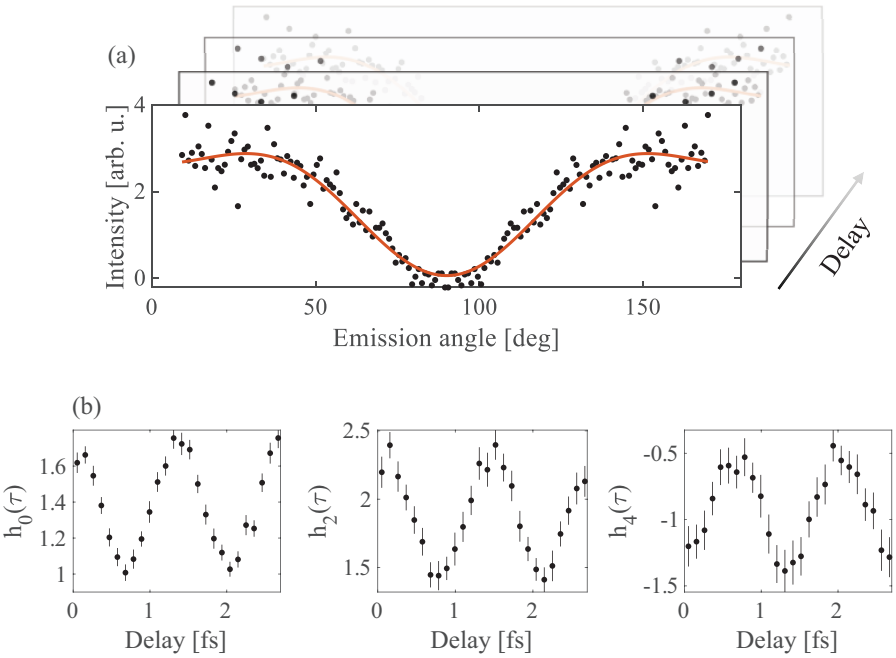

Figure 3.9: (a) Fit of equation 3.16 (red line) to the photoelectron angular distribution (black dots), which is repeated for all recorded delay steps. Each fit results in one point in (b), showing the delay dependence of the obtained coefficients $h_i(\tau)$, $i = 0, 2, 4$ for sideband 18. The error bars correspond to one standard deviation returned from the fit.

3.4 Radial Amplitude and Phase Extraction

The final step consists in connecting the experimental observables for the one- and two-photon cases to the unknown quantities describing the outgoing electron. Firstly, the single-photon phases are extracted from the two-photon emission spectra. In order to do so, Equation 3.12 can be written for all possible states:

$$\begin{aligned} I_{SB}(\theta,\tau) \propto \int \mathrm{d}\phi \Big| &\Big(\Big[M^{+}_{1010} + M^{+}_{1210}\Big] Y_{10}(\theta,\phi) + M^{+}_{3210} Y_{30}(\theta,\phi)\Big) \mathrm{e}^{\mathrm{i}\omega\tau} \\ &\Big(\Big[M^{-}_{1010} + M^{-}_{1210}\Big] Y_{10}(\theta,\phi) + M^{-}_{3210} Y_{30}(\theta,\phi)\Big) \mathrm{e}^{-\mathrm{i}\omega\tau}\Big|^2 \\ &+ 2\Big|\Big(M^{+}_{1211} Y_{11}(\theta,\phi) + M^{+}_{3211} Y_{31}(\theta,\phi)\Big) \mathrm{e}^{\mathrm{i}\omega\tau} \\ &\Big(M^{-}_{1211} Y_{11}(\theta,\phi) + M^{-}_{3211} Y_{31}(\theta,\phi)\Big) \mathrm{e}^{-\mathrm{i}\omega\tau}\Big|^2 \end{aligned} \tag{3.17}$$

This can be further expanded by replacing the products of spherical harmonics by an expansion in associated Legendre polynomials, using the following relation:

$$Y_{Lm}(\theta,\phi) = (-1)^m \sqrt{\frac{(2L+1)(L-m)!}{4\pi(L+m)!}} P_L^m(\cos\theta) e^{\mathrm{i}m\phi} \tag{3.18}$$

The absolute square in equation 3.17 results in squared and cross terms between odd Legendre polynomials, which can be replaced by the following identities:

$$\begin{aligned}
\left(P_1^0\right)^2 &= \frac{1}{3}\left(P_0^0 + 2P_2^0\right) \\
P_1^0 P_3^0 &= \frac{1}{7}\left(3P_2^0 + P_4^0\right) \\
\left(P_3^0\right)^2 &= \frac{1}{7}P_0^0 + \frac{4}{21}P_2^0 + \frac{18}{77}P_4^0 + \frac{100}{231}P_6^0 \\
\left(P_1^1\right)^2 &= \frac{2}{3}\left(P_0^0 - P_2^0\right) \\
P_1^1 P_3^1 &= \frac{12}{7}\left(P_2^0 - P_4^0\right) \\
\left(P_3^1\right)^2 &= \frac{12}{7}\left(P_0^0 + P_2^0\right) + \frac{36}{77}P_4^0 - \frac{300}{77}P_6^0
\end{aligned}$$

Note that the associated Legendre polynomials are equal to the regular ones for $m = 0$ and thus $P_L^0 = P_L$ for $L = 0, 2, 4$. The angular coefficients $C_{l,l+1}^m$ are derived by calculating the angular transition matrix element between an initial state with angular momentum ℓ and a final state with angular momentum $\ell + 1$ as:

$$C_{\ell,\ell+1}^m = (-1)^{\ell+m-1}(\ell+1)^{1/2} \begin{pmatrix} \ell+1 & 1 & \ell \\ -m & 0 & m \end{pmatrix}.$$

Finally, only Legendre polynomials of the 0$^{\text{th}}$, 2$^{\text{nd}}$ and 4$^{\text{th}}$ order are left, as all sixth-order terms vanish. Hence, we recover the general form: $I_{\text{SB}}(\theta,\tau) = h_0(\tau) + h_2(\tau)P_2(\cos\theta) + h_4(\tau)P_4(\cos\theta)$, which is identical to equation 3.16. The three

parameters $h_i,\ i = 0, 2, 4$ can thus be identified as:

$$
\begin{aligned}
h_0(\tau) = {} & \frac{25}{9}\Big[(\sigma^+_{101})^2 + (\sigma^-_{101})^2\Big] + \frac{34}{9}\Big[(\alpha^+_2\sigma^+_{321})^2 + (\alpha^-_2\sigma^-_{321})^2\Big] \\
& + 4\Big[(\sigma^+_{321})^2 + (\sigma^-_{321})^2\Big] + \frac{40}{9}\Big[\alpha^+_2\sigma^+_{101}\sigma^+_{321}\cos\big(\varphi^+_{01} - \varphi^+_{21} + \phi^+_{10} - \phi^+_{12}\big) \\
& + \alpha^-_2\sigma^-_{101}\sigma^-_{321}\cos\big(\varphi^-_{01} - \varphi^-_{21} + \phi^-_{10} - \phi^-_{12}\big)\Big] \\
& + \frac{50}{9}\,\sigma^+_{101}\sigma^-_{101}\cos\big(2\omega\tau + \Delta\Phi_{2q} + \varphi^+_{01} - \varphi^-_{01} + \phi^+_{10} - \phi^-_{10}\big) \\
& + \frac{40}{9}\Big[(\alpha^-_2\sigma^+_{101}\sigma^-_{321}\cos\big(2\omega\tau + \Delta\Phi_{2q} + \varphi^+_{01} - \varphi^-_{21} + \phi^+_{10} - \phi^-_{12}\big) \\
& + \alpha^+_2\sigma^+_{321}\sigma^-_{101}\cos\big(2\omega\tau + \Delta\Phi_{2q} + \varphi^+_{21} - \varphi^-_{01} + \phi^+_{12} - \phi^-_{10}\big)\Big] \\
& + \frac{68}{9}\alpha^+_2\alpha^-_2\sigma^+_{321}\sigma^-_{321}\cos\big(2\omega\tau + \Delta\Phi_{2q} + \varphi^+_{21} - \varphi^-_{21} + \phi^+_{12} - \phi^-_{12}\big) \\
& + 8\,\sigma^+_{321}\sigma^-_{321}\cos\big(2\omega\tau + \Delta\Phi_{2q} + \varphi^+_{21} - \varphi^-_{21} + \phi^+_{32} - \phi^-_{32}\big)
\end{aligned}
$$

$$
\begin{aligned}
h_4(\tau) = {} & \frac{24}{7}\Big[(\sigma^+_{321})^2 + (\sigma^-_{321})^2\Big] + \frac{16}{7}\Big[\alpha^+_2(\sigma^+_{321})^2\cos\big(\phi^+_{32} - \phi^+_{12}\big) \\
& + \alpha^-_2(\sigma^-_{321})^2\cos\big(\phi^-_{32} - \phi^-_{12}\big)\Big] + \frac{80}{7}\Big[\sigma^+_{101}\sigma^+_{321}\cos\big(\varphi^+_{01} - \varphi^+_{21} + \phi^+_{10} - \phi^+_{32}\big) \\
& + \sigma^-_{101}\sigma^-_{321}\cos\big(\varphi^-_{01} - \varphi^-_{21} + \phi^-_{10} - \phi^-_{32}\big)\Big] \\
& + \frac{48}{7}\,\sigma^+_{321}\sigma^-_{321}\cos\big(2\omega\tau + \Delta\Phi_{2q} + \varphi^+_{21} - \varphi^-_{21} + \phi^+_{32} - \phi^-_{32}\big) \\
& + \frac{16}{7}\Big[\alpha^-_2\sigma^+_{321}\sigma^-_{321}\cos\big(2\omega\tau + \Delta\Phi_{2q} + \varphi^+_{21} - \varphi^-_{21} + \phi^+_{32} - \phi^-_{12}\big) \\
& + \alpha^+_2\sigma^+_{321}\sigma^-_{321}\cos\big(2\omega\tau + \Delta\Phi_{2q} + \varphi^+_{21} - \varphi^-_{21} + \phi^+_{12} - \phi^-_{32}\big)\Big] \\
& + \frac{80}{7}\Big[\sigma^+_{321}\sigma^-_{101}\cos\big(2\omega\tau + \Delta\Phi_{2q} + \varphi^+_{21} - \varphi^-_{01} + \phi^+_{32} - \phi^-_{10}\big) \\
& + \sigma^+_{101}\sigma^-_{321}\cos\big(2\omega\tau + \Delta\Phi_{2q} + \varphi^+_{01} - \varphi^-_{21} + \phi^+_{10} - \phi^-_{32}\big)\Big]
\end{aligned}
$$

$$
\begin{aligned}
h_2(\tau) = {} & \frac{50}{9}\Big[(\sigma_{101}^{+})^2 + \sigma_{101}^{-})^2\Big] + \frac{14}{9}\Big[(\alpha_2^{+}\sigma_{321}^{+})^2 + (\alpha_2^{-}\sigma_{321}^{-})^2\Big] \\
& + \frac{32}{7}\Big[(\sigma_{321}^{+})^2 + (\sigma_{321}^{-})^2\Big] \\
& + \frac{80}{9}\Big[\alpha_2^{+}\sigma_{101}^{+}\sigma_{321}^{+}\cos\big(\varphi_{01}^{+} - \varphi_{21}^{+} + \phi_{10}^{+} - \phi_{12}^{+}\big) \\
& + \alpha_2^{-}\sigma_{101}^{-}\sigma_{321}^{-}\cos\big(\varphi_{01}^{-} - \varphi_{21}^{-} + \phi_{10}^{-} - \phi_{12}^{-}\big)\Big] \\
& + \frac{96}{7}\Big[\alpha_2^{+}(\sigma_{321}^{+})^2\cos\big(\phi_{32}^{+} - \phi_{12}^{+}\big) + \alpha_2^{-}(\sigma_{321}^{-})^2\cos\big(\phi_{32}^{-} - \phi_{12}^{-}\big)\Big] \\
& + \frac{60}{7}\big[\sigma_{101}^{+}\sigma_{321}^{+}\cos\big(\varphi_{01}^{+} - \varphi_{21}^{+} + \phi_{10}^{+} - \phi_{32}^{+}\big) \\
& + \sigma_{101}^{-}\sigma_{321}^{-}\cos\big(\varphi_{01}^{-} - \varphi_{21}^{-} + \phi_{10}^{-} - \phi_{32}^{-}\big)\big] \\
& + \frac{100}{9}\sigma_{101}^{+}\sigma_{101}^{-}\cos\big(2\omega\tau + \Delta\Phi_{2q} + \varphi_{01}^{+} - \varphi_{01}^{-} + \phi_{10}^{+} - \phi_{10}^{-}\big) \\
& + \frac{80}{9}\Big[\alpha_2^{-}\sigma_{101}^{+}\sigma_{321}^{-}\cos\big(2\omega\tau + \Delta\Phi_{2q} + \varphi_{01}^{+} - \varphi_{21}^{-} + \phi_{10}^{+} - \phi_{12}^{-}\big) \\
& + \alpha_2^{+}\sigma_{321}^{+}\sigma_{101}^{-}\cos\big(2\omega\tau + \Delta\Phi_{2q} + \varphi_{21}^{+} - \varphi_{01}^{-} + \phi_{12}^{+} - \phi_{10}^{-}\big)\Big] \\
& + \frac{60}{7}\Big[\sigma_{321}^{+}\sigma_{101}^{-}\cos\big(2\omega\tau + \Delta\Phi_{2q} + \varphi_{21}^{+} - \varphi_{01}^{-} + \phi_{32}^{+} - \phi_{10}^{-}\big) \\
& + \sigma_{101}^{+}\sigma_{321}^{-}\cos\big(2\omega\tau + \Delta\Phi_{2q} + \varphi_{01}^{+} - \varphi_{21}^{-} + \phi_{10}^{+} - \phi_{32}^{-}\big)\Big] \\
& + \frac{28}{9}\,\alpha_2^{+}\alpha_2^{-}\sigma_{321}^{+}\sigma_{321}^{-}\cos\big(2\omega\tau + \Delta\Phi_{2q} + \varphi_{21}^{+} - \varphi_{21}^{-} + \phi_{12}^{+} - \phi_{12}^{-}\big) \\
& + \frac{64}{7}\sigma_{321}^{+}\sigma_{321}^{-}\cos\big(2\omega\tau + \Delta\Phi_{2q} + \varphi_{21}^{+}\varphi_{21}^{-} + \phi_{32}^{+} - \phi_{32}^{-}\big) \\
& + \frac{96}{7}\Big[\alpha_2^{-}\sigma_{321}^{+}\sigma_{321}^{-}\cos\big(2\omega\tau + \Delta\Phi_{2q} + \varphi_{21}^{+} - \varphi_{21}^{-} + \phi_{32}^{+} - \phi_{12}^{-}\big) + \\
& \alpha_2^{+}\sigma_{321}^{+}\sigma_{321}^{-}\cos\big(2\omega\tau + \Delta\Phi_{2q} + \varphi_{21}^{+} - \varphi_{21}^{-} + \phi_{12}^{+} - \phi_{32}^{-}\big)\Big]
\end{aligned}
$$

As is clear from these equations, each $h_i(\tau)$ oscillates with the delay τ at frequency 2ω. The values for $\alpha_\lambda^{(\pm)}$ and $\phi_{L\lambda}^{(\pm)}$ are taken from figures 3.3 and 3.4. The nine unknown quantities are now determined through a simultaneous fit of the three analytical expressions of $h_i(\tau)$ (equations above), to the experimentally measured coefficients $h_i(\tau)$ in figure 3.9. The result of this global fit is shown in figure 3.10 for sideband 18. The extracted phases are however not completely independent, since they only appear as differences in the analytical expressions above, which means that they carry a global offset and are not absolute. However, if one of the phases is locked, e.g. φ_{01}^{-}, all of the others can be determined. To map out the

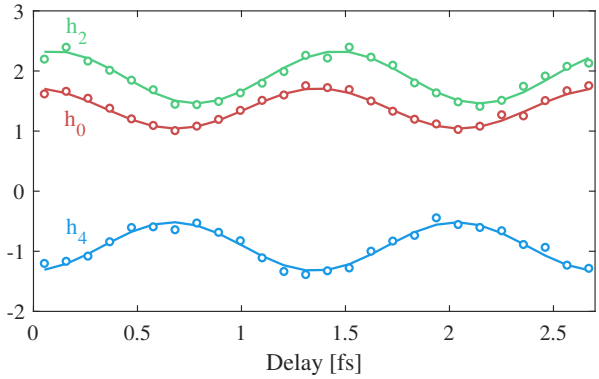

Figure 3.10: Global fit results of sideband 18 for all three asymmetry parameters h_i, where $i = 0, 2, 4$ are shown in red, green and blue respectively.

energy dependence of the one-photon phases, the global fit is repeated for each sideband. Using the fact that $\varphi^{-}_{\lambda 1}(SB_n) = \varphi^{+}_{\lambda 1}(SB_{n+2})$, the evolution of the one-photon phases as a function of energy is iteratively retrieved. Consequently, the superscript $(\pm)$ can be neglected, since in the following the phases are shown as a function of the kinetic energy.

Figure 3.11 displays the extracted phases for $\lambda = 0$ (green) and $\lambda = 2$ (blue). The solid lines correspond to calculated values, based on the angular-channel-resolved many-body perturbation theory. As explained above, the procedure only enables us to determine the phases up to a global phase offset. After adjusting this phase offset, the theoretical and experimental results are in excellent agreement: both the energy dependence and the difference between the s- and the d-channel is well reproduced by the experimental results. The deviation of the highest energy might be due to low statistics caused by the comparably low intensity of the 25^{th} harmonic.

The phase $\varphi_{\lambda\ell}$ results from the radial part of the final scattering state, as introduced in equation 3.5 and is a sum of the Coulomb phase ς_λ, a contribution δ_λ from the short-range potential and a contribution from the centrifugal barrier $-\pi\lambda/2$. In order to investigate the influence of each term, figure 3.11 also shows the Coulomb phases ς_λ (dashed lines), as well as $\varsigma_\lambda + \delta_\lambda - \pi\lambda/2$ (dotted lines), where δ_λ are taken from Kennedy and Manson [94]. The calculated as well as the experimentally retrieved phases are very close to $\varsigma_\lambda + \delta_\lambda - \pi\lambda/2$ (cf. the solid and dotted lines). The difference between φ_{01} and ς_0 is due to the short range potential contributing with $\sim 1.2\pi$, while that between φ_{02} and ς_2 is mainly a result of the effect of the centrifugal barrier, leading to a π phase shift. Both phase shifts are indicated by black arrows. For $\lambda = 2$, short range effects are small because of

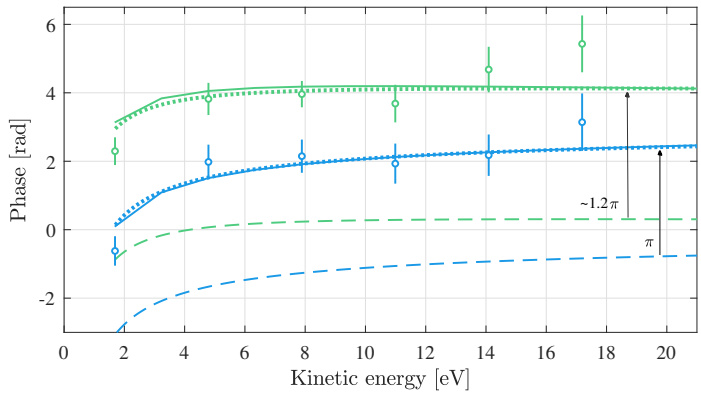

Figure 3.11: Extracted one-photon scattering phases φ_{01} (green) and φ_{21} (blue) for experimental (dots) and simulated data (solid lines). The dashed lines show the contributions from the Coulomb phase ς_λ, where for the dotted lines the effect of the short-range potential and the centrifugal effect is added: $\varsigma_\lambda + \delta_\lambda - \pi\lambda/2$. For $\lambda = 0$ this shift is dominated by the short range potential ($\delta_0 \approx 1.2\pi$) and for $\lambda = 2$ by the centrifugal effect (π), as indicated by the arrows.

the centrifugal barrier that prevents the d-electron from coming close to the core. Since the effect of the short-range potential for the s-electron is comparable to that of the centrifugal barrier for the d-electron, the two contributions almost cancel each other out. Hence, the difference between φ_{01} and φ_{21} is primarily due to the difference in Coulomb phases. The increase of the phases for low energies and the asymptotic behavior for higher energies also follows the behavior of the Coulomb phases.

Finally, in order to fully characterize single photon ionization, the radial amplitudes $\sigma_{\lambda\ell}$ are determined as described above. Again, equation 3.13 is rewritten in terms of Legendre polynomials (equation 3.15) where the coefficients h_0 and h_2 result in:

$$h_0 = \frac{1}{12\pi}\left[\sigma_{01}^2 + \sigma_{21}^2\right], \tag{3.19}$$

$$h_2 = \frac{1}{3\pi}\left[\frac{1}{2}\sigma_{21}^2 + \sigma_{01}\sigma_{21}\cos(\varphi_{01} - \varphi_{21})\right]. \tag{3.20}$$

The coefficients h_0 and h_2 are extracted from the experimental data. Using the single-photon phases obtained previously, the relative radial amplitudes of the $\lambda = 0$ and $\lambda = 2$ channel are determined from equation 3.19 and 3.20. The absolute values of the amplitudes depend on the experimental parameters, in particular the harmonic intensity, which is why figure 3.12 displays the ratio between them. The black solid line corresponds to the calculated values. As can be seen, the ratio is above one for all energies, which agrees well with Fano's propensity rule for one-photon absorption [95].

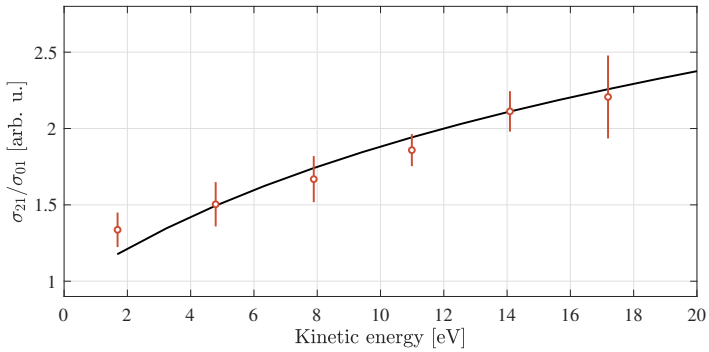

Figure 3.12: Ratio between one-photon amplitudes σ_{21} and σ_{01} extracted from XUV only data (dots). The black line shows the result of the calculations.

The above mentioned extraction of amplitude and phase of the s and d ionization channels fully characterizes the individual matrix elements and thus the photoionization dynamics. In particular, the study of the phases of the different angular momentum channels, unravels the interplay between short-range, correlation and/or centrifugal effects. The method is general and can be applied to other atomic shells (e.g. d).

Chapter 4

Photodissociation

The following chapter focuses on the dissociation dynamics of carbon-based molecules upon ionization by XUV pulses. Paper IV sets out how the Intense XUV Beamline was used to study the diamondoid adamantane based on correlated ion and electron spectroscopy using the double-sided VMIS. Characterizing the charged fragments enabled a detailed investigation of the individual dissociation channels.

Further, as described in papers VI and VII, experiments were carried out at Free-Electron-Lasers (FELs) using pump-probe schemes to resolve dissociation dynamics on a femtosecond timescale.

4.1 Dissociation Dynamics of Adamantane

The molecule adamantane, $C_{10}H_{16}$, is the smallest of all diamondoids with a well-defined structure, shown in figure 4.1, forming a cage of carbon atoms, where each one is fully terminated by hydrogen atoms. Studying adamantane is of interest due to its natural appearance on earth and in space [96, 97, 98].

The ionization threshold of adamantane lies between 8-9 eV, which leads to the production of unstable cations followed by dissociation. Previous studies indicate that the dissociation takes place via several fragmentation channels accompanied by hydrogen migration and often a prior opening of the carbon cage [99, 100]. In a series of studies, we examined the dissociation dynamics of the adamantane dication. The double-ionization threshold of adamantane at 23.9 eV is reached by using harmonics generated in argon with photon energies spanning from 20 to

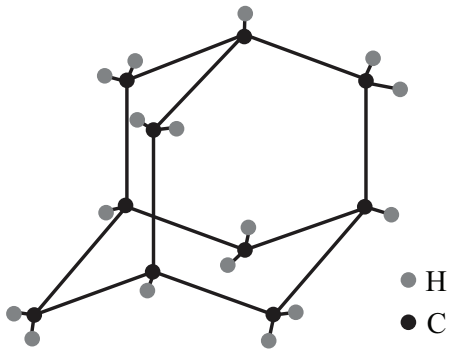

Figure 4.1: Schematic illustration of the structure of adamantane

45 eV. The resulting charged particles were detected using the double-sided VMIS to simultaneously record the ion and electron momentum distributions and the time-of-flight spectrum.

The adamantane sample, which is solid at room temperature, was introduced into the application chamber using the Even-Lavie valve. The powder was inserted into a cartridge, which was heated to 100° C to ensure a constant vapor pressure and the gaseous sample was then picked up by a helium carrier gas with a 1 bar backing pressure injected through the cartridge.

4.1.1 Fragmentation Landscape

Figure 4.2 presents the mass spectrum, retrieved from the time-of-flight spectrum. A rich fragmentation landscape can be observed. The strongest peak at m/q=2 u/e originates from the helium carrier gas. The peak at m/q=136 u/e corresponds to the singly charged parent ion. In between can be seen the production of a wide distribution of $C_nH_x^+$. Individual islands can be identified corresponding to groups of C_n, $n = 2 - 9$. The peaks within each group arise from various amounts of hydrogen atoms attached to the carbon chain, as shown in the inset in figure 4.2. This is an indication of strong intranuclear rearrangements, in particular hydrogen migration. If such rearrangements take place prior to the fragmentation, a cage opening is likely to occur, as indicated by Candian *et al.* [99]. It is not possible to see the dication or any other doubly-charged fragments in the mass spectrum at the time of the detection. However, there are indications in the spectrum hinting towards dynamics initiated by multiple ionization of the parent ion. For instance, the peak of the C_2H_5 fragment appears to be widened compared to its neighboring peaks, as shown in the inset in figure 4.2, signifying a higher kinetic energy distribution.

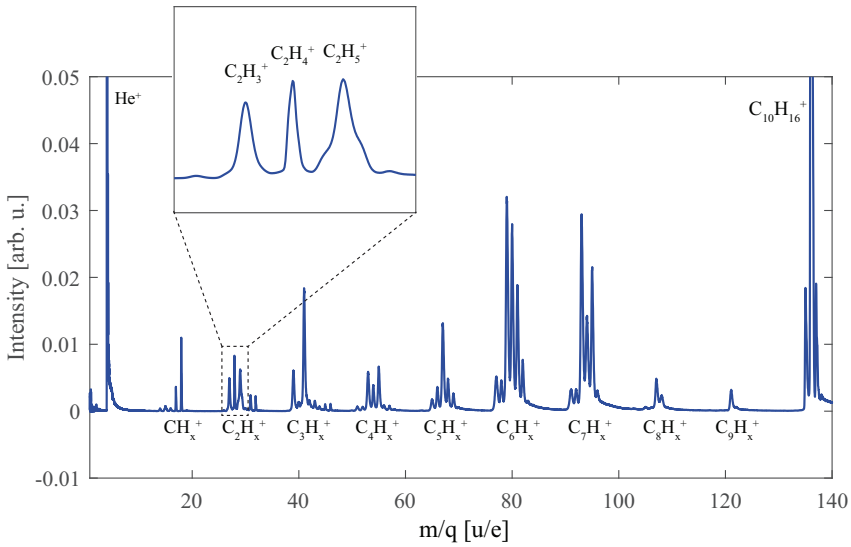

Figure 4.2: The mass spectrum of ionization induced dissociation of adamantane molecules injected using a helium carrier gas. The two highest peaks correspond to helium ions at m/q=2 u/e and the parent ion at m/q=136 u/e. The islands in between represent all fragmentation products. The inset shows a zoom-in on three of the fragments.

In order to unravel the dynamics initiated by the double ionization process, figure 4.3 shows the key energy levels of the cage opening as well as various two-body and three-body fragmentation channels obtained using *ab initio* molecular dynamics calculations performed as part of our collaboration with the Autonomous Uni-

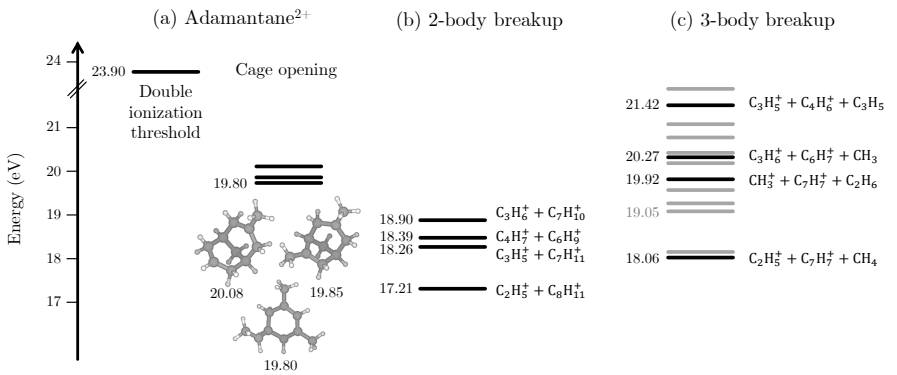

Figure 4.3: Key energy levels of the fragmentation process starting from the dication. (a) Doubly ionized states including the double ionization threshold and the lowest energy configuration for an open cage geometry. (b,c) Lowest energies of final levels for two- and three-body break-up channels. Figure adapted from paper IV.

versity of Madrid. Interestingly, all two- and three-body break-up channels lie energetically lower than the double ionization threshold. Hence, the dication of adamantane is unstable and will dissociate. In between the energy levels of the dication and the break-up channels, the energies corresponding to the cage opening geometries can be found. The calculations indicate time scales of hundreds of femtoseconds for the fragmentation process, with a dependence on the excitation energy. The cage-opening takes place within a few tens of femtoseconds after the ionization. For both the two- and three-body break-ups, the lowest lying channels are the ones leading to the production of C_2H_5 fragments, where the two-body breakup is energetically favorable. However, the mass spectrum as shown in figure 4.2 does not provide enough information to distinguish different fragmentation channels leading to the same fragment. Therefore, the next chapter introduces a method that allows the measurement of shot-to-shot correlations between different fragments and thus an unraveling of the fragmentation pathways.

4.1.2 Covariance Analysis

In this experiment, the high event rate per laser pulse (several tens of counts per shot) enables the use of covariance techniques [101]. Based on the idea that the Poisson-distributed probability distribution of the individual dissociation channels is imprinted in the shot-to-shot varying fragmentation landscape, correlated fragmentation products within this landscape should carry the same imprints. Extracting the so-called *covariance* between those fragmentation products determines how strong these correlations are and makes it possible to distinguish them from uncorrelated fragments. This is done by the following calculation: $\mathbf{X} = \{X^{(i)}\}$ and $\mathbf{Y} = \{Y^{(i)}\}, i = 1...N$ are the shot-to-shot yields of two different fragments. The covariance between $\mathbf{Y}$ and $\mathbf{Y}$ is given by:

$$\mathrm{cov}(\mathbf{X}, \mathbf{Y}) = \langle (\mathbf{X} - \langle \mathbf{X} \rangle)(\mathbf{Y} - \langle \mathbf{Y} \rangle) \rangle = \langle \mathbf{XY} \rangle - \langle \mathbf{X} \rangle \langle \mathbf{Y} \rangle , \tag{4.1}$$

$$\text{where } \langle \mathbf{X} \rangle = \frac{1}{N} \sum_{i=1}^{N} X^{(i)} \text{ and } \langle \mathbf{XY} \rangle = \frac{1}{N} \sum_{i=1}^{N} X^{(i)} Y^{(i)} \tag{4.2}$$

Equation 4.1 has a simple interpretation: $\langle \mathbf{XY} \rangle$ measures the common occurrences of $\mathbf{X}$ and $\mathbf{Y}$, including all correlated and uncorrelated events. $\langle \mathbf{X} \rangle \langle \mathbf{Y} \rangle$ estimates the uncorrelated common events and thus corrects the previous term such that the result reduces to all correlated events. In practice, false correlations caused by systematic variation, e.g., fluctuations of the laser, often affect the result of covariance calculations. If such variations are also detected on a shot-to-shot basis, it is possible to compensate for them using partial covariance. Consequently,

the covariance between $\mathbf{X}$ or $\mathbf{Y}$ and the variation is calculated and subtracted from the covariance between the $\mathbf{X}$ and $\mathbf{Y}$.

4.1.3 The C_2H_5-C_8H_{11} Fragmentation Channel

Figure 4.4 displays the application of this technique to the detected ions in the time-of-flight (TOF) spectra. The covariance between each recorded TOF channel is calculated with all other TOF channels for each recorded laser shot. A positive signal designates a high correlation between two channels. As can be seen in the figure, several correlation islands can be identified, each corresponding to a pair of ions and the associated fragmentation channel. The strength of the islands is the branching ratio of the respective fragmentation channel. The inset in figure 4.4 shows the region with the strongest contributions at around 2250 ns on the x-axis, which corresponds to the $C_2H_5^+$ ion. The top island represents the correlation with $C_8H_{11}^+$, which has the strongest branching ratio overall. The underlying two-body breakup channel can be formulated as:

$$C_{10}H_{16}^{2+} \longrightarrow C_2H_5^+ + C_8H_{11}^+ \tag{4.3}$$

The shape of the identified island plays an important role in understanding the dynamics. Generally, the elongation of each island indicates a spread of the mo-

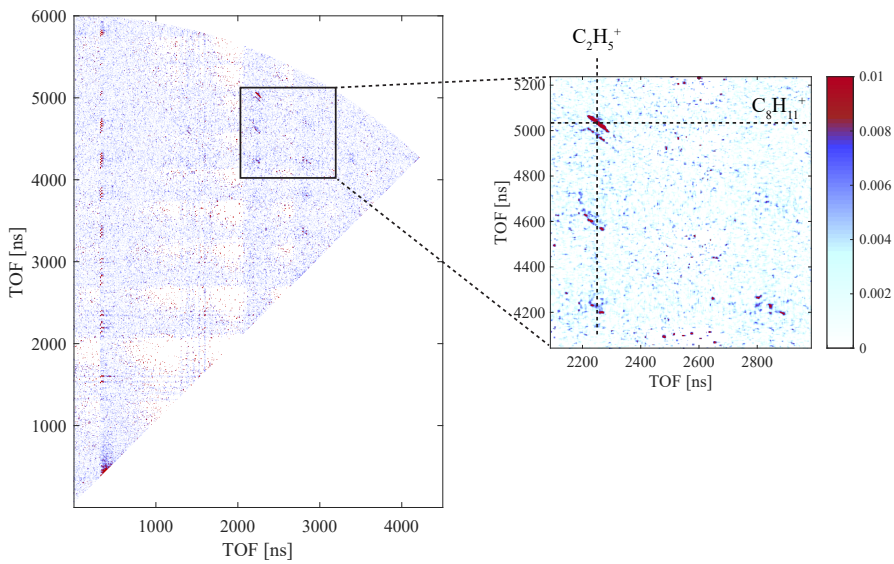

Figure 4.4: Ion-ion correlation map retrieved from the covariance analysis of the time-of-flight spectrum of adamantane. The inset shows a zoom-in on the correlations with the $C_2H_5^+$ fragment.

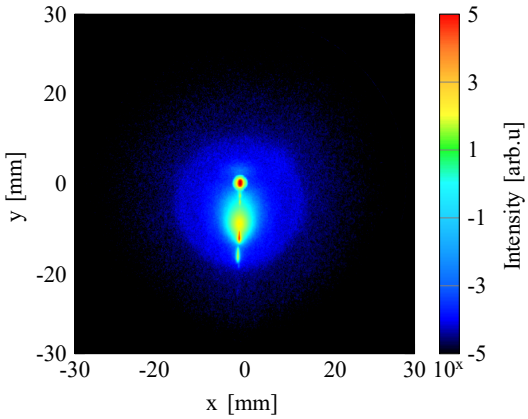

Figure 4.5: Total ion VMI map of adamantane after XUV irradiation averaged over all recorded shots. Figure reproduced from [103].

menta between the two ions, leading to the shoulders of the widened peaks in the mass spectrum described previously. This is due to the kinetic energy released in the charge separation, which is shared between the two fragments and divided according to momentum conservation. Confirmation of this was obtained by the slope of -1 of the correlation island, as expected for a two-body break-up [102]. The other islands found in the inset of figure 4.4 can be associated to further break-up channels of the $C_2H_5^+$ ion.

In order to access the distribution of momenta between ions, the ion VMI image is recorded in addition to the TOF. Figure 4.5 shows the recorded total ion velocity map image. The image shows several features along the vertical axis, which can be associated to different fragments. Due to their initial velocity in the jet, they are displaced downwards on the detector depending on their mass, with the heavier fragments further from the center. However, drawing conclusion about the individual fragments is not possible. While the camera is unable to record the momentum distributions for individual fragments, correlated information can be used to disentangle them.

In a similar fashion to what is described above, the covariance between individual peaks in the mass spectrum, i.e., individual fragments, and each pixel of the ion velocity map image is calculated. The results are covariance maps indicating which parts of the velocity map are caused by the corresponding fragment. Figure 4.6 shows the result of such calculations, where the entire mass spectrum is displayed at the bottom, while the insets exhibit the covariance maps for the individual fragments. Most fragments show a strong central feature, which can be associated to ions with little or no additional kinetic energy, resulting from dissociative channels

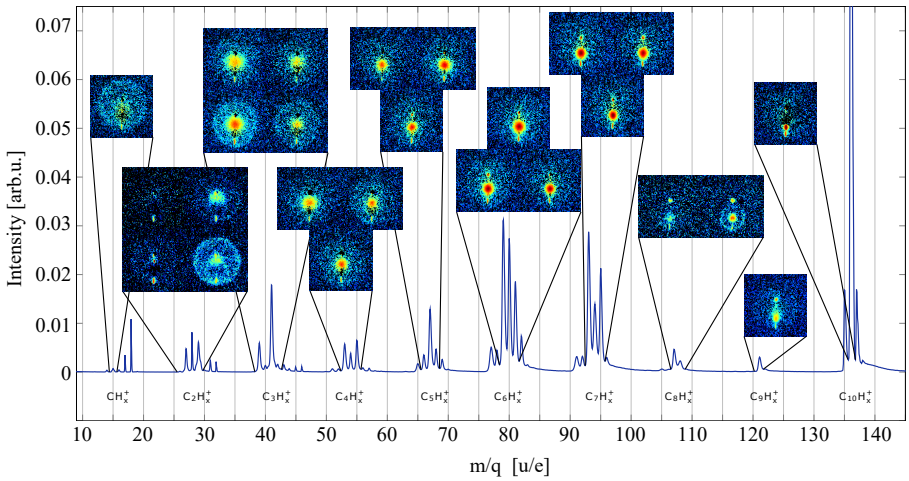

Figure 4.6: Mass spectrum of fragments of adamantane and the correlation maps of each fragment obtained from a covariance analysis between the time-of-flight channels and the VMI images. Figure reproduced from [103].

from the cation. For certain fragments, a disk-like structure is visible around the central peak. Again, this indicates that the ions carry momentum, arising from a Coulomb explosion process. Due to the charges that both ions have, they repel each other in opposing directions. The resulting momentum distribution depends on the mass ratio of the ion pair.

In particular, the C_2H_5 and C_8H_{11} fragments discussed above show pronounced ring structures, which is why they are displayed in figure 4.7 in more detail. The covariance maps are inversely Abel-inverted, portrayed in the right half of figure 4.7 (a) and (c). In figure 4.7 (b) and (d) we can see the angle integrated momentum distributions, recalibrated to the respective kinetic energies. For C_2H_5, a peak is found at around 2.6 eV. The value for C_8H_{11} can be calculated assuming the momentum is conserved:

$$E_{\text{kin}}^{[C_8H_{11}]^+} = \frac{m_{[C_2H_5]^+}}{m_{[C_8H_{11}]^+}} E_{\text{kin}}^{[C_2H_5]^+} = \frac{29}{107}\ 2.6\ \text{eV} = 0.71\ \text{eV} \tag{4.4}$$

The resulting value of 0.71 eV is in excellent agreement with the peak in figure 4.7 (d). This supports the interpretation of the predicted two-body break-up channel followed by the dication into C_2H_5 and C_8H_{11}.

All in all, the results of the TOF-TOF covariance as well as the TOF-VMI covariance present a correlated, conserved distribution of momenta between the C_2H_5 and the C_8H_{11} fragments. Convincingly, the measured photoion kinetic energies confirm that the two fragments are created by a dissociative channel of the

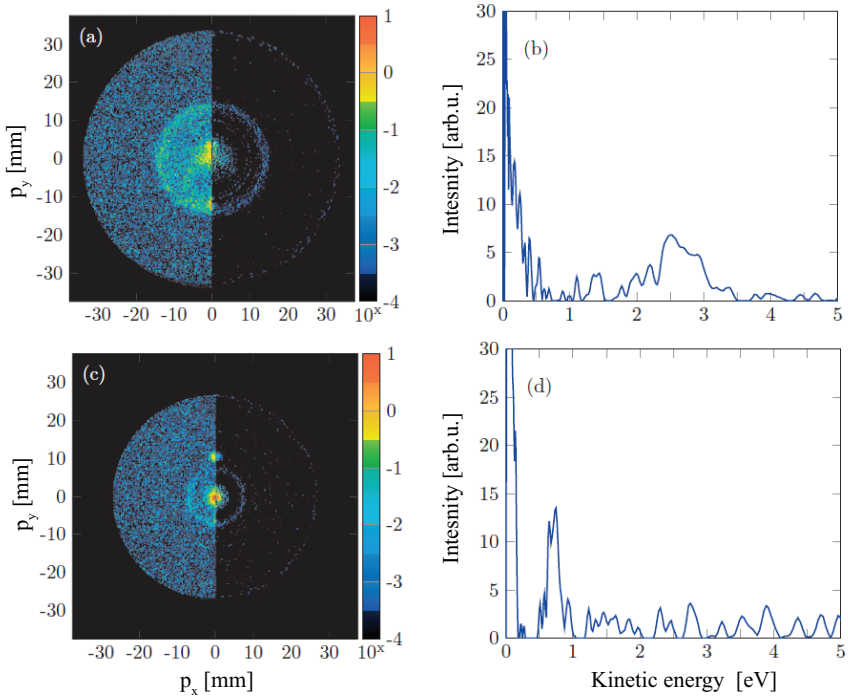

Figure 4.7: Covariance maps of the $C_2H_5^+$ (a,b) and $C_8H_{11}^+$ (c,d) fragments. (a,c) show 2D maps obtained by a covariance analysis between the retrieved VMI images and the corresponding time-of-flight channels in the left part. The right part shows an inverse Abel-inversion of the covariance maps. (b,d) show the angle-integrated and energy calibrated spectra. Figure reproduced from [103].

dication followed by a Coulomb explosion. This is in good agreement with the predictions from the calculated energy surfaces shown in figure 4.3. The two-body C_2H_5-C_8H_{11} breakup channel has the lowest energy, which makes it energetically favorable. Given that several other fragments in figure 4.6 show similar ring structures, it seems obvious to think that more dissociation channels undergo the same dynamics. However, due to the lower branching ratios, the statistics are not high enough to achieve equally convincing results in the covariance analysis.

4.1.4 Time-resolved Results in Adamantane

The calculations presented above indicate time-scales in the hundreds of fs. In order to reveal insights into such time-scales, a time-resolved experiment was performed at the Lund Laser Centre. Two light pulses are used, where the first one induces the dynamics and the second one probes the state of the system, ideally

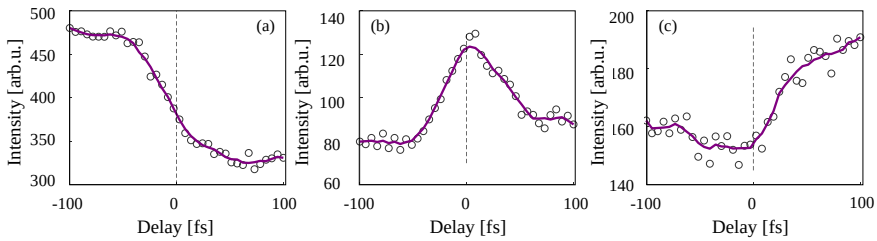

Figure 4.8: Delay-dependent yields of the adamantane parent ion (a), the $C_2H_5^+$ fragment (b) and the $C_6H_7^+$ fragment (c). The dots represent the measured values, where the purple line is a running average.

without introducing further dynamics. For the current study, infrared pulses from a 1 kHz laser were utilized to generate high-order harmonics with photon energies between 20-45 eV in the nJ regime. An infrared-XUV interferometer synchronized an auxiliary part of the fundamental infrared beam to the generated harmonics and introduced a delay between the two pulses over a range of hundreds of femtoseconds. For details about the setup the interested reader is referred to [104]. The mass-spectrum was recorded as a function of the delay, which allowed us to access the time-resolved fragmentation landscape. The analysis is still ongoing, however figure 4.8 shows preliminary results and thus provides insights into the time-scales involved. The yield of different species, namely the parent ion (a) and two carbon groups, $C_2H_5^+$ (b) and $C_6H_7^+$ (c), are shown as a function of the delay. Negative delays correspond to the infrared pulses arriving before the XUV pulses.

As can be seen, the yield of the parent ion decreases as a function of the delay indicating a depletion due to fragmentation induced by the XUV pulses. In contrast, the yield of the $C_6H_7^+$-fragment increases, representing one of the many fragmentation channels. The dynamics of the parent ion and the $C_6H_7^+$-fragment take place on time scales of around 100 fs. The channel of the $C_2H_5^+$-fragment shows an additional increase around the temporal overlap at zero delay. The peak-like shape has a duration of around 50 fs, which matches the simulated time-scales of the cage-opening process.

4.2 Time-resolved Fragmentation Dynamics studied with FELs

Pump-probe studies have also been performed at the FELs FLASH at DESY in Hamburg, Germany, and SACLA at the Spring8 facility in Sayo, Japan. Compared with HHG-based sources, FELs have the advantage of tunable wavelengths and higher amounts of photons per pulse. In particular, using photons in the x-ray regime enables probing of inner-shell electrons, rendering it possible to target the pump or probe only at specific atoms within the molecule.

Papers VI and VII present time-resoled results using an XUV/x-ray photon from an FEL and an infrared/UV photon from an optical laser. The studies were conducted on carbon-based molecules, namely three different polycyclic aromatic hydrocarbons (PAH) in paper VI and thiophene in paper VII. The authors contribution to these papers was mainly experimental, which is why this chapter, after a short introduction to FELs, only presents a summary of selected results.

4.2.1 Free-Electron Lasers

A Free-Electron Laser (FEL) is a source of photons emitted by electrons accelerated to relativistic velocities passing through an alternating magnetic field. The electrons are released into a vacuum and picked up by a linear accelerator, in which they reach kinetic energies up to several GeV. The relativistic electrons enter a set of opposing magnets, called undulators, with alternating magnetic fields, as illustrated in figure 4.9. The Lorentz force causes an oscillating motion of the electrons perpendicular to the magnetic field and their direction of motion. The alternating radial acceleration leads to the emission of synchrotron radiation in a cone directed towards the propagation direction of the electrons. So far, the emitted radiation

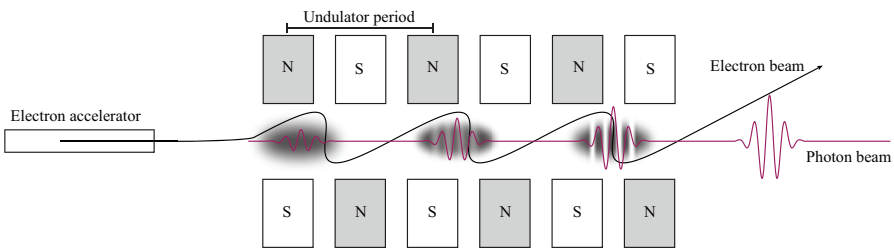

Figure 4.9: Schematic illustration of the working principle of a FEL. The accelerated electron beam (black arrows) enters a set of undulators and is forced onto an oscillating motion. The radial acceleration of the electrons produces synchrotron radiation (purple line). Microbunching of the electrons ensures constructive interference of the emitted field.

is created with a random phase. However, after a certain propagation distance through the undulators, the interaction between the generated field and electrons leads to a modulation of the electron density into microbunches, as shown in figure 4.9. As a consequence, the emitted radiation by the microbunches is in phase, increasing the emitted intensity. This process is called self-amplified spontaneous emission (SASE) [22, 105, 106] and is deployed at most XUV and x-ray FELs. The principle was first employed for photons in the XUV regime at the FEL FLASH facility in 2005 [107, 108]. Generally, FELs are available from the microwave [109] to the x-ray regime [110], where the wavelength is set by the undulator period. However, for high-energy photons in the x-ray regime the electron kinetic energy must be high enough, which is why linear accelerators of x-ray FELs are usually over several kilometers long.

4.2.2 Fragmentation Dynamics

Paper VII presents a study of the dissociation of the carbon-based molecule thiophene (C_4H_4S). Using 180 eV photons from the FEL SACLA, electrons were emitted from the $2p$ orbital of the sulfur atom leading to a subsequent Auger process leaving the molecule in a dicationic state. Hence, the starting point was similar to the experiment described in the previous chapter, however with much higher excitation energies due to the x-ray induced ionization. An 800 nm optical laser monitored the evolution of the dynamics in a pump-probe setup. The resulting ions were detected by a momentum-imaging ion time-of-flight spectrometer with a Roentdek HEX120 detector [111]. Instead of detecting several ionization events per shot like in the previous experiment, only one event was identified, allowing an instant correlation of the fragmentation products. By doing so, it is not only possible to measure the yield of an isolated fragment, but also to instantaneously detect correlated ion pairs formed through the same fragmentation channel. This technique is called coincidence detection and generally requires a high repetition rate and/or long acquisition times.

Figure 4.10 shows the retrieved yield of selected fragmentation pairs as a function of the delay, where negative delays correspond to the infrared pulses arriving before the x-ray pulses. In panel 4.10(a), the yield of the strongest two-body break-up channel is shown, corresponding to $C_4SH_4^{2+} \rightarrow CSH^+ + C_3H_3^+$. A clear drop at ≈ 110 fs is seen with a slow rise at large delays. In 4.10(b), an example of an ion-pair ($C_2H_2^+$,S^+) from the three-body break-up channel $C_4SH_4^{2+} \rightarrow C_2H_n^+ + S^+ + C_2H_{4-n}$ is presented. A remarkably different behavior can be seen: the yield of the ion pair increases drastically when the two pulses overlap and then quickly decreases. This behavior is more short-lived than the negative variation

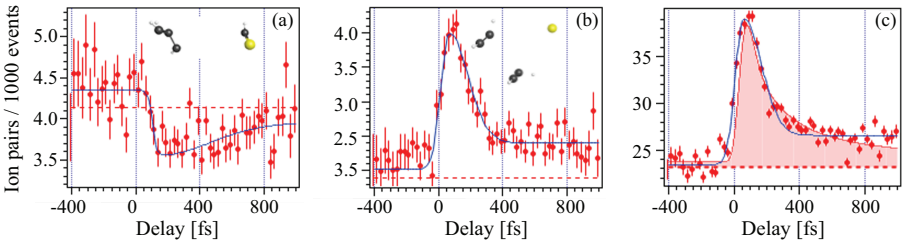

Figure 4.10: Delay-dependent yields of different ion-pairs resulting from the dissociation of thiophene. (a) shows the yield of (CSH^+, $C_3H_3^+$) representing a two-body break-up channel. In (b) an example for an individual ion pair ($C_2H_2^+$,S^+) resulting from a multibody break-up channel is shown, where (c) shows the yield of all ion pairs from multibody break-up channels. The dashed lines correspond to the yield of the corresponding ion pair upon ionization by only the x-ray pulse. Figure adapted from paper VII.

in the two-body break-up channel, which indicates that the two processes are not induced by the same dynamics. A similar enhancement is present in all ion pairs from multibody break-up channels, for which the combined yield is shown in 4.10(c).

Based on the results of self-consistent charge-density functional tight-binding simulations performed by our collaborators at the University of Turku, we can explain the experimental findings by a very fast opening of the ring structure of thiophene followed by the formation of a transient linear geometry of the parent dication. The ring-opening is followed by the two- and three-body break-up dissociation shown in figure 4.10. The lifetime of the transient linear geometry depends on the internal energy after the x-ray induced ionization and ranges from tens to hundreds of femtoseconds. When the two pulses overlap in time, the effect of the infrared beam is primarily ionizing. Hence, the x-ray induced dicationic state is further transferred to a triply charged state. The primary consequence of this is the enhancement of the multibody break-up seen in figure 4.10.

Paper VI presents a similar study of the fragmentation dynamics of three PAHs, namely fluorene, phenanthrene and pyrene. An equally rich fragmentation landscape was detected for all molecules. Interestingly, a similar transient enhancement as in the previous experiment was seen in the time-resolved ion yield of selected fragments. In this study, the effect was also attributed to an enhanced dissociation due to the formation of an unstable triply charged state of the parent ion when the two pulses overlap in time. In addition, the paper determines the lifetime of the excited states of the single charged parent ions.

In general, the break-up into two or more fragments leads to a dynamical transfer of energy between the fragmentation products, which is why the momentum of the resulting ions is an interesting observable. In the next section an example of

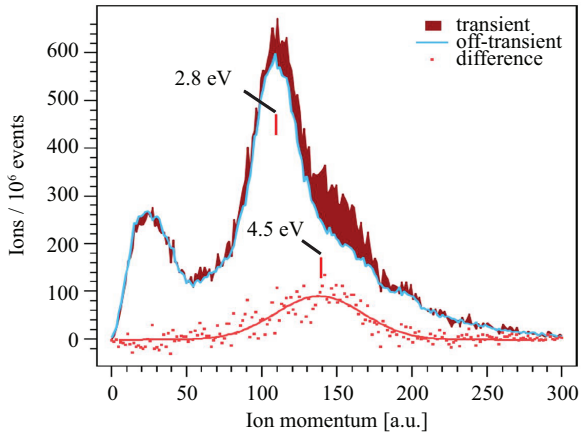

Figure 4.11: Momentum distribution of the S^+ ion for delay ranges outside (blue) and inside (red) the transient region. The red dots correspond to the difference between the two curves together with a fitted Gaussian function. Figure adapted from paper VII.

such a measurement is presented.

4.2.3 Time-resolved Ion Momentum Spectroscopy

The transient enhancement in the multibody fragmentation of thiophene, presented in the previous section, suggests an impact on the kinematics of the resulting ions. The additional charged fragments lead to an increased momentum of individual ions after dissociation. In paper VII, we present results of the ion momentum distribution of the S^+ ion, which are reproduced in figure 4.11. Shown are the momentum distributions within and outside the delay range of the transient enhancement as well as the difference between them. The first peak is attributed to O_2^+ ions from a residual contamination in the chamber. Oxygen has the same mass as sulfur wherefore they cannot be distinguished from S^+ ions.

The main peak lies at 2.8 eV kinetic energy, while the difference curve shows a peak at 4.5 eV kinetic energy. Similarly to the results presented in section 4.1.3, such values can be explained by a Coulomb explosion following the dissociation. Paper VII puts forward results of a simple calculation, indicating that the formation of a triply charged transient linear geometry followed by a multibody break-up leads to S^+ ions of higher kinetic energies ($\sim$ 4.2 eV) than the same process starting from a doubly charged state ($\sim$ 2.2 eV). This supports the interpretation that in the transient delay region, which shows a shift towards higher kinetic energies, the enhancement of the multibody break-up is due to the more energetic fragmentation of the triply-charged system.

Chapter 5

Summary and Outlook

The objective of the research presented herein has been to investigate ultrafast dynamics in atomic and molecular systems using intense XUV attosecond pulses. Chapters 2-4 summarize the work conducted during my last four years in Lund, including theoretical tools, technical designs as well as experimental and simulated results.

The second chapter portrays the process of HHG, introducing the results presented in papers II, III, V, IX and X. After an introduction to the basic principles, the IXB at the Lund Laser Centre is detailed. The design of a new vacuum chamber housing, among other things, the in-vacuum compressor is described, as it was a major part of my work. With the aim of generating intense XUV attosecond pulses, the Intense XUV Beamline (IXB) delivers pulse energies in the μJ regime, and, when focused tightly (paper IX), intensities high enough to induce multiphoton ionization. However, despite the high pulse energies, it remains a challenge to carry out an XUV-XUV pump-probe experiment using the split-and-delay unit. The upgrade to a new OPCPA laser system in 2022 should dramatically improve the generation of intense harmonics, as driving pulses with pulse energies of 60 mJ and a duration of sub-10 fs are expected.

The next part of chapter 2 outlines the extensive studies around the spatial and temporal properties of the generated XUV pulses, as presented in papers II, III, VIII and IX. In particular, studying the effects of the dipole phase taught us the importance of a well-chosen focusing geometry in order to achieve high intensities. The first results of the IR-XUV interferometer are presented and the RABBIT technique was applied to reconstruct the temporal structure of the attosecond pulse train. A pulse duration of 313 as was extracted.

Chapter 3 and paper 1 discuss laser-assisted photoionization. Making use of the angular resolution of the VMIS, we investigated the interference between electrons released via different angular momentum channels from the $2p^6$ ground state of neon. Using a fitting algorithm, we characterized the amplitude and phase of the single-photon matrix elements of each angular momentum channel and thus the full ionization process. The difference in phase between the channels as well as the energy dependence of the extracted values is well reproduced by calculations based on angular-channel-resolved many-body perturbation theory. The presented method paves the way for further experiments, as its approach is universal and can be applied to other atomic systems. When it comes to molecules, the effect of the cc-transition has to be considered differently, as the electron in the continuum encounters a more complex potential. Nevertheless, angular-resolved RABBIT will provide novel insights into molecular dynamics on attosecond time scales.

During the analysis of the angle-resolved RABBIT experiments in neon we came across an interesting feature in the photoelectron spectrum shown in figure 5.1. Within the peak corresponding to photoelectrons produced by the absorption of the 15$^{\text{th}}$ harmonic, a sub-structure can be identified. Mostly along the polarization axis, three sub-peaks are visible in the momentum map, as can be seen in figure 5.1 (a). As the 15$^{\text{th}}$ harmonic is the lowest order to overcome the ionization energy of neon, the 13$^{\text{th}}$ harmonic may excite the ground state electron to a resonance close to threshold, which is then ionized by absorption of two infrared photons. This electron carries the same kinetic energy as that due to absorption of the 15$^{\text{th}}$

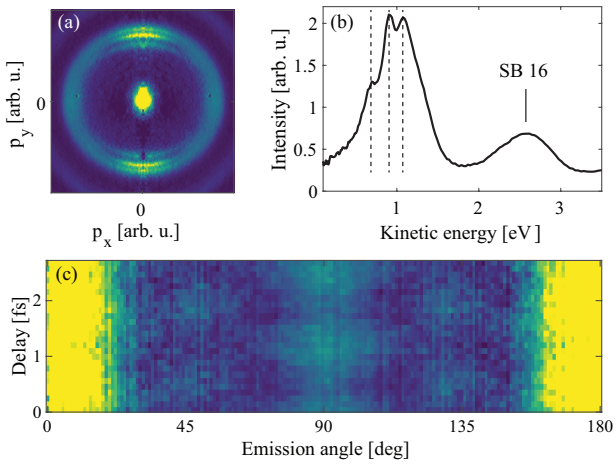

Figure 5.1: Sub-structures seen in the photoelectron spectrum for electrons produced by the absorption of the 15$^{\text{th}}$ harmonic. (a) shows the electron momentum map and (b) the angle-integrated photoelectron spectrum. In (c) the energy integrated range around 1 eV is shown as a function of angle and delay.

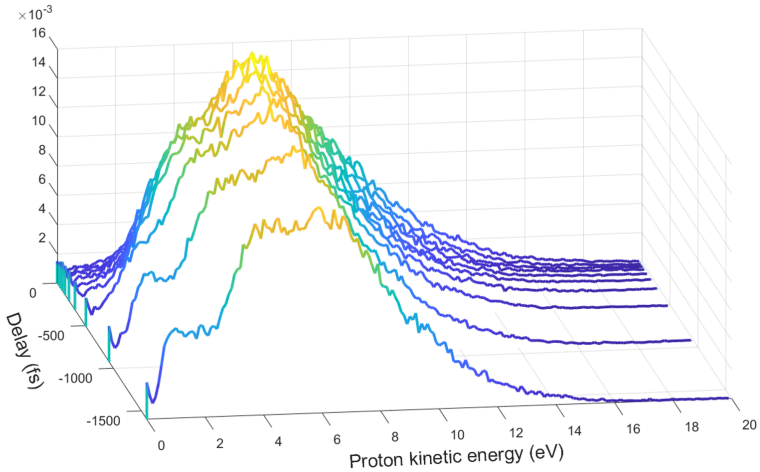

Figure 5.2: Ion kinetic energy distribution of protons resulting from the dissociation of adamantane after XUV induced ionization as a function of the delay.

harmonic, which means they interfere. The structure seen in the photoelectron spectrum can be caused by such an interference. Further analysis indicates that in the delay dependent angular distribution, shown in figure 5.1(c), oscillations at 45° appear, out of phase with the oscillations at 90°. We are currently investigating these results further aiming to extract information allowing us to study resonant photoionization.

Lastly, the results of papers IV and VI-VIII on the dissociation of organic molecules are introduced in chapter 4. Paper IV discusses experimental results of the diamondoid adamantane performed at the IXB, together with molecular dynamics calculations. The different fragmentation dynamics are identified using covariance analysis techniques. The dissociation of the doubly charged parent ion is followed by a Coulomb explosion process, leading predominantly to the C_2H_5 and C_8H_{11} fragmentation channels. Preliminary results are shown from an infrared-XUV pump-probe experiment, indicating time scales on the sub 100 fs scale. Looking ahead, we are currently working on the analysis of an XUV-XUV pump-probe experiment performed at the FL26 at FLASH at DESY. The first preliminary results show time-dependent signals in many of the fragmentation channels. Additionally, we see a shift of the momentum distribution in the protons, as shown in figure 5.2. The interpretation of the results is however still ongoing.

Papers VI and VII introduce results of time-resolved experiments in organic molecules performed at the FELs FLASH at DESY in Hamburg, Germany, and SACLA at the Spring8 facility in Sayo, Japan. Using infrared-XUV/x-ray pump-probe techniques, the fragmentation landscape was studied. For the PAHs discussed in paper

VI and thiophene described in paper VII, the double and triple ionization of the parent molecule lead to a dissociation within hundreds of femtoseconds. Based on the results presented in paper VI a subsequent beamtime was granted and performed in August 2021 with the aim to investigate the observed dynamics in further detail and extend the experiments to other PAHs.

On the way towards pump-probe experiments using intense XUV pulses on the attosecond time scale, this thesis provides a promising outlook for both HHG and FEL sources. However, technical advances are required in order to perform "pure" experiments. For HHG, the attosecond resolution is realized, as shown in chapter 2.23, but most applications rely on techniques like RABBIT for which assumptions are required in order to extract information about the underlying physics. This works well for atomic systems, as in the case of neon presented in chapter 3, but is more complex for molecules and solids. For FELs on the other hand, the temporal resolution prevents the detection of ultrafast processes, like pre-dissociative charge migration. All in all however, HHG and FELs are on the way to delivering the required technical advances. The Extreme Light Infrastructure Attosecond Light Pulse Source (ELI-ALPS) facility in Szeged, Hungary and will take HHG on another level [112]. In particular the "long" beamline with 55 m focusing and a 6 m gas cell will generate intese high-order harmonics on an unprecedented scale. At FELs on the other hand, tunable isolated attosecond X-ray pulses were recently generated using at the Linac Coherent Light Source at the SLAC institute [27]. This gives a promising outlook towards experiments using XUV-XUV pump-probe techniques. Performing such experiments, in combination with advanced photoelectron and -ion detection schemes, is the aim for these "next-generation" ultrafast time-resolved experiments and will shine new light on the fundamental processes behind chemical and biological transformations.

Acknowledgments

First of all, I would like to thank you, Per. Your support and your trust from day one gave me the confidence I needed to start my journey at the (at first incredibly overwhelming) intense beamline. Not later than on our first beamtime at Flash, I got to realize how passionate you are about tweaking buttons, inverting VMI images and solving experimental mysteries. That inspired me. Your sense for people was the foundation for the spirit within the 10Hz team, which made the decision to start this PhD incredibly easy. To many more Currywürste!

Thank you, Anne, for all the hours we got to work together towards the end of my PhD. The combination of your Swedish diplomacy and your French honesty taught me a lot about my strengths, but also my weaknesses, which I appreciate a lot. Your dedication for atomic physics is highly encouraging for young researchers like me. I am surely not the first one to stay in research following your lead by example.

Merci Sylvain, for being the teacher guiding me through my first years of science. I am however even more grateful for the friendship between us, which led to something much bigger than the work we shared in the lab. Certainly you taught me a thing or two about experimental physics, but more importantly you became an inspiration also outside the lab. Together with Lana, you two made me part of your family, which I am immensely thankful for. Also you, Lana, became a great friend. Your perspectives and opinions are important to me and influenced who I became over the last five years. I don't want to miss any of the memories I share with all three of you.

Talking about memories: Many moments of joy, frustration and even triumph were shared with you Hampus (strangely often in states of extreme tiredness). Thank you for that! Jan, you have been a great companion along the way and I am excited for hopefully many more rounds of 'dubbelhuvud' to come. Thank you to Linnea, Filippo, Hélène and Piotr for paving my way into science and the support you gave me as a young and sometimes lost master student.

Thank you to the new 10Hz generation! You, Marius, are also much more than a co-worker. Your critical mind taught me a lot and led to many long (some would argue unnecessary) discussions. I don't want to miss a single one of them. Thank you Maria for the time we got to spend together in and outside the lab. I wish you all the best for the future and we'll see each other out on the Öresund!

A big thanks to the rest of the Attogroup for making these four years as short as they were. Mercias David, for your scientific expertise as well as the many joyful moments we shared outside the physics world. Thanks to Giada and Alexander for the moral support during many encounters in the laser room and the growing bond between HHG and plasmas, also outside the lab. I am very thankful for the support from you, Anders, we would have seen a lot less photons without you. Thank you Mathieu, see you at the next conference, I'll bring the ouzo. I want to thank Felipe and Mattias for your help with the Legendre polynomial gymnastics. And big thanks to the rest of the team: Cord, Hugo, Emma, Jan V., Samuel, Sara, Neven, Chen, Anne-Lise, Anna, Ann-Kathrin, Ivan, Saikat, Robin, Yu-Chen, Shiyang. Finally, I want to express my gratitude for the support from Anne Petersson Jungbeck, Åke Johansson, Jakob Testad and Maria Algotsson.

On a more private note, I would like to thank the 👩‍🦰⬛-family. In particular during the last year, our friendships were put to the test while being locked up in an apartment together. I am however sure that I wouldn't have made it through these months equally seamless, without the three of you.

Zum Schluss möchte ich meiner Familie danken, ohne die ich hier sicherlich nicht stehen würde. Insbesondere dir, Julius, der du mir in den letzten Jahren ein noch engerer Begleiter geworden bist.

References

[1] A. Zewail. *Femtochemistry: Atomic-Scale Dynamics of the Chemical Bond*. J. Phys. Chem. A, 104:5660 (2000).

[2] A. McPherson, G. Gibson, H. Jara, U. Johann, T. S. Luk, I. A. McIntyre, K. Boyer, and C. K. Rhodes. *Studies of multiphoton production of vacuum-ultraviolet radiation in the rare gases*. J. Opt. Soc. Am. B, 4:595 (1987).

[3] M. Ferray, A. L'Huillier, X. Li, L. Lompre, G. Mainfray, and C. Manus. *Multiple-harmonic conversion of 1064 nm radiation in rare gases*. J. Phys. B, **21**:L31 (1988).

[4] F. Krausz and M. Ivanov. *Attosecond physics*. Rev. Mod. Phys., 81:163–234 (2009).

[5] T. Popmintchev, M. C. Chen, P. Arpin, M. M. Murnane, and H. C. Kapteyn. *The attosecond nonlinear optics of bright coherent X-ray generation*. Nature Photonics, 4(12):822–832 (2010).

[6] F. Calegari, G. Sansone, S. Stagira, C. Vozzi, and M. Nisoli. *Advances in attosecond science*. Journal of Physics B: Atomic, Molecular and Optical Physics, 49(6):062001 (2016).

[7] M. Drescher, M. Hentschel, R. Kienberger, M. Uiberacker, V. Yakovlev, A. Scrinzi, T. Westerwalbesloh, U. Kleineberg, U. Heinzmann, and F. Krausz. *Time-resolved atomic inner-shell spectroscopy*. Nature, 419:803 (2002).

[8] M. Uiberacker, T. Uphues, M. Schultze, A. J. Verhoef, V. Yakovlev, M. F. Kling, Rauschenberger, N. M. Kabachnik, H. Schröder, M. Lezius, K. L. Kompa, H.-G. Muller, M. J. J. Vrakking, S. Hendel, U. Kleineberg, U. Heinzmann, M. Drescher, and F. Krausz. *Attosecond real-time observation of electron tunnelling in atoms*. Nature, 446:627 (2007).

[9] M. Schultze, M. Fieß, N. Karpowicz, J. Gagnon, M. Korbman, M. Hofstetter, S. Neppl, A. L. Cavalieri, Y. Komninos, T. Mercouris, C. A. Nicolaides, R. Pazourek, S. Nagele, J. Feist, J. Burgdörfer, A. M. Azzeer, R. Ernstorfer, R. Kienberger, U. Kleineberg, E. Goulielmakis, F. Krausz, and V. S. Yakovlev. *Delay in Photoemission*. Science, 328:1658–1662 (2010).

[10] J. Mauritsson, T. Remetter, M. Swoboda, K. Klünder, A. L'Huillier, K. J. Schafer, O. Ghafur, F. Kelkensberg, W. Siu, P. Johnsson, M. J. J. Vrakking, I. Znakovskaya, T. Uphues, S. Zherebtsov, M. F. Kling, F. Lepine, E. Benedetti, F. Ferrari, G. Sansone, and M. Nisoli. *Attosecond Electron Spectroscopy Using a Novel Interferometric Pump-Probe Technique*. Phys. Rev. Lett., 105:053001 (2010).

[11] M. Isinger, R. J. Squibb, D. Busto, S. Zhong, A. Harth, D. Kroon, S. Nandi, C. L. Arnold, M. Miranda, J. M. Dahlström, E. Lindroth, R. Feifel, M. Gisselbrecht, and A. L'Huillier. *Photoionization in the time and frequency domain*. Science, 358(6365):893–896 (2017).

[12] G. Sansone, F. Kelkensberg, J. F. Pérez-Torres, F. Morales, M. F. Kling, W. Siu, O. Ghafur, P. Johnsson, M. Swoboda, E. Benedetti, F. Ferrari, F. Lépine, J. L. Sanz-Vicario, S. Zherebtsov, I. Znakovskaya, A. L'Huillier, M. Y. Ivanov, M. Nisoli, F. Martìn, and M. J. J. Vrakking. *Electron localization following attosecond molecular photoionization*. Nature, 465:763–766 (2010).

[13] F. Kelkensberg, C. Lefebvre, W. Siu, O. Ghafur, T. T. Nguyen-Dang, O. Atabek, A. Keller, V. Serov, P. Johnsson, M. Swoboda, T. Remetter, A. L'Huillier, S. Zherebtsov, G. Sansone, E. Benedetti, F. Ferrari, M. Nisoli, F. Lépine, M. F. Kling, and M. J. J. Vrakking. *Molecular Dissociative Ionization and Wave-Packet Dynamics Studied Using Two-Color XUV and IR Pump-Probe Spectroscopy*. Physical Review Letters, 103(12):123005 (2009).

[14] C. Neidel, J. Klei, C.-H. Yang, A. Rouzée, M. J. J. Vrakking, K. Klünder, M. Miranda, C. L. Arnold, T. Fordell, A. L'Huillier, M. Gisselbrecht, P. Johnsson, M. P. Dinh, E. Suraud, P.-G. Reinhard, V. Despré, M. A. L. Marques, and F. Lépine. *Probing Time-Dependent Molecular Dipoles on the Attosecond Time Scale*. Phys. Rev. Lett., 111:033001 (2013).

[15] A. L. Cavalieri, N. Müller, T. Uphues, V. S. Yakovlev, A. Baltuška, B. Horvath, B. Schmidt, L. Blümel, R. Holzwarth, S. Hendel, M. Drescher, U. Kleineberg, P. M. Echenique, R. Kienberger, F. Krausz, and U. Heinzmann. *Attosecond spectroscopy in condensed matter*. Nature, 449:1029 (2007).

[16] M. Schultze, E. M. Bothschafter, A. Sommer, S. Holzner, W. Schweinberger, M. Fiess, M. Hofstetter, R. Kienberger, V. Apalkov, V. S. Yakovlev, M. I. Stockman, and F. Krausz. *Controlling dielectrics with the electric field of light*. Nature, 493(7430):75–78 (2013).

[17] A. Picón, L. Plaja, and J. Biegert. *Attosecond x-ray transient absorption in condensed-matter: a core-state-resolved Bloch model*. New Journal of Physics, 21(4):043029 (2019).

[18] P. Tzallas, E. Skantzakis, C. Kalpouzos, E. P. Benis, G. D. Tsakiris, and D. Charalambidis. *Generation of intense continuum extreme-ultraviolet radiation by many-cycle laser fields*. Nature Phys., 3:846 (2007).

[19] Y. Wu, E. Cunningham, H. Zang, J. Li, M. Chini, X. Wang, Y. Wang, K. Zhao, and Z. Chang. *Generation of high-flux attosecond extreme ultraviolet continuum with a 10 TW laser*. Applied Physics Letters, 102(20):201104 (2013).

[20] B. Manschwetus, L. Rading, F. Campi, S. Maclot, H. Coudert-Alteirac, J. Lahl, H. Wikmark, P. Rudawski, C. M. Heyl, B. Farkas, T. Mohamed, A. L'Huillier, and P. Johnsson. *Two-photon double ionization of neon using an intense attosecond pulse train*. Phys. Rev. A, 93:061402 (2016).

[21] B. Senfftleben, M. Kretschmar, A. Hoffmann, M. Sauppe, J. Tümmler, I. Will, T. Nagy, M. J. J. Vrakking, D. Rupp, and B. Schütte. *Highly non-linear ionization of atoms induced by intense high-harmonic pulses*. Journal of Physics: Photonics, 2(3):034001 (2020).

[22] W. Ackermann, G. Asova, V. Ayvazyan, A. Azima, N. Baboi, J. Bähr, V. Balandin, B. Beutner, A. Brandt, A. Bolzmann, R. Brinkmann, O. I. Brovko, M. Castellano, P. Castro, L. Catani, E. Chiadroni, S. Choroba, A. Cianchi, J. T. Costello, D. Cubaynes, J. Dardis, W. Decking, H. Delsim-Hashemi, A. Delserieys, G. Di Pirro, M. Dohlus, S. Düsterer, A. Eckhardt, H. T. Edwards, B. Faatz, J. Feldhaus, K. Flöttmann, J. Frisch, L. Fröhlich, T. Garvey, U. Gensch, C. Gerth, M. Görler, N. Golubeva, H. J. Grabosch, M. Grecki, O. Grimm, K. Hacker, U. Hahn, J. H. Han, K. Honkavaara, T. Hott, M. Hüning, Y. Ivanisenko, E. Jaeschke, W. Jalmuzna, T. Jezynski, R. Kammering, V. Katalev, K. Kavanagh, E. T. Kennedy, S. Khodyachykh, K. Klose, V. Kocharyan, M. Körfer, M. Kollewe, W. Koprek, S. Korepanov, D. Kostin, M. Krassilnikov, and G. Kube *et al. Operation of a free-electron laser from the extreme ultraviolet to the water window*. Nature Photonics, 1(6):336–342 (2007).

[23] Y. Nabekawa, H. Hasegawa, E. J. Takahashi, and K. Midorikawa. *Production of Doubly Charged Helium Ions by Two-Photon Absorption of an Intense Sub-10-fs Soft X-Ray Pulse at 42 eV Photon Energy*. Phys. Rev. Lett., 94:043001 (2005).

[24] A. Sorokin, M. Wellhöfer, S. Bobashev, K. Tiedtke, and M. Richter. *X-ray-laser interaction with matter and the role of multiphoton ionization: Free-electron-laser studies on neon and helium*. Physical Review A, 75(5):051402 (2007).

[25] R. Moshammer, Y. H. Jiang, L. Foucar, A. Rudenko, T. Ergler, C. D. Schröter, S. Lüdemann, K. Zrost, D. Fischer, J. Titze, T. Jahnke, M. Schöffler, T. Weber, R. Dörner, T. J. M. Zouros, A. Dorn, T. Ferger, K. U. Kühnel, S. Düsterer, R. Treusch, P. Radcliffe, E. Plönjes, and J. Ullrich. *Few-Photon Multiple Ionization of Ne and Ar by Strong Free-Electron-Laser Pulses*. Phys. Rev. Lett., 98:203001 (2007).

[26] A. Rudenko, L. Foucar, M. Kurka, T. Ergler, K. U. Kühnel, Y. H. Jiang, A. Voitkiv, B. Najjari, A. Kheifets, S. Lüdemann, T. Havermeier, M. Smolarski, S. Schössler, K. Cole, M. Schöffler, R. Dörner, S. Düsterer, W. Li, B. Keitel, R. Treusch, M. Gensch, C. D. Schröter, R. Moshammer, and J. Ullrich. *Recoil-Ion Momentum Distributions for Two-Photon Double Ionization of He and Ne by 44 eV Free-Electron Laser Radiation*. Physical Review Letters, 101(7) (2008).

[27] J. Duris, S. Li, T. Driver, E. G. Champenois, J. P. MacArthur, A. A. Lutman, Z. Zhang, P. Rosenberger, J. W. Aldrich, R. Coffee, G. Coslovich, F.-J. Decker, J. M. Glownia, G. Hartmann, W. Helml, A. Kamalov, J. Knurr, J. Krzywinski, M.-F. Lin, J. P. Marangos, M. Nantel, A. Natan, J. T. O'Neal, N. Shivaram, P. Walter, A. L. Wang, J. J. Welch, T. J. A. Wolf, J. Z. Xu, M. F. Kling, P. H. Bucksbaum, A. Zholents, Z. Huang, J. P. Cryan, and A. Marinelli. *Tunable isolated attosecond X-ray pulses with gigawatt peak power from a free-electron laser*. Nature Photonics, 14(1):30–36 (2020).

[28] P. K. Maroju, C. Grazioli, M. Di Fraia, M. Moioli, D. Ertel, H. Ahmadi, O. Plekan, P. Finetti, E. Allaria, L. Giannessi, G. De Ninno, C. Spezzani, G. Penco, S. Spampinati, A. Demidovich, M. B. Danailov, R. Borghes, G. Kourousias, C. E. Sanches Dos Reis, F. Billé, A. A. Lutman, R. J. Squibb, R. Feifel, P. Carpeggiani, M. Reduzzi, T. Mazza, M. Meyer, S. Bengtsson, N. Ibrakovic, E. R. Simpson, J. Mauritsson, T. Csizmadia, M. Dumergue, S. Kühn, H. Nandiga Gopalakrishna, D. You, K. Ueda, M. Labeye, J. E. Bækhøj, K. J. Schafer, E. V. Gryzlova, A. N.

Grum-Grzhimailo, K. C. Prince, C. Callegari, and G. Sansone. *Attosecond pulse shaping using a seeded free-electron laser*. Nature, 578(7795):386–391 (2020).

[29] P. Paul, E. Toma, P. Breger, G. Mullot, F. Augé, P. Balcou, H. Muller, and P. Agostini. *Observation of a train of attosecond pulses from high harmonic generation*. Science, 292:1689 (2001).

[30] K. C. Kulander, K. J. Schafer, and J. L. Krause. *Dynamics of short-pulse excitation, ionization and harmonic conversion*. In *Super-Intense Laser-Atom Physics*. Plenum Press, New York (1993).

[31] M. Lewenstein, P. Balcou, M. Ivanov, A. L'Huillier, and P. Corkum. *Theory of high-order harmonic generation by low-frequency laser fields*. Phys. Rev. A, 49:2117 (1994).

[32] D. E. Spence, P. N. Kean, and W. Sibbett. *60-fsec pulse generation from a self-mode-locked Ti:sapphire laser*. Opt. Lett., **16**:42 (1991).

[33] D. Strickland and G. Mourou. *Compression of amplified chirped optical pulses*. Opt. Commun., **56**:219 (1985).

[34] S. Svanberg, J. Larsson, A. Persson, and C.-G. Wahlström. *Lund High-Power Laser Facility – Systems and First Results*. Physica Scripta, **49**:187 (1994).

[35] C. G. Wahlström, J. Larsson, A. Persson, T. Starczewski, S. Svanberg, P. Salieres, P. Balcou, and A. L'Huillier. *High-order harmonic generation in rare gases with an intense short-pulse laser*. Phys. Rev. A, 48:4709 (1993).

[36] G. Cantono, A. Permogorov, J. Ferri, E. Smetanina, A. Dmitriev, A. Persson, T. Fülöp, and C.-G. Wahlström. *Laser-driven proton acceleration from ultrathin foils with nanoholes*. Scientific Reports, 11(1):5006 (2021).

[37] J. Björklund Svensson, D. Guénot, J. Ferri, H. Ekerfelt, I. Gallardo González, A. Persson, K. Svendsen, L. Veisz, and O. Lundh. *Low-divergence femtosecond X-ray pulses from a passive plasma lens*. Nature Physics (2021).

[38] G. Cheriaux, P. Rousseau, F. Salin, J. P. Chambaret, B. Walker, and L. F. Dimauro. *Aberration-free stretcher design for ultrashort-pulse amplification*. Opt. Lett., 21(6):414–416 (1996).

[39] P.-A. Belanger and C. Pare. *Self-focusing of Gaussian beams: an alternate derivation*. Appl. Opt., 22(9):1293–1295 (1983).

[40] V. S. Popov. *Tunnel and multiphoton ionization of atoms and ions in a strong laser field (Keldysh theory)*. Physics-Uspekhi, 47(9):855–885 (2004).

[41] P. Corkum. *Plasma perspective on strong-field multiphoton ionization*. Phys. Rev. Lett., 71:1994 (1993).

[42] K. J. Schafer, B. Yang, L. F. DiMauro, and K. C. Kulander. *Above threshold ionization beyond the high harmonic cutoff*. Phys. Rev. Lett., 70:1599 (1993).

[43] J. L. Krause, K. J. Schafer, and K. C. Kulander. *High-order harmonic generation from atoms and ions in the high intensity regime*. Phys. Rev. Lett., **68**:3535 (1992).

[44] T. Popmintchev, M.-C. Chen, D. Popmintchev, P. Arpin, S. Brown, S. Alisauskas, G. Andriukaitis, T. Balciunas, O. Mücke, A. Pugzlys, A. Baltuska, B. Shim, S. Schrauth, A. Gaeta, C. Hernandez-Garcia, L. Plaja, A. Becker, A. J.-B., M. Murnane, and H. Kapteyn. *Bright Coherent Ultrahigh Harmonics in the keV X-ray Regime from Mid-Infrared Femtosecond Lasers*. Science, 336(6086):1287–1291 (2012).

[45] S. M. Teichmann, F. Silva, S. L. Cousin, M. Hemmer, and J. Biegert. *0.5-keV Soft X-ray attosecond continua*. Nature Communications, 7(1):11493 (2016).

[46] Y. Mairesse, A. de Bohan, L. J. Frasinski, H. Merdji, L. C. Dinu, P. Monchicourt, P. Breger, M. Kovačev, R. Taïeb, B. Carré, H. G. Muller, P. Agostini, and P. Salières. *Attosecond synchronization of high-harmonic soft X-rays*. Science, 302:1540 (2003).

[47] S. Carlström. *Sub-Cycle Control of Strong-Field Processes on the Attosecond Timescale*. Division of Atomic Physics, Department of Physics, Lund University, Lund, Sweden (2017).

[48] K. Varjú, Y. Mairesse, B. Carre, M. B. Gaarde, P. Johnsson, S. Kazamias, R. Lopez-Martens, J. Mauritsson, K. J. Schafer, P. Balcou, A. L'Huillier, and P. Salières. *Frequency chirp of harmonic and attosecond pulses*. J. Mod. Opt., 52:379 (2005).

[49] N. Dudovich, O. Smirnova, J. Levesque, Y. Mairesse, M. Y. Ivanov, D. M. Villeneuve, and P. B. Corkum. *Measuring and controlling the birth of attosecond XUV pulses*. Nature Phys., 2:781 (2006).

[50] C. M. Heyl, C. L. Arnold, A. Couairon, and A. L'Huillier. *Introduction to macroscopic power scaling principles for high-order harmonic generation*. Journal of Physics B: Atomic, Molecular and Optical Physics, 50(1):013001 (2016).

[51] B. E. A. Saleh and M. C. Teich. *Fundamentals of Photonics*. John Wiley and Sons (2007).

[52] E. Constant, D. Garzella, P. Breger, E. Mével, C. Dorrer, C. L. Blanc, F. Salin, and P. Agostini. *Optimizing High Harmonic Generation in Absorbing Gases: Model and Experiment*. Phys. Rev. Lett., 82:1668 (1999).

[53] C. M. Heyl, H. Coudert-Alteirac, M. Miranda, M. Louisy, K. Kovacs, V. Tosa, E. Balogh, K. Varjú, A. L'Huillier, A. Couairon, and C. L. Arnold. *Scale-invariant nonlinear optics in gases*. Optica, 3(1):75–81 (2016).

[54] F. Brunner. *Focus optimization of intense attosecond XUV pulses*. Master Thesis, Lund University / ETH Zürich (2017).

[55] H. Wolter. *Spiegelsysteme streifenden Einfalls als abbildende Optiken für Röntgenstrahlen*. Annalen der Physik, 445:94–114 (1952).

[56] U. Even. *Pulsed Supersonic Beams from High Pressure Source: Simulation Results and Experimental Measurements*. Advances in Chemistry, 2014:636042 (2014).

[57] A. T. J. B. Eppink and D. H. Parker. *Velocity map imaging of ions and electrons using electrostatic lenses: Application in photoelectron and photofragment ion imaging of molecular oxygen*. Rev. Sci. Instr., 68:3477 (1997).

[58] L. M. Smith and D. R. Keefer. *Abel inversion using transform techniques*. J. Quant. Spectrosc. Radial. Transfer, 39:367 (1988).

[59] M. J. J. Vrakking. *An iterative procedure for the inversion of two-dimensional ion/photoelectron imaging experiments*. Rev. Sci. Instr., 72:4084 (2001).

[60] G. A. Garcia, L. Nahon, and I. Powis. *Two-dimensional charged particle image inversion using a polar basis function expansion*. Review of Scientific Instruments, 75(11):4989–4996 (2004).

[61] J. Ullrich, R. Moshammer, A. Dorn, R. Dörner, L. P. H. Schmidt, and H. Schniidt-Böcking. *Recoil-ion and electron momentum spectroscopy: reaction-microscopes*. Reports on Progress in Physics, 66(9):1463–1545 (2003).

[62] F. Zernike and F. Stratton. *Diffraction Theory of the Knife-Edge Test and its Improved Form, The Phase-Contrast Method*. Monthly Notices of the Royal Astronomical Society, 94(5):377–384 (1934).

[63] R. Cubalchini. *Modal wave-front estimation from phase derivative measurements*. J. Opt. Soc. Am., 69(7):972–977 (1979).

[64] W. Southwell. *Wave-front estimation from wave-front slope measurements*. J. Opt. Soc. Am., 70(8):998–1006 (1980).

[65] F. Campi. *An Intense Attosecond Light Source - Towards Extreme Ultraviolet Pump-Probe Experiments*. PhD Thesis, Faculty of Engineering, LTH (2017).

[66] R. Trebino, K. W. DeLong, D. N. Fittinghoff, J. Sweetser, M. A. Krumbügel, and B. Richman. *Measuring ultrashort laser pulses in the time-frequency domain using frequency-resolved optical gating*. Rev. Sci. Instrum., **68**:1 (1997).

[67] S. Akturk, C. D'Amico, and A. Mysyrowicz. *Measuring ultrashort pulses in the single-cycle regime using frequency-resolved optical gating*. J. Opt. Soc. Am. B, 25(6):A63–A69 (2008).

[68] C. Iaconis and I. A. Walmsley. *Spectral phase interferometry for direct electric field reconstruction of ultrashort optical pulses*. Opt. Lett., 23:792 (1998).

[69] M. Miranda, T. Fordell, C. Arnold, A. L'Huillier, and H. Crespo. *Simultaneous compression and characterization of ultrashort laser pulses using chirped mirrors and glass wedges*. Opt. Express, 20(1):688–697 (2012).

[70] J. Itatani, J. Levesque, D. Zeidler, H. Niikura, H. Pépin, J. C. Kieffer, P. B. Corkum, and D. M. Villeneuve. *Tomographic imaging of molecular orbitals*. Nature, 432:867 (2004).

[71] A. Paul, R. A. Bartels, R. Tobey, H. Green, S. Weiman, I. P. Christov, M. M. Murnane, H. C. Kapteyn, and S. Backus. *Quasi-phase-matched generation of coherent extreme-ultraviolet light*. Nature, **421**:51 (2003).

[72] F. Campi, H. Coudert-Alteirac, M. Miranda, L. Rading, B. Manschwetus, P. Rudawski, A. L'Huillier, and P. Johnsson. *Design and test of a broadband split-and-delay unit for attosecond XUV-XUV pump-probe experiments*. Review of Scientific Instruments, 87(2):023106 (2016).

[73] H. Wikmark. *Spatial and temporal aspects of intense attosecond pulses for pump-probe experiments*. Division of Atomic Physics, Department of Physics, Lund University, Lund, Sweden (2019).

[74] H. Muller. *Reconstruction of attosecond harmonic beating by interference of two-photon transitions*. Appl. Phys. B, 74:17 (2002).

[75] U. Becker. Comments At. Mol. Phys., 1(1):41–44 (1969).

[76] U. Becker. *Complete photoionisation experiments*. Journal of Electron Spectroscopy and Related Phenomena, 96(1):105–115 (1998).

[77] M. Eminyan, K. B. MacAdam, J. Slevin, and H. Kleinpoppen. *Measurements of Complex Excitation Amplitudes in Electron-Helium Collisions by Angular Correlations Using a Coincidence Method*. Phys. Rev. Lett., 31:576–579 (1973).

[78] L. H. Haber, B. Doughty, and S. R. Leone. *Photoelectron Angular Distributions and Cross Section Ratios of Two-Color Two-Photon Above Threshold Ionization of Argon*. The Journal of Physical Chemistry A, 113(47):13152–13158 (2009).

[79] T. Mazza, M. Ilchen, A. J. Rafipoor, C. Callegari, P. Finetti, O. Plekan, K. C. Prince, R. Richter, M. B. Danailov, A. Demidovich, G. De Ninno, C. Grazioli, R. Ivanov, N. Mahne, L. Raimondi, C. Svetina, L. Avaldi, P. Bolognesi, M. Coreno, P. O'Keeffe, M. Di Fraia, M. Devetta, Y. Ovcharenko, T. Möller, V. Lyamayev, F. Stienkemeier, S. Düsterer, K. Ueda, J. T. Costello, A. K. Kazansky, N. M. Kabachnik, and M. Meyer. *Determining the polarization state of an extreme ultraviolet free-electron laser beam using atomic circular dichroism*. Nature Communications, 5(1):3648 (2014).

[80] K. Klünder, J. M. Dahlström, M. Gisselbrecht, T. Fordell, M. Swoboda, D. Guénot, P. Johnsson, J. Caillat, J. Mauritsson, A. Maquet, R. Taïeb, and A. L'Huillier. *Probing Single-Photon Ionization on the Attosecond Time Scale*. Phys. Rev. Lett., 106:143002 (2011).

[81] J. M. Dahlström, D. Guénot, K. Klünder, M. Gisselbrecht, J. Mauritsson, A. L'Huillier, A. Maquet, and R. Taïeb. *Theory of attosecond delays in laser-assisted photoionization*. Chem. Phys., 414:53–64 (2013).

[82] D. Busto. *Quantum interference effects in attosecond photoionization dynamics*. Division of Atomic Physics, Department of Physics, Lund University, Lund, Sweden (2020).

[83] C. Cirelli, C. Marante, S. Heuser, C. L. M. Petersson, Á. J. Galán, L. Argenti, S. Zhong, D. Busto, M. Isinger, S. Nandi, S. Maclot, L. Rading, P. Johnsson, M. Gisselbrecht, M. Lucchini, L. Gallmann, J. M.

Dahlström, E. Lindroth, A. L'Huillier, F. Martín, and U. Keller. *Anisotropic photoemission time delays close to a Fano resonance*. Nature Communications, 9(1):955 (2018).

[84] J. Fuchs, N. Douguet, S. Donsa, F. Martin, J. Burgdörfer, L. Argenti, L. Cattaneo, and U. Keller. *Time delays from one-photon transitions in the continuum*. Optica, 7(2):154–161 (2020).

[85] S. Heuser, A. Jiménez Galán, C. Cirelli, C. Marante, M. Sabbar, R. Boge, M. Lucchini, L. Gallmann, I. Ivanov, A. S. Kheifets, J. M. Dahlström, E. Lindroth, L. Argenti, F. Martín, and U. Keller. *Angular dependence of photoemission time delay in helium*. Phys. Rev. A, 94:063409 (2016).

[86] D. Busto, J. Vinbladh, S. Zhong, M. Isinger, S. Nandi, S. Maclot, P. Johnsson, M. Gisselbrecht, A. L'Huillier, E. Lindroth, and J. M. Dahlström. *Fano's Propensity Rule in Angle-Resolved Attosecond Pump-Probe Photoionization*. Phys. Rev. Lett., 123:133201 (2019).

[87] J. Vinbladh, J. M. Dahlström, and E. Lindroth. *Many-body calculations of two-photon, two-color matrix elements for attosecond delays*. Phys. Rev. A, 100:043424 (2019).

[88] K. Klünder. *Electron Wave Packet Dynamics on the Attosecond Time Scale*. Ph.D. thesis, Lund University (2012).

[89] S. A. Aseyev, Y. Ni, L. J. Frasinski, H. G. Muller, and M. J. J. Vrakking. *Attosecond Angle-Resolved Photoelectron Spectroscopy*. Phys. Rev. Lett., 91:223902 (2003).

[90] D. M. Villeneuve, P. Hockett, M. J. J. Vrakking, and H. Niikura. *Coherent imaging of an attosecond electron wave packet*. Science, 356(6343):1150–1153 (2017).

[91] K. Taylor. *Photoelectron angular-distribution beta parameters for neon and argon*. Journal of Physics B: Atomic and Molecular Physics, 10(18):L699 (1977).

[92] K. L. Reid. *Photoelectron angular distributions*. Annu. Rev. Phys. Chem, 54(1):397–424 (2003).

[93] E. Arnous, S. Klarsfeld, and S. Wane. *Angular Distribution in the Two-Quantum Atomic Photoeffect*. Phys. Rev. A, 7:1559–1568 (1973).

[94] D. J. Kennedy and S. T. Manson. *Photoionization of the Noble Gases: Cross Sections and Angular Distributions*. Phys. Rev. A, 5:227 (1972).

[95] U. Fano. *Effects of configuration interaction on intensities and phase shifts*. Phys. Rev., 124(6):1866 (1961).

[96] T. Henning and F. Salama. *Carbon in the Universe*. Science, 282(5397):2204–2210 (1998).

[97] E. Anders and E. Zinner. *Interstellar Grains in Primitive Meteorites: Diamond, Silicon Carbide, and Graphite*. Meteoritics, 28(4):490–514 (1993).

[98] H. Schwertfeger, A. Fokin, and P. Schreiner. *Diamonds are a Chemist's Best Friend: Diamondoid Chemistry Beyond Adamantane*. Angewandte Chemie International Edition, 47(6):1022–1036 (2008).

[99] A. Candian, J. Bouwman, P. Hemberger, A. Bodi, and A. G. G. M. Tielens. *Dissociative ionisation of adamantane: a combined theoretical and experimental study*. Phys. Chem. Chem. Phys., 20:5399–5406 (2018).

[100] M. Steglich, F. Huisken, J. E. Dahl, R. M. K. Carlson, and T. Henning. *Electronic Spectroscopy of FUV-Irradiated Diamondoids: A Combined Experimental and Theoretical Study*. The Astrophysical Journal, 729(2):91 (2011).

[101] L. J. Frasinski. *Covariance mapping techniques*. Journal of Physics B: Atomic, Molecular and Optical Physics, 49(15):152004 (2016).

[102] E. Itälä, D. Ha, K. Kooser, E. Nõmmiste, U. Joost, and E. Kukk. *Fragmentation patterns of core ionized uracil*. International Journal of Mass Spectrometry, 306(1):82–90 (2011).

[103] J. Lahl. *Investigation of Ultrafast Molecular Dynamics via Covariance Mapping*. Division of Atomic Physics, Department of Physics, Lund University, Lund, Sweden (2019).

[104] M. Isinger. *Time-Frequency Analysis in Attosecond Spectroscopy*. Division of Atomic Physics, Department of Physics, Lund University, Lund, Sweden (2018).

[105] A. M. Kondratenko and E. L. Saldin. *Generation of coherent radiation by a relativistic electron beam in an ondulator**. Zhurnal Tekhnicheskoi Fiziki, 10:207–216 (1980).

[106] Y. Derbenev, A. Kondratenko, and E. Saldin. *On the possibility of using a free electron laser for polarization of electrons in storage rings*. Nuclear Instruments and Methods in Physics Research, 193(3):415–421 (1982).

[107] S. Schreiber. *First Lasing at 32 nm of the VUV-FEL at DESY*. 27th International Free Electron Laser Conference, page 12 (2005).

[108] V. Ayvazyan, N. Baboi, J. Bahr, V. Balandin, B. Beutner, A. Brandt, I. Bohnet, A. Bolzmann, R. Brinkmann, O. Brovko, J. Carneiro, S. Casalbuoni, M. Castellano, P. Castro, L. Catani, E. Chiadroni, S. Choroba, A. Cianchi, H. Delsim-Hashemi, G. Di Pirro, M. Dohlus, S. Dusterer, H. Edwards, B. Faatz, A. Fateev, J. Feldhaus, K. Flottmann, J. Frisch, L. Frohlich, T. Garvey, U. Gensch, N. Golubeva, H. Grabosch, B. Grigoryan, O. Grimm, U. Hahn, J. Han, M. Hartrott, and K. Honkavaara *et al. First operation of a free-electron laser generating GW power radiation at 32 nm wavelength*. Eur. Phys. J. D., 37(2):297–303 (2006).

[109] D. Oepts, A. van der Meer, and P. van Amersfoort. *The Free-Electron-Laser user facility FELIX*. Infrared Physics Technology, 36(1):297–308 (1995). Proceedings of the Sixth International Conference on Infrared Physics.

[110] B. W. J. McNeil and N. R. Thompson. *X-ray free-electron lasers*. Nature Photonics, 4(12):814–821 (2010).

[111] H. Fukuzawa, K. Nagaya, and K. Ueda. *Advances in instrumentation for gas-phase spectroscopy and diffraction with short-wavelength free electron lasers*. Nuclear Instruments and Methods in Physics Research Section A: Accelerators, Spectrometers, Detectors and Associated Equipment, 907:116–131 (2018).

[112] S. Kühn, M. Dumergue, S. Kahaly, S. Mondal, M. Füle, T. Csizmadia, B. Farkas, B. Major, Z. Várallyay, E. Cormier, M. Kalashnikov, F. Calegari, M. Devetta, F. Frassetto, E. Månsson, L. Poletto, S. Stagira, C. Vozzi, M. Nisoli, P. Rudawski, S. Maclot, F. Campi, H. Wikmark, C. L. Arnold, C. M. Heyl, P. Johnsson, A. L'Huillier, R. Lopez-Martens, S. Haessler, M. Bocoum, F. Boehle, A. Vernier, G. Iaquaniello, E. Skantzakis, N. Papadakis, C. Kalpouzos, P. Tzallas, F. Lépine, D. Charalambidis, K. Varjú, K. Osvay, and G. Sansone. *The ELI-ALPS facility: the next generation of attosecond sources*. Journal of Physics B: Atomic, Molecular and Optical Physics, 50(13):132002 (2017).

Publications

Author contributions

Paper I: Complete characterization of multi-channel single photon ionization

During the first RABBIT experiments at the Intense XUV Beamline, I participated in the measurements using the newly developed IR-XUV interferometer for the first time. I reviewed and analysed the data, co-developed the theoretical model and performed the fitting procedure in order to extract the one photon scattering phases and amplitudes. Finally, I wrote the manuscript draft and implemented the revisions.

Paper II: Focusing properties of high-order harmonics

I took part in designing and performing the knife-edge measurements to determine focus positions of different harmonic orders when being refocused. I contributed to the analysis and the interpretation, gave feedback on the manuscript drafts and supported the revisions.

Paper III: Spatiotemporal coupling of attosecond pulses

This paper was the begin of a series of studies on the impact of the infrared focusing conditions on the XUV beam properties, which ultimately led to the experiments performed in paper II. Shown in the paper are the measured Gaussian beam properties as a function of the infrared focus position, for which I participated in the experimental studies. During the analysis, I took part in the discussions and reviewed the manuscript draft.

Paper IV: Dissociation dynamics of the diamondoid adamantane upon photoionization by XUV femtosecond pulses

I participated in the experiments performed in the frame of a Laser Lab Europe campaign investigating the dissociation dynamics of adamantane. As the first re-

sult of a molecular sample at the Intense XUV Beamline, I contributed to the analysis and interpretation of the multi-body break-up dynamics upon the single and double ionization of the parent molecule. Finally, I gave feedback on the manuscript drafts.

Paper v: A 10-gigawatt attosecond source for non-linear XUV optics and XUV-pump-XUV-probe studies

My contribution to the paper was conducted during a study visit to the FORTH institute in Heraklion, Greece. We performed a general study of the generation of intense high-order harmonics, as presented in the paper, as well as the multi-ionization experiments in argon and neon. An attempt to record an XUV-XUV autocorrelation measurement in argon was not successful during my stay, but was accomplished a few weeks later by the team at Forth.

Paper vi: Time-Resolved Relaxation and Fragmentation of Polycyclic Aromatic Hydrocarbons Investigated in the Ultrafast XUV-IR Regime

During this experimental campaign, performed at Beamline I at the FEL FLASH at DESY in Hamburg, Germany, I participated in the integration of the molecular source in the experimental setup. During the beamtime, I co-developed the software controlling the scan procedure and took part in the data acquisition. During an analysis workshop in Lund, I was involved in the covariance analysis of the data. I contributed to the discussions during the data analysis and reviewed the manuscript draft.

Paper vii: Formative period in the X-ray-induced photodissociation of organic molecules

I participated in the presented experiment performed at the FEL SACLA at the synchrotron radiation facility SPring-8 in Sayo Town, Japan. During the beamtime, I contributed to the data analysis, in particular the time-resolved mass spectroscopy and the ion momentum imaging. Finally, I gave feedback on the manuscript draft.

Paper viii: Single-shot extreme-ultraviolet wavefront measurements of high-order harmonics

This paper was a result of a Laser Lab Europe campaign performed at the Intense XUV Beamline. I was involved in preparing the beamline for the XUV wavefront sensing and in the data acquisition during the experiments. Later on, I gave feedback on the drafts.

Paper IX: Micro-focusing of broadband high-order harmonic radiation by a double toroidal mirror

In this paper, I was mostly involved in the experiments concerning the wavefront measurements and optimization of the focusing optics. I took part in the discussions during the analysis and reviewed the paper drafts.

Paper X: A versatile velocity map ion-electron covariance imaging spectrometer for high-intensity XUV experiments

In this paper, the double-sided VMIS was commissioned and tested, which I was partly involved in. In particular, I participated in the acquisition of the data showing the ionization of N_2. I contributed to the corresponding discussions concerning the covariance analysis of the data and reviewed the manuscript drafts.

Paper I

J. Peschel, D. Busto, M. Plach, M. Bertolino, M. Hoflund, S. Maclot, H. Wikmark, F. Zapata, J. M. Dahlström, A. L'Huillier and P. Eng-Johnsson
Complete characterization of multi-channel single photon ionization
Submitted, arXiv:2109.01581

Complete characterization of multi-channel single photon ionization

Jasper Peschel[1,*], David Busto[1,2,*], Marius Plach[1], Mattias Bertolino[1], Maria Hoflund[1], Sylvain Maclot[1,†], Jimmy Vinbladh[1,3], Hampus Wikmark[1,‡], Felipe Zapata[1], Eva Lindroth[3], Mathieu Gisselbrecht[1], Jan Marcus Dahlström[1], Anne L'Huillier[1], and Per Eng-Johnsson[1]

[1] Department of Physics, Lund University, P.O. Box 118, 22100 Lund, Sweden
[2] Physikalisches Institut, Albert-Ludwigs-Universität, Stefan-Meier-Strasse 19, 79104 Freiburg, Germany
[3] Department of Physics, Stockholm University, AlbaNova University Center, SE-106 91 Stockholm, Sweden
[†] Current address: Department of Physics, Gothenburg University, Box 100, 405 30, Gothenburg, Sweden
[‡] Current address: Department of Physics and Astronomy, Uppsala University, Box 516, 751 20, Uppsala, Sweden
[*] These authors contributed equally to this work

Abstract. Ionization of atoms and molecules by absorption of a light pulse results in electron wavepackets carrying information on the atomic or molecular structure as well as on the dynamics of the ionization process. These wavepackets can be described as a coherent sum of waves of given angular momentum, called partial waves, each characterized by an amplitude and a phase. The complete characterization of the individual angular momentum components is experimentally challenging, requiring the analysis of the interference between partial waves both in energy and angle. Using a two-photon interferometry technique based on extreme ultraviolet attosecond and infrared femtosecond pulses, we characterize the individual partial wave components in the photoionization of the $2p^6$ shell in neon. The study of the phases of the angular momentum channels allows us to unravel the influence of short-range, correlation and centrifugal effects. This approach enables the complete reconstruction of photoionization electron wavepackets in time and space, providing insight into the photoionization dynamics.

Photoionization is a fundamental process that happens when electromagnetic radiation of high enough frequency is absorbed by matter. Since the 70s, synchrotron radiation has been used for photoionization studies [1,2,3], playing an important role for our understanding of the quantum nature of matter and its interaction with light. In general, an electron is released into the continuum via various ionization channels corresponding to different initial or final angular momenta. In these channels, the probability to find the released electron in space is proportional to the square of a spherical harmonic function, as exemplified in Figure 1 for the case of the ejection of an electron from the $2p^6$ shell of neon. The characterization of the photoionization process requires the determination of the amplitudes of the different channels and, when they add coherently, their relative phases. Experimentally this requires angular detection, to analyse the interference between different outgoing angular momentum channels [4,5]. Additionally, energy resolution is needed to disentangle ionization pathways leading to different ionic states or distinguish between different excitation schemes.

In order to perform "complete" experiments, where the outgoing electron wavepacket is reconstructed, additional experimental information is usually needed [3,6,7]. Advances in this direction have been made by preparing atoms in aligned or oriented excited states, using light with several frequency and polarization components [8,9,10]. Recent experiments have extended such studies to ground state atoms using two-photon schemes combining either laser-generated attosecond extreme ultraviolet (XUV) pulses [11,12] or free-electron laser

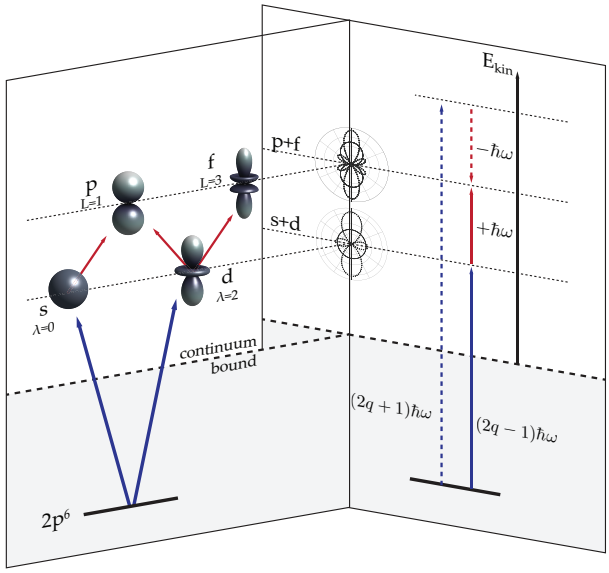

FIG. 1: **Angular momenta and energy level diagram:** Angular channels involved in the one- and two-photon transitions addressed in the present work (left panel) and principle of the interferometric RABBIT technique (right panel). The photoionization from the $2p^6$-ground state of neon towards s- and d- continuum states (blue arrows) is followed by the absorption or stimulated emission of an additional IR photon (red arrows, solid and dashed lines, right panel), leading to final p- and f-states. The left panel presents the quantum paths corresponding to the initial state $m = 0$. For $m = \pm 1$, the path going via $\lambda = 0$ is forbidden.

femtosecond pulses [13] with infrared (IR) laser pulses. These have been limited, however, to the characterization of the final two-photon wavepacket [14,12,13].

In this article, we completely characterize one-photon ionization from the $2p^6$-ground state of neon, obtaining the amplitude and relative phase of the electric dipole transition matrix elements towards s- and d-continuum states. To extract channel-resolved one-photon ionization (scattering) phases, we apply the reconstruction of attosecond beating by interference of two-photon transitions (RABBIT) technique [11] while detecting electrons with full angular resolution [15,16,17,18]. We use XUV pulses from high-order harmonic generation (HHG) [19] in argon in the 20-50 eV range and delayed weak IR pulses from the laser driving the HHG process. The phase extraction relies on the fact that transitions between continuum states are universal, *i.e.* independent of the atom. We then determine the channel-resolved one-photon amplitudes from measurements with only the XUV field. The retrieved values for the scattering phases and channel amplitudes are in excellent agreement with calculations using angular-channel-resolved many-body perturbation theory [20,21,22].

Figure 1 describes the principle of our experiment. Photoionization from the $2p^6$-ground state of neon leads to photoelectrons of different angular momenta s or d. Additional absorption or emission of IR photons, through transitions between continuum states, called "continuum-continuum" (cc) transitions, leads to sidebands in the photoelectron spectrum. These sidebands can be reached by two interfering quantum paths (solid and dashed lines in Figure 1) [11,23]. Our experiment consists in recording the photoelectron spectra as a

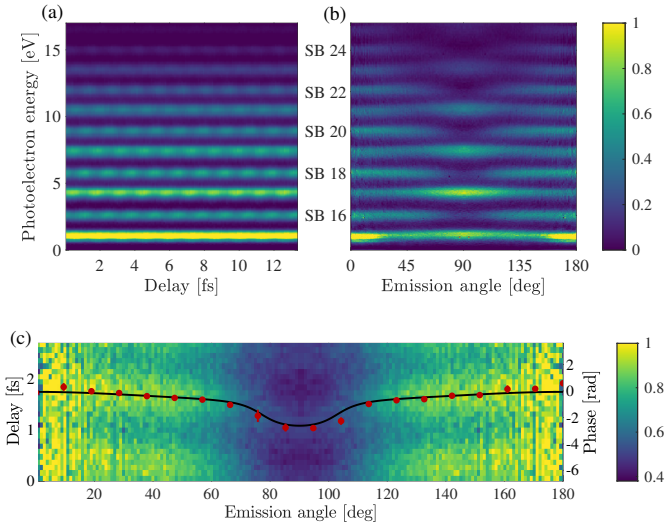

FIG. 2: **Angle and delay-dependence of photoelectron spectra:** (a) Angle-integrated spectrum as a function of the delay; (b) Angle-resolved two-photon photoelectron spectrum integrated over all delays; (c) Energy-integrated sideband 16 as a function of angle and delay. The red dots show the extracted phase, and the black line shows the result of a simulation (see Methods section).

function of delay between the XUV and IR pulses and emission angle (see experimental details in the Methods section).

Figure 2 presents angular-integrated delay-dependent (a) as well as angular-resolved delay-integrated photoelectron spectra (b). It shows contributions from absorption of harmonics 15 to 25 as well as sidebands 16 to 24 (the number indicates the total energy absorbed in units of the IR photon energy), as a result of the interaction between released electrons and the infrared field. The sidebands in Figure 2(a) oscillate at frequency 2ω, where ω is the angular frequency of the driving laser. As shown in [14], the phase of the oscillation depends on the intrinsic group delay of the attosecond pulses as well as on a delay due to the photoionization process. The photoelectron peaks corresponding to absorption of harmonics oscillate with opposite phase, due to redistribution of the electrons from the main absorption peaks to the sidebands [24]. Figure 2(b) presents the angular dependence of the delay-integrated photoelectron signal. The sidebands are maximized at the angles of 0° and 180°, corresponding to emission along the common polarization axis of the XUV and IR fields. In contrast the main absorption peaks present a maximum at 90°.

Finally, Figure 2(c) shows the delay and angle dependence of sideband 16. The oscillation phase is extracted by fitting a cosine to the temporal evolution for each angle. The red dots in Figure 2(c) show the measured phase as a function of the emission angle. The phase variation around 80° is close to 2 rad. The experimental data is compared to simulations (black line) based on calculations presented in the Methods section.

The observed angular structure of the sidebands depends not only on the interference between the different partial waves of the angular momentum channels reached via single photon ionization, but is also strongly influenced by the cc-transitions [16,18]. The additional interaction with the IR field leads to an increase in the number of angular channels (see Figure 1, where only the $m = 0$ angular path is indicated), and modifies the radial am-

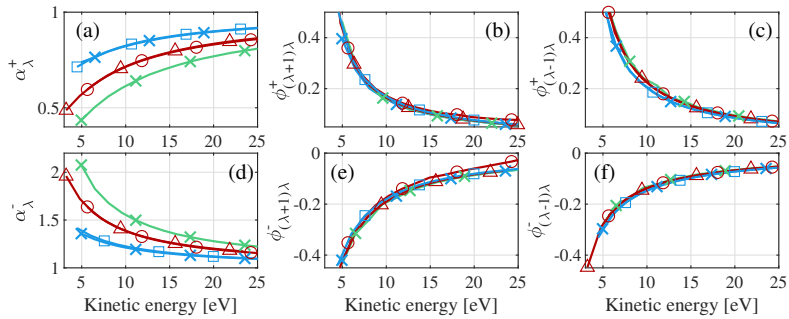

FIG. 3: **Continuum-continuum transitions:** Calculated amplitude ratios $\alpha^{\pm}_{\lambda\ell}$ (a,d) and continuum-continuum phases $\phi^{\pm}_{L\lambda}$ (b-c and e-f) for the absorption (a-c) and emission (d-f) processes. For the amplitude ratios, the curves correspond to different intermediate states (λ=1,2,3 in blue, red, green, respectively) and different atoms/initial states (square, He, 1s initial state); (cross, Kr, 3d); (triangle, Ne, 2p); (circle, Ar, 3p). (b,e) refer to transitions with increasing angular momentum, $L = \lambda + 1$, while in (c,f), $L = \lambda - 1$.

plitude and phase of the outgoing photoionization wavepacket [25,26,27]. In the following, we present a general method to retrieve the amplitude and phase of each photoionization angular channel from experimental data.

The angle- and delay-dependent sideband intensity can be written as

$$I_{SB}(\theta,\tau) \propto \int d\phi \sum_{m=0,\pm1} \Big| \sum_{\substack{L=1,3\\ \lambda=0,2}} \mathcal{M}^{+}_{L\lambda\ell m} Y_{Lm}(\theta,\phi) \mathrm{e}^{\mathrm{i}\omega\tau} + \mathcal{M}^{-}_{L\lambda\ell m} Y_{Lm}(\theta,\phi) \mathrm{e}^{-\mathrm{i}\omega\tau} \Big|^2, \tag{1}$$

where $(\pm)$ refers to the pathways with IR absorption $(+)$ or emission $(-)$, $\mathcal{M}^{\pm}_{L\lambda\ell m}$ is the two-photon transition matrix element with final state angular momentum L, intermediate state orbital angular momentum λ, initial state orbital angular momentum ℓ ($\ell = 1$ in the case studied here) and initial magnetic quantum number m, which is kept constant in the two-photon transition, since the XUV and IR fields are linearly polarized in the same direction. $Y_{Lm}(\theta,\phi)$ are spherical harmonics and $\mathrm{e}^{\pm\mathrm{i}\omega\tau}$ is the phase term introduced by absorption and emission of the IR photon with angular frequency ω, which depends on the delay τ between the XUV and IR fields. The transition matrix element can be decomposed into amplitude and phase terms as

$$\mathcal{M}^{\pm}_{L\lambda\ell m} = C^{m}_{L\lambda} C^{m}_{\lambda\ell}\, \sigma^{\pm}_{L\lambda\ell}\, \mathrm{e}^{\mathrm{i}(\phi^{\pm}_{L\lambda} + \varphi^{\pm}_{\lambda\ell} + \Phi_{2q\mp1})}. \tag{2}$$

Here, $C^{m}_{L\lambda}, C^{m}_{\lambda\ell}$ are known angular coefficients (See Eq. (S1) of the Supplementary Material, SM) and $\sigma^{\pm}_{L\lambda\ell}$ is the radial amplitude. The phase term includes three different contributions: $\varphi^{\pm}_{\lambda\ell}$ is the phase associated to the one-photon ionization channel $\ell \to \lambda$, $\phi^{\pm}_{L\lambda}$ is the cc-phase, and $\Phi_{2q\mp1}$ the phase of the $(2q\mp1)^{\text{th}}$ harmonic field. The characterization of multi-channel one-photon ionization using two-photon interferometry requires the determination of all these quantities, from either theoretical arguments or experimental measurements.

Applying and extending the results of previous work [25,26,28], we use the universal behavior of the cc-transitions to determine some of the terms in Eq. (2), thus reducing the number of unknown quantities. Figure 3 (a,d) presents the ratios between the two-photon transition radial amplitudes, calculated as described in the methods section and defined as

$$\alpha^{\pm}_{\lambda\ell} = \frac{\sigma^{\pm}_{(\lambda-1)\lambda\ell}}{\sigma^{\pm}_{(\lambda+1)\lambda\ell}}, \tag{3}$$

for increasing or decreasing angular momentum from the same intermediate state as the function of the kinetic energy of the electron. The different curves correspond to different intermediate states (λ=1,2,3 in blue, red and green) and different atoms and initial states. The ratio shows an universal behavior [28], independent of the atom. Only the orbital angular momentum of the intermediate state, λ, is of importance.

We present $\phi^{\pm}_{L\lambda}$ in Figure 3 for increasing (b,e) and decreasing (c,f) angular momenta, in the absorption (b,c) and emission cases (e,f). The colors and symbols, corresponding to different intermediate angular momenta and atoms/initial states are indicated in the figure caption. These results show that the variation of the continuum-continuum phase is universal, depending mainly on whether the IR photon is absorbed or emitted. For the absorption process, the cc-phase decreases as a function of kinetic energy and is positive, while for the emission, it increases and is negative. Note that the phases are not mirror image of each other, i.e. $\phi^{+}_{L\lambda} \neq -\phi^{-}_{L\lambda}$. The cc-phases depend on whether the angular momentum increases or decreases, especially at low kinetic energy, as observed by comparing (b) and (c), or (e) and (f). Finally, the cc-phases depend only slightly on the intermediate angular momentum (compare blue and red curves) and not at all on the atomic system (e.g. compare circle and triangle) in the range of energies studied here.

Our channel-resolved amplitude and phase retrieval is based on the knowledge of the cc-transitions. The unknown and known quantities in Eq. (1), after having expressed the transition matrix elements as in Eq. (2), and used the available information in Fig. 3, are indicated in Table 1 for an initial $\ell = 1$ state. We note that only the phase difference $\Delta\Phi_{2q} = \Phi_{2q+1} - \Phi_{2q-1}$, and not the individual high-order harmonic phases, plays a role in Eq. (1). The number of unknown quantities is therefore nine. While here the case of $\ell = 1$ is shown, this is also true for higher initial angular momenta.

TABLE 1: Unknown and known quantities involved in Eq. (1)

	Unknown quantities	Known quantities
Atomic phases	$\varphi^{\pm}_{01}$, $\varphi^{\pm}_{21}$	$\phi^{\pm}_{10}$, $\phi^{\pm}_{12}$, $\phi^{\pm}_{32}$, from Fig. 3(b,c,e,f)
2-photon amplitudes	$\sigma^{\pm}_{101}$, $\sigma^{\pm}_{321}$	$\alpha^{\pm}_{21}$, from Fig. 3(a,d)
		$\rightarrow\ \sigma^{\pm}_{121} = \alpha^{\pm}_{21}\sigma^{\pm}_{321}$
Harmonic phase	$\Delta\Phi_{2q} = \Phi_{2q-1} - \Phi_{2q+1}$	

We determine these nine unknown quantities using a global fit to our experimental measurements. In general, multiphoton electron angular distributions can be written as an expansion in Legendre polynomials [26,27,29,30]. For a two-photon transition, without parity mixing, the expansion needs only three polynomials, $P_0(x) = 1$, $P_2(x) = (3x^2 - 1)/2$, and $P_4(x) = (35x^4 - 30x^2 + 3)/8$, reading as

$$I_{\mathrm{SB}}(\theta, \tau) = h_0(\tau) + h_2(\tau)P_2(\cos\,\theta) + h_4(\tau)P_4(\cos\,\theta). \tag{4}$$

The theoretical expressions for the coefficients $h_i(\tau)$, $i = 0, 2, 4$, can be obtained by expanding Eq. (1) and replacing the products of spherical harmonics by Legendre polynomials, leading to Eqs. (S2-S4) of the SM. Figure 4 shows the variation of $h_i(\tau)$ extracted from the experimental data for each delay (black points). As is clear from Eqs. (S2-S4) in the SM and from Figure 4, each $h_i(\tau)$ oscillates with the delay τ at the frequency 2ω and is therefore fully determined by three quantities: mean value, amplitude and phase. Thus, a total of nine parameters describe the angle and delay dependence of the sideband signal $I_{\mathrm{SB}}(\theta, \tau)$. This implies that the nine unknown quantities in table 1 can be determined through a global fit

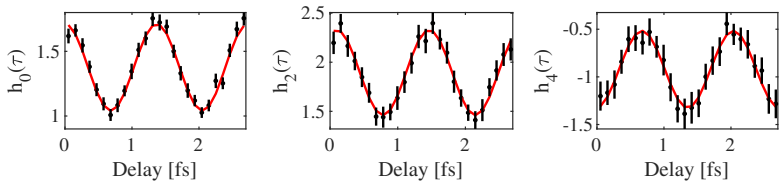

FIG. 4: **Global fit to experimental data:** Delay dependence of the coefficients $h_i(\tau)$, $i = 0, 2, 4$ for sideband 18. The black dots are obtained from the angular distributions (Eq. 4) for each delay and the error bars correspond to one standard deviation. The red curves are the result of a simultaneous fit of the delay dependent h_i functions using Eqs. (S2-S4) in the SM.

of the three analytical expressions of $h_i(\tau)$ given in the SM, to the experimentally measured coefficients in Figure 4. The result of such a global fit is shown by the red lines in Figure 4.

The nine unknown quantities in table 1 are not completely independent, since the one-photon ionization phases only appear as differences in Eqs. (S2-S4) (SM). We therefore lock φ_{01}^{-} for the first sideband and determine all of the others (φ_{01}^{+},$\varphi_{21}^{\pm}$). To map out the energy dependence of the one-photon phases, the global fit is repeated for each sideband. Using the fact that $\varphi_{\lambda 1}^{-}(SB_n) = \varphi_{\lambda 1}^{+}(SB_{n+2})$, we iteratively retrieve the one-photon phases, as a function of energy, for the two possible angular momenta. From now on, we drop the $\pm$ superscript to describe the one-photon phase, as it only refers to the path used for the determination. The experimental results for φ_{01} and φ_{21} are shown in Fig. 5(a) in green and blue symbols respectively, together with the phases calculated using many-body perturbation theory, as described in the methods section (solid lines).

The phase $\varphi_{\lambda\ell}$ can be written as the sum of the scattering phase η_λ and a contribution from the centrifugal barrier $-\pi\lambda/2$ [25]. The scattering phase is itself the sum of the Coulomb phase $\varsigma_\lambda = \arg\Gamma(\lambda+1-iZ/k)$ and a contribution δ_λ from the short range potential. (Here Z is the atomic number, $k = \sqrt{2mE}/\hbar$ the wavenumber and Γ, the gamma function). In order to emphasize the influence of the short range potential, we also show in Figure 5(a) ς_0 and ς_2 (green and blue dashed lines), as well as $\varsigma_0+\delta_0$ and $\varsigma_2+\delta_2-\pi$ (green and blue dot-dashed lines), where δ_λ are taken from Kennedy and Manson [1]. The calculated phases are very close to $\varsigma_\lambda + \delta_\lambda - \pi\lambda/2$ (compare solid and dot-dashed lines). The difference between φ_{01} and ς_0 is due to the short range potential contributing by $\sim 1.2\pi$, while that between φ_{02} and ς_2 is mainly due to the effect of the centrifugal barrier, leading to a π phase shift. For $\lambda = 2$, short range effects are small due to the centrifugal barrier that prevents the electron to come close to the core. The measured phases are also in excellent agreement with the predictions from quantum defect theory at threshold, leading to $\delta_\lambda = \pi\mu_\lambda \simeq 1.3\pi$ for $\lambda = 2$ and $\delta_\lambda \simeq 0$ for $\lambda = 0$, (μ_λ is the quantum defect extracted from experimental energy values) [31]. Since the short range effects for the s-electron are comparable to the effect of the centrifugal barrier for the d-electron, the difference between φ_{01} and φ_{21} therefore mostly reflects the difference in Coulomb phases. The increase of the phases with energy, which is similar for the two angular momenta also follows the behavior of the Coulomb phases.

As explained above, our procedure allows us to determine the phases as function of energy and angular momentum up to a global phase offset. After adjustment of this phase offset, the theoretical and experimental results are found to be in excellent agreement. Both the energy dependence and the difference between the angular channels is well reproduced by the experimental results. The observed deviation for the highest energy might be due to low statistics originating from the low intensity of the 25^{th} harmonic.

Finally, in order to fully characterize single photon ionization, it is necessary to also determine the one-photon amplitudes $\sigma_{\lambda\ell}$. However, it is not possible to extract $\sigma_{\lambda\ell}$ from the two-photon ionization data. Instead, we perform additional measurements in the absence

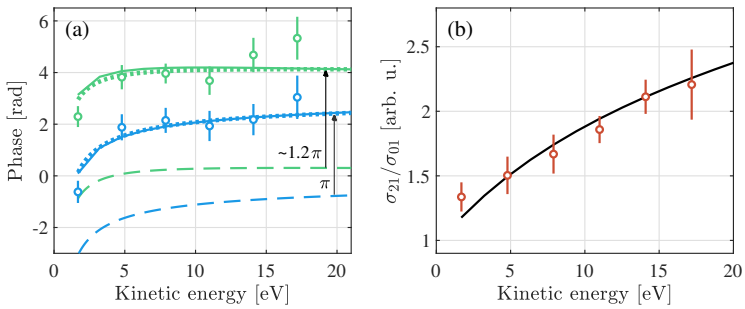

FIG. 5: **Extracted one-photon amplitudes and phases as a function of the kinetic energy.** (a) Scattering phases φ_{01} (green) and φ_{21} (blue) for experimental (dots) and simulated data (solid lines). The dashed lines correspond to the contributions from the Coulomb phase ς_0 (green) and ς_2 (blue), where for the dotted lines the effect of the short-range potential and the centrifugal effect is added: $\varsigma_\lambda + \delta_\lambda - \pi\lambda/2$. For $\lambda = 0$ this shift is dominated by the short range potential ($\delta_0 \approx 1.2\pi$) and for $\lambda = 2$ by the centrifugal effect (π), as indicated by the arrows. (b) Ratio between amplitudes σ_{21} and σ_{01} extracted from XUV only data (dots). The black line shows the result of angular-channel-resolved many-body perturbation simulation.

of the IR field, in order to access directly the one-photon transition amplitudes. The one-photon angle-dependent photoelectron signal is written as:

$$I_{\mathrm{H}}(\theta) \propto \int d\phi \sum_{m=0,\pm1} \Big| \sum_{\lambda=0,2} M_{\lambda\ell m} Y_{\lambda m}(\theta,\phi) \Big|^2 . \tag{5}$$

Here, $M_{\lambda\ell m}$ is the one-photon matrix element from the ground state with angular momentum ℓ and magnetic quantum number m to the continuum state with angular momentum λ, which can be written as

$$M_{\lambda\ell m} \approx C^m_{\lambda\ell}\ \sigma_{\lambda\ell}\ \mathrm{e}^{\mathrm{i}(\varphi_{\lambda\ell}+\Phi_{2q+1})}, \tag{6}$$

where $2q+1$ is the order of the harmonic used for the photoionization. $I_{\mathrm{H}}(\theta)$ can be written as an expansion of Legendre polynomials P_0 and P_2 [see Eqs. (S5) and (S6) in the SM]. The coefficients of the expansion h_0 and h_2 are extracted from the experimental data. Using the one-photon phases obtained previously, we determine the relative radial amplitudes of the $\lambda = 0$ and $\lambda = 2$ channels. The ratio between these amplitudes is shown in Figure 5(b), together with the calculated one. The ratio is above one for all energies, thus in agreement with Fano's propensity rule for one-photon absorption.

The retrieval of the amplitudes and phases of angular momentum channels in photoionization has been a major challenge during the last decades, and has only been realized for specially prepared atoms or for single angular channels. Here, we present a method using laser-assisted photoionization, based on the universality of the continuum-continuum transitions to retrieve the one-photon photoionization amplitudes and phases for the different angular channels. We apply the method both experimentally and numerically to characterize photoionization from the $2p^6$ shell of neon. Our method is general and can be applied to other shells (e.g. d) and thus to more complex atomic systems. In particular, the study

of the phases of the different angular momentum channels, unravels the interplay between short-range, correlation and/or centrifugal effects.

1 Acknowledgments

The authors acknowledge support from the Swedish Research Council, the European Research Council (advanced grant QPAP), the Knut and Alice Wallenberg Foundation, and the Crafoord Foundation.

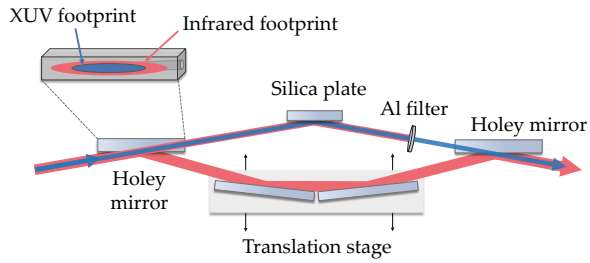

FIG. 6: **Schematic drawing of the XUV-infrared interferometer.** Two holey mirrors split and recombine the XUV and infrared components of the beam and a linear translation stage introduces a time delay between them.

Methods

The XUV attosecond pulse trains (ATPs) used in the experiments are synthesized using high-order harmonic generation (HHG) by focusing 40 fs, 806 nm, ∼45 mJ pulses from a 10 Hz Ti:sapphire laser into a pulsed gas jet of Argon in a loose focusing geometry (∼8.7 m focal length) [32]. The obtained XUV spectrum spans from ∼20 to 45 eV. The beamline is designed to generate high-flux high-order harmonics, hence the loose focusing geometry [33].

The APTs are separated from the fundamental infrared field by taking advantage of the lower divergence of the XUV beam. Figure 6 shows a scheme of the newly developed interferometer, which consists of a set of holey mirrors creating two interferometric arms. The hole diameter is chosen in a way such that the entire XUV beam propagates through the hole, whereas the reflected part only consists of fundamental infrared radiation. A translation stage in the infrared arm varies the path difference between both arms and hence introduces a time delay. A 200 nm thick aluminum filter in the XUV arm blocks the remaining infrared and the intense low-order harmonics. Due to the long beamline design, traditional interferometers add the risk of pointing instabilities and temporal jitters, while propagating over such long distances. Hence, we designed this compact in-line interferometer, such that the path difference is kept as short as possible, which results in excellent temporal and spatial stability.

Both beams, after being collinearly overlapped, are focused tightly using two toroidal mirrors in a Wolter configuration [34]. In focus they interact with the neon target gas introduced using a pulsed Even-Lavie valve [35] and a set of two skimmers. The resulting photoelectrons are detected by a velocity map imaging spectrometer (VMIS) with the ability to record angle-resolved momentum distribution [36,37]. The 2D projections of the momentum distribution of the photoelectrons is recorded by a CCD camera imaging a phosphor screen coupled to a set of multi-channel plates. Since the VMIS is recording the 2D projection of the 3D momentum distribution, an inverse Abel transform has to be applied, which is done using an iterative method [38].

Our calculations are based on a one-electron Hamiltonian, with a Dirac-Fock potential plus a correction that ensures the correct long-range potential for ionized photoelectrons [20]. The absorption of one ionizing photon is treated within the Relativistic Random Phase Approximation with Exchange (RPAE) resulting in a so-called perturbed wave function describing the ionized electron. The method accounts for important many-body effects such as inter-channel coupling and ground-state correlation. Exterior complex scaling is used in order to be able to use a finite numerical box.

The complex-valued two-photon matrix elements, expressed in Eq. (2), are then calculated as the transition from the perturbed wave function to the final continuum state in each angular momentum channel, following the procedure described in [20,21,22] for the

non-relativistic case. The integration is performed numerically out to a distance far outside the atomic core, but within the unscaled region, while the last part of the integral is carried out using analytical Coulomb waves along the imaginary radial axis. The amplitude and phase shift of these Coulomb waves are determined from the numerical solutions for the perturbed wave function and for the final state describing a free electron within the potential of the remaining ion. The numerical stability is monitored by comparison of different "break points" between the numerical and analytical descriptions.

References

1. D. J. Kennedy and S. T. Manson. Photoionization of the Noble Gases: Cross Sections and Angular Distributions. *Phys. Rev. A*, 5:227, 1972.
2. Volker Schmidt. Photoionization of atoms using synchrotron radiation. *Rep. Prog. Phys.*, 55:1483–1659, 1992.
3. Uwe Becker. Complete photoionisation experiments. *Journal of Electron Spectroscopy and Related Phenomena*, 96(1):105–115, 1998.
4. J. Cooper and R. N. Zare. Angular Distribution of Photoelectrons. *J. Chem. Phys*, 48:942, 1968.
5. J. W. Cooper. Photoelectron-angular-distribution parameters for rare-gas subshells. *Phys. Rev. A*, 47:1841–1851, Mar 1993.
6. Uwe Becker. *Comments At. Mol. Phys.*, 1(1):41–44, 1969.
7. M. Eminyan, K. B. MacAdam, J. Slevin, and H. Kleinpoppen. Measurements of complex excitation amplitudes in electron-helium collisions by angular correlations using a coincidence method. *Phys. Rev. Lett.*, 31:576–579, Aug 1973.
8. K. Godehusen, P. Zimmermann, A. Verweyen, A. von dem Borne, Ph. Wernet, and B. Sonntag. A complete photoionization experiment with polarized atoms using magnetic dichroism and phase tilt measurements. *Phys. Rev. A*, 58:R3371–R3374, Nov 1998.
9. N.A. Cherepkov. Complete experiments in photoionization of atoms and molecules. *Journal of Electron Spectroscopy and Related Phenomena*, 144-147:1197–1201, 2005. Proceeding of the Fourteenth International Conference on Vacuum Ultraviolet Radiation Physics.
10. F J Wuilleumier and M Meyer. Pump–probe experiments in atoms involving laser and synchrotron radiation: an overview. *Journal of Physics B: Atomic, Molecular and Optical Physics*, 39(23):R425–R477, nov 2006.
11. P.M. Paul, E.S. Toma, P. Breger, G. Mullot, F. Augé, Ph. Balcou, H.G. Muller, and P. Agostini. Observation of a train of attosecond pulses from high harmonic generation. *Science*, 292:1689, 2001.
12. Louis H. Haber, Benjamin Doughty, and Stephen R. Leone. Photoelectron angular distributions and cross section ratios of two-color two-photon above threshold ionization of argon. *The Journal of Physical Chemistry A*, 113(47):13152–13158, Nov 2009.
13. T. Mazza, M. Ilchen, A. J. Rafipoor, C. Callegari, P. Finetti, O. Plekan, K. C. Prince, R. Richter, M. B. Danailov, A. Demidovich, G. De Ninno, C. Grazioli, R. Ivanov, N. Mahne, L. Raimondi, C. Svetina, L. Avaldi, P. Bolognesi, M. Coreno, P. O'Keeffe, M. Di Fraia, M. Devetta, Y. Ovcharenko, Th. Möller, V. Lyamayev, F. Stienkemeier, S. Düsterer, K. Ueda, J. T. Costello, A. K. Kazansky, N. M. Kabachnik, and M. Meyer. Determining the polarization state of an extreme ultraviolet free-electron laser beam using atomic circular dichroism. *Nature Communications*, 5(1):3648, Apr 2014.
14. K. Klünder, J. M. Dahlström, M. Gisselbrecht, T. Fordell, M. Swoboda, D. Guénot, P. Johnsson, J. Caillat, J. Mauritsson, A. Maquet, R. Taïeb, and A. L'Huillier. Probing single-photon ionization on the attosecond time scale. *Phys. Rev. Lett.*, 106:143002, 2011.
15. S. A. Aseyev, Y. Ni, L. J. Frasinski, H. G. Muller, and M. J. J. Vrakking. Attosecond Angle-Resolved Photoelectron Spectroscopy. *Phys. Rev. Lett.*, 91:223902, 2003.
16. Sebastian Heuser, Álvaro Jiménez Galán, Claudio Cirelli, Carlos Marante, Mazyar Sabbar, Robert Boge, Matteo Lucchini, Lukas Gallmann, Igor Ivanov, Anatoli S. Kheifets, J. Marcus Dahlström, Eva Lindroth, Luca Argenti, Fernando Martín, and Ursula Keller. Angular dependence of photoemission time delay in helium. *Phys. Rev. A*, 94:063409, Dec 2016.
17. D. M. Villeneuve, Paul Hockett, M. J. J. Vrakking, and Hiromichi Niikura. Coherent imaging of an attosecond electron wave packet. *Science*, 356(6343):1150–1153, 2017.

18. Claudio Cirelli, Carlos Marante, Sebastian Heuser, C. L. M. Petersson, Álvaro Jiménez Galán, Luca Argenti, Shiyang Zhong, David Busto, Marcus Isinger, Saikat Nandi, Sylvain Maclot, Linnea Rading, Per Johnsson, Mathieu Gisselbrecht, Matteo Lucchini, Lukas Gallmann, J. Marcus Dahlström, Eva Lindroth, Anne L'Huillier, Fernando Martín, and Ursula Keller. Anisotropic photoemission time delays close to a fano resonance. *Nature Communications*, 9(1):955, Mar 2018.
19. M. Ferray, A. L'Huillier, X.F. Li, L.A. Lompre, G. Mainfray, and C. Manus. Multiple-harmonic conversion of 1064 nm radiation in rare gases. *J. Phys. B*, **21**:L31, 1988.
20. JM Dahlström, Thomas Carette, and Eva Lindroth. Diagrammatic approach to attosecond delays in photoionization. *Phys. Rev. A*, 86(6):061402, 2012.
21. J M Dahlström and E Lindroth. Study of attosecond delays using perturbation diagrams and exterior complex scaling. *J. Phys. B*, 47(12):124012, 2014.
22. Jimmy Vinbladh, Jan Marcus Dahlström, and Eva Lindroth. Many-body calculations of two-photon, two-color matrix elements for attosecond delays. *Phys. Rev. A*, 100:043424, Oct 2019.
23. V. Véniard, R. Taïeb, and A. Maquet. Phase dependence of (N+1) - color (N>1) ir-uv photoionization of atoms with higher harmonics. *Phys. Rev. A*, **54**:721, 1996.
24. Mattias Bertolino and Jan Marcus Dahlström. Multiphoton interaction phase shifts in attosecond science. *Phys. Rev. Research*, 3:013270, Mar 2021.
25. J Marcus Dahlström, Diego Guénot, Kathrin Klünder, Matthieu Gisselbrecht, Johan Mauritsson, Anne L'Huillier, Alfred Maquet, and Richard Taïeb. Theory of attosecond delays in laser-assisted photoionization. *Chem. Phys.*, 414:53–64, 2013.
26. Jaco Fuchs, Nicolas Douguet, Stefan Donsa, Fernando Martin, Joachim Burgdörfer, Luca Argenti, Laura Cattaneo, and Ursula Keller. Time delays from one-photon transitions in the continuum. *Optica*, 7(2):154–161, Feb 2020.
27. J Joseph, F Holzmeier, D Bresteau, C Spezzani, T Ruchon, J F Hergott, O Tcherbakoff, P D'Oliveira, J C Houver, and D Dowek. Angle-resolved studies of XUV–IR two-photon ionization in the RABBITT scheme. *Journal of Physics B: Atomic, Molecular and Optical Physics*, 53(18):184007, aug 2020.
28. David Busto, Jimmy Vinbladh, Shiyang Zhong, Marcus Isinger, Saikat Nandi, Sylvain Maclot, Per Johnsson, Mathieu Gisselbrecht, Anne L'Huillier, Eva Lindroth, and Jan Marcus Dahlström. Fano's propensity rule in angle-resolved attosecond pump-probe photoionization. *Phys. Rev. Lett.*, 123:133201, 2019.
29. Katharine L Reid. Photoelectron angular distributions. *Annu. Rev. Phys. Chem*, 54(1):397–424, 2003.
30. E. Arnous, S. Klarsfeld, and S. Wane. Angular distribution in the two-quantum atomic photoeffect. *Phys. Rev. A*, 7:1559–1568, May 1973.
31. H. Friedrich. *Theoretical atomic physics*. Springer Verlag, 1994.
32. B. Manschwetus, L. Rading, F. Campi, S. Maclot, H. Coudert-Alteirac, J. Lahl, H. Wikmark, P. Rudawski, C. M. Heyl, B. Farkas, T. Mohamed, A. L'Huillier, and P. Johnsson. Two-photon double ionization of neon using an intense attosecond pulse train. *Phys. Rev. A*, 93:061402, Jun 2016.
33. P. Rudawski, C. M. Heyl, F. Brizuela, J. Schwenke, A. Persson, E. Mansten, R. Rakowski, L. Rading, F. Campi, B. Kim, P. Johnsson, and A. L'Huillier. A high-flux high-order harmonic source. *Review of Scientific Instruments*, 84(7):–, 2013.
34. H. Coudert-Alteirac, H. Dacasa, E. Campi, F.and Kueny, B. Farkas, F. Brunner, S. Maclot, B. Manschwetus, H. Wikmark, J. Lahl, L. Rading, J. Peschel, B. Major, K. Varjú, G. Dovillaire, P. Zeitoun, P. Johnsson, A. L'Huillier, and P. Rudawski. Micro-focusing of broadband high-order harmonic radiation by a double toroidal mirror. *Appl. Sci.*, 7:1159, 2017.
35. U. Even. Pulsed supersonic beams from high pressure source: Simulation results and experimental measurements. *Advances in Chemistry*, 2014:636042, Aug 2014.
36. A. T. J. B. Eppink and D. H. Parker. Velocity map imaging of ions and electrons using electrostatic lenses: Application in photoelectron and photofragment ion imaging of molecular oxygen. *Rev. Sci. Instr.*, 68:3477, 1997.
37. Linnea Rading, Jan Lahl, Sylvain Maclot, Filippo Campi, Hélène Coudert-Alteirac, Bart Oostenrijk, Jasper Peschel, Hampus Wikmark, Piotr Rudawski, Mathieu Gisselbrecht, and Per Johnsson. A versatile velocity map ion-electron covariance imaging spectrometer for high-intensity xuv experiments. *Applied Sciences*, 8(6), 2018.
38. M. J. J. Vrakking. An iterative procedure for the inversion of two-dimensional ion/photoelectron imaging experiments. *Rev. Sci. Instr.*, 72:4084, 2001.

Paper II

M. Hoflund, **J. Peschel**, M. Plach, H. Dacasa, K. Veyrinas, E. Constant, P. Schmorenburg, C. Guo, C. Arnold, A. L'Huillier, P. Eng-Johnsson
Focusing properties of high-order harmonics
Ultrafast Science 2021, 9797453 (2021)

AAAS
Ultrafast Science
Volume 2021, Article ID 9797453, 8 pages
https://doi.org/10.34133/2021/9797453

Ultrafast Science
A SCIENCE PARTNER JOURNAL

Research Article

Focusing Properties of High-Order Harmonics

Maria Hoflund,[1] **Jasper Peschel**,[1] **Marius Plach**,[1] **Hugo Dacasa**,[1] **Kévin Veyrinas**,[2] **Eric Constant**,[3] **Peter Smorenburg**,[4] **Hampus Wikmark**,[1] **Sylvain Maclot**,[1] **Chen Guo**,[1] **Cord Arnold**,[1] **Anne L'Huillier**,[1] **and Per Eng-Johnsson**[1]

[1]*Department of Physics, Lund University, P.O. Box 118, 22100 Lund, Sweden*
[2]*Université de Bordeaux, CNRS, CEA, Centre Laser Intenses et Applications (CELIA), 43 Rue P. Noailles, 33400 Talence, France*
[3]*Univ Lyon, Univ Claude Bernard Lyon 1, CNRS, Institut Lumière Matière, F-69622 Villeurbanne, France*
[4]*ASML Research, ASML Netherlands B.V., 5504 DR Veldhoven, Netherlands*

Correspondence should be addressed to Maria Hoflund; maria.hoflund@fysik.lth.se

Received 29 April 2021; Accepted 27 July 2021; Published 29 August 2021

Many applications of the extreme ultraviolet (XUV) radiation obtained by high-order harmonic generation (HHG) in gases require a small focus area in order to enable attosecond pulses to reach a high intensity. Here, high-order harmonics generated in Ar with a multiterawatt laser system in a loose focusing geometry are focused to a few micrometers using two toroidal mirrors in a Wolter configuration with a high demagnification factor. Using a knife-edge measurement technique, we determine the position and size of the XUV foci as a function of harmonic order. We show that the focus properties vary with harmonic order and the generation conditions. Simulations, based on a classical description of the harmonic dipole phase and assuming that the individual harmonics can be described as Gaussian beams, reproduce the experimental behavior. We discuss how the generation geometry affects the intensity and duration of the focused attosecond pulses.

1. Introduction

High-order harmonic generation (HHG) is a highly nonlinear process that converts intense low-frequency light into attosecond pulse trains in the extreme ultraviolet (XUV) spectral region. In spite of a low conversion efficiency [1–3], the choice of appropriate gas targets combined with the use of loose focusing geometries has led to high pulse energies on the order of microjoules [4–8]. The high intensity that can potentially be achieved by focusing this radiation opens the way to multiphoton ionization processes in the XUV range [7, 9–12], and in particular to nonlinear XUV pump-XUV probe studies with attosecond resolution [13–15]. While XUV and X-ray radiation from free-electron lasers provide the required intensities for these types of studies [16, 17], they have only recently started to demonstrate the generation of attosecond pulses [18]. Using these sources for experiments is still very challenging, whereas HHG-based sources already provide a mature technology for nonlinear pump-probe experiments in the attosecond range.

To obtain both high intensity and attosecond pulse duration in the interaction with a low-density gas target, it is important to focus the broadband radiation on a small spot. This requires focusing the different harmonic components at the same position. Focusing of high-order harmonics has been achieved using ellipsoidal mirrors [19, 20], pairs of toroidal mirrors at grazing incidence [21–23], or spherical mirrors at normal incidence for low photon energy [8, 24]. Focal spot sizes of the order of a few μm for the emitted harmonics in a certain spectral range are typically obtained. The methods used for measuring these spot sizes vary from direct techniques like the knife-edge method [20, 25–27] or microscopy [21] to indirect ones based on wavefront determination [23, 28–30]. Recently, focus sizes of the order of $0.3 \times 0.4\,\mu\text{m}^2$ have been measured for harmonics between 10 and 20 nm (i.e., 60-120 eV) focused with an ellipsoidal mirror [31].

Previous studies [30, 32–36] have shown that high-order harmonics have different wavefronts at the exit of the nonlinear medium, which can be convergent or divergent [35], corresponding to a real or virtual focus, respectively. The

wavefront curvature of the harmonics is the sum of that of the driving laser and an additional contribution originating from the process behind the generation of high-order harmonics. The resulting harmonic radius of curvature and spatial profile [37] depends on harmonic order, laser intensity, and generation position. When they are refocused, this results in separated waist positions along the propagation direction, thus affecting the focusing properties of the harmonics and the peak intensity and pulse duration of the focused attosecond pulses. Although theoretically predicted in [34, 35], and experimentally shown for the total harmonic beam in [38], no experiments have yet quantitatively examined the influence of the generation geometry on the focus position, waist, and intensity of individual harmonics and attosecond pulses.

In the present study, we generate high-order harmonics in argon using a 45 mJ, 40 fs, Ti:Sapphire laser in a loose focusing geometry. We refocus the XUV radiation with a pair of toroidal mirrors in a Wolter configuration [23, 39] in order to achieve broadband focusing with a high demagnification factor. A knife-edge technique [20, 25–27] is used to measure the individual harmonic focus positions for different locations of the gas target relative to the laser focus in the generation chamber. In some cases, the harmonics are found to be refocused at positions that evolve strongly with the harmonic order. The observed experimental trends can be explained by a simple model which takes into account the intensity dependence of the spectral phase of the attosecond pulses, also called the dipole phase [34, 35]. We find that the chromatic aberrations induced by the dipole phase affect strongly the temporal profile and intensity of the focused attosecond pulses.

2. Experimental Method

The experimental setup used in this study is sketched in Figure 1. We use a multiterawatt Ti:Sapphire laser system delivering 40 fs, 806 nm, and 45 mJ pulses [7]. A deformable mirror (DM), used together with an infrared wavefront sensor, allows us to correct for spatial aberrations and to control the IR focusing position with respect to the generation medium by introducing a slight curvature to the beam. After aberration correction, the measured laser wavefront has an RMS value of about $\lambda/40$, corresponding to a Strehl ratio of 0.97. After going through an iris, the infrared beam is loosely focused with an 8.7 m spherical mirror into a 1 cm long, pulsed, Ar gas cell, generating high-order harmonics up to 45 eV. We estimate that the IR waists are approximately 340-360 μm with corresponding Rayleigh lengths of 45 to 50 cm for the different focal lengths used in the experiment.

The XUV radiation is reflected, at a 10° grazing incidence angle, by a fused silica (FS) plate, which is antireflection-coated for the IR, and spectrally filtered by a 200 nm Al filter. The FS plate and Al filter allow us to completely eliminate the IR. Further, the broadband beam is refocused by Wolter optics, consisting of a prealigned assembly of two toroidal mirrors from Thales SESO, designed to image the generation medium, after 6 m propagation, with a high demagnification factor and minimal aberrations in the XUV range. The grazing incidence angle on the two toroidal mirrors is 15°, giving a total deviation angle of 60°. The Wolter optics assembly is aligned in our beamline by using a homemade XUV Hartmann wavefront sensor. The tangential focal lengths are 265.3 mm and 545.2 mm for the first and second mirror while the sagittal focal lengths are 265.0 mm and 544.4 mm. The combined focal length of 164.2 mm provides a demagnification factor of 35. A homemade flat-field spectrometer, based on a Hitachi aberration-corrected concave grating, images the focus in the vertical direction onto a microchannel plate (MCP). In this configuration, no entrance slit is needed and the entire beam is characterized. The grating disperses the harmonics along the vertical axis of the MCP, while the far field spatial profile is recorded along the horizontal axis.

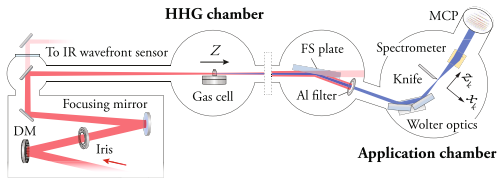

FIGURE 1: Schematic representation of the experimental setup. The spatially filtered IR beam (red) is first wavefront-corrected by a deformable mirror before it goes through an iris and is reflected by a focusing mirror. High-order harmonics (blue) are generated in an argon gas cell. The IR is filtered out by an IR antireflection-coated fused silica plate followed by an aluminum filter. In the application chamber, the harmonic beam is focused by the Wolter optics. The knife is placed around the focus, and the beam is detected by a flat-field spectrometer.

For each position of the cell relative to the IR focus along the propagation direction Z, called "generation position," we measure the focus position of the harmonics in the application chamber. Harmonic spectra are recorded for different x_k (transverse to the beam) and z_k (along the beam) positions of a knife-edge located close to the focus (see Figure 1). A rough estimate of the focus position for each harmonic can be obtained by looking at the diffraction image position of the knife-edge on the spatial profile recorded by the spectrometer. If the knife is after the focus, the shadow is on the same side as the knife, while if the focus is after, it is on the opposite side. This is illustrated in Figure 2, showing spectra obtained without the knife-edge (a) and for three positions of the knife-edge (b–d). In (b) (respectively, d), the knife is before (after) the focus for all harmonic orders and the shadow is observed on the right (left) sides of the profile. In (c), the shadow of the knife is on the right side for the lower-order harmonics while it is on the left side for the higher-order harmonics. This means that the knife is before the focus for the lower-order harmonics, and after the focus for the higher orders. The harmonics in the middle are less affected by the knife, which indicates that it is located close to their focus. These results show that the harmonics are indeed focused at different positions along the propagation axis.

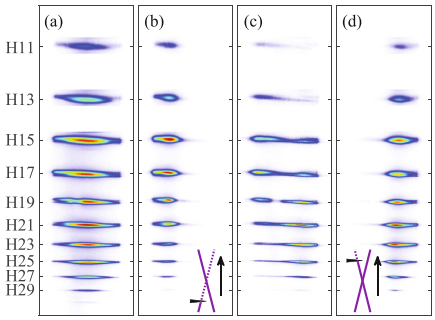

FIGURE 2: Measured spectra with no knife (a), the knife before (b) and after (d) the focus, and the knife in the focal region (c). The second-order diffraction from the spectrometer grating is numerically filtered out. The insets in (b) and (d) illustrate the position of the knife relative to the focus and its shadow. The knife positions in (b–d) are $z_k = -8.3$, $z_k = 0$ mm, and $z_k = 9.1$ mm.

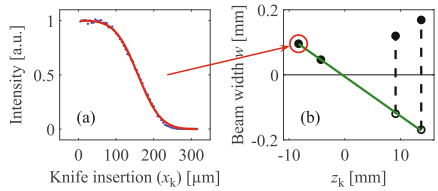

FIGURE 3: Illustration of our analysis method for one harmonic order (21). (a) Normalized harmonic intensity as a function of knife-edge insertion (blue dots). An error function is fitted to the data (red curve), allowing us to determine the beam width at $1/e^2$, marked with a red circle in (b). (b) Measured beam widths for four different knife-edge positions along the propagation direction (black dots). A linear fit (green curve) is performed between these widths, after mirroring two of them relative to the horizontal axis (black circles). The focus is the position where the fit crosses zero.

Mapping out the individual harmonic focus positions requires scanning both x_k and z_k in small steps. Instead, we use a faster and less tedious method based on measurements at only four positions in z_k, outside the Rayleigh range ($z_R \approx 1$ mm), two before and two after the focus, which is sufficient to extract the position of each focus. Figure 3 illustrates this method for the 21st harmonic. The harmonic intensity as a function of knife insertion (x_k) is recorded for each knife-edge position along the propagation direction (z_k) (see Figure 3(a)). Assuming Gaussian beams, this data is then fitted to a normalized error function, $f(x_k) = \{\mathrm{erf}\,[b(x_k - c)] + 1\}/2$, representing the integral of a Gaussian function $\exp\,[-b^2(x-c)^2]$ from $-\infty$ to x_k. For each knife-edge position, the $1/e^2$ beam waist radius ($w_q = \sqrt{2}/b$) is obtained from the fit. The position of the harmonic focus (z_q) can be determined by performing a linear fit of the beam widths, after mirroring those corresponding to the knife-edge position behind the focus (Figure 3(b)). If we assume that the harmonics are ideal Gaussian beams with $\mathbb{M}^2 = 1$, the beam waists (w_q) can also be estimated as $\lambda_q/(\pi\theta_q)$, where λ_q is the wavelength of the q^{th} harmonic and θ_q the (half) divergence angle. Note that w_q represents a lower limit to the beam waist and that a better estimation would require a measurement of the quality factor $\mathbb{M}^2$, which has not been done in the present work.

3. Theoretical Model

HHG can be described by a three-step process: tunneling ionization, electron acceleration by the laser field, and recombination [40, 41]. In the second step, the electron wave packet accumulates a phase, called the dipole phase, which is then transferred to the harmonic field. Two families of trajectories, related to the time spent by the electron in the continuum ("short" or "long"), have been identified and observed experimentally [42, 43]. The dipole phase is often expressed as αI, where α depends on the harmonic order and electron trajectory, and I is the intensity of the driving laser [44]. This expression is derived by using the strong-field approximation to solve the time-dependent Schrödinger equation (TDSE) of the single-atom response. Instead, we use an analytical expression derived by solving Newton's equation of motion [34, 45]:

$$\Phi_i(q, I) = \alpha_i I + t_{pi}(q\omega - \omega_p) + \frac{\gamma_i}{I}(q\omega - \omega_p)^2, \qquad (1)$$

where i refers to the trajectory (short or long), q is the harmonic order, I and ω are the fundamental intensity and angular frequency, respectively, ω_p is the angular frequency corresponding to the ionization energy, and t_{pi} is a return time, as explained in [34]. We here consider only the contribution from the short trajectory, which is mainly observed in our experiment. In Equation (1), the quantity α_i is independent of the harmonic order and is equal to zero for the short trajectory, while the quantity γ_i is equal to $1.03 \times 10^{-18}\,\mathrm{s}^2\,\mathrm{W\,cm}^{-2}$ for a driving laser of 800 nm. The first and third terms depend on the laser intensity, leading to an order-dependent wavefront curvature.

We assume that high-order harmonics are generated at position Z relative to the IR focus (located at $Z = 0$) in a thin medium [46]. For a Gaussian fundamental beam, with a profile $I_0 \exp\,[-2r^2/w^2(Z)]$, where I_0 is the peak intensity, r is the radial coordinate, and $w(Z)$ is the beam width at position Z, the r-dependence of the dipole phase can be approximated by

$$-\frac{2\alpha_i I_0 w_0^2}{w^4(Z)} r^2 - \frac{2\gamma_i(q\omega - \omega_p)^2}{I_0 w_0^2} r^2. \qquad (2)$$

The generated harmonic field also includes an r-dependent phase contribution from the fundamental, which is equal to $qkr^2/2R(Z)$, where k is the fundamental wavevector and $R(Z)$ is its radius of curvature. The total radius of

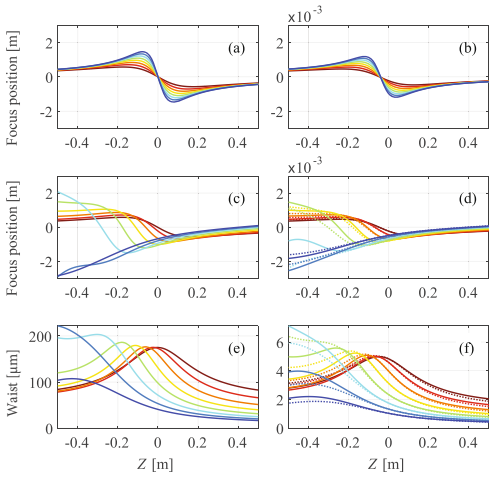

FIGURE 4: Calculated harmonic focus positions as a function of generation position Z, in the HHG chamber (a, c) and after being refocused, in the application chamber (b, d). In (e, f), the corresponding waists are shown. The simulation is run without (a, b) and with (c–f) the dipole phase included. The harmonic order goes from 11 (red) to 25 (blue). The dashed lines in (d) and (f) simulate the experimental conditions, where the relative medium-laser focus distance is varied by changing the focal length of the generating laser with a deformable mirror.

curvature of the harmonic field, corresponding to one trajectory i, is given by

$$\frac{1}{R_i(Z)} = \frac{1}{R(Z)} - \frac{4\alpha_i I_0 w_0^2 c}{w^4(Z) q\omega} + \frac{4\gamma_i (q\omega - \omega_p)^2 c}{I_0 w_0^2 q\omega}, \quad (3)$$

where c is the speed of light and w_0 is the fundamental beam waist [34].

To fully characterize the harmonic beams, the width at the generation position is estimated by assuming that the harmonic intensity (I_q) is proportional to the fundamental intensity to the power of p ($I_q \propto I_0^p$) [46–50], where the degree of nonlinearity, p, is assumed to be equal to 4, which is confirmed by TDSE calculations [34]. The harmonic width, at the position of the gas target, is then simply half the width of the driving laser. Assuming Gaussian optics for the harmonic beam, knowing the width and radius of curvature at the generation position Z allows us to determine the beam properties at any position.

Figure 4 shows the calculated focus positions and waist size, with respect to the IR focus, for harmonic 11 to 25 as a function of generation position Z. The left column shows the (virtual or real) focus positions and waists at generation while the right column shows the foci and waists of the refocused beams. The first row (a, b) shows results obtained without the dipole phase. In this case, the harmonics have the same wavefront, which is equal to that of the fundamental. When they are generated at the IR waist, they have the same focus, which is identical to the IR focus (Figure 4(a)). However, for this generation position ($Z = 0$), the harmonics are not refocused at the same focus position in the application chamber (Figure 4(b)). In this very loose focusing geometry, some harmonics have very long Rayleigh lengths. Consequently, the focusing optics is not fully in the far field, so that the curvatures of the harmonics at this position are slightly harmonic-dependent. Therefore, the harmonics will be focused at slightly different positions. In this case, where the dipole phase is not included, the foci in the application chamber are overlapped for all harmonics, when the generation medium is slightly before the IR focal spot. This is a clear deviation from the predictions of geometrical optics, due to the long Rayleigh lengths mentioned above.

The second row (c, d) is calculated including the dipole phase. This leads to an asymmetric focus position distribution for positive and negative generation positions. Furthermore, there is no generation position where all harmonics are focused at the same position. We also show in (e, f) the harmonic waists both in the generation and application chambers, including the dipole phase in the calculations.

Finally, we also simulate the experimental conditions, where the cell position is fixed and where the focal length is slightly varied in order to change the relative position between the generation and the IR focus. As expected, the results, shown as dashed lines in Figures 4(d) and 4(f), present the same qualitative behavior as when the focal length is not varied (solid lines), and only minor quantitative differences. The simulation with the varying focal length is used in the comparison with the experimental results.

4. Results

To describe our experimental geometry, where the generation cell is fixed and the position of the IR focus varied, we introduce $\Delta Z = Z_m - Z_0$, which is the medium position (Z_m) relative to the IR focus (Z_0). Similarly, in the application chamber, we refer to the refocused focus positions in the coordinate $\Delta z = z_q - z_0$, where z_0 is the position of the refocused IR, which was estimated from the simulations. The 19th harmonic is removed from the dataset because its position on the detector coincides with a damaged area on the microchannel plate of the spectrometer, making its detection unreliable.

The results of our knife-edge measurements are shown in Figures 5(a)–5(e), for different generation positions, as shown at the top of the figure. The experimental data are compared with simulations (dashed line) using the model presented above. The different harmonics are found to be focused at different positions, with a separation of up to 1.5 mm, which is significant since the harmonic Rayleigh lengths are typically around 1 mm. This effect decreases as the generation position moves towards and beyond the laser focus. When the medium is before the focus (see Figures 5(a)–5(c)), the lower-order harmonics are focused approximately one mm after the higher-order harmonics, on different sides of the IR focus. When the generation medium is centered at the infrared focus or beyond (see Figures 5(d) and 5(e)), all of the harmonics are focused much

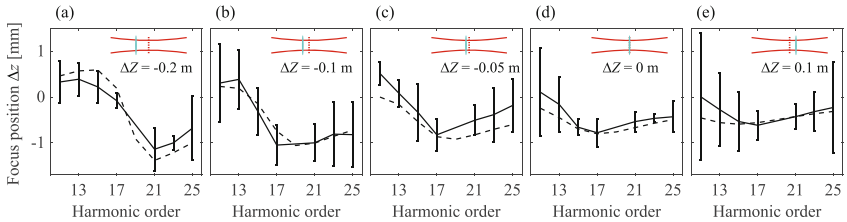

FIGURE 5: Measured (solid line) and simulated (dashed line) focus positions of harmonics 11-25 for five different generation positions in relation to the IR focus. The insets indicate the geometry of the generation in the five cases. The medium is represented by the vertical blue line, while the position of the IR focus is indicated in red. The error bars are obtained from the standard deviation of the fit performed in Figure 3.

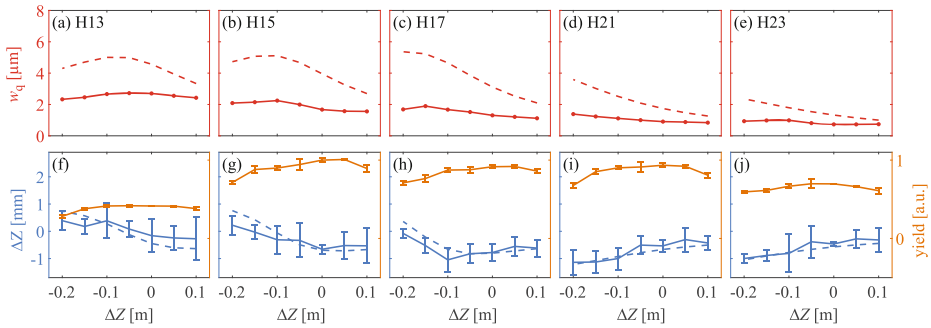

FIGURE 6: Simulated (dashed red) and measured waist size (solid red) as a function of generation position, for harmonic 13, 15, 17, 21, and 23 (a–e). Measured (solid blue) and simulated (dashed blue) focus positions, and measured yield (orange) as a function of generation position for the same harmonic orders (f–j).

closer to each other, at a position before the IR focus. Simulations reproduce the main features of the experimental data, which indicates that, despite its simplicity, our model describes the physics behind the focusing properties of high-order harmonics well [34, 35].

In Figures 6(a)–6(e), we present the measured (solid line) and simulated (dashed line) beam waists (w_q), for a few harmonics (13, 15, 17, 21, and 23), as a function of generation position. As explained in the experimental section, the measured beam waists should be considered lower limits. We find that the harmonic waist sizes decrease with order. For harmonics 13, 15, and 17 (a–c), the generation position leading to the maximum waist moves progressively from around $\Delta Z = 0$ to negative values. The measured values for the harmonic beam waists are consistent with (but slightly below) previous spectrally integrated measurements, which were performed by wavefront analysis of the total beam combined with numerical back-propagation and gave 3.6×4 μm^2 FWHM ($3.1 \times 3.4\,\mu m^2$ half-width at $1/e^2$) [23]. The simulations in Figure 6 (a–e, dashed lines) follow qualitatively the experimental results, with slightly larger waists. This difference might be due to a deviation of the experimental laser (and consequently harmonic) beams from a Gaussian behavior (i.e., $\mathbb{M}^2 > 1$). Another possible cause of the discrepancy between the experimental results and our simulations could be that the dipole phase is more complex than the model dipole or that phase-matching impacts also the wavefront of the XUV beam. Despite the approximation of our model, the agreement is very satisfactory.

Figures 6(f)–6(j) show the focus positions (blue) and yield (orange) for the same harmonics, as a function of generation position. Simulations, indicated by dashed lines, agree well with the experimental measurements. As shown in Figure 5, the harmonic focus position varies with the generation geometry, especially for the lower-order harmonics. The harmonic yield, on the other hand, is relatively insensitive to the generation position over the studied range.

5. Discussion

Our results can be used to estimate not only the intensity of the refocused individual harmonics but also that of the attosecond pulses in the train, in which case the relative phase of the harmonics has to be included [8]. The electric field describing the attosecond pulse train can be expressed as

$$E(t, r, z) = \sum_q \sqrt{I_q(t, r, z)}\, \exp\left(iq\omega t + i\phi_q(t, r, z)\right), \quad (4)$$

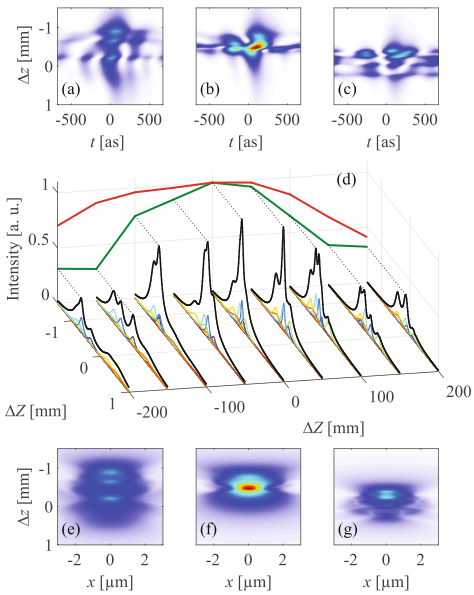

Figure 7: Estimated on-axis intensity as a function of time and Δz for generation positions: $\Delta Z = -150$ mm (a), $\Delta Z = 0$ (b), and $\Delta Z = 150$ mm (c). (d) Peak intensity (black) varying along the propagation axis (Δz) for different generation positions (ΔZ). The harmonic intensities (multiplied by two) are plotted for each ΔZ, going from order 11 (red) to 25 (blue). Measured total yield (red) and peak intensity (green) as a function of ΔZ are plotted in the intensity-ΔZ-plane. Estimated peak intensity as a function of the transverse coordinate x and Δz for generation positions: $\Delta Z = -150$ mm (e), $\Delta Z = 0$ (f), and $\Delta Z = 150$ mm (g).

where I_q are the relative experimental harmonic intensities. The phases, ϕ_q, are the sum of the Gouy phase obtained by using the experimentally determined position of the focus and Rayleigh length for each harmonic and the inherent phase due to the generation process (see Equation (1)), also called attochirp [51].

In Figures 7(a)–7(c), we show the estimated attosecond pulse intensity on axis in the application chamber, as a function of time and position along the propagation axis (Δz), for three generation positions, $\Delta Z = -150$ mm (a), $\Delta Z = 0$ (b), and $\Delta Z = 150$ mm (c). This is obtained using Equation (4) for each Δz and taking the absolute square to get the intensity. The peak of the attosecond pulse intensity is extracted from these results and shown in Figure 7(d) in black as a function of Δz, for different generation positions (ΔZ). The intensity variation for each harmonic is marked in color going from the 11^{th} (red) to 25^{th} (blue). Figure 7(d) also shows the maximum XUV peak intensity (green) and the total yield (red) for each generation position. Furthermore, the intensity distribution as a function of the transverse coordinate x and Δz is shown for $\Delta Z = -150$ mm (e), $\Delta Z = 0$ (f), and $\Delta Z = 150$ mm (g).

As seen in Figure 7, the distribution of harmonic focus positions is clearly broader when the cell is before the IR focus (negative ΔZ), as shown in panels (a) and (e). In contrast, the foci are closer to each other along the propagation axis when the cell is located at the IR focus or beyond, as shown in panels (b, c) and (f, g). The maximum intensity is obtained for $\Delta Z = 0$ and $\Delta z = -0.47$ mm, as seen in panels (b) and (f). When $\Delta Z < 0$, the harmonics are focused at different positions, while when $\Delta Z > 0$, the generation efficiency decreases. The total yield and the maximum intensity vary differently with respect to the generation position, as shown in Figure 7(d).

From the estimated spatiotemporal intensities in Figure 7, we find for the conditions where the maximum intensity is obtained ($\Delta Z = 0$ and $\Delta z = -0.47$ mm), an average pulse duration of the individual attosecond pulses of ~ 200 as and a beam waist of $\sim 1.5\,\mu$m. Combining this with the XUV pulse energy, measured using an X-ray CCD camera (Andor) to be 1.6 nJ, and a harmonic pulse duration of 20 fs (half of the IR pulse duration, according to the same power law used for the harmonic beam widths above), gives an estimate of the maximum XUV peak intensity of 10^{13} W/cm^2. This corresponds to an intensity of 1 on the vertical axis in Figure 7(d).

6. Conclusion

By inserting a knife before and after the focus and scanning it through the XUV beam, we have mapped out the focus position and estimated the waist size of each individual harmonic, as a function of the position of the gas cell relative to the IR focus. The key conclusion of this work is that the harmonics' focusing properties are found to depend on the order and the generation position. We interpret this effect as a consequence of the intensity-dependent dipole phase. The experimental data agree with relatively simple simulations based on an analytical expression for the dipole phase [34, 35], the assumption that the harmonics can be represented as Gaussian beams [33], and without taking into account propagation effects in the nonlinear medium. These measurements allow us to estimate the focused intensity of the individual harmonics and the attosecond pulses in the train and to define the optimal conditions to achieve high-intensity attosecond illumination. We find that these optimal conditions do not necessarily coincide with those leading to the highest yield. Even when the yield is approximately constant, the harmonic focusing properties can change significantly and thus affect the pulse duration and intensity of the attosecond pulses.

Data Availability

All data discussed in the article will be made available upon request.

Disclosure

Hugo Dacasa's present address is Department of Physical Chemistry, Complutense University of Madrid, Ciudad

Universitaria, 28040 Madrid, Spain. Kévin Veyrinas' present address is Amplitude Laser Group, 11, avenue de Canteranne, Cité de la Photonique, 33600 Pessac, France. Hampus Wikmark's present address is Department of Physics and Astronomy, Uppsala University, Box 516, SE-751 20, Uppsala, Sweden. Sylvain Maclot's present address is Department of Physics, Gothenburg University, Box 100, 405 30 Gothenburg, Sweden.

Conflicts of Interest

The authors declare no conflict of interest.

Authors' Contributions

M.H, J.P., M.P., and H.D. performed the experiments. P.E.-J, J.P., and C.A. designed the experiment. K.V., E.C., H.W., and S.M. contributed to building the experimental setup and preparing the experiment. M.H. did the data analysis and the simulations based on theory that P.S., H.W., C.G., C.A., and A.L. developed. M.H., A.L., P.E.-J., J.P., and M.P. wrote the article, with feedback from all the authors.

Acknowledgments

The authors acknowledge support from the Swedish Research Council, the European Research Council (advanced grant QPAP), the Knut and Alice Wallenberg Foundation, and the Crafoord Foundation. The research leading to these results has received funding from LASERLAB-EUROPE (grant agreement no. 654148, European Union's Horizon 2020 research and innovation programme). S.M. acknowledges financial support from the COST Action CA18212-Molecular Dynamics in the GAS phase (MD-GAS), supported by COST (European Cooperation in Science and Technology).

References

[1] P. Agostini and L. F. DiMauro, "The physics of attosecond light pulses," *Reports on Progress in Physics*, vol. 67, no. 6, pp. 813–855, 2004.

[2] J. Tate, T. Auguste, H. G. Muller, P. Salières, P. Agostini, and L. F. DiMauro, "Scaling of wave-packet dynamics in an intense midinfrared field," *Physical Review Letters*, vol. 98, no. 1, article 013901, 2007.

[3] A. D. Shiner, C. Trallero-Herrero, N. Kajumba et al., "Wavelength scaling of high harmonic generation efficiency," *Physical Review Letters*, vol. 103, no. 7, article 073902, 2009.

[4] Y. Kobayashi, T. Ohno, T. Sekikawa, Y. Nabekawa, and S. Watanabe, "Pulse width measurement of high-order harmonics by autocorrelation," *Applied Physics B: Lasers and Optics*, vol. 70, no. 3, pp. 389–394, 2000.

[5] J.-F. Hergott, M. Kovacev, H. Merdji et al., "Extreme-ultraviolet high-order harmonic pulses in the microjoule range," *Physical Review A*, vol. 66, no. 2, article 021801, 2002.

[6] P. Rudawski, C. M. Heyl, F. Brizuela et al., "A high-flux high-order harmonic source," *Review of Scientific Instruments*, vol. 84, no. 7, article 073103, 2013.

[7] B. Manschwetus, L. Rading, F. Campi et al., "Two-photon double ionization of neon using an intense attosecond pulse train," *Physical Review A*, vol. 93, no. 6, article 061402, 2016.

[8] I. Makos, I. Orfanos, A. Nayak et al., "*A* 10-gigawatt attosecond source for non-linear XUV optics and XUV-pump-XUV- probe studies," *Scientific Reports*, vol. 10, no. 1, p. 3759, 2020.

[9] K. Midorikawa, Y. Nabekawa, and A. Suda, "XUV multiphoton processes with intense high-order harmonics," *Progress in Quantum Electronics*, vol. 32, no. 2, pp. 43–88, 2008.

[10] E. J. Takahashi, P. Lan, O. D. Mücke, Y. Nabekawa, and K. Midorikawa, "Attosecond nonlinear optics using gigawatt-scale isolated attosecond pulses," *Nature Communications*, vol. 4, no. 1, 2013.

[11] A. Nayak, I. Orfanos, I. Makos et al., "Multiple ionization of argon via multi-xuv-photon absorption induced by 20-gw high-order harmonic laser pulses," *Physical Review A*, vol. 98, no. 2, article 023426, 2018.

[12] B. Senfftleben, M. Kretschmar, A. Hoffmann et al., "Highly nonlinear ionization of atoms induced by intense high-harmonic pulses," *Journal of Physics: Photonics*, vol. 2, no. 3, 2020.

[13] P. A. Carpeggiani, P. Tzallas, A. Palacios, D. Gray, F. Martín, and D. Charalambidis, "Disclosing intrinsic molecular dynamics on the 1-fs scale through extreme-ultraviolet pump-probe measurements," *Physical Review A*, vol. 89, no. 2, article 023420, 2014.

[14] P. Tzallas, D. Charalambidis, N. A. Papadogiannis, K. Witte, and G. D. Tsakiris, "Direct observation of attosecond light bunching," *Nature*, vol. 426, no. 6964, pp. 267–271, 2003.

[15] Y. Nabekawa, H. Hasegawa, E. J. Takahashi, and K. Midorikawa, "Production of doubly charged helium ions by two-photon absorption of an intense sub-10-fs soft X-ray pulse at 42 eV photon energy," *Physical Review Letters*, vol. 94, no. 4, article 043001, 2005.

[16] C. Pellegrini, A. Marinelli, and S. Reiche, "The physics of x-ray free-electron lasers," *Reviews of Modern Physics*, vol. 88, no. 1, article 015006, 2016.

[17] L. Young, K. Ueda, M. Gühr et al., "Roadmap of ultrafast x-ray atomic and molecular physics," *Journal of Physics B: Atomic, Molecular and Optical Physics*, vol. 51, no. 3, p. 032003, 2018.

[18] J. Duris, S. Li, T. Driver et al., "Tunable isolated attosecond x-ray pulses with gigawatt peak power from a free-electron laser," *Nature Photonics*, vol. 14, no. 1, pp. 30–36, 2020.

[19] A. Suda, H. Mashiko, and K. Midorikawa, "Focusing intense high-order harmonics to a micron spot size," in *Progress in Ultrafast Intense Laser Science II*, pp. 183–198, Springer Berlin Heidelberg, Berlin, Heidelberg, 2007.

[20] H. Motoyama, T. Sato, A. Iwasaki et al., "Development of high-order harmonic focusing system based on ellipsoidal mirror," *Review of Scientific Instruments*, vol. 87, no. 5, article 051803, 2016.

[21] C. Valentin, D. Douillet, S. Kazamias et al., "Imaging and quality assessment of high-harmonic focal spots," *Optics Letters*, vol. 28, no. 12, pp. 1049–1051, 2003.

[22] F. Frassetto, S. Anumula, F. Calegari, A. Trabattoni, M. Nisoli, and L. Poletto, "Microfocusing beamline for xuv-xuv pump-probe experiments using hh generation," in *Adaptive X-Ray Optics III*, vol. 9208, pp. 159–167, September 2014.

[23] H. Coudert-Alteirac, H. Dacasa, F. Campi et al., "Micro-focusing of broadband highorder harmonic radiation by a double toroidal mirror," *Applied Sciences*, vol. 7, no. 11, p. 1159, 2017.

[24] I. Orfanos, I. Makos, I. Liontos et al., "Non-linear processes in the extreme ultraviolet," *Journal of Physics: Photonics*, vol. 2, no. 4, 2020.

[25] J. A. Arnaud, W. M. Hubbard, G. D. Mandeville, B. de la Clavière, E. A. Franke, and J. M. Franke, "Technique for fast measurement of Gaussian laser beam parameters," *Applied Optics*, vol. 10, no. 12, pp. 2775-2776, 1971.

[26] D. R. Skinner and R. E. Whitcher, "Measurement of the radius of a high-power laser beam near the focus of a lens," *Journal of Physics E: Scientific Instruments*, vol. 5, no. 3, pp. 237-238, 1972.

[27] L. le Déroff, P. Salières, and B. Carré, "Beam-quality measurement of a focused high-order harmonic beam," *Optics Letters*, vol. 23, no. 19, pp. 1544–1546, 1998.

[28] D. G. Lee, J. J. Park, J. H. Sung, and C. H. Nam, "Wave-front phase measurements of high-order harmonic beams by use of point-diffraction interferometry," *Optics Letters*, vol. 28, no. 6, pp. 480–482, 2003.

[29] E. Frumker, G. G. Paulus, H. Niikura, D. M. Villeneuve, and P. B. Corkum, "Frequency-resolved high-harmonic wavefront characterization," *Optics Letters*, vol. 34, no. 19, pp. 3026–3028, 2009.

[30] D. R. Austin, T. Witting, C. A. Arrell et al., "Lateral shearing interferometry of high-harmonic wavefronts," *Optics Letters*, vol. 36, no. 10, pp. 1746–1748, 2011.

[31] H. Motoyama, A. Iwasaki, Y. Takei et al., "Broadband nanofocusing of high-order harmonics in soft x-ray region with ellipsoidal mirror," *Applied Physics Letters*, vol. 114, no. 24, article 241102, 2019.

[32] D. T. Lloyd, K. O'Keeffe, and S. M. Hooker, "Complete spatial characterization of an optical wavefront using a variable-separation pinhole pair," *Optics Letters*, vol. 38, no. 7, pp. 1173–1175, 2013.

[33] E. Frumker, G. G. Paulus, H. Niikura, A. Naumov, D. M. Villeneuve, and P. B. Corkum, "Order-dependent structure of high harmonic wavefronts," *Optics Express*, vol. 20, no. 13, article 13870, p. 13877, 2012.

[34] H. Wikmark, C. Guo, J. Vogelsang et al., "Spatiotemporal coupling of attosecond pulses," *Proceedings of the National Academy of Sciences*, vol. 116, no. 11, pp. 4779–4787, 2019.

[35] L. Quintard, V. Strelkov, J. Vabek et al., "Optics-less focusing of XUV high-order harmonics," *Science Advances*, vol. 5, no. 4, article eaau7175, 2019.

[36] H. Dacasa, H. Coudert-Alteirac, C. Guo et al., "Single-shot extreme-ultraviolet wavefront measurements of high-order harmonics," *Optics Express*, vol. 27, no. 3, pp. 2656–2670, 2019.

[37] C. Hernández-García, A. Picón, J. San Román, and L. Plaja, "Attosecond extreme ultraviolet vortices from high-order harmonic generation," *Physical Review Letters*, vol. 111, no. 8, article 083602, 2013.

[38] S. Chatziathanasiou, S. Kahaly, D. Charalambidis, P. Tzallas, and E. Skantzakis, "Imaging the source of high-harmonics generated in atomic gas media," *Optics Express*, vol. 27, no. 7, pp. 9733–9739, 2019.

[39] H. Wolter, "Spiegelsysteme streifenden Einfalls als abbildende Optiken für Röntgenstrahlen," *Annalen der Physik*, vol. 445, no. 1-2, pp. 94–114, 1952.

[40] P. B. Corkum, "Plasma perspective on strong field multiphoton ionization," *Physical Review Letters*, vol. 71, no. 13, pp. 1994–1997, 1993.

[41] K. J. Schafer, B. Yang, L. F. DiMauro, and K. C. Kulander, "Above threshold ionization beyond the high harmonic cutoff," *Physical Review Letters*, vol. 70, no. 11, pp. 1599–1602, 1993.

[42] M. Bellini, C. Lyngå, A. Tozzi et al., "Temporal coherence of ultrashort high-order harmonic pulses," *Physical Review Letters*, vol. 81, no. 2, pp. 297–300, 1998.

[43] P. Salières, B. Carré, L. le Déroff et al., "Feynman's path-integral approach for intense-laser-atom interactions," *Science*, vol. 292, no. 5518, pp. 902–905, 2001.

[44] M. Lewenstein, K. C. Kulander, K. J. Schafer, and P. H. Bucksbaum, "Rings in above-threshold ionization: a quasiclassical analysis," *Physical Review A*, vol. 51, no. 2, pp. 1495–1507, 1995.

[45] C. Guo, A. Harth, S. Carlström et al., "Phase control of attosecond pulses in a train," *Journal of Physics B: Atomic Molecular and Optical Physics*, vol. 51, no. 3, article 034006, 2018.

[46] C. Hernández-García, J. S. Román, L. Plaja, and A. Picón, "Quantum-path signatures in attosecond helical beams driven by optical vortices," *New Journal of Physics*, vol. 17, no. 9, article 093029, 2015.

[47] F. Catoire, A. Ferré, O. Hort et al., "Complex structure of spatially resolved high-order-harmonic spectra," *Physical Review A*, vol. 94, no. 6, 2016.

[48] L. Rego, J. S. Román, A. Picón, L. Plaja, and C. Hernández-García, "Nonperturbative twist in the generation of extreme-ultraviolet vortex beams," *Physical Review Letters*, vol. 117, no. 16, 2016.

[49] J. A. Pérez-Hernández, L. Roso, and L. Plaja, "Harmonic generation beyond the Strong-Field approximation: the physics behind the short-wave-infrared scaling laws," *Optics Express*, vol. 17, no. 12, pp. 9891–9903, 2009.

[50] C. G. Durfee, A. R. Rundquist, S. Backus, C. Herne, M. M. Murnane, and H. C. Kapteyn, "Phase matching of high-order harmonics in hollow waveguides," *Physical Review Letters*, vol. 83, no. 11, pp. 2187–2190, 1999.

[51] Y. Mairesse, A. de Bohan, L. J. Frasinski et al., "Attosecond synchronization of high-harmonic soft X-rays," *Science*, vol. 302, no. 5650, pp. 1540–1543, 2003.

Paper III

H. Wikmark, C. Guo, J. Vogelsang, P. W. Smorenburg, H. Coudert-Alteirac, J. Lahl, **J. Peschel**, P. Rudawski, H. Dacasa, S. Carlström, S. Maclot, M. B. Gaarde, P. Johnsson, C. L. Arnold, and A. L'Huillier
Spatiotemporal coupling of attosecond pulses
Proc. Natl. Acad. Sci. 116, 4779–4787 (2019)

Spatiotemporal coupling of attosecond pulses

Hampus Wikmark[a,1], Chen Guo[a,1], Jan Vogelsang[a,1], Peter W. Smorenburg[b], Hélène Coudert-Alteirac[a], Jan Lahl[a], Jasper Peschel[a], Piotr Rudawski[a], Hugo Dacasa[a], Stefanos Carlström[a,2], Sylvain Maclot[a], Mette B. Gaarde[c], Per Johnsson[a], Cord L. Arnold[a], and Anne L'Huillier[a,3]

[a]Department of Physics, Lund University, SE-221 00 Lund, Sweden; [b]ASML Research, ASML Netherlands B.V., 5504 DR Veldhoven, The Netherlands; and [c]Department of Physics and Astronomy, Louisiana State University, Baton Rouge, LA 70803-4001

This contribution is part of the special series of Inaugural Articles by members of the National Academy of Sciences elected in 2018.

Contributed by Anne L'Huillier, January 18, 2019 (sent for review October 12, 2018; reviewed by David Attwood and Margaret M. Murnane)

The shortest light pulses produced to date are of the order of a few tens of attoseconds, with central frequencies in the extreme UV range and bandwidths exceeding tens of electronvolts. They are often produced as a train of pulses separated by half the driving laser period, leading in the frequency domain to a spectrum of high, odd-order harmonics. As light pulses become shorter and more spectrally wide, the widely used approximation consisting of writing the optical waveform as a product of temporal and spatial amplitudes does not apply anymore. Here, we investigate the interplay of temporal and spatial properties of attosecond pulses. We show that the divergence and focus position of the generated harmonics often strongly depend on their frequency, leading to strong chromatic aberrations of the broadband attosecond pulses. Our argument uses a simple analytical model based on Gaussian optics, numerical propagation calculations, and experimental harmonic divergence measurements. This effect needs to be considered for future applications requiring high-quality focusing while retaining the broadband/ultrashort characteristics of the radiation.

attosecond pulse | high-order harmonic generation | Gaussian optics | spatiotemporal coupling | focusing of XUV radiation

Electromagnetic waves are usually mathematically described by a product of purely spatial and purely temporal terms. This approximation often fails for broadband femtosecond laser pulses (ref. 1 and references therein), and spatiotemporal couplings need to be considered. Spatiotemporal couplings for visible or infrared (IR) light may be introduced by refractive and dispersive elements, such as lenses, gratings, or prisms. The noncollinear amplification in optical parametric crystals may also potentially lead to spatiotemporal couplings, and it is important to develop characterization methods to measure and reduce their effects (2–4). In some cases, these couplings may be advantageously used, as, for example, demonstrated by Vincenti and Quéré (5) for the so-called "lighthouse" effect (6, 7).

The shortest light pulses, generated by high-order harmonic generation (HHG) in gases, are in the extreme UV (XUV)/soft X-ray region and in the range of 100 as (8–11), with bandwidths of a few tens or even hundreds of electronvolts (12, 13). These pulses are generated in a three-step process (14, 15). When an atom is exposed to a strong laser field, an electron in the ground state can tunnel through the atomic potential bent by the laser field, propagate in the continuum, and recombine back to the ground state when (and if) returning close to the ionic core. In this process, an XUV photon is emitted, with energy equal to the ionization energy plus the electron kinetic energy at return. Two main families of trajectories leading to the same photon energy can be identified. They are characterized by the "short" or "long" time of travel of the electron in the continuum (16, 17). Interferences of attosecond pulses emitted at each laser half-cycle leads to a spectrum of odd-order harmonics.

The investigation of spatiotemporal coupling of attosecond pulses requires measurements of their spatial properties, as a function of time or, equivalently, frequency. Wavefronts of high-order harmonics have been measured by several groups, using different techniques such as Spectral Wavefront Optical Reconstruction by Diffraction (18–20), lateral shearing interferometry (21), point-diffraction interferometry (22), and Hartmann diffraction masks (23, 24). In particular, Frumker et al. (25) pointed out that the variation of wavefront and intensity profile with harmonic order leads to spatiotemporal coupling of the attosecond pulses, with temporal properties depending on where they are measured.

The spatial and spectral properties of high-order harmonics strongly depend on the geometry of the interaction and, in particular, on whether the gas medium in which the harmonics are generated is located before or after the focus of the driving laser beam (26). The asymmetry between "before" and "after" can be traced back to the phase of the emitted radiation, which is equal to that of the incident laser field multiplied by the process order, as in any frequency upconversion process, plus the dipole phase which is accumulated during the generation and mostly originates from electron propagation in the continuum. While the former is usually antisymmetric relative to the laser focus, the latter depends on the laser intensity and is therefore symmetric (21, 27). The total phase and thus the divergence properties are different before and after the laser focus, leading to a strong dependence of the spatiotemporal properties of the harmonic

Significance

In most optics textbooks, one writes the electric field describing an optical wave as a product of temporal and spatial amplitudes. This approximation often breaks down for short optical pulses. An example of such spatiotemporal coupling is chromatic aberrations, where the focal properties of the radiation vary with frequency over the pulse bandwidth. In this work, we point out significant chromatic aberrations of attosecond pulses, which depend on the geometry of the generation process. These aberrations are intrinsic to the generation process and need to be eliminated in applications requiring attosecond pulses to be focused over a small region.

Author contributions: H.W., C.G., J.V., P.W.S., H.C.-A., P.R., P.J., C.L.A., and A.L. designed research; H.W., C.G., J.V., P.W.S., H.C.-A., J.L., J.P., P.R., H.D., S.C., S.M., M.B.G., P.J., C.L.A., and A.L. performed research; C.G., J.V., P.W.S., H.C.-A., S.C., S.M., and M.B.G. contributed with analytic tools; H.W., C.G., J.V., P.W.S., H.C.-A., J.P., P.R., S.M., and C.L.A. analyzed data; and H.W. and A.L. wrote the paper.

Reviewers: D.A., University of California, Berkeley; and M.M.M., University of Colorado and NIST.

The authors declare no conflict of interest.

See QnAs on page 4767.

[1]H.W., C.G., and J.V. contributed equally to this work.

[2]Present address: Max Born Institute, 12489 Berlin, Germany.

[3]To whom correspondence should be addressed. Email: anne.lhuillier@fysik.lth.se.

Published online March 1, 2019.

radiation on the generation conditions. In some conditions, harmonics can be emitted with a flat wavefront (21) or even as a converging beam (28, 29). Another phenomenon leading to an asymmetry of HHG with respect to the generation conditions is ionization-induced reshaping of the fundamental field, which depends on whether the beam is converging or diverging when entering the gas medium (20, 30–32).

In the present work, we show that the frequency components of attosecond pulses generated by HHG in gases have different divergence properties, which depend on the geometry of the interaction and in particular on where the generating medium is located relative to the laser focus. In some conditions, the position of the focus and divergence strongly vary with frequency, leading to chromatic aberrations, as sketched in Fig. 1, similar to the effect that a chromatic lens has on broadband radiation (33, 34). Any imaging optical component will focus the frequency components of the attosecond pulses at different locations, resulting in spatiotemporal couplings. Depending on the position where the pulses are characterized or used, they will have different central frequencies, pulse durations, and spatial widths. We use an analytical expression for the dipole phase (35) combined with traditional Gaussian optics to predict the radius of curvature, position of focus, and divergence of the two trajectory contributions to HHG (29). This model, which assumes generation in a thin slab (36, 37), is validated by using numerical simulations of HHG (38) for both thin and thick generating media. We also present experimental measurements of the harmonic divergence as a function of position of generation relative to the laser focus. Finally, we discuss the implications of our results for the focusing of broadband attosecond pulses.

Analytical Expression of the Dipole Phase

The single-atom response of HHG is well described by an approximate solution of the time-dependent Schrödinger equation (TDSE) for an atom in a strong laser field, called the strong-field approximation (SFA) (39). This theory leads to a simple analytical expression of the dipole phase, equal to αI, where α depends on the harmonic order and on the trajectory contributing to HHG (16, 26, 40, 41) and where I is the laser intensity. This expression has been used in numerous investigations of the harmonic properties (17, 29, 41, 42). Here, we use a more general analytical expression for the phase (35), based on the semiclassical description of attosecond pulse generation (14, 15).

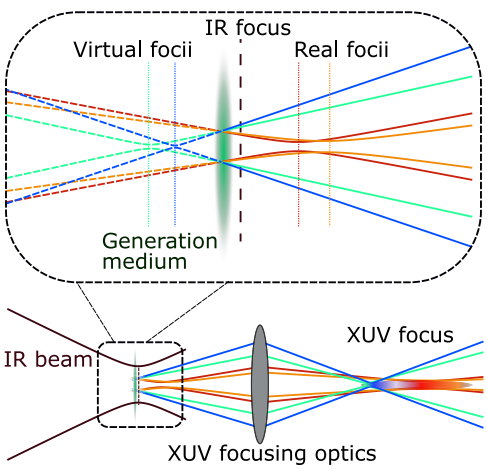

Fig. 1. Illustration of spatiotemporal coupling for an attosecond pulse: different frequencies (harmonic orders 31, 35, 59, and 67, with red, orange, green, and blue colors respectively), generated with varying wavefront curvatures and different divergences, as indicated in *Inset*, will be refocused by XUV optics (here represented as a lens) at different positions, leading to strong chromatic aberrations and an extended focus, both transversally and longitudinally. The fundamental driving field is indicated by the dark brown/black line.

In this approximation, the second step of the process is described by solving Newton's equation of motion for a free particle in the laser field. Fig. 2 shows the frequency (Ω) of the emitted XUV radiation as a function of electron return time for two different fundamental field intensities, indicated by the solid and dashed curves. The frequency varies from Ω_p, corresponding to the ionization threshold ($\hbar\Omega_p = I_p$, I_p denoting the ionization energy and $\hbar$ the reduced Planck constant) to the cutoff frequency Ω_c ($\hbar\Omega_c = 3.17U_p + I_p$). U_p denotes the ponderomotive energy, equal to

$$U_p = \frac{\alpha_{FS}\hbar I\lambda^2}{2\pi c^2 m}, \quad [1]$$

where α_{FS} is the fine structure constant, m the electron mass, c the speed of light, and λ the laser wavelength. The frequency variation can be approximated by piecewise straight lines, as indicated by the black solid lines. After inversion from $\Omega(t)$ to $t(\Omega)$, for each straight line, we have

$$t_i(\Omega) = t_{pi} + \frac{t_{ci} - t_{pi}}{\Omega_c - \Omega_p}(\Omega - \Omega_p), \quad [2]$$

where $i = s, \ell$ refers to the electron trajectory (short or long), and t_{pi} and t_{ci} are defined as indicated by the dashed black lines in Fig. 2. The values of t_{pi} and t_{ci}, in both laser cycles and femtoseconds (at $\lambda = 800$ nm), are summarized in Table 1. We also indicate the return times for the short and long electron trajectories leading to the threshold frequency (t_{ts}, $t_{t\ell}$) and the return time for the trajectory leading to the cutoff frequency (t_c). Neglecting the frequency dependence of the time for tunneling and recombination, $t_i(\Omega)$ can be interpreted as the group delay of the emitted radiation. Its integral is the spectral phase

$$\Phi_i(\Omega) = \Phi_i(\Omega_p) + t_{pi}(\Omega - \Omega_p) + \frac{t_{ci} - t_{pi}}{\Omega_c - \Omega_p}\frac{(\Omega - \Omega_p)^2}{2}. \quad [3]$$

As shown in Fig. 2, the return times t_{pi}, t_{ci}, and therefore the second term in Eq. **3** do not depend on laser intensity. Using $\Omega_c - \Omega_p = 3.17U_p/\hbar$, the coefficient in the third term can be written as

$$\frac{t_c - t_{pi}}{\Omega_c - \Omega_p} = \frac{2\gamma_i}{I}, \quad [4]$$

where

$$\gamma_i = \frac{(t_{ci} - t_{pi})\pi c^2 m}{3.17\alpha_{FS}\lambda^2}. \quad [5]$$

In this classical calculation, $\Phi_i(\Omega_p)$ is equal to zero for the short trajectory, while it is proportional to the laser intensity for the long: $\Phi_\ell(\Omega_p) = \alpha_\ell I$. The value of α_ℓ can be obtained numerically within the classical approach used in this work (43) and is found to be close to that given within the SFA, equal to $4\pi^2\alpha_{FS}/m\omega^3$, where Ω is the laser frequency (16, 41). The parameters needed to describe $\Phi_i(\Omega)$ for 800-nm radiation are $\gamma_s = 1.03 \times 10^{-18}$ s^2·W·cm^{-2}, $\gamma_\ell = -0.874 \times 10^{-18}$ s^2·W·cm^{-2}, α_s=0, and $\alpha_\ell = -2.38 \times 10^{-13}$ W^{-1}·cm^2.

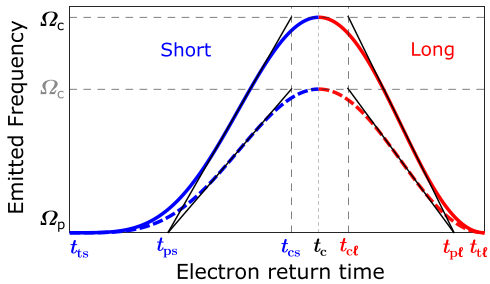

Fig. 2. Emitted XUV frequency as a function of return time for two laser intensities, corresponding to the solid and dashed blue/red curves. The blue curves describes the short trajectories, while the red lines refer to the long trajectory. $t_{ts,t\ell}$ are the return times for the short and long electron trajectories leading to the threshold frequency Ω_p. t_c is the return time for the trajectory leading to the cutoff frequency Ω_c. t_{pi} and t_{ci} (i = s, ℓ) are return times obtained by approximating $\Omega(t)$ as piecewise straight lines. Values for these return times are indicated in Table 1.

The dipole phase can be approximated for the two families of trajectories by the expansion:

$$\Phi_i(\Omega) = \alpha_i I + t_{pi}(\Omega - \Omega_p) + \frac{\gamma_i}{I}(\Omega - \Omega_p)^2. \quad [6]$$

The present expression gives very similar results to, e.g., the numerical results presented in ref. 40, obtained by solving saddle-point equations within the SFA, with the advantage of being analytical.

Wavefront and Spatial Width of XUV Radiation

We now use this analytical expression for the dipole phase together with traditional Gaussian optics to predict the radius of curvature, position of focus, and divergence of the two trajectory contributions to HHG. A similar derivation has been proposed, independently, by Quintard et al. (29) with, however, a different analytical formulation of the dipole phase. We neglect the influence of propagation, considering an infinitely thin homogeneous gas medium (36, 37, 44). Such an approximation is valid in a loose focusing geometry, where the generating medium length is much smaller than the Rayleigh length. We also assume that the fundamental field is Gaussian, with intensity $I(r,z)$, radial width $w(z)$ at $1/e^2$, radius of curvature $R(z)$, and peak intensity I_0, z denoting the coordinate along the propagation axis and r the radial coordinate. The focus position is $z=0$ and the waist $w_0 = w(0)$. Considering only the contribution of one trajectory i, the phase of the qth harmonic field can be approximated by

$$\Phi_q(r,z) = q\phi(r,z) + \Phi_i(r,z). \quad [7]$$

The phase of the fundamental Gaussian beam is $\phi(r,z) = kz - \zeta(z) + kr^2/2R(z)$, where k is the wavevector equal to ω/c and $\zeta(z)$ the Gouy phase (45). This article is mainly concerned with the third term, giving the curvature of the beam. The dipole phase $\Phi_i(r,z)$ is given by Eq. **6**, for $I = I(r,z)$ and $\Omega = q\omega$. Omitting the second term in Eq. **6**, which does not depend on intensity and therefore on space, $\Phi_i(r,z)$ can be expressed as

$$\Phi_i(r,z) = \frac{\alpha_i I_0 w_0^2}{w^2(z)} e^{-\frac{2r^2}{w^2(z)}} + \frac{\gamma_i(\Omega-\Omega_p)^2 w^2(z)}{I_0 w_0^2} e^{\frac{2r^2}{w^2(z)}}. \quad [8]$$

We use a Taylor expansion close to the center of the beam to approximate $\Phi_i(r,z)$ (Eq. **8**). To determine the harmonic wavefront, we only keep the terms proportional to r^2 in Eq. **8**, to which we add the r^2-dependent contribution from the fundamental, equal to $qkr^2/2R(z)$. The resulting r^2-dependent contribution to the phase of the harmonic field can be written as $qkr^2/2R_i$, with

$$\frac{1}{R_i} = \frac{1}{R(z)} - \frac{4\alpha_i I_0 w_0^2 c}{w^4(z)\Omega} + \frac{4\gamma_i(\Omega-\Omega_p)^2 c}{I_0 w_0^2 \Omega}. \quad [9]$$

For simplicity of the notations, we omit to explicitly indicate the z dependence of R_i. The curvature of the harmonic field is equal to that of the fundamental (first term) plus that induced by the dipole phase. The second term is only present for the long trajectory. This equation outlines the dependence of the XUV radiation wavefront on frequency (Ω), electron trajectory (i), intensity at focus (I_0), and generation position (z). Eq. **9** is illustrated in Fig. 3*A*, representing the wavefronts induced by the fundamental (black) and due to the dipole phase for the short trajectory (green) as a function of the generation position. The fundamental wavefront changes from convergent to divergent through the focus, while that induced by the dipole phase is always divergent and independent of the generation position (z).

Using the reduced coordinate $Z = z/z_0$, where $z_0 = \pi w_0^2/\lambda$ is the fundamental Rayleigh length, Eq. **9** can be written as

$$\frac{z_0}{R_i} = \frac{1}{Z + 1/Z} - \frac{\eta_i}{(1+Z^2)^2} + \mu_i, \quad [10]$$

where $\eta_i = 2\alpha_i I_0/q$ and $\mu_i = 2\gamma_i\omega^2(q-q_p)^2/qI_0$ are dimensionless quantities ($q_p = \Omega_p/\omega$). For the short trajectory, since $\alpha_s = 0$, the positions where the radius of curvature diverges, corresponding to a flat phase front, can be calculated analytically by solving a second-order equation in Z,

$$Z^2 + \frac{Z}{\mu_s} + 1 = 0. \quad [11]$$

For $\mu_s \leq 0.5$, the solutions to this equation are real and the radius of curvature diverges at

$$Z_\pm = -\frac{1}{2\mu_s} \pm \sqrt{\frac{1}{4\mu_s^2} - 1}. \quad [12]$$

This discussion is illustrated graphically in Fig. 3*B* for the 23rd harmonic of 800-nm radiation generated in Ar, with $I_0 = 3 \times 10^{14}$ W·cm^{-2}. In these conditions, we have $\eta_s = 0$, $\mu_s = 0.253$, $\eta_\ell = -6.38$, and $\mu_\ell = -0.215$. Fig. 3*B* presents the radius of curvature in reduced units R_i/z_0 for the short (blue) and long (red) trajectory contributions. Over the range shown in the

Table 1. Return times for the short and long trajectories relative to the zero of the electric field

Return time	Brief description	Cycle	fs
t_{ts}	Short, threshold	0	0
t_{ps}	Short, threshold, model	0.18	0.48
t_{cs}	Short, cut-off, model	0.40	1.07
t_c	Cut-off	0.45	1.20
$t_{c\ell}$	Long, cut-off, model	0.50	1.35
$t_{p\ell}$	Long, threshold, model	0.69	1.85
$t_{t\ell}$	Long, threshold	0.75	2.00

For the last column, a laser wavelength of 800 nm is used.

figure, between $-2z_0$ and z_0, R_s/z_0, represented by the blue curve, diverges at $Z_+ = -0.272$. The other solution of Eq. **11** is $Z_- = -3.68$ which is outside the scale of the figure. For the long trajectory, the radius of curvature, represented by the red solid line, diverges at $Z \simeq -1.4$. This behavior is quite general for all harmonics, as discussed in the last section of this work.

To estimate in a simple way the spatial width of the harmonic field at the generation position, we assume that its amplitude is proportional to the fundamental amplitude to a power p (36, 37, 44, 46, 47). This exponent is quite constant in the plateau region and typically of the order of 4, as confirmed by our TDSE calculations presented below. The harmonic width is then simply equal to $W = w(z)/\sqrt{p}$ (here, as well, we omit to write explicitly the z-dependence of W).

Focus Position and Beam Waist

Knowing the beam radius of curvature and width at a given position z, it is a simple exercise within Gaussian optics to determine the position of the focus and the corresponding waist (e.g., ref. 45). The position of focus relative to the generation position z is given by

$$z_i = -\frac{R_i}{1 + (\lambda_q R_i/\pi W^2)^2}, \qquad [13]$$

with $\lambda_q = \lambda/q$. By using reduced coordinates relative to the fundamental Rayleigh length, Eq. **13** can be written as

$$\frac{z_i}{z_0} = -\frac{R_i}{z_0}\left(1 + \left[\frac{pR_i}{qz_0(1+Z^2)}\right]^2\right)^{-1}. \qquad [14]$$

The corresponding waist at focus is

$$w_i = \frac{W}{\sqrt{1 + (\pi W^2/\lambda_q R_i)^2}}, \qquad [15]$$

or, relative to the fundamental waist,

$$\frac{w_i}{w_0} = \left(\frac{1+Z^2}{p}\right)^{\frac{1}{2}}\left(1 + \left[\frac{qz_0(1+Z^2)}{pR_i}\right]^2\right)^{-\frac{1}{2}}. \qquad [16]$$

Fig. 4 shows the position of the harmonic focus (z_i/z_0) relative to that of the generation position (z/z_0) (*A*) and the normalized far-field divergence $\theta_i/\theta_0 = w_0/w_i$ (*B*) for the two trajectories, short (blue solid line) and long (red solid line). The color plots represent harmonic intensities obtained from a simulation presented in *Numerical Calculations*. The divergence of the fundamental θ_0 is defined as $\lambda/\pi w_0$. Let us emphasize that the zero of the horizontal scale is the laser focus, while in *A*, zero on the vertical scale means that the focus of the harmonic field coincides with the generation position. The focus position and divergence strongly vary with z and quite differently for the two trajectories. In both cases, the focus position changes sign, and the divergence goes through a minimum when the radius of curvature goes to infinity (Fig. 3).

For the short trajectory and $Z \le Z_+$, the focus is real, and it is located after the generation position ($z_i \ge 0$) along the propagation direction. The negative curvature of the convergent fundamental beam is larger in magnitude than the positive curvature induced by the dipole phase, and the harmonics are generated as a convergent beam (29). When $Z > Z_+$, the focus is virtual and located before the generation position. Two cases can be considered: When $0 > Z > Z_+$, i.e., when the generation position is before the IR focus, the negative curvature of the fundamental beam is smaller in magnitude than the positive curvature induced by the dipole phase: The harmonics are generated as a divergent beam. When $Z \ge 0$, both curvatures are positive, and the harmonics are generated as a divergent beam. The divergence is smallest in the region close to Z_+.

The same reasoning applies for the long trajectory contribution, except that Z_+ is now replaced by $Z \approx -1.4$ (Fig. 3). In this case, in the region with enough intensity for HHG, i.e., $|Z| \le 1.5$, corresponding to $I = 9 \times 10^{13}$ W·cm^{-2}, the harmonic focus is located just before the generation position, and the divergence is much larger than that of the short trajectory contribution.

At the positions where the radius of curvature diverges (indicated by the dashed line in Fig. 4 for the short trajectory), the harmonics are generated with a flat wavefront and with a large focus (low divergence). In contrast, harmonics generated far away from the divergence minima will inherit a curvature from the fundamental and the dipole phase contribution which corresponds to a significantly smaller beam waist in the real or virtual focus and thus in a significantly larger divergence. The variation of the divergence with generation position is due partly to the dipole phase contribution, but also to the mismatch between the harmonic order q and the amplitude variation here described by a power law with exponent $p = 4$ (Eq. **16**).

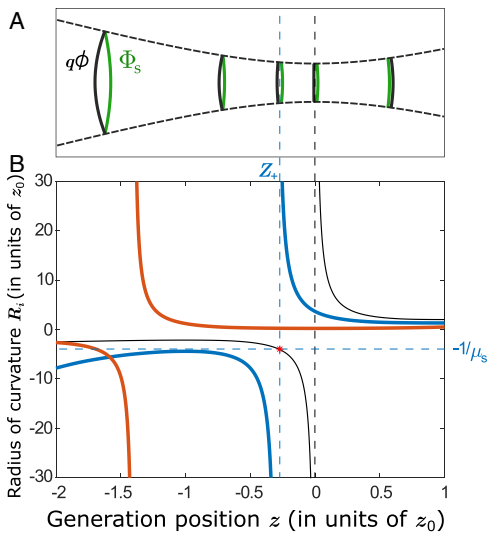

Fig. 3. (*A*) Representation of different contributions to the harmonic wavefront, due to the fundamental (black) and due to the dipole phase for the short trajectory (green) at different generation positions (*z*). The fundamental beam profile variation is indicated by the thick black dashed line. (*B*) Radius of curvature of the 23rd harmonic as a function of generation position. The laser wavelength is 800 nm, and the peak intensity at focus is 3×10^{14} W·cm^{-2}. The blue (red) solid line is obtained for the short (long) trajectory. The thin solid line shows the radius of curvature of the fundamental. At the position Z_+, where $R(z) = -z_0/\mu_s$, R_s/z_0 diverges. As can be seen in *A*, this is when the two phase contributions cancel out, as shown by the horizontal blue dashed line. In both *A* and *B*, the vertical thin dashed lines indicate the position of the harmonic focus (for the short trajectory, in blue) and the fundamental focus (black). The symbols are defined in the text; Eqs. **7**, **10**, and **12**.

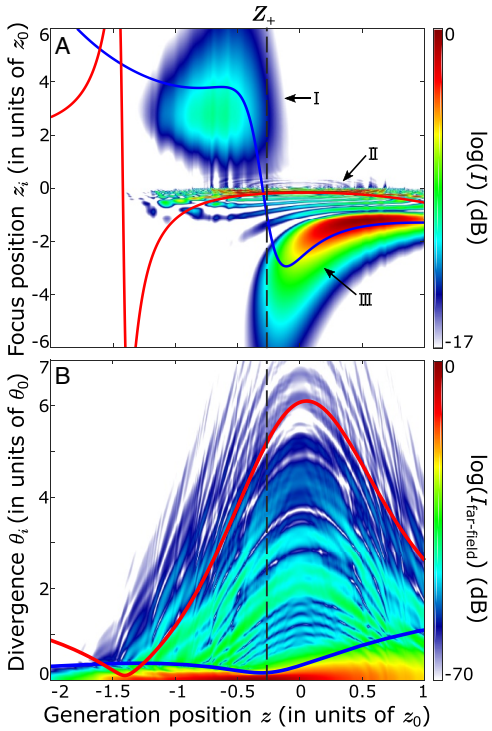

Fig. 4. Position of the focus of the 23rd harmonic relative to the generation position (*A*) and far-field divergence (*B*) as a function of the generation position relative to the laser focus. The results for the short and long trajectory are indicated by the blue and red curves, respectively. The dashed line corresponds to the position Z_+, where the radius of curvature for the short trajectory diverges. The color plots indicate results of a calculation based on the solution of the TDSE, where HHG is assumed to occur in an infinitely thin plane. In *A*, the on-axis intensity at a certain position along the propagation axis is plotted as a function of generation position on a logarithmic scale. Three different focal regions, labeled I–III can be identified. In *B*, the radial intensity calculated at a distance of $50z_0$ from the generation position, long enough to reach the far field, and normalized to the fundamental radial intensity at the same distance is indicated.

Numerical Calculations

To validate the Gaussian model presented in this work, we performed calculations based on single-atom data obtained by solving the TDSE for a single active electron in Ar exposed to a constant intensity. The time-dependent dipole response was calculated for 5,000 intensity points. This allows us, for each harmonic frequency, to precisely unwrap the amplitude and phase variation as a function of intensity, and thus to accurately describe the interferences of the trajectories. The complex electric-field distribution at a given harmonic frequency is obtained by integrating in time the polarization induced by the fundamental field in an arbitrarily thin sheet of homogeneous Ar gas. The field is then propagated to different positions relative to the generation position by calculating the diffraction integral in Fresnel approximation using Hankel transforms. The influence of ionization is not taken into account. This procedure is repeated for different gas target positions relative to the laser focus. We use a fundamental wavelength of 800 nm, a pulse duration of 45 fs, and a peak intensity of 3×10^{14} W·cm^{-2}.

Fig. 4*A* presents a color plot of the 23rd harmonic on-axis intensity for different generation positions (horizontal axis). The regions with the warmest colors (i.e., toward red) represent the focal regions. The small regions with high peak intensity (dark red, like that labeled II) correspond to the smallest focus. The agreement between the numerical predictions and those of the Gaussian model is striking. When $Z \leq Z_+$, the 23rd harmonic is focused after the generation position (region I). When $Z \geq Z_+$, two focal regions can be identified, a very thin one close to the generation position (region II) and a larger one at larger negative z_i (region III). The agreement with the results of the Gaussian model allows us to interpret the main contribution to these regions: short trajectory for I and III and long trajectory for II. While the focus position for the long trajectory contribution remains close to (just before) the generation plane, the focus position of the short trajectory contribution strongly depends on the generation position. The harmonic radiation often exhibits two foci, due to the two trajectories.

Fig. 4*A* presents a series of interference structures, some vertical, others almost horizontal. To identify the physical reason for these structures, we have performed simulations allowing us to separate the contributions of the trajectories, using the thin medium approximation and harmonic fields as in our model. Instead of Gaussian optics, however, we used diffraction integrals for the propagation. These simulations show that the horizontal fringes (e.g., between regions II and III) concern the short trajectory contribution and come from the fact that the harmonic phase front and intensity profile are not those of a Gaussian beam (37). The vertical features (e.g., between I and II), however, are a manifestation of quantum path interferences (41, 42), since they only appear when both contributions are coherently added.

The color plot in Fig. 4*B* is the 23rd harmonic radial intensity at a distance of $50z_0$, as a function of generation position. This distance is long enough to reach the far field region, so that the radial intensity is proportional to the far field divergence. As for the focus position, the comparison with the prediction of the Gaussian model allows us to distinguish the contribution of the two trajectories, with quite different divergence, especially for $|Z| \leq 1$. The red (blue) curves represent the $1/e^2$ divergence within the Gaussian model for the long (short) trajectories. The blue-green colored regions in *B* can be attributed to the long trajectory, while the red–yellow–bright green regions are due to the short trajectory.

An important question is whether these results are still valid after propagation in a finite medium. We used the single-atom data described as input in a propagation code based on the slowly varying envelope and paraxial approximations (38). We present in Fig. 5 results obtained for a 5.4-mm-long (*A*), 30-mm-long (*B*), and 60-mm-long (*C*) homogeneous medium, using a 2-mbar gas pressure and a fundamental waist size of $w_0 = 350$ μm. While Fig. 5*A* compares very well with the results shown in Fig. 4*A*, as expected, Fig. 5 *B* and *C* shows clear effects of propagation, related to ionization-induced defocusing of the fundamental laser beam. In fact, two different phase-matching regimes appear: one similar to what is present in absence of propagation and which agrees well with the predictions of the Gaussian model (compare regions I and III in Fig. 5 *A* and *B*), and a second one, which also follows a similar model but for a fundamental focus moved to the left (see regions I′ and III′ in Fig. 5*B*), as expected for a fundamental beam that is defocused due to partial ionization of the medium (20, 30–32). To examine in more details the effect of propagation goes beyond the scope of this paper.

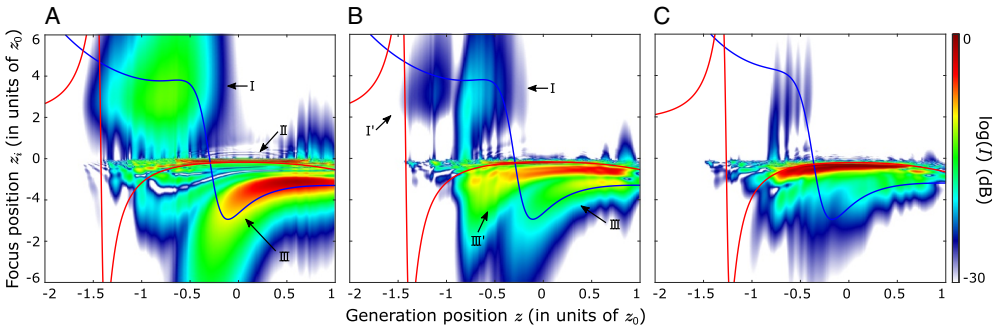

Fig. 5. Results of propagation calculations for the 23rd harmonic for a 5.4-mm-long (*A*), 30-mm-long (*B*), and 60-mm-long (*C*) gas cell. The on-axis intensity at a certain position along the propagation axis is plotted as a function of generation position on a logarithmic scale. The results of the Gaussian model are indicated by the blue and red solid lines for the short and long trajectories and are identical to those of Fig. 4*A*.

Experimental Divergence Measurements

Experiments were performed at the intense XUV beamline of the Lund Laser Centre (48, 49), by using a multiterawatt 45-fs titanium–sapphire laser operating at a 10-Hz repetition rate. The beam was (slightly) apertured to 27 mm and focused by using a spherical mirror with focal length $f = 8$ m. The laser aberrations were minimized by using a deformable mirror coupled to an IR Shack–Hartmann wavefront sensor. The harmonics were generated in a 60-mm gas cell filled with Ar by a pulsed valve. We measured the divergence of the emitted harmonics using a flat-field XUV spectrometer with an entrance slit located approximately 6 m after the generation. For each harmonic, the width was estimated by fitting a Gaussian function onto the transverse (spatial) direction of the spectrometer. The IR focus was moved relative to the gas cell along the direction of propagation by changing the voltage of the actuator which controls the curvature of the deformable mirror. The limits of the scan were imposed by the decrease of the harmonic yield, which is slightly asymmetric relative to the laser focus (26).

The widths of the 13th–19th harmonics are shown in Fig. 6*A* and compared with theoretical predictions in *B*–*D*, obtained by using a laser waist of 220 μm and a maximum intensity of 2.5×10^{14} W·cm^{-2} (the Rayleigh length is estimated to 0.2 m). The harmonic widths were calculated as $(z_i + L)\theta_i$, where $L = 6$ m is the distance from the gas cell to the measurement point. Fig. 6*B* presents results of numerical calculations based on solving the TDSE and the propagation equations, using parameters mimicking the experimental conditions as well as possible. In Fig. 6*C*, the results of the Gaussian model for the short trajectory are shown, while in Fig. 6*D*, a "truncated" Gaussian model is used, where the expressions for the beam waist, radius of curvature, and intensity variation of the fundamental beam now include the effect of a circular aperture (50, 51), taken to be equal to the experimental one. Going from the left to the right in all of the plots in Fig. 6, the harmonic widths first decrease (or stay approximately constant for the highest orders) and then increase. The harmonic widths vary more strongly in the Gaussian model than in the other calculations and in the experiment. We investigated the reason for this difference by varying the parameters used in the propagation simulations, such as medium length, gas pressure, aperture diameter, and pulse energy. Unlike the conditions used in Fig. 5 *B* and *C*, effects due to propagation, e.g., induced by ionization-defocusing, are negligible, and the main reason for the difference between Fig. 6 *B* and *C* is the beam truncation due to the aperture, as confirmed by Fig. 6*D*. Effects due to propagation in the nonlinear medium, which become nonnegligible at higher laser intensity, actually lead to faster variation of the beam divergence on both sides of the laser focus.

Chromatic Aberrations of Attosecond Pulses

Finally, we study the variation of the focus position and beam waist over a large spectral bandwidth. To obtain a broad spectral region, we consider generation of high-order harmonics in neon atoms. HHG spectra obtained in Ne (52) are broader and flatter than those in Ar, which exhibit a strong modulation due to a Cooper minimum at ∼45 eV. Fig. 7 shows the predictions of the Gaussian model, for the 31st to the 71st harmonics of 800-nm radiation, at an intensity of 5×10^{14} W·cm^{-2}. We only consider here the contribution from the short trajectory. The Gaussian model is used here for simplicity. It should be

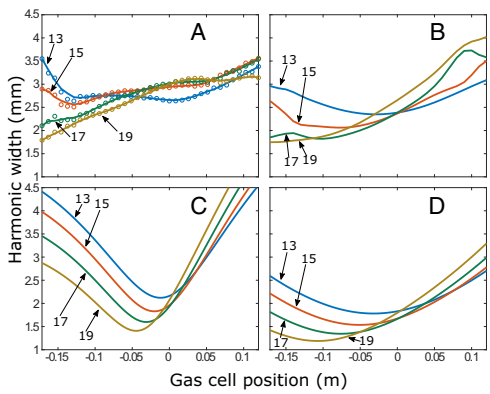

Fig. 6. (*A*) Spatial widths of harmonics 13–19 generated in Ar and measured approximately 6 m after generation as a function of the cell position. The solid lines are fit to the experimental data indicated by the circles. (*B*–*D*) Spatial widths of the same harmonics as a function of generation position, obtained by the numerical simulations solving the TDSE and the propagation equations (*B*) and predicted by the Gaussian model for the short trajectory (*C*) and the same model using a truncated Gaussian beam (*D*). The peak intensity in vacuum is 2.5 × 10^{14} W·cm^{-2}, and the laser beam waist is 220 μm.

reasonably accurate in conditions of thin medium, not too high degree of ionization, which is the case for Ne atoms at the intensity used, and high spatial quality, nontruncated, fundamental beam.

The variation of the focus position as a function of generation position strongly depends on the process order. This is due to the frequency dependence of Eq. **9** and, in particular, depends on whether the radius of curvature diverges. Since μ_s increases with frequency, the two zeros $Z_\pm$ of Eq. **9** move closer to each other, as is clear in Fig. 7*A* by comparing, e.g., harmonics 41 and 43 ($Z_\pm$ correspond to the two maxima in the figure). At a certain frequency, corresponding to harmonic 45 in Fig. 7*A*, $-1/\mu_s$ becomes tangent to $R(z)$ at $z=-z_0$ (see also Fig. 3). Above this frequency, the radius of curvature does not diverge and remains negative. The harmonic focus position is then always located before the generation position. As $-1/\mu_s \to 0$, when the frequency increases, the focus position becomes largely independent from the generation. In this region, the harmonics are much more focused, as shown by the blue lines in Fig. 7*B*.

To estimate the consequence of these spatial properties on the spectral characteristics of the attosecond pulses (25), we examine the variation of the on-axis spectrum at different positions (labelled ① to ④), for the generation position indicated by the dashed line. This is equivalent to examining the properties of

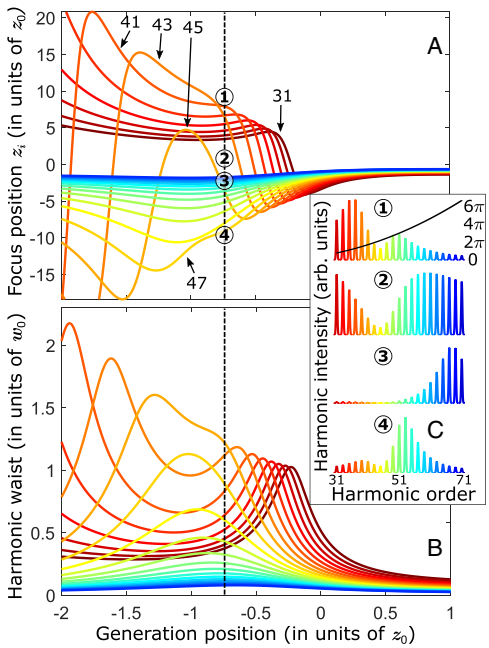

Fig. 7. Position of harmonic focus z_i (*A*) and waist (*B*) as a function of generation position for harmonics 31–71. The different harmonic orders are indicated by different rainbow color codes, from brown (31) to dark blue (71). *C* shows harmonic spectra at four different positions along z_i, indicated from top to bottom by the numbered circles, for the generation position marked by the dashed line in *A*. The spectral phase of the attosecond pulse is shown in black for the first observation point, being largely independent of the observation position. arb. units, arbitrary units.

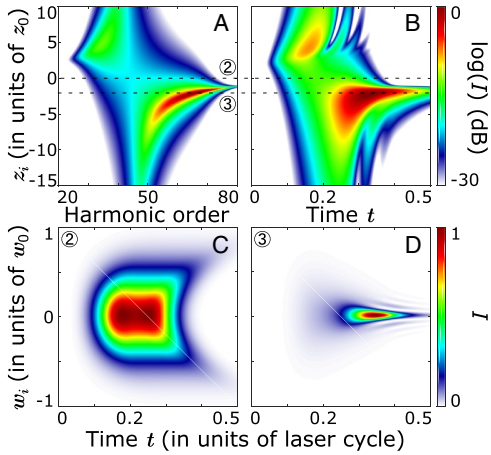

Fig. 8. (*A* and *B*) Graphs show the on-axis spectral and temporal intensity, respectively, in logarithmic scales, as a function of the observation position, when generating at $z=-0.75\ z_0$. The positions ② and ③ (see Fig. 7*A*) are indicated by dashed lines. *C* and *D* show retrieved attosecond pulses at two different detection positions, i.e., ② and ③ in Fig. 7*A*, in a linear scale.

the generated radiation after refocusing as illustrated in Fig. 1, for different "detection positions" in the focal region. We here assume equal strength of the generated harmonics, but account for the frequency variation in beam waist size (Fig. 7*B*) and position (Fig. 7*A*). The harmonic spectra shown in Fig. 7*C* are found to be strongly dependent on the detection position, with, in some cases, strong bandwidth reduction and displacement of the central frequency. In contrast, the on-axis harmonic phase is dominated by the attosecond chirp, given by the last term in Eq. **6** and indicated by the black line in Fig. 7*C*, and does not vary much with the detection position.

Spatiotemporal Coupling of Attosecond Pulses

Finally, we estimate the influence of the chromatic aberrations on the temporal properties of the attosecond pulses. We consider a flat spectrum between harmonics 31 and 71 at the generation position indicated by the dashed line in Fig. 7, in the same conditions as in the previous paragraph. We propagate the harmonic fields using diffraction integrals and coherently add them to obtain the resulting attosecond pulse train in space and time at different detection positions. We take into account the different focus positions and divergences of the frequency components of the attosecond pulses, as well as the attosecond positive chirp.

Fig. 8 shows the spectral (*A*) and temporal (*B*) intensity (in color) of the generated attosecond pulse on-axis as function of the detection position relative to the generation position, here equal to $z=-0.75\ z_0$ (dashed line in Fig. 7). In these conditions, the central frequency and pulse duration of the attosecond pulse vary distinctively, indicating strong spatiotemporal couplings. In particular, the high-frequency components (high harmonic orders) form a tight virtual focus before the generation position, while the low-frequency components have a more loose and real focus behind (Fig. 8*A*). The highest intensity is obtained before the generation position, while the shortest pulse is obtained afterward, as follows from Fig. 8*B*. The attosecond pulse is not the shortest at the generation position, where the spectral bandwidth is the largest, because the

attosecond chirp stretches the pulse in time. Fig. 8 *A* and *B* strikingly show that the shortest pulse and the highest intensity of the attosecond pulse are obtained in different positions, illustrating the difficulty of refocusing high-order harmonics, particularly for applications requiring high intensity.

Finally, Fig. 8 *C* and *D* shows the spatiotemporal intensity profiles of the attosecond pulse at the positions where is it spectrally broadest (*C*, ②) and where it is most intense (*D*, ③). The difference between the two cases is a signature of the strong spatiotemporal couplings of the generated attosecond pulses. These couplings, here studied at $z = -0.75\ z_0$ (dashed line in Fig. 7), strongly depend on the position of generation.

Conclusion

In this work, we examine the focusing properties of high-order harmonics generated in gases. We use a simple Gaussian optics model, valid for a thin generating medium, assuming a fundamental Gaussian beam, and based on an analytical expression of the frequency- and intensity-dependent dipole phase. This model allows us to predict the focus and divergence of the two trajectory contributions to HHG. We validate the predictions of the model by numerical calculations based on solving the TDSE for the single-atom response and propagation equations for the response from the macroscopic medium. Experimental divergence measurements performed at the intense XUV beamline of the Lund Laser Centre show similar trends as those predicted by the numerical calculations, as well as by an extension of the Gaussian model, which includes the effect of a circular aperture. We also discuss the consequences of the fact that the harmonics have different focus positions and beam waists on the resulting spectra and pulse durations. The relative harmonic amplitudes are found to vary with the detection position, thus strongly affecting the spatiotemporal properties of the corresponding attosecond pulses.

The effects investigated in the present work have a strong impact on applications of attosecond pulses, requiring a small focal spot (e.g., to reach a high XUV intensity) over a broad bandwidth or during a short (attosecond) duration. These spatiotemporal couplings may be reduced by locating the generation medium after the laser focus and/or by minimizing the influence of the dipole phase, using a shaped fundamental beam (53, 54) or generating in waveguides (capillaries) (47, 55).

ACKNOWLEDGMENTS. This research was supported by the Swedish Research Council; the Swedish Foundation for Strategic Research; European Research Council Grant 339253 PALP; the Knut and Alice Wallenberg Foundation; and National Science Foundation Grant PHY-1713761. This project received funding from the European Union's Horizon 2020 research and innovation program under Marie Skłodowska-Curie Grant Agreements 641789 MEDEA and 793604 ATTOPIE.

1. Akturk S, Gu X, Bowlan P, Trebino R (2010) Spatio-temporal couplings in ultrashort laser pulses. *J Opt* 12:093001–093020.
2. Miranda M, et al. (2014) Spatiotemporal characterization of ultrashort laser pulses using spatially resolved Fourier transform spectrometry. *Opt Lett* 39:5142–5145.
3. Pariente G, Gallet V, Borot A, Gobert O, Quéré F (2016) Space–time characterization of ultra-intense femtosecond laser beams. *Nat Photon* 10:547–553.
4. Harth A, et al. (2017) Compact 200 kHz HHG source driven by a few-cycle OPCPA. *J Opt* 20:014007.
5. Vincenti H, Quéré F (2012) Attosecond lighthouses: How to use spatiotemporally coupled light fields to generate isolated attosecond pulses. *Phys Rev Lett* 108:113904.
6. Kim KT, et al. (2013) Photonic streaking of attosecond pulse trains. *Nat Photon* 7: 651–656.
7. Louisy M, et al. (2015) Gating attosecond pulses in a noncollinear geometry. *Optica* 2:563–566.
8. Sansone G, et al. (2006) Isolated single-cycle attosecond pulses. *Science* 314:443–446.
9. Goulielmakis E, et al. (2008) Single-cycle nonlinear optics. *Science* 320:1614–1617.
10. Li J, et al. (2017) 53-attosecond X-ray pulses reach the carbon K-edge. *Nat Commun* 8:186.
11. Gaumnitz T, et al. (2017) Streaking of 43-attosecond soft-X-ray pulses generated by a passively CEP-stable mid-infrared driver. *Opt Express* 25:27506–27518.
12. Popmintchev T, et al. (2012) Bright coherent ultrahigh harmonics in the keV X-ray regime from mid-infrared femtosecond lasers. *Science* 336:1287–1291.
13. Cousin SL, et al. (2017) Attosecond streaking in the water window: A new regime of attosecond pulse characterization. *Phys Rev X* 7:041030.
14. Schafer KJ, Yang B, DiMauro LF, Kulander KC (1993) Above threshold ionization beyond the high harmonic cutoff. *Phys Rev Lett* 70:1599–1602.
15. Corkum PB (1993) Plasma perspective on strong-field multiphoton ionization. *Phys Rev Lett* 71:1994–1997.
16. Lewenstein M, Kulander KC, Schafer KJ, Bucksbaum PH (1995) Rings in above-threshold ionization: A quasiclassical analysis. *Phys Rev A* 51:1495–1507.
17. Bellini M, et al. (1998) Temporal coherence of ultrashort high-order harmonic pulses. *Phys Rev Lett* 81:297–300.
18. Frumker E, Paulus GG, Niikura H, Villeneuve DM, Corkum PB (2009) Frequency-resolved high-harmonic wavefront characterization. *Opt Lett* 34:3026–3028.
19. Lloyd DT, O'Keeffe K, Anderson PN, Hooker SM (2016) Gaussian-Schell analysis of the transverse spatial properties of high-harmonic beams. *Sci Rep* 6:30504.
20. Johnson AS, et al. (2018) High-flux soft X-ray harmonic generation from ionization-shaped few-cycle laser pulses. *Sci Adv* 4:eaar3761.
21. Austin DR, et al. (2011) Lateral shearing interferometry of high-harmonic wavefronts. *Opt Lett* 36:1746.
22. Lee DG, Park JJ, Sung JH, Nam CH (2003) Wave-front phase measurements of high-order harmonic beams by use of point-diffraction interferometry. *Opt Lett* 28: 480–482.
23. Valentin C, et al. (2008) High-order harmonic wave fronts generated with controlled astigmatic infrared laser. *J Opt Soc Am B* 25:B161–B166.
24. Freisem L, Jansen GSM, Rudolf D, Eikema KSE, Witte S (2018) Spectrally resolved single-shot wavefront sensing of broadband high-harmonic sources. *Opt Express* 26:6860–6871.
25. Frumker E, et al. (2012) Order-dependent structure of high harmonic wavefronts. *Opt Express* 20:13870–13877.
26. Salières P, L'Huillier A, Lewenstein M (1995) Coherence control of high-order harmonics. *Phys Rev Lett* 74:3776–3779.
27. Balcou P, Salières P, L'Huillier A, Lewenstein M (1997) Generalized phase-matching conditions for high harmonics: The role of field-gradient forces. *Phys Rev A* 55:3204–3210.
28. Quintard L (2017) Caractérisation et contrôle des profils spatiaux, spectraux et temporels de faisceaux XUV obtenus par génération d'harmoniques d'ordres élevés dans des gaz. PhD thesis (Université de Bordeaux, Bordeaux, France). French.
29. Quintard L, et al. (2018) Mirrorless focusing of XUV high-order harmonics. arxiv:1810.07282. Preprint, posted October 16, 2018.
30. Miyazaki K, Takada H (1995) High-order harmonic generation in the tunneling regime. *Phys Rev A* 52:3007–3021.
31. Tamaki Y, Itatini J, Nagata Y, Obara M, Midorikawa K (1999) Highly efficient, phase matched high-harmonic generation by a self-guided laser beam. *Phys Rev Lett* 82:1422–1425.
32. Lai CJ, Kärtner FX (2011) The influence of plasma defocusing in high harmonic generation. *Opt Express* 19:22377–22387.
33. Bor Z (1989) Distortion of femtosecond laser pulses in lenses. *Opt Lett* 14:119–121.
34. Bor Z, Horváth ZL (1992) Distortion of femtosecond pulses in lenses. Wave optical description. *Opt Commun* 94:249–258.
35. Guo C, et al. (2018) Phase control of attosecond pulses in a train. *J Phys B At Mol Opt Phys* 51:034006.
36. Hernández-García C, San Román J, Plaja L, Picón A (2015) Quantum-path signatures in attosecond helical beams driven by optical vortices. *New J Phys* 17:093029.
37. Catoire F, et al. (2016) Complex structure of spatially resolved high-order-harmonic spectra. *Phys Rev A* 94:063401.
38. L'Huillier A, Balcou P, Candel S, Schafer KJ, Kulander KC (1992) Calculations of high-order harmonic-generation processes in xenon at 1064 nm. *Phys Rev A* 46:2778–2790.
39. Lewenstein M, Balcou P, Ivanov M, L'Huillier A, Corkum P (1994) Theory of high-order harmonic generation by low-frequency laser fields. *Phys Rev A* 49:2117–2132.
40. Varjú K, et al. (2005) Frequency chirp of harmonic and attosecond pulses. *J Mod Opt* 52:379–394.
41. Carlström S, et al. (2016) Spatially and spectrally resolved quantum path interference with chirped driving pulses. *New J Phys* 18:123032.
42. Zaïr A, et al. (2008) Quantum path interferences in high-order harmonic generation. *Phys Rev Lett* 100:143902.
43. Guo C (2018) A high repetition rate attosecond light source based on optical parametric amplification. Ph.D. thesis (Lund University, Lund, Sweden).
44. Rego L, San Román J, Picón A, Plaja L, Hernández-García C (2016) Nonperturbative twist in the generation of extreme-ultraviolet vortex beams. *Phys Rev Lett* 117:163202.
45. Saleh BEA, Teich MC (2007) *Fundamentals of Photonics* (John Wiley and Sons, New York).
46. Pérez-Hernández JA, Roso L, Plaja L (2009) Harmonic generation beyond the strong-field approximation: The physics behind the short-wave-infrared scaling laws. *Opt Express* 17:9891–9903.
47. Durfee CG III, et al. (1999) Phase matching of high-order harmonics in hollow waveguides. *Phys Rev Lett* 83:2187–2190.
48. Manschwetus B, et al. (2016) Two-photon double ionization of neon using an intense attosecond pulse train. *Phys Rev A* 93:061402.
49. Coudert-Alteirac H, et al. (2017) Micro-focusing of broadband high-order harmonic radiation by a double toroidal mirror. *Appl Sci* 7:1159.

50. Horváth ZL, Bor Z (2003) Focusing of truncated Gaussian beams. *Opt Commun* 222: 51–68.
51. Gillen GD, Seck CM, Guha S (2010) Analytical beam propagation model for clipped focused-Gaussian beams using vector diffraction theory. *Opt Express* 18:4023–4040.
52. Macklin JJ, Kmetec JD, Gordon CL III (1993) High-order harmonic generation using intense femtosecond pulses. *Phys Rev Lett* 70:766–769.
53. Boutu W, et al. (2011) High-order-harmonic generation in gas with a flat-top laser beam. *Phys Rev A* 84:063406.
54. Dubrouil A, et al. (2011) Controlling high harmonics generation by spatial shaping of high-energy femtosecond beam. *Opt Lett* 36:2486–2488.
55. Popmintchev T, Chen MC, Arpin P, Murnane MM, Kapteyn HC (2010) The attosecond nonlinear optics of bright coherent X-ray generation. *Nat Photon* 4:822–832.

Paper IV

S. Maclot, J. Lahl, **J. Peschel**, H. Wikmark, P. Rudawski, F. Brunner, H. Coudert-Alteirac, S. Indrajith, B. A. Huber, S. Díaz-Tendero, N. F.Aguirre, P. Rousseau, and P. Johnsson
Dissociation dynamics of the diamondoid adamantane upon photoionization by XUV femtosecond pulses
Sci. Reports 10, 2884 (2020)

SCIENTIFIC REPORTS
nature research

OPEN

Dissociation dynamics of the diamondoid adamantane upon photoionization by XUV femtosecond pulses

Sylvain Maclot[1,2*], Jan Lahl[1], Jasper Peschel[1], Hampus Wikmark[1], Piotr Rudawski[1], Fabian Brunner[1], Hélène Coudert-Alteirac[1], Suvasthika Indrajith[3], Bernd A. Huber[3], Sergio Díaz-Tendero[4,5,6], Néstor F. Aguirre[7], Patrick Rousseau[3] & Per Johnsson[1*]

This work presents a photodissociation study of the diamondoid adamantane using extreme ultraviolet femtosecond pulses. The fragmentation dynamics of the dication is unraveled by the use of advanced ion and electron spectroscopy giving access to the dissociation channels as well as their energetics. To get insight into the fragmentation dynamics, we use a theoretical approach combining potential energy surface determination, statistical fragmentation methods and molecular dynamics simulations. We demonstrate that the dissociation dynamics of adamantane dications takes place in a two-step process: barrierless cage opening followed by Coulomb repulsion-driven fragmentation.

Diamondoids are a class of carbon nanomaterials based on carbon cages with well-defined structures formed by $C(sp^3)$-$C(sp^3)$-hybridized bonds and fully terminated by hydrogen atoms. All diamondoids are variants of the adamantane molecule, the most stable among all of the isomers with the formula $C_{10}H_{16}$, shown in Fig. 1. On Earth, diamondoids are naturally found in petroleum deposits and natural gas reservoirs, and their most common applications are for the characterization of petroleum and gas fields, offering possibilities to e.g. trace the source of oil spills[1]. Today, diamondoids are attracting increasing interest for use as an applied nanomaterial in e.g. nano- and optoelectronics as well as in biotechnology and medicine due to their high thermal stability and well-defined structure in combination with no known toxicity[2]. In space, diamondoids have been found to be the most abundant component of presolar grains[3], and due to their high stability they are thus also expected to be abundant in the interstellar medium[4].

However, when compared to laboratory measurements based on infrared spectroscopy[5], astronomical observations show a deficiency of diamondoids in the interstellar medium which to date is not completely understood[6]. The first ionization limit in diamondoids lies around 8–9 eV with a maximum in the ionization yield between 10 and 11 eV[7], close to the hydrogen Lyman-α line, and the efficient production of cations followed by dissociation has been suggested as a possible explanation for the apparent lack of diamondoids in the interstellar medium. Steglich *et al.* investigated the stability of diamondoid cations using ultraviolet irradiation, finding that rapid loss of a neutral hydrogen followed ionization[8]. Since then, further studies have suggested that small hydrocarbons are also created as dissociation products. In a recent work at the Swiss Light Source, vacuum ultraviolet radiation (9–12 eV) was used in combination with threshold photoelectron and photoion coincidence detection to determine the appearance energies and branching ratios of the resulting photofragments of the singly charged adamantane cation[9]. The study reveals, in addition to the expected hydrogen loss, dissociation via a number of parallel channels which all start with an opening of the carbon cage and hydrogen migration indicating that the

[1]Department of Physics, Lund University, P.O. Box 118, 22100, Lund, Sweden. [2]Biomedical and X-Ray Physics, Department of Applied Physics, AlbaNova University Center, KTH Royal Institute of Technology, SE-10691, Stockholm, Sweden. [3]Normandie Université, ENSICAEN, UNICAEN, CEA, CNRS, CIMAP, 14000, Caen, France. [4]Departamento de Química, Módulo 13, Universidad Autónoma de Madrid, 28049, Madrid, Spain. [5]Condensed Matter Physics Center (IFIMAC), Universidad Autónoma de Madrid, 28049, Madrid, Spain. [6]Institute for Advanced Research in Chemical Sciences (IAdChem), Universidad Autónoma de Madrid, 28049, Madrid, Spain. [7]Theoretical Division, Los Alamos National Laboratory, Los Alamos, New Mexico, 87545, USA. *email: smaclot@gmail.com; per.johnsson@fysik.lth.se

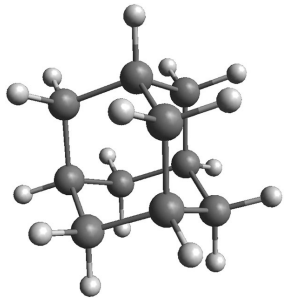

Figure 1. Structure of adamantane.

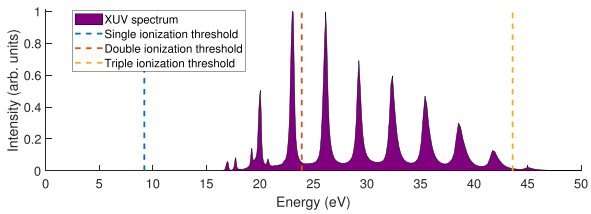

Figure 2. XUV spectrum and the first three ionization thresholds of adamantane.

low photostability of adamantane could explain its deficiency in astronomical observations. While this study was recently complemented by a first time-resolved study[10], to date no results have been published on the dissociation dynamics of multiply charged adamantane molecules.

In this work, we study the fragmentation dynamics of the adamantane dication after ionization by extreme ultraviolet (XUV) femtosecond pulses, the use of which ensures prompt and well-defined ionization. The experimental technique used in this study is based on correlated ion and electron spectroscopy, enabling the characterization of the charged products of interaction (identification and energetics). The support of various theoretical methods such as molecular dynamics simulations, potential energy surface determination and statistical fragmentation models, helps to unravel the fragmentation dynamics of such a complex molecular system.

Methods

Experiments. The high-intensity XUV beamline at the Lund Attosecond Science Centre provides trains of attosecond pulses in the XUV spectral region using the high-order harmonic generation (HHG) technique[11,12]. This is achieved by focusing an intense infrared (IR) pulse (high-power Ti:Sapphire chirped pulse amplification laser with a pulse energy of 50 mJ, a central wavelength of 810 nm, a pulse duration of 45 fs and a repetition rate of 10 Hz) into an argon gas medium (6 cm long cell) in a loose focusing geometry (~8 m focal length)[13]. The train of XUV attosecond pulses, with a total duration of 20 fs, contains around 15 attosecond pulses with an estimated individual pulse duration of approximately 300 as, spaced by 1.35 fs. The photon energy spectrum of the produced XUV light is a characteristic harmonic comb spanning from ~20 to 45 eV (Fig. 2). Then, the XUV light is micro-focused (~5×5 μm^2) on target via a double toroidal mirror[14] and with a pulse train energy on target of around 10 nJ this leads to intensities of the order of 10^{12} W · cm^{-2}.

Adamantane molecules, $C_{10}H_{16}$ (powder from Aldrich with >99% purity), are produced in the gas phase by a pulsed Even-Lavie valve[15,16], heated to 100 °C and using He as a carrier gas, in the form of a cold and collimated supersonic jet.

The photon-molecule interaction leads to the formation of highly excited singly and doubly charged adamantane molecules (single and double ionization thresholds IT_1~9.2 eV and IT_2~23.9 eV - see Fig. 2). The trication is only produced in negligible amounts since the triple ionization threshold is IT_3~43.6 eV (Fig. 2) and thus is not discussed in the following. The charged products of interaction are detected by a double-sided velocity map imaging (VMI) spectrometer[17] giving access to the kinetic energy distributions of ions and electrons on a shot-to-shot basis. In addition, the ion side of the spectrometer can measure the time-of-flight (TOF) of the ions, providing the mass spectrum. Despite the high count rates (several tens of counts per pulse), the use of the partial covariance technique[18] enables us to disentangle the contributions of the different fragmentation channels. For instance, applying this technique on single-shot ion TOF spectra gives the possibility to produce ion-ion correlation maps that reveal the dissociation dynamics of the doubly charged adamantane molecules. In addition, the use of this

technique on single-shot ion TOF spectra and the single-shot ion VMI data gives access to the kinetic energy distribution of specific ionic fragments.

Theory. Three different theoretical methods have been used: (i) molecular dynamics (MD) simulations in the framework of the density functional theory (DFT) and the density functional tight binding (DFTB) method, (ii) exploration of the potential energy surface (PES) employing the DFT, and (iii) statistical fragmentation using the Microcanonical Metropolis Monte-Carlo (M3C) method.

Molecular dynamics simulations. The molecular dynamics approach, using the DFTB method[19,20], has been used to compute the lifetime of doubly-ionized and excited adamantane. To this end, we have considered double ionization of adamantane in a Franck-Condon way; that is, our molecular dynamics simulations start from the optimized geometry of the neutral adamantane molecule after removal of two electrons. We assume that the electronic excitation energy is rapidly redistributed into the nuclear degrees of freedom and thus we run these simulations in the electronic ground state of the dication Ada^{2+}, taking the equilibrium geometry of the neutral ground state as initial point. We have taken four values of excitation energy corresponding to the relative energy of the highest order of harmonics in the XUV spectrum (Fig. 2) with respect to IT_2 (8.46, 11.50, 14.63 and 17.80 eV, which correspond to temperature values 2520, 3450, 4360 and 5300 K, respectively). The used E_{exc} values can be considered as the upper limits of the remaining electronic excitation energy after ionization with the four highest energy harmonics, assuming that the kinetic energy of the ejected electrons is zero, thus $E_{ph} = E_{exc}$. This excitation energy is randomly distributed into the nuclear degrees of freedom in each trajectory (i.e., in the velocity components v_x^i, v_y^i, v_z^i of each atom i). Molecular dynamics trajectories are propagated up to a maximum time of $t_{max} = 1, 5, 10$, 20 and 100 ps. For each value of excitation energy and propagation time a set of 1000 independent trajectories are considered (that is, the initial conditions are separately established in each set of trajectories). Statistics are then carried out over these trajectories to obtain information on the survival time of the doubly-ionized adamantane with different excitation energies. To ensure adiabaticity in the simulations a time step of $\Delta t = 0.1$ fs is used. These simulations have been carried out with the deMonNano code[21] and the results show that even with these relatively high excitation energies the dication does not fully fragment until after tens to hundreds of picoseconds making it computationally too heavy to perform full MD simulations at the DFT level (see SI).

Potential energy surface calculations. We have explored the PES using DFT, in particular we have employed the B3LYP functional[22–24] in combination with the 6-31G(d) basis set. This part of the study provides useful energetic and structural information of the experimentally measured exit channels. In order to identify the most relevant stationary points of the PES we have adopted the following strategy:

(1) We have first performed molecular dynamics simulations at the same DFT-B3LYP/6-31G(d) level, to mimic the evolution of the system during the first femtoseconds after the ionization and excitation. This part of the simulations also starts by computing the energy required to doubly ionize adamantane in a Franck-Condon transition from the optimized neutral structure. This is our starting point for the dynamics. 160 trajectories were carried out using the ADMP method with a maximum propagation time of 500 fs, and considering a time step of $\Delta t = 0.1$ fs, and a fictitious mass of $\mu = 0.1$ au. Thus, after propagation of the doubly charged excited adamantane, we have obtained the evolution of the system in the first femtoseconds.
(2) Then, using the last step in the dynamics as an initial guess, we have optimized the geometry of the produced species.
(3) Finally, geometry optimization of fragments observed in the experiments has also been computed. To this end, we have considered several structures for each $C_nH_x^{q+}$ fragment, thus obtaining the relative energy of the exit channels observed in the experiment. Harmonic frequencies have been computed after geometry optimization to confirm that the obtained structures are actual minima in the PES (no imaginary frequencies) and to evaluate the Zero-Point-Energy correction. These calculations were carried out with the Gaussian09 package[25]. The proposed strategy was used in the past with success to study the fragmentation dynamics of ionized biomolecules (see e.g.[26–28]).

Notice that we are not performing a complete exploration of the full PES. The very large number of degrees of freedom makes such study unfeasible. However, with the followed strategy, we are confident that the most populated fragmentation channels are taken into account, and the minima of the relevant energy paths are located.

Statistical fragmentation simulations. We study statistical fragmentation of doubly ionized adamantane with the recently developed M3C method[29,30], using the constrained approach presented in[31]. The key aspect of this methodology is that it provides a random way to move in the phase space (the so-called Markov chain) until a region of maximum entropy is reached, where the physical observables are computed. This description should be equivalent to an MD simulation in the infinite integration time limit. In this work, we focus on two observables: (1) the probability of each fragmentation channel as a function of internal energy (the so-called breakdown curves), and (2) the distribution of the internal energy of the system in its components. This method was successfully used in the past to describe the fragmentation of carbonaceous species[29,31–34].

The main ingredients of the M3C simulations, i.e. structures, energies, and vibrational frequencies of the fragments, are those obtained in the PES exploration at the B3LYP/6-31G(d) level. In total, 148 molecules are included in the fragmentation model (see SI for details). Geometries are available as an additional file in the SI and in the M3C-store project database[35].

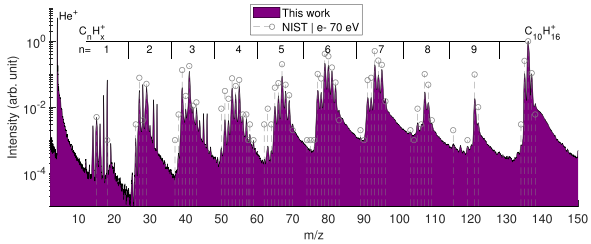

Figure 3. Mass spectrum of cationic products resulting from the interaction between XUV pulses and neutral adamantane molecules (purple). The dashed gray lines correspond to the mass spectrum obtained by electron impact at 70 eV[39].

The statistical simulations have been carried out such that the sum of angular momenta from all fragments exactly compensates the orbital momentum resulting in a total angular momentum equal to zero. We set the radius of the system to 30.0 Å. Implementation of larger radii implies similar Coulomb interaction among fragments, but requires increased sampling to achieve convergence; on the other hand, a smaller radius results in an artificial overestimation of the fragments' angular momentum. We have performed a scan of the internal energy from 0 to 10 eV. 10000 numerical experiments for each value of internal energy have been carried out in order to estimate the error in the computed observables (and thus to use them as convergence criteria). The numerical experiments each differ from one another in their initial values for vibrational energy, angular momentum, and molecular orientation, which were randomly chosen. All numerical experiments start from the most stable structure of the doubly charged $C_{10}H_{16}^{2+}$. The sequence `5*V,T,R,S:0,5*V,T,R,S:-1:1` has been used as a Markov chain, including a total of 2000 events; among them 10% have been used as a burn-in period (see ref. [29] for details).

In summary, a complete picture of the fragmentation of excited doubly-charged adamantane is obtained with the theoretical simulations: dynamic, energetic and entropic approaches allow us to infer the main factors governing the experimentally observed processes, also providing complementary information.

Results and Discussion

The experimental total mass spectrum of the charged products of interaction (Fig. 3) is obtained by calibration of the TOF spectrum recorded after 275000 laser shots. The most intense peak (excluding helium) corresponds to the singly charged parent ion at $m/z = 136$. The loss of one hydrogen atom is observed at a mass-to-charge ratio of $m/z = 135$ with an intensity of 9% of the parent ion. The losses of two and three hydrogen atoms are also observed, however they have an intensity two orders of magnitude lower than that of the single hydrogen loss. As a general feature, the production of a wide distribution of $C_nH_x^+$ fragments resulting from dissociation of singly and doubly charged adamantane molecules is observed. The most intense peaks of each C_n group are attributed to CH_3^+, $C_2H_5^+$, $C_3H_5^+$, $C_4H_7^+$, $C_5H_7^+$, $C_6H_7^+$, $C_7H_9^+$, $C_8H_{11}^+$ and $C_9H_{13}^+$ (respectively $m/z = 15$, 29, 41, 55, 67, 79, 93, 107 and 121) and are rather similar to the ones observed in the case of ionization by electron impact at 70 eV (dashed line in Fig. 3). On the other hand, the main fragments of the C_n groups $n = 3$, 4 and 8 are different from the ones found by Candian *et al.*[9] (photodissociation around first ionization threshold), *i.e.* $C_3H_7^+$, $C_4H_8^+$ and $C_8H_{12}^+$ respectively, demonstrating that the dynamics of fragmentation is sensitive to the ionization/excitation energy.

Most of the fragments indicate strong intramolecular rearrangements with multiple hydrogen migrations and/or hydrogen losses. Some of these rearrangements may occur before fragmentation and lead to the cage opening of adamantane cations. The corresponding cage opening of the singly charged cation was already studied by Candian *et al.* using DFT and RRKM simulations[9]. In the case of the doubly charged adamantane, the results of our *ab initio* molecular dynamics calculations (ADMP using DFT-B3LYP up to 500 fs) followed by PES exploration are summarized in Fig. 4. The three lowest energy configurations (Fig. 4(a)), appearing ≈ 4 eV below the double ionization threshold, have an open-cage geometry and have at least one hydrogen migration (CH_3 termination).

Dication fragmentation pattern. In order to help to understand the complex energetic picture of the dication dynamics, Fig. 5 shows a schematic dissociative potential energy curve for the dication, including the different energetic quantities that are useful for the discussion. We consider the vertical ionization (Franck-Condon region) from the neutral ground state with a photon of energy $h\nu$ (purple arrow), such as $h\nu > IT_2$. The excess energy after photoionization is defined as $E_{ph} = h\nu - IT_2$. We already know that the relaxation from the double ionization threshold IT_2 to the ground state of the dication has a fixed energy of $E_{relax} \approx 4.1$ eV (see Fig. 4(a)). The kinetic energy of the electron pair involved in the double ionization is called E_{2e^-} and the internal energy of the dication ground state is denoted E_{int}. Under our assumptions, the internal energy is the sum of the rapidly redistributed electronic excitation energy (E_{exc}) and the relaxation energy (E_{relax}), and thus $E_{int} \geq E_{relax} \approx 4.1$ eV. The final ionic products of the dissociation have a total energy equal to the sum of their internal energy ($E_{intfrag}$) and the kinetic energy release (KER). This total energy also corresponds to the sum of the

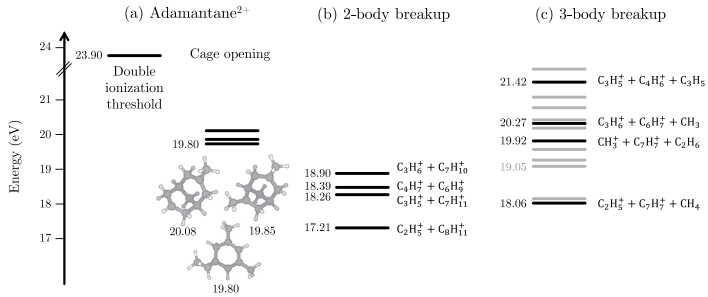

Figure 4. Key energy levels of adamantane dication processes. (**a**) Double ionization threshold and lowest energy configurations for doubly charged adamantane found in the PES exploration. (**b,c**) Final energy levels of the fragmentation channels of the adamantane dication (2- and 3-body breakups) corresponding to the ones in Table 1. Energy levels in gray are not explicitly labelled but can be found in Table 1. The energy values are relative to the neutral ground state in units of eV.

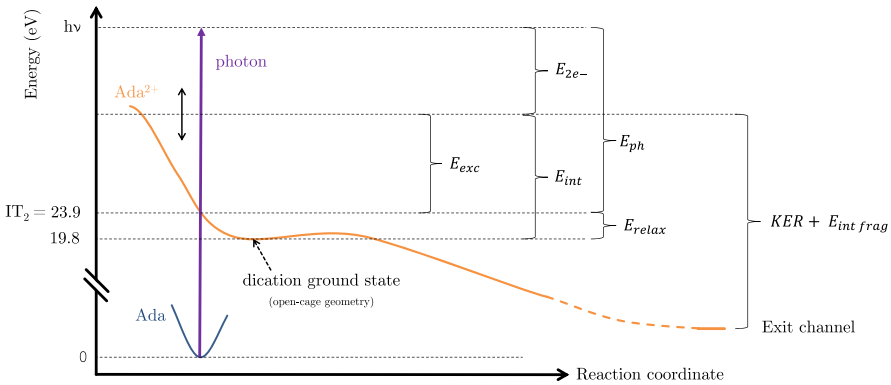

Figure 5. Schematic of the dissociation of adamantane dication displaying the different energy quantities involved.

initial internal energy of the dication (E_{int}) and the energy difference between the dication ground state and the energy levels of the exit channel.

Experimentally, the intact doubly charged parent ion is not observed in the mass spectrum (Fig. 3) at the timescale of the detection (a few microseconds). Moreover, no doubly charged fragments are detected. While the total mass spectrum is dominated by the fragments of singly charged adamantane molecules, the use of the partial covariance technique[18,36] on the ion TOF spectrum enables to case correlate singly charged ions coming from the dissociation of the dication of adamantane using an ion-ion correlation map representation (Fig. 6). Correlation islands in this map give the ion pairs that are summarized in Table 1 as well as the branching ratios (BR) of these fragmentation channels. In addition, the PES exploration provides the final energy levels of the dication fragmentation channels referred to the neutral ground state (ΔE), which are represented in Fig. 4 and given in Table 1. The energy levels of the 2-body breakup channels appear at lower energies than most of the 3-body breakup ones. It is interesting to notice that all the energy levels are below the double ionization threshold, meaning that the dication of adamantane is metastable and will spontaneously dissociate (if no barrier, *i.e.* transition state, at higher energy than the double ionization threshold is involved).

Statistical fragmentation simulations. Assuming a low internal energy after the ionization, the fragmentation time of doubly charged adamantane is expected to be very long ($\gtrsim$ 100 ps, according to our DFTB simulation, see SI) and therefore we cannot afford to carry out simulations with *ab* initio molecular dynamics. Thus, we use the M3C statistical method to obtain complementary information. This method was developed to study the fragmentation of molecular systems based on entropic criteria (see[29–31] for details).

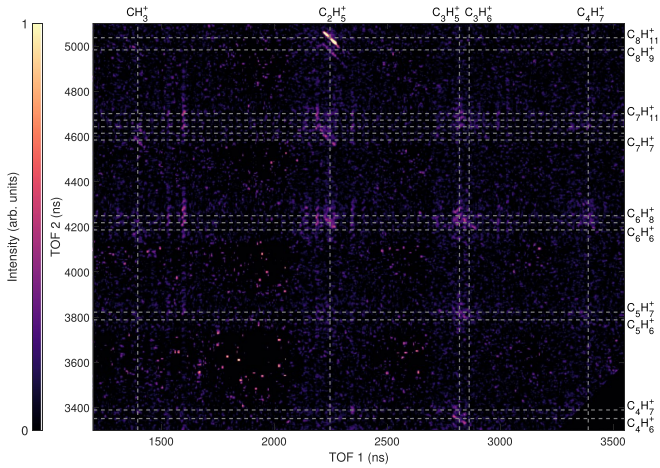

Figure 6. Ion-ion correlation map resulting from the fragmentation of adamantane dications.

Fragment 1		Fragment 2		Neutral loss		BR	ΔE
Formula	m (a.u.)	Formula	m (a.u.)	Formula	m (a.u.)	%	(eV)
CH_3^+	15	$C_8H_9^+$	105	CH_4	16	2.8 ± 0.2	19.27
		$C_7H_9^+$	93	C_2H_4	28	2.7 ± 0.2	20.32
		$C_7H_7^+$	91	C_2H_6	30	4.3 ± 0.2	19.92
		$C_6H_6^+$	78	C_3H_7	43	2.3 ± 0.2	22.24
$C_2H_5^+$	29	$C_8H_{11}^+$	107	—	—	23.3 ± 0.3	17.21
		$C_8H_9^+$	105	H_2	2	6.3 ± 0.2	18.11
		$C_7H_8^+$	92	CH_3	15	5.4 ± 0.2	20.18
		$C_7H_7^+$	91	CH_4	16	6.1 ± 0.2	18.06
		$C_6H_7^+$	79	C_2H_4	28	7.1 ± 0.2	19.05
$C_3H_5^+$	41	$C_7H_{11}^+$	95	—	—	2.5 ± 0.2	18.26
		$C_6H_8^+$	80	CH_3	15	5.3 ± 0.2	20.31
		$C_5H_7^+$	67	C_2H_4	28	5.3 ± 0.2	19.78
		$C_4H_7^+$	55	C_3H_4	40	4.6 ± 0.2	21.06
		$C_4H_6^+$	54	C_3H_5	41	6.6 ± 0.2	21.42
$C_3H_6^+$	42	$C_7H_{10}^+$	94	—	—	2.8 ± 0.2	18.90
		$C_6H_7^+$	79	CH_3	15	6.4 ± 0.2	20.27
		$C_5H_6^+$	66	C_2H_4	28	3.7 ± 0.2	20.80
$C_4H_7^+$	55	$C_6H_9^+$	81	—	—	2.3 ± 0.2	18.39

Table 1. List of correlated singly charged fragments coming from the dissociation of adamantane dication observed experimentally. In the case of n-body breakups with $n > 2$, the neutral losses are given in mass losses such that the chemical formulae have to be seen as chemical element indicators and not necessarily as fragments. BR stands for branching ratio and is given in percent. ΔE is the calculated final energy level of the dication fragmentation channels (2- and 3-body breakups) referred to the neutral ground state (in eV).

Breakdown curves. In Fig. 7, showing the breakdown curves, the gray areas mark the inaccessible regions of internal energy ($E_{int} < E_{relax}$). The probabilities for the 2-body channels (Fig. 7(a)) all peak below E_{relax}, with tails reaching into the accessible internal energy region. This is consistent with the fact that they appear in the lowest energy region in the PES (Fig. 4). Above E_{relax}, only the $C_2H_5^+/C_8H_{11}^+$ has a significant probability, while the other 2-body breakup channels $C_3H_5^+/C_7H_{11}^+$, $C_3H_6^+/C_7H_{10}^+$ and $C_4H_7^+/C_6H_9^+$ are almost not populated. The 3-body breakups channels (Fig. 7(b)) all peak around 6 eV, also consistent with their higher energy levels according to the PES in Fig. 4.

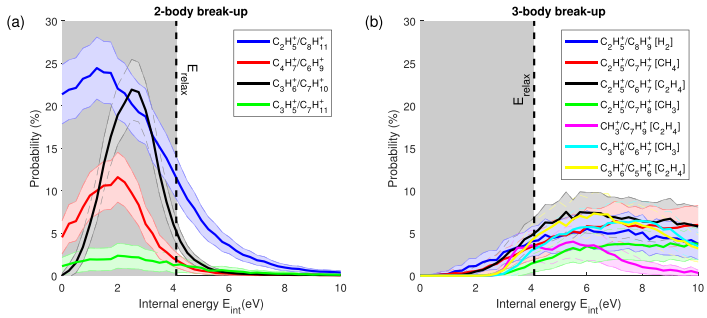

Figure 7. Breakdown curves of the channels observed in the experiments for 2-body breakups (**a**) and 3-body breakups (**b**). The errors (shaded areas around curves) correspond to the standard deviation. The black dashed lines indicate the minimum of internal energy that we can reach in our case, meaning E_{relax}, and the gray areas mark the regions of internal energy that are inaccessible in the experiment.

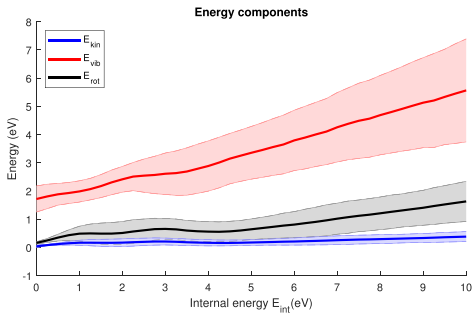

Figure 8. The average of the energy components E_{int}, E_{vib}, and E_{rot} is shown as a function of the internal energy. The errors (shaded areas around curves) correspond to the standard deviation.

Comparing the calculated breakdown cuves with the experimentally measured branching ratios in Table 1, suggests that the internal energy of the adamantane dications is close to E_{relax} under the current conditions, since in this region the $C_2H_5^+/C_8H_{11}^+$ channel dominates the other 2-body breakup channels, in good agreement with the experiment (BR > 23% vs. BR < 3%). If the internal energy was higher, the 3-body breakup channels would start to dominate, which is not observed in the experiment.

Under our assumption that the electronic excitation energy is considered to be rapidly redistributed into the nuclear degrees of freedom, this implies that most of the dications remain in the ground state or low excited states after ionization, and that the internal energy of the system mainly corresponds to the relaxation energy.

Energy storage in the fragments. We have further obtained additional valuable information by analyzing how the internal energy is distributed after ionization using the statistical simulations with the M3C code. Note that this analysis is based on the ergodic assumption, i.e. at infinite time when the system has reached equilibrium and the maximum entropy region in the phase space is populated.

We can decompose the internal energy as

$$E_{int} = E_{kin} + E_{pot} + E_{vib} + E_{rot}$$

where E_{kin}, E_{pot}, E_{vib}, and E_{rot} represent the kinetic or translational, the potential, the vibrational, and the rotational energy components, respectively. The potential energy E_{pot} is the energy difference between different geometrical configurations, in this case the exit channel and the most stable dication structure (see Fig. 4). While the potential energy is important for the total available energy, we now focus on how the latter is distributed between the remaining degrees of freedom, i.e. between E_{kin}, E_{vib} and E_{rot}. Fig. 8 shows the average and the standard deviation of these energy components as a function of the internal energy E_{int}. It is clear that in the considered internal energy range the vibrational contribution is most prominent, with smaller contributions of the rotational and

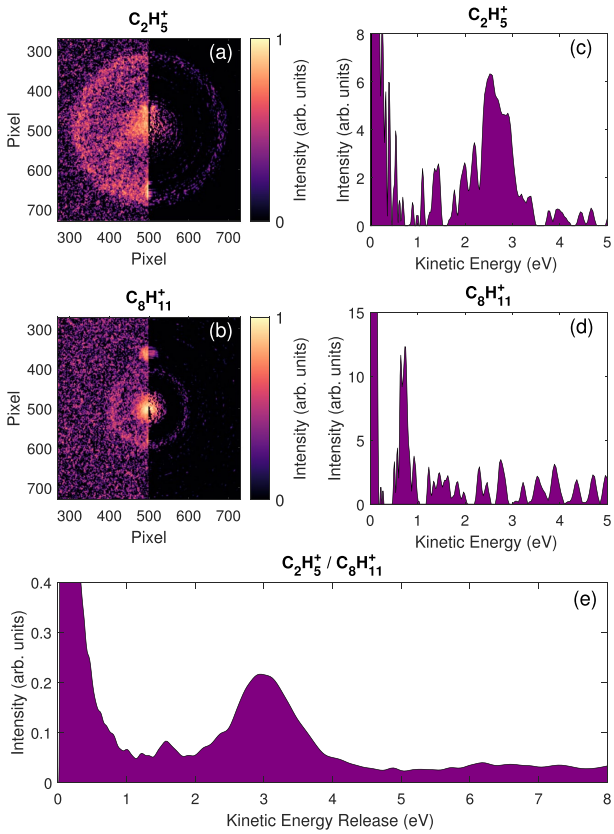

Figure 9. VMI images obtained after filtering using the partial covariance method on the TOF peaks correspond to the fragments $C_2H_5^+$ (**a**) and $C_8H_{11}^+$ (**b**) (left part: raw data and right part: inverted data). Artefacts are coming from intense signal (helium and parent ion) that were not filtered out by covariance analysis (see SI for more details). (**c,d**) Ion kinetic energy distributions of the respective fragments obtained by angular integration of the inverted data avoiding the artefacts signal and energy calibrated using ion trajectory simulations (SIMION[40]). (**e**) Kinetic energy release distribution (KERd) for the channel $C_2H_5^+$ / $C_8H_{11}^+$ obtained by convolution of the kinetic energy distributions of the two fragments.

kinetic energy components. As already shown, the fragmentation is the dominant process in the relaxation of the adamantane dication; thus, the available energy of the system is primarily absorbed by the vibrational component, i.e. the produced fragments can store a large amount of energy in nuclear degrees of freedom (mainly vibrations). Assuming an internal energy of ~4.1 eV (corresponding to the relaxation energy), ~70% of the available energy is stored in vibration and ~15% in rotation while the remaining 15% are shared among the other components.

The main fragmentation channel $C_2H_5^+/C_8H_{11}^+$ - experimental evidence of a two-step process. As we have seen, the channel $C_2H_5^+/C_8H_{11}^+$ is strongly dominating the fragmentation dynamics of the dication with a branching ratio ~23.3% whereas the other channels are at least three times less intense (Fig. 6 and Table 1). This can be roughly interpreted by looking at the energy levels of the different fragmentation channels obtained from the exploration of the PES of the adamantane dication (Fig. 4 and Table 1). This main channel is energetically favorable since it has the lowest energy level at around ~7 eV below the double ionization threshold. In addition, we have seen from the M3C calculations that the breakdown curve (Fig. 7(a)) of this channel was dominant at low accessible internal energy (~4 − 5 eV), thus being also entropically favorable in this energy region.

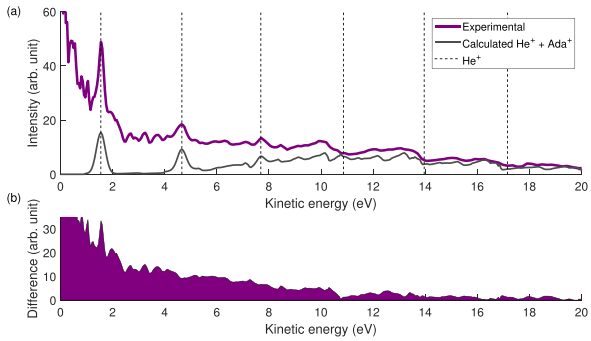

Figure 10. (**a**) Total photoelectron spectrum (purple). The black dashed lines indicate the position of helium photoelectrons. The gray line is the calculated sum of helium photoelectrons (Gaussian) and of the photoelectrons coming from the singly charged adamantane (taken from[38]) considering our XUV spectrum and the photoabsorption cross section of adamantane[8]. (**b**) Estimated photoelectron spectrum coming from double ionization of adamantane obtained as the difference between the purple and the gray curves of panel (a).

In order to have a better insight into the energetics of the main fragmentation channel, we can regard the ion kinematics of the dissociation process, particularly the kinetic energy release distribution (KERd). Performing partial covariance analysis between the ion TOF and the ion VMI data gives the "mass-selected" velocity map images displayed on the left parts of panels (a,b) in Fig. 9. The right parts in Fig. 9(a,b) show the result of Abel inversion using an iterative method[37]. The angular integration of the inverted images gives, after energy calibration, the kinetic energy distributions of the fragments $C_2H_5^+$ and $C_8H_{11}^+$ (Fig. 9(c,d)). The intense signal close to zero corresponds to the contribution from the dissociation of the singly charged adamantane. At higher energies, clear peaks show contributions at ~2.5 eV and ~0.7 eV respectively due to the Coulomb repulsion of the 2-body breakup of the dication and verify the momentum conservation principle. It is possible to obtain the KERd of the channel $C_2H_5^+/C_8H_{11}^+$ by convolution of the two individual kinetic energy distributions (Fig. 9(e)). The peak at ~3 eV indicates the main energy contribution of this channel.

The small value of the KER reflects complex fragmentation dynamics with strong molecular rearrangement before the charge separation takes place: In a first step, a cage opening leading, most probably, to one of the structures in Fig. 4; then a second molecular reorganization producing both charged fragments; and finally charge repulsion between them. The energy difference between the open structures in Fig. 4 and the $C_2H_5^+/C_8H_{11}^+$ exit channel is between ~2.6 and ~2.9 eV, which is consistent within a multiple step fragmentation as the one presented here. Considering the Coulomb repulsion between the two positive charges, the energy released is C/R, with $C = 14.4$ eV · Å and R the initial inter-charge distance in [Å]. An energy release of ~ 3.0 eV, as measured in the experiment, corresponds to an inter-charge distance of 4.8 Å. However, the maximum distance between two C atoms in the closed-cage adamantane structure is ~3.5 Å, discarding the assumption of an instantaneous double ionization followed by prompt fragmentation. Thus, structural rearrangements before the charge separation would produce a considerable extension of the structure, thus increasing the inter-charge distance up to 4.8 Å (as inferred from the experiment). This further confirms the multi-step processes with cage opening preceding Coulomb repulsion.

Photoelectron spectrum. Figure 10(a) (purple line) shows the total photoelectron energy spectrum obtained by angular integration of the electron VMI data after inversion using an iterative method[37]. Electrons coming from the ionization of the helium buffer gas can be seen around the dashed lines and were used for energy calibration. The contribution to the photoelectron spectrum associated with single ionization by the harmonics is found in the higher energy part of the total spectrum. The expected contribution, shown by the gray line Fig. 10(a), is calculated using the measured photoelectron spectrum for singly charged adamantane[38], the harmonic spectrum (see Fig. 2), and the photoabsorption cross section of adamantane[8]. In this estimated contribution, the calculated photoelectron spectrum from ionization of helium has also been included, and by subtracting this from the total photoelectron spectrum, the expected spectrum of the photoelectrons associated with double ionization is obtained and shown in Fig. 10(b).

Although the absolute signal in the resulting spectrum is sensitive to the scaling of the calculated spectrum, it is clear that the photoelectrons primarily occupy the low-energy part of the spectrum (<10 eV) compared to the photoelectrons from single ionization. From the harmonic spectrum (Fig. 2) the maximum total electron pair energy is $E_{2e^-} \approx 21$ eV, assuming that the dications remain in the ground state or in low excited states after ionization. Thus, the observed cut-off at ~10 eV, suggests that the available energy is shared rather evenly between the two electrons. All-in-all, the shape of the photoelectron energy distribution supports the assumption of low excitation, apart from the unexpectedly strong contribution at energies below 2 eV. The latter feature is a possible indication of excitation of higher-lying electronic states, resulting in low energy electrons. Possible candidates

for such states are found through a calculation of the excited states of the adamantane dication (see SI for more details) exhibiting a dense band of excited states between 35 and 40 eV (relative to the ground state of the neutral) that would result in large internal energy values E_{int} between 15 and 20 eV, and values of E_{2e-} in the 5–10 eV range following ionization by the cut-off harmonics. Such excitation could not be inferred from the experimental fragmentation pattern, nor is included in the current level of theory, which calls for further investigation.

Conclusion

We have performed a detailed study of the photodissociation of adamantane, focused on the fragmentation dynamics of the dication. By combining the experimental analysis with multiple theoretical methods we unraveled key processes governing charge and energy distribution after the ultrafast photoionizaton and the subsequent fragmentation dynamics.

We found that the most stable structures of the dication of adamantane present an open-cage geometry, appearing at ~4 eV below the double ionization threshold, that can be reached in a few tens of femtoseconds after the ionization. However, these structures are metastable and evolve producing several fragments in a Coulomb repulsion process. Much like other carbonaceous species, adamantane dications are quite efficient energy reservoirs, being able to store a large amount of energy in particular in vibrational modes. This occurs when the internal energy generated in the photoionization, together with the energy produced in the Coulomb explosion, is redistributed among the nuclear degrees of freedom of the produced fragments.

Among the different fragmentation pathways, the most populated channel $C_2H_5^+/C_8H_{11}^+$ is the lowest in energy in the PES (~2.6 eV below the most stable structure of the adamantane dication) leading us to conclude that the fragment distribution is mainly governed by energetic criteria. We have shown that the ion KERd of this channel peaks at ~3 eV with a width of 1 eV allowing us to experimentally confirm that the cage opening takes place prior to fragmentation. A qualitative comparison between the experimental branching ratios and the results of statistical fragmentation simulations suggests that the internal energy of the dication largely consists of the relaxation energy from the cage opening, with only minor contribution from redistribution of electronic excitation energy. Finally, measurements of the photoelectron kinetic energy spectrum largely confirms these observations, but also indicate the possible existence of electronic excitation which could not be further investigated in the current experiment.

The presented results highlight the complexity of, and provides pieces of information on, the fragmentation of multiply charged diamondoids. While this study was able to identify the dominant fragmentation pathways and shine light on the redistribution of energy and charge, the further elucidation of the ultrafast excitation dynamics, and in particular the timescales involved, calls for time-resolved experiments. Such experiments can be envisaged using ultrashort single wavelength XUV pulses, e.g. from free electron lasers, in combination with multicoincidence ion-electron spectroscopy techniques.

Received: 11 December 2019; Accepted: 29 January 2020;
Published online: 19 February 2020

References

1. Schwertfeger, H., Fokin, A. & Schreiner, P. Diamonds are a chemist's best friend: Diamondoid chemistry beyond adamantane. *Angewandte Chemie Int. Ed.* **47**, 1022–1036, https://doi.org/10.1002/anie.200701684 (2008).
2. Stauss, S. & Terashima, K. *Diamondoids: Synthesis, Properties, and Applications* (CRC Press, 2017).
3. Anders, E. & Zinner, E. Interstellar grains in primitive meteorites: Diamond, silicon carbide, and graphite. *Meteorit.* **28**, 490–514, https://doi.org/10.1111/j.1945-5100.1993.tb00274.x (1993).
4. Henning, T. & Salama, F. Carbon in the universe. *Sci.* **282**, 2204–2210, https://doi.org/10.1126/science.282.5397.2204 (1998).
5. Oomens, J. *et al.* Infrared spectroscopic investigation of higher diamondoids. *J. Mol. Spectrosc.* **238**, 158–167, https://doi.org/10.1016/j.jms.2006.05.001 (2006).
6. Acke, B. & van den Ancker, M. E. A survey for nanodiamond features in the 3 micron spectra of herbig ae/be stars. *Astron. & Astrophys.* **457**, 171–181, https://doi.org/10.1051/0004-6361:20065612 (2006).
7. Lenzke, K. *et al.* Experimental determination of the ionization potentials of the first five members of the nanodiamond series. *The J. Chem. Phys.* **127**, 084320, https://doi.org/10.1063/1.2773725 (2007).
8. Steglich, M., Huisken, F., Dahl, J. E., Carlson, R. M. K. & Henning, T. Electronic spectroscopy of fuv-irradiated diamondoids: a combined experimental and theoretical study. *The Astrophys. J.* **729**, 91, https://doi.org/10.1088/0004-637x/729/2/91 (2011).
9. Candian, A., Bouwman, J., Hemberger, P., Bodi, A. & Tielens, A. G. G. M. Dissociative ionisation of adamantane: a combined theoretical and experimental study. *Phys. Chem. Chem. Phys.* **20**, 5399–5406, https://doi.org/10.1039/C7CP05957D (2018).
10. Marciniak, A. *et al.* Electron correlation driven non-adiabatic relaxation in molecules excited by an ultrashort extreme ultraviolet pulse. *Nat. communications* **10**, 1–8, https://doi.org/10.1038/s41467-018-08131-8 (2019).
11. Ferray, M. *et al.* Multiple-harmonic conversion of 1064 nm radiation in rare gases. *J. Phys. B: At. Mol. Opt. Phys.* **21**, L31–L35, https://doi.org/10.1088/0953-4075/21/3/001 (1988).
12. McPherson, A. *et al.* Studies of multiphoton production of vacuum-ultraviolet radiation in the rare gases. *J. Opt. Soc. Am. B* **4**, 595–601, https://doi.org/10.1364/JOSAB.4.000595 (1987).
13. Manschwetus, B. *et al.* Two-photon double ionization of neon using an intense attosecond pulse train. *Phys. Rev. A* **93**, 061402, https://doi.org/10.1103/PhysRevA.93.061402 (2016).
14. Coudert-Alteirac, H. *et al.* Micro-focusing of broadband high-order harmonic radiation by a double toroidal mirror. *Appl. Sci.* **7**, 1159, https://doi.org/10.3390/app7111159 (2017).
15. Even, U. Pulsed supersonic beams from high pressure source: Simulation results and experimental measurements. *Adv. Chem.* **2014**, 11, https://doi.org/10.1155/2014/636042 (2014).
16. Even, U. The even-lavie valve as a source for high intensity supersonic beam. *EPJ Tech. Instrumentation* **2**, 17, https://doi.org/10.1140/epjti/s40485-015-0027-5 (2015).
17. Rading, L. *et al.* A versatile velocity map ion-electron covariance imaging spectrometer for high-intensity xuv experiments. *Appl. Sci.* **8**, 998, https://doi.org/10.3390/app8060998 (2018).
18. Frasinski, L. J. Covariance mapping techniques. *J. Phys. B: At. Mol. Opt. Phys.* **49**, 152004, https://doi.org/10.1088/0953-4075/49/15/152004 (2016).

19. Porezag, D., Frauenheim, T., Köhler, T., Seifert, G. & Kaschner, R. Construction of tight-binding-like potentials on the basis of density-functional theory: Application to carbon. *Phys. Rev. B* **51**, 12947–12957, https://doi.org/10.1103/PhysRevB.51.12947 (1995).
20. Seifert, G., Porezag, D. & Frauenheim, T. Calculations of molecules, clusters, and solids with a simplified lcao-dft-lda scheme. *International Journal of Quantum Chemistry*, **58**, 185–192, 10.1002/(SICI)1097-461X(1996)58:2<185::AID-QUA7>3.0.CO;2-U (1996).
21. Heine, T. *et al.* demon-nano Jacobs University Bremen: Bremen, Germany (2009).
22. Lee, C., Yang, W. & Parr, R. G. Development of the colle-salvetti correlation-energy formula into a functional of the electron density. *Phys. Rev. B* **37**, 785–789, https://doi.org/10.1103/PhysRevB.37.785 (1988).
23. Miehlich, B., Savin, A., Stoll, H. & Preuss, H. Results obtained with the correlation energy density functionals of becke and lee, yang and parr. *Chem. Phys. Lett.* **157**, 200–206, https://doi.org/10.1016/0009-2614(89)87234-3 (1989).
24. Becke, A. D. Density-functional thermochemistry. iii. the role of exact exchange. *The J. Chem. Phys.* **98**, 5648–5652, https://doi.org/10.1063/1.464913 (1993).
25. Frisch, M. J. *et al.* Gaussian 09 Revision E.01 (2013). Gaussian Inc. Wallingford CT 2013.
26. Maclot, S. *et al.* Dynamics of glycine dications in the gas phase:ultrafast intramolecular hydrogen migration versus coulomb repulsion. *The J. Phys. Chem. Lett.* **4**, 3903–3909, https://doi.org/10.1021/jz4020234 (2013).
27. Piekarski, D. G. *et al.* Unusual hydroxyl migration in the fragmentation of β-alanine dication in the gas phase. *Phys. Chem. Chem. Phys.* **17**, 16767–16778, https://doi.org/10.1039/C5CP01628B (2015).
28. Maclot, S. *et al.* Determination of energy-transfer distributions in ionizing ion-molecule collisions. *Phys. Rev. Lett.* **117**, 073201, https://doi.org/10.1103/PhysRevLett.117.073201 (2016).
29. Aguirre, N. F., Díaz-Tendero, S., Hervieux, P.-A., Alcamí, M. & Martín, F. M3C: A Computational Approach To Describe Statistical Fragmentation of Excited Molecules and Clusters. *J. Chem. Theory Comput.* **13**, 992–1009, https://doi.org/10.1021/acs.jctc.6b00984 (2017).
30. Aguirre, N. F., Díaz-Tendero, S., Hervieux, P.-A., Alcamí, M. & Martín, F. M3C Software Package, https://github.com/nfaguirrec/M3C, https://doi.org/10.5281/zenodo.3533987 (2019).
31. Aguirre, N. F. *et al.* Fully versus constrained statistical fragmentation of carbon clusters and their heteronuclear derivatives. *The J. Chem. Phys.* **150**, 144301, https://doi.org/10.1063/1.5083864 (2019).
32. Martinet, G. *et al.* Fragmentation of highly excited small neutral carbon clusters. *Phys. Rev. Lett.* **93**, 063401, https://doi.org/10.1103/PhysRevLett.93.063401 (2004).
33. Díaz-Tendero, S., Hervieux, P.-A., Alcamí, M. & Martín, F. Statistical fragmentation of small neutral carbon clusters. *Phys. Rev. A* **71**, 033202, https://doi.org/10.1103/PhysRevA.71.033202 (2005).
34. Erdmann, E., Labuda, M., Aguirre, N. F., Díaz-Tendero, S. & Alcamí, M. Furan fragmentation in the gas phase: New insights from statistical and molecular dynamics calculations. *The J. Phys. Chem. A* **122**, 4153–4166, https://doi.org/10.1021/acs.jpca.8b00881 (2018).
35. Aguirre, N. F. *et al.* M3C-store dataset, https://github.com/nfaguirrec/M3C-store, https://doi.org/10.5281/zenodo.2632188 (2019).
36. Frasinski, L. J., Codling, K. & Hatherly, P. A. Covariance mapping: A correlation method applied to multiphoton multiple ionization. *Sci.* **246**, 1029–1031, https://doi.org/10.1126/science.246.4933.1029 (1989).
37. Vrakking, M. J. J. An iterative procedure for the inversion of two-dimensional ion/photoelectron imaging experiments. *Rev. Sci. Instruments* **72**, 4084–4089, https://doi.org/10.1063/1.1406923 (2001).
38. Schmidt, W. Photoelectron spectra of diamondoid molecules: Adamantane, silamantane and urotropine. *Tetrahedron* **29**, 2129–2134, https://doi.org/10.1016/0040-4020(73)80153-X (1973).
39. Wallace, W. E. *"Mass Spectra" by NIST Mass Spectrometry Data Center in NIST Chemistry WebBook, NIST Standard Reference Database Number 69, Eds. P.J. Linstrom and W.G. Mallard* (National Institute of Standards and Technology, Gaithersburg MD, 20899, 2019).
40. Dahl, D. A. Simion for the personal computer in reflection. *Int. J. Mass Spectrom.* **200**, 3–25 (2000).

Acknowledgements

A special thanks is given to A. Persson for his support for the high-power laser and to M. Gisselbrecht for critical reading of the manuscript. This research was supported by the Swedish Research Council, the Swedish Foundation for Strategic Research and the Crafoord Foundation. This project has received funding from the European Union's Horizon 2020 research and innovation program under the Marie Sklodowska-Curie Grant Agreement No. 641789 MEDEA and under grant agreement no 654148 Laserlab-Europe. The research was conducted in the framework of the International Associated Laboratory (LIA) Fragmentation DYNAmics of complex MOlecular systems - DYNAMO, funded by the Centre National de la Recherche Scientifique (CNRS). The authors acknowledge the generous allocation of computer time at the Centro de Computación Científica at the Universidad Autónoma de Madrid (CCC-UAM). This work was partially supported by the project CTQ2016-76061-P of the Spanish Ministerio de Economía y Competitividad (MINECO). Financial support from the MINECO through the "María de Maeztu" Program for Units of Excellence in R&D (MDM-2014-0377) is also acknowledged.

Author contributions

P.R., P.J. and S.M. designed the experiments, S.M., J.L., J.P., H.W., P.R., P.R., S.I., F.B., H.C.-A. and B.A.H. performed the experiment, S.M. and J.L. analysed the results. S.D.-T. performed the potential energy surface and the molecular dynamics calculations, and N.F.A. the M3C simulations. S.M., S.D.-T. and P.J. wrote the original draft, S.D.-T. and N.F.A. wrote the theoretical sections and part of the discussion and all authors reviewed the manuscript.

Competing interests

The authors declare no competing interests.

Additional information

Supplementary information is available for this paper at https://doi.org/10.1038/s41598-020-59649-1.

Correspondence and requests for materials should be addressed to S.M. or P.J.

Reprints and permissions information is available at www.nature.com/reprints.

Paper v

I. Makos, I. Orfanos, A. Nayak, **J. Peschel**, B. Major, I. Liontos, E. Skantzakis, N. Papadakis, C. Kalpouzos, M. Dumergue, S. Kühn, K. Varju, P. Johnsson, A. L'Huillier, P. Tzallas, and D. Charalambidis
A 10-gigawatt attosecond source for non-linear XUV optics and XUV-pump-XUV-probe studies
Sci. Reports 10, 3759 (2020)

SCIENTIFIC REPORTS
nature research

OPEN

A 10-gigawatt attosecond source for non-linear XUV optics and XUV-pump-XUV-probe studies

I. Makos[1,2,7], I. Orfanos[1,2,7], A. Nayak[1,3,6], J. Peschel[5], B. Major[3], I. Liontos[1], E. Skantzakis[1], N. Papadakis[1], C. Kalpouzos[1], M. Dumergue[3], S. Kühn[3], K. Varju[3,4], P. Johnsson[5], A. L'Huillier[5], P. Tzallas[1,3] & D. Charalambidis[1,2,3*]

The quantum mechanical motion of electrons and nuclei in systems spatially confined to the molecular dimensions occurs on the sub-femtosecond to the femtosecond timescales respectively. Consequently, the study of ultrafast electronic and, in specific cases, nuclear dynamics requires the availability of light pulses with attosecond (asec) duration and of sufficient intensity to induce two-photon processes, essential for probing the intrinsic system dynamics. The majority of atoms, molecules and solids absorb in the extreme-ultraviolet (XUV) spectral region, in which the synthesis of the required attosecond pulses is feasible. Therefore, the XUV spectral region optimally serves the study of such ultrafast phenomena. Here, we present a detailed review of the first 10-GW class XUV attosecond source based on laser driven high harmonic generation in rare gases. The pulse energy of this source largely exceeds other laser driven attosecond sources and is comparable to the pulse energy of femtosecond Free-Electron-Laser (FEL) XUV sources. The measured pulse duration in the attosecond pulse train is 650 ± 80 asec. The uniqueness of the combined high intensity and short pulse duration of the source is evidenced in non-linear XUV-optics experiments. It further advances the implementation of XUV-pump-XUV-probe experiments and enables the investigation of strong field effects in the XUV spectral region.

In the 20 years of attosecond science[1,2], numerous exciting ideas have been conceived and sound applications have been demonstrated, the majority of which is based on pump-probe studies, exploiting combinations of infrared (IR) and XUV pulses.

Already the domain of attosecond pulse characterization gave access to fascinating physics, novel methodologies and innovative technologies. Those are to be found in the Reconstruction of Attosecond Beating By Interference of two-photon Transitions (RABBIT)[3], Frequency Resolved Optical Gating for Complete Reconstruction of Attosecond Bursts (FROG-CRAB)[4], Phase Retrieval by Omega Oscillation Filtering (PROOF)[5,6], Rainbow RABBIT[7], *In-situ*[8], Spectral Phase Interferometry for the Direct Electric Field Reconstruction (SPIDER)[9,10], atto-clock[11], double-blind holography[12], attosecond spatial interferometry[13], and the attosecond streaking[14] methods and in the devices developed towards their implementation. A summary of these approaches is presented in the perspective article on attosecond pulse metrology[15].

In parallel, abundant, significant proof of principle experiments enriched the pallet of attosecond applications. Atomic inner-shell spectroscopy[16], real-time observation of ionization[17], light wave electronics[18], and molecular optical tomography[19] are some examples of such experiments. Other more recent applications of attosecond pulses include ionization delays in solids[20] and atoms[21,22], electron dynamics[23], charge migration[24,25], build-up of a Fano-Beutler resonance[7], and ionization dynamics in chiral molecules[26]. It should be noted that the above examples are only a representative fraction of many studies performed in attosecond laboratories.

Following a somewhat different path, a group of attosecond laboratories focused for several years their efforts towards the development of high photon flux attosecond beam lines. The aim of these efforts was to reach sufficiently high attosecond pulse intensities as to induce observable two- (or more) XUV-photon transitions, a

[1]Foundation for Research and Technology - Hellas, Institute of Electronic Structure & Laser, GR71110, Heraklion, Crete, Greece. [2]Department of Physics, University of Crete, GR71003, Heraklion, Crete, Greece. [3]ELI-ALPS, ELI-Hu Non-Profit Ltd., Dugonics tér 13, H-6720, Szeged, Hungary. [4]Department of Optics and Quantum Electronics, University of Szeged, Dom tér 9, 6720, Szeged, Hungary. [5]Department of Physics, Lund University, SE-221 00, Lund, Sweden. [6]Institute of Physics, University of Szeged, Dom tér 9, 6720, Szeged, Hungary. [7]These authors contributed equally: I. Makos and I. Orfanos. *email: chara@iesl.forth.gr

central prerequisite for XUV-pump-XUV-probe experiments in the one femtosecond (fs) and sub-fs temporal regime[27–29]. The importance of XUV-pump-XUV-probe schemes relies on the fact that when temporarily overlapping IR and XUV pulses are used for pump-probe studies, the high IR intensities that have to be employed may cause distortions to the system under investigation obscuring its intrinsic dynamics[30]. XUV-pump-XUV-probe experiments benefit substantially from the existence of intense isolated[27,28] or essentially isolated[31] XUV pulses. At the same time, observable two-(or more) XUV-photon transitions allow temporal characterization of attosecond pulses based on non-linear XUV autocorrelation (AC) measurements[32–38], bypassing complications that may arise from IR-XUV cross-correlation based pulse characterization techniques[39]. It should be noted that these developments were a follow up of pioneering non-linear XUV experiments completed with individual harmonics in the few tens of fs temporal regime, including two-[40], three-[41] and four-XUV-photon[42] ionization, two-XUV-photon double ionization[43,44] as well as the corresponding 2nd [40,43] and 4th order AC measurements[42], two-XUV-photon above threshold ionization (ATI)[45] and even a FROG based XUV pulse reconstruction[46].

Towards reaching high XUV photon fluxes there are certain hurdles including depletion of the generating medium above a certain threshold of the driving laser intensity, XUV radiation reabsorption by the generating medium, as well as phase mismatch due to high generating gas pressures and high degree of ionization of the generating medium (see the review article of ref. [47]). A way to overcome these obstacles is to use non depleting media as non-linear harmonic generation targets. This is the case in the generation of harmonics from laser induced surface plasma[48–53], often referred to as plasma mirrors[54]. Indeed, for surface plasma harmonics, very high photon fluxes have been predicted in particle in cell (PIC) simulations[55] and sub-fs temporal confinement has been experimentally demonstrated[56]. Laser surface plasma harmonic generation requires however, increased technological demands such as high laser peak to background contrast, including elimination of unwanted laser pre-pulses, demanding "cleaning" procedures of the laser pulse through additional plasma mirrors, tedious control of the plasma density gradient[53], μm positioning of the focus on the target and debris to mention a few. Although laser surface plasma harmonic generation holds promise of high photon flux attosecond pulses, the so far achieved maximum XUV pulse energy is 40 μJ[56].

The alternative to laser surface plasma harmonic generation in avoiding the above mentioned obstacles is to use gas targets combined with loose focusing of the driving laser beam. The scalability of gas phase harmonic generation sources has been recently studied in ref. [57]. The work by Heyl *et al.* demonstrates that long focal lengths combined with low pressure gas cells, allowing control of phase matching, can lead to high throughputs and thus to high XUV photon fluxes. At the same time it has been recently shown that multi-cycle high peak power laser beams, focused in the generation medium using long focal lengths of several meters, in combination with quasi-phase matching[58] arrangements, achieved through a chain of small length gas media i.e. pulsed gas jets, can reach emission of 20-GW XUV harmonic power at the source in the spectral region of 15–30 eV[59]. In the work of Nayak *et al.* apart from the measurement of the harmonic source power the high focused XUV intensities achieved were evidenced through the observation of multi-XUV-photon multiple ionization of argon atoms. While FEL sources have much higher peak brightness at shorter wavelengths and in particular in the x-ray regime, in the spectral region of 15–30 eV the measured peak brightness of the harmonic spectra is competing with that of FELs[52].

In the present work we provide an in-detail presentation of the 20-GW XUV source developed at the Instutute of Electronic Structure and Laser of the Foundation for Research and Technology-Hellas (FORTH-IESL) together with multi-XUV-photon multiple atomic ionization measurements in helium, argon and neon, while 10 GW attosecond pulse trains have been demonstrated at this source. Two-photon ionization of helium atoms and argon ions is used in second order intensity volume autocorrelation (2nd IVAC) measurements of the pulse duration of the attosecond pulse train (APT). Since the measured duration of the pulses in the train is found to be $\tau_{XUV} = 670 \pm 80$ asec and $\tau_{XUV} = 650 \pm 80$ asec in He and Ar respectively, the present work introduces the most powerful table top XUV attosecond source.

The structure of the manuscript is as follows. In section 2 we give a detailed illustration of the XUV beam-line. In section 3 we report a quantitative characterization of the different parameters of the beam-line. In section 4 we present results of non-linear XUV-optics experiments. In section 5 results of the attosecond pulse trains temporal characterization are shown, followed by the concluding section of the work. It should be noted that after submission of the present work tunable attosecond x-ray pulses with 100 GW peak power were demonstrated in the SLAC FEL large scale infrastructure[60].

The High XUV Photon Flux Source

The high XUV-photon flux beam-line mentioned in the previous section has been recently developed and tested in the Attosecond Science & Technology laboratory of FORTH-IESL[59]. In this section, a detailed description of the beam line and its characterization is presented.

The 20-GW XUV beam-line. The high photon throughput of the XUV beam-line relies on the exploitation of: I) 9 m focal length optics focusing the laser beam into the non-linear medium, as to increase the number of harmonic emitters in the interaction cross section, keeping the driving intensity below the ionization saturation thresholds of the generating medium, II) a dual gas jet as target with variable jet distance as to achieve optimal phase matching, III) optimized gas pressure in both jets, and IV) Xe gas as non-linear medium, the conversion efficiency of which is the highest of all rare gasses[61,62] with the trade-off of the low cut-off photon energy. However, in test measurements Ar gas was also used as generating medium.

The beam-line, as shown in Fig. 1, consists of the following units: (a) laser beam steering/shaping, placed in the "compressor chamber" and "IR steering optics and Polarization Gating" chambers, (b) laser beam focusing, placed in the "IR focusing optics" chamber, (c) XUV generation, placed in the "HHG" chamber, (d) XUV separation/steering, placed in the "XUV separation/steering" chamber, (e) XUV manipulation and diagnostics, placed

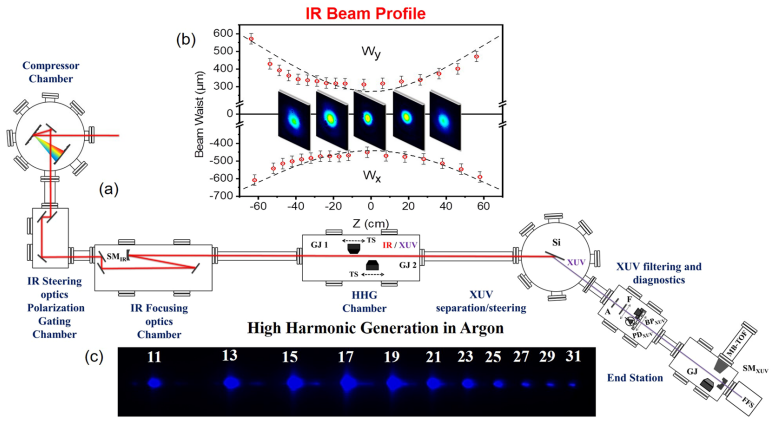

Figure 1. The 20-GW XUV beam line. (**a**) Optical layout of the 20-GW XUV beam-line. SM_{IR}: spherical mirror of 9-m focal length. $GJ_{1,2}$: dual-pulsed-jet configuration placed on translation stages (TS). Si: silicon plate. F: Al or Sn filter. A: aperture. BP_{XUV}: XUV beam profiler. SM_{XUV}: gold coated spherical mirror of 5-cm focal length. Ar-GJ: Ar gas jet. MB-TOF: magnetic bottle time-of-flight spectrometer. PD_{XUV}: calibrated XUV photodiode. FFS: flat-field spectrometer. (**b**) IR beam profile around the focus measured with a CCD camera. (**c**) measured HHG spectrum produced in Argon gas phase medium spreading up to 48 eV corresponding to the 31st harmonic of the fundamental frequency of the driving field. Part of the figure is copied from reference[59].

in the "XUV filtering and diagnostics" chamber and (e) XUV pulse temporal characterization and XUV radiation use unit placed in the "end station".

The laser steering and shaping takes place in two different vacuum chambers. In the first one a two grating arrangement compresses the amplified laser beam (Amplitude Technologies Ti:Sapphire chain) and delivers pulses of 800 nm central wavelength, ≈400 mJ maximum energy and ≈24 fs duration at 10 Hz repetition rate. Since 400 mJ pulse energy would deplete the harmonic generation medium at the used geometry the energy is reduced to 25–45 mJ after compression depending on the gas used for the generation.

The beam is then steered into the focusing unit through three plane mirrors placed in the second chamber. The same mirror set up is used for the alignment of the laser through the entire beam-line. This second chamber hosts also a Polarization Gating (PG) optical arrangement for the generation of isolated attosecond pulses. Since no isolated pulses are used in the present work the PG arrangement is not described here but can be found in previous works[63–65]. The polarization of the laser beam entering the focusing unit is *parallel* to the optical table. The beam diameter is $D \approx 2.3$ cm. The focusing unit uses three silver protected low dispersion plane mirrors and a spherical mirror (SM) of 9 m focal length. The optical layout shown in Fig. 1a aims to reduce astigmatism introduced by the spherical mirror due to the deviation from the normal incidence. The angle of incidence at the spherical mirror is as close as possible to normal (~3°). In this way the astigmatism is kept low but is not negligible. Figure 1b shows the beam profile at the focus of the IR beam (measured with a CCD camera) which reveals a small degree of elongation along the x-axis. The confocal parameter is measured to be $b \approx 70$ cm which is a factor of ≈ 1.22 larger than the value obtained according to the relation $b = 2\pi R^2/\lambda_L$ (where R and λ_L is the radius and the wavelength of the IR beam) given by Gaussian optics. Although these imperfections of the IR beam do not affect the XUV beam profile (measured with an XUV beam profiler placed after the metal filter in the "XUV diagnostics" chamber) as can be seen in Fig. 1 of ref. [59] and further down in this work, according to ref. [66], they may introduce distortions in XUV wavefront and hence influence the duration of the emitted attosecond pulses at the "end station" where the XUV beam is refocused. This matter will be further discussed in Section 4 of the manuscript. Further measurements of the IR profile have been performed at several positions around the focus as shown in Fig. 1b.

The XUV generation unit can host up to four gas-jets placed on x, y, z translation stages. All gas-jets of the beamline are home made piezoelectric crystal based gas-jets. These translations are used for optimization of the laser-gas interaction. In addition, the translation in the z direction (beam propagation direction) permits the variation of the inter-jet distance, optimizing phase matching. Due to the large focal length, the distance between the jets is several cm and thus phase matching can be accurately controlled through translation in the z direction. The minimum step of the stage was 5 μm, much smaller than the needed accuracy in the range of cm. In the present study only two gas jets (GJ_1, GJ_2) have been used with the scanning step of the translation stages set at 0.75 cm. The gas jets are operated by piezoelectrically driven pulsed nozzles. For comparison reasons a 10 cm long gas cell bounded by two pinholes (entrance-exit pinholes) of 2 mm diameter has also been used in one of the experiments. The generated XUV co-propagates with the IR towards the "XUV separation/steering" chamber. The two beams (IR, XUV) first impinge a silicon plate (Si) placed at the Brewster angle (~75°) of the IR radiation. This plate significantly attenuates the IR and reflects ~60% of the XUV radiation deflecting the XUV beam

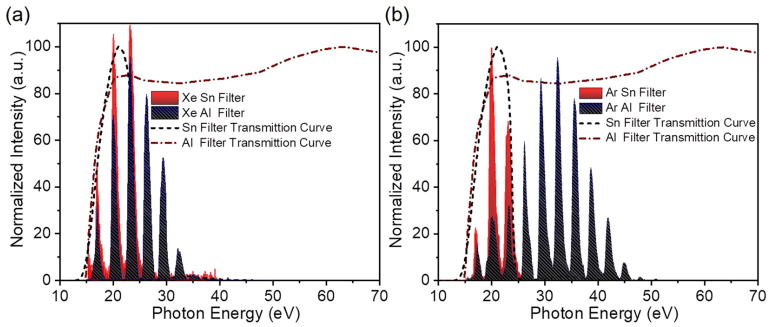

Figure 2. Harmonic spectra recorded by FFS after spectral selection by metallic foils. The generation medium was (**a**) Xe and (**b**) Ar gas. In both panels, the blue and red peaks correspond to harmonics after transmission through 150 nm thick Al and Sn respectively, while the red dash-dotted (Al) and black dashed (Sn) are transmission curves for 150 nm thickness.

towards the "XUV filtering and diagnostics" and "end station" chambers. In the "XUV filtering and diagnostics" chamber, the beam after passing through a 7 mm diameter aperture, is spectrally selected by 150 nm thick metal foils (Al or Sn) mounted on an *x*, *y* translation stage. The foils are acting as band pass filters in the XUV spectral range and eliminate any residual IR radiation. The transmission curve of these filters is shown in Fig. 2 together with harmonic spectra obtained using xenon (Fig. 2a) and argon (Fig. 2b) as generating gas, recorded by the XUV flat-field-spectrometer (FFS).

In the "XUV filtering and diagnostics" chamber the pulse energy of the XUV radiation was also measured introducing a calibrated XUV photodiode (PD_{XUV}) into the XUV beam and its beam profile was recorded introducing an XUV beam profiler (BP_{XUV}) (consisting of a pair of multichannel plates (MCPs) and a phosphor screen followed by a CCD camera). Figure 3 shows the XUV beam profiles recorded after the filtering through Al foil with the GJ_1 to be placed at the focusing position of the driving field. For further investigation, recordings have been carried out for several positions of the GJ_1 producing the XUV radiation. No significant change was observed when GJ_1 was placed before ($z_{GJ1} = -b, -b/2$), on ($z_{GJ1} = 0$) or after ($z_{GJ1} = b, b/2$) the driving laser focus. For an IR focus displacement of $\approx \pm 30$ cm relative to the gas jet position, a significant change in the beam XUV profile is expected when both the short and long trajectory harmonics are recorded by the beam profiler. This is because, as it is well known, the divergence of the short trajectory harmonics is smaller than the long trajectory harmonics which have an annular-like beam profile. Focusing the IR beam before (after) the gas jet, the contribution of the short (long) trajectory harmonics is dominating. In the present measurements, the diameter of the aperture that has been placed before the beam profiler was reduced to ≈ 5 mm, thus selecting mainly the short trajectory harmonics (without excluding the presence of the long trajectories for harmonics lying close to the cut-off spectral region), and thus it does not "significantly" change when moving the jet before and after the focus. To double check the spatial intensity distribution of the XUV beam recorded by the BP_{XUV}, the knife edge technique was also used for $z_{GJ1} = 0$. The XUV radiation photoionizes argon gas and the photoelectron yield is measured as a function of the knife edge position. The measured curve shown in Fig. 3c (black dots) is then differentiated resulting in the intensity distribution (red dots). The colored area is defined by a Gaussian fit to the measured data. The results of the knife edge measurements were in agreement with the values of the XUV beam radius obtained by the BP_{XUV}.

The last chamber (end station) of the beam-line is the temporal characterization and pump-probe unit. It hosts an attosecond delay line based on a split spherical gold coated mirror of 5 cm focal length, fixed on a multiple-translation-rotation stage. This stage enables control in 3 degrees of freedom for the one D-shaped half of the mirror i.e. the displacement along the *z* axis (i.e. the beam propagation axis) with a maximum value of 80 μm and rotation in the x-z and y-z plane. The other part of the mirror position is altered only along the propagation direction with a maximum translation of 400 μm. All movements of the split-mirror are controlled by piezo crystals operated in closed loop mode. A 1.5 nm minimum step of the translation of the first, as described above, of the two parts of the bisected mirror introduces a temporal delay between the two parts of the beam. It is worth noting that for such time delays (80 μm total translation), effects of spatial displacements of the two parts of the focused beam are negligibly small[36]. The XUV beam is focused in front of a pulsed gas jet whose forefront serves also as a repeller of a magnetic bottle time of flight (MB-TOF) spectrometer. The TOF can be operated either in an ion mass spectrometer or electron energy analyzer mode measuring the products of the interaction of the XUV pulses with the gas target. This arrangement is used either for performing 2nd IVAC measurements of the XUV pulse duration or in XUV-pump-XUV-probe experiments. Finally, the FFS is placed at the end of the beam line monitoring and recording the XUV radiation spectrum that is "leaking" through the slit of the bisected mirror.

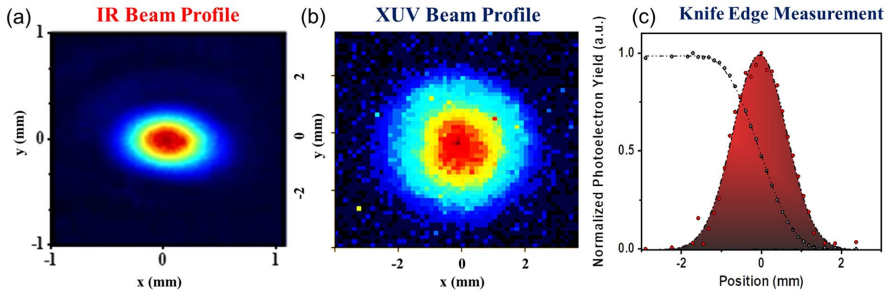

Figure 3. IR and XUV beam profiles. (**a**) IR beam profile at the focal plane measured by a commercial CCD profile camera. (**b**) XUV beam profile recorded using the BP_{XUV}. For this measurement Xe gas was used as harmonic generation medium. (**c**) Knife edge measurement of the XUV beam profile presented with black dots while the red dots show the obtained intensity distribution. The colored area is defined by a Gaussian fit to the measured data. In both (**b**,**c**) measurements, harmonics are generated using xenon with the GJ placed at the IR focus.

Characterization of the XUV Beam-line

In this section, vacuum, XUV pulse energy, attosecond delay line stability and temporal resolution measurements are discussed.

Vacuum conditions. The rest vacuum, i.e. the vacuum when all gas jets are off, in all chambers of the beam-line is: ~10^{-6} mbar except for the "end station" chamber in which it is ~10^{-7} mbar. The generating nozzles are operating with a backing pressure in the range of 2 bar. The estimated gas pressure of the jets in the interaction area is ~25 mbar as reported in a previous work[39]. When the two generation jets are on, the pressure in the HHG chamber increases to ~10^{-4} mbar. The jet pressure conditions in the detection chamber depend on the type of experiment that is performed. A 1000 l/min turbo-molecular pump in the "end station" chamber secures an adequate vacuum pressure during operation of the gas target jet. An additional turbo pump differentially pumping the FFS spectrometer ensures that the pressure where the multichannel plate detector is located, is lower than 10^{-6} mbar.

Measurement and optimization of the XUV pulse energy. Typical harmonic spectra generated in Ar and Xe, recorded by the FFS after the XUV radiation has passed through 150 nm thick Al or Sn filters are shown in Fig. 2. The harmonic cut-off region when Xe gas and Al filter are used is around 30 eV (and the highest harmonic observed is the 23rd), while harmonics higher than the 15th are not transmitted through the Sn filter. In Ar the cut-off region extends to about 48 eV (the highest harmonic observed is the 31st).

Figure 4 shows the dependence of the energy of the XUV radiation (integrated over the Al-filter-selected harmonics spectrum and measured with the PD_{XUV}) on the argon gas pressure (changed by varying the delay of the gas nozles, both positioned at z = 0, with respect to the arrival time of the laser pulse) as well as the comparison between one gas jet and one gas cell with respect to the XUV energy emission. In particular, Fig. 4a shows the emitted XUV pulse energy as a function of the time delay between the trigger pulse of the GJ_1 nozzle opening and the laser pulse, for an arbitrary IR intensity well below the saturation threshold. The emission maximizes for a time delay of 600 μs. At this value the harmonic signal was then further optimized by setting the IR intensity just below the ionization saturation intensity. Figure 4b shows essentially the same behavior for GJ_1 and GJ_2. Figure 4c is devoted to the comparison between the XUV pulse energy obtained when using a single gas jet and a cell in the present beam line. It presents the XUV pulse energy emitted by (i) GJ_1 as a function of the pulsed nozzle time delay and (ii) by the gas cell as a function of the cell gas pressure. For the given cell length of 10 cm, the emission maximizes for a pressure value between 8 and 9 mbar. The maximum harmonic yield in the cell is found to be slightly lower (~25%) than the one of the gas jet. In these measurements Ar is used as generating medium and thus the pulse energy throughput is not the highest possible. Apart from the gas-jet/cell comparison measurement, the beam-line is operated exclusively with gas-jets, mainly because at 10 Hz repetition rate they consume less gas, and because of their demonstrated slightly higher measured XUV energy throughput. After opting for the GJ configuration as the preferable one for the beamline of this work, experimental investigations focused on maximizing the photon flux of the emitted XUV radiation. Measurements of the single GJ emission by varying the medium position relatively to the driving pulse's focus are depicted in Fig. 5a,b for Ar and Xe respectively. The *x*-axis reveals the harmonic order, measured in the photoelectron spectrum produced by the unfocused XUV beam, the y-axis depicts the distance of gas jet from the position of the IR focus and the z-axis the XUV pulse energy. Having optimized the emission resulting from the single GJ configuration further enhancement of the harmonic yield was achieved by applying quasi- phase-matching conditions using two gas jets. The same gas is used in both jets. Results are shown in Fig. 5c,d. The dependence of the harmonic yield, generated by Ar and Xe gas, on the distance between GJ_2 and GJ_1 is shown in Fig. 5c,d, respectively. The x-axis denotes the distance

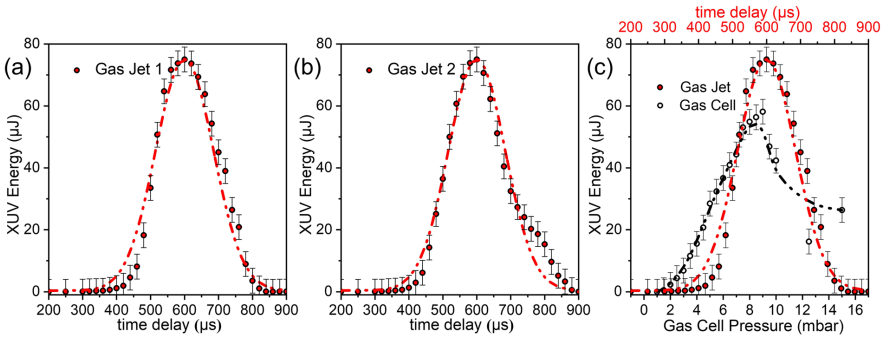

Figure 4. Harmonic emission using a single pulsed gas-jet and the comparison with a single gas-cell. (**a**,**b**) Pulse energy of the XUV radiation emitted by GJ_1 and GJ_2, respectively, as a function of the delay between the laser pulse arrival at the focus and the opening of the nozzle. Both jets are positioned at z = 0. The time delay of ≈600 μs corresponds to the value where the laser pulse meets the maximum atomic density. The dots are the measured data and the red line is a Gaussian fit. (**c**) Comparison of a single gas jet vs 10 cm long gas cell yield for optimized conditions.The upper part axis represents the time delay of the pulsed nozzle while the lower one the measured pressure of the Gas cell. In all panels the generated medium was Ar, while the XUV energy was determined by PD_{XUV} placed after an Al filter.

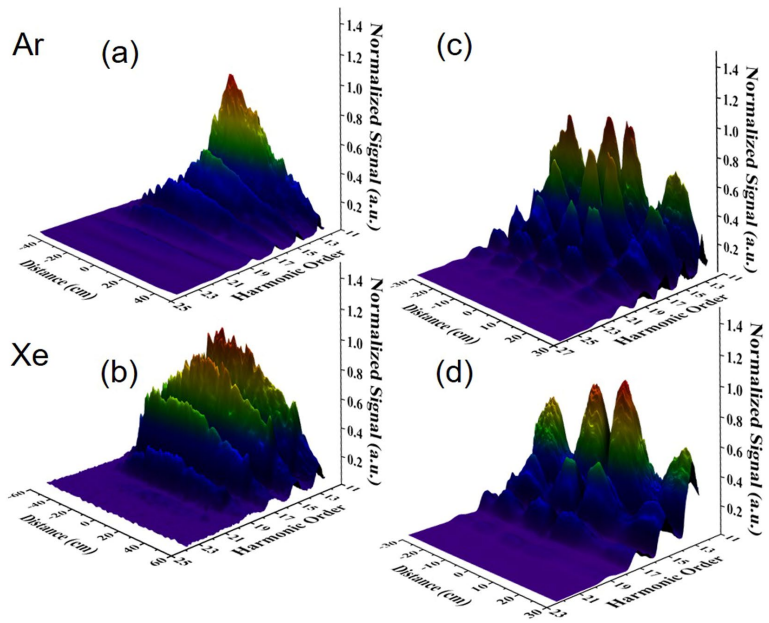

Figure 5. Harmonic generation in single and dual gas-jet configuration. Generation of GW high-harmonics using single (**a**,**b**) and dual gas-jet (**c**,**d**) configuration for Xe and Ar. In all panels the corresponding harmonic signal was determined by recording the single-photon photoelectron spectra produced by the interaction of Ar gas with the incoming XUV beam after passing trough the Al filter.

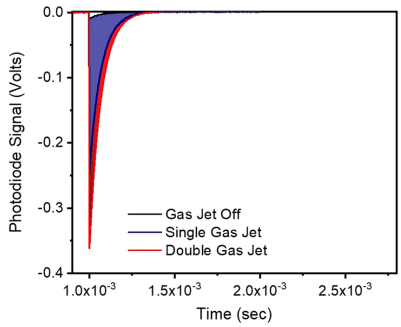

Figure 6. Measurement of the XUV energy. XUV photodiode signal obtained with one GJ (blue shaded area), two GJs (red shaded) and with the harmonic generation switched off (black line). For the extraction of the pulse energy the XUV photodiode quantum efficiency as a function of photon energy provided by the manufacturing company Opto Diode Corp was used.

between the two jets, the y-axis the harmonic order and the z-axis the XUV pulse enegy. GJ_1 is positioned at fixed $z \approx 0$ while GJ_2 moves at variable positions.

All spectra emitted by Ar extend to higher cut-off energies than those emitted by Xe due to the higher ionization energy of Ar, while the pulse energy is lower than the one in Xe due to the lower conversion efficiency of Ar[61,62]. When two jets (filled with the same gas) are used a clear modulation of the signal is observed as a function of the jet distance. This is attributed to the quasi-phase matching resulting from the jet distance dependent Gouy phase and it is verified by numerical calculations[59]. The maximum measured pulse energy at the source is: I) 75 μJ (one jet) and 130 μJ (two jets), for Ar driven by 45 mJ IR pulse energy; and II) 135 μJ (one jet) and 230 μJ (two jets), for Xe driven by 25 mJ IR pulse energy. This last value corresponds to ~$5 \cdot 10^{13}$ photons/pulse, a photon flux that competes with photon fluxes of FELs in this spectral region. More details on the above quasi-phase-matching generation scheme and XUV throughputs can be found in ref. [59].

The pulse energy measurement procedure followed is described below. Once optimization of harmonic emission is achieved, the XUV Photodiode (Opto Diode AXUV100G) is placed after the Sn filter (F). Figure 6 shows the photodiode signal of the radiation transmitted through the Sn filter produced with the single (blue shaded area) and the dual (red shaded area) GJ configuration. The black line is IR light detected by the PD_{XUV}, when the gas jet of the HH generation was off. Although significantly small, this signal was subtracted from the measured total one, when harmonic generation was on.

The signal was measured with an oscilloscope (50 Ω input impedance) and the measured trace was integrated. The pulse energy E_{PD} measured at the position where the photodiode was placed is calculated by

$$E_{PD} = \sum_q \frac{n_e \cdot w \cdot h\nu_q}{\eta_q} \cdot e$$

where q is the harmonic order, n_e is the number of produced photoelectrons, w is the statistical weight of the qth harmonic, $h\nu_q$ is the harmonic photon energy, η_q is the photodiode quantum efficiency of the photodiode and e is the electron charge. The photoelectron number is given by

$$n_e = \frac{S_T - S_{IR}}{e \cdot R}$$

where S_T *is* the total time integrated photodiode signal, S_{IR} *is* the time integrated photodiode signal when the harmonic generation is off, e is the electron charge and R is the oscilloscope impedance. The quantum efficiency of the photodiode as a function of the photon energy is provided by the manufacturing company (See legend of Fig. 6). The pulse energy E at the harmonic generation source is given by:

$$E = \sum_q \frac{n_e \cdot w \cdot h\nu_q}{\eta_q \cdot R_q^{Si} \cdot T_q^{Sn}} \cdot e$$

where T_q^{Sn} is the 4% transmission of the Sn filter in this spectral region measured by recording the harmonic spectrum with and without filter, and R_q^{Si} is the ~50–60% reflectivity of the Si plate. It is worth noting that after having published in ref. [59] the above given XUV pulse energies, a second slightly different calibration curve was published in the documents of the manufacturing company of the photodiode. Using this second calibration curve the above given and in ref. [59] published XUV pulse energy values reduce by 35% i.e. for Ar 48 μJ (one jet) and 85 μJ (two jets) and for Xe 88 μJ (one jet) and 150 μJ (two jets) for Xe.

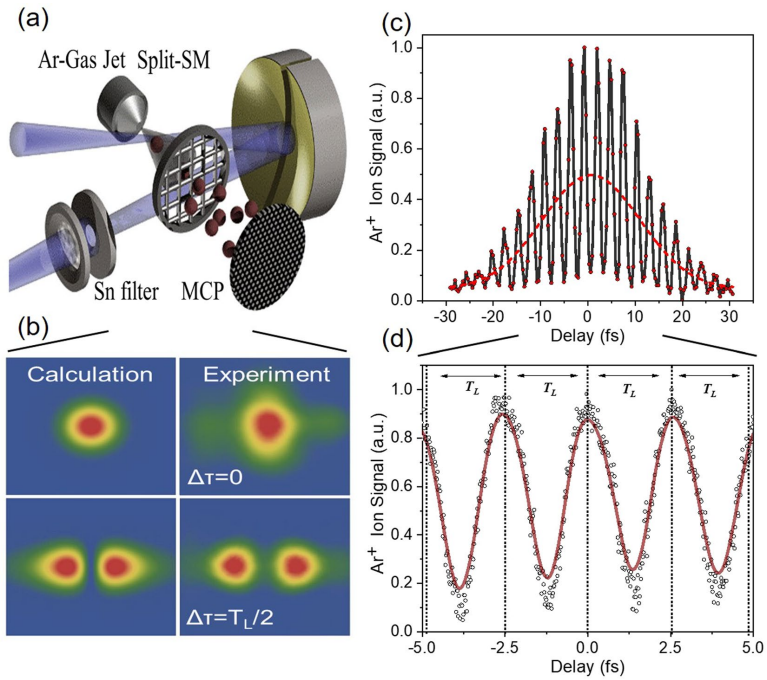

Figure 7. Split mirror arrangement. (**a**) A schematic of the experimental set-up of the autocorrelator consisting of a split spherical mirror and a TOF spectrometer. (**b**) Calculated (left panels) and measured (right panels) transverse intensity distribution of a CW 532 nm laser at the focus of the spherical mirror for $\Delta\tau = 0$ and $\Delta\tau = T_L/2$ (double maximum distribution) delay. (**c**) High-order autocorrelation trace of the fundamental laser field (IR) obtained measuring the Ar^+ yield as a function of the time delay between the two pulses produced by the split mirror. For this acquisition, the harmonic generation was turned off and the Sn filter was removed. (**d**) Expanded area of the AC trace. The signal is oscillating at the laser period of 2.67 fs.

Temporal resolution. The temporal resolution of the beam line has been tested by measuring the beam pointing stability at the end station, the performance of the split mirror device and its interferometric stability. This has been done using the IR laser beam and a CW diode laser at 532 nm wavelength.

Figure 7a shows a schematic of the split mirror assembly. The focal area of the gold coated spherical mirror was magnified by a lens and imaged by a CCD camera. Figure 7b shows the calculated (left panels) and measured (right panels) images of the focal spot area for two different delays, i.e. for two different displacements of the one-half of the mirror. The upper pannels show the intensity distribution at the focus formed when the phase difference between the two parts of the laser wave-front reflected by the two mirror halves is equal or close to $2n\pi$, $n = 0, 1, 2, 3\ldots$, i.e. when the delay between the two wave-fronts is $\sim nT_L$, with T_L being the period of the laser field.

The phase difference is controlled by finely adjusting the position of the piezoelectric translator connected with the one part of the split mirror. The position of the piezo translation stage was measured by a capacitive sensor feedback system of the piezo system. When the phase difference of the two wave-fronts becomes equal or close to $(2n+1)\pi$, $n = 0, 1, 2, 3\ldots$, i.e. when the delay between the two wave-fronts is $(n+1/2)T_L$, the intensity distribution at the focus splits into two bright spots shown at the lower part of Fig. 7b. The two bright spots ideally have the same intensity. Additionally, a higher-order autocorrelation trace of the fundamental laser field (IR) was recorded. For this acquisition, the harmonic generation was turned off and all filters were removed, thus ionization of Ar occurs only through the fundamental laser frequency by multi-IR-photon absorption.

The measured trace is shown in Fig. 7c where the interferometric interference fringes are clearly visible. The red dashed line is the cycle average of the data. The interference fringes are used for the calibration of the delay scale of the measured autocorrelation traces. The period of the observed oscillation, depicted in the expanded AC area trace in Fig. 7d is equal to the laser period that is 2.67 fs, where the red line is a cosine fit in the measured data.

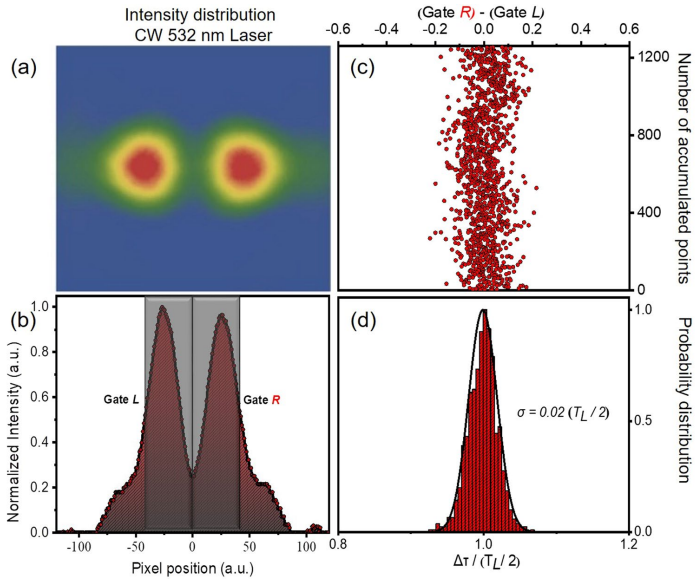

Figure 8. Stability measurements of the split-mirror autocorrelator. (**a**,**b**) Measured transverse intensity distribution of a CW 532 nm laser at the focus of the spherical mirror for $\Delta\tau = T_L/2$ (double maximum distribution) delay. It is noted that in this graph T_L corresponds to the period of the 532 nm CW laser. (**c**) The difference of the integrated signals of the Gate *L* and *R*. (**d**) Probability distribution of the above difference (1260 points were accumulated). The standard deviation of the mean yields a temporal resolution of ~17 asec.

Shot-to-shot fluctuations of the XUV intensity distribution may be introduced because of: i) the non-perfect pointing stability of the laser and consequently of the XUV beam and ii) mechanical instabilities of the split mirror arrangement. The above factors affect the interferometric stability of the delay line. The interferometric stability of the split mirror was measured using a CW laser of $\lambda = 532$ nm by the following procedure. The displacement of the two halves of the spherical mirror was fixed such as introducing a delay of $T_L/2$ (Fig. 8a). Consequently in the line-out of the focal spot area, the integrated areas of the two gates *L* and *R*, introduced in Fig. 8b, are essentially equal. Any deviation from this picture can be correlated to the instability of the split spherical mirror, since it originates from the optical path difference between the two interfering wave fronts. The interferometric stability of the split mirror device is extracted from the standard deviation of the mean value of the probability distribution for 1260 points as a function of time and is found to be ≈17 asec (Fig. 8c,d).

The interferometric stability of the device may be different when the IR laser is used as its pointing stability is not the same with that of the CW one. The pointing stability of the IR was measured with an IR beam profiler placed just in front of the split mirror. The shot to shot position of the maximum of the intensity distribution is plotted in Fig. 9 for 150 laser shots. The mean FWHM of the contour is about 75 μm and thus substantially smaller than the 3 mm FWHM of the XUV intensity distribution at the split mirror, not affecting the measured interferometric stability and time resolution.

Non-Linear XUV Optics Using the 20-GW XUV Beam-Line

The highest focused XUV intensity achieved was ~$7 \cdot 10^{15}$ W/cm^2 assuming a 10 fs long pulse train envelope[59], an XUV focal spot size of 2 μm measured with an ion-microscope[67], the gold reflectivity (~12%) of the spherical mirror, the ~60% reflectivity of the Si plate, the ~20% transmition of the Sn filter for the given wavelengths and the 230 μJ generated pulse energy at the harmonic source. Such intensity allows the investigation of multi-XUV-photon multiple ionization. Here, we summarize the results obtained in He, Ar and Ne atoms. Some of the multi-XUV-photon schemes of this chapter have been used for the measurement of the attosecond pulse duration through 2nd IVAC measurements (schemes in He and Ar), which will be described in the next section.

Figure 10a shows the measured ion mass spectrum of He, in which He^+ is clearly observable. It should be noted that for this measurement an Sn filter was used. The XUV intensity dependence of the ion yield is depicted in Fig. 10b. The slope of the fitted line in the He^+ data is 2.1 ± 0.2, as expected for the underlying two photon ionization process, while the slope of the line fitted in the H_2O+ date is 1.2 ± 0.1, as water molecules are single photon ionized at the XUV photon energies used. The verified two-XUV-photon ionization of He is a very convenient process in performing 2nd order autocorrelation measurements of XUV radiation with wavelengths ≥51 nm. The

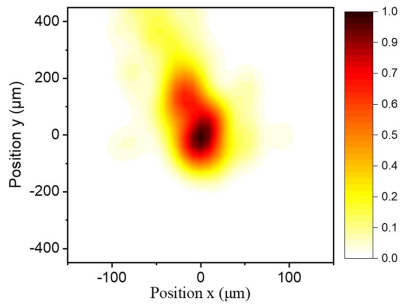

Figure 9. Measurement of the IR laser pointing instability. The contour illustrates the shot to shot distribution of the maximum of the IR laser intensity distribution measured just before the split mirror. The colorbar shows the normalized probability distribution of laser shots.

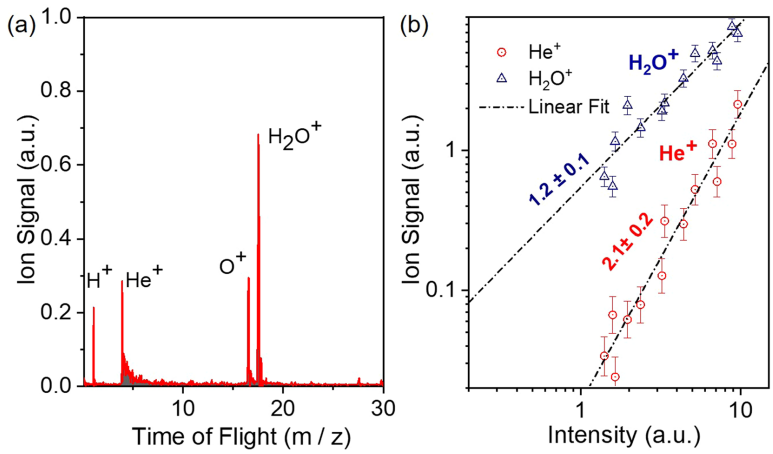

Figure 10. 2-XUV-photon ionization process of He. (**a**) TOF mass spectrum produced by the interaction of the XUV comb (11^{th}−15^{th}) with He gas.(**b**) XUV intensity dependence of the He^+. The slope of 2.1 ± 0.2 ascertains the second-order nonlinearity of the ionization process. The intensity axis in (b) has been calibrated using the O^+ ion signal, which is linear with the XUV intensity.

Ar and Ne ion TOF mass spectra are shown in Fig. 11a,b respectively. The latter reveals the formation of singly and doubly charged Ne, while the former shows recorded charge states of Ar up to +4 (Ar^{4+}). Figure 12 depicts the ionization schemes of Ne and Ar, while Fig. 13a shows the dependence of the Ar^{2+}, Ar^{3+} and $N_2{}^+$ yield and Fig. 13b the dependence of the Ne^+, Ne^{2+} and $N_2{}^+$ yield on the XUV pulse intensity I_{XUV}.

The Ar^+ ion mass peak of Fig. 11b was used for the calibration of the XUV energy scale (x-axis) of the Ne ion yield power dependence graph (Fig. 13b). The black dashed-dot lines in Fig. 13 are linear fits to the raw data. The error bars represent one standard deviation of the mean.

The results for Ar gas have been extensively discussed in ref. [59]. In brief, intensity dependence measurements performed for Ar^+, Ar^{2+} and Ar^{3+} were supported by numerical calculations revealing the dominant channels of these multi-XUV-photon multiple ionization studies. Comparison with the data obtained using FEL source indicates that there are differences in multiphoton ionization induced by the two different sources, which can be attributed to the different photon statistics of the two sources[59].

As expected for a single-photon ionization process, the dependence of the Ne^+ and $N_2{}^+$ yields on I_{XUV} is linear (Fig. 13b). The slope of the Ne^{2+} yield is found to be 3.1 ± 0.4 compatible with a three-photon ionization process. For the photon energies employed in this experiment both the sequential and the direct double ionization of Neon are three photon processes. Above the ionization saturation intensity the slope becomes 1.5±0.1. For the

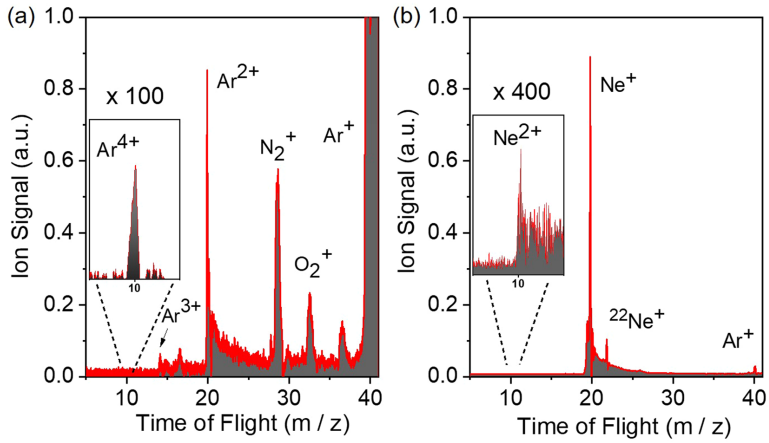

Figure 11. Time of Flight mass spectrum of Ar and Ne. (**a**) TOF mass spectrum produced by the interaction of the focused 11^{th}–15^{th} harmonics with Ar. The spectrum shows multiple charged Ar ions (Ar^{n+}) with n up to +4. (**b**) Measured Ne ion mass spectrum produced by the XUV radiation. In the spectrum two Ne^+ ion mass peaks are to be seen corresponding to the two most abundant isotopes, ^{20}Ne and ^{22}Ne. A small Ne^{2+} peak and an Ar^+ peak are also observed. The Ar^+ peak originating from residual Ar gas is used for calibration of the mass ion spectrometer.

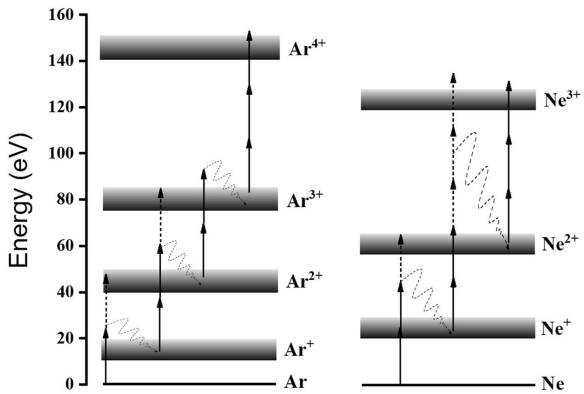

Figure 12. Multi-XUV-photon multiple ionization scheme. The ionization energy level schemes for Ar and Ne (excluding higher order processes (ATI) and decays to excited ionic states) depicting the direct and sequential channels.

next charge state, i.e. Ne^{3+}, six or more photon absorption is required. This charge state is not observable in the measured ion mass spectra.

Temporal Characterization of the Attosecond Pulse Trains

After having set up, characterized and tested the high photon flux beam-line, measurements towards temporal characterization of the APTs synthesized by the harmonic spectrum have been performed. It is worth noting that in these measurements the diameter of the aperture (A) in the "XUV filtering and diagnostics" chamber (Fig. 1) was reduced as to decrease the XUV signal to about half of its maximum value. Thus the outer part of the XUV beam cross-section was blocked. Consequently i) aberrations in the XUV beam were reduced and ii) the ratio of the short to long trajectory contribution in the transmitted XUV beam was increased. The method used is the 2^{nd}

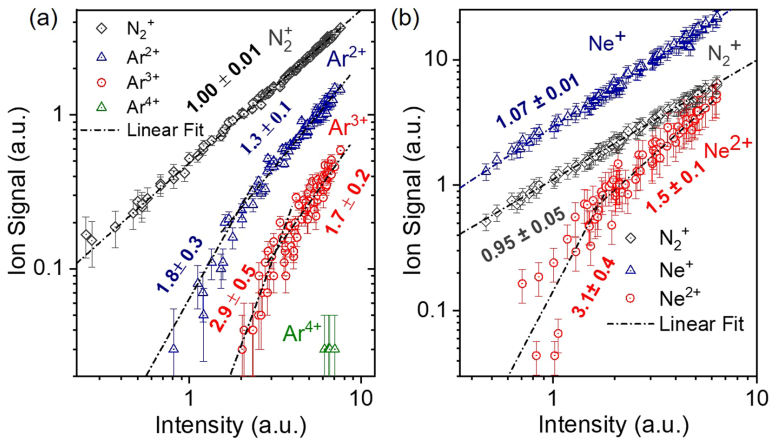

Figure 13. Ion yield dependence on the XUV radiation. XUV intensity dependence of different charge states of Ar (**a**) and Ne (**b**). In both panels the black dashed lines depict a linear fit on the raw data and the error bars represent one standard deviation of the mean. The slopes of the lines in both measurements, are in agreement with lowest-order pertubation theory i.e. with the order of the underlying non-linear process.

IVAC utilizing the delay line and TOF spectrometer discussed in section 3 and shown in Fig. 7a. As second order non-linear process, the two-XUV-photon ionization of both Ar^+ and He were used. This is in order to demonstrate different two-photon schemes that can be used in pulse duration measurements at higher photon energies. In performing the 2nd IVAC measurements the gas pressure in the interaction area was kept as low as possible in order to minimize the space charge effects which become visible by broadening the TOF ion-mass peaks. In Ar the traces are obtained by the superposition of the harmonics transmitted through the Sn filter. Before saturation, the Ar^{2+} yield as a function of the I_{XUV} in log-log scale has a linear dependence with slope ~2[59]. This slope is compatible with either two-XUV-photon direct double ionization of Ar or two-XUV-photon ionization of Ar^+ after saturation of the single photon ionization of Ar (see Fig. 12). Numerical calculations in[59] have shown that the latter channel, i.e. saturated single photon ionization of Ar followed by two photon ionization of Ar^+ is the dominant channel in the I_{XUV} range in which the present experiments have been performed.

Measured 2nd IVAC traces are shown in Fig. 14a,b. The blue rhombus is the trace obtained from the single photon ionization of H_2O. As expected for a linear process the IVAC shows no modulation. The Ar^{2+} ion yield (produced by the XUV radiation generated using only one gas jet) is measured here as a function of the delay between the two XUV pulses introduced by the translation of one part of the bisected spherical mirror. The gas jet in the HHG chamber was set at 20 cm after the laser focus in order to minimize the contribution of the long electron trajectory. Low temporal resolution scans recorded with a step of 350 asec have been performed in determining the duration of the APT envelope (Fig. 14a). The red points are the raw data, averages of 50 laser points and the error bar corresponds to the standard deviation of the mean value. The black curve is a Gaussian fit to the data. The fit results in an XUV pulse envelope having a duration of 9.8 ± 0.9 fs, verifying the estimated duration used in ref. [59]. A fine scan using a time delay step of 50 asec is shown in Fig. 14b. The Ar^{2+} ion yield, as expected, is modulated with the half period of the driving field. The gray circles are the recorded raw data (averages of 50 laser shots). The raw data in the fine scan of Fig. 14b are fluctuating around the mean value mainly due to interferometric instabilities (within the cycle of the XUV field) and XUV beam pointing instabilities, which are both enhanced by the non-linearity of the process. Long averaging and calculating moving averages substantially reduce the strong shot-to-shot fluctuation of the recoded data. The red circles are the moving averages of the raw data taken over 10 points. The black curve is fit of a series of Gaussian distributions to the averaged points. In this fit the free parameters are the common width, height of the Gaussians as well as the peak to peak distance. Furthermore the comb of Gaussians are multiplied by a fixed envelope distribution taken from the fit of Fig. 14a. The pulse width resulting from the Gaussian distributions is found to be $\tau_{XUV} = 650 \pm 80$ asec. The error of 80 asec appearing in all measurements is the largest resulted standard deviation, among all the fits in the raw data of all measured traces. The above pulse duration of the attosecond pulses in the APT is synthesized essentially by the three harmonics 11th, 13th and 15th. Since here only one gas jet was utilized, the APT beam-line power to be rigorously reported is 11.0 ± 3.5 GW, the error originating mainly from the uncertainty in the calibration of the XUV photodiode.

The two-XUV-photon ionization of He^+ has also been used to measure the produced APTs through 2nd IVAC, shown in Fig. 15a and alongside with Fig. 15b showing a 2nd IVAC trace of Ar^{2+}. The trace of Fig. 15b is a different run than the one shown in Fig. 14b verifying reproducibility of the results. All points, error bars and curves are as those in Fig. 14b. with the only difference being that here we do not use any envelope distribution in the fit either

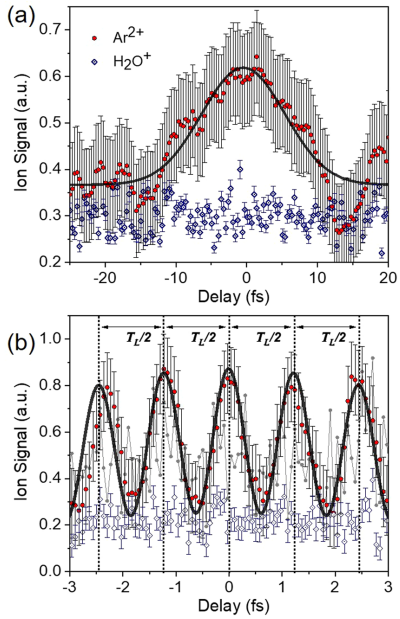

Figure 14. Measured 2nd IVAC trace i.e. Ar^{2+} ion signal as a function of the XUV-XUV delay line. The XUV radiation is produced by a single gas jet of xenon and is transmitted through a Sn filter. (**a**) A coarse time delay scan with 350 asec step is revealing a modulation in Ar^{2+} ion signal represented by the red circles, while the blue rhombus depicting the single photon ionization of H_2O shows no modulation. A Gaussian fit in the data points of Ar^{2+} yields a time duration of $\tau_{XUV} = 9.8 \pm 0.9$ fs. (**b**) A fine scan with time delay step of 50 asec. The gray circles correspond to the raw data recorded for Ar^{2+}. The moving averages of the raw data taken over 10 points are represented by the red circles. The black curve is a fit of a sequence of gaussian pulses in the averaged points.

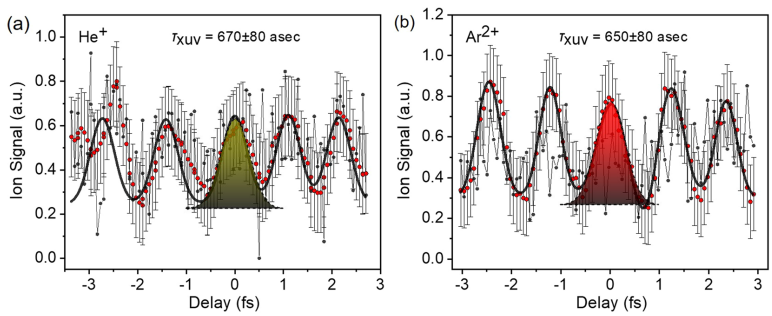

Figure 15. (**a**) Measured 2nd IVAC trace of the He^+ (**b**) 2nd IVAC trace of the Ar^{2+} ion signal as a fuction of the delay of the XUV-XUV delay line. The gray circles correspond to the raw data recorded, the moving averages of the raw data taken over 10 points are represented by the red circles. The black curves is a Gaussian fit over the averaged points. The temporal width of the Gaussian fit corresponds to a pulse duration of 670 ± 80 as and 650 ± 80, for He^+ and Ar^{2+} respectively.

Harmonic order	9	11	13	15	17
λ_q(nm)	88.9	72.7	61.5	53.3	47.0
α_S	1	0.435	−0.4	−1.5	−2.96
α_L	−23.97	−23.56	−22.88	−21.96	−20.71
θ_S(mrad)	0.195	0.15	0.127	0.126	0.148
θ_L(mrad)	1.74	1.40	1.15	0.96	0.79

Table 1. Parameters of the 9th to the 17th harmonics generated in Xe. The intensity of the laser field used is 10^{14} W/cm^2 and the unit for α is 10^{-14} W^{-1}·cm^2.

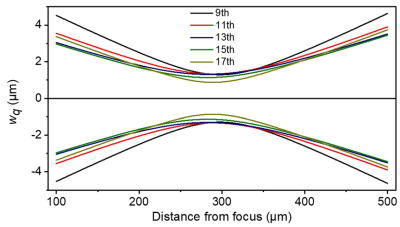

Figure 16. Calculated focal areas of the five harmonics 9th, 11th, 13th, 15th and 17th. The graph depicts the harmonic beam waist as a function of the distance from the focus of the spherical mirror. The x-axis shows the focus position of the harmonics on the propagation axis. The focus position of the harmonics is found to be ≈ 290 μm away from the focus of the 5 cm mirror. Their beam waist ratios are 0.99:1.01:1:0.87:0.67 for harmonic 9th, 11th, 13th, 15th and 17th respectively.

for the He or the Ar trace. This is because in these runs the peak height distribution within the error bars did not depict any envelope type modulation. The pulse duration measured using He as non-linear medium is 670 ± 80 asec and the one of the superposition of harmonics 11th, 13th and 15th measured in Ar^{2+} is the same as the one of Fig. 14b. The two values are well within the error bar and thus essentially identical.

The measured durations here are similar to those retrieved in previous experiments implemented in a 3 m focal length beam-line applying 2nd IVAC in two photon ionization of He but about 65% longer than those measured through the RABBIT technique[39]. The discrepancy between the 2nd IVAC and RABBIT originates from the fact that 2nd IVAC measures averages of spatiotemporally dependent pulse durations and the contribution of both long and short trajectories, while RABBIT measures average phases[39]. An additional effect to be considered is pointed out recently in refs. [66,68]. Different harmonics, due to their different divergence are focused at different positions, have different focal spots and therefore lead to only partial spatial overlap of the superimposed harmonics and to different Gouy phase contributions in the harmonic superposition. At specific conditions, e.g. spectrum with harmonics of very different order, the spatial overlap becomes notably small and the Gouy phase difference large, thus reducing a lot the temporal confinement. 2nd IVAC is sensitive to these effects and thus reveals fairly realistic pulse durations. However, for the three harmonics employed in this experiment substantial spatial overlap is present as indicated by the results of a recent work[69], were separation of the harmonic foci was not observed.

In order to verify the significant spatial overlap of the three harmonics used in the 2nd IVAC measurements we have performed calculations of the focal areas of the three harmonics, for a bandwidth spanning from the 9th to the 17th harmonic and Xe gas as harmonic generating medium. We are using the expression $\theta_{S,L} = \frac{\lambda_q}{\pi w_q}\sqrt{1 + 4\alpha_{S,L}^2 I_L^2 \frac{w_q^4}{w_f^4}}$ of the divergence of the harmonics originating from the electron short (S) and long (L) trajectories at the point of the interaction for the harmonic order q, as given in ref. [70]. λ_q, w_q, are the wavelength and the beam waist of the harmonic q, w_f is the waist size of the laser beam, $\alpha_{S,L}$ is the S and L trajectory coefficient and I_L is the IR driving laser peak intensity. The beam waist was measured at the emission plane and it was found to be $w_f \approx 350$ μm. Using Gaussian optics the harmonic beam waist can be obtained by $w_q = \frac{w_f}{\sqrt{q_{eff}}}$ where q_{eff} is the effective nonlinearity coefficient with $q_{eff} \approx 5$ for all the harmonics laying in the plateau of the harmonic spectrum[69,71,72]. For a peak intensity 10^{14} W/cm^2 all the studied harmonics are laying in the plateau and the trajectory coefficient $\alpha_{S,L}$ is extracted by solving the three-step semi-classical model[73]. The results are summarized in Table 1.

After extracting the divergence of the different harmonics, the virtual source positions for each of the generated harmonics is calculated assuming only short trajectory contribution. The focus positions of the harmonics, after reflection on the spherical mirror of focal length $f = 5$ cm, are calculated using geometrical optics. Here the paraxial approximation is applied since the divergence of the harmonics is below the paraxial limit. The results of the calculations are shown in Fig. 16.

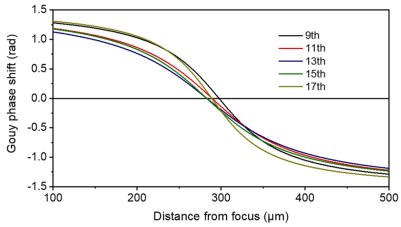

Figure 17. Calculated Gouy phase shift of the five harmonics 9th, 11th, 13th, 15th and 17th. The x-axis shows the focus position of the harmonics on the propagation axis. The focus position of the harmonics is found to be ≈ 290 μm away from the focus position of the 5 cm mirror.

The distance of the positions of the five foci is 8.2 μm between the 9th and 11th, 6.3 μm between the 11th and 13th harmonic, ~0 μm between the 13th and 15th harmonic, 5.9 μm between the 15th and 17th harmonic and thus it is negligibly small with respect to their confocal parameter (≈170 μm for 13th harmonic). The size of the focal spots is slightly different. The ratios for the beam waists at the focus are 0.99:1.01:1:0.87:0.67 for the harmonics 9th, 11th, 13th, 15th and 17th respectively. Under these conditions, the spatial overlap of the five harmonics is substantial. The Gouy phase at the beam waist for each harmonic can be calculated and is shown in Fig. 17. Its variation for the different harmonics (assuming as central frequency the 13th harmonic) $\varphi_9 = 0.24$ rad, $\varphi_{11} = 0.08$ rad, $\varphi_{13} = 0$ rad, $\varphi_{15} = 0$ rad, $\varphi_{17} = 0.13$ rad is also negligibly small. In this case, the duration of the APT pulses is not significantly affected. In fact, the different beam waists of the 11th, 13th, 15th harmonics lead to more similar amplitudes of the interfering harmonics than those generated.

Similar calculations have been further performed for the long electron trajectories, which present larger harmonic divergence. In this case, the virtual foci are placed closer to the focusing element. It is found that the difference of the foci positions between *L* and *S* trajectories is ≈30 μm which is consistent with previous experimental findings[69,72,74] and also smaller than the confocal parameter, thus not substantially affecting the APT pulse duration in particular because the long trajectory contributions are reduced through the geometry used.

Conclusions

In summary, a detailed description of an ultra-intense attosecond XUV beam line has been presented. A ten GW class average peak power attosecond source in the XUV spectral region 15–25 eV is demonstrated. These specifications are to our knowledge unique for an XUV source. While in a previous publication the high power of the source (20 GW) was reported[59] attosecond confinement, although expected, could not be rigorously claimed as the previous work did not include any pulse duration measurements. In the present work, APT durations of the order of 650 asec have been measured opening the way to ten-GW class attosecond XUV sources. The source is based on harmonic generation in long (9 m) focusing geometry of the driving IR laser radiation. The pulse duration of both the APT pulses and the envelope have been measured though 2nd IVAC i) in He employing two-XUV-photon ionization as a second order process as well as ii) in Ar exploiting two-XUV-photon ionization of Ar^+ under saturation of neutral Ar ionization. Measurements with both gases resulted in the same pulse durations within the experimental error. High non-linear XUV-optics in terms of multiple multi-XUV-photon ionization of He, Ar and Ne atoms, have been further demonstrated using the above beam line. The combination of high pulse energy and short duration opens up excellent perspectives for sub-fs XUV-pump-XUV-probe experiments in all states of matter. At the same time the XUV intensity levels reached enable the study of strong field effects in the XUV spectral region. As a further perspective, scaling previous parameters of isolated attosecond pulses[64], our source holds promise of generating few μJ level isolated attosecond pulses through polarization gating approaches. Those are advanced perspectives for the Hellenic National Research Infrastructure HELLAS-CH, part of which is the present beam line.

The results of the present work further hints towards an unprecedented performance of the two 1-kHz repetition rate attosecond beam lines of the Extreme Light Infrastructure – Attosecond Light Pulse Source (ELI-ALPS) facility currently being under implementation[75], driven by shorter laser pulses with similar pulse energies. The geometry of one of the two beam-lines of ELI-ALPS is very close to that of the present source, while the second one is several times longer and offers phase matching control capacities. Thus, it is expected to further scale up the source throughput. The 1 kHz repetition rate of these sources in combination with the CEP stabilized driving laser will provide the by far best ever conditions for attosecond XUV-pump-XUV-probe investigations using isolated attosecond pulses and kinematically nearly complete experiments through e-e, e-ion and ion-ion coincidence measurements.

Received: 29 November 2019; Accepted: 29 January 2020;
Published online: 28 February 2020

References

1. Träger, F. ed. *Springer handbook of lasers and optics* (Springer, Dordrecht, New York, 2012).
2. Krausz, F. & Ivanov, M. Attosecond physics. *Rev. Mod. Phys.* **81**, 163–234, https://doi.org/10.1103/RevModPhys.81.163 (2009).
3. Paul, P. M. *et al.* Observation of a train of attosecond pulses from high harmonic generation. *Science (New York, N.Y.)* **292**, 1689–1692, https://doi.org/10.1126/science.1059413 (2001).

4. Mairesse, Y. & Quéré, F. Frequency-resolved optical gating for complete reconstruction of attosecond bursts. *Phys. Rev. A* **71**, 803, https://doi.org/10.1103/PhysRevA.71.011401 (2005).
5. Chini, M., Gilbertson, S., Khan, S. D. & Chang, Z. Characterizing ultrabroadband attosecond lasers. *OPTICS EXPRESS* **18**, 13006–13016, https://doi.org/10.1364/OE.18.013006 (2010).
6. Conference on Lasers and Electro-Optics (CLEO), 2013. 9–14 June 2013, San Jose, CA, USA (IEEE, Piscataway, NJ, 2013).
7. Gruson, V. *et al*. Attosecond dynamics through a Fano resonance: Monitoring the birth of a photoelectron. *Science (New York, N.Y.)* **354**, 734–738, https://doi.org/10.1126/science.aah5188 (2016).
8. Spanner, M., Bertrand, J. B. & Villeneuve, D. M. *In situ* attosecond pulse characterization techniques to measure the electromagnetic phase. Phys. Rev. A 94; https://doi.org/10.1103/PhysRevA.94.023825 (2016).
9. Mairesse, Y. *et al*. High harmonic XUV spectral phase interferometry for direct electric-field reconstruction. *Phys. Rev. Lett.* **94**, 173903, https://doi.org/10.1103/PhysRevLett.94.173903 (2005).
10. Iaconis, C. & Walmsley, I. A. Self-Referencing Spectral Interferometry For Measuring Ultrashort Optical Pulses - Quantum Electronics, IEEE Journal of // Self-referencing spectral interferometry for measuring ultrashort optical pulses. *IEEE J. Quantum Electron.* **35**, 501–509, https://doi.org/10.1109/3.753654 (1999).
11. Eckle, P. *et al*. Attosecond angular streaking. *Nat Phys* **4**, 565–570, https://doi.org/10.1038/nphys982 (2008).
12. Pedatzur, O. *et al*. Double-blind holography of attosecond pulses. *Nature Photonics* **13**, 91–95, https://doi.org/10.1038/s41566-018-0308-z (2019).
13. Carpeggiani, P. *et al*. Vectorial optical field reconstruction by attosecond spatial interferometry. *Nature Photon* **11**, 383–389, https://doi.org/10.1038/nphoton.2017.73 (2017).
14. Constant, E., Taranukhin, V. D., Stolow, A. & Corkum, P. B. Methods for the measurement of the duration of high-harmonic pulses. *Phys. Rev. A* **56**, 3870–3878, https://doi.org/10.1103/PhysRevA.56.3870 (1997).
15. Orfanos, I. *et al*. Attosecond pulse metrology. *APL Photonics* **4**, 80901, https://doi.org/10.1063/1.5086773 (2019).
16. Drescher, M. *et al*. Time-resolved atomic inner-shell spectroscopy. *Nature* **419**, 803–807, https://doi.org/10.1038/nature01143 (2002).
17. Uiberacker, M. *et al*. Attosecond real-time observation of electron tunnelling in atoms. *Nature* **446**, 627–632, https://doi.org/10.1038/nature05648 (2007).
18. Goulielmakis, E. *et al*. Direct measurement of light waves. *Science (New York, N.Y.)* **305**, 1267–1269, https://doi.org/10.1126/science.1100866 (2004).
19. Itatani, J. *et al*. Tomographic imaging of molecular orbitals. *Nature* **432**, 867–871, https://doi.org/10.1038/nature03183 (2004).
20. Cavalieri, A. L. *et al*. Attosecond spectroscopy in condensed matter. *Nature* **449**, 1029–1032, https://doi.org/10.1038/nature06229 (2007).
21. Schultze, M. *et al*. Delay in photoemission. *Science (New York, N.Y.)* **328**, 1658–1662, https://doi.org/10.1126/science.1189401 (2010).
22. Isinger, M. *et al*. Photoionization in the time and frequency domain. *Science (New York, N.Y.)* **358**, 893–896, https://doi.org/10.1126/science.aao7043 (2017).
23. Goulielmakis, E. *et al*. Real-time observation of valence electron motion. *Nature* **466**, 739–743, https://doi.org/10.1038/nature09212 (2010).
24. Calegari, F. *et al*. Ultrafast electron dynamics in phenylalanine initiated by attosecond pulses. *Science (New York, N.Y.)* **346**, 336–339, https://doi.org/10.1126/science.1254061 (2014).
25. Kraus, P. M. *et al*. Measurement and laser control of attosecond charge migration in ionized iodoacetylene. *Science (New York, N.Y.)* **350**, 790–795, https://doi.org/10.1126/science.aab2160 (2015).
26. Beaulieu, S. *et al*. Attosecond-resolved photoionization of chiral molecules. *Science (New York, N.Y.)* **358**, 1288–1294, https://doi.org/10.1126/science.aao5624 (2017).
27. Tzallas, P., Skantzakis, E., Nikolopoulos, L. A. A., Tsakiris, G. D. & Charalambidis, D. Extreme-ultraviolet pump–probe studies of one-femtosecond-scale electron dynamics. *Nat Phys* **7**, 781–784, https://doi.org/10.1038/nphys2033 (2011).
28. Carpeggiani, P. A. *et al*. Disclosing intrinsic molecular dynamics on the 1-fs scale through extreme-ultraviolet pump-probe measurements. Phys. Rev. A 89; https://doi.org/10.1103/PhysRevA.89.023420 (2014).
29. Nabekawa, Y. *et al*. Sub-10-fs control of dissociation pathways in the hydrogen molecular ion with a few-pulse attosecond pulse train. *Nature communications* **7**, 12835, https://doi.org/10.1038/ncomms12835 (2016).
30. Palacios, A., González-Castrillo, A. & Martín, F. Molecular interferometer to decode attosecond electron-nuclear dynamics. *Proceedings of the National Academy of Sciences of the United States of America* **111**, 3973–3978, https://doi.org/10.1073/pnas.1316762111 (2014).
31. Takahashi, E. J., Lan, P., Mucke, O. D., Nabekawa, Y. & Midorikawa, K. Attosecond nonlinear optics using gigawatt-scale isolated attosecond pulses. *Nature communications* **4**, 2691, https://doi.org/10.1038/ncomms3691 (2013).
32. Tzallas, P., Charalambidis, D., Papadogiannis, N. A., Witte, K. & Tsakiris, G. D. Direct observation of attosecond light bunching. *Nature* **426**, 267–271, https://doi.org/10.1038/nature02091 (2003).
33. Nikolopoulos, L. A. A. *et al*. Second order autocorrelation of an XUV attosecond pulse train. *Physical review letters* **94**, 113905, https://doi.org/10.1103/PhysRevLett.94.113905 (2005).
34. Nabekawa, Y. *et al*. Interferometric autocorrelation of an attosecond pulse train in the single-cycle regime. *Physical review letters* **97**, 153904, https://doi.org/10.1103/PhysRevLett.97.153904 (2006).
35. Nabekawa, Y. *et al*. Conclusive evidence of an attosecond pulse train observed with the mode-resolved autocorrelation technique. *Physical review letters* **96**, 83901, https://doi.org/10.1103/PhysRevLett.96.083901 (2006).
36. Faucher, O. *et al*. Four-dimensional investigation of the 2nd order volume autocorrelation technique. *Appl. Phys. B* **97**, 505–510, https://doi.org/10.1007/s00340-009-3559-z (2009).
37. Heissler, P. *et al*. Two-photon above-threshold ionization using extreme-ultraviolet harmonic emission from relativistic laser–plasma interaction. *New J. Phys.* **14**, 43025, https://doi.org/10.1088/1367-2630/14/4/043025 (2012).
38. Kolliopoulos, G. *et al*. Single-shot autocorrelator for extreme-ultraviolet radiation. *J. Opt. Soc. Am. B* **31**, 926, https://doi.org/10.1364/JOSAB.31.000926 (2014).
39. Kruse, J. E. *et al*. Inconsistencies between two attosecond pulse metrology methods. A comparative study. Phys. Rev. A 82; https://doi.org/10.1103/PhysRevA.82.021402 (2010).
40. Kobayashi, Y., Sekikawa, T., Nabekawa, Y. & Watanabe, S. 27-fs extreme ultraviolet pulse generation by high-order harmonics. *Opt. Lett.* **23**, 64, https://doi.org/10.1364/OL.23.000064 (1998).
41. Descamps, D., Roos, L., Delfin, C., L'Huillier, A. & Wahlström, C.-G. Two- and three-photon ionization of rare gases using femtosecond harmonic pulses generated in a gas medium. *Phys. Rev. A* **64**, 273, https://doi.org/10.1103/PhysRevA.64.031404 (2001).
42. Sekikawa, T., Ohno, T., Yamazaki, T., Nabekawa, Y. & Watanabe, S. Pulse Compression of a High-Order Harmonic by Compensating the Atomic Dipole Phase. *Phys. Rev. Lett.* **83**, 2564–2567, https://doi.org/10.1103/PhysRevLett.83.2564 (1999).
43. Nabekawa, Y., Hasegawa, H., Takahashi, E. J. & Midorikawa, K. Production of doubly charged helium ions by two-photon absorption of an intense sub-10-fs soft x-ray pulse at 42 eV photon energy. *Physical review letters* **94**, 43001, https://doi.org/10.1103/PhysRevLett.94.043001 (2005).
44. Manschwetus, B. *et al*. Two-photon double ionization of neon using an intense attosecond pulse train. *Phys. Rev. A* **93**; https://doi.org/10.1103/PhysRevA.93.061402 (2016).

45. Miyamoto, N. *et al.* Observation of two-photon above-threshold ionization of rare gases by xuv harmonic photons. *Physical review letters* **93**, 83903, https://doi.org/10.1103/PhysRevLett.93.083903 (2004).
46. Sekikawa, T., Katsura, T., Miura, S. & Watanabe, S. Measurement of the intensity-dependent atomic dipole phase of a high harmonic by frequency-resolved optical gating. *Physical review letters* **88**, 193902, https://doi.org/10.1103/PhysRevLett.88.193902 (2002).
47. Chatziathanasiou, S. *et al.* Generation of Attosecond Light Pulses from Gas and Solid State Media. *Photonics* **4**, 26, https://doi.org/10.3390/photonics4020026 (2017).
48. Chen, S., Rever, M., Zhang, P., Theobald, W. & Umstadter, D. Observation of relativistic cross-phase modulation in high-intensity laser-plasma interactions. *Physical review. E, Statistical, nonlinear, and soft matter physics* **74**, 46406, https://doi.org/10.1103/PhysRevE.74.046406 (2006).
49. Gordienko, S., Pukhov, A., Shorokhov, O. & Baeva, T. Relativistic Doppler effect: universal spectra and zeptosecond pulses. *Phys. Rev. Lett.* **93**, 115002, https://doi.org/10.1103/PhysRevLett.93.115002 (2004).
50. Bulanov, S. V., Naumova, N. M. & Pegoraro, F. Interaction of an ultrashort, relativistically strong laser pulse with an overdense plasma. *Physics of Plasmas* **1**, 745–757, https://doi.org/10.1063/1.870766 (1994).
51. Tarasevitch, A., Lobov, K., Wünsche, C. & Linde, Dvonder Transition to the relativistic regime in high order harmonic generation. *Phys. Rev. Lett.* **98**, 103902, https://doi.org/10.1103/PhysRevLett.98.103902 (2007).
52. Jafari, B. & Soofi, H. High bandwidth and responsivity mid-infrared graphene photodetector based on a modified metal-dielectric-graphene architecture. *Applied optics* **58**, 6280–6287, https://doi.org/10.1364/AO.58.006280 (2019).
53. Kahaly, S. *et al.* Direct observation of density-gradient effects in harmonic generation from plasma mirrors. *Physical review letters* **110**, 175001, https://doi.org/10.1103/PhysRevLett.110.175001 (2013).
54. Thaury, C. *et al.* Plasma mirrors for ultrahigh-intensity optics. *Nat Phys* **3**, 424–429, https://doi.org/10.1038/nphys595 (2007).
55. Tsakiris, G. D., Eidmann, K., Meyer-ter-Vehn, J. & Krausz, F. Route to intense single attosecond pulses. *J. Opt. Soc. Am. B* **8**, 19, https://doi.org/10.1088/1367-2630/8/1/019 (2006).
56. Nomura, Y. *et al.* Attosecond phase locking of harmonics emitted from laser-produced plasmas. *Nat Phys* **5**, 124–128, https://doi.org/10.1038/nphys1155 (2008).
57. Heyl, C. M., Arnold, C. L., Couairon, A. & L'Huillier, A. Introduction to macroscopic power scaling principles for high-order harmonic generation. *J. Phys. B: At. Mol. Opt. Phys.* **50**, 13001, https://doi.org/10.1088/1361-6455/50/1/013001 (2017).
58. Seres, J. *et al.* Coherent superposition of laser-driven soft-X-ray harmonics from successive sources. *Nat Phys* **3**, 878–883, https://doi.org/10.1038/nphys775 (2007).
59. Nayak, A. *et al.* Multiple ionization of argon via multi-XUV-photon absorption induced by 20-GW high-order harmonic laser pulses. *Phys. Rev. A* **98**, 66, https://doi.org/10.1103/PhysRevA.98.023426 (2018).
60. Duris, J. *et al.* Tunable isolated attosecond X-ray pulses with gigawatt peak power from a free-electron laser. *Nature Photonics* **14**, 30–36, https://doi.org/10.1038/s41566-019-0549-5 (2020).
61. Constant, E. *et al.* Optimizing High Harmonic Generation in Absorbing Gases: Model and Experiment. *Phys. Rev. Lett.* **82**, 1668–1671, https://doi.org/10.1103/PhysRevLett.82.1668 (1999).
62. Hergott, J.-F. *et al.* Extreme-ultraviolet high-order harmonic pulses in the microjoule range. Phys. Rev. A 66; https://doi.org/10.1103/PhysRevA.66.021801 (2002).
63. Tzallas, P. *et al.* Generation of intense continuum extreme-ultraviolet radiation by many-cycle laser fields. *Nat Phys* **3**, 846–850, https://doi.org/10.1038/nphys747 (2007).
64. Skantzakis, E., Tzallas, P., Kruse, J., Kalpouzos, C. & Charalambidis, D. Coherent continuum extreme ultraviolet radiation in the sub-100-nJ range generated by a high-power many-cycle laser field. *Opt. Lett.* **34**, 1732–1734, https://doi.org/10.1364/OL.34.001732 (2009).
65. Kolliopoulos, G., Carpeggiani, P. A., Rompotis, D., Charalambidis, D. & Tzallas, P. A compact collinear polarization gating scheme for many cycle laser pulses. *The Review of scientific instruments* **83**, 63102, https://doi.org/10.1063/1.4725590 (2012).
66. Dacasa, H. *et al.* Single-shot extreme-ultraviolet wavefront measurements of high-order harmonics. *Opt. Express* **27**, 2656–2670, https://doi.org/10.1364/OE.27.002656 (2019).
67. Tzallas, P. *et al.* Time gated ion microscopy of light-atom interactions. *J. Opt.* **20**, 24018, https://doi.org/10.1088/2040-8986/aaa326 (2018).
68. Isinger, M. *et al.* Accuracy and precision of the RABBIT technique. *Philosophical transactions. Series A, Mathematical, physical, and engineering sciences* **377**, 20170475, https://doi.org/10.1098/rsta.2017.0475 (2019).
69. Chatziathanasiou, S., Kahaly, S., Charalambidis, D., Tzallas, P. & Skantzakis, E. Imaging the source of high-harmonics generated in atomic gas media. *Opt. Express* **27**, 9733, https://doi.org/10.1364/OE.27.009733 (2019).
70. He, X. *et al.* Spatial and spectral properties of the high-order harmonic emission in argon for seeding applications. *Phys. Rev. A* **79**, 888, https://doi.org/10.1103/PhysRevA.79.063829 (2009).
71. Wahlstroem, C.-G. *et al.* High-order harmonic generation in rare gases with an intense short-pulse laser. *Phys. Rev. A* **48**, 4709–4720, https://doi.org/10.1103/PhysRevA.48.4709 (1993).
72. Quintard, L. *et al.* Optics-less focusing of XUV high-order harmonics. *Science advances* **5**, eaau7175, https://doi.org/10.1126/sciadv.aau7175 (2019).
73. Lewenstein, M., Balcou, P., Ivanov, M. Y., L'Huillier, A. & Corkum, P. B. Theory of high-harmonic generation by low-frequency laser fields. *Phys. Rev. A* **49**, 2117–2132, https://doi.org/10.1103/PhysRevA.49.2117 (1994).
74. Wikmark, H. *et al.* Spatiotemporal coupling of attosecond pulses. Proceedings of the National Academy of Sciences of the United States of America; https://doi.org/10.1073/pnas.1817626116 (2019).
75. Kühn, S. *et al.* The ELI-ALPS facility. The next generation of attosecond sources. *J. Phys. B: At. Mol. Opt. Phys.* **50**, 132002, https://doi.org/10.1088/1361-6455/aa6ee8 (2017).

Acknowledgements

We acknowledge support of this work by the LASERLAB- EUROPE (EC's Seventh Framework Programme Grant No. 284464), Hellenic Foundation for Research and Innovation (HFRI) and the General Secretariat for Research and Technology (GSRT) under grant agreements [GAICPEU (Grant No 645)] and the HFRI PhD Fellowship grant (GA. no. 4816), "HELLAS-CH" (MIS Grant No. 5002735) [which is implemented under the "Action for Strengthening Research and Innovation Infrastructures," funded by the Operational Program "Competitiveness, Entrepreneurship and Innovation" (NSRF 2014–2020) and co-financed by Greece and the European Union (European Regional Development Fund)], and the European Union's Horizon 2020 research ELI-ALPS is supported by the European Union and cofinanced by the European Regional Development Fund (GINOP Grant No. 2.3.6-15-2015-00001), and innovation program under Marie Sklodowska-Curie MEDEA Grant No. 641789. JP, PJ and ALH acknowledge the support of the Swedish Research Council, the Swedish Foundation for Strategic Research and the Knut and Alice Wallenberg Foundation. We thank G. Konstantinidis and G. Deligiorgis from the Materials and Devices Division of FORTH-IESL for their support in maintaining the quality of the optical components.

Author contributions

I.M., I.O., E.S., I.L. have participated in all experimental runs, in the data analysis and in the preparation of the manuscript, and P.T. has designed the beamline and participated in all parts of the work, A.N. participated in the Ar measurements and did numerical calculation, J.P. and B.M. participated in the Ne and He measurements, C.K. did laser work and participated in the preparation of the manuscript, N.P. has performed all I.T. and automation work, M.D. and S.K. took part in initial experimental runs and in the data analysis, K.V., P.J. and A.L'H. contributed to the evaluation of the beam-line, to the preparation of the non-linear studies and to the preparation of the manuscript and DC has coordinated the work and contributed to the majority of its different parts.

Competing interests

The authors declare no competing interests.

Additional information

Correspondence and requests for materials should be addressed to D.C.

Reprints and permissions information is available at www.nature.com/reprints.

Publisher's note Springer Nature remains neutral with regard to jurisdictional claims in published maps and institutional affiliations.

Paper VI

J. W. L. Lee, D. S. Tikhonov, P. Chopra, S. Maclot, A. L. Steber, S. Gruet, F. Allum, R. Boll, X. Cheng, S. Düsterer, B. Erk, D. Garg, L. He, D. Heathcote, M. Johny, M. M. Kazemi, H. Köckert, J. Lahl, A. K. Lemmens, D. Loru, R. Mason, E. Müller, T. Mullins, P. Olshin, C. Passow, **J. Peschel**, D. Ramm, D. Rompotis, N. Schirmel, S. Trippel, J. Wiese, F. Ziaee, S. Bari, M. Burt, J. Küpper, A. M. Rijs, D. Rolles, S. Techert, P. Eng-Johnsson, M. Brouard, C. Vallance, B. Manschwetus, and M. Schnell

Time-Resolved Relaxation and Fragmentation of Polycyclic Aromatic Hydrocarbons Investigated in the Ultrafast XUV-IR Regime

Accepted in Nature Communications

Time-Resolved Relaxation and Fragmentation of Polycyclic Aromatic Hydrocarbons Investigated in the Ultrafast XUV-IR Regime

J. W. L. Lee,[†,‡,⊥⊥] D. S. Tikhonov,[†,¶,⊥⊥] P. Chopra,[†,¶] S. Maclot,[§,‖] A. L. Steber,[†,¶,⊥] S. Gruet,[†] F. Allum,[‡] R. Boll,[#] X. Cheng,[†] S. Düsterer,[†] B. Erk,[†] D. Garg,[†,@] L. He,[△] D. Heathcote,[‡] M. Johny,[△] M. M. Kazemi,[†] H. Köckert,[‡] J. Lahl,[§] A. K. Lemmens,[▽,††] D. Loru,[†,¶] R. Mason,[‡] E. Müller,[†] T. Mullins,[△] P. Olshin,[‡‡] C. Passow,[†] J. Peschel,[§] D. Ramm,[†] D. Rompotis,[#,†] N. Schirmel,[†] S. Trippel,[△,⊥] J. Wiese,[△,¶¶] F. Ziaee,[§§] S. Bari,[†] M. Burt,[‡] J. Küpper,[△,⊥,@,¶¶] A. M. Rijs,[▽] D. Rolles,[§§] S. Techert,[†,‖‖] P. Johnsson,[§] M. Brouard,[‡] C. Vallance,[‡] B. Manschwetus,[*,†] and M. Schnell[*,†,¶]

†*Deutsches Elektronen-Synchrotron DESY, Notkestraße 85, 22607 Hamburg, Germany*

‡*The Chemistry Research Laboratory, University of Oxford, United Kingdom*

¶*Institute of Physical Chemistry, Christians-Albrecht-Universität zu Kiel, Kiel, Germany*

§*Atomic Physics, Department of Physics, Lund University, Sweden*

‖*Physics Department, University of Gothenburg, Sweden*

⊥*Center for Ultrafast Imaging, Universität Hamburg, Germany*

#*European XFEL, Schenefeld, Germany*

@*Department of Physics, Universität Hamburg, Germany*

△*Center for Free-Electron Laser Science, Deutsches Elektronen-Synchrotron DESY, Hamburg, Germany*

▽*Radboud University, FELIX Laboratory, The Netherlands*

††*Van't Hoff Institute for Molecular Sciences, University of Amsterdam*

‡‡*Saint Petersburg State University, Saint Petersburg, Russia*

¶¶*Department of Chemistry, Universität Hamburg, Germany*

§§*J.R. Macdonald Laboratory, Department of Physics, Kansas State University, Manhattan, KS, USA*

‖‖*Institute for X-Ray Physics, Georg-August-Universität, Göttingen, Germany*

⊥⊥*These authors contributed equally to this work.*

E-mail: bastian.manschwetus@desy.de; melanie.schnell@desy.de

Abstract

Polycyclic aromatic hydrocarbons (PAHs) play an important role in interstellar chemistry and are subject to high energy photons that can induce excitation, ionization, and fragmentation. Previous studies have demonstrated electronic relaxation of parent PAH monocations over 10-100 femtoseconds as a result of beyond-Born-Oppenheimer coupling between the electronic and nuclear dynamics. Here, we investigate three PAH molecules, fluorene, phenanthrene, and pyrene, using ultrafast XUV and IR laser pulses. Simultaneous measurements of the ion yields, ion momenta, and electron momenta as a function of laser pulse delay allow a detailed insight into the various molecular processes. Relaxation times are reported for the electronically excited PAH^*, PAH^{+*} and PAH^{2+*} states, and the time-dependent conversion between fragmentation pathways is also shown. Recoil-frame covariance analysis between recorded ion images demonstrates that the dissociation of the PAH^{2+} ions favors reaction pathways involving two-body breakup and/or loss of neutral fragments totaling an even number of carbon atoms.

Graphical TOC Entry

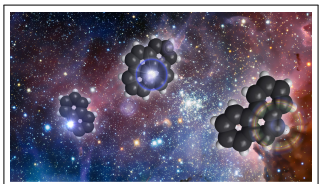

Polycyclic aromatic hydrocarbons play an important role in interstellar chemistry and are subject to high energy photon radiation. Ultrafast relaxation and fragmentation processes are investigated in time-dependent pump-probe XUV-IR experiments.

I Introduction

Polycyclic aromatic hydrocarbons (PAHs) are abundant molecules in the interstellar medium (ISM), accounting for approximately 10% of the total galactic carbon, according to infrared (IR) emission spectra measured by the Spitzer Space Telescope.[1,2] PAHs undergo a variety of processes upon irradiation, including ionization, dehydrogenation, fragmentation, and isomerization, and the influence of PAHs on the thermodynamics and chemistry of the ISM has motivated laboratory research for many decades.[3,4] The conditions of low temperature, low density, and strong photon radiation means that these unimolecular reactions become more important compared to a terrestrial environment and are key to the structure and evolution of the ISM.[5–7]

Previous studies into the ionization and fragmentation of PAHs have employed synchrotron and rare gas lamps as photon sources up to the extreme ultraviolet (XUV) and X-ray wavelengths.[8–12] Photoelectron photoion photoion coincidence (PEPIPICO) experiments demonstrated that the interaction of PAHs with XUV photons yielded a PAH^{2+}/PAH^{+} ratio of approximately 0.25 for naphthalene at the highest photon energy of 40.8 eV.[13] These studies also investigated the decay mechanisms of doubly-charged PAHs (naphthalene-d_8, naphthalene-h_8, and azulene), revealing prominent dissociation channels into two monocations where zero, two and four carbon atoms were lost in neutral co-fragments.[14,15] Such experiments provide important information on the photofragmentation products and give an insight into molecules that may exist in the ISM but have not yet been assigned by spectral features.

PAHs also provide a framework to explore ultrafast dynamics and beyond-Born-Oppenheimer effects. Within the Born-Oppenheimer approximation, electrons are assumed to move much faster than the nuclei, and the electronic and nuclear frameworks can therefore be treated separately. If the electronic and nuclear motion are instead strongly coupled, this can result in the ultrafast energy transfer from electronic excitation into nuclear motion, and the Born-Oppenheimer approximation breaks down.[16–20] Non-adiabatic electronic relaxation has been demonstrated in recent ultrafast time-resolved studies on a series of small PAHs revealing electronic lifetimes of the monocation in the range 30 - 55 fs.[21] Theoretical calculations suggest the presence of conical intersections facilitating the rapid electronic relaxation. Experiments by the same group indicate that the electronic lifetimes increase with both the molecular size and the cationic excitation energy, and that multi-electronic and non-Born-Oppenheimer

effects must be accounted for to provide accurate theoretical calculations.[22–24]

Here, we present femtosecond XUV-IR pump-probe experiments from the Free-Electron Laser (FEL) FLASH in Hamburg,[25] studying the ultrafast photoinduced dynamics of fluorene (FLU), phenanthrene (PHE), and pyrene (PYR). The structure of these molecules is shown in Figure 1. This comparative study using 30.3 nm (40.9 eV) XUV photons, corresponding to the He II emission line, a dominant spectral line in the interstellar environment, provides valuable insight into the stability and the accessible reaction pathways of these complex molecules.[26] The time-resolved photodynamics of these PAHs are investigated by concurrently recording the photoelectrons using velocity-map imaging (VMI) and the photoions by VMI and time-of-flight mass spectrometry. In addition to determining PAH^{+*} excited state lifetimes similar to those reported in the HHG study by Marciniak *et al.*,[21] our measurements demonstrate ultrafast relaxation for the PAH^{*} and PAH^{2+*} species. Furthermore, the application of recoil-frame covariance analysis to the ion images provides a detailed mechanistic insight into the fragmentation pathways of the PAH^{2+} ions, demonstrating a strong preference for dissociation into two monocations, where neutral co-fragments contain an even number of carbon atoms.[27–31] Theoretical calculations, reported in Sections S1 and S8 of the SI, support both the electronic relaxation times and the fragmentation channels observed.

II Results

A. Time-Independent Results

The mass spectra obtained following irradiation of FLU, PHE, and PYR with 30.3 nm FEL light are shown in Figure 1. The spectra are dominated by the cations (PAH^{+}) and dications (PAH^{2+}) of the respective parents, with small signals from triply ionized molecules also visible. Multiple fragment ions are also seen. The FEL power was set to minimize the formation of PAH^{2+} and PAH^{3+} ions whilst maximizing the PAH^{+} ion yield to avoid multi-photon interactions. In line with the results of previous studies, fragmentation is more pronounced for the two smaller PAHs, FLU and PHE, than for PYR.[32] The parent ion peaks are generally much sharper than the fragment peaks as a result of peak broadening associated with kinetic energy release during the fragmentation process. To illustrate this

further, the insets to Figure 1 show the symmetrized velocity-map ion images for the PAH^{2+} dication and one of the fragmentation products, $C_2H_x^+$, for FLU. The velocity distribution of the dication reflects that of the neutral parent molecule within the molecular beam, which is essentially unaffected by loss of two electrons, while the fragment ion ($C_2H_x^+$) possesses significant recoil velocity as a result of the kinetic energy released during the parent ion dissociation. The nomenclature of, for example, $C_2H_x^+$ and $C_8H_y^+$, is used throughout this discussion to refer to all monocations with two and eight carbon atoms, respectively, where x and y encapsulate the possible hydrogen atom values for the fragment.

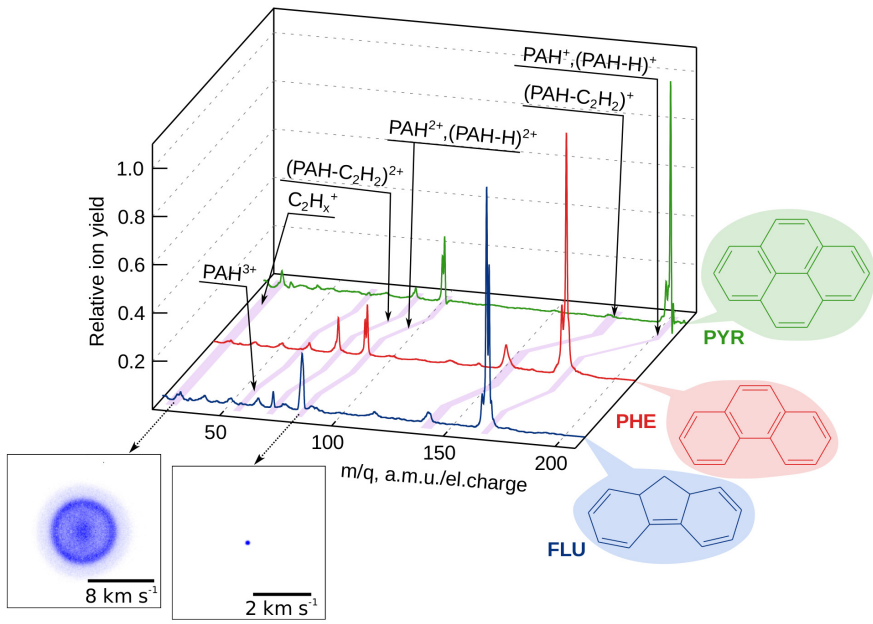

Figure 1: Ion mass spectra for the three PAH molecules, pyrene (PYR), phenanthrene (PHE), and fluorene (FLU), after irradiation with the FEL FLASH at 30.3 nm. Intensities are normalized on the height of the respective parent ion PAH^+. Insets show the velocity-map images for the PAH^{2+} dication and $C_2H_x^+$ for FLU (four-fold symmetrization about the laser polarization and vertical axis applied).

The velocity-map images provide the 2D projection of the velocity distribution of each detected fragment. Because the velocity distributions for all fragments are recorded simultaneously for each laser pulse, a covariance analysis of the data set allows statistical correlations between the velocities of two or

more fragments to be investigated.[27] This provides the correlated velocity distributions of two fragments from the data set, which is a powerful tool for determining the fragmentation processes occuring. The covariance-mapping procedure has been described in previous publications[28–31] and is detailed further in the Methods section. Briefly, in a covariance image, cov(A, B), one of the two fragments is chosen to be the 'reference' ion (B), and the covariance-map image reveals the velocity distribution of the ion of interest (A) relative to the trajectory direction of the reference ion. In the simplest example, for a parent dication undergoing unimolecular dissociation into two monocations, A and B, the trajectories of A and B will always be directly opposed due to conservation of momentum. Therefore, assuming no other formation pathways, the appearance of cov(A, B) would strongly resemble a single point directly opposed from the reference direction. Due to rotational freedom of the molecule in and out of the detector plane, signal leading from the point to the center of the covariance image would also be expected.

In this experiment, as hydrogen loss is difficult to resolve using ion imaging (limited by the phosphor screen decay time and the time resolution of the PImMS sensor), the discussion focuses on fragmentation of the carbon framework. Figure 2(a) shows the raw velocity-map images recorded for the $C_3H_x^+$ and $C_{10}H_y^+$ fragments of the dissociative ionization of FLU, $C_{13}H_{10}$. The two images potentially contain contributions from the dissociation of singly-charged, doubly-charged, and more highly charged parent ions. Performing the covariance analysis isolates the fragmentation of the doubly-charged parent ion to form two monocations, which corresponds to the higher velocity ring component seen in the velocity-map images. Figure 2(b) shows the recoil-frame covariance images of $C_3H_x^+$ relative to the $C_{10}H_y^+$ reference ion (left), and vice versa (right), with black arrows indicating the direction of the reference ion. As expected for a two-body dissociation, the two fragments recoil in opposite directions, i.e., the covariance signal is seen 180° from the reference direction, due to conservation of momentum, as described above. The relative speeds of the two fragments are determined by their individual masses: the heavier $C_{10}H_y^+$ recoils more slowly than the lighter $C_3H_x^+$ fragment, yielding a covariance signal closer to the center of the image. Converting the spatial coordinates in the covariance images to momentum units and performing an angular integration gives the momentum profiles shown in Figure 2(c)(ii). As expected, there is excellent agreement between the momentum profiles obtained from the cov($C_3H_x^+$,$C_{10}H_y^+$) and

cov($C_{10}H_x^+$,$C_3H_y^+$) covariance maps.

Further to this, the recoil-frame covariance analysis can be performed between all $C_nH_x^+$ species for the PAHs. The resulting covariance maps for the FLU fragment ions are plotted as a matrix in Figure 3, providing a rich basis for elucidating the formation mechanisms for each fragment. The initial focus is on the covariance maps along the main diagonal of the matrix, highlighted by black squares in Figure 3. These correspond to the two-body dissociations of the doubly-charged parent, similar to the reaction $FLU^{2+} \rightarrow C_3H_x^+ + C_{10}H_y^+$ discussed above. Clear covariance signals can be seen for each of the ion pairs, demonstrating that, except for loss of a single carbon atom, all two-body dissociation processes of the carbon framework resulting in two monocations are possible from the PAH^{2+} parent. This may seem surprising given the extensive rearrangement of the carbon backbone that must occur for several of the dissociation pathways. Calculated dissociation energies for various channels of PAH^+ and PAH^{2+}, resulting in neutral, singly-, and doubly-charged fragments, are shown in Section S1 of the supplementary material. These energies were calculated assuming that absorption of an XUV photon primarily populates highly excited states where dissociation occurs rapidly without time for isomerization. Pathways that correspond to a doubly-charged parent ion fragmenting into two singly-charged ions, for example $C_{10}H_7^+ + C_3H_3^+$ or $C_9H_6^+ + C_4H_4^+$, are predicted to have relatively low dissociation energies, which are energetically consistent with the observation of many such fragmentation channels in the covariance map images. Each of the two-body dissociation processes also shows excellent momentum matching in the covariance maps, as plotted in Figure 2(c)(i)-(v).

In addition to seeing covariances between the ion pairs that have masses totaling the molecular mass, prominent covariances are seen between ion pairs that are an even number of carbon units deficient from the parent mass. Ion pairs that are two and four carbon units deficient from the parent mass are highlighted with blue and red squares, respectively, in Figure 3. The covariance signal between $C_3H_x^+$ and $C_8H_y^+$ in Figure 3 demonstrates a dissociation pathway that would be consistent with the reaction $C_{13}H_{10}^{2+} \rightarrow C_3H_x^+ + C_8H_y^+ + C_2H_2$, and the velocities of the $C_3H_x^+$ and $C_8H_y^+$ ions match the Coulombic repulsion expected between two monocations. Similarly, the covariance signals between $C_3H_x^+$ and $C_6H_y^+$ demonstrate two-body dissociation from the parent dication with four carbon atoms lost in neutral fragments. Previous PEPIPICO studies investigating the dissociative ionization of PAH

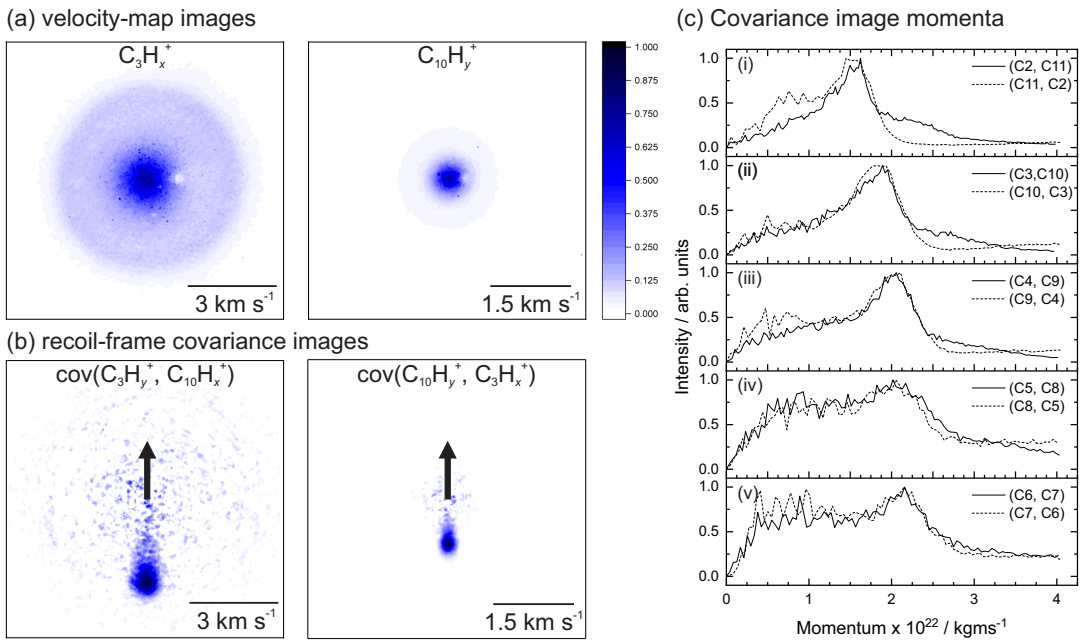

Figure 2: (a) Velocity-map images and (b) covariance-map images for the $C_3H_x^+$ and $C_{10}H_y^+$ fragment ions arising from dissociative ionization of FLU, $C_{13}H_{10}$. Each image is individually normalized. The velocity-map images are presented without symmetrization or Abel-inversion to provide a better comparison to the covariance images. The small areas lacking signal near the center of the velocity-map images are attributed to damage in the MCP/phosphor detector. Black arrows in the covariance images indicate the direction of the reference ion. (c) Momentum profiles of the ion pairs resulting from the two-body dissociative ionization of fluorene. An angular integration is performed on the covariance images, and the spatial coordinates are converted to momentum units. Cov(A, B) refers to the covariance of ion A with B as the reference ion. Discrepancies between the plots in (i) are attributed to physical defects in the detector and background ions affecting the ion images differently.

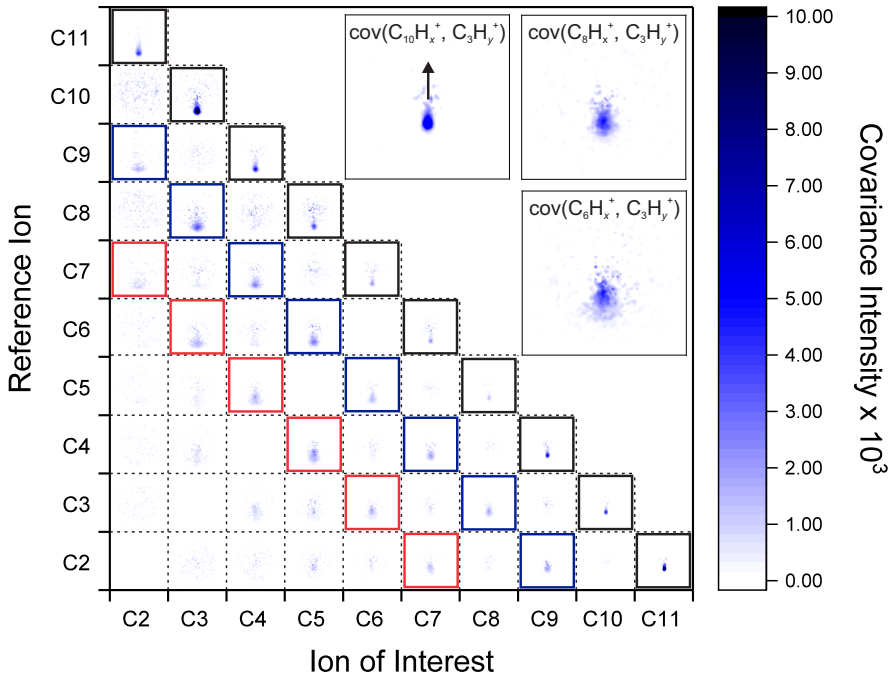

Figure 3: (a) The covariance-map images between all ion species produced from FLU. Axis labels refer to the number of carbons in the monocationic species and omit the number of hydrogen atoms. Fragment ion pairs that have a total number of carbons greater than that of the parent ion, for example, between $C_8H_x^+$ and $C_9H_x^+$, show no covariance as they cannot be formed as partners from the same parent molecule; these have been omitted for clarity. Any ion species will also always show covariance with itself (autocovariance), and these entries have also been omitted. Notably, signal in the cells along the main diagonal of the matrix (highlighted in black) corresponds to the two-body dissociation pathways from the FLU^{2+} ion. Additionally, the cells highlighted in blue and red correspond to the dissociation pathways where two and four carbon atoms, respectively, are lost in neutral co-fragments. Inset: expansions for the maps corresponding to cov($C_{10}H_x^+$, $C_3H_y^+$), cov($C_8H_x^+$, $C_3H_y^+$), cov($C_6H_x^+$, $C_3H_y^+$) showing increased blurring as more carbon atoms are lost in neutral co-fragments. The black arrow indicates the direction of the reference ion in all covariance-maps.

molecules at XUV wavelengths have attributed similar observations to the loss of one or more neutral acetylene (C_2H_2) molecules.[13,14]

It is observed that as more carbon atoms are lost in neutral molecules, the covariance maps become successively more blurred, e.g. as shown in the insets in Figure 3 comparing cov($C_{10}H_x^+$, $C_3H_y^+$), cov($C_8H_x^+$, $C_3H_y^+$), and cov($C_6H_x^+$, $C_3H_y^+$). Assuming that the two carbons are lost as a neutral C_2H_2 molecule, this may result either from secondary fragmentation ($PAH^{2+} \rightarrow m_1^+ + m_2^+ \rightarrow m_1^+ + m_3^+ + C_2H_2$) or from deferred charge separation reactions ($PAH^{2+} \rightarrow C_2H_2 + m_1^{2+} \rightarrow C_2H_2 + m_2^+ + m_3^+$). In both cases, blurring in the covariance images would be expected. These pathways would usually be differentiated by observing the gradient of the regression line in an ion-TOF ion-TOF covariance plot,[33] as previously performed for naphthalene-d8, demonstrating deferred charge separation.[14] The ion-TOF ion-TOF partial covariance plots for the PAH molecules in our study are shown in Section S2 of the SI, following correction for the FEL and IR shot-to-shot intensity fluctuations. Some two-body dissociation pathways from the parent dication are visible, but three-body dissociations cannot be discerned above the noise level, preventing this technique from being applied. There is currently ongoing work exploring the use of the ion images to create an ion-momentum ion-momentum covariance plot to differentiate the dissociation pathways.

The recoil-frame covariance results for PHE and PYR are shown in Section S3 of the SI. These similarly demonstrate a propensity for dissociation pathways from the parent dication into two monocations, with either zero or an even number of carbon atoms lost in neutral co-fragments. The signal levels for PYR^{2+} fragmentation are notably lower than for FLU^{2+} and PHE^{2+}, matching previous studies commenting that larger PAH molecules such as PYR tend to form stable parent cations and undergo less dissociative ionization compared to smaller PAHs.[34,35]

B. Time-Dependent Results

In this section, we present the effect of applying a 30.3 nm XUV pulse and 810 nm pulse at various delays on the three PAHs. This analysis integrates the electron VMI, ion VMI, and ion TOF measurements. Analysis of the helium carrier gas photoelectron sideband lines in the electron images provides an independent and accurate measurement of when the two laser pulses overlap in time (t_0), outlined in

more detail in Section S4 of the SI. For the PAHs in this investigation, there are two major two-color reaction pathways depending on which laser pulse arrives first, as shown in the schematic in Figure 4(b):

- Scenario 1: The XUV pulse interacts with the PAH to produce an electronically excited charged molecule, which can rapidly decay to produce a vibrationally hot parent species. Absorption of one or more IR photons before electronic relaxation can cause electronic excitation and/or promote the molecule to the next charge state. If further ionization is induced, the ejected electron typically has low kinetic energy (LKE), as each IR photon is low in energy. In this analysis, LKE electrons are defined as having a kinetic energy lower than 2 eV, compared to the 1.53 eV of the IR photons. Increasing the delay between the XUV and the IR pulse allows the molecule to electronically relax, thus increasing fragmentation caused by the IR pulse through loss of H, C_2H_2 or other neutral or charged species.

- Scenario 2: The IR pulse interacts with the PAH, producing a vibrationally and electronically excited neutral molecule by multiphoton excitation. In the excited state, absorption of an XUV photon has an increased probability of leading to ionization or dissociative ionization. Evidence for this scenario is demonstrated in the analysis of the time-dependent PAH parent ions described below, where the fits were significantly improved by introducing a channel representing this pathway, i.e., before t_0. The IR pulse is strong enough to produce PAH^+ ions directly but in a negligible quantity compared to the XUV pulse. Comparative TOF spectra are shown in Section S5 of the SI.

For all PAHs, the XUV/IR laser regime creates significant quantities of both fragment and parent ions. The delay-dependent yields of these are considered separately in the following sections.

B.1 Fragment Ions

The XUV/IR pump-probe experiments create all possible singly-charged ions with the exception of CH_x^+, consistent with previous studies.[13,14] For each fragment ion, a velocity-map image was extracted from the PImMS data and Abel-inverted using the polar onion-peeling method.[36] After performing an angular integral, the velocity distribution was converted to momentum and plotted as a function of

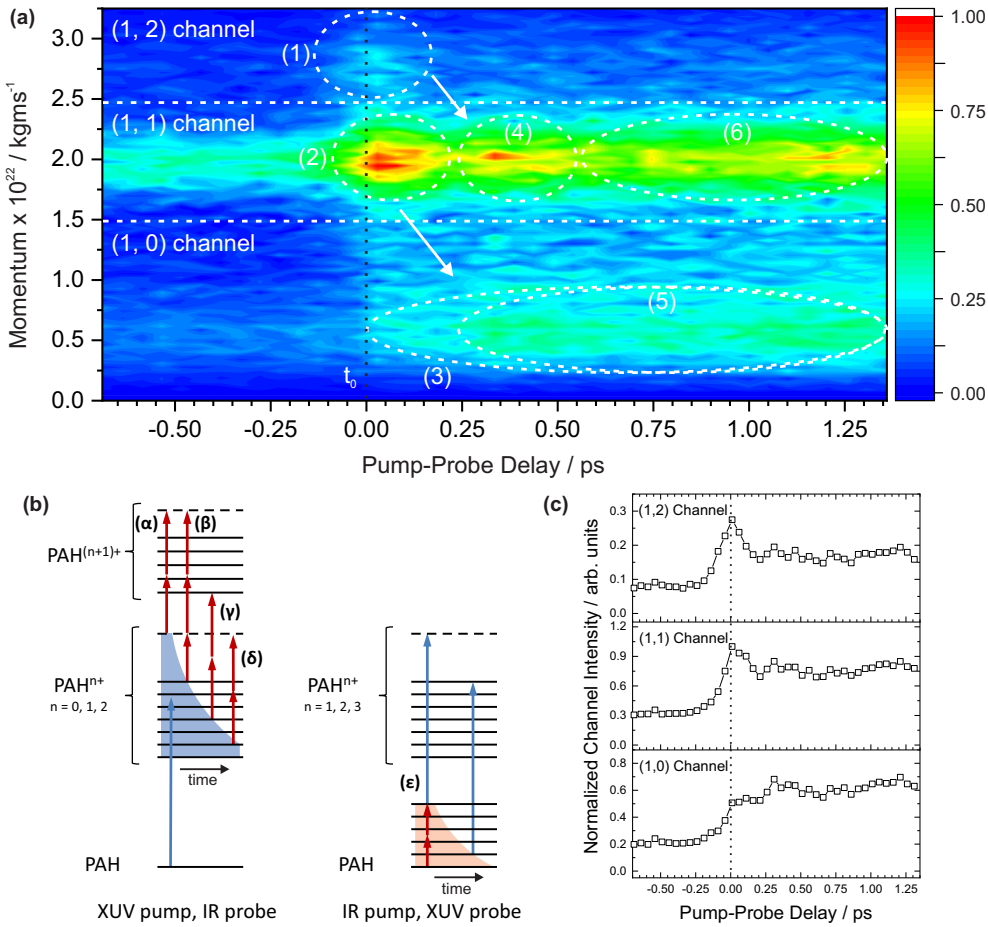

Figure 4: (a) The $C_3H_x^+$ momentum profile formed from FLU as a function of XUV-IR laser pulse delay. The IR pulse interacting with the molecular beam before the XUV pulse gives negative pump-probe delay values, whereas for positive pump-probe values, the XUV pulse interacts first. Channels and numbered features are described in the text. White arrows highlight the shift in channel yields from pathway β and γ to pathway δ, as denoted in (b). The vertical black dotted line indicates t_0 determined by the helium electron sidebands. (b) Schematic of the PAH states involved in this experiment. Solid black lines and dashed lines represent bound and dissociative electronic states, respectively. Blue and red arrows represent the effects of the XUV laser and IR laser pulses, respectively. The pump pulses are able to populate a multitude of electronic states, as represented by the blue and red shaded areas for the XUV and IR pulses, respectively. Electronic relaxation of the wavepacket over time is represented by the curvature in the shaded areas. The change in electronic states due to relaxation alters the product of the probe pulse. (c) Integrated plots of the (1, 0), (1, 1), and (1, 2) channels from (a). Plots are normalized to the maximum signal detected in the (1, 1) channel, and t_0 is represented by the dotted black line.

pump-probe delay. This discussion focuses on the $C_3H_x^+$ ion formation from FLU, shown in Figure 4(a), which had strong signal levels across the three PAHs studied. Momentum plots for $C_3H_x^+$ from PHE and PYR are shown in Section 3 of the SI, and other fragments will be discussed in a follow-up publication. The momentum plot can be divided into three regions:

- high momentum, referred to as the (1, 2) channel, with the $C_3H_x^+$ ion primarily recoiling against a dication or two other monocations.
- medium momentum, referred to as the (1, 1) channel, where $C_3H_x^+$ recoils against a monocation.
- low momentum, referred to as the (1, 0) channel, where there is no charged partner in the dissociation.

The (1, 2) and (1, 1) channels were confirmed by performing a covariance analysis between ion pairs, as described above. The integrated channel yields are plotted in Figure 4(c).

A transient increase in signal around t_0 is highlighted as feature (1) in Figure 4(a). At negative pump-probe delays, the IR pulse arrives before the XUV pulse, creating vibrationally and electronically excited PAH^* molecules. If the pump-probe delay is short (-100 to 0 fs), the PAH^* molecules remain in an excited state and the XUV pulse can induce ionization to PAH^{n+} (n = 1, 2, 3) states, as represented by path ε in Figure 4(b). Dissociation from the PAH^{3+} states produces fragments in the (1, 2) channel, explaining the increase in signal in feature (1) before t_0. After t_0, the XUV pulse precedes the IR pulse, and the XUV-only mass spectrum in Figure 1 demonstrates that the primary products are PAH^+ and PAH^{2+} ions. The IR pulse can induce dissociative ionization of the electronically hot PAH^{2+*}, represented by pathways α and β in Figure 4(b). This also produces ions in the (1, 2) channel.

Electronic relaxation following the initial laser pulse is represented in Figure 4(b) by the curvature in the blue and red shaded areas for the XUV pulse and IR pulse, respectively. Electronically excited PAH^{2+*} molecules produced by the XUV pulse relax during the time of the pump-probe delay; as the delay is increased, more energy is required from the IR pulse to initiate dissociative ionization. Consequently, the (1, 2) channel yield diminishes, and the IR pulse begins to favor dissociating the PAH^{2+} ion instead of promoting it to a PAH^{3+} state. This is represented in Figure 4(b) by pathways α, β, and γ converting to pathway δ as the molecule relaxes and is similar to the wavepacket evolution

identified for the PAH^{2+} ion in a previous HHG study.[21] This causes a signal increase in the (1, 1) channel after approximately 250 fs, labeled as feature (4) in Figure 4(a).

In the (1, 1) channel, an increase in signal can be seen around t_0, labeled feature (2). As noted for the (1, 2) channel, prior to t_0, the IR pulse primarily creates PAH^* molecules. Whilst electronically excited, the XUV pulse can more easily promote PAH^* to a dissociative PAH^{2+} state, as represented by pathway ε with n = 2. At positive pump-probe delay values, the XUV pulse creates significant quantities of PAH^+ and PAH^{2+}, which are subsequently promoted to a dissociative PAH^{2+} state by the IR pulse. These processes are represented by pathways β and δ with n = 1 and 2, respectively.

Two increases in signal are visible in the (1, 0) channel, one beginning at t_0, labeled feature (3), and one beginning after approximately 250 fs, labeled feature (5). Feature (3) is attributed primarily to the XUV pulse creating excited PAH^{+*}, which is dissociated by the IR pulse. This is represented by pathway δ with n = 1. Notably, the signal increase only begins after t_0, implying that the IR-pump, XUV-probe regime contribution to this channel is negligibly small. Feature (5) has a similar origin to feature (4) – the XUV pulse initially creates an ensemble containing highly excited PAH^{+*} ions which can be readily promoted to a PAH^{2+} state by the IR laser pulse at short pump-probe delays. However, at longer delay values, the ions electronically relax causing the IR laser to induce dissociation rather than ionization. Again, this can be represented as a shift from pathways α, β, and γ to δ.

An overall increase in signal is seen when the IR pulse arrives after the XUV pulse, even for very long pump-probe delays; for example the signal level in feature (6) compared to the signal before t_0. This is attributed to the XUV pulse creating excited parent ions PAH^{+*}, PAH^{2+*}, and PAH^{3+*}, which relax to their ground electronic states. The IR pulse induces dissociation in a fraction of the molecules so the PAH^+, PAH^{2+}, and PAH^{3+} ions contribute to the (1, 0), (1, 1), and (1, 2) fragment channels, respectively. This is shown by pathway δ in Figure 4(b).

B.2 Parent Ions

The delay-dependent formations of all ions can be plotted by integrating the appropriate arrival times of the TOF spectrum recorded from the MCP current. This provides a more accurate quantification of the ion signal compared to the ion images which are susceptible to saturation, particularly for parent

ions, which are always incident in the center of the detector. In addition, the behavior of LKE electrons can be monitored using the electron velocity-map images. Yields for the LKE electrons, the PAH^{2+} parent, and the (1, 2) $C_3H_x^+$ ions extracted from the ion images for FLU, PHE and PYR are shown in Figure 5. A Monte Carlo sampling procedure was used to produce the relaxation times of the excited PAH, PAH^+, and PAH^{2+} species.[37] A summarized description of the analysis is detailed below, and the analysis procedure is described briefly in the Methods section and in full in S6 of the SI. The relaxation constants for all PAH species are given in Table 1.

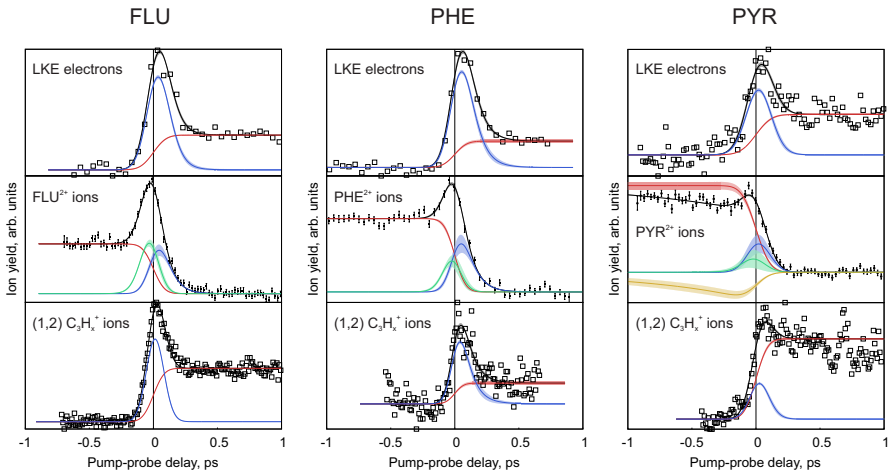

Figure 5: Delay-dependent yields of the LKE electrons, PAH^{2+}, and $C_3H_x^+$ ions from the (1, 2) channel formed from FLU, PHE, and PYR. The vertical black line represents t_0. LKE electrons are defined as having a kinetic energy below 2 eV. Details for the fitting procedure are described in the Methods section. The blue and green peak functions represent the XUV-pump, IR-probe and the IR-pump, XUV-probe laser regimes, respectively. The red sigmoidal curves represent the change in the PAH ionization states due to the pump laser. The PYR^{2+} curve additionally contains another peak function (in yellow) to account for slowly changing IR-pump dynamics reproduced over multiple measurements. The black curves show the sum of the peak functions and sigmoidal. Each data point in the PAH^{2+} plots results from averaging 1300 ± 200, 2000 ± 400, and 900 ± 400 measurements for FLU, PHE, and PYR, respectively (variation arises from jitter in the FEL pulse timing).

PAH^{+*} Lifetime When the IR pulse induces ionization, the molecule absorbs IR photons until the ionization energy is reached and the electron is ejected. As each photon is low in energy, the electron typically has low kinetic energy (LKE), defined in this study as below 2 eV. Figure 1 demonstrates that PAH^+ is the dominant product after interaction with the XUV pulse. This suggests that the transient

Table 1: Exponential decay lifetimes for the excited state of various charged parent species. The listed error values refer to the fit errors.

Exponential Lifetime / fs				
Charge State	FLU	FLU (Theory)	PHE	PYR
PAH^*	35 ± 8	54 ± 2	29 ± 17	62 ± 71
PAH^{+*}	57 ± 13	42 ± 8	76 ± 14	24 ± 11
PAH^{2+*}	17 ± 5	–	74 ± 19	28 ± 10

increase in the LKE electron yield is primarily due to ionization of PAH^{+*} to PAH^{2+} by the IR pulse. By fitting the LKE electron yield, the PAH^{+*} lifetime can be extracted for each PAH.

PAH^* Lifetime There are a significant number of possible processes leading to both the creation and depletion of the PAH^{2+} ion. For example, the XUV photon may form PAH^{2+*} directly, which is depleted by further ionization or dissociation by the IR pulse. However, as the yields of the other parent and fragment species are comparatively low, it is reasonable to fit the transient behavior using two major pathways, namely (i) the absorption of an XUV photon to form PAH^{+*} followed by ionization to PAH^{2+} by the IR pulse; and (ii) the IR pulse interacting with the molecule to generate an excited neutral PAH^*, which is ionized by the XUV pulse to generate PAH^{2+}. The transient behavior is therefore dependent on the relaxation times of both the PAH^{+*} and PAH^* species. By using the values for t_0 and the PAH^{+*} relaxation lifetimes determined from the electron data, the fitting procedure can isolate the PAH^* relaxation times. The PYR^{2+} trace was found to have a slow decrease in signal at t_0 (visible in Figure 5) that was reproduced over multiple scans. An additional peak function was used to fit this trace in order to produce the associated PYR* lifetime.

PAH^{2+*} Lifetime As discussed in Section B.1, the transient signal increase for $C_3H_x^+$ in the (1, 2) channel is dependent upon two pathways. Firstly, before t_0, the IR pulse creates an excited neutral PAH^* species, which undergoes dissociative ionization with an XUV photon to a PAH^{3+} state. Secondly, after t_0, the XUV laser pulse induces formation of PAH^{2+*}, which the IR laser pulse promotes to a dissociative PAH^{3+*} state. The time-dependence of the $C_3H_x^+$ ions in the (1, 2) channel is therefore governed by the lifetimes of the PAH^* and PAH^{2+*} states, which can be determined from the fitting procedure. The transient increase showed a good fit using a single Gaussian representing XUV-pump, IR-probe (centered after t_0), indicating the IR-pump, XUV-probe contribution to be small. Therefore, the (1, 2) channel for $C_3H_x^+$ was fitted using only the XUV-pump, IR-probe channel, allowing the PAH^{2+*} lifetime

to be extracted.

Theoretical Model Extensive theoretical calculations were performed to support the experimental results. Due to the computational requirements, these studies were restricted to calculating the FLU^* and FLU^{+*} electronic lifetimes. The approaches are described in the Methods section and in more detail in Section S8 of the SI.

To calculate the FLU^* lifetime, the effect of the IR laser pulse on an ensemble of molecules in various orientations was simulated explicitly. Following this, DFT-based trajectory surface hopping molecular dynamics (TSH-MD) calculations were used to track the dynamics of the states formed over 400 fs. The photoionization cross section of each electronic state was calculated to simulate the XUV laser pulse probing these states. Combining the population of the states and the photoionization cross section allows the time-dependent change in FLU^+ yield to be estimated at 54 ± 2 fs.

For the FLU^+ lifetimes, the effect of the XUV pulse on a ground state FLU molecule was simulated. 480 FLU^+ electronic states can be populated by an XUV photon, of which 180 are high enough in energy to be further ionized to FLU^{2+} by a 810 nm photon. Given the high number of states and the complicated potential energy surface topology, a linear vibronic coupling (LVC) model was used to perform TSH-MD simulations over 50 fs. The population that can be ionized by a 810 nm photon decreases as the population decays over time, thus giving rise to a decay constant of 42 ± 8 fs for the FLU^+ ion.

III Discussion

The PAHs studied are different sizes with different levels of bonding between the carbon rings; nonetheless, ultrafast electronic relaxation in the range 10-100 fs was observed for all molecules in all charge states, indicating that electronic relaxation on this timescale is likely to be ubiquitous across PAHs. Theoretical calculations show that with the high range of accessible electronic states, the populations resulting from IR or XUV excitation undergo ultrafast relaxation within this time range. Our value of 24 ± 11 fs for the PYR^{+*} lifetime (Table 1) roughly matches the measurement of 37 ± 3 fs by Marciniak *et al*,[21] with discrepancies primarily attributed to the difference in XUV photon energy (16-20 eV compared to 40.9 eV in this study).

Overall, our results provide a comprehensive view of the electronic and fragmentation dynamics of PAH molecules. The propensity for molecules to fragment with neutral fragments containing zero or an even number of carbon atoms provides valuable information for modelling the ISM, both in terms of the species that might be detected and potential reagents for interstellar chemistry. The abundance of accessible dissociation pathways consistent with the loss of one or more neutral C_2H_2 echoes the widely-accepted model for PAH growth called the hydrogen abstraction C_2H_2 addition (HACA) model.[38–40] Furthermore, the ubiquity of ultrafast relaxation times indicates that electronically-excited PAHs are generally short lived and such molecules in the ISM can be assumed to be in the electronic ground state. This greatly simplifies interstellar chemical modelling involving PAHs by reducing the number of accessible reaction pathways. Our work demonstrates how ultrafast XUV experiments can be used to simultaneously investigate the dissociation and ionization dynamics of complex systems and provide a more complete picture of the molecular processes.

IV Methods

A. Experiment

The time-resolved pump-probe experiments were performed at FLASH[41] using the CFEL-ASG Multi Purpose (CAMP) endstation[42] at beamline 1 (BL1). The CAMP endstation houses a double-sided velocity-map imaging (VMI) spectrometer for simultaneous measurement of the electron and ion kinetic energy and angular distributions. The FEL provided 30.3 nm (40.9 ± 0.4 eV) XUV pulses, which, from the electron pulse durations, were estimated to be 90 fs FWHM with a pulse energy of 25 µJ. In addition, to perform pump-probe measurements, the present study used 60 fs FWHM IR laser pulses at 810 nm. By measuring the IR laser pulse intensity and the focal spot size before the beam enters the chamber, the intensity of the IR laser pulse is estimated to be 1×10^{13} W/cm^2. The intensity was tuned so that the IR laser pulse was strong enough to induce a small level of single ionization of the parent molecules without causing significant fragmentation or double ionization (see supplementary material). An overview of the laser settings is given in Section S7 in the SI, and the laser is described by Redlin *et al.*[43]

The sample molecules FLU ($C_{13}H_{10}$, melting point (mp) = 116 °C), PHE ($C_{14}H_{10}$, mp = 101 °C), and PYR ($C_{16}H_{10}$, mp = 145 °C) were purchased from Sigma-Aldrich with 98% purity and used without further purification. The structures of these molecules are shown in Figure 1. The samples were placed in an in-vacuum reservoir and heated to approximately 220–230 °C to increase their respective vapor pressures. Using helium as a carrier gas (1.5-2 bar backing pressure), the molecules were then introduced into vacuum *via* a supersonic expansion produced by an Even-Lavie high-temperature pulsed valve,[44] using valve opening times of a few tens of microseconds. The resulting molecular beam was skimmed twice to yield well-collimated pulses of isolated PAH molecules.

In terms of the laser pulses employed, two experiments were performed: a) irradiating the molecules with the XUV light only, in order to explore its effect on the molecules and to allow the FEL pulse intensity to be tuned to minimize multi-photon effects by the FEL and b) time-resolved pump-probe experiments employing both the 30.3 nm FEL and 810 nm laser pulses. In the pump-probe experiments, the two laser pulses interacting with the molecules have a defined, adjustable time delay with respect to each other. The pump-probe delay is derived by subtracting the arrival time of the XUV pulse from the arrival time of the IR pulse; hence a positive pump-probe delay refers to the XUV pulse interacting with the molecules first, while a negative pump-probe delay refers to the IR pulse interacting with the molecules first. All pump-probe data was sorted into delay bins according to the bunch arrival monitors of the FLASH FEL in order to account for the FEL jitter.[45]

Ions were velocity-mapped onto a position-sensitive detector comprising a pair of microchannel plates (MCPs) coupled to a P47 phosphor screen.[46,47] The ion time-of-flight (TOF) spectra were recorded by coupling out the voltage drop at the back side of the MCP with a 2 GHz ADC (ADQ412AC-4G-MTCA) through a resistor-capacitor circuit. The ion images from the phosphor screen were captured by a Pixel Imaging Mass Spectrometry 2 (PImMS2) multi-mass imaging sensor housed within a PImMS camera,[48,49] enabling images to be acquired for all fragment ions on each laser cycle. Data from the PImMS2 sensor was processed to obtain time-of-flight mass spectra and two-dimensional projections of the three-dimensional momentum distribution for each detected product. These were analyzed to extract their kinetic energy and angular distributions.[36] A conversion curve from spatial coordinates to kinetic energy was created by modeling the instrument using SIMION.[50]

Electrons were velocity-mapped onto a separate position sensitive detector mounted opposite to the ion detector. This comprised a pair of MCPs and a P20 phosphor screen. Electron images on the phosphor screen were recorded with a CCD camera (PIKE F145B). Following background correction, the 2D projections of the electron momentum distributions were fully symmetrized (top/bottom/left/right), corrected for ellipticity, and Abel-inverted to obtain time-resolved electron kinetic energy spectra.[51]

B. Recoil-Frame Covariance Analysis

Details of the covariance-mapping procedure have been provided in previous publications.[28–31] Performing this analysis requires the data for each species of interest to be recorded for each experimental cycle, in this case, using the PImMS sensor to record the ion image for each species for every laser pulse. Applying recoil-frame covariance analysis to the ion-imaging data allows the investigation of channels producing two or more cations. Covariance analysis is optimal for regimes such as FLASH1, where the FEL operates at 10 Hz with each laser pulse producing significant quantities of ions (e.g. > 100). Conversely, lasers operating in the 1 kHz or faster regime generally produce better results under coincidence conditions, in which fewer than one event is detected per laser pulse.

Briefly, the covariance between two variables A and B is defined as the product of their deviations from their mean values:

$$\mathrm{cov}(A, B) = \langle (A - \langle A \rangle) \times (B - \langle B \rangle) \rangle = \langle AB \rangle - \langle A \rangle \langle B \rangle \tag{1}$$

where $\langle\rangle$ indicates a mean. Here, A and B are the velocities of the two fragments of interest, and $\langle AB \rangle$ and $\langle A \rangle \langle B \rangle$ are referred to as the 'coincidence image' and 'false covariance image', respectively. The covariance of a two-dimensional ion image with another two-dimensional ion image produces a four-dimensional covariance dataset; however, such a data set is generally difficult to interpret. In practice, for each laser pulse, the signal for ion A is rotated relative to the reference ion B and summed into the coincidence term. In the common case where more than one A or B ion associated with that laser pulse is detected, the process is repeated for each B ion and a proportionate signal for A is added to the covariance image. The false covariance image is constructed in a similar manner using the mean A and

B ion images from the whole data set, i.e., $\langle A \rangle$ and $\langle B \rangle$. For each pixel in the $\langle B \rangle$ image that contains signal, the $\langle A \rangle$ image is rotated to the reference direction, and a proportional amount of signal is added to the false covariance image. Subtracting the false covariance image from the coincidence image yields the covariance image. The covariance images shown in this study are referred to as 'positive covariance images' where negative values have been set to 0 for clarity.

C. Fitting of the Delay Dependent Yields

The equations used to derive the PAH^{n+*} relaxation lifetimes are given in Section S6 of the SI. Briefly, the functions used to approximate the LKE electrons, PAH^{2+}, and (1, 2) $C_3H_x^+$ ions consist of the following components:

- A sigmoidal curve centered at t_0. t_0 is independently determined from the He(1s) photoelectron line, described in more detail in Section S4 of the SI. The sigmoidal curves represent the change in the signal due to the pump pulse altering the molecular charge state; for example, as demonstrated in Figure 5, the yield of PAH^{2+} for the PAHs studied is always greater at a pump-probe delay of -0.5 ps compared to +0.5 ps. Before t_0, this is interpreted as the IR pulse primarily causing internal excitation and the XUV pulse promoting the excited neutral PAH to PAH^{2+}. After t_0, the XUV pulse interacts with the PAH first and can generate PAH^{2+}. Following electronic relaxation to the PAH^{2+} ground state, the IR pulse can induce dissociation causing the PAH^{2+} yield to be depleted.

- A transient peak function representing electronic relaxation following excitation by the XUV-pump pulse, probed by the IR pulse. Specifically, the XUV pulse is expected to initiate ionization and electronic excitation, and the peak function accounts for the change in IR-probe yield as electronic relaxation takes place. The maximum of this transient appears after t_0.

- A transient peak function representing electronic relaxation following excitation by the IR-pump pulse, probed by the XUV pulse. The IR pulse primarily creates electronically excited neutral PAH molecules; electronic relaxation will change the effect of the XUV pulse. This maximum of this transient appears before t_0, and it is only used when fitting PAH^{2+}.

The model sampled two types of non-linear parameters: relaxation lifetimes of the intermediate PAH species and cross-correlation time, which accounts for the finite duration of the pump and probe pulses, the number of pump and probe photons involved in creating the observed product, and the jitter between the pulses. The parameter distributions were obtained using Monte-Carlo sampling of the likelihood function with the Metropolis algorithm.[52] The sampling procedure also sampled the determined uncertainty in t_0, with the initial t_0 value determined by analysis of the helium photoelectrons (Section S4 in the SI).

D. Dissociation Energies Computations

For all three PAHs, structural optimizations on the ground electronic states of the neutral species were performed. Based on these geometries, we calculated the vertical ionization potentials (VIP) and estimated bounds for the dissociation energy corresponding to reactions of the types ${}^{m_0}\mathrm{PAH}^{q_0+} \rightarrow {}^{m_1}(\mathrm{PAH\text{-}X})^{q_1+} + {}^{m_2}\mathrm{X}^{q_2+}$, where q and m are the charge and multiplicity of the species, X = H, C_2H_2, C_3H_3, and C_4H_4, and (PAH-X) refers to a fragment where the moiety X has been removed from the PAH. For this purpose, single point energy calculations of the PAHs, (PAH-X), and X fragments at the geometries of the ground state optimized PAHs were performed. All calculations were performed at the UKS-DFT/def2-TZVPP level using the ORCA 4.0 software[53] with ωB97[54] and M06-2x[55] functionals. The latter functionals have been shown to reproduce various properties of PAHs and aromatic allotropes of carbon.[56,57]

E. Simulation of the Beyond-Born-Oppenheimer Internal Conversion

Trajectory surface hopping molecular dynamics (TSH-MD) simulations[58] of FLU were done with the SHARC software[59–61] interfaced with Orca 4.[53] All the simulations were performed with or based on calculations at the PBE/def2-SV(P) level of theory.[62,63] Excited states were calculated with TD-DFT at the chosen level of theory using the Tamm-Dancoff approximation (TDA). To speed up the (TD-)DFT calculations the resolution-of-identity (RI) approximation was used.[64–66] Simulations of the FLU^+ dynamics excited to the correlation bands were done using a linear vibronic coupling (LVC) model[67] as implemented in SHARC.[68] The initial conditions for trajectories were sampled from the Wigner

distribution of the ground vibrational state. A full description of the procedure including the calculation of the photoionization cross-sections is available in Section S8 of the SI.

Acknowledgement

This work was supported by the ERC Starting Grant ASTROROT, grant number 638027, and the project CALIPSOplus under the grant agreement 730872 from the EU Framework Programme for Research and Innovation HORIZON 2020. The experimental parts of this research were carried out at beamline BL1 FLASH at DESY, a member of the Helmholtz Association (HGF). We acknowledge the Max Planck Society for funding the development and the initial operation of the CAMP endstation within the Max Planck Advanced Study Group at CFEL and for providing this equipment for CAMP@FLASH. The installation of CAMP@FLASH was partially funded by the BMBF grants 05K10KT2, 05K13KT2, 05K16KT3 and 05K10KTB from FSP-302. We acknowledge financial support by the European Union's Horizon 2020 research and innovation program under the Marie Skłodowska-Curie Grant Agreement 641789 "Molecular Electron Dynamics investigated by Intense Fields and Attosecond Pulses" (MEDEA), the Clusters of Excellence "Center for Ultrafast Imaging" (CUI, EXC 1074, ID 194651731), the "Advanced Imaging of Matter" (AIM, EXC 2056, ID 390715994) of the Deutsche Forschungsgemeinschaft (DFG), and the Helmholtz Gemeinschaft through the "Impuls-und Vernetzungsfond". Additionally, the project was supported by The Netherlands Organization for Scientific Research (NWO) and is part of the Dutch Astrochemistry Network (DAN) II (Project No. 648.000.029). S.M., J.L., J.P. and P.J. acknowledge support from the Swedish Research Council and the Swedish Foundation for Strategic Research. The authors are additionally thankful for support from the following funding bodies: the UK EPSRC (M.Br. and C.V. - EP/L005913/1; M.Bu. - EP/S028617/1), STFC (PNPAS award and mini-IPS Grant No. ST/J002895/1), the Chemical Sciences, Geosciences, and Biosciences Division, Office of Basic Energy Sciences, Office of Science, US Department of Energy (F.Z. - DE-FG02-86ER13491); the National Science Foundation (D.Rol. - PHYS-1753324); and the Helmholtz Initiative and Networking Fund through the Young Investigators Group Program (S.B.).

V Author Contributions

B.M. and M.S. conceived and designed the experiments. J.W.L.L., P.C., S.M., A.L.S., S.G., F.A., R.B., X.C., S.D, B.E., L.H., D.H., M.J., M.M.K., H.K., J.L., A.L., D.L., R.M., E.M., T.M., P.O., C.P., J.P., D.Ra., D.Rom., N.S., S.Tr., J.W., F.Z., S.B., M.Bu., D.Rol., S.Te., P.J., B.M. and M.S. performed the experiments. J.W.L.L., D.S.T., P.C., S.M., A.S., S.G., D.G., and E.M. analyzed the data. J.W.L.L., D.S.T., P.C., S.M., A.S., S.G., F.A., M. Bu., J.K., A.R., D.Rol., P.J., M.Br., C.V., B.M. and M.S. performed detailed discussions of the results. J.W.L.L., D.S.T., B.M. and M.S. wrote the manuscript.

VI Competing Interests

The authors declare no competing interests.

VII Additional Information

Supplementary information is available for this paper.

Correspondence and requests for materials should be addressed to B.M. and M.S.

References

(1) Joblin, C.; Tielens, A. 25 years of PAH hypothesis. *European Astronomical Society Publications Series* **2011**, *46*, 3–10.

(2) Lagache, G.; Dole, H.; Puget, J.-L.; Pérez-González, P.; Le Floc'h, E.; Rieke, G. H.; Papovich, C.; Egami, E.; Alonso-Herrero, A.; Engelbracht, C. et al. Polycyclic Aromatic Hydrocarbon Contribution to the Infrared Output Energy of the Universe at z≈2. *The Astrophysical Journal Supplement Series* **2004**, *154*, 112.

(3) Leach, S. Laboratory studies of polycyclic aromatic hydrocarbons, fullerenes and linear carbon chains in an astrophysical context. *Planetary and Space Science* **1995**, *43*, 1153–1164.

(4) Dabestani, R.; Ivanov, I. N. A compilation of physical, spectroscopic and photophysical properties of polycyclic aromatic hydrocarbons. *Photochemistry and photobiology* **1999**, *70*, 10–34.

(5) Herbst, E.; van Dishoeck, E. F. Complex Organic Interstellar Molecules. *Annual Review of Astronomy and Astrophysics* **2009**, *47*, 427–480.

(6) Tielens, A. 25 years of PAH hypothesis. *EAS Publications Series* **2011**, *46*, 3–10.

(7) Snow, T. P.; Le Page, V.; Keheyan, Y.; Bierbaum, V. M. The interstellar chemistry of PAH cations. *Nature* **1998**, *391*, 259–260.

(8) Jochims, H.; Baumgärtel, H.; Leach, S. Photoionization quantum yields of polycyclic aromatic hydrocarbons. *Astronomy and Astrophysics* **1996**, *314*, 1003–1009.

(9) Jochims, H.; Rühl, E.; Baumgärtel, H.; Tobita, S.; Leach, S. VUV peaks in absorption spectra and photoion yield curves of polycyclic aromatic hydrocarbons and related compounds. *International journal of mass spectrometry and ion processes* **1997**, *167*, 35–53.

(10) Jochims, H.; Baumgärtel, H.; Leach, S. Structure-dependent photostability of polycyclic aromatic hydrocarbon cations: Laboratory studies and astrophysical implications. *The astrophysical journal* **1999**, *512*, 500.

(11) Boschman, L.; Cazaux, S.; Spaans, M.; Hoekstra, R.; Schlathölter, T. H2 formation on PAHs in photodissociation regions: a high-temperature pathway to molecular hydrogen. *Astronomy & Astrophysics* **2015**, *579*, A72.

(12) Reitsma, G.; Boschman, L.; Deuzeman, M.; Hoekstra, S.; Hoekstra, R.; Schlathölter, T. Near edge X-ray absorption mass spectrometry on coronene. *The Journal of chemical physics* **2015**, *142*, 024308.

(13) Leach, S.; Eland, J.; Price, S. Formation and dissociation of dications of naphthalene, azulene and related heterocyclic compounds. *The Journal of Physical Chemistry* **1989**, *93*, 7575–7583.

(14) Leach, S.; Eland, J.; Price, S. Formation and dissociation of dications of naphthalene-d8. *The Journal of Physical Chemistry* **1989**, *93*, 7583–7593.

(15) Ruehl, E.; Price, S. D.; Leach, S. Single and double photoionization processes in naphthalene between 8 and 35 eV. *The Journal of Physical Chemistry* **1989**, *93*, 6312–6321.

(16) Domcke, W.; Yarkony, D. R. Role of conical intersections in molecular spectroscopy and photoinduced chemical dynamics. *Annual review of physical chemistry* **2012**, *63*, 325–352.

(17) Joalland, B.; Mori, T.; Martínez, T. J.; Suits, A. G. Photochemical dynamics of ethylene cation C2H4+. *The journal of physical chemistry letters* **2014**, *5*, 1467–1471.

(18) Galbraith, M.; Scheit, S.; Golubev, N.; Reitsma, G.; Zhavoronkov, N.; Despré, V.; Lepine, F.; Kuleff, A.; Vrakking, M.; Kornilov, O. et al. Few-femtosecond passage of conical intersections in the benzene cation. *Nature communications* **2017**, *8*, 1–7.

(19) Bazzi, S.; Welsch, R.; Vendrell, O.; Santra, R. Challenges in XUV photochemistry simulations: A case study on ultrafast fragmentation dynamics of the benzene radical cation. *The Journal of Physical Chemistry A* **2018**, *122*, 1004–1010.

(20) Curchod, B. F.; Martínez, T. J. Ab initio nonadiabatic quantum molecular dynamics. *Chemical reviews* **2018**, *118*, 3305–3336.

(21) Marciniak, A.; Despré, V.; Barillot, T.; Rouzée, A.; Galbraith, M.; Klei, J.; Yang, C.-H.; Smeenk, C.; Loriot, V.; Reddy, S. N. et al. XUV excitation followed by ultrafast non-adiabatic relaxation in PAH molecules as a femto-astrochemistry experiment. *Nature Communications* **2015**, *6*.

(22) Hervé, M.; Despré, V.; Nash, P. C.; Loriot, V.; Boyer, A.; Scognamiglio, A.; Karras, G.; Brédy, R.; Constant, E.; Tielens, A. et al. Ultrafast dynamics of correlation bands following XUV molecular photoionization. *Nature Physics* **2020**, 1–5.

(23) Reitsma, G.; Hummert, J.; Dura, J.; Loriot, V.; Vrakking, M. J.; Lépine, F.; Kornilov, O. Delayed relaxation of highly excited cationic states in naphthalene. *The Journal of Physical Chemistry A* **2019**, *123*, 3068–3073.

(24) Marciniak, A.; Despré, V.; Loriot, V.; Karras, G.; Hervé, M.; Quintard, L.; Catoire, F.; Joblin, C.; Constant, E.; Kuleff, A. et al. Electron correlation driven non-adiabatic relaxation in molecules excited by an ultrashort extreme ultraviolet pulse. *Nature communications* **2019**, *10*, 1–8.

(25) Ackermann, W. a.; Asova, G.; Ayvazyan, V.; Azima, A.; Baboi, N.; Bähr, J.; Balandin, V.; Beutner, B.; Brandt, A.; Bolzmann, A. et al. Operation of a free-electron laser from the extreme ultraviolet to the water window. *Nature photonics* **2007**, *1*, 336–342.

(26) Craig, N.; Abbott, M.; Finley, D.; Jessop, H.; Howell, S. B.; Mathioudakis, M.; Sommers, J.; Vallerga, J. V.; Malina, R. F. TheExtreme Ultraviolet ExplorerStellar Spectral Atlas. *The Astrophysical Journal Supplement Series* **1997**, *113*, 131–193.

(27) Frasinski, L. J. Covariance mapping techniques. *Journal of Physics B: Atomic, Molecular and Optical Physics* **2016**, *49*, 152004.

(28) Slater, C. S.; Blake, S.; Brouard, M.; Lauer, A.; Vallance, C.; John, J. J.; Turchetta, R.; Nomerotski, A.; Christensen, L.; Nielsen, J. H. et al. Covariance imaging experiments using a pixel-imaging mass-spectrometry camera. *Physical Review A* **2014**, *89*, 011401.

(29) Slater, C. S.; Blake, S.; Brouard, M.; Lauer, A.; Vallance, C.; Bohun, C. S.; Christensen, L.; Nielsen, J. H.; Johansson, M. P.; Stapelfeldt, H. Coulomb-explosion imaging using a pixel-imaging mass-spectrometry camera. *Physical Review A* **2015**, *91*, 053424.

(30) Allum, F.; Burt, M.; Amini, K.; Boll, R.; Köckert, H.; Olshin, P. K.; Bari, S.; Bomme, C.; Braußе, F.; Cunha de Miranda, B. et al. Coulomb explosion imaging of CH3I and CH2ClI photodissociation dynamics. *The Journal of chemical physics* **2018**, *149*, 204313.

(31) Amini, K.; Boll, R.; Lauer, A.; Burt, M.; Lee, J. W.; Christensen, L.; Brauβe, F.; Mullins, T.; Savelyev, E.; Ablikim, U. et al. Alignment, orientation, and Coulomb explosion of difluoroiodobenzene studied with the pixel imaging mass spectrometry (PImMS) camera. *The Journal of chemical physics* **2017**, *147*, 013933.

(32) Hagan, D.; Eland, J. Formation and decay of doubly charged ions in n-alkanes from methane to triacontane. *Organic mass spectrometry* **1992**, *27*, 855–863.

(33) Eland, J. The dynamics of three-body dissociations of dications studied by the triple coincidence technique PEPIPICO. *Molecular Physics* **1987**, *61*, 725–745.

(34) West, B.; Castillo, S. R.; Sit, A.; Mohamad, S.; Lowe, B.; Joblin, C.; Bodi, A.; Mayer, P. M. Unimolecular reaction energies for polycyclic aromatic hydrocarbon ions. *Physical Chemistry Chemical Physics* **2018**, *20*, 7195–7205.

(35) West, B. J.; Lesniak, L.; Mayer, P. M. Why Do Large Ionized Polycyclic Aromatic Hydrocarbons Not Lose C2H2? *The Journal of Physical Chemistry A* **2019**, *123*, 3569–3574.

(36) Roberts, G.; Nixon, J.; Lecointre, J.; Wrede, E.; Verlet, J. Toward real-time charged-particle image reconstruction using polar onion-peeling. *Review of Scientific Instruments* **2009**, *80*, 053104.

(37) Vishnevskiy, Y. V.; Schwabedissen, J.; Rykov, A. N.; Kuznetsov, V. V.; Makhova, N. N. Conformational and bonding properties of 3, 3-dimethyl-and 6, 6-dimethyl-1, 5-diazabicyclo [3.1. 0] hexane: a case study employing the Monte Carlo method in gas electron diffraction. *The Journal of Physical Chemistry A* **2015**, *119*, 10871–10881.

(38) Bockhorn, H.; Fetting, F.; Wenz, H. Investigation of the formation of high molecular hydrocarbons and soot in premixed hydrocarbon-oxygen flames. *Berichte der Bunsengesellschaft für physikalische Chemie* **1983**, *87*, 1067–1073.

(39) Richter, H.; Howard, J. B. Formation of polycyclic aromatic hydrocarbons and their growth to soot—a review of chemical reaction pathways. *Progress in Energy and Combustion science* **2000**, *26*, 565–608.

(40) Shukla, B.; Koshi, M. A novel route for PAH growth in HACA based mechanisms. *Combustion and flame* **2012**, *159*, 3589–3596.

(41) Feldhaus, J. FLASH—the first soft x-ray free electron laser (FEL) user facility. *Journal of Physics B: Atomic, Molecular and Optical Physics* **2010**, *43*, 194002.

(42) Erk, B.; Müller, J. P.; Bomme, C.; Boll, R.; Brenner, G.; Chapman, H. N.; Correa, J.; Düsterer, S.; Dziarzhytski, S.; Eisebitt, S. et al. CAMP@FLASH: an end-station for imaging, electron- and

ion-spectroscopy, and pump–probe experiments at the FLASH free-electron laser. *Journal of Synchrotron Radiation* **2018**, *25*, 1529–1540.

(43) Redlin, H.; Al-Shemmary, A.; Azima, A.; Stojanovic, N.; Tavella, F.; Will, I.; Düsterer, S. The FLASH pump–probe laser system: Setup, characterization and optical beamlines. *Nuclear Instruments and Methods in Physics Research Section A: Accelerators, Spectrometers, Detectors and Associated Equipment* **2011**, *635*, S88–S93.

(44) Even, U. The Even-Lavie valve as a source for high intensity supersonic beam. *EPJ Techniques and Instrumentation* **2015**, *2*, 17.

(45) Savelyev, E.; Boll, R.; Bomme, C.; Schirmel, N.; Redlin, H.; Erk, B.; Düsterer, S.; Müller, E.; Höppner, H.; Toleikis, S. et al. Jitter-correction for IR/UV-XUV pump-probe experiments at the FLASH free-electron laser. *New Journal of Physics* **2017**, *19*, 043009.

(46) Eppink, A. T.; Parker, D. H. Velocity map imaging of ions and electrons using electrostatic lenses: Application in photoelectron and photofragment ion imaging of molecular oxygen. *Review of Scientific Instruments* **1997**, *68*, 3477–3484.

(47) Parker, D. H.; Eppink, A. T. Photoelectron and photofragment velocity map imaging of state-selected molecular oxygen dissociation/ionization dynamics. *The Journal of chemical physics* **1997**, *107*, 2357–2362.

(48) Clark, A. T.; Crooks, J. P.; Sedgwick, I.; Turchetta, R.; Lee, J. W.; John, J. J.; Wilman, E. S.; Hill, L.; Halford, E.; Slater, C. S. et al. Multimass velocity-map imaging with the pixel imaging mass spectrometry (PImMS) sensor: an ultra-fast event-triggered camera for particle imaging. *The Journal of Physical Chemistry A* **2012**, *116*, 10897–10903.

(49) Amini, K.; Blake, S.; Brouard, M.; Burt, M.; Halford, E.; Lauer, A.; Slater, C.; Lee, J.; Vallance, C. Three-dimensional imaging of carbonyl sulfide and ethyl iodide photodissociation using the pixel imaging mass spectrometry camera. *Review of Scientific Instruments* **2015**, *86*, 103113.

(50) Dahl, D.; Delmore, J.; Appelhans, A. SIMION PC/PS2 electrostatic lens design program. *Review of Scientific Instruments* **1990**, *61*, 607–609.

(51) Vrakking, M. J. An iterative procedure for the inversion of two-dimensional ion/photoelectron imaging experiments. *Review of Scientific Instruments* **2001**, *72*, 4084–4089.

(52) Press, W. H.; Teukolsky, S. A.; Vetterling, W. T.; Flannery, B. P. *Numerical recipes 3rd edition: The art of scientific computing*; Cambridge university press, 2007.

(53) Neese, F. The ORCA program system. *Wiley Interdisciplinary Reviews: Computational Molecular Science* **2012**, *2*, 73–78.

(54) Chai, J.-D.; Head-Gordon, M. Systematic optimization of long-range corrected hybrid density functionals. *The Journal of Chemical Physics* **2008**, *128*, 084106.

(55) Zhao, Y.; Truhlar, D. G. The M06 suite of density functionals for main group thermochemistry, thermochemical kinetics, noncovalent interactions, excited states, and transition elements: two new functionals and systematic testing of four M06-class functionals and 12 other functionals. *Theoretical Chemistry Accounts* **2008**, *120*, 215–241.

(56) Rayne, S.; Forest, K. Benchmarking semiempirical, Hartree–Fock, DFT, and MP2 methods against the ionization energies and electron affinities of short- through long-chain [n]acenes and [n]phenacenes. *Canadian Journal of Chemistry* **2016**, *94*, 251–258.

(57) Zhou, B.; Hu, Z.; Jiang, Y.; He, X.; Sun, Z.; Sun, H. Benchmark study of ionization potentials and electron affinities of armchair single-walled carbon nanotubes using density functional theory. *Journal of Physics: Condensed Matter* **2018**, *30*, 215501.

(58) Tully, J. C.; Preston, R. K. Trajectory Surface Hopping Approach to Nonadiabatic Molecular Collisions: The Reaction of H+ with D2. *The Journal of Chemical Physics* **1971**, *55*, 562–572.

(59) Mai, S.; Richter, M.; Heindl, M.; Menger, M. F. S. J.; Atkins, A.; Ruckenbauer, M.; Plasser, F.; Ibele, L. M.; Kropf, S.; Oppel, M. et al. SHARC2.1: Surface Hopping Including Arbitrary Couplings — Program Package for Non-Adiabatic Dynamics. sharc-md.org, 2019.

(60) Richter, M.; Marquetand, P.; González-Vázquez, J.; Sola, I.; González, L. SHARC: ab initio Molecular Dynamics with Surface Hopping in the Adiabatic Representation Including Arbitrary Couplings. *J. Chem. Theory Comput.* **2011**, *7*, 1253–1258.

(61) Mai, S.; Marquetand, P.; González, L. Nonadiabatic Dynamics: The SHARC Approach. *WIREs Comput. Mol. Sci.* **2018**, *8*, e1370.

(62) Perdew, J. P.; Burke, K.; Ernzerhof, M. Generalized Gradient Approximation Made Simple. *Phys. Rev. Lett.* **1996**, *77*, 3865–3868.

(63) Weigend, F.; Ahlrichs, R. Balanced basis sets of split valence, triple zeta valence and quadruple zeta valence quality for H to Rn: Design and assessment of accuracy. *Phys. Chem. Chem. Phys.* **2005**, *7*, 3297–3305.

(64) Weigend, F. Accurate Coulomb–fitting basis sets for H to Rn. *Phys. Chem. Chem. Phys.* **2006**, *8*, 1057–1065.

(65) Neese, F.; Wennmohs, F.; Hansen, A.; Becker, U. Efficient, approximate and parallel Hartree–Fock and hybrid DFT calculations. A 'chain-of-spheres' algorithm for the Hartree–Fock exchange. *Chemical Physics* **2009**, *356*, 98–109, Moving Frontiers in Quantum Chemistry:.

(66) Izsák, R.; Neese, F. An overlap fitted chain of spheres exchange method. *The Journal of Chemical Physics* **2011**, *135*, 144105.

(67) Köuppel, H.; Domcke, W.; Cederbaum, L. S. *Advances in Chemical Physics*; John Wiley & Sons, Ltd, 1984; pp 59–246.

(68) Plasser, F.; Gómez, S.; Menger, M. F. S. J.; Mai, S.; González, L. Highly efficient surface hopping dynamics using a linear vibronic coupling model. *Phys. Chem. Chem. Phys.* **2019**, *21*, 57–69.

Paper VII

E. Kukk, H. Fukuzawa, J. Niskanen, K. Nagaya, K. Kooser, D. You, **J. Peschel**, S. Maclot, A. Niozu, S. Saito, Y. Luo, E. Pelimanni, E. Itälä, J. D. Bozek, T. Takanashi, M. Berholts, P. Johnsson, and K. Ueda
Formative period in the X-ray-induced photodissociation of organic molecules
Phys. Rev. Res. 3, 013221 (2021)

Formative period in the x-ray-induced photodissociation of organic molecules

E. Kukk,[1] H. Fukuzawa,[2,3] J. Niskanen,[1] K. Nagaya,[4] K. Kooser,[1,5] D. You,[2] J. Peschel,[6] S. Maclot,[6] A. Niozu,[4] S. Saito,[2] Y. Luo,[2] E. Pelimanni,[7] E. Itälä,[1] J. D. Bozek,[8] T. Takanashi,[2] M. Berholts,[5,8] P. Johnsson,[6] and K. Ueda[2,3]

[1]*Department of Physics and Astronomy, University of Turku, FI-20014 Turku, Finland*
[2]*Institute of Multidisciplinary Research for Advanced Materials, Tohoku University, Sendai 980-8577, Japan*
[3]*RIKEN SPring-8 Center, Kouto 1-1-1, Sayo, Hyogo 679-5148, Japan*
[4]*Department of Physics, Kyoto University, Kyoto 606-8502, Japan*
[5]*Institute of Physics, University of Tartu, Wilhelm Ostwaldi 1, EE-50411 Tartu, Estonia*
[6]*Department of Physics, Lund University, SE-22100 Lund, Sweden*
[7]*Nano and Molecular Systems Research Unit, Faculty of Science, University of Oulu, FI-90014 Oulu, Finland*
[8]*Synchrotron SOLEIL, L'Orme des Merisiers, Saint-Aubin, BP 48, FR-91192 Gif-sur-Yvette Cedex, France*

(Received 14 July 2020; revised 10 December 2020; accepted 7 December 2020; published 9 March 2021)

Absorption of x-ray photons by atomic inner shells of light-element organics and biomolecules often leads to formation of dicationic electronic states and to molecular fragmentation. We investigated the x-ray-induced dissociation landscape of a representative medium-sized organic molecule, thiophene, by femtosecond x-ray pulses from the Super Photon Ring-8 GeV (SPring-8) Angstrom Compact Free-Electron Laser (SACLA). Holes, created in the sulfur $2p$ orbital by photoemission, were filled by the Auger process that created dicationic molecular states within a broad range of internal energies—a starting point particular to x-ray-induced dynamics. The evolution of the ionized molecules was monitored by a pump-probe experiment using a near-infrared (800 nm) laser pulse. Ion-ion coincidence and ion momentum analysis reveals enhanced yields of ionic fragments from multibody breakup of the ring, attributed to additional ionization of the highly excited fraction of the dicationic parent molecular states. The transient nature of the enhancement and its decay with about a 160-fs time constant indicate formation of an open-ring parent geometry and the statistical survival time of the parent species before the dissociation events. By probing specific Auger final states of transient, highly excited nature by near-infrared light, we demonstrate how pump-probe signatures can be related to the key features in dynamics during the early period of the x-ray-induced damage of organic molecules and biomolecules.

DOI: 10.1103/PhysRevResearch.3.013221

I. INTRODUCTION

Absorption of light by molecules leads to a rich variety of photochemistry and photophysics. These processes can be initiated by nonionizing absorption of ultraviolet (UV) light, such as the ubiquitous and important $\pi \rightarrow \pi^*$ transitions in organic molecules [1,2], by valence ionization with vacuum ultraviolet (VUV) radiation, or by deeper atomic inner-shell ionization using x rays. The latter originate from either natural or artificial sources as in medical imaging and radiotherapy. When x rays interact with biomolecules and organic molecules consisting mainly of light elements, they remove electrons from the atomic inner shells. In a few femtoseconds, the electronic structure transitions to a lower-energy state via a radiationless Auger process, in which the inner-shell vacancy is filled, another electron is emitted, and two outer-shell vacancies are created. The resulting doubly ionized molecules most likely break up, releasing neutral and charged fragments into the surroundings, spreading radiation damage. In this paper, we focus on the early period following inner-shell (core) ionization by x rays of the organic molecule thiophene. This aromatic nine-atom molecule is in the size range of the building blocks of large biomolecules and was chosen for its feature-rich dissociation landscape representing diverse molecular dynamics. Thiophene is also the basis of poly- and oligothiophenes that are promising organic materials for technological applications [3].

Fundamental interest in the early photoinduced dynamics in small quantum systems arises since it largely defines the dissociation landscape—the various fragmentation pathways and the branching ratios between them. Theoretical treatment of the evolution during the first tens and hundreds of femtoseconds following photoionization is challenging due to strongly coupled and concurrent electron and nuclear dynamics in the system [4,5]. Furthermore, the properties of dicationic states and their dynamics, in which Coulomb repulsion and charge separation play an important role [6], are very different from the dynamics of cations, prevalently created by VUV and extreme ultraviolet (XUV) absorption.

The emergence of short-pulse ionizing light sources such as free-electron lasers (FELs) and high-order-harmonic generation (HHG) sources has revolutionized femtochemistry

and related physics, allowing us to follow photodynamics in real time [7]. Various pump-probe techniques combining two light pulses with either the same or even vastly different wavelengths provide glimpses into the evolution of quantum systems ranging from single atoms to molecules and to clusters of thousands of atoms [8–10]. A popular approach to study ultrafast molecular dynamics is realized by ionizing the valence or inner-valence orbitals by VUV or XUV light and then probing the development of the cationic states by pulses of longer wavelength such as near-infrared (NIR) light [11]. NIR radiation has been shown to successfully probe VUV- or XUV-induced photodynamics, from the classic experiment of the acetylene isomerization [11–14] to the much more complex processes in thymidine [15]. In the x-ray regime, experimentalists often take advantage of the extreme intensity of the short FEL pulses, creating highly charged exotic states by multiphoton absorption that undergo destructive Coulomb explosions [16–19,19–24]—a dynamics again very different from the evolution of a low-charge state. In contrast, in this paper we used strongly attenuated short (60 fs), soft x-ray pulses produced by a FEL to create a *core-ionized* state. We demonstrate how the subsequent probing of the photodynamics by NIR pulses reveals the early evolution of a much gentler but at the same time much more common and practically relevant event in organic molecules and biomolecules: single-photon core ionization followed by Auger decay.

Time-resolved probing of the early period of the x-ray-induced dissociation landscape allows us to address some key factors defining the final dissociation landscape and test the underlying assumptions in theoretical modeling of the photodynamics. It can reveal, for example, whether the molecules embark on a certain pathway immediately after the Auger decay of the parent dicationic species, or have a certain "survival" time. With the increasing size of the system, answering such questions by detailed mapping of the potential-energy surfaces of the many states involved becomes infeasible. However, simulation results of molecular dynamics of thiophene dications [25] suggest another description: The system embarks on a chosen dissociation pathway once the interference of the many vibrational modes creates a favorable local concentration of energy for bond breaking. Depending on the average energy of the vibrational modes and the initial conditions such as the charge state, such an event could occur with a significant delay. In time-resolved experiments with highly charged small quantum systems, survival of the intact system for any significant time is unlikely as a violent Coulomb explosion immediately follows the intense FEL pulse. However, in a doubly charged system even with very high excess internal energy—the most common starting point of x-ray-induced molecular dynamics of organic molecules and biomolecules—the *parent survival time* might be a very significant factor in the formative period of the dissociation.

A characteristic feature of the early dynamics is the rapidly changing electronic structure, the details of which are sensitive to how the initial state is created. Auger decay can leave the molecule in highly excited electronic states tens of eV above the lowest dicationic level. Recent research in biomolecular building-block molecules (in the size range of thiophene) has found that electronic relaxation of excited states through conical intersections is much more common than once thought [13,15,26]. How quickly do such processes happen, how do they affect the dissociation landscape, and what are the implications for theoretical modeling of the molecular dynamics? In a common approximation the electronic relaxation to the dicationic ground state is assumed to be so fast that all electronic energy is converted to heat that then drives the dynamics on the dicationic ground-state potential-energy surface. However, if this energy conversion happens on a timescale comparable to or even longer than the time period in which the dissociation pathways are chosen, a more rigorous theoretical treatment of excited electronic states could be required.

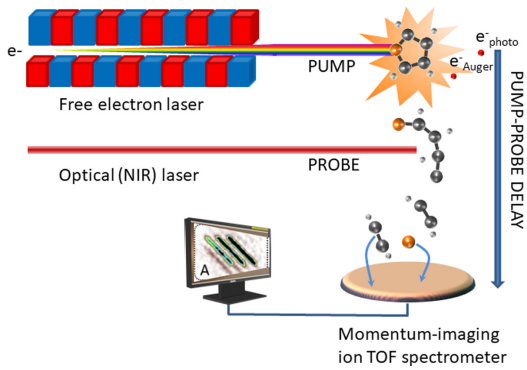

FIG. 1. Schematic of the experiment.

Last but not least, this study introduces a novel approach for obtaining experimental time-dependent information on the very complex electron-nuclear dynamics of the very commonplace dicationic molecular states, created by x-ray absorption after the initial Auger relaxation of the core hole. We employ the near-infrared laser probe pulse to follow up on the x-ray ionization event. Such a probe would not be sensitive to these Auger final states but for the recently discovered (single photon) laser-enabled Auger decay (LEAD) effect [27]. We demonstrate how the LEAD-activated NIR-probe technique works and creates strong time-dependent signatures of the state of the system—not only a medium-sized organic molecule as in the present case but also a biosystem undergoing x-ray absorption and subsequent radiation damage in radiotherapy, for example.

II. EXPERIMENTAL SETUP

The experiments were carried out at Beamline 1 [28] of the Super Photon Ring-8 GeV (SPring-8) Angstrom Compact Free-Electron Laser (SACLA) FEL facility [29] operating at a repetition rate of 60 Hz, with the approval of the Japan Synchrotron Radiation Research Institute (JASRI) (Proposal No. 2018B8014). The arrangement of the experiment is depicted in Fig. 1. The sample [thiophene ($\geqslant$ 98.0% purity), purchased from Nacalai Tesque] was evaporated at room temperature from liquid phase without further purification and introduced into the focal spot of the FEL and NIR beams through a pulsed valve.

The duration of the FEL pulse was estimated to be about 60 fs. The photon energy of 180 eV was selected as the third harmonic of the undulator radiation, tuned to the maximum cross section of the sulfur $2p$ photoabsorption. The first harmonic was removed by a 0.1-μm Sn filter with a 0.016% transmission at 60 eV and about 4400-times-higher transmission at 180 eV. The fraction of the total FEL-pulse energy that contained the third harmonic is 0.15–0.6%. The removal of the first harmonic thus greatly reduced the pulse intensity, bringing the experiment to the intended single-photon inner-shell absorption regime. The 800-nm NIR pulses were generated by a Ti:sapphire laser and arrived at the interaction point with an adjustable time delay (positive or negative) relative to the arrival of the FEL pulse. The pulse duration of the NIR laser was about 30 fs [30], the chosen attenuated pulse energy was 150 μJ (FWHM), and the power density in the waist of the beam was about 6×10^{13} W/cm^2. The NIR-pulse intensity for this experiment was chosen to minimize direct multiphoton ionization of the thiophene molecules by NIR radiation only, while maintaining a sufficient cross section for the NIR pulses to interact with the FEL-ionized target.

The beamline is equipped with a cross-correlation pulse arrival time monitor [30]. Recording the measured FEL-to-NIR delays for each pump-probe pulse allows us to take into account the timing jitter and improve the instrumental delay-time resolution by removing the jitter component, which in the present experiment had a standard deviation of 55 fs. The narrowest recorded broadening was $w = 35(7)$ fs at the rising edge of Xe^{2+} (from Xe clusters) yield, fitted by Eq. (3).

Positive ions were detected by a multicoincidence momentum-imaging ion time-of-flight (TOF) spectrometer equipped with a Roentdek HEX120 position-sensitive ion detector [31]. Multiple ions could be detected per pump-probe event, and for each ion, its TOF and the hit coordinates on the 120-mm-diameter detector were recorded. From these variables, the mass-to-charge values of the ions as well as their momentum vectors were derived.

III. RESULTS

A. Dissociation landscape of the thiophene dication after core ionization

Before presenting our experimental findings and their interpretation in light of the above questions, we review briefly the dissociation landscape of thiophene dications and the predictions of theoretical simulations.

Interleaved with time-resolved measurements, the dissociation products of the thiophene dication were recorded in a single-pulse "FEL-only" experiment at a photon energy of 180 eV. The raw data consist of fragment ion TOF values and reconstructed momentum vectors for all ions, collected for each FEL pulse. The FEL-only experiment provided reference values for the analysis of pump-probe data.

A schematic representation of the electron and nuclear dynamics is presented in Fig. 2. In the absence of the second, NIR pulse, the molecule evolves mostly along the various dicationic potential-energy surfaces guiding it to any of the possible dissociation pathways.

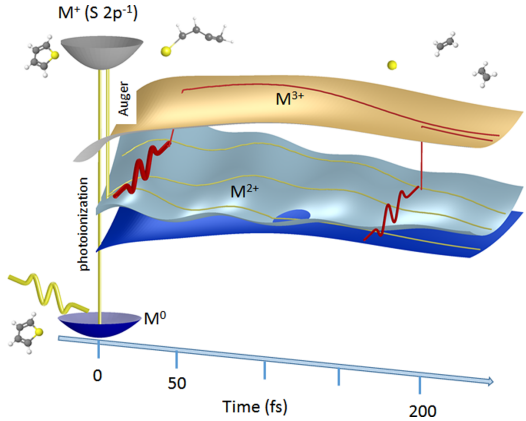

FIG. 2. Schematic depiction of the processes involved in the x-ray-pump–NIR-probe experiment of thiophene following S $2p$ core ionization. The x-ray-induced transitions and evolution of the system on the dicationic (M^{2+}) potential-energy surfaces are marked in yellow, while the absorption of the NIR radiation lifting the dynamics onto the (M^{3+}) surfaces is shown in red. The evolution of molecular geometry is shown at a few points in time. The actual number of the surfaces is much larger than the few sketched.

The FEL-only measurement can be summarized in the form of a two-dimensional histogram, the photoion-photoion coincidence (PIPICO) map as shown in Fig. 3, plotting all possible ion pairs that can be formed from the ions per each

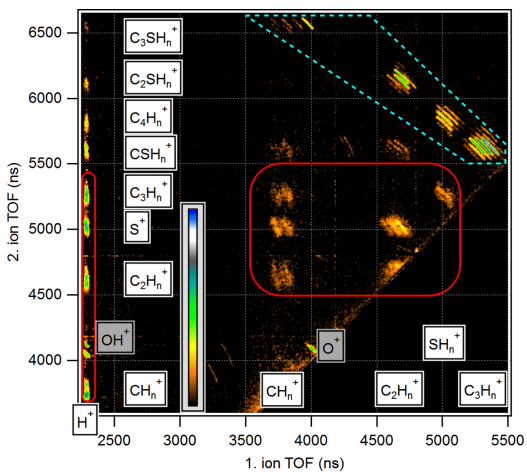

FIG. 3. Photoion-photoion coincidence (PIPICO) map of the dissociation of the thiophene dication following the S $2p$ core ionization. The time-of-flight ranges of ionic species are indicated by the row and column of labels near the corresponding axis. The regions surrounded by the red line indicate the ion pairs for which strong pump-probe effects were observed. The region within the dashed blue line covers the two-body processes.

FEL pulse against their flight times. The false-color scale represents the counts of ion pairs, and the islands appearing in the PIPICO map represent the various dissociation pathways. Thus the full PIPICO map is an experimental representation of the dissociation landscape of the thiophene dication. In constructing the PIPICO map of Fig. 3, the contribution from false coincidences (ion pairs formed by ions from different parent molecules) was subtracted. The ion TOFs depend not only on the ions' mass-to-charge ratio but also on the kinetic-energy release (KER) in the dissociation process. Ion pairs with significant KER form patterns with negative slopes in the PIPICO map due to the momentum correlation between the two ions; such patterns are a reliable indication of true coincidence events. Some patterns, (O^+, O^+), (H^+, O^+), and (H^+, OH^+), are due to residual water or molecular oxygen ionization. All ions contributing to Fig. 3 are singly charged, except a weak pattern at around ($TOF_1 \approx 4300$, $TOF_2 \approx 5600$), where the first ion is $C_3H_3^{2+}$.

Figure 3 shows a very feature-rich dissociation landscape. For classification purposes, we will use the terms *two-body* and *multibody* dissociation, referring to the number of C- and S-containing ring fragments that are produced. The emission of hydrogen atoms or protons is referred to as *H loss*, and it can accompany both the two-body and multibody processes or occur from a stable parent dication.

The intense, narrow patterns surrounded by the dashed blue line are due to two-body fragmentation, often accompanied by H loss and/or migration (creating the narrow stripes within the patterns). The central region of the PIPICO map encircled by the red line shows a number of more diffuse patterns that are due to a multibody fragmentation, also frequently accompanied by H loss or migration, such as

$$\begin{aligned} &C_4SH_4^{2+} \rightarrow C_2H_n^{0,+} + SH_m^{0,+} + C_2H_p^{0,+} + kH^{0,+}, \\ &C_4SH_4^{2+} \rightarrow C_3H_n^{0,+} + SH_m^{0,+} + CH_p^{0,+} + kH^{0,+}, \\ &k = 4 - n - m - p. \end{aligned} \quad (1)$$

All combinations of the localization of the two positive charges on the right side of (1) are observable in Fig. 3. Ion pairs involving an ejected proton correspond to the encircled steeply sloped patterns on the left-hand side of the PIPICO map.

B. Initial stages of dissociation as predicted by theory

Although prior experiments [25,32] could not follow the early dynamics in the thiophene molecular dication, it could be investigated by theoretical self-consistent charge-density-functional tight-binding (SCC-DFTB) simulations, where the internal energy of the molecular dication was in the form of heat (the vibrational motion of atoms). In Ref. [25], a total of 12 000 dissociation trajectories were simulated for internal energies ranging from 5.2 to 27 eV, and the individual trajectories at each temperature point were obtained by randomly varying the initial atomic velocity vectors at a set total kinetic energy.

Let us concentrate on the features of the simulations in the first few hundred femtoseconds. The calculations showed that fragmentation is almost universally preceded by a very fast opening of the ring and the formation of a transient linear geometry of the parent dication. The location of the opening bond along the ring varies, with the highest (54–66%) probability for the C-S bond to open. Once the ring opens, two-body or multibody fragmentation follows. Two example animations of such trajectories are given in the Supplemental Material [33]. The ring opening and fragmentation are often accompanied by H loss or migration.

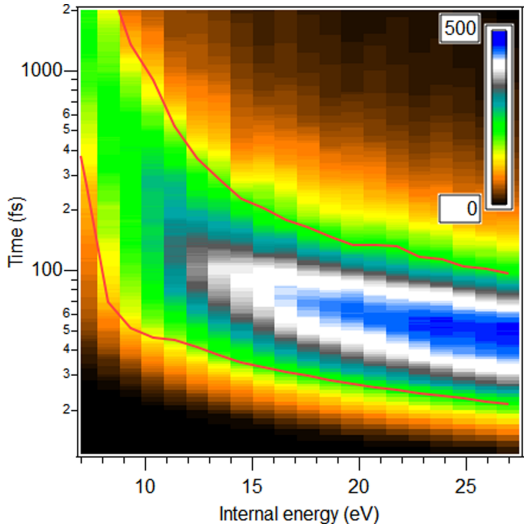

FIG. 4. Population of the transient linear geometry of the parent dication during molecular dynamics according to the SCC-DFTB simulations shown as a function of time and dependent on the internal energy of the molecule. Red curves mark the times of reaching the half-maximum population.

Figure 4 shows how the transient linear geometry is created by ring opening and then depleted by dissociation, from a statistical analysis of 500 trajectories simulated for each internal vibrational energy value. Figure 4 thus represents the birth and survival of the transient geometry in the parent molecular dication. We can see a strong dependency of the relevant time constants (red curves) on the internal energy. In the present experiment, large internal energies of over ≈ 40 eV in the molecular dication arise from populating highly excited final states in the course of the Auger decay [25,32].

In general, the SCC-DFTB simulations [25] match well with the observed dissociation landscape. The strongest individual dissociation pathway in both is

$$C_4SH_4^{2+} \rightarrow CSH^+ + C_3H_3^+. \quad (2)$$

The simulations predict all the observed two-body pathways (surrounded by dashed blue line area in Fig. 3) and also the numerous multibody fragmentation pathways, corresponding to the regions encircled by red lines in Fig. 3 (see also the animations in the Supplemental Material Ref. [33]) and single or multiple H-loss events. Only two-body events occur at the internal energies below 12 eV, while the multibody events become significant at higher energies.

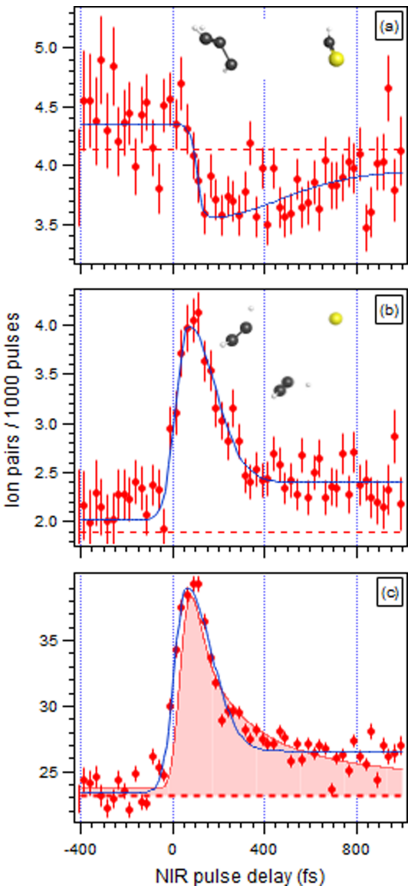

FIG. 5. (a) Measured ion-pair yield (CSH^+, $C_3H_3^+$) from the strongest two-body pathway and (b) multibody fragmentation ion-pair yield (S^+, $C_2H_n^+$), per 1000 pump-probe events. (c) Total multibody ion-pair yield from the areas encircled by the red lines in Fig. 3. Dashed lines are the yield values from a FEL-only measurement, and the blue curves are fits of the model function of (3) to the data. The shaded area in (c) shows the internal-energy-averaged population of the transient linear geometry from the SCC-DFTB simulations, convoluted by the temporal instrument function. Data error bars are based on Poisson statistics of ion-pair counting.

C. Time-dependent effects of adding the NIR probe

We begin the quantitative analysis of the structures already seen in the PIPICO map (Fig. 3) as ion-pair yields, adding the dimension of time delay between the FEL and the NIR pulses (the "NIR delay"; Fig. 5). In the experiment, the arrival time of the NIR pulse was scanned continuously across the FEL pulse, so that it in fact became the pump pulse at the negative delay values and the probe pulse at the positive ones. The data points of the yield curves in Fig. 5 were obtained by counting specific types of ion pairs formed in the pump-probe events. The dashed lines indicate the ion-pair yields in the reference FEL-only measurement.

Figure 5(a) shows the ion-pair yield in the strongest individual two-body dissociation pathway (2), where one can see a clear drop of about 20% starting from a NIR delay of ≈ 110 fs. The effect is mostly transient with a slow recovery time of several hundred femtoseconds. From all two-body pathways seen in Fig. 3, only this pathway (2) shows statistically significant NIR-induced effects; overall the two-body processes are affected very little (see Appendix). Analyzing the yields of individual ions in this pathway narrows the effect down further as the depletion of the $C_3H_3^+$ ion yield, while the SCH^+ population remains unaffected by NIR.

Figure 5(b) is an example of ion-pair yield (CH_n^+, S^+) from a multibody pathway $C_4SH_4^{2+} \rightarrow C_2H_n^+ + S^+ + C_2H_{4-n}$. Here, a dramatically different behavior is seen: The yield more than doubles immediately when the NIR pulse arrives together with or after the FEL pulse. This strong transient enhancement is more short-lived than the negative effect in the two-body channel. Similar behavior, although of varying strength, is exhibited by all individual multibody ion-pair yields (see Appendix), and so we summarize our main experimental finding as a single curve in Fig. 5(c). It shows the multibody events corresponding to the ion pairs from the regions encircled by red in the PIPICO map in Fig. 3. Comparing the total multibody ion-pair yield [Fig. 5(c)] in the pump-probe experiment with the FEL-only yield confirms that an early NIR pulse (negative NIR delay) has no statistically significant effect. In the FEL-pump–NIR-probe region, one can identify a persistent component and a transient component of the enhancement. The ion, ion-pair, and ion-triplet yield curves were fitted using the following model function:

$$Y(t) = Y_0 + A_p \mathrm{erf}\left(\frac{t - t_0}{w}\right) + A_t \exp\left(\frac{-(t - t_g)^2}{(w + w_{t>t_g})^2}\right), \quad (3)$$

where the broadening parameter w of the error function also defines the left-hand-side width of the asymmetric Gaussian. The half-maximum position of the Gaussian is aligned with the zero crossing of the error function by the term $t_g = t_0 + \sqrt{\ln 2}w$, creating a common rising edge, and the right-hand-side width of the Gaussian is modified by the additional broadening $w_{t>t_g}$. The intensity parameters are Y_0, A_p, and A_t. The FEL-delay scale was calibrated by the rising-edge position obtained from the fit of Fig. 5(c) (zeroing the model parameter t_0). All yield curves in Fig. 5 (see also additional yield curves in the Supplemental Material Ref. [33]) are given on this delay scale, regardless of their own fitted edge positions t_0 (see Table I). Using the Xe^{2+} yields from reference measurements for the delay scale calibration according to Ref. [34] is compatible with the above procedure within ± 20 fs. Additional ion pair and triplet yields are given in the Appendix.

The blue curves in Fig. 5 show the fit of a model function representing both the persistent (error function) and the transient (asymmetric Gaussian) effects. The time constants from the fits of the multibody ion-pair yields in Fig. 5(b) and others are given in Table I.

From the fit of the ion-pair yield in Fig. 5(a), the NIR effect on the two-body process is delayed by 106(15) fs, but

TABLE I. Edge positions and the edge and decay widths (in femtoseconds) of the transient NIR enhancements from least-squares fitting of ion-pair yields. Time delay $t_0 = 0$ is defined as the edge position in the fit of the combined multibody ion yield. The width parameters are according to Eq. (3) ($w_{\text{edge}} = w$ and $w_{\text{decay}} = w + w_{t>t_0}$).

Pair	t_0	w_{edge}	w_{decay}
	Multibody yields		
CH_n, CH_n	−7(15)	63(35)	222(91)
CH_n, C_2H_n	−8(7)	44(17)	214(43)
CH_n, S	11(7)	60(16)	173(36)
CH_n, C_3H_n	9(10)	27(33)	241(78)
C_2H_n, S	9(9)	71(21)	128(44)
S, C_3H_n	−21(18)	105(37)	80(78)
H_n, CH_n	10(6)	81(14)	145(31)
H_n, C_2H_n	−24(13)	85(31)	190(71)
H_n, S	8(7)	69(15)	104(31)
H_n, C_3H_n	−11(12)	12(134)	198(253)
Combined	0.0(2.2)	66(5)	158(12)
	Two-body yield		
CSH, C_3H_3	106(11)	42(30)	455(98)

then the falling-edge width of 42(30) fs can be fully ascribed to the temporal instrument function. The transient depletion partly recovers with the width of 455(100) fs. From the total multibody ion-pair yield in Fig. 5(c), we obtain a transient enhancement of 55% over the FEL-only level and a persistent enhancement of 13%. The broadening of the rising edge is 66(5) fs, and the decay width is 158(12) fs.

Comparing the pump-probe effects in the curves in Figs. 5(a) and 5(c), the first observation to make is that both the transient and persistent enhancements in the total multibody yields are much stronger than the decrease in the two-body yield. If the NIR effect were mainly enhanced dissociation due to the increase in the internal energy by nonionizing absorption, it would transfer intensity from the two-body yield to multibody yield, with mirroring behavior. This is not observed, leading to the conclusion that the NIR effect is primarily ionizing, transferring the post-Auger system evolving along any of the M^{2+} potential-energy surfaces (Fig. 2) to the M^{3+} surfaces. The primary consequence of this is the increased number of ionized multibody fragments produced (at the expense of the neutral fragments in multibody processes), leading to a higher count of all possible multibody ion pairs. In the experiment, total ion-pair count from multibody processes increased by as much as 70% [Fig. 5(c)].

With the transient enhancements in ion-pair yields due to additional NIR ionization of the dicationic transient geometry, we expect changes also in the multibody kinematics, since an additional charged fragment would increase the momenta of individual ions in dissociation. The clearest experimental momentum data were obtained by investigating the S^+ ion, since it shows transient enhancements in all channels in which it appears and is accompanied by only a very low contribution of SH^+ ions, making its momentum determination the most accurate among the multibody fragments.

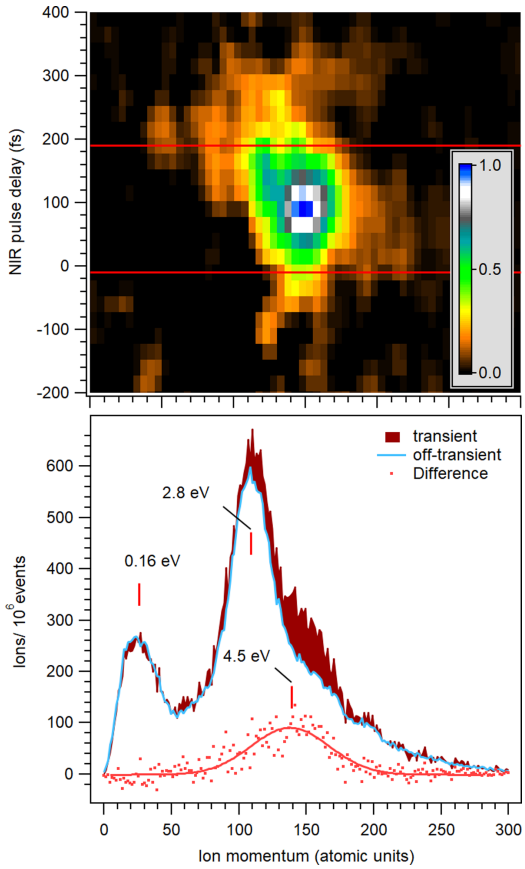

FIG. 6. Top: momentum distribution of S^+ ions as a function of the NIR delay, after subtracting the averaged NIR-early momentum distribution (NIR delay < −300 fs). The color scale is set relative to the peak value of the distribution function over the shown range of ion momenta and pulse delays. Bottom: momentum distribution of the S^+ ions in the transient (between the red lines in the top panel) and off-transient regions of the NIR delay. Dots with a fitted Gaussian function are the difference of the two curves. The ion kinetic energies corresponding to the peak maxima are marked.

The top panel of Fig. 6 is a two-dimensional histogram of the momenta of all the S^+ ions detected in the pump-probe measurement, binned according to the NIR delays of the pump-probe events producing them. The histogram is given as a difference from the NIR-pump–FEL-probe momentum distribution, by subtracting the distribution curve of the S^+ ions produced in the events where the NIR pulse arrives more than 300 fs before the FEL pulse. It is clearly seen that the ions from the NIR enhancement fall into a well-defined momentum range around 140 a.u., with a time profile of the transient enhancement region.

The bottom panel of Fig. 6 shows the S^+ ion's momentum distributions within and outside the transient NIR-delay range

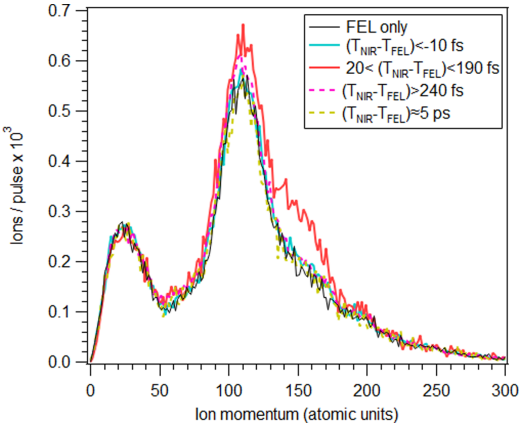

FIG. 7. Momentum distribution of S^+ ions in various NIR-delay ranges and in the FEL-only measurement (black line). The range of the transient effects was set to the 20-to-190 fs FEL-NIR-pulse delay (red curve) and also the pre-transient (cyan curve), after-transient (dashed pink) and long FEL-delay (dashed yellow) ranges are shown.

and Fig. 7 gives a more detailed breakdown of the dependency of the momentum distribution on the pump-probe delay. Both momentum distribution curves in Fig. 6 show a first maximum corresponding to very small kinetic energy which is attributed to the residual O_2^+ contamination or a small amount of S^+ fragments from direct valence ionization. The main maximum corresponds to 2.8-eV kinetic energy, while the ions from the transient enhancement have an average of 4.5-eV kinetic energy.

Ion triplet yields provide even more dissociation-channel-specific information on multi-body fragmentation events, but suffer from lower statistics than the ion-pair yields.

We confirmed the assignment of the two maxima to the two- and three-ion pathways by a simple point-charge Coulomb explosion model [24,35], starting from the linear transient geometry and using the centers of mass of the fragments as starting coordinates. In a three-body concerted dicationic dissociation where, in addition to S^+, only one C_2H_2 fragment obtains charge, the S^+ ion receives either 1.34 or 2.22 eV of kinetic energy. If one considers also the possibility of a two-step process, first releasing the S^+ ions by $C_4SH_4^{2+} \rightarrow S^+ + C_4H_4^+$, then S^+ obtains 2.35 eV of energy. In a concerted dissociation of a triply charged system with S^+ and two $C_2H_2^+$ ions, S^+ receives 4.19 eV of kinetic energy (4.46 eV in the case of a two-step process $C_4SH_4^{2+} \rightarrow S^+ + C_4H_4^{2+}$). These guideline values support our interpretation of the transient enhancement as due to quite a different process from the prevalent dicationic dissociation, namely, the more energetic breakup of a triply charged system.

IV. DISCUSSION

A. Probing the early dynamics

At the starting point of molecular dynamics, the Auger decay populates numerous dicationic potential-energy surfaces (PESs), two of which are shown schematically in Fig. 2, up to about 40 eV above the double-ionization potential (DIP) [25]. Some of these states lie above the triple-ionization potential (TIP) and can therefore decay further onto the triply ionized PESs, leading to triple ion coincidences observable already in the FEL-only experiment (see Appendix for the ion-triplet yields). Consistently, the momentum distribution of the S^+ ions (Fig. 6, blue curve) has a tail in the region corresponding to the triply ionized dissociation even without the NIR-induced enhancement.

We concluded that the NIR probe facilitates the transfer of the system to the triply ionized PESs. First, we calculated the ionization potentials along one chosen dissociation trajectory from the SCC-DFTB simulations. The calculated TIP lies above the DIP by 23.3, 19.9, or 17.4 eV in the ground-state, open-linear, and dissociated (with the S, C_2H_2, and C_2H_2 fragments) geometries, respectively. (The edges of the bottom M^{2+} and the M^{3+} surfaces in Fig. 2 are from this calculation.) This energy is too high for efficient NIR ionization from M^{2+} to M^{3+} PESs. In the basic picture, Auger decay replaces the inner-shell vacancy with two vacancies in the outer- or inner-valence molecular orbitals. Such a description of the Auger final states has been shown to be rather simplified, however, since due to the correlated motion of all valence electrons, an electron can transfer to an initially empty, Rydberg-like orbital [36]. These excited electrons have smaller binding energies than valence electrons, more easily overcome by the absorption of one or a few NIR photons. The combination of high-energy Auger final states and the presence of excited electrons due to electron correlation creates a suitable environment for efficient NIR ionization, such as observed in the laser-enabled Auger decay (LEAD) process [27,36,37]. It is worth emphasizing the key point of the NIR probing of the particular electron-correlated dicationic states involving an excited electron. The NIR probe acting on the pure two-hole states (in valence and inner-valence orbitals) would, consistent with the present experimental results, be quite insensitive to such a system, and the FEL-NIR pump-probe approach would not be a suitable one to study the dynamics in dicationic states that are prevalent after x-ray absorption in organic molecules and biomolecules. However, the electron correlation of the two-hole states with the states involving an excited Rydberg electron (three-hole, one-excited-electron states) makes the NIR probe sensitive to the dicationic states.

Such an environment arises very shortly after the core ionization, following the core-hole lifetime of a few femtoseconds, and creates the observed fast-rising edge of the transient NIR effects. The next questions are, What changes in the evolving systems cause these effects to fade, and what transient properties do we actually probe?

Let us first look at the early evolution of the molecular geometry. Figure 4 showed the population of the transient geometry of the parent dication as a function of time and internal energy, from the SCC-DFTB simulations. In Fig. 5(c), it is compared with the experimental total multibody ion-pair yield, after calculating a weighted average over the Auger final-state energies according to their theoretical density of states in the Auger spectrum [25]. The Auger final states

with less than 10 eV (10 000 K) internal energy were excluded, since the likelihood of NIR-induced third ionization from these states should be negligible. This particular cutoff energy was also chosen since neither the simulated trajectories nor the electron-energy-resolved experiment [25] show any multibody fragmentation channels below that energy. As the comparison shows, the temporal behavior of the transient linear parent geometry is quantitatively well matched with the NIR enhancement.

Turning to the changes in the electronic structure, one recognizes that the relaxation of the high-energy dicationic states towards the lowest-energy state can take place over time. This *internal conversion* transfers energy from electrons to the nuclear motion and is a fundamental mechanism of energy dissipation in organic molecules [2,38,39]. As the energy is transferred from the electronic to the nuclear subsystem, the initially excited dicationic electronic states are depleted, and the NIR-ionization probability by LEAD decreases accordingly. The internal conversion is not a process easily modeled and can occur in different systems over a broad time range [40]. Our observation of the decay width of the transient enhancement, about 160 fs, sets the lower limit to the internal-conversion time constant.

It is of interest to consider briefly the relevant findings in other studies, although their different photoexcitation conditions (involving valence rather than the inner electron shells) do not allow for a direct comparison. Photoinduced thiophene ring opening has been observed following neutral excitations from the ground state to the S_1 state by Weinkauf *et al.* [1], who determined in a UV pump-probe experiment a time constant of 80 fs, associated with the ring opening by the cleavage of the C-S bond (the prevalent cleavage site in our simulations also [25]). A subsequent theoretical study of the S_1 excited state in thiophene found that the subsequent dynamics of the open-ring structures is characterized by the interplay of internal conversion and intersystem crossing [41]. Other femtosecond pump-probe studies in the XUV energy range have drawn inferences about the timescale of the internal conversion in a dissociating molecular system. In a study by Månsson *et al.* [15], the authors observed transient effects in cationic states of thymidine. Their decay time constants of less than 200 fs were interpreted as due to rapid decay via nonadiabatic coupling between electronic states. In another study of the radiosensitizer molecule 5-fluorouracil, both fast nonadiabatic-relaxation (30 fs) and slow (2.3 ps) internal-conversion timescales were proposed as creating the transient pump-probe effects [42].

B. Probing the late dynamics

In the FEL-pump–late-NIR-probe region beyond the transient structures we observe weak persistent enhancements over the FEL-only baseline in multibody ion-pair yields, such as the plateau beyond ≈ 400-fs delay in Fig. 5(c). The plateau continues to much longer FEL-NIR delays (was observed even at 5 ps) and therefore must be related to the interaction of the NIR pulse with the *fragment species*, produced by the FEL ionization. The most likely persistent NIR contribution to the multibody ion-pair yields comes from the ionization of neutral fragments, such as $C_{1-3}H_{1-4}$. The ionization energies of the neutral fragments are comparable to or even lower (starting from 6.6 eV for the cyclopropenyl radical C_3H_3 [43]) than that of neutral thiophene, which is weakly ionized by the NIR pulse. Fundamentally, the persistent and transient NIR interactions are similar, but the former occurs in a nonevolving environment of stable neutral fragment species likely as multiphoton ionization.

The ion momentum distributions are also useful in probing the late dynamics. The S^+ ions showed a clear triple-ionization high-momentum transient enhancement. In contrast, the momentum distributions in the late persistent enhancement region are identical in shape to the pretransient region and also to the FEL-only distribution (more detailed ion momentum curves are given in the Appendix). The persistent component is seen as a slight increase in the ions with momenta corresponding to the doubly charged process. Although the NIR pulse eventually releases the third charge, the neutral fragments are ionized at larger separations where its Coulomb interaction with the two initially charged fragments is much weaker. Since the fragment separation at the time of the arrival of the NIR pulse is delay dependent, shorter pump-probe delays close to the transient region should give a larger change in the momenta of ions, and at long delays the change becomes negligible. Some tentative indications of such delay dependency of the momentum of the persistent enhancement are seen in the top panel of Fig. 6.

Lastly, we note that the NIR-probe effect on two-body channels can only be depletive. Generally, the two-body pathways are affected very little in our experiment. This is readily understood since the NIR pulse requires highly excited dicationic states for efficient ionization (depleting the two-body channels) but the two-body pathways are primarily associated with the *low-energy* dicationic states. The only two-body process exhibiting the NIR effects [Fig. 5(a)] exhibits a delayed onset of the transient NIR effect. The ≈ 100-fs delay is well in line with the fragment separation time in the two-body process (2): A point-charge calculation using the center-of-mass positions of the two fragments in the ground-state geometry of thiophene as a starting point showed that in 100 fs their separation increases from 1.9 to 6.4 Å—a reasonable distance to describe a fragmented system. The slow decay time of about 500 fs of the depleting NIR effect likely represents the timescale of the internal conversion of electronic energy within the $C_3H_3^+$ fragment and/or geometry relaxation, slowly reducing the NIR pulse's ability to interact with it.

V. SUMMARY

We have demonstrated how the FEL-NIR pump-probe experiments shed light on the early period of the x-ray-induced molecular dissociation of organic molecules and can be suitable also for larger biomolecules. We suggest that the NIR enhancement is linked to the creation of highly excited electronic states by the Auger decay of the core-ionized molecules, as a particular feature of x-ray ionization. These excited states likely involve electrons promoted to

Rydberg-type orbitals, allowing the NIR probe to interact efficiently. However, this interaction is transient since the highly excited states are continually depleted by internal conversion, transferring energy to vibrational motion. Exactly how the electronic structure changes and accommodates to the changing geometry has a direct bearing on the ability of the NIR probe to interact with the system.

The observations on our sample system, thiophene, in combination with theoretical modeling led us to conclude that the cyclic parent thiophene dication quickly opens up into a linear geometry, which then dissociates. Calculations suggest that the dissociation has a certain latency, since that linear geometry can occasionally survive for tens, even hundreds, of femtoseconds, even at high internal energies. We suggest that it is this open-ring parent geometry that ibeing probed and that the time structure of the transient NIR-induced enhancements reflects the statistical survival probability (lifetime) of this transient geometry. Eventually, the NIR effect fades into much weaker, persistent interaction with the stable fragment species. Perhaps surprisingly, our study also leads to the conclusion that the decay of the energetic electronic states by internal conversion is slow enough, over ≈ 160 fs, to allow for significant concurrent nuclear dynamics.

The prominence of electronic relaxation and geometry changes in the early photodynamics underscores the importance of nonadiabatic couplings in this period. Both the survival of the parent dication even at strongly unfavorable conditions and the redistribution of the internal energy over time are properties that have relevance well beyond the technicalities of pump-probe experiments. The first might significantly affect the final extent and nature of the radiation damage as fragments are released over time by the primary and secondary (electron and fragment collisions) ionizations. The second affects our ability to accurately model the dissociation landscape in larger quantum systems.

New time-resolved experimental opportunities offered by the FEL facilities with very high pulse repetition rates will certainly reveal new details of the formative periods of the photodissociation landscapes of molecules. Here, we demonstrated how, in the FEL-NIR pump-probe scheme, the NIR probe becomes sensitive to transient excited dicationic states of the molecule, created by the Auger relaxation of core-hole states. We showed the feasibility of this experimental approach in the example of a medium-sized organic molecule. This technique would likely also be beneficial, for example, in time-tracing the early evolution of x-ray radiation damage in the molecular building blocks of much larger biomolecules.

Using pump-probe schemes such as the one in this paper and adding selectivity to the internal energy by also recording the Auger electrons' energies will help in investigating the parent molecule's survival times and the fast energy conversions following the ionization event.

ACKNOWLEDGMENTS

This study was supported by the X-ray Free Electron Laser Utilization Research Project and the X-ray Free Electron Laser Priority Strategy Program of the Ministry of Education, Culture, Sports, Science and Technology of Japan (MEXT), by the Proposal Program of SACLA Experimental Instruments of RIKEN, by the research program "Dynamic Alliance for Open Innovation Bridging Human, Environment and Materials" at the Network Joint Research Center for Materials and Devices, by the IMRAM project, and by the Japan Society for the Promotion of Science (JSPS). E.K., J.N., and E.P. acknowledge financial support from the Academy of Finland, and D.Y. was supported by a grant-in-aid from Tohoku University Institute for Promoting Graduate Degree Programs, Division for Interdisciplinary Advanced Research and Education. J.P. and P.J. acknowledge support from the Swedish Research Council and the Swedish Foundation for Strategic Research. We thank the staff of the SACLA facility for their help in preparation of and during the experiment.

APPENDIX: ION-PAIR AND ION-TRIPLET YIELDS

In this appendix, further details on the ion-pair and ion-triplet yields as a function of time are presented. Firstly, Fig. 8 shows the total ion-pair yield from all detected two-body dissociation channels.

Figure 9 gives ion-pair yields from eight observed strong multibody dissociation channels within the circled regions of Fig. 3.

Ion-triplet yields provide even more dissociation-channel-specific information on multibody fragmentation events but suffer from lower statistics than the ion-pair yields. Some examples are shown in Fig. 10.

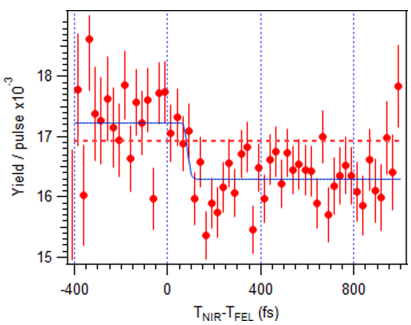

FIG. 8. Combined ion-pair yield of all two-body channels, as a function of NIR-delay. Dashed line is the yield value from a FEL-only measurement.

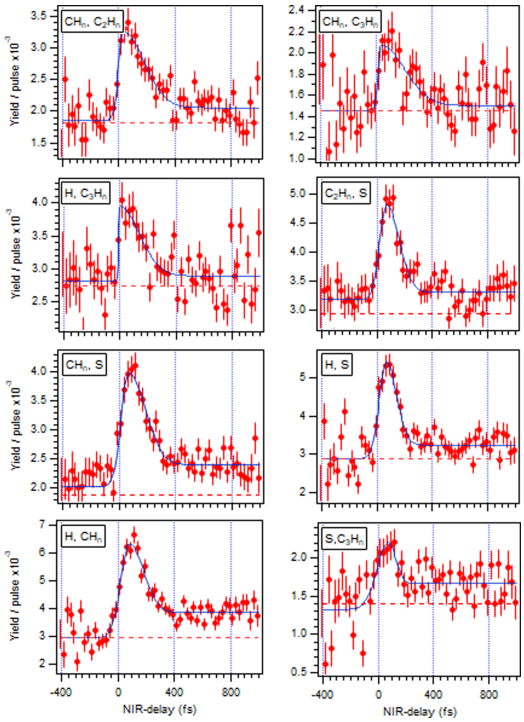

FIG. 9. Ion-pair yields of multi-body fragmentation events, as a function of NIR-delay. Dashed lines are yield values from a FEL-only measurement.

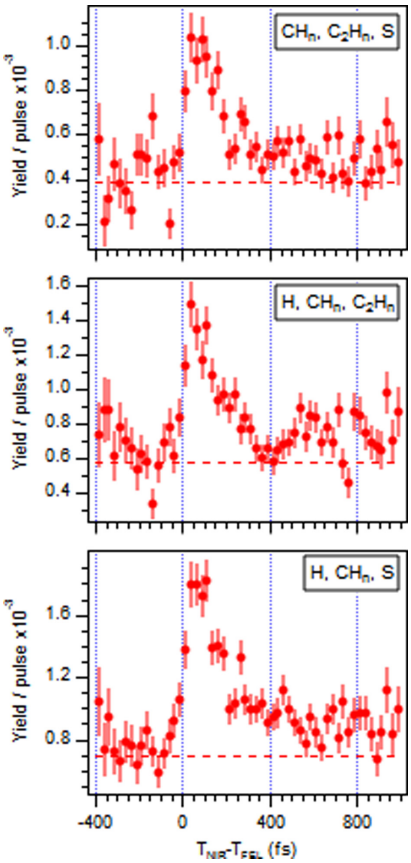

FIG. 10. Ion triplet yields of some prominent multi-body channels, as a function of NIR-delays. Dashed lines are the yield values from a FEL-only measurement.

[1] R. Weinkauf, L. Lehr, E. W. Schlag, S. Salzmann, and C. M. Marian, Ultrafast dynamics in thiophene investigated by femtosecond pump probe photoelectron spectroscopy and theory, Phys. Chem. Chem. Phys. **10**, 393 (2008).

[2] T. J. A. Wolf, R. H. Myhre, J. P. Cryan, S. Coriani, R. J. Squibb, A. Battistoni, N. Berrah, C. Bostedt, P. Bucksbaum, G. Coslovich, R. Feifel, K. J. Gaffney, J. Grilj, T. J. Martinez, S. Miyabe, S. P. Moeller, M. Mucke, A. Natan, R. Obaid, T. Osipov *et al.*, Probing ultrafast $\pi\pi^*/n\pi^*$ internal conversion in organic chromophores via K-edge resonant absorption, Nat. Commun. **8**, 29 (2017).

[3] *Handbook of Thiophene-Based Materials*, edited by I. F. Perepichka and D. F. Perepichka (Wiley, Chichester, UK, 2009).

[4] I. Luzon, E. Livshits, K. Gope, R. Baer, and D. Strasser, Making sense of Coulomb explosion imaging, J. Phys. Chem. Lett. **10**, 1361 (2019).

[5] S. Scheit, S. Goswami, H.-D. Meyer, and H. Köppel, Fully quantal treatment of nonadiabatic molecular photodynamics: General considerations and application to the benzene cation, Comput. Theor. Chem. **1150**, 71 (2019).

[6] S. Hsieh and J. H. Eland, Reaction dynamics of three-body dissociations in triatomic molecules from single-photon double ionization studied by a time- and position-sensitive coincidence method, J. Phys. B: At., Mol. Opt. Phys. **30**, 4515 (1997).

[7] R. J. Squibb, M. Sapunar, A. Ponzi, R. Richter, A. Kivimäki, O. Plekan, P. Finetti, N. Sisourat, V. Zhaunerchyk, T. Marchenko, L. Journel, R. Guillemin, R. Cucini, M. Coreno, C. Grazioli, M. Di Fraia, C. Callegari, K. C. Prince, P. Decleva, M. Simon *et al.*, Acetylacetone photodynamics at a seeded free-electron laser, Nat. Commun. **9**, 63 (2018).

[8] J. Ullrich, A. Rudenko, and R. Moshammer, Free-electron lasers: New avenues in molecular physics and photochemistry, Annu. Rev. Phys. Chem. **63**, 635 (2012).

[9] L. Young, K. Ueda, M. Gühr, P. H. Bucksbaum, M. Simon, S. Mukamel, N. Rohringer, K. C. Prince, C. Masciovecchio, M. Meyer, A. Rudenko, D. Rolles, C. Bostedt, M. Fuchs, D. A. Reis, R. Santra, H. Kapteyn, M. Murnane, H. Ibrahim, F. Légaré *et al.*, Roadmap of ultrafast x-ray atomic and molecular physics, J. Phys. B: At., Mol. Opt. Phys. **51**, 032003 (2018).

[10] K. Ueda, E. Sokell, S. Schippers, F. Aumayr, H. Sadeghpour, J. Burgdörfer, C. Lemell, X.-M. Tong, T. Pfeifer, F. Calegari, A. Palacios, F. Martin, P. Corkum, G. Sansone, E. V. Gryzlova, A. N. Grum-Grzhimailo, M. N. Piancastelli, P. M. Weber, T. Steinle, K. Amini *et al.*, Roadmap on photonic, electronic and atomic collision physics: I. Light-matter interaction, J. Phys. B: At., Mol. Opt. Phys. **52**, 171001 (2019).

[11] J. van Tilborg, T. K. Allison, T. W. Wright, M. P. Hertlein, R. W. Falcone, Y. Liu, H. Merdji, and A. Belkacem, Femtosecond isomerization dynamics in the ethylene cation measured in an EUV-pump NIR-probe configuration, J. Phys. B: At., Mol. Opt. Phys. **42**, 081002 (2009).

[12] Y. H. Jiang, A. Rudenko, O. Herrwerth, L. Foucar, M. Kurka, K. U. Kühnel, M. F. Lezius, M. Kling, J. van Tilborg, A. Belkacem, K. Ueda, S. Düsterer, R. Treusch, C. D. Schröter, R. Moshammer, and J. Ullrich, Ultrafast Extreme Ultraviolet Induced Isomerization of Acetylene Cations, Phys. Rev. Lett. **105**, 263002 (2010).

[13] T. K. Allison, H. Tao, W. J. Glover, T. W. Wright, A. M. Stooke, C. Khurmi, J. van Tilborg, Y. Liu, R. W. Falcone, T. J. Martínez, and A. Belkacem, Ultrafast internal conversion in ethylene. II. Mechanisms and pathways for quenching and hydrogen elimination, J. Chem. Phys. **136**, 124317 (2012).

[14] N. Hartmann, S. Bhattacharyya, F. Schlaepfer, M. Volkov, Z. Schumacher, M. Lucchini, L. Gallmann, U. Rothlisberger, and U. Keller, Ultrafast nuclear dynamics of the acetylene cation $C_2H_2^+$ and its impact on the infrared probe pulse induced C-H bond breaking efficiency, Phys. Chem. Chem. Phys. **21**, 18380 (2019).

[15] E. P. Månsson, S. De Camillis, M. C. Castrovilli, M. Galli, M. Nisoli, F. Calegari, and J. B. Greenwood, Ultrafast dynamics in the DNA building blocks thymidine and thymine initiated by ionizing radiation, Phys. Chem. Chem. Phys. **19**, 19815 (2017).

[16] B. F. Murphy, L. Fang, M.-H. Chen, J. D. Bozek, E. Kukk, E. P. Kanter, M. Messerschmidt, T. Osipov, and N. Berrah, Multiphoton *L*-shell ionization of H_2S using intense x-ray pulses from a free-electron laser, Phys. Rev. A **86**, 053423 (2012).

[17] O. Kornilov, M. Eckstein, M. Rosenblatt, C. P. Schulz, K. Motomura, A. Rouzée, J. Klei, L. Foucar, M. Siano, A. Lübcke, F. Schapper, P. Johnsson, D. M. P. Holland, T. Schlathölter, T. Marchenko, S. Düsterer, K. Ueda, M. J. J. Vrakking, and L. J. Frasinski, Coulomb explosion of diatomic molecules in intense XUV fields mapped by partial covariance, J. Phys. B: At., Mol. Opt. Phys. **46**, 164028 (2013).

[18] B. Erk, D. Rolles, L. Foucar, B. Rudek, S. Epp, M. Cryle, C. Bostedt, S. Schorb, J. Bozek, A. Rouzee, A. Hundertmark, T. Marchenko, M. Simon, F. Filsinger, L. Christensen, S. De, S. Trippel, J. Küpper, H. Stapelfeldt, S. Wada *et al.*, Ultrafast Charge Rearrangement and Nuclear Dynamics upon Inner-Shell Multiple Ionization of Small Polyatomic Molecules, Phys. Rev. Lett. **110**, 053003 (2013).

[19] B. Erk, R. Boll, S. Trippel, D. Anielski, L. Foucar, B. Rudek, S. W. Epp, R. Coffee, S. Carron, S. Schorb, K. R. Ferguson, M. Swiggers, J. D. Bozek, M. Simon, T. Marchenko, J. Kupper, I. Schlichting, J. Ullrich, C. Bostedt, D. Rolles *et al.*, Imaging charge transfer in iodomethane upon x-ray photoabsorption, Science **345**, 288 (2014).

[20] B. Rudek, S.-K. Son, L. Foucar, S. W. Epp, B. Erk, R. Hartmann, M. Adolph, R. Andritschke, A. Aquila, N. Berrah, C. Bostedt, J. Bozek, N. Coppola, F. Filsinger, H. Gorke, T. Gorkhover, H. Graafsma, L. Gumprecht, A. Hartmann, G. Hauser *et al.*, Ultra-efficient ionization of heavy atoms by intense X-ray free-electron laser pulses, Nat. Photonics **6**, 858 (2012).

[21] A. Rudenko, L. Inhester, K. Hanasaki, X. Li, S. J. Robatjazi, B. Erk, R. Boll, K. Toyota, Y. Hao, O. Vendrell, C. Bomme, E. Savelyev, B. Rudek, L. Foucar, S. H. Southworth, C. S. Lehmann, B. Kraessig, T. Marchenko, M. Simon, K. Ueda *et al.*, Femtosecond response of polyatomic molecules to ultra-intense hard X-rays, Nature (London) **546**, 129 (2017).

[22] K. Motomura, E. Kukk, H. Fukuzawa, S.-i. Wada, K. Nagaya, S. Ohmura, S. Mondal, T. Tachibana, Y. Ito, R. Koga, T. Sakai, K. Matsunami, A. Rudenko, C. Nicolas, X.-J. Liu, C. Miron, Y. Zhang, Y. Jiang, J. Chen, M. Anand *et al.*, Charge and nuclear dynamics induced by deep inner-shell multiphoton ionization of CH_3I molecules by intense x-ray free-electron laser pulses, J. Phys. Chem. Lett. **6**, 2944 (2015).

[23] K. Nagaya, K. Motomura, E. Kukk, Y. Takahashi, K. Yamazaki, S. Ohmura, H. Fukuzawa, S. Wada, S. Mondal, T. Tachibana, Y. Ito, R. Koga, T. Sakai, K. Matsunami, K. Nakamura, M. Kanno, A. Rudenko, C. Nicolas, X.-J. Liu, C. Miron *et al.*, Femtosecond charge and molecular dynamics of I-containing organic molecules induced by intense X-ray free-electron laser pulses, Faraday Discuss. **194**, 537 (2016).

[24] E. Kukk, H. Myllynen, K. Nagaya, S. Wada, J. D. Bozek, T. Takanashi, D. You, A. Niozu, K. Kooser, T. Gaumnitz, E. Pelimanni, M. Berholts, S. Granroth, N. Yokono, H. Fukuzawa, C. Miron, and K. Ueda, Coulomb implosion of tetrabromothiophene observed under multiphoton ionization by free-electron-laser soft-x-ray pulses, Phys. Rev. A **99**, 023411 (2019).

[25] E. Kukk, D. T. Ha, Y. Wang, D. G. Piekarski, S. Diaz-Tendero, K. Kooser, E. Itälä, H. Levola, M. Alcamí, E. Rachlew, and F. Martín, Internal energy dependence in x-ray-induced molecular fragmentation: An experimental and theoretical study of thiophene, Phys. Rev. A **91**, 043417 (2015).

[26] M. S. Schuurman and A. Stolow, Dynamics at conical intersections, Annu. Rev. Phys. Chem. **69**, 427 (2018).

[27] D. You, K. Ueda, M. Ruberti, K. L. Ishikawa, P. A. Carpeggiani, T. Csizmadia, L. G. Oldal, H. N G, G. Sansone, P. K. Maroju, K. Kooser, C. Callegari, M. D. Fraia, O. Plekan, L. Giannessi, E. Allaria, G. D. Ninno, M. Trovó, L. Badano, B. Diviacco *et al.*, A detailed investigation of single-photon laser enabled Auger decay in neon, New J. Phys. **21**, 113036 (2019).

[28] S. Owada, K. Togawa, T. Inagaki, T. Hara, T. Tanaka, Y. Joti, T. Koyama, K. Nakajima, H. Ohashi, Y. Senba, T. Togashi, K. Tono, M. Yamaga, H. Yumoto, M. Yabashi, H. Tanaka, and T. Ishikawa, A soft X-ray free-electron laser beamline at SACLA:

The light source, photon beamline and experimental station, J. Synchrotron Radiat. **25**, 282 (2018).

[29] M. Yabashi, H. Tanaka, and T. Ishikawa, Overview of the SACLA facility, J. Synchrotron Radiat. **22**, 477 (2015).

[30] S. Owada, K. Nakajima, T. Togashi, T. Katayama, H. Yumoto, H. Ohashi, and M. Yabashi, Arrival timing diagnostics at a soft X-ray free-electron laser beamline of SACLA BL1, J. Synchrotron Radiat. **26**, 887 (2019).

[31] H. Fukuzawa, K. Nagaya, and K. Ueda, Advances in instrumentation for gas-phase spectroscopy and diffraction with short-wavelength free electron lasers, Nucl. Instrum. Methods Phys. Res., Sect. A **907**, 116 (2018).

[32] R. G. Hayes and W. Eberhardt, Electron-ion coincidences studies of the fragmentation of thiophene and of tetrahydrothiophene upon core ionization, J. Chem. Phys. **94**, 397 (1991).

[33] See Supplemental Material at http://link.aps.org/supplemental/10.1103/PhysRevResearch.3.013221 for example animations of the ring opening and fragmentation.

[34] D. Rolles, R. Boll, B. Erk, D. Rompotis, and B. Manschwetus, An experimental protocol for femtosecond NIR/UV - XUV pump-probe experiments with free-electron lasers, J. Visualized Exp. **140**, e57055 (2018).

[35] E. Kukk, K. Motomura, H. Fukuzawa, K. Nagaya, and K. Ueda, Molecular dynamics of XFEL-induced photo-dissociation, revealed by ion-ion coincidence measurements, Appl. Sci. **7**, 531 (2017).

[36] B. Cooper and V. Averbukh, Single-Photon Laser-Enabled Auger Spectroscopy for Measuring Attosecond Electron-Hole Dynamics, Phys. Rev. Lett. **111**, 083004 (2013).

[37] D. Iablonskyi, K. Ueda, K. L. Ishikawa, A. S. Kheifets, P. Carpeggiani, M. Reduzzi, H. Ahmadi, A. Comby, G. Sansone, T. Csizmadia, S. Kuehn, E. Ovcharenko, T. Mazza, M. Meyer, A. Fischer, C. Callegari, O. Plekan, P. Finetti, E. Allaria, E. Ferrari *et al.*, Observation and Control of Laser-Enabled Auger Decay, Phys. Rev. Lett. **119**, 073203 (2017).

[38] M. Fagnoni, Modern Molecular Photochemistry of Organic Molecules. Von Nicholas J. Turro, V. Ramamurthy und Juan C. Scaiano, Angew. Chem. **122**, 6859 (2010).

[39] R. R. Valiev, V. N. Cherepanov, G. V. Baryshnikov, and D. Sundholm, First-principles method for calculating the rate constants of internal-conversion and intersystem-crossing transitions, Phys. Chem. Chem. Phys. **20**, 6121 (2018).

[40] H. Kuhn, H.-D. Försterling, and D. H. Waldeck, *Principles of Physical Chemistry*, 2nd ed. (Wiley, Hoboken, NJ, 2009).

[41] T. Schnappinger, P. Kölle, M. Marazzi, A. Monari, L. González, and R. de Vivie-Riedle, *Ab initio* molecular dynamics of thiophene: The interplay of internal conversion and intersystem crossing, Phys. Chem. Chem. Phys. **19**, 25662 (2017).

[42] P. Çarçabal, D. Descamps, S. Petit, Y. Mairesse, V. Blanchet, and R. Cireasa, Using high harmonic radiation to reveal the ultrafast dynamics of radiosensitiser molecules, Faraday Discuss. **194**, 407 (2016).

[43] *NIST Chemistry WebBook: NIST Standard Reference Database Number 69*, edited by P. J. Linstrom and W. G. Mallard (National Insitute of Standards and Technology, Gaithersburg, MD, 2000).

Paper VIII

H. Dacasa, H. Coudert-Alteirac, C. Guo, E. Kueny, F. Campi, J. Lahl, J. Peschel, H. Wikmark, B. Major, E. Malm, D. Alj, K. Varjú, C. L. Arnold,G. Dovillaire, P. Johnsson, A. L'Huillier, S. Maclot, P. Rudawski, and P. Zeitoun
Single-shot extreme-ultraviolet wavefront measurements of high-order harmonics
Opt. Express 27, 2656–2670 (2019)

Research Article | Vol. 27, No. 3 | 4 Feb 2019 | OPTICS EXPRESS 2656
Optics EXPRESS

Single-shot extreme-ultraviolet wavefront measurements of high-order harmonics

HUGO DACASA,[1,2,*] HÉLÈNE COUDERT-ALTEIRAC,[2] CHEN GUO,[2] EMMA KUENY,[2] FILIPPO CAMPI,[2] JAN LAHL,[2] JASPER PESCHEL,[2] HAMPUS WIKMARK,[3] BALÁZS MAJOR,[4] ERIK MALM,[2] DOMENICO ALJ,[3] KATALIN VARJÚ,[4] CORD L. ARNOLD,[2] GUILLAUME DOVILLAIRE,[3] PER JOHNSSON,[2] ANNE L'HUILLIER,[2] SYLVAIN MACLOT,[2] PIOTR RUDAWSKI,[2] AND PHILIPPE ZEITOUN[1]

[1]*Laboratoire d'Optique Appliquée, École Nationale Supérieure de Techniques Avancées, École Polytechnique, CNRS UMR7639, Chemin de la Hunière, 91761 Palaiseau Cedex, France*
[2]*Department of Physics, Lund University, P. O. Box 118, SE-22100 Lund, Sweden*
[3]*Imagine Optic, 18 Rue Charles de Gaulle, 91400 Orsay, France*
[4]*ELI-ALPS, ELI-HU Non-Profit Ltd., Dugonics ter 13, Szeged 6720, Hungary*
[*]*hugo.dacasa@fysik.lth.se*

Abstract: We perform wavefront measurements of high-order harmonics using an extreme-ultraviolet (XUV) Hartmann sensor and study how their spatial properties vary with different generation parameters, such as pressure in the nonlinear medium, fundamental pulse energy and duration as well as beam size. In some conditions, excellent wavefront quality (up to $\lambda/11$) was obtained. The high throughput of the intense XUV beamline at the Lund Laser Centre allows us to perform single-shot measurements of both the full harmonic beam generated in argon and individual harmonics selected by multilayer mirrors. We theoretically analyze the relationship between the spatial properties of the fundamental and those of the generated high-order harmonics, thus gaining insight into the fundamental mechanisms involved in high-order harmonic generation (HHG).

1. Introduction

High-order harmonic generation (HHG) in gases [1, 2] is a highly nonlinear process which provides spatially and temporally coherent ultrashort pulses [3, 4] in the extreme ultraviolet (XUV) and X-ray domains [5–7]. HHG has applications in many research fields, such as nonlinear XUV optics [8], attosecond physics [9, 10], XUV spectroscopy [11], and plasma physics [12, 13].

Generating high-order harmonic beams with high spatial quality is of crucial importance for applications like imaging [14], holography [15], or as a seed of a plasma amplifier [16] or a free-electron laser [17]. Good spatial quality also allows for tighter focusing [18–21], leading to higher intensities, important for experiments involving nonlinear phenomena, such as two-photon ionization of gases [22, 23]. The study of harmonic wavefronts can lead to better knowledge of the physical process of HHG, and suggest new ways of optimizing the resulting XUV beams in terms of power and spatial quality.

One of the first experiments performed to study the wavefronts of high-order harmonics made use of the technique of point diffraction interferometry [24] with, however, limited precision in the wavefront measurements. Furthermore, only the defocus was characterized, without measuring other aberrations such as astigmatism or coma. Other similar techniques include lateral shearing interferometry [25] and slit diffraction, also called spectral wavefront optical reconstruction by diffraction (SWORD) [26, 27]. The latter involves measuring the radiation diffracted from a slit scanned in front of a spectrometer, thus measuring the wavefronts and intensity profiles along

#349968 https://doi.org/10.1364/OE.27.002656
Journal © 2019 Received 2 Nov 2018; revised 19 Dec 2018; accepted 19 Dec 2018; published 28 Jan 2019

one direction for all harmonic orders simultaneously. This method is well suited for sources where rotational symmetry can be assumed, which is not the case in the present work. Complete two-dimensional measurements of the wavefront can be achieved by rotating the measurement setup by 90°. In either case, this technique always requires many laser shots per measurement.

XUV Hartmann wavefront sensors (WFS), while lacking the spectral resolution found in SWORD, provide high accuracy and allow for the measurement of the two-dimensional wavefront and intensity profile of a light pulse simultaneously [28]. Previous measurements of the wavefronts of high-order harmonics with this method use multiple shots [29, 30], required for HHG with infrared (IR) lasers with pulse energies in the few mJ range, repetition rates of the order of kHz, and short focal lengths. Thousands of shots are typically needed to be accumulated in order to record usable wavefront and intensity maps, thus providing only averages and no information on shot-to-shot stability. Hartmann sensors have, however, the potential for single-shot acquisitions provided that the measured pulse carries enough energy.

In HHG, a spectrum of several odd-order harmonics of the fundamental is obtained, corresponding in the time domain to an attosecond pulse train (APT). Depending on the application, it is interesting to measure the wavefront of the APT or of the individual harmonic components. The latter measurements require separation or selection of the harmonics, e.g. with multilayer mirrors, or the use of spectrally-resolved techniques such as SWORD or the Hartmann sensor-based method developed in [31]. Full beam APT wavefront measurements are useful to optimize and characterize the focus of attosecond pulses [21].

In this paper, we report the results of an experiment carried out at the intense XUV beamline at the Lund Laser Centre, with the main goal of investigating how the harmonic wavefront relates to the spatial properties of the driving IR beam. Another goal was to study in detail how it varies depending on the generation parameters, such as pressure of the nonlinear medium, diameter of the fundamental beam, and its pulse energy and duration. This is, to the best of our knowledge, the first systematic study of the effects these parameters have on the wavefronts of APTs based on single-shot measurements. Such measurements were made possible by the high throughput of this beamline, and provide useful information about the shot-to-shot variations of the XUV wavefronts. Additionally, we used multilayer mirrors to measure how the spatial properties change with the harmonic order. The obtained data can thus give insight on the fundamental mechanisms involved in HHG. We then present a new theoretical model of the wavefront transfer from the fundamental pulse to the harmonics, as well as numerical simulations based on it to explain the data from the experiment. Lastly, we use a deformable mirror (DM) on the IR beampath to modify the wavefront of the driving beam, and we studied its influence on the harmonic wavefronts. We found that using it led to significant improvement of the spatial quality of the high-order harmonics as well as the conversion efficiency.

2. Experimental setup

The setup used in this experiment is shown in Fig. 1(a). The Ti:Sapphire laser emits linearly polarized 40-fs pulses of 800-nm wavelength, at a repetition rate of 10 Hz. The high-order harmonics are generated in loose focusing geometry to optimize the conversion efficiency [32], by using a lens with a focal length of 8.7 m, and a 6-cm-long cylindrical gas cell filled with argon. The IR beam, which has a $1/e^2$ diameter of 35 mm, can be apertured by an iris placed before the lens. Between this iris and the lens there is a DM used at normal incidence. It contains 32 actuators which can modify the IR wavefront aberrations as well as its curvature. The DM was not used for the measurements reported in sections 3 and 4.

After the cell, the harmonic and IR beams propagate towards a fused silica plate, set at a grazing angle of 10°. The plate reflects XUV radiation (R = 50%), but transmits most of the IR energy thanks to an anti-reflective coating. The beams then propagate through a 200-nm-thick aluminum filter, that blocks the remaining IR field, and towards a gold-coated flat mirror. The

Optics EXPRESS

mirror can be rotated in order to reflect the harmonic beam towards a spectrometer, the XUV Hartmann WFS, or a CCD camera to record its far-field intensity profile. The camera has been calibrated so that it can measure XUV energies as well. Figure 1(b) shows a typical harmonic spectrum generated in this setup.

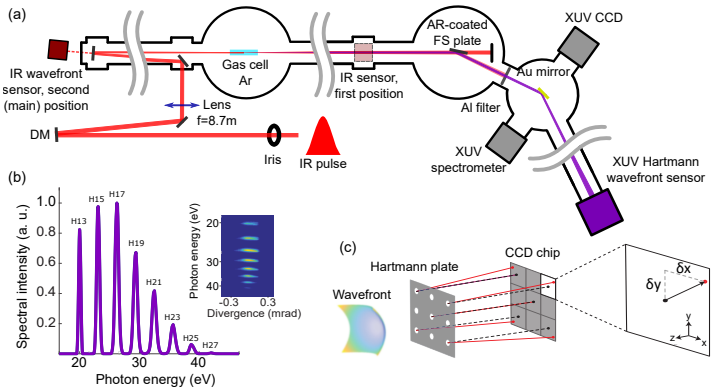

Fig. 1. (a) Schematic drawing of the experimental setup for the measurement of single-shot high-order harmonic wavefronts. The Au mirror can be rotated to send the beam towards the XUV CCD camera or the spectrometer as well. (b) Typical harmonic spectrum generated in argon, including raw data showing the beam divergence. (c) Working principle of the XUV Hartmann wavefront sensor. The sensor contains an array of square subpupils and a CCD camera. An incoming wavefront is diffracted in each of them and propagated in a direction depending on the local slope. The resulting diffraction pattern is recorded on the CCD camera allowing for wavefront reconstruction. AR: Anti-reflective, FS: fused silica.

The working principle of the XUV Hartmann WFS is illustrated in Fig. 1(c). The WFS consists of a mask, also called a Hartmann plate, containing an array of holes, subsequently referred to as subpupils, placed before a CCD camera at a known distance. The direction of propagation of the beamlets upon diffraction by the subpupils is given by the local slope of the wavefront at the plane of the plate. The resulting diffraction patterns are recorded by the CCD camera, and their positions are then compared to reference positions, obtained via a previous calibration of the WFS, in order to reconstruct the wavefront [33].

The sensor used in this experiment was built and calibrated by the Laboratoire d'Optique Appliquée and Imagine Optic. The Hartmann plate contains 34x34 square subpupils of side 110 µm, separated by 387 µm. They are rotated by 25° to prevent adjacent diffraction patterns from overlapping each other on the CCD camera [28], which is placed 211 mm after the Hartmann plate. Due to the low divergence of the harmonic beam, of the order of 0.2 mrad (see Fig. 1(b)), the sensor had to be placed as far as possible from the gas cell, about 9.5 m, in order to illuminate enough subpupils for an accurate wavefront reconstruction. The leakage from a flat mirror was used to monitor the wavefront of the driving IR beam with a Shack-Hartmann WFS [34].

It is important to note that the harmonic beam is reflected by two mirrors before being measured by the WFS. These optics introduce additional aberrations in the wavefront which might be significant, and must then be taken into account. To do so, we calibrated the optics by spatially filtering the high-order harmonic beam with a 100-µm pinhole placed in the beam path. This creates a beam with a known reference wavefront which is then reflected by the optics and measured by the WFS. Any aberrations present on this beam are thus solely caused by the optics.

Optics EXPRESS

3. Full-beam wavefronts

3.1. Single-shot high-order harmonic wavefronts

Throughout this experiment, we measured single-shot wavefronts for different values of the generation parameters. Figure 2 shows one such measurement, taken in the same generation conditions as the spectrum presented in Fig. 1(b). The measured quantity is the spatial phase variation perpendicular to the propagation axis. The obtained wavefront is compared to a perfect parabolic wavefront, and the difference is expressed in units of the central wavelength λ, where one λ corresponds to a 2π radian phase variation. The quality of the wavefront is characterized by the root mean square (RMS) of the difference. In our case, the central wavelength is $\lambda = \lambda_{H19} = 42$ nm, corresponding to the 19th harmonic order. All RMS values are given as averages of five shots, together with the corresponding standard deviation, in order to show the shot-to-shot stability of the high-order harmonic beam.

As shown in Fig. 1(b), our HHG spectrum comprises mainly five harmonics. Using a theoretical model described in [42], in the conditions used in the present work, we find that the curvature difference between the harmonic wavefronts stays lower than 5% and close to the curvature of the full beam. In general, the full beam wavefront is expected to be an average of that of the individual harmonics.

Figures 2(a) and 2(b) show the intensity distribution and wavefront, respectively, of a single APT, after filtering out the defocus (i.e. the Zernike polynomial $2r^2 - 1$) and tilt components. In this case, the generated wavefront has an RMS value of $(0.287 \pm 0.064)\lambda$, close to $\lambda/4$, averaged over five separate single-shot measurements.

It is dominated by astigmatism at 0°, which is consistent with previous experiments carried out at high repetition rates [29]. The contribution of astigmatism to the wavefront can be numerically filtered out, resulting in Fig. 2(c). In this case, the RMS is only $(0.062 \pm 0.006)\lambda$, indicating the much lower contribution of all other aberrations, such as coma or spherical aberration.

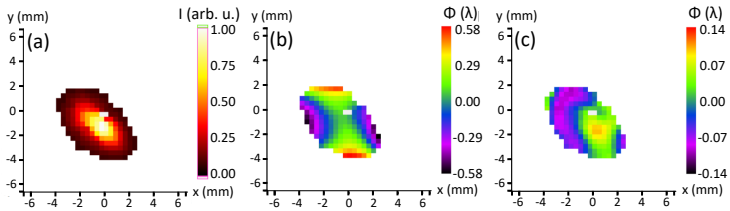

Fig. 2. Typical single-shot intensity distribution (a) and wavefront (b) of the harmonic beam, along with the resulting wavefront after numerically ruling out astigmatism (c).

The main results obtained during the experiment are summarized in Fig. 3, where the harmonic wavefront RMS values are plotted with the energies of the APTs, measured with the calibrated CCD camera, when varying the IR pulse energy, the aperture diameter, the argon pressure, and the IR pulse duration (and with it the IR intensity). The latter is modified by introducing group delay dispersion (GDD) to the pulse with the compressor of the Ti:Sapphire laser chain. In each set of measurements, one parameter was varied, while the other ones were kept constant. All data points represent the average of five consecutive single-shot measurements, and the error bars represent the standard deviation.

The wavefront RMS was observed to vary significantly as a function of the generation conditions, even becoming as low as $\lambda/10$ or as high as λ in some cases. It is also interesting to note that high APT energies are often paired with larger wavefront aberrations, so that a compromise must be made between having higher energies or better wavefronts. In all cases,

Optics EXPRESS

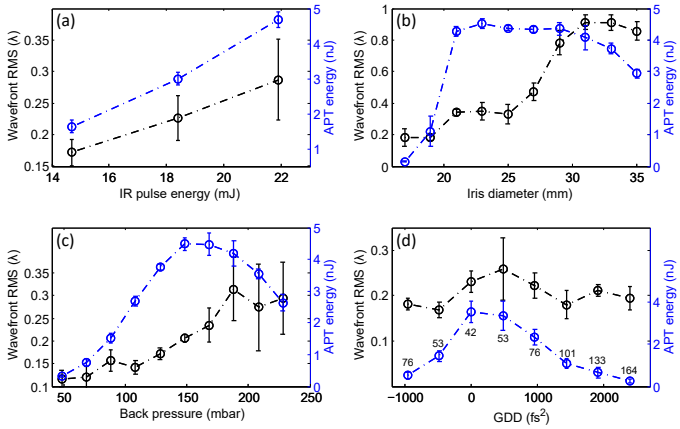

Fig. 3. Main data obtained in the experiment, representing the average wavefront RMS (black) of a single APT as well as its average energy (blue) as a function of (a) IR pulse energy, (b) iris diameter, (c) argon back pressure, and (d) GDD. The latter includes the calculated FWHM (full width at half maximum) duration of the IR pulses for each case, in fs, next to each data point.

however, the harmonic wavefronts were dominated by astigmatism, which may be corrected with appropriate focusing optics [21, 35, 36]. Additionally, the relative standard deviation for the wavefront RMS takes values between 15% and 20% in most cases, thus revealing a relatively good source stability, except for the most extreme cases such as those where the pressure was too high, or the iris was fully open.

The astigmatism always has similar directions, with only slight variations. We investigated the possibility that this direction is defined by the polarization of the IR beam by measuring harmonic wavefronts with three different IR polarization angles: vertical, horizontal, and at 45°. The direction of astigmatism, as well as the wavefront itself, remained constant, showing that the IR polarization has barely any influence on it or none at all. The calibration wavefront measured prior to the experiment has an RMS of $(0.022 \pm 0.005)\lambda$, around 10 times smaller than the full wavefront, indicating that the optics do not introduce any significant aberrations.

3.2. *Relation between the IR and harmonic wavefronts*

Being a secondary source of radiation, the spatial properties of harmonic radiation are expected to be influenced by those of the driving pulse. For this reason, the IR wavefront was measured prior to the experiment, by placing the IR Shack-Hartmann WFS 1.5 m after the gas cell (see Fig. 1). This step was carried out at atmospheric pressure and without argon in the gas cell. Several neutral-density filters were placed before the focus to protect the sensor and to avoid nonlinear effects in air. A single-shot IR wavefront is shown in Fig. 4, obtained with typical beamline conditions. After these measurements, the sensor was placed behind a mirror to monitor the IR wavefront during generation through a leak in a mirror. Both positions of the IR sensor are equivalent in terms of distance to the focusing lens.

The IR beam is slightly elliptical, and the measured wavefront has an average RMS value of $(0.095 \pm 0.003)\lambda_{\mathrm{IR}}$, better than $\lambda_{\mathrm{IR}}/10$. Astigmatism, which largely dominates every XUV wavefront measured throughout the experiment, is much less significant in the driving beam.

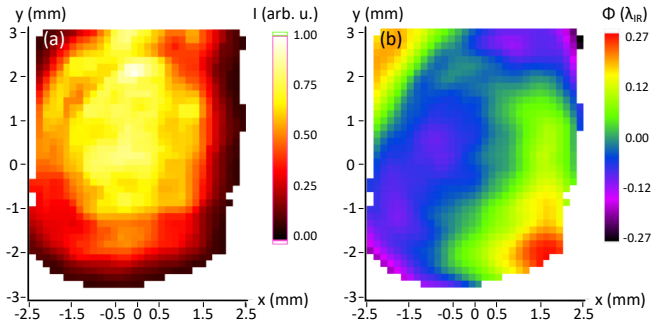

Fig. 4. Intensity distribution (a) and wavefront (b) of the direct IR beam in typical working conditions (λ_{IR} = 800nm).

Additionally, the IR wavefront was observed to be constant throughout the experiment.

The IR focal spot in the gas cell reconstructed via back propagation of the measured far-field wavefront can be seen in Fig. 5(a). It has a slightly elliptical shape as well, and the average FWHM size was 239 ± 1 µm along the major axis and 178 ± 1 µm along the minor axis. Figure 5(b) presents the calculated harmonic source shape, obtained through back propagation of the measured spatial profile for typical generation conditions (see Fig. 2). Its average FWHM size was 211 ± 5 µm and 104 ± 3 µm along both axes. The size of the harmonic source was observed to vary depending on the generation conditions used, being smaller than the IR focal spot. This, in turn, is most likely caused by the nonlinearity of the HHG process, since the outer parts of the IR focus are not intense enough to efficiently generate XUV radiation.

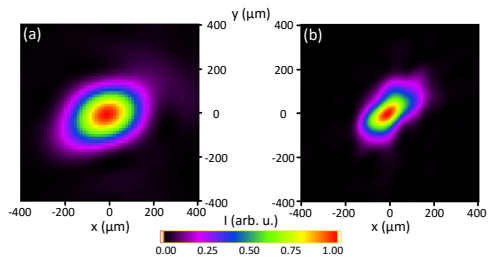

Fig. 5. Side by side comparison between the reconstructed infrared focus (a) and high-order harmonic source (b). Both images represent typical generation conditions.

4. Wavefronts of single harmonic orders

Different harmonic orders have been found to contain differences in their wavefronts [27]. For this reason, we used three dielectric multilayer mirrors, with peak reflectivities at different wavelengths, in order to isolate single harmonic orders in different parts of the spectrum and compare their wavefronts to each other and to that of the full beam. The optics were placed before the silica plate and the XUV Hartmann WFS was moved to a new position, as shown in Fig. 6. Since the silica plate is no longer used to filter the IR beam, two flat silicon mirrors at

Brewster's angle are placed instead shortly before the mirrors. The multilayer mirrors consist of alternating layers of Al/Mo/SiC on fused silica substrates. They are all made for optimal use at 45° incidence, providing reflectivities around 35% for the wavelengths 41.4 nm (H19), 35 nm (H23) and 23.9 nm (H33). A 200-nm-thick aluminum filter is placed before the WFS. A calibration procedure such as the one described in section 2 was performed with each mirror, in order to rule out any aberrations they might introduce on the beam upon reflection [37].

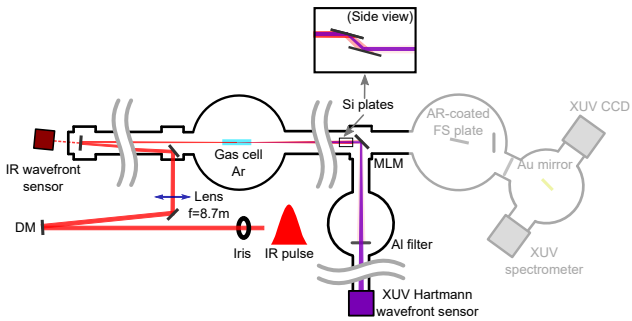

Fig. 6. Experimental setup for the measurement of single harmonic orders with the use of multilayer mirrors, showing the new placement of the XUV WFS. Inset shows a side view of the silicon plates used to attenuate the IR beam. MLM: multilayer mirror.

Although only one harmonic order was reflected by each mirror, the APTs had enough energy to allow for single-shot wavefront acquisitions, mostly due to the higher reflectivities of the involved optics, as well as the beam being smaller on the sensor due to the shorter distance to the cell, close to 7 m. As was done previously, five single-shot measurements were taken and averaged, to account for instabilities. Harmonics 19 and 23 were generated with very similar conditions. However, in order to observe a sufficient intensity of harmonic 33, the pressure and the aperture diameter had to be significantly increased. The XUV intensity profiles obtained with the three mirrors are presented in Figs. 7(a)-7(c). In general, the beam profiles are very similar for single harmonics and for the full beam shown above, except for the 33rd order, which is more elongated. This shape was also observed for the full beam at high pressures, which were required in order to generate this order efficiently.

The obtained wavefronts are presented in Figs. 7(d)-7(f), each represented in terms of its corresponding wavelength (denoted as λ_{H19}, λ_{H23}, and λ_{H33}). The aberrations introduced by the mirrors were calibrated and subtracted from these measurements. It can be seen that the 19th order presents no astigmatism, in contrast with the full beam, where astigmatism at 0° was always present. Slight astigmatism appears in the 23rd order, but it is still very low compared to the full beam. The 33rd order, on the other hand, is completely dominated by astigmatism at 0°. In particular, its angle of astigmatism is, on average, 8.0°, very close to the typical values observed in the full beam.

The average RMS values corresponding to the three orders were $0.062\lambda_{H19} = \lambda_{H19}/16$, $0.084\lambda_{H23} = \lambda_{H23}/12$, and $0.715\lambda_{H33} = \lambda_{H33}/1.3$. In terms of units of length, these RMS values are 2.57 nm, 2.94 nm, and 17.09 nm, respectively. The relative standard deviation is close to 10% in all cases. In comparison, the full-beam wavefronts seen in Fig. 3 present values typically around $\lambda_{H19}/4$ and $\lambda_{H19}/3$ for conditions similar to those used for harmonics 19 and 23, which are observed to have much better wavefronts when isolated. Harmonic 33 is not generally observed in the setup, so the generation conditions were different from the other two orders. In particular,

Optics EXPRESS

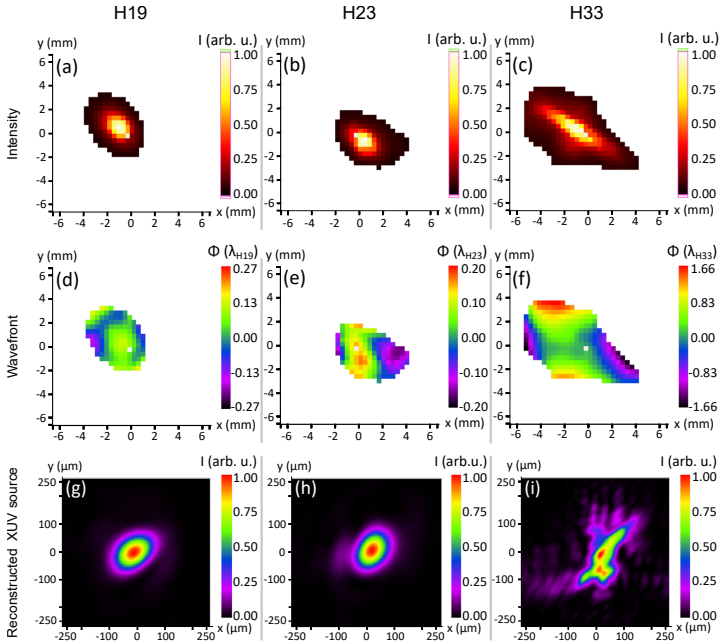

Fig. 7. Single-shot high-order harmonic intensity distributions (a-c), wavefronts (d-f), and reconstructed harmonic sources (g-i) for the 19th, 23rd, and 33rd harmonic orders. Note that the wavefronts are expressed in terms of each order's particular wavelength.

the pressure and IR pulse energies had to be increased, leading to distortions of the IR pulse in the medium via nonlinear effects [38], which may account for the more aberrated wavefront found in this harmonic order.

Lastly, the harmonic sources for each harmonic order, obtained via back propagation, are also presented in Figs. 7(g)-7(i). As expected from the measured wavefronts, the calculated sources for the 19th and 23rd orders are regular and slightly elliptical, similar to the best cases measured for the full harmonic beam, while it is slightly larger and highly distorted for the 33rd. This order has, however, much lower intensity than the other two in typical working conditions, so it will not provide a large contribution to the shape of the full beam.

5. Theoretical interpretation

In order to better understand the spatial properties of high-order harmonics, we develop a simple model based on propagation by means of diffraction integrals and on a semi-classical description of the HHG process, neglecting propagation effects. The fundamental field evaluated in a certain plane z_{IR} (see Fig. 8) can be written as a product of an amplitude and a phase term, as

$$E(x, y, z_{IR}) \propto |E(x, y, z_{IR})| \exp(-i\phi(x, y, z_{IR})). \quad (1)$$

This field is then propagated to the generation position by calculating [39]

Optics EXPRESS

$$E(x, y, z_G) = \mathrm{FT}^{-1}\left[\tilde{E}(k_x, k_y, z_{IR}) \exp\left(-i(z_G - z_{IR})\sqrt{k^2 - k_x^2 - k_y^2}\right)\right], \quad (2)$$

where $\tilde{E}_q(k_x, k_y, z_{IR})$ is the spatial Fourier transform of the IR field $E(x, y, z_{IR})$. z_G was chosen to be -80 mm for H19 and H23 in the simulations presented below, and -130 mm for H33, in order to be consistent with the experimental measurements shown above.

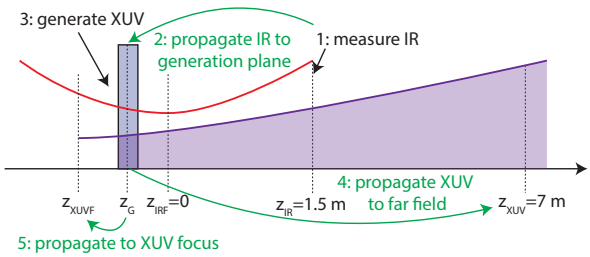

Fig. 8. Principle of the simulations. The IR field is obtained from the experimental wavefronts and intensity maps recorded at position z_{IR}. It is back propagated to the position z_G, where the harmonics are generated. The harmonic field is then propagated to the position z_{XUV}, where it is analyzed. Finally it can also be back propagated to its focus z_{XUVF}.

The generated q^{th} harmonic field is approximated by

$$E_q(x, y, z_G) \propto |E(x, y, z_G)|^p \exp\left[-iq\phi(x, y, z_G) - i\phi_d(x, y, z_G)\right]. \quad (3)$$

The amplitude is assumed to vary slowly with the amplitude of the fundamental field, with a power p typically of the order of 4 [40]. The phase of the harmonic field is the sum of q times the phase $\phi(x, y, z_G)$ of the IR field and the dipole phase $\phi_d(x, y, z_G)$ originating from the generation process. Note that this simple model does not take into account propagation in the nonlinear medium or phase-matching effects. Considering only the short trajectory of the electron in the continuum, assumed to be classical, and neglecting spatially-independent terms, this phase can be approximated as [41, 42]

$$\phi_d(x, y, z_G) = \frac{\gamma_s(q - q_p)^2\omega^2}{I(x, y, z_G)}, \quad (4)$$

where $\gamma_s = 1.030 \times 10^{-18}$ s^{2}Wcm^{-2} for 800 nm wavelength and $I(x, y, z_G)$ is the IR intensity. The intensity is chosen to be 3×10^{14} W/cm^2 for H19 and H23, and 4×10^{14} W/cm^2 for H33, in order to replicate the experimental conditions. The quantity q_p is defined as $I_p/\hbar\omega$, where I_p is the ionization potential and ω is the IR frequency. The harmonic field is then propagated to a plane where it is spatially characterized (z_{XUV}) as in Eq. (2). It can also be back propagated to its focus (z_{XUVF}).

Figure 9 presents calculations of the 19th, 23rd and 33rd harmonic fields using the measured IR field presented in Fig. 4. These simulated results can be compared with the experimental results in Fig. 7. In each case, we present the far field profile calculated at $z = z_{XUV} = 7$ m, the wavefront and the reconstructed XUV source, calculated via back propagation. Experiments and simulations agree reasonably well for the far field intensity profiles. The beams were quite astigmatic around the XUV focal region in the simulations. The presented results are those obtained at approximately the medial focus. Finally, the XUV wavefronts are found to be

Optics EXPRESS

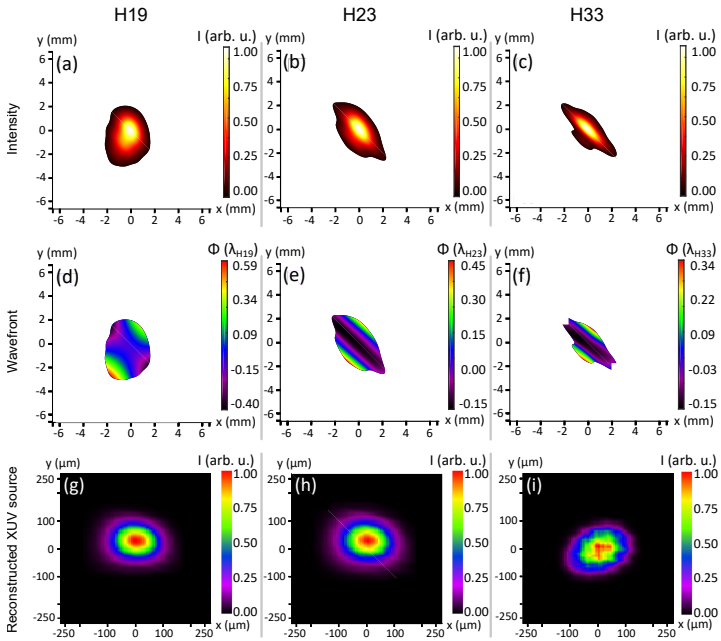

Fig. 9. Simulations of high-order harmonic intensity distributions (a-c), wavefronts (d-f), and reconstructed harmonic sources (g-i) for the 19th, 23rd, and 33rd harmonic orders.

dominated by astigmatism, as in the experiment. The simulations reproduce qualitatively the measured wavefront.

In Fig. 10, we show the respective influence of the IR phase aberrations which are transferred to the XUV and the effect of the dipole phase, which depends on the elliptical intensity profile of the IR, on the spatial properties of the 19th order. Comparing the wavefronts plotted in Figs. 10(e) and 7(d), we can conclude that the wavefront of the 19th harmonic, which exhibits astigmatism at $\simeq 45°$, is mostly influenced by the IR phase. However, the harmonic intensity profile (see Fig. 9(a)) cannot be reproduced by considering only the IR phase transfer, and shows a strong influence of the dipole phase. In conclusion, both effects must be taken into account in order to understand the spatial properties of the generated harmonics, since they have a similar order of magnitude. Note that the interplay between IR phase transfer and dipole phase strongly depends on the generation conditions.

6. Using IR adaptive optics to improve the XUV wavefronts

Having demonstrated that the spatial properties of the high-order harmonics are strongly influenced by the wavefront and focusing of the driving pulses, it should then be possible to improve them by modifying the IR focus by means of adaptive optics. In this study, we analyzed how the spatial properties of the high-order harmonic beam, as well as the conversion efficiency, are modified with the use of the IR DM.

DMs have been used in the past to modify the wavefront of the driving beam for HHG in

Optics EXPRESS

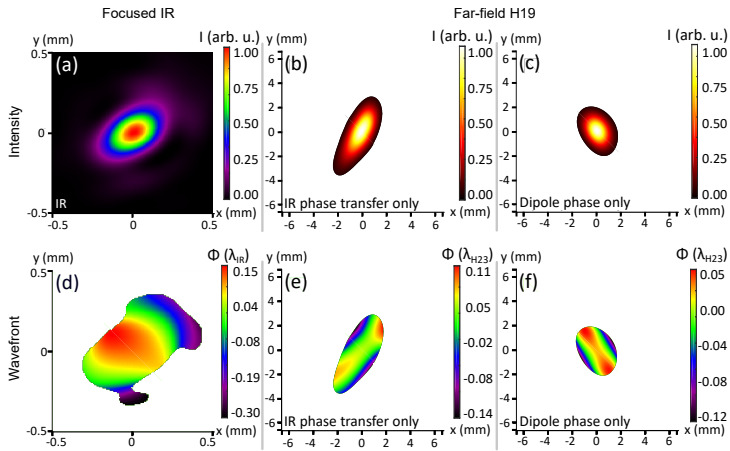

Fig. 10. Simulations of intensity distributions (a-c) and wavefronts (d-f) for the focused IR beam and far-field 19th harmonic with the IR-phase transfer only and with dipole phase only.

setups with high repetition rates. This has been done to modify the astigmatism in the harmonic wavefront [29], and also to improve phase matching and thus the energy in the resulting APTs [43]. In the present work, we investigate the influence of the IR wavefront on the spatial properties of single high-order harmonic APTs, including all generated harmonic orders.

We simultaneously measured IR and harmonic wavefronts for different DM configurations, while all other previously mentioned generation parameters were kept unchanged. Figure 11 presents several measurements of the IR wavefront and the wavefront of the full harmonic beam, taken while modifying the DM in order to improve the latter. Each wavefront is normalized to its corresponding wavelength, with the RMS values included in the figure. The harmonic spectrum did not change significantly when varying the settings on the DM (see Fig. 1(b)).

Each column of Fig. 11 shows the IR and harmonic wavefronts, as well as the harmonic intensity distribution for one of the three cases presented. The first IR wavefront, seen in Fig. 11(a), has larger IR astigmatism than the rest. The resulting harmonic wavefront presents large astigmatism as well, but at 45°. The beam is also larger and has low energy. Figure 11(b) presents an intermediate case, where the DM configuration improves the IR wavefront and thus both the conversion efficiency and the harmonic wavefront. The resulting harmonic beam is smaller and less elliptical than observed in Figs. 2 and 7, as well as three times more energetic. However, consistently with previous measurements, the harmonic wavefront is mainly astigmatic at 0°, whereas the IR wavefront presents more astigmatism at 45°. In the final configuration, shown in Fig. 11(c), the IR wavefront presents less aberration than in both 11(a) and 11(b). However, this improvement does not significantly change the harmonic wavefront, which is only slightly better, having an RMS of $\lambda/11$. The energy was not further increased from the previous measurement. In summary, by tweaking the DM to improve the IR wavefront, we were able to reduce the average XUV wavefront aberrations from $\lambda/4$ to $\lambda/11$, as well as to increase the energy of the APTs by a factor of 3.

These results again show the importance of the IR beam's spatial properties on the HHG process, since it affects not only the high-order harmonic beam wavefront, but also its shape and size, as well as the conversion efficiency. The experimental results clearly show that the

Optics EXPRESS

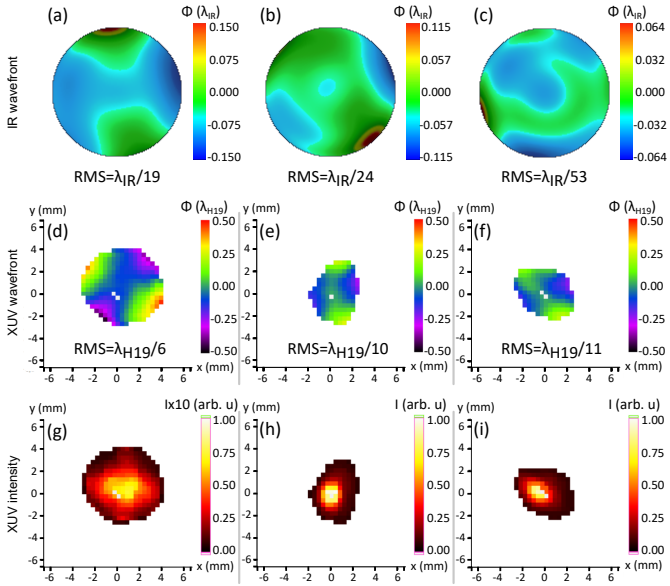

Fig. 11. Direct comparison between the IR wavefronts measured with three different DM configurations (a-c) and the corresponding full-spectrum single-shot XUV wavefronts (d-f) and far-field intensity distributions for each case (g-i). The RMS values are included under each wavefront. Note that the intensity scale is different in (g) to make the beam more visible due to its lower energy.

XUV wavefront results from more than a just a direct transfer from the IR to the XUV, which is confirmed by the model presented above. The IR wavefront, however, is especially important due to how it affects its focusing. The use of the DM provided significant wavefront improvement with respect to the values typically found in previous measurements performed without it. The control it provides on the XUV wavefront is complex, since changing the IR wavefront modifies the intensity distribution at focus and thus the dipole phase during HHG (see previous section). Nonetheless, using an IR DM provides a cheaper alternative to the use of less accessible DMs for the XUV domain [44].

7. Conclusions

The XUV Hartmann sensor provides a versatile tool for spatial metrology of pulsed XUV beams. The single-shot harmonic wavefronts measured in this experiment had typical RMS values of the order of $\lambda/4$. The high XUV energies obtained in this beamline allowed us to take single-shot high-order harmonic wavefront measurements, in turn providing information on the shot-to-shot wavefront stability. The relative standard deviation of the wavefront RMS takes values between 15% and 20% in most cases, thus revealing a relatively good source stability, except for the most extreme cases such as those with the highest pressures, or where the iris was fully open. It is also interesting to note that high XUV energies are often paired with larger wavefront aberrations.

The results of our single-shot wavefront measurements are similar to previously published

studies involving multishot measurements in beamlines with high repetition rates, in that the harmonic wavefront always presents a very prominent astigmatism, which was not observed in the IR beam. The fact that astigmatism is also observed in other high-order harmonic beamlines can be attributed to the difficulty in focusing the IR beam in a perfectly symmetrical manner. The observed predominant direction of astigmatism, around 0°, might be due to the optics used to handle the IR beam. These include in particular a compressor at the end of the amplification chain, which has a similar geometry in most Ti:Sapphire laser systems and might introduce small aberrations that cause the focal spot to deviate from a perfect Gaussian profile. Other aberrations such as coma or spherical aberration are much less significant. In fact, if the astigmatism is corrected with appropriate focusing optics, RMS values lower than $\lambda/10$ can be obtained, even diffraction-limited beams in some of the cases reported here before the use of the DM. It was found, however, that the best wavefronts are generally obtained at the cost of low harmonic energies. During this experiment, we also confirmed that the direction of polarization of the IR pulse has no influence on the harmonic wavefront. Additionally, the study of single harmonic orders by means of multilayer mirrors suggests that not all orders carry the same amount of astigmatism.

The experimental data indicate that the full spatial profile (amplitude and phase) of the IR affects the harmonics, rather than just its wavefront. We thus propose a theoretical model which describes the transfer of the spatial profile from the IR to the harmonics through two effects, the direct transfer from IR wavefront to XUV wavefront by frequency upconversion and the transfer from the IR intensity profile to the XUV wavefront through the dipole phase. The curvature induced by the dipole phase is generally comparable in magnitude to that due to the IR beam curvature, so it must be taken into account as well. It must be noted that the model does not account for phase matching effects or propagation of the IR pulse in the gas, so its results are not perfectly accurate at this stage. The simulations presented here show a satisfactory agreement with the experimental data when using typical generation conditions.

In conclusion, while the generation parameters affect the harmonic wavefront RMS, the shape of the IR focus was found to have a larger impact on the spatial properties of the XUV beam. We demonstrate that they can be improved to a large extent by using IR adaptive optics to modify the IR wavefront, and thus its focus. This also had a significant effect on the APT energy, increasing it by a factor of up to three compared to previous measurements without the DM. Being able to tailor the spatial properties of the harmonics with this method provides a useful alternative to the use of a more expensive DM for the XUV domain, which would also provide lower reflectivity. Furthermore, a computerized closed-loop program could be implemented in the beamline, which would use data from the XUV sensor to find the DM configuration which provides the best harmonic wavefront, the highest energy, or the most circular beam shape.

Future steps involve improving the theoretical model as well as performing further experiments to learn more about the transfer of spatial properties in order to improve the quality of the generated XUV beams, as well as to compare the experimental results with the simulations. This, in turn, will lead to better focusing and thus higher XUV intensities.

Funding

Svenska Forskningsrådet Formas; Stiftelsen för Strategisk Forskning; Knutoch Alice Wallenbergs Stiftelse; H2020 European Research Council (339253 PALP); LASERLAB-EUROPE (LLC002276); European Cooperation in Science and Technology (MP1203 and CM1204); Horizon 2020 Framework Programme (665207); H2020 Marie Skłodowska-Curie (641789 MEDEA); European Regional Development Fund.

Optics EXPRESS

References

1. A. McPherson, G. Gibson, H. Jara, U. Johann, T. S. Luk, I. A. McIntyre, K. Boyer, and C. K. Rhodes, "Studies of multiphoton production of vacuum-ultraviolet radiation in the rare gases," JOSA B **4**(4), 595–601 (1987).
2. M. Ferray, A. L'Huillier, X. F. Li, L. A. Lompré, G. Mainfrays, and C. Manus, "Multiple-harmonic conversion of 1064 nm radiation in rare gases," J. Phys. B **21**(3), L31–L35 (1988).
3. R. A. Bartels, A. Paul, H. Green, H. C. Kapteyn, M. M. Murnane, S. Backus, I. P. Christov, Y. Liu, D. Attwood, C. Jacobsen, "Generation of spatially coherent light at extreme ultraviolet wavelengths," Science **297**(5580), 376–378 (2002).
4. C. Lyngå, M. B. Gaarde, C. Delfin, M. Bellini, T. W. Hänsch, A. L'Huillier, and C.-G. Wahlström, "Temporal coherence of high-order harmonics," Phys. Rev. A **60**(6), 4823 (1999).
5. Z. Chang, A. Rundquist, H. Wang, M. M. Murnane, and H. C. Kapteyn, "Generation of coherent soft X rays at 2.7 nm using high harmonics," Phys. Rev. Lett. **79**(16), 2967 (1997).
6. M. Schnürer, Ch. Spielmann, P. Wobrauschek, C. Streli, N. H. Burnett, C. Kan, K. Ferencz, R. Koppitsch, Z. Cheng, T. Brabec, and F. Krausz, "Coherent 0.5-keV X-ray emission from helium driven by a sub-10-fs laser," Phys. Rev. Lett. **80**(15), 3236 (1998).
7. T. Popmintchev, M.-C. Chen, D. Popmintchev, P. Arpin, S. Brown, S. Ališauskas, G. Andriukaitis, T. Balčiunas, O. D. Mücke, A. Pugzlys, A. Baltuška, B. Shim, S. E. Schrauth, A. Gaeta, C. Hernández-García, L. Plaja, A. Becker, A. Jaron-Becker, M. M. Murnane, H. C. Kapteyn, "Bright coherent ultrahigh harmonics in the keV X-ray regime from mid-infrared femtosecond lasers," Science **336**, 1287-1291 (2012).
8. D. Descamps, L. Roos, C. Delfin, A. L'Huillier, and C.-G. Wahlström, "Two-and three-photon ionization of rare gases using femtosecond harmonic pulses generated in a gas medium," Phys. Rev. A **64**(3), 31404 (2001).
9. Y. Mairesse, A. de Bohan, L. J. Frasinski, H. Merdji, L. C. Dinu, P. Monchicourt, P. Breger, M. Kovačev, R. Taïeb, B. Carré, H. G. Muller, P. Agostini, P. Salières, "Attosecond synchronization of high-harmonic soft x-rays," Science **302**(5650), 1540–1543 (2003).
10. E. Goulielmakis, M. Schultze, M. Hofstetter, V. S. Yakovlev, J. Gagnon, M. Uiberacker, A. L. Aquila, E. M. Gullikson, D. T. Attwood, R. Kienberger, F. Krausz, and U. Kleineberg, "Single-Cycle Nonlinear Optics," Science **320**(5883), 1614–1617 (2008).
11. S. L. Sorensen, O. Björneholm, I. Hjelte, T. Kihlgren, G. Öhrwall, S. Sundin, S. Svensson, S. Buil, D. Descamps, A. L'Huillier, J. Norin, and C.-G. Wahlström, "Femtosecond pump-probe photoelectron spectroscopy of predissociative Rydberg states in acetylene," J. Chem. Phys. **112**(18), 8038–8042 (2000).
12. W. Theobald, R. Hässner, C. Wülker, and R. Sauerbrey, "Temporally Resolved Measurement of Electron Densities ($> 10^{23}$cm^{-3}) with High Harmonics," Phys. Rev. Lett. **77**(2), 298-301 (1996).
13. B. Kettle, T. Dzelzainis, S. White, L. Li, B. Dromey, M. Zepf, C. L. S. Lewis, G. Williams, S. Künzel, M. Fajardo, H. Dacasa, Ph. Zeitoun, A. Rigby, G. Gregori, C. Spindloe, R. Heathcote, and D. Riley, "Experimental measurements of the collisional absorption of XUV radiation in warm dense aluminium," Phys. Rev. E **94**(2), 023203 (2016).
14. R. L. Sandberg, A. Paul, D. A. Raymondson, S. Hädrich, D. M. Gaudiosi, J. Holtsnider, R. I. Tobey, O. Cohen, M. M. Murnane, H. C. Kapteyn, C. Song, J. Miao, Y. Liu, and F. Salmassi, "Lensless Diffractive Imaging Using Tabletop Coherent High-Harmonic Soft-X-Ray Beams," Phys. Rev. Lett. **99**(9), 098103 (2007).
15. A.-S. Morlens, J. Gautier, G. Rey, Ph. Zeitoun, J.-P. Caumes, M. Kos-Rosset, H. Merdji, S. Kazamias, K. Cassou, and M. Fajardo, "Submicrometer digital in-line holographic microscopy at 32 nm with high-order harmonics," Opt. Lett. **31**(21), 3095–3097 (2006).
16. Ph. Zeitoun, G. Faivre, S. Sebban, T. Mocek, A. Hallou, M. Fajardo, D. Aubert, Ph. Balcou, F. Burgy, D. Douillet, S. Kazamias, G. de Lachèze-Murel, T. Lefrou, S. le Pape, P. Mercère, H. Merdji, A. S. Morlens, J. P. Rousseau, and C. Valentin, "A high-intensity highly coherent soft X-ray femtosecond laser seeded by a high harmonic beam," Nature **431**(7007), 426–429 (2004).
17. G. Lambert, T. Hara, D. Garzella, T. Tanikawa, M. Labat, B. Carre, H. Kitamura, T. Shintake, M. Bougeard, S. Inoue, Y. Tanaka, P. Salieres, H. Merdji, O. Chubar, O. Gobert, K. Tahara, and M.-E. Couprie, "Injection of harmonics generated in gas in a free-electron laser providing intense and coherent extreme-ultraviolet light," Nat. Phys. **4**, 296–300 (2008).
18. H. Mashiko, A. Suda, and K. Midorikawa, "Focusing coherent soft-x-ray radiation to a micrometer spot size with an intensity of 10^{14}W/cm^2," Opt. Lett. **29**(16), 1927 (2004).
19. C. Valentin, D. Douillet, S. Kazamias, Th. Lefrou, G. Grillon, F. Augé, G. Mullot, Ph. Balcou, P. Mercère, and Ph. Zeitoun, "Imaging and quality assessment of high-harmonic focal spots," Opt. Lett. **28**(12), 1049–1051 (2003).
20. S. Kazamias, D. Douillet, C. Valentin, Th. Lefrou, G. Grillon, G. Mullot, F. Augé, P. Mercère, Ph. Zeitoun, and Ph. Balcou, "Optimization of the focused flux of high harmonics," Eur. Phys. J. D **26**(1), 47–50 (2003).
21. H. Coudert-Alteirac 1, H. Dacasa, F. Campi, E. Kueny, B. Farkas, F. Brunner, S. Maclot, B. Manschwetus, H. Wikmark, J. Lahl, L. Rading, J. Peschel, B. Major, K. Varjú, G. Dovillaire, Ph. Zeitoun, P. Johnsson, A. L'Huillier, and P. Rudawski, "Micro-focusing of broadband high-order harmonic radiation by a double toroidal mirror," Appl. Sci. **7**(11), 1159 (2017).
22. T. Nakajima and L. A. A. Nikolopoulos, "Use of helium double ionization for autocorrelation of an xuv pulse," Phys. Rev. A **66**(4), 041402(R) (2002).
23. B. Manschwetus, L. Rading, F. Campi, S. Maclot, H. Coudert-Alteirac, J. Lahl, H. Wikmark, P. Rudawski, C. M. Heyl, B. Farkas, T. Mohamed, A. L'Huillier, and P. Johnsson, "Two-photon double ionization of neon using an intense

Optics EXPRESS

attosecond pulse train," Phys. Rev. A **93**, 061402(R) (2016).
24. D. G. Lee, J. J. Park, J. H. Sung, and C. H. Nam, "Wave-front phase measurements of high-order harmonic beams by use of point-diffraction interferometry," Opt. Lett. **28**(6), 480–482 (2003).
25. D. R. Austin, T. Witting, C. A. Arrell, F. Frank, A. S. Wyatt, J. P. Marangos, J. W. G. Tisch, and I. A. Walmsley, "Lateral shearing interferometry of high-harmonic wavefronts," Opt. Lett. **36**, 1746–1748 (2011).
26. E. Frumker, G. G. Paulus, H. Niikura, D. M. Villeneuve, and P. B. Corkum, "Frequency-resolved high-harmonic wavefront characterization," Opt. Lett. **34**, 3026–3028 (2009).
27. E. Frumker, G. G. Paulus, H. Niikura, A. Naumov, D. M. Villeneuve, and P. B. Corkum, "Order-dependent structure of high harmonic wavefronts," Opt. Express **20**(13), 13870-13877 (2012).
28. P. Mercère, Ph. Zeitoun, M. Idir, S. Le Pape, D. Douillet, X. Levecq, G. Dovillaire, S. Bucourt, K. A. Goldberg, P. P. Naulleau, and S. Rekawa , "Hartmann wave-front measurement at 13.4 nm with λ_{EUV}/120 accuracy," Opt. Lett. **28**(17), 1534–1536 (2003).
29. C. Valentin, J. Gautier, J.-Ph. Goddet, C. Hauri, T. Marchenko, E. Papalazarou, G. Rey, S. Sebban, O. Scrick, Ph. Zeitoun, G. Dovillaire, X. Levecq, S. Bucourt, and M. Fajardo, "High-order harmonic wave fronts generated with controlled astigmatic infrared laser," JOSA B **25**(7), B161–B166 (2008).
30. J. Gautier, Ph. Zeitoun, C. Hauri, A.-S. Morlens, G. Rey, C. Valentin, E. Papalarazou, J.-Ph. Goddet, S. Sebban, F. Burgy, P. Mercère, M. Idir, G. Dovillaire, X. Levecq, S. Bucourt, M. Fajardo, H. Merdji, and J.-Ph. Caumes, "Optimization of the wave front of high order harmonics," Eur. Phys. Jour. D **48**(3), 459–463 (2008).
31. L. Freisem, G. S. M. Jansen, D. Rudolf, K. S. E. Eikema, and S. Witte, "Spectrally resolved single-shot wavefront sensing of broadband high-harmonic sources," Opt. Express **26**(6), 6860-6871 (2018).
32. S. Kazamias, D. Douillet, F. Weihe, C. Valentin, A. Rousse, S. Sebban, G. Grillon, F. Augé, D. Hulin, and Ph. Balcou, "Global Optimization of High Harmonic Generation," Phys. Rev. Lett. **90**, 193901 (2003).
33. W. H. Southwell, "Wave-front estimation from wave-front slope measurements," JOSA **70**(8), 998–1006 (1980).
34. B. C. Platt and R. Shack, "History and Principles of Shack-Hartmann Wavefront Sensing," J. Refract. Surg. **17**(5), S573–S577 (2001).
35. L. Poletto, F. Frassetto, F. Calegari, S. Anumula, A. Trabattoni, and M. Nisoli, "Micro-focusing of attosecond pulses by grazing-incidence toroidal mirrors," Opt. Express **21**(11), 13040–13051 (2013).
36. C. Bourassin-Bouchet, M. M. Mang, F. Delmotte, P. Chavel, and S. de Rossi, " How to focus an attosecond pulse ," Opt. Express **21**(2), 2506–2520 (2013).
37. H. Dacasa, "Spatial and temporal metrology of coherent ultrashort pulses in the extreme-ultraviolet domain," PhD Thesis, Université Paris-Saclay (2017).
38. V. Tosa, K. Kovács, B. Major, E. Balogh, and K. Varjú, "Propagation effects in highly ionised gas media," Quantum Electron. **46**(4), 321–326 (2016).
39. D. G. Voelz and M. C. Roggemann, "Digital simulation of scalar optical diffraction: revisiting chirp function sampling criteria and consequences," Appl. Opt. **48**(32), 6132–6142 (2009).
40. C. G. Durfee III, A. R. Rundquist, S. Backus, C. Herne, M. M. Murnane, and H. C. Kapteyn, "Phase matching of high-order harmonics in hollow waveguides," Phys. Rev. Lett. **83**(11), 2187 (1999).
41. C. Guo, A. Harth, S. Carlström, Y.-C. Cheng, S. Mikaelsson, E. Mårsell, C. Heyl, M. Miranda, M. Gisselbrecht, M. B. Gaarde, K. J. Schafer, A. Mikkelsen, J. Mauritsson, C. L. Arnold, and A. L'Huillier, "Phase control of attosecond pulses in a train," J. Phys. B **51**(3), 034006 (2018).
42. H. Wikmark, C. Guo, J. Vogelsang, H. Coudert-Alteirac, J. Lahl, J. Peschel, P. Rudawski, H. Dacasa, S. Maclot, C. Arnold, P. Johnsson, and A. L'Huillier, "Spatio-temporal coupling of attosecond pulses," *manuscript in preparation*.
43. D. Yoshitomi, J. Nees, N. Miyamoto, T. Sekikawa, T. Kanai, G. Mourou, and S. Watanabe, "Phase-matched enhancements of high-harmonic soft X-rays by adaptive wave-front control with a genetic algorithm," Appl. Phys. B **78**(3), 275–280 (2004).
44. A. J. Corso, S. Bonora, P. Zuppella, P. Baksh, M. Miszczak, W. Brocklesby, Z. Wang, P. Nicolosi, M. G. Pelizzo, "Developing an EUV multilayer adaptive mirror: the first results," Proc. SPIE 9963, 99630K (2016).

Paper IX

H. Coudert-Alteirac, H. Dacasa, F. Campi, E. Kueny, B. Farkas, F. Brunner, S. Maclot, B. Manschwetus, H. Wikmark, J. Lahl, L. Rading, **J. Peschel**, B. Major, K. Varjú, G. Dovillaire, P. Zeitoun, P. Johnsson, A. L'Huillier, and P. Rudawski
Micro-focusing of broadband high-order harmonic radiation by a double toroidal mirror
Appl. Sci. 7, 1159 (2017)

applied sciences

MDPI

Article

Micro-Focusing of Broadband High-Order Harmonic Radiation by a Double Toroidal Mirror

Hélène Coudert-Alteirac [1,*], Hugo Dacasa [2], Filippo Campi [1], Emma Kueny [1,†,‡], Balázs Farkas [3], Fabian Brunner [1], Sylvain Maclot [1], Bastian Manschwetus [1,†], Hampus Wikmark [1], Jan Lahl [1], Linnea Rading [1], Jasper Peschel [1], Balázs Major [3], Katalin Varjú [3], Guillaume Dovillaire [4], Philippe Zeitoun [2], Per Johnsson [1], Anne L'Huillier [1] and Piotr Rudawski [1]

1 Department of Physics, Lund University, P. O. Box 118, SE-22100 Lund, Sweden; filippo.campi@fysik.lth.se (F.C.); emma.kueny@desy.de (E.K.); fbrunner@ethz.ch (F.B.); sylvain.maclot@fysik.lth.se (S.M.); bastian.manschwetus@desy.de (B.Man.); hampus.wikmark@fysik.lth.se (H.W.); jan.lahl@fysik.lth.se (J.L.); linnea.k.rading@gmail.com (L.R.); jasper.peschel@fysik.lth.se (J.P.); per.johnsson@fysik.lth.se (P.J.); anne.lhuillier@fysik.lth.se (A.L.); piotr.rudawski@fysik.lth.se (P.R.)

2 Laboratoire d'Optique Applique, ENSTA ParisTech, École Polytechnique, CNRS-UMR7639, Chemin de la Hunière, 91761 Palaiseau CEDEX, France; hugo.dacasa@ensta-paristech.fr (H.D.); philippe.zeitoun@ensta-paristech.fr (P.Z.)

3 ELI-ALPS, ELI-HU Non-Profit Ltd., Dugonics tr 13, 6720 Szeged, Hungary; farkas.balazs@eli-alps.hu (B.F.); major.balazs@eli-alps.hu (B.Maj.); varju.katalin@eli-alps.hu (K.V.)

4 Imagine Optic, 18 Rue Charles de Gaulle, 91400 Orsay, France; gdovillaire@imagine-optic.com

* Correspondence: helene.coudert@fysik.lth.se

† Current adress: Deutsches Elektronen-Synchrotron (DESY), Notkestrasse 85, 22607 Hamburg, Germany.

‡ Current adress: Department of Physics, Universitt Hamburg, Luruper Chaussee 149, 22761 Hamburg, Germany.

Received: 10 October 2017; Accepted: 7 November 2017; Published: 12 November 2017

Abstract: We present an optical system based on two toroidal mirrors in a Wolter configuration to focus broadband extreme ultraviolet (XUV) radiation. Optimization of the focusing optics alignment is carried out with the aid of an XUV wavefront sensor. Back-propagation of the optimized wavefront to the focus yields a focal spot of 3.6 × 4.0 μm^2 full width at half maximum, which is consistent with ray-tracing simulations that predict a minimum size of 3.0 × 3.2 μm^2. This work is important for optimizing the intensity of focused high-order harmonics in order to reach the nonlinear interaction regime.

Keywords: high-order harmonic generation; ultrafast nonlinear optics; extreme ultraviolet; XUV focusing; wavefront sensing; attosecond pulses

1. Introduction

High-order harmonic generation (HHG) [1,2] in gases is one of the main sources of attosecond pulses in the extreme ultraviolet (XUV) and soft X-ray regime [3,4]. These pulses, generated through highly nonlinear interaction between laser pulses and atoms, are coherent and of broad bandwidth, typically several tens of eV wide. If sufficiently intense, they can be used to investigate multiphoton phenomena in atoms and molecules to unravel ultrafast dynamics [5–8]. These nonlinear experiments require high intensity, on the order of 10^{12}–10^{14} W/cm^2. Numerous studies report optimization of the pulse energy. The highest energies, up to the µJ level, were demonstrated through loose focusing scaling techniques [9–13]. The generation of extremely short pulses of the order of 100 as or shorter was also reported [14,15]. Short isolated attosecond pulses in the µJ range have even been generated using a combination of two-color field synthesis and energy-scaling aforementioned techniques [16]. However, few studies tackle the problem of focusing the HHG radiation [17,18]. The challenge is to

focus an XUV beam to a small focal spot, while maintaining the broad bandwidth of the radiation and the short pulse duration, as well as minimizing the loss in the pulse energy.

Refractive optics cannot be used for XUV radiation, since it is strongly absorbed when propagating in materials. Spherical mirrors, used at near-normal incidence, allow high-aperture beams to be focused on small focal spots. However, they are effectively designed only for narrow bandwidth radiation. Although larger bandwidths can be handled by aperiodic multilayer mirrors, their reflectivity is often very low [18,19]. Diffractive optics, such as zone plates [20], also have low transmission and are designed for monochromatic radiation. The best option to focus a broadband XUV beam with high reflectivity is therefore by using curved mirrors at grazing incidence [21]. Ellipsoidal mirrors are in principle able to perfectly focus the radiation in the second focus of the ellipsoid, if the point source is located in the first focus. An ellipsoidal mirror was used to focus harmonics between 24 and 38 nm (33 to 51 eV) with a full width at half maximum (FWHM) measured to be 2.5 µm [22]. However, these mirrors are challenging to manufacture as well as to align, since strong aberrations appear if the source is extended or if it moves slightly out of the first focus of the ellipsoid [23].

Configurations with multiple toroidal mirrors have been used [21] to overcome the limitation of ellipsoidal mirrors. The concept is to mutually compensate the coma [24] with successive mirrors. A Z-shape configuration with two toroidal mirrors was used to focus high-order harmonics between 30 and 70 nm (17 to 38 eV) to an 8-µm FWHM spot [17,25]. In the 1950s, Wolter [26] demonstrated that some combinations of two confocal conic sections, such as ellipsoids, paraboloids, and hyperboloids, can minimize aberrations. This idea is widely used in astronomy for X-ray telescopes [27], for focusing neutron beams [28,29], and for inertial confinement fusion imaging experiments [30,31].

Focusing of XUV radiation requires not only good optics but also precise alignment and therefore accurate measurement techniques. The focus size can be determined by knife-edge [32], point diffraction [33], slit diffraction [34], lateral shearing interferometry [35], or direct imaging with a microscope [17]. This direct technique requires the insertion of a component in the focus, which hinders simultaneous application experiments. Wavefront sensors [36], on the other hand, can be located far from the focus and thus provide on-line diagnostics of beam spatial characteristics. Shack–Hartmann sensors, based on microlens arrays, are routinely used in the visible or infrared regime, but their use in the XUV regime is more challenging [37]. Therefore, the Hartmann technique, based upon diffraction through small apertures, is often used [36]. This sensor allows the determination of wavefront aberrations after focusing, and thus provides convenient feedback for the alignment of the focusing optics. The focus location and spot shape can be estimated by performing back-propagation calculations.

In this work, we use two toroidal mirrors in a Wolter configuration to focus broadband high-order harmonic radiation between 20 and 50 eV. This design allows us to use a large demagnification of approximately 35 between the HHG source, located at 6 m from the optics, and the image position, at 170 mm from the mirror pair. We optimize the focusing of an XUV beam with an XUV wavefront sensor, using single-shot measurements, and back-propagate the measured intensity profile and wavefront to the focal plane which yields a spot of 3.6×4.0 µm^2 FWHM. These results are consistent with ray-tracing simulations that predict a minimum size of 3.0×3.2 µm^2 FWHM.

In Section 2, we describe the experimental setup, including the XUV generation and focusing geometry. Wavefront measurements and focal spot optimization are presented in Section 3. We conclude in Section 4.

2. Experimental Setup

2.1. Beamline

The intense XUV beamline [8] (Figure 1a) is driven by a Ti: sapphire chirped pulse amplification laser system delivering pulses at a 10-Hz repetition rate with duration of 45 fs, energy around 20 mJ,

and a beam diameter of 24 mm (FWHM). The vertically polarized beam, apertured to a diameter of 22 mm, is focused by a 8.7-m focal length lens into a 60-mm-long gas cell statically filled with argon. Prior to focusing, residual aberrations of the infrared (IR) beam are compensated by a deformable mirror operating in closed loop with an IR wavefront sensor. The mirror also allows for adjustment of the focal position with respect to the cell in 1-mm steps. The aperture size, the gas pressure, the position of the cell, and the laser focus are optimized for the maximum of the XUV signal. The IR and XUV radiation are then co-propagating towards a fused silica (FS) plate placed at a 10° grazing angle 4 m after the gas cell. The plate is given anti-reflection (AR) coating to transmit the IR while the XUV beam is reflected. The residual IR radiation is blocked by a 200-nm-thick aluminum filter. In the next chamber, a gold-coated mirror on a rotation stage is used to fold the XUV radiation towards an XUV flat-field spectrometer. A typical HHG spectrum is shown in Figure 1b. It is composed of nine harmonic orders, from 15 to 31, with photon energies from 23 to 45 eV. Their spatial profiles in the far field are plotted in the inset. The divergence is estimated to 0.33 mrad (FWHM) for harmonic 19. The transmission of the beamline from the generation cell to the entrance of the application chamber is estimated to be 22%, for XUV photons with energies from 20 to 50 eV. This value is calculated using the measured transmission of the Luxel aluminum filter (34%) and the calculated reflectivity of the AR-coated fused silica plate (the top layer of the coating is SiO_2 with reflectivity of 65%). During nonlinear experiments, the XUV beam is focused into a target gas jet, and a double-sided ion/electron spectrometer is placed around the focus as shown in Figure 1.

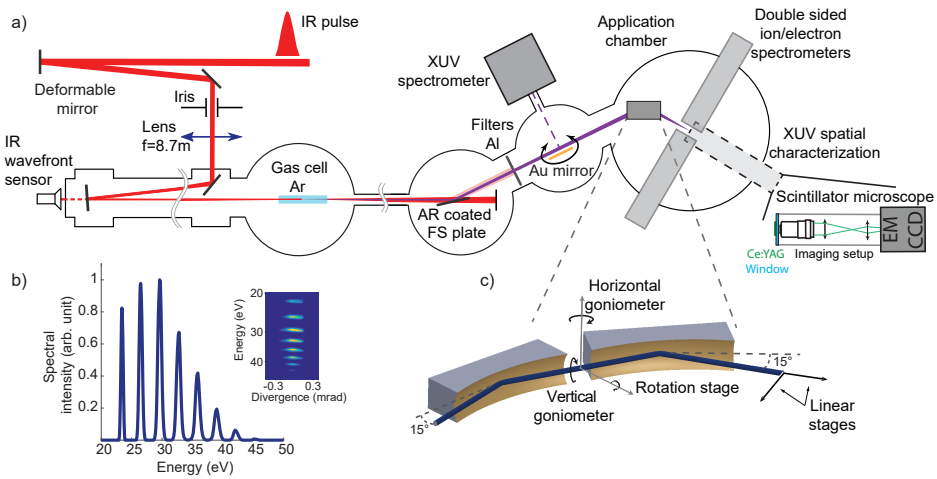

Figure 1. (**a**) Scheme of the intense extreme ultraviolet (XUV) beamline; (**b**) typical high-order harmonic generation (HHG) spectrum; and (**c**) double toroidal mirror setup in a Wolter configuration. The black lines indicate the translation axes (straight solid arrows) and the pivoting axes for the revolutions (curved solid arrows). AR: anti-reflection; FS: fused silica.

2.2. Micro-Focusing

With the intent of maintaining the broad spectrum and high throughput, the XUV radiation is focused in the experimental region by means of two toroidal mirrors in grazing incidence configuration. The XUV beam is not recollimated prior to refocusing, but instead the object, i.e., the generation volume in the gas cell, is imaged into the interaction region in the application chamber. The object arm measures approximately 6 m, while the image arm measures 170 mm, resulting in a demagnification of 35. The combination of the two toroidal mirrors is designed to achieve a total deflection of 60°, arising from a 15° grazing incidence on each mirror.

Figure 1c shows a schematic representation of the Wolter assembly. It is composed of two toroidal mirrors which are 30 mm long and 10 mm high. The center-to-center distance between the two mirrors is 30 mm. The mirrors are coated with gold because of its broadband reflectivity in the XUV range. In fact, between 20 and 50 eV, the gold layer yields a 61% reflectivity for s-polarized light and for a 15° grazing angle. The theoretical throughput of the optical setup is then 37%. However, the roughness of the surface is not taken into account in this calculation and the real throughput is expected to be smaller. The two mirrors were installed and pre-aligned by the manufacturer Thales SESO (Aix-en-Provence, France). This assembly is mounted on a 5-axis stage, whose degrees of freedom are sketched in Figure 1c. These axes are actuated by piezo-driven stick-and-slip positioners in open-loop configuration.

As mentioned in the introduction, ellipsoidal mirrors are in principle the ideal solution for imaging. However, the toroidal surface represents a good local approximation to the ellipsoidal surface with the advantage that the two focal lengths, f_T and f_S, corresponding to the tangential (the plane which includes both the optical axis and the normal to the mirror surface) and the sagittal (normal to the tangential plane and containing the optical axis) planes, respectively, are not coupled and can be set independently according to the following equations:

$$f_T = \frac{R_T \sin\theta}{2}, \tag{1}$$

$$f_S = \frac{R_S}{2\sin\theta}, \tag{2}$$

where R denotes the radius of curvature, and the subscripts T and S refer to the tangential and sagittal planes, respectively. θ is the grazing angle. Table 1 shows the curvatures and focal lengths of the individual mirrors in the two planes, as well as the combined focal length.

Table 1. Radii of curvature (provided by the manufacturer), focal lengths of the individual mirrors in the two planes, and the equivalent focal length of the assembly.

	Tangential		**Sagittal**	
	R_T **[mm]**	f_T **[mm]**	R_S **[mm]**	f_S **[mm]**
First mirror	2050	265.3	137.2	265.0
Second mirror	4213	545.2	281.8	544.4
Combined	Focal length = 164.2 mm			

The curvatures of each of the two mirrors are adjusted so that the resulting focal lengths in both planes are almost the same, to prevent astigmatism. The equivalent focal length of the assembly is about 164 mm (from the center of the second mirror), calculated in the paraxial approximation. This implies that our source, located 6 m before the mirrors, is imaged at 170 mm from the center of the second mirror.

2.3. Direct Focus Measurements

In order to directly record an image of the focal spot, we used a Ce-doped yttrium aluminum garnet (Ce:YAG) scintillation crystal [17,25,38], which converts the XUV radiation into visible light with 550-nm central wavelength. The resulting luminescence spot was imaged onto a cooled electron multiplying charge-coupled device (EMCCD) camera by using an optical system composed of a microscope objective (Mitutoyo M Plan Apo 100X) and two lenses for relay imaging (see inset to Figure 1a). The crystal was fixed to a thin fused silica window and placed under vacuum, while the imaging system with the camera was under atmospheric pressure. The field of view

and resolution were estimated to be 50 µm and 2 µm, respectively. A limiting factor for the measurement was the nonlinear dependence of the luminescence yield as a function of the XUV intensity [17,39] and, in particular, its saturation. To limit this phenomenon, we used a 2-µm-thick Al filter after the fused silica plate (see Figure 1), which decreased the HHG energy by two orders of magnitude. Consequently, the luminescence yield was reduced, and the detection required a single-photon-sensitive camera. Furthermore, it was crucial to record single-shot images of the focal spot, since accumulating several shots led to a seemingly larger spot size, because of the pointing instability of the incoming beam.

These measurements confirm that the Wolter optics compensate efficiently for coma aberrations. Astigmatism could be observed in non-optimized focusing conditions. However, it was not possible to determine precisely the spot size, which was found to be systematically a factor two or three times larger than the wavefront-based measurements presented in Section 3. This probably indicates that this measurement method is still hampered by the nonlinearity of the crystal or other technical limitations.

3. Wavefront Measurements and Optimization of the Focal Spot Size

3.1. Hartmann Wavefront Sensor

The wavefront sensor, presented schematically in Figure 2a, is composed of a Hartmann mask and an XUV charge-coupled device (CCD) camera [36]. Flat, non-tilted wavefronts result in individual diffraction spots being equidistantly distributed on the camera chip (see black dots in Figure 2b), whereas in the case of distorted wavefronts, the positions deviate (red dots). These deviations are compared to a reference measurement with a known wavefront profile, here a spherical wavefront created from the diffraction of an HHG beam onto a pinhole. The local wavefront slopes in the mask plane, $(\partial W/\partial x, \partial W/\partial y)$ with W denoting the wavefront, are proportional to these deviations ($\vec{h}$ in the figure), and are calculated for each hole. Subsequently, a wavefront reconstruction is performed to retrieve the wavefront over the whole aperture.

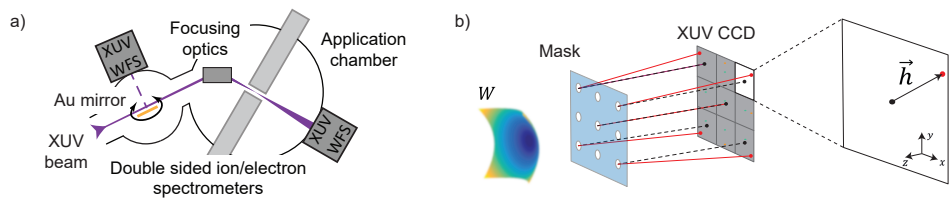

Figure 2. (**a**) Positions of the sensor in the beamline; and (**b**) principle of the Hartmann wavefront sensor. WFS: Wavefront sensor.

To measure XUV wavefronts after the focusing setup, we used a wavefront sensor (collaboration between Imagine Optics and the Laboratoire d'Optique Applique, LOA) placed 50 cm after the focus. This distance was chosen to match the beam size to the sensor aperture. The Hartmann mask is a 100-µm-thick nickel plate, which contains an array of 34 × 34 holes. The holes are squares with a size of 110 µm and a pitch of 387 µm, and are tilted to prevent the diffraction patterns from consecutive holes to overlap. During previous calibration measurements performed at the LOA, the absolute accuracy of the sensor was estimated to be 0.6 nm root mean square (RMS), which corresponds to $\lambda/70$ RMS for a wavelength of 42 nm. The sensor was mounted on a manual hexapod to ensure optimal alignment. The analysis was performed for the 19th harmonic (42 nm/29.5 eV), chosen as the weighted center of our spectrum. The validity of single-wavelength wavefront retrieval for broadband radiation in the visible regime was discussed with a Shack–Hartmann sensor [40] and was proven to be satisfying.

There are two main types of wavefront reconstruction from the measured slopes [41]. The first one is called zonal reconstruction, which corresponds to the direct numerical integration of the local slopes. The other type is modal reconstruction, a decomposition of the wavefront in the basis of orthogonal polynomials, which correspond to a set of different aberrations. It thus allows the aberrations to be extracted independently, with the drawback of fitting them over a circular pupil, which is not always matching real beam profiles and leads to slightly underestimated aberrations [42]. The basis of orthogonal polynomials is provided by Zernike polynomials $Z_n^m(x, y)$, which are often the preferred choice to extract and study aberrations independently. The wavefront is then expanded as:

$$W(x, y) = \sum_{m,n} c_n^m Z_n^m(x, y), \tag{3}$$

where c_n^m are the weights of the individual polynomials. The first coefficients in Equation (3) are known as piston (c_0^0), x-tilt (c_1^{-1}), y-tilt (c_1^1), defocus (c_2^0), astigmatism at 0° (c_2^2), astigmatism at 45° (c_2^{-2}), and coma at 0° (c_3^1) and 90° (c_3^{-1}). The coefficients can be determined by fitting the polynomials' derivatives to the measured local slopes.

For the analysis of the wavefronts presented in this work, when using the zonal method, the pupil was chosen to be the entire illuminated area, about 10×10 mm^2. When using the modal method, a circular pupil with a radius of 2.3 mm was centered around the peak of the beam profile. The analysis was performed using the first 32 Zernike polynomials with a standard peak-to-valley (PV) normalization. All wavefronts presented here are single-shot measurements. Contributions from defocus and tilts have been numerically removed.

3.2. Alignment of the Focusing Optics

In order to evaluate the sensitivity of the wavefront aberrations to the alignment of the focusing optics, we scanned the rotation stage and goniometers described in Figure 1c while recording single-shot wavefronts. As there is no absolute characterization of the stage rotation angles, we express them in number of steps. We extracted the RMS of the wavefronts by zonal reconstruction, as well as the corresponding Strehl ratio [43], which is defined as the ratio of the peak intensities of the focal distribution in the aberrated and unaberrated cases. A good approximation of the Strehl ratio S, used in the present work, is given by $S = \exp(-\sigma^2/\lambda^2)$, where σ is the wavefront RMS [44].

The results are presented in Figure 3, where Figures 3a, 3b and 3c correspond to scans of the rotation stage, and the horizontal and vertical goniometers, respectively, with the other axes around the optimum. Due to shot-to-shot fluctuations, for each point, the average value of several (~ 5) single-shot measurements with corresponding RMS error bars is plotted. A sharp V-shaped trend is visible for every graph. It means that for each actuator, it is possible to find a position minimizing the aberrations. The RMS minima are 0.028 ± 0.015 λ ($\simeq \lambda/36$) in Figure 3a, 0.088 ± 0.012 λ in Figure 3b and 0.111 ± 0.034 λ in Figure 3c. The values for Figure 3b and Figure 3c are slightly higher because of residual aberrations or misalignments.

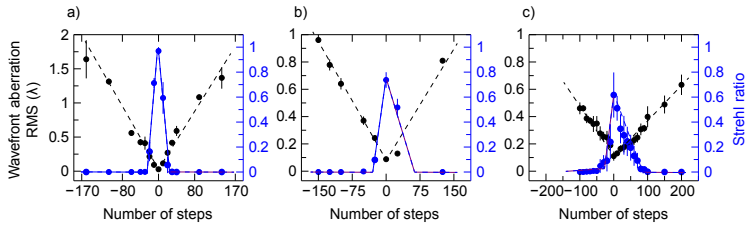

Figure 3. Evolution of the XUV wavefront root mean square (RMS) as a function of the focusing optics relative angle (number of steps) along the different axes: (**a**) rotation stage; (**b**) horizontal goniometer; and (**c**) vertical goniometer. The RMS is plotted in black dots in units of lambda for $\lambda = 42$ nm (left axis), with error bars coming from several single-shot measurements. The corresponding Strehl ratios are plotted in blue dots (right axis). The qualitative trends are plotted in dashed lines.

In order to better understand which aberrations are accounting for most of the wavefront distortions, we used the modal technique to decompose the wavefronts in a weighted sum of Zernike polynomials, as explained above. Our analysis shows that astigmatism is the dominant aberration, accounting for most of the deviation from a perfect wavefront. Figure 4 presents the Zernike coefficients for astigmatism (0° and 45°) and coma (average value of 0° and 90°) as a function of the number of steps. For all three cases, the coma is found to be negligible, which means that if the first mirror introduces coma, it is completely compensated by the second one, thus validating the double toroidal mirror Wolter configuration. The horizontal goniometer introduces mostly 0° astigmatism while the rotation stage and the vertical goniometer introduce 45° astigmatism. These different behaviors allow us to determine which axis is misaligned, and is thus very useful for fast optimization. For example, during the vertical goniometer scan shown in Figure 4c, there was residual 0° astigmatism (green dots), meaning that the horizontal goniometer was not perfectly aligned in this case. Good alignment could be reached after a few iterations.

In order to validate these results, we carried out simulations of the XUV beam propagation through the setup with the ray-tracing software FRED Optical Engineering (Version 14, Photon Engineering LLC, Tucson, AZ, USA), based upon Gaussian beamlet decomposition [45]. The wavelength was chosen to be 42 nm, corresponding to harmonic 19. The results are plotted in Figure 4 as solid lines, using the same colors as the experimental data for the different coefficients. Here, the relative angle is indicated in degrees. The ray-tracing simulations show the same behavior as the experimental data, with the sharp V-shape for the dependence of the main Zernike coefficient for a given axis. The simulations also confirm that each goniometer is affecting mainly a specific aberration. For the Zernike coefficients, simulations and respectively experimental data have been normalized to 1 at -0.8 degrees (respectively at -160 steps) of the rotation stage in Figure 4a. We also used the zonal wavefront reconstruction method for both experiment and simulation to extract the wavefront RMS. This allowed us to estimate the step size as a function of rotation angle for each axis.

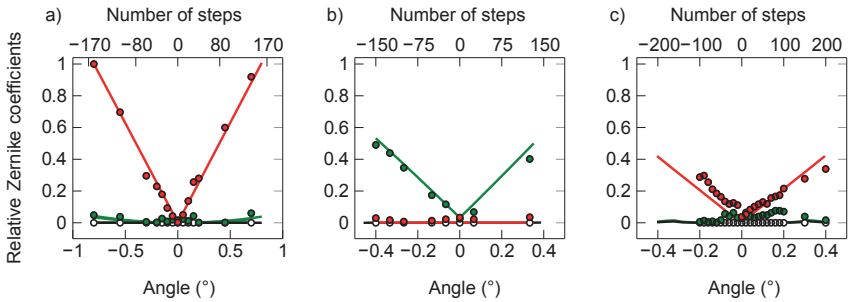

Figure 4. Relative Zernike coefficients for the main aberrations as a function of the angle of the (**a**) rotation stage; (**b**) horizontal goniometer; and (**c**) vertical goniometer. The experimental data are represented as circled colored dots, plotted as a function of the number of steps (top axis). The ray-tracing simulation data is represented as solid lines, plotted as a function of the angle in degrees (bottom axis). Red corresponds to 45° astigmatism, green to 0° astigmatism, and white to the averaged coma.

Figure 5 is a comparison between the beam before the focusing optics, intensity and wavefront in Figure 5a,c respectively, and after optimization (Figure 5b,d). The beam before focusing optics has some 0° astigmatism, with an RMS value of 0.11 λ (=λ/9). After optimization of the focusing optics, we obtain an RMS value of 0.028 ± 0.015 λ (λ/36). It shows that the focusing optics can not only be aligned to introduce the least possible aberrations, but can also correct the pre-existing ones.

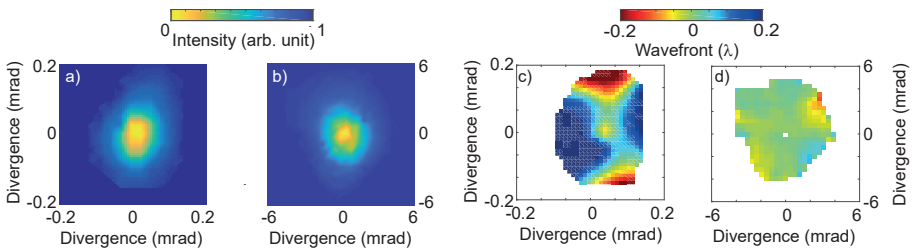

Figure 5. Intensity and wavefront of the XUV beam before (**a**,**c**) and after (**b**,**d**) focusing.

3.3. Size of the Focal Spot

To estimate the focal spot size, the measured wavefront and spatial intensity distribution are back-propagated to the focus by applying a Fourier transform. The wavefront $W(x,y)$ is written as the sum of the first three terms in the expansion (tilts and defocus, the piston is ignored) plus a residual wavefront $\tilde{W}(x,y)$. The contributions of defocus and tilts to the wavefront are strong and usually dominate the higher-order aberrations. Their back-propagation requires a very fine sampling of the xy-plane over the pupil such that the wavefront never changes by more than a fraction of the wavelength from one sample point to the next. We thus need to treat the defocus and tilt contributions separately in order to optimize the numerical calculation. The wavefront tilts represent the propagation direction of the beam and they can be added later to obtain the final result. The electric field $E(x,y,z)$, at the position of the Hartmann mask ($z = 0$), is described by

$$E(x,y,0) = U(x,y,0)\, e^{-ikc_2^0 Z_2^0(x,y)} \qquad \text{with} \qquad U(x,y,0) = \sqrt{I(x,y,0)}\, e^{-ik\tilde{W}(x,y)}\,. \tag{4}$$

$I(x,y,z=0)$ is the spatial intensity distribution measured at the position of the mask and $k = 2\pi/\lambda$ the wavevector. Since the defocus component $c_2^0 Z_2^0$ describes a quadratic phase, $E(x,y,0)$ represents the field after an ideal lens with focal length $f = r^2/(4c_2^0)$, with r being the pupil radius, and $U(x,y,0)$ being the field before the lens. The field in the focus is then given by the Fourier transform of $U(x,y,0)$

$$I(x',y',z_{foc}=f) = |E(x',y',z_{foc})|^2 \propto \left| \iint U(x,y,0)\, e^{i2\pi(\nu_x x+\nu_y y)}\, dx\, dy \right|^2 . \quad (5)$$

Taking into account the tilts' contribution to the focal spot position, the rescaled coordinates in the focal plane are $x' = \nu_x \lambda f + c_1^{-1} f/r$ and $y' = \nu_y \lambda f + c_1^1 f/r$. The defocus component of the wavefront determines the focus position along the beam path, whereas the tilts determine its position in the $x'y'$-plane.

With this method, we back-propagated the least aberrated field (optimized alignment of the focusing setup), presented in Figure 5b,d, and obtained the focal spot plotted in Figure 6a. The focus size is estimated to be 3.6×4.0 μm^2 (FWHM).

We also performed ray-tracing simulations for aligned focusing optics, assuming a perfect Gaussian beam, with the experimentally measured divergence. The focal spot is shown in Figure 6b with its profiles. The FWHM beam size is 3.0 × 3.2 μm^2. The focal spot size obtained by back-propagation of the wavefront is in good agreement with the one obtained by the ray-tracing simulations. The 20% difference in size can be explained by the difficulty of estimating precisely the divergence of the beam used for the ray-tracing simulations, and by distortions of the experimental intensity profile.

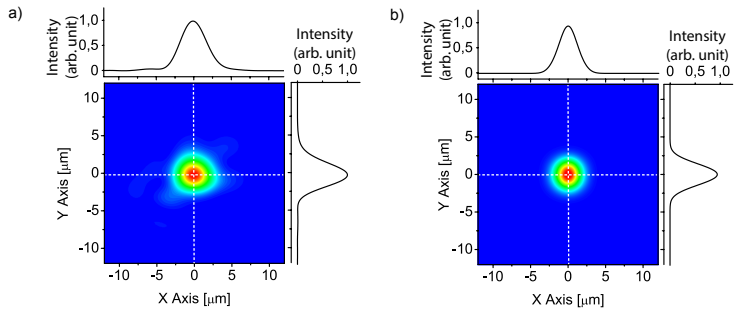

Figure 6. Focal spot (**a**) calculated from wavefront measurement by back-propagation; and (**b**) calculated from ray-tracing simulations.

The intensity of the focused attosecond pulse train is estimated to 7 × 10^{12} W/cm^2, using the back-propagated spot size of 3.6 × 4.0 μm^2 and typical energies of 5 nJ, measured in the focal region with a calibrated Andor XUV camera and an XUV photodiode. For this estimation we assume a train of 15 pulses with individual duration of ≈300 as [8].

4. Conclusions

We have presented a micro-focusing setup for a broadband harmonic beam based on two toroidal mirrors in a Wolter configuration. The setup is capable of focusing the beam to a spot size of 3.6 × 4.0 μm^2, which was optimized and characterized using an XUV wavefront sensor. The focus dimensions agree well with the expected value according to the ray-tracing simulations. The wavefront sensor was found to be an excellent tool to optimize the focusing optics alignment, providing quick and precise feedback. Pre-existing aberrations of the XUV beam could also be corrected. The non-invasive property of wavefront measurements makes it possible to control the focusing quality and thus guarantees the highest intensity on target during experiments.

Acknowledgments: The research was supported by the Swedish Research Council, the Swedish Foundation for Strategic Research, the European Research Council (grant 339253 PALP), LASERLAB-EUROPE (proposal LLC002276), and the European COST Actions MP1203 and CM1204. This project received funding from the European Union's Horizon 2020 research and innovation program under Marie Skłodowska-Curie Grant Agreement No. 641789 MEDEA and the FET-open grant No. 665207 VOXEL. The authors would like to thank Johan Axelsson and Anders Mikkelsen for lending high-sensitivity cameras. The ELI-ALPS project (GINOP-2.3.6-15-2015-00001) is supported by the European Union and co-financed by the European Regional Development Fund.

Author Contributions: H.C.-A., H.D., K.V., P.Z., P.J., A.L.H, and P.R. conceived and designed the experiments; B.F., H.C.-A., S.M., and P.R. performed the spot characterization by the scintillator microscope; B.Man. designed the scintillator microscope; H.C.-A., H.D., P.R., F.C., E.K., S.M., H.W., J.L., L.R., J.P., and B.Maj. performed the wavefront optimization experiments; F.C. and H.C.-A. performed the ray-tracing simulations; F.B. performed the back-propagation of the wavefronts and intensity recorded by the wavefront sensor; G.D. contributed to the analysis tools. All authors participated in writing the manuscript.

Conflicts of Interest: The authors declare no conflict of interest.

References

1. McPherson, A.; Gibson, G.; Jara, H.; Johann, U.; Luk, T.S.; McIntyre, I.A.; Boyer, K.; Rhodes, C.K. Studies of multiphoton production of vacuum-ultraviolet radiation in the rare gases. *J. Opt. Soc. Am. B* **1987**, *4*, 595.
2. Ferray, M.; L'Huillier, A.; Li, X.F.; Lompre, L.A.; Mainfray, G.; Manus, C. Multiple-harmonic conversion of 1064 nm radiation in rare gases. *J. Phys. B At. Mol. Opt. Phys.* **1988**, *21*, L31–L35.
3. Ishii, N.; Kaneshima, K.; Kitano, K.; Kanai, T.; Watanabe, S.; Itatani, J. Carrier-envelope phase-dependent high harmonic generation in the water window using few-cycle infrared pulses. *Nat. Commun.* **2014**, *5*, doi:10.1038/ncomms4331.
4. Li, J.; Ren, X.; Yin, Y.; Cheng, Y.; Cunningham, E.; Wu, Y.; Chang, Z. Polarization gating of high harmonic generation in the water window. *Appl. Phys. Lett.* **2016**, *108*, doi:10.1063/1.4953402.
5. Tzallas, P.; Charalambidis, D.; Papadogiannis, N.A.; Witte, K.; Tsakiris, G.D. Direct observation of attosecond light bunching. *Nature* **2003**, *426*, 267–271.
6. Tzallas, P.; Skantzakis, E.; Nikolopoulos, L.A.A.; Tsakiris, G.D.; Charalambidis, D. Extreme-ultraviolet pump–probe studies of one-femtosecond-scale electron dynamics. *Nat. Phys.* **2011**, *7*, 781–784.
7. Nabekawa, Y.; Hasegawa, H.; Takahashi, E.J.; Midorikawa, K. Production of Doubly Charged Helium Ions by Two-Photon Absorption of an Intense Sub-10-fs Soft X-Ray Pulse at 42 eV Photon Energy. *Phys. Rev. Lett.* **2005**, *94*, doi:10.1103/PhysRevLett.94.043001.
8. Manschwetus, B.; Rading, L.; Campi, F.; Maclot, S.; Coudert-Alteirac, H.; Lahl, J.; Wikmark, H.; Rudawski, P.; Heyl, C.M.; Farkas, B.; et al. Two-photon double ionization of neon using an intense attosecond pulse train. *Phys. Rev. A* **2016**, *93*, 1–5.
9. Hergott, J.F.; Kovacev, M.; Merdji, H.; Hubert, C.; Mairesse, Y.; Jean, E.; Breger, P.; Agostini, P.; Carré, B.; Salières, P. Extreme-ultraviolet high-order harmonic pulses in the microjoule range. *Phys. Rev. A* **2002**, *66*, doi:10.1103/PhysRevA.66.021801.
10. Takahashi, E.; Nabekawa, Y.; Otsuka, T.; Obara, M.; Midorikawa, K. Generation of highly coherent submicrojoule soft x rays by high-order harmonics. *Phys. Rev. A* **2002**, *66*, doi:10.1103/PhysRevA.66.021802.
11. Midorikawa, K.; Nabekawa, Y.; Suda, A. XUV multiphoton processes with intense high-order harmonics. *Progress Quantum Electron.* **2008**, *32*, 43–88.
12. Rudawski, P.; Heyl, C.M.; Brizuela, F.; Schwenke, J.; Persson, A.; Mansten, E.; Rakowski, R.; Rading, L.; Campi, F.; Kim, B.; et al. A high-flux high-order harmonic source. *Rev. Sci. Instrum.* **2013**, *84*, doi:10.1063/1.4812266.
13. Kühn, S.; Dumergue, M.; Kahaly, S.; Mondal, S.; Füle, M.; Csizmadia, T.; Farkas, B.; Major, B.; Várallyay, Z.; Cormier, E.; et al. The ELI-ALPS facility: The next generation of attosecond sources. *J. Phys. B At. Mol. Opt. Phys.* **2017**, *50*, doi;10.1088/1361-6455/aa6ee8.
14. Zhao, K.; Zhang, Q.; Chini, M.; Wu, Y.; Wang, X.; Chang, Z. Tailoring a 67 attosecond pulse through advantageous phase-mismatch. *Opt. Lett.* **2012**, *37*, 3891–3893.
15. Li, J.; Ren, X.; Yin, Y.; Zhao, K.; Chew, A.; Cheng, Y.; Cunningham, E.; Wang, Y.; Hu, S.; Wu, Y.; et al. 53-attosecond X-ray pulses reach the carbon K-edge. *Nat. Commun.* **2017**, *8*, doi:10.1038/s41467-017-00321-0.
16. Takahashi, E.J.; Lan, P.; Mücke, O.D.; Nabekawa, Y.; Midorikawa, K. Attosecond nonlinear optics using gigawatt-scale isolated attosecond pulses. *Nat. Commun.* **2013**, *4*, doi:10.1038/ncomms3691.

17. Valentin, C.; Douillet, D.; Kazamias, S.; Lefrou, T.; Grillon, G.; Augé, F.; Mullot, G.; Balcou, P.; Mercère, P.; Zeitoun, P. Imaging and quality assessment of high-harmonic focal spots. *Opt. Lett.* **2003**, *28*, 1049–1051.
18. Morlens, A.S.; López-Martens, R.; Boyko, O.; Zeitoun, P.; Balcou, P.; Varjú, K.; Gustafsson, E.; Remetter, T.; L'Huillier, A.; Kazamias, S.; et al. Design and characterization of extreme-ultraviolet broadband mirrors for attosecond science. *Opt. Lett.* **2006**, *31*, 1558–1560.
19. Ménesguen, Y.; De Rossi, S.; Meltchakov, E.; Delmotte, F. Aperiodic multilayer mirrors for efficient broadband reflection in the extreme ultraviolet. *Appl. Phys. A Mater. Sci. Process.* **2010**, *98*, 305–309.
20. Wieland, M.; Wilheim, T.; Spielmann, C.; Kleinberg, U. Zone-plate interferometry at 13 nm wavelength. *Appl. Phys. B Lasers Opt.* **2003**, *76*, 885–889.
21. Poletto, L.; Frassetto, F.; Calegari, F.; Trabattoni, A.; Nisoli, M. Micro-focusing of attosecond pulses by grazing-incidence toroidal mirrors. *Opt. Express* **2013**, *21*, 13040–13051.
22. Suda, A.; Mashiko, H.; Midorikawa, K. Focusing intense high-order harmonics to a micron spot size. *Springer Ser. Chem. Phys.* **2007**, *85*, 183–198.
23. Bourassin-Bouchet, C.; Mang, M.M.; Delmotte, F.; Chavel, P.; de Rossi, S. How to focus an attosecond pulse. *Opt. Express* **2013**, *21*, 2506–2520.
24. Underwood, J.H. Imaging properties and aberrations of spherical optics and nonspherical optics. In *Experimental Methods in the Physical Sciences*; Academic Press: Cambridge, MA, USA, 1998; Volume 31.
25. Frassetto, F.; Anumula, S.; Calegari, F.; Trabattoni, A.; Nisoli, M.; Poletto, L. Microfocusing beamline for XUV-XUV pump-probe experiments using HH generation. In Proceedings of the Society of Photo-Optical Instrumentation Engineers SPIE 9208, San Diego, CA, USA, 5 September 2014.
26. Wolter, H. Spiegelsysteme streifenden Einfalls als abbildende Optiken für Röntgenstrahlen. *Ann. Phys.* **1952**, *445*, 94–114.
27. Gaetz, T.J.; Jerius, D.; Edgar, R.J.; Van Speybroeck, L.P.; Schwartz, D.A.; Markevitch, M.L.; Taylor, S.C.; Schulz, N.S. Orbital verification of the CXO high-resolution mirror assembly alignment and vignetting. In Proceedings of the Society of Photo-Optical Instrumentation Engineers SPIE 4012, Munich, Germany, 18 July 2000.
28. Mildner, D.F.R.; Gubarev, M.V. Wolter optics for neutron focusing. *Nucl. Instrum. Meth. A* **2011**, *634*, 7–11.
29. Khaykovich, B.; Gubarev, M.V.; Bagdasarova, Y.; Ramsey, B.D.; Moncton, D.E. From x-ray telescopes to neutron scattering: Using axisymmetric mirrors to focus a neutron beam. *Nucl. Instrum. Meth. A* **2011**, *631*, 98–104.
30. Bennett, G.R. Advanced laser-backlit grazing-incidence x-ray imaging systems for inertial confinement fusion research. I. Design. *Appl. Opt.* **2001**, *40*, 4570–4587.
31. Ellis, R.J.; Trebes, J.E.; Phillion, D.W.; Kilkenny, J.D.; Glendinning, S.G.; Wiedwald, J.D.; Levesque, R.A. Four-frame gated Wolter x-ray microscope. *Rev. Sci. Instrum.* **1990**, *61*, 2759–2761.
32. Le Déroff, L.; Salières, P.; Carré, B. Beam-quality measurement of a focused high-order harmonic beam. *Opt. Lett.* **1998**, *23*, 1544–1546.
33. Lee, D.G.; Park, J.J.; Sung, J.H.; Nam, C.H. Wave-front phase measurements of high-order harmonic beams by use of point-diffraction interferometry. *Opt. Lett.* **2003**, *28*, 480–482.
34. Frumker, E.; Paulus, G.G.; Niikura, H.; Villeneuve, D.M.; Corkum, P.B. Frequency-resolved high-harmonic wavefront characterization. *Opt. Lett.* **2009**, *34*, 3026–3028.
35. Austin, D.R.; Witting, T.; Arrell, C.A.; Frank, F.; Wyatt, A.S.; Marangos, J.P.; Tisch, J.W.G.; Walmsley, I.A. Lateral shearing interferometry of high-harmonic wavefronts. *Opt. Lett.* **2011**, *36*, 1746–1748.
36. Mercère, P.; Zeitoun, P.; Idir, M.; Le Pape, S.; Douillet, D.; Levecq, X.; Dovillaire, G.; Bucourt, S.; Goldberg, K.A.; Naulleau, P.P.; et al. Hartmann wave-front measurement at 134 nm with λ_EUV/120 accuracy. *Opt. Lett.* **2003**, *28*, 1534–1536.
37. Le Pape, S.; Zeitoun, P.; Idir, M.; Dhez, P.; Rocca, J.J.; François, M. Electromagnetic-Field Distribution Measurements in the Soft X-Ray Range: Full Characterization of a Soft X-Ray Laser Beam. *Phys. Rev. Lett.* **2002**, *88*, doi:10.1103/PhysRevLett.88.1839011.
38. Moszyński, M.; Ludziejewski, T.; Wolski, D.; Klamra, W.; Norlin, L. Properties of the YAG:Ce scintillator. *Nucl. Instrum. Meth. A* **1994**, *345*, 461–467.
39. Jaeglé, P.; Sebban, S.; Carillon, A.; Jamelot, G.; Klisnick, A.; Zeitoun, P.; Rus, B.; Nantel, M.; Albert, F.; Ros, D. Ultraviolet luminescence of CsI and CsCl excited by soft x-ray laser. *J. Appl. Phys.* **1997**, *81*, 2406–2409.

40. Hauri, C.P.; Biegert, J.; Keller, U.; Schaefer, B.; Mann, K.; Marowski, G. Validity of wave-front reconstruction and propagation of ultrabroadband pulses measured with a Hartmann-Shack sensor. *Opt. Lett.* **2005**, *30*, 1563–1565.
41. Southwell, W. Wave-front estimation from wave-front slope measurements. *J. Opt. Soc. Am.* **1980**, *70*, 998–1006.
42. Lakshminarayanan, V.; Fleck, A. Zernike polynomials: A guide. *J. Mod. Opt.* **2011**, *58*, 545–561.
43. Chériaux, G.; Rousseau, J.P.; Ferré, S.; Notebaert, L.; Pittman, M.; Chambaret, J.P. Caractérisation et contrôle de la répartition d'énergie et du front d'onde d'impulsions femtosecondes. In *Systèmes Femtosecondes*; Number 1 in Intégrations Des Savoirs Et Savoir-Faire; Publications de l'Université de Saint-Étienne: Saint-Étienne, France; 2001; pp. 141–156.
44. Mahajan, V.N. Strehl ratio for primary aberrations in terms of their aberration variance. *J. Opt. Soc. Am.* **1983**, *73*, 860–861.
45. Harvey, J.E.; Irvin, R.G.; Pfisterer, R.N. Modeling physical optics phenomena by complex ray tracing. *Opt. Eng.* **2015**, *54*.

Paper x

L. Rading, J. Lahl, S. Maclot, F. Campi, H. Coudert-Alteirac, B. Oostenrijk, **J. Peschel**, H. Wikmark, P. Rudawski, M. Gisselbrecht, and P. Johnsson
A versatile velocity map ion-electron covariance imaging spectrometer for high-intensity XUV experiments
Appl. Sci. 8(6), 998, (2018)

applied sciences

MDPI

Article

A Versatile Velocity Map Ion-Electron Covariance Imaging Spectrometer for High-Intensity XUV Experiments

Linnea Rading †, Jan Lahl *,†, Sylvain Maclot †, Filippo Campi, Hélène Coudert-Alteirac, Bart Oostenrijk, Jasper Peschel, Hampus Wikmark, Piotr Rudawski, Mathieu Gisselbrecht and Per Johnsson *

Department of Physics, Lund University, P.O. Box 118, 22100 Lund, Sweden;
linnea.k.rading@gmail.com (L.R.); sylvain.maclot@fysik.lth.se (S.M.); filiuqwerty@gmail.com (F.C.); helene.coudert@fysik.lth.se (H.C.-A.); bart.oostenrijk@sljus.lu.se (B.O.); jasper.peschel@fysik.lth.se (J.P.); hampus.wikmark@fysik.lth.se (H.W.); piotr.rudawski@fysik.lth.se (P.R.); mathieu.gisselbrecht@sljus.lu.se (M.G.)
* Correspondence: jan.lahl@fysik.lth.se (J.L.); per.johnsson@fysik.lth.se (P.J.)
† These authors contributed equally to this work.

Received: 22 April 2018; Accepted: 15 June 2018; Published: 19 June 2018

Abstract: We report on the design and performance of a velocity map imaging (VMI) spectrometer optimized for experiments using high-intensity extreme ultraviolet (XUV) sources such as laser-driven high-order harmonic generation (HHG) sources and free-electron lasers (FELs). Typically exhibiting low repetition rates and high single-shot count rates, such experiments do not easily lend themselves to coincident detection of photo-electrons and -ions. In order to obtain molecular frame or reaction channel-specific information, one has to rely on other correlation techniques, such as covariant detection schemes. Our device allows for combining different photo-electron and -ion detection modes for covariance analysis. We present the expected performance in the different detection modes and present the first results using an intense high-order harmonic generation (HHG) source.

Keywords: high-order harmonic generation; velocity map imaging; extreme ultraviolet; covariance; ultrafast nonlinear optics; particle correlation

1. Introduction

During recent years, emerging short pulse high-intensity extreme ultraviolet (XUV) and X-ray sources such as laser-driven high-order harmonic generation (HHG) [1–5] and free-electron lasers (FELs) [6–9] have opened up new fields of science. They made it possible to study ultrafast dynamics induced and probed with wavelengths in the XUV/X-ray regimes on femtosecond (FELs) [10] and even attosecond (HHG) [11,12] time scales. In addition, the high intensities and short pulse durations enable the study of hitherto inaccessible ionization processes [13–16], as well as single shot imaging of macromolecular complexes [17,18] by circumventing the resolution limit set by radiation damage for long exposures [19]. However, compared to traditional laser or synchrotron experiments, experiments using short pulse high-intensity XUV and X-ray sources typically have to deal with very large single-shot signals (∼1000 events/shot), often at relatively low repetition rates (∼10–100 Hz), which calls for adapted detection schemes.

In experiments employing photo-induced ionization or fragmentation, the information about the interaction process lies in the energy and angular distribution of the emitted photo-electrons and -ions. One way of obtaining this information is by means of the application of a reaction microscope (REMI) [20], where the initial three-dimensional momentum of particles is deduced from measurements

of their impact coordinates on the detector, as well as from the flight time, acquired by means of, e.g., delay-line detectors. REMI gives access to complete, correlated, 3D velocity information of all particles detected in coincidence, as long as the count rates are sufficiently low (<1 event/shot) to avoid detecting fragments from more than one target atom or molecule on the same shot.

With high-intensity sources, the repetition rates are typically low, while the single-shot count rates can be very high, which in many cases makes it difficult to use techniques relying on detecting coincidences. Another approach is to use the so-called velocity map imaging (VMI) technique [21], which uses an extraction field configuration that makes the impact coordinates on the detector independent of the location of the ionization event within the interaction volume, as well as of the momentum along the detector axis. This allows for the use of a micro-channel plate (MCP) and a phosphor screen where the impact of a large number of particles can be accumulated on every shot. Under the condition of cylindrical symmetry of the ionization process, the initial three-dimensional momentum distribution of the particles can be recovered from the measured two-dimensional projection using numerical inversion procedures [22,23].

There are several demonstrations of using VMI, under low count rate conditions, for photoelectron-photoion coincidence spectroscopy (PEPICO) [24], for example using electron VMI combined with ion time-of-flight (TOF), ion VMI together with electron spectroscopy and electron VMI with ion VMI [25–29].

An obvious drawback of VMI in high count rate conditions is that one cannot rely on coincidence detection for extracting information about different electrons or ions coming from the same target molecule. An elegant way to overcome this lack of correlated information in VMI, without sacrificing the high count rates, is to use covariance mapping [30]. Briefly, for any two variables, $\mathbf{X} = [X_1, X_2, \ldots, X_N]$ and $\mathbf{Y} = [Y_1, Y_2, \ldots, Y_N]$, sampled synchronously in a repetitive measurement, one can calculate the covariance, which is a measure of how well correlated the variations of the two variables are. Covariance mapping has successfully been applied in several laser and FEL experiments for different detection schemes, demonstrating ion-ion, electron-electron and ion-electron covariance mapping [31–34]. There are also a few examples where not only the mass or energy, but also the momentum of the particles has been studied through so-called covariance imaging [35–38]. Recently, a double-sided electron-ion momentum imaging spectrometer has been installed at the Laser Applications in Material Processing (LAMP)end-station at the Linac Coherent Light Source (LCLS). It features a complex lens design that allows operation either as a REMI or a VMI spectrometer, and for the simultaneous detection of scattered XUV/X-ray photons on a pn charge-coupled device (pnCCD)photon detector [39]. While offering high flexibility, such devices by necessity compromise the imaging capabilities to some extent, due to the adapted electrode design, as well as to the absence of additional shielding of the interaction region from external fields.

Here, we present the design and performance of a double VMI spectrometer (VMIS) for covariance imaging of electrons and positively-charged ions, optimized for experiments using high-intensity XUV and X-ray sources. With minimal compromising of the imaging capabilities, the instrument is versatile and allows for combining photo-electron and -ion detection modes, such as ion TOF, ion VMI and electron VMI, in different ways, depending on the required information and the process under study. The performance of the different detection modes is estimated with simulations and tested in experiments using an intense HHG source, with promising first results using the ion TOF signal for species selection in ion VMI and extraction of channel-specific information from electron VMI data.

In Section 2, we describe the design of the apparatus, discuss technical requirements and the motivation of important design details such as the electrode geometry and the mounting, which allow floating voltages. Further, we describe the simulation procedure and present data on the estimated performance in the different operation modes. In Section 3, we show results from measurements with the spectrometer at the high-intensity XUV beamline at the Lund Attosecond Science Center. Finally, we conclude in Section 4.

2. Apparatus

The design of the double VMIS is an extension of the standard VMIS suggested by Eppink and Parker in 1997 [21]. The standard VMIS, corresponding to the left side in Figure 1a, consists of a repeller plate, an open extractor plate and a field-free flight tube. In the simplest case, where the flight tube is grounded ($V_F^e = 0$), the ratio between the extractor voltage (V_E^e) and the repeller voltage (V_R) defines the imaging mode of the VMIS. In the general case, the ratio can be written as:

$$\eta = \frac{V_E^e - V_F^e}{V_R - V_F^e}. \quad (1)$$

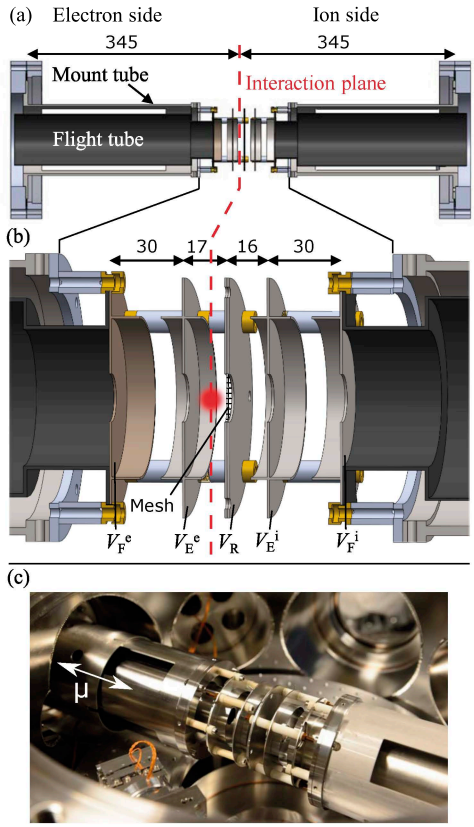

Figure 1. Drawing of the double velocity map imaging spectrometer (VMIS) (**a**) and an expanded view of the electrode package (**b**); dimensions are in mm. The indicated voltages are applied to the electron side flight tube (V_F^e), the electron side extractor (V_E^e), the repeller (V_R), the ion side extractor (V_E^i) and the ion side flight tube (V_F^i). A photo of the spectrometer mounted in the experimental chamber is shown in (**c**). The sliding μ-metal shield is marked by the letter μ.

By changing η, the curvature of the field in the interaction region is changed, allowing for different imaging modes. Velocity map imaging mode is usually achieved for $\eta \approx 0.75$, with the exact value depending on the specific design geometry [21]. In this mode, electrons (or ions) with the same momentum in the plane parallel to the detection plane will be projected onto the same spot on the detector even if they are generated at different positions in the interaction region.

The full three-dimensional momentum distribution can be obtained through inversion procedures, as long as there is an axis of cylindrical symmetry in the ionization process [22,23]. Another mode of operation, often referred to as the spatial imaging mode, is achieved for $\eta \approx 1$ [40]. The particle impact position on the detector is then most sensitive to where the charged particle is created, and therefore, the interaction region can be imaged. This is a useful mode for alignment purposes, providing a means of ensuring precise positioning of the XUV light focal spot, as well as good overlap between the laser beam and the molecular beam [40]. Moreover, by choosing η between 0.78 and 0.8, a Wiley–McLaren ion time-of-flight mode can be achieved [41].

2.1. Design

The design of the double VMIS was made with the following goals: First, we wanted to add the capability to detect positively-charged ions without compromising the resolution on the electron side as compared to a standard VMIS. Second, as molecules have a typical ionization potential of 7–15 eV and, with HHG, the typical photon energies are up to 100 eV, the spectrometer should be able to focus electrons with energies up to ≈90 eV and ions with kinetic energies up to ≈10 eV, typical for, e.g., Coulomb explosion. Third, the spectrometer had to be compatible with the existing experimental chamber of the high-intensity XUV beamline at the Lund Attosecond Science Center containing the all-reflective short focal length XUV focusing optics [42,43].

Extending the single-sided spectrometer to be able to record positively-charged ions and electrons simultaneously was the aim of this work. To that end, the design of the electron side, adapted from [44], was retained and the repeller electrode replaced by an electrode with a mesh, as shown in Figure 1b. On the ion side, an open extractor electrode and a flight tube, similar to that on the electron side, were added. There are two advantages with this choice of design. First, we are not changing the imaging conditions on the electron side, and second, once the optimum voltages have been found for the electrons, the voltages on the ion side can be tuned independently without affecting the electron image quality. The drawbacks are that the ions are to some extent scattered by the mesh, which has a transmission of ∼80%, and that they pass through a drift region before they pass the repeller and are focused by the fields on the ion side. This affects the energy resolution that can be achieved for the ion imaging, which will be discussed in Section 2.3.

The maximum electron or ion energy is restricted by the fact that the electrons or ions move away from the detector axis due to their initial velocity perpendicular to it. To increase the maximum detectable energy, one needs to either decrease the flight tube length, increase the flight tube and detector diameters or use higher acceleration voltages. In our case, the maximum detector size and the flight tube diameters were set by the existing chamber to ∼100 mm, leading to the choice of a standard MCP detector with a diameter of 75 mm, mounted on a CF160 flange. Similarly, the minimum flight tube lengths were set by the flange-to-flange distance (690 mm) of the existing experimental chamber to 345 mm. In principle, shorter flight tube lengths could have been achieved by a design where the MCPs are mounted inside the vacuum chamber, but this would have led to a more complicated design and a deteriorated TOF resolution, and was thus avoided.

With restrictions imposed on the detector size and flight tube length, the ratio between the maximum detectable kinetic energy and the acceleration voltage scales approximately as $(r/L)^2$, where r is the detector radius and L is the flight tube length. Under the chosen conditions, this means that particles with kinetic energies up to ≈1% of the acceleration voltage can be detected, meaning that a total voltage difference of almost 10 kV between the front of the electron MCP and the front of the ion MCP is required to detect electrons and ions with 90 eV and 10 eV of kinetic energy, respectively.

The design of the assembly was made in such a way that both detectors, electrodes and flight tubes could be supplied with floating voltages of ±10 kV. While the front of the MCPs are not electrically connected to the flight tubes, for the following discussion and simulations, we assume that the same voltage is applied to the front of the MCP and the flight tube.

The resulting design of the double VMIS is shown in Figure 1 together with the relevant dimensions. The spectrometer is mounted horizontally, and the electron and ion sides are separable between the repeller electrode and the ion extractor electrode to facilitate mounting of the spectrometer on the two opposite CF200 flanges of the experimental chamber. The mounting flanges are CF200 to CF160 zero-length reducers, allowing for convenient mounting of the detectors after the spectrometer has been installed. In order to allow for floating voltages on the flight tubes, ceramic spacers are used between these and the supporting grounded mount tubes, which are made of stainless steel. While the ion flight tube is made of stainless steel, the electron flight tube is made of μ-metal to provide shielding from external magnetic fields. In addition, a sliding μ-metal cylinder with holes for the laser beam and the molecular beam, visible on the far left in Figure 1c, can be moved in to shield also the electrode assembly. The flight tubes have a front brim, which is supported by four rods via ceramic spacers (white parts in Panel (b)) and bushings (yellow parts in Panel (b)). These brims also hold the electrodes, which can be conveniently reached and exchanged from the top of the chamber without unmounting the flight tube assemblies. The electrodes are mounted with ceramic bushings (yellow parts in Panel (b)) on rods made out of Vespel®, separated by ceramic spacers (white parts in Panel (b)). No electrode or grounded parts are closer than 10 mm apart to allow for large voltage differences without the risk of arcing.

The final design offers a large versatility by allowing for voltages of $\pm$10 kV to be applied to any of the spectrometer components (electrodes or flight tubes), and the choice of a mesh in the repeller electrode allows for independent tuning of the ion sides without affecting the electron imaging. The physical design makes it easy to mount and dismount the whole or parts of the spectrometer, and while being dimensioned for use in the existing experimental chamber, the assembly can be easily transferred also to chambers with other geometries.

2.2. Operation Modes

The spectrometer can be operated in different photo-electron and -ion detection modes. A selection of spectroscopically-relevant modes is listed below:

1. High resolution ion modes:
   (a) Ion TOF,
   (b) Ion VMI.
2. High resolution electron modes:
   (a) Electron VMI, ion TOF,
   (b) Electron VMI, ion VMI.

In the high resolution ion modes, the voltages are set to accelerate and detect ions on the electron side, as a standard single-side VMI, either in TOF mode (1(a)) under Wiley-McLaren conditions [41] or in VMI mode (1(b)). With this setting, the mesh in the repeller electrode does not impose any restriction on the achievable mass or energy resolution, since the ion side of the spectrometer is not used (see Figure 1). In the high resolution electron modes, the electron side of the spectrometer is configured for optimum VMI conditions for electrons, while the ion side voltages are set either for ion TOF (2(a)) or ion VMI (2(b)). The different modes are explored in Section 2.3.

2.3. Simulations

To evaluate the expected performance of the spectrometer, simulations were carried out using SIMION [45] for the different operation modes listed above. An interaction region, defined by the overlap between the laser beam and the molecular beam, with a conservatively chosen size of $(100 \times 100 \times 2000)$ μm^3 was used. For the VMI calculations, electron kinetic energies were chosen in steps of 5 eV from 10–90 eV and ion kinetic energies in steps of 1 eV from 2 to 10 eV. For each

operation mode, we found optimum voltages, defined as the voltages for which the best resolution is obtained for electrons with a kinetic energy of 30 eV and singly-charged ions with a kinetic energy of 6 eV and a mass of $m = 100$ u. The kinetic energies were chosen based on the typical energies of the photoelectrons and photoions of interest using high-order harmonics generated in argon to ionize molecules with ionization potentials in the 10–20-eV range, and the mass was chosen because it is typical for systems that are of current scientific interest, like small polycyclic aromatic hydrocarbons.

To find the optimum voltages for the VMI modes, a simplified simulation procedure was used, in which the trajectories of 27 particles arranged on a $3 \times 3 \times 3$ grid covering the interaction region and with their velocity component perpendicular to the detector axis were calculated and the energy or mass resolution calculated from the particle impact position distribution on the detector. For the optimum voltages found (summarized in Table 1), a procedure based on Monte Carlo sampling was used [46], resulting in more realistic resolution estimates. The method consisted of launching a large number of electrons or ions ($\sim 10^6$) with a random starting position chosen from a Gaussian distribution over the interaction volume and with a random, isotropically-distributed 3D initial momentum. The particle impacts on the detector were then sampled to generate a simulated detector image or TOF trace, which was treated similarly to experimental data in order to extract the resolution. The simulated images were inverted using an iterative algorithm [23] to retrieve the 3D momentum distribution from the 2D image. From the 3D momentum distribution, the energy spectrum was calculated, and the energy resolution, $\Delta E/E$, was estimated by obtaining ΔE from the full width at half maximum of a Gaussian fit to the peaks in the spectrum. For the TOF simulations, only the Monte Carlo method was used, and the mass resolution, $m/\Delta m$, was calculated by obtaining Δm from the full width at half maximum of a Gaussian fit to the peaks in the mass spectrum. They were performed both for ions with zero kinetic energy and for ions with an initial velocity in the direction of the molecular beam. The latter represents the more realistic scenario of target molecules with a mass of 100 u that are brought into the interaction region by a carrier gas, e.g., helium. This carrier gas typically travels at a speed of 1000 m/s, which corresponds to a kinetic energy of 520 meV for molecules with a mass of 100 u.

Table 1. Simulated optimum voltages for the different operation modes. For Mode 1(a), the exact optimum voltage V_E^e depends on the initial velocity of the ions.

Operation Mode	η (Equation (1))	V_F^e (kV)	V_E^e (kV)	V_R (kV)	V_E^i (kV)	V_F^i (kV)
1(a) Ion TOF	0.76–0.78	0	2.275–2.354	3.000	not used	not used
1(b) Ion VMI	0.76	0	2.275	3.000	not used	not used
2(a) Electron VMI + ion TOF	0.76	5.000	−5.775	−9.200	−10.000	−10.000
2(b) Electron VMI + ion VMI	0.76	5.000	−5.775	−9.200	−8.802	−10.000

2.3.1. High Resolution Ion Modes

For the high resolution ion modes, ions are detected on the electron side of the spectrometer, and for the simulations, the choice was made to ground the front of the MCP and the flight tube ($V_F^e = 0$ kV). The repeller voltage was set to $V_R = 3$ kV. Figure 2a shows the resulting mass resolution in Operation Mode 1(a) for extractor voltages from 1400–3000 V. For zero kinetic energy ions, the optimum extractor voltage was found to be $V_E^e = 2.354$ kV ($\eta = 0.78$, black curve). The resolution of $m/\Delta m =$ 35,000 is clearly over-estimated, and for the more realistic case of ions with an initial drift velocity, the best resolution of $m/\Delta m = 2000$ was found for a voltage of $V_E^e = 2.275$ kV ($\eta = 0.76$, blue curve).

Figure 2b shows the resulting energy resolution for ion VMI in Operation Mode 1(b) for three different settings for the extractor voltage, V_E^e, calculated using the 27-particle model (blue, green and orange lines). The optimum extractor voltage, for which the best resolution was achieved for a photoion kinetic energy of 6 eV, was found to be $V_E^e = 2.275$ kV ($\eta = 0.76$), and for this setting, the resulting energy resolution from the Monte Carlo simulation is shown (black line), indicating an energy resolution better than 1.5% for kinetic energies between 6 and 10 eV. In Figure 2c,d, the corresponding

simulated detector image and the 3D momentum distribution after inversion are shown, respectively. Figure 2e shows the kinetic energy spectrum calculated from the 3D momentum distribution.

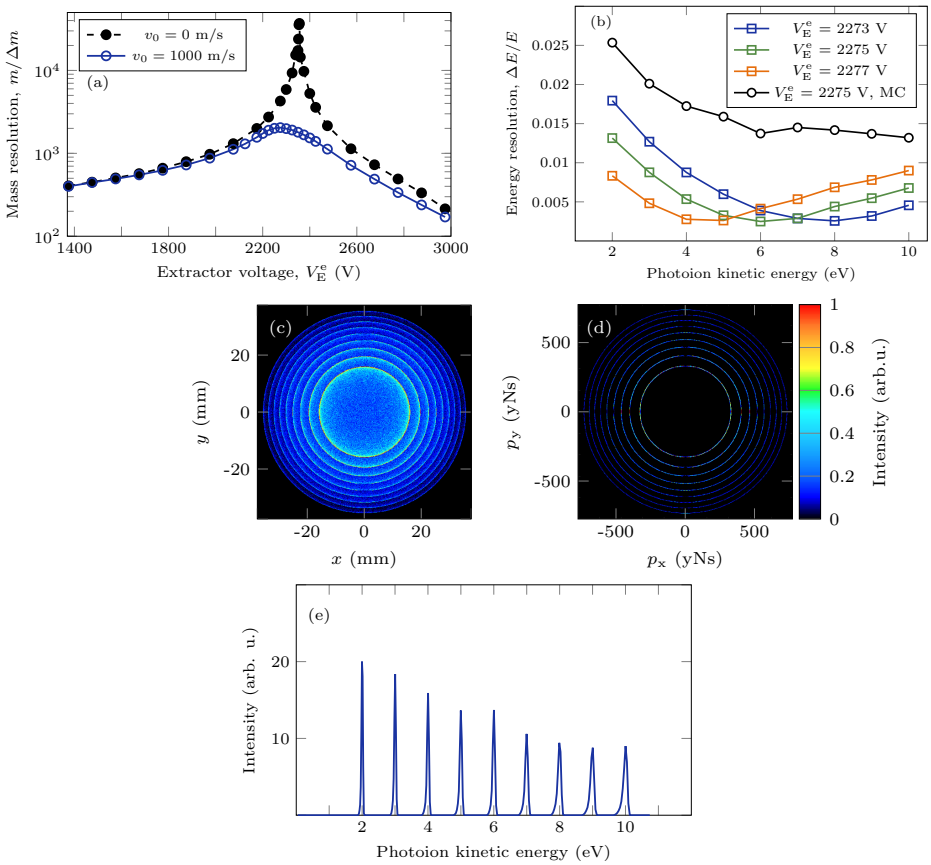

Figure 2. Simulation results for the high resolution ion modes. (**a**) shows the resulting mass resolution at mass $m = 100$ u as a function of extractor voltage, V_E^e, for ions with zero initial kinetic energy (black) and ions with an initial velocity of $v_0 = 1000$ m/s in the direction of the molecular beam (blue); (**b**) shows the resulting VMI energy resolution for three different extractor voltages (V_E^e) using the 27-particle model (blue, green and orange lines) and the Monte Carlo model for the optimum setting (black line); (**c**,**d**) show the simulated detector image and the 3D momentum distribution after inversion, for the optimum voltages; (**e**) shows the kinetic energy spectrum calculated from the 3D momentum distribution.

2.3.2. High Resolution Electron Modes

For the high resolution electron modes, electrons and ions are detected on their respective sides of the spectrometer. To maximize the possible total voltage difference over the spectrometer, the voltage on the electron side flight tube (and thus, the front of the electron MCP) was set to $V_F^e = 5$ kV, so that the phosphor screen could still be operated at its full voltage bias of 5 kV relative to the front of the MCP without exceeding the limit of the electrical feedthroughs. The repeller voltage was set to $V_R = -9.2$ kV to allow for detection of electrons with kinetic energies up to 90 eV, while allowing for extraction and imaging of ions with kinetic energies up to 10 eV.

Figure 3a shows the resulting energy resolution for electron VMI for three different settings for the extractor voltage, V_E^e, calculated using the 27-particle model (blue, green and orange lines). The optimum extractor voltage, for which the best resolution was achieved for a photoelectron energy of 30 eV, was found to be $V_E^e = -5.775$ kV ($\eta = 0.76$), and for this setting, the resulting energy resolution from the Monte Carlo simulation is shown (black line), indicating an energy resolution better than 2% for photoelectron energies between 30 and 85 eV. In Figure 3b,c, the corresponding simulated detector image and the 3D momentum distribution after inversion are shown, respectively. Figure 3d shows the photoelectron energy spectrum calculated from the 3D momentum distribution.

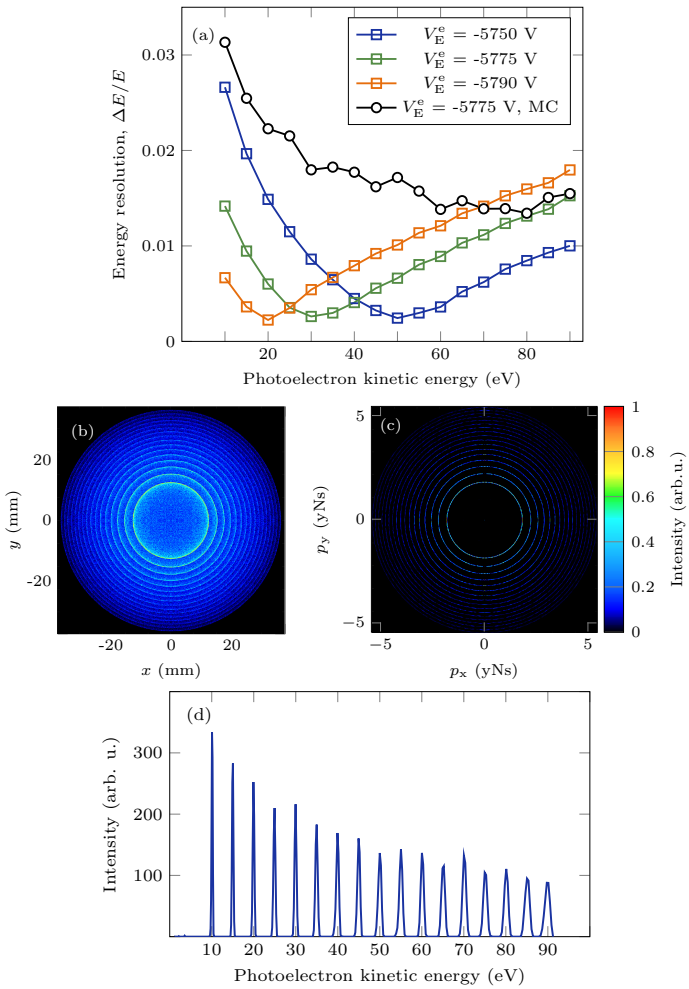

Figure 3. Simulation results for high resolution electron VMI mode. (**a**) shows the resulting energy resolution for three different extractor voltages (V_E^e) using the 27-particle model (blue, green and orange lines) and the Monte Carlo model for the optimum setting (black line); (**b**,**c**) show the simulated detector image and the 3D momentum distribution after inversion, for the optimum voltages; (**d**) shows the photoelectron energy spectrum calculated from the 3D momentum distribution.

With the electron side conditions optimized for electron VMI and the voltage on the ion side flight tube set to $V_F^i = -10$ kV to detect ions with kinetic energies up to 10 eV, the ion side can be tuned either for TOF (Operation Mode 2(a)) or VMI (Operation Mode 2(b)) by varying the ion extractor electrode voltage, V_E^i.

Figure 4a shows the resulting mass resolution in Operation Mode 2(a) for ions with an initial velocity of 1000 m/s in the direction of the molecular beam, for different extractor voltages, V_E^i. It is clear that it is not possible to reach Wiley–McLaren conditions within the voltage limits of the setup, due to the initial drift region between the interaction point and the mesh through which the ions have to travel. In addition, the best mass resolution of $m/\Delta m = 110$, achieved for $V_E^i = -10$ kV, is a factor of 18 worse than that achieved in Operation Mode 1(a). In fact, the mass resolution is in this case limited by the influence of the drift region and not by the initial velocity of the ions, and the mass resolution for zero kinetic energy ions (not shown) coincides with the mass resolution shown in Figure 4a. Figure 4b shows the resulting energy resolution for ion VMI in Operation Mode 2(b) for three different settings for the extractor voltage, V_E^i, calculated using the 27-particle model (blue, green and orange lines). The optimum extractor voltage, for which the best resolution was achieved for a kinetic energy of 6 eV, was found to be $V_E^i = -8.802$ kV, and for this setting, the resulting energy resolution from the Monte Carlo simulation is shown (black line), indicating an energy resolution better than 2.5% for kinetic energies between 3 and 10 eV. This is a small degradation in resolution as compared to the resolution obtained in Operation Mode 1(b) (shown by the dashed black line), but it is still an acceptable resolution for ions in most experiments. It is interesting to note that even in Operation Mode 2(b), for $V_E^i = -8.802$ kV, the mass resolution of the ion TOF is $m/\Delta m = 100$, which is acceptable unless isotope resolution of heavier fragments is required. In Figure 4c,d, the corresponding simulated detector image and the 3D momentum distribution after inversion are shown, respectively. Figure 4e shows the kinetic energy spectrum calculated from the 3D momentum distribution.

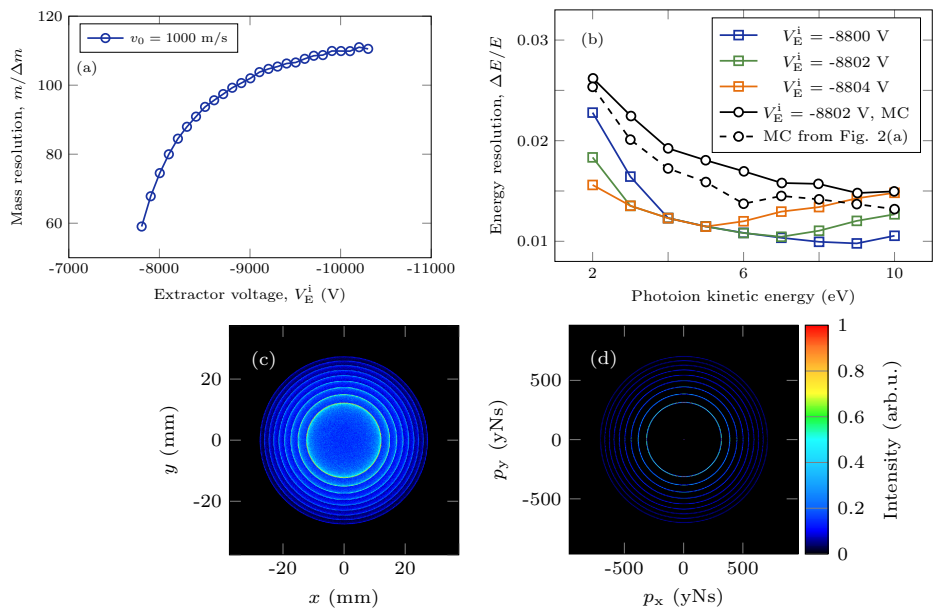

Figure 4. Cont.

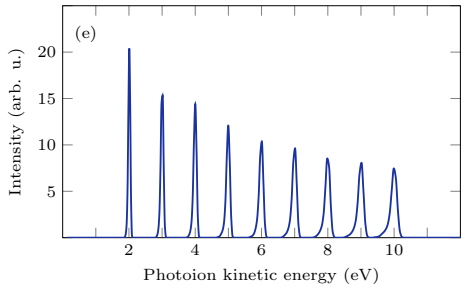

Figure 4. Simulation results for ion detection when the electron side is optimized for electron VMI (Operation Modes 2(a) and 2(b)). (**a**) shows the resulting mass resolution as a function of extractor voltage, V_E^i, for ions with an initial velocity of $v_0 = 1000$ m/s in the direction of the molecular beam; (**b**) shows the resulting VMI energy resolution for three different extractor voltages using the 27-particle model (blue, green and orange lines) and the Monte Carlo model for the optimum setting (solid black line). The dashed black line shows the resolution in Operation Mode 1(b) obtained by the Monte Carlo method, reproduced from Figure 2; (**c**,**d**) show the simulated detector image and the 3D momentum distribution after inversion, for the optimum voltages; (**e**) shows the kinetic energy spectrum calculated from the 3D momentum distribution.

3. Experimental Results

To evaluate the performance of the instrument, measurements have been done at the high-intensity XUV beamline at the Lund Attosecond Science Center [42], where high-flux XUV pulses generated through the HHG process were focused by reflective optics into the interaction region of the double VMIS. The target gas was introduced using a pulsed molecular beam from an Even–Lavie solenoid valve, able to produce high density pulses with durations as short as 10 µs [47,48]. In Figure 5, the spectrum of the XUV pulses generated in argon and recorded by an XUV spectrometer is displayed. It contains photons from harmonic order 13 (20.0 eV) up to harmonic order 29 (44.7 eV). Lower photon energy contributions and the remaining driving laser light are absorbed by a 200 nm-thick aluminum filter. The XUV light is redirected to the XUV spectrometer by a rotatable gold mirror prior to the focusing into the interaction region of the double VMIS, and thus, the spectrum cannot be recorded during measurements with the double VMIS. The displayed XUV spectrum has been corrected for the spectral responses of the employed grating and MCP detector. In the further analysis, the corrected spectrum is used.

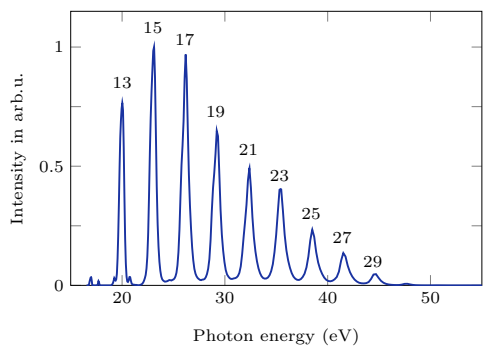

Figure 5. XUV spectrum recorded by the XUV spectrometer. The spectrum contains photons from harmonic order 13 (20.0 eV) up to harmonic order 29 (44.7 eV), indicated above the peaks.

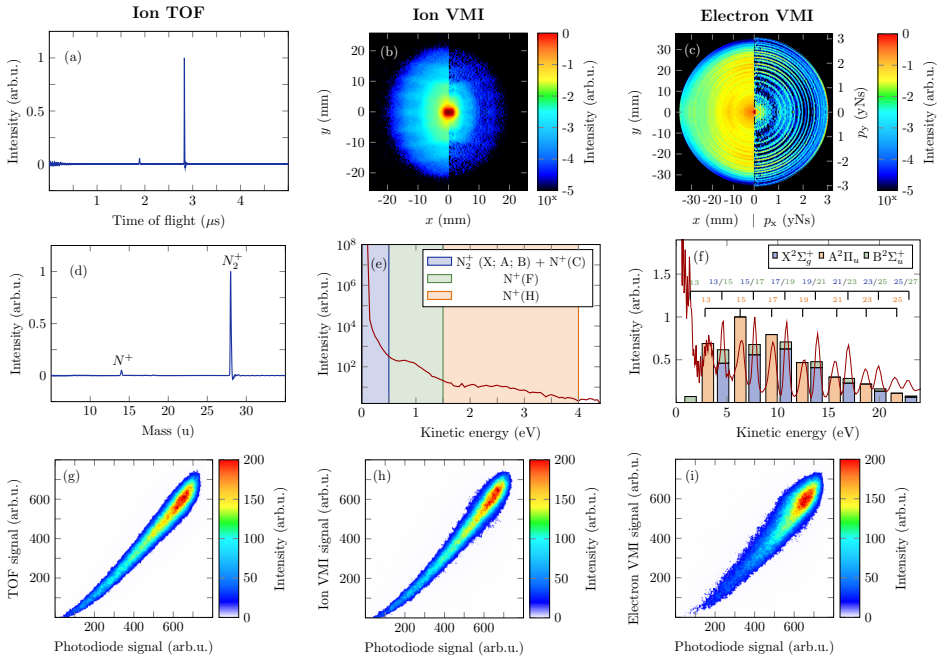

Figure 6. Experimental results in the high resolution electron mode 2(b) using high-order harmonics generated in argon to ionize N_2. (**a**,**d**,**g**) show ion TOF data (**a**), with the calibrated mass spectrum in (**d**) and the correlation between the total ion TOF signal and the XUV intensity measured by the XUV photodiode visualized by a color-coded scatter plot in (**g**); (**b**,**e**,**h**) show ion VMI data, with the average detector image (left part) and inverted image (right part) in (**b**). The inverted images represent the reconstructed initial 3D momentum distributions obtained by inversion of the 2D projections recorded on the detector [23]. The photoion kinetic energy spectrum is displayed in (**e**) with its attributed contributions shaded in different colors, calculated from the inverted image (**b**). The correlation between the total ion VMI signal and the XUV intensity is exhibited in (**h**); (**c**,**f**,**i**) show electron VMI data, with the average detector image (left part) and inverted image (right part) in (**c**). The photoelectron kinetic energy spectrum is displayed in panel (**f**) with the attributed electronic molecular channels and the color-coded corresponding harmonic orders. The correlation between the total electron VMI signal and the XUV intensity is shown in (**i**). The slight bend observed for low intensities in the correlation plots is likely caused by a non-linear behavior of the photodiode in this signal region.

To be able to apply covariance analysis, synchronized single-shot data need to be acquired. At the high-intensity XUV beamline, the repetition rate is 10 Hz, and acquisition of single-shot data is relatively straightforward. However, the intensity of the XUV light generated by laser-driven HHG typically varies on a shot-to-shot basis, introducing false correlations between channels that are physically not correlated. To circumvent this problem, a partial covariance method was used [49], through which the covariance maps were corrected for the fluctuating source intensity, recorded on a single-shot basis by an in-vacuum XUV photodiode placed after the focus of the XUV pulses. In this section, we describe the acquisition of data and the subsequent proof-of-principle application of ion-ion and ion-electron covariance mapping.

3.1. Data Acquisition

The successful implementation of the partial covariance analysis technique, discussed above, requires that the different single-shot observables can be reliably recorded in a synchronized fashion. In order to achieve this, a timestamp server was set up. After receiving the trigger from the laser master clock, the acquisition programs signal their readiness to the server. If all programs signal within a set timeout, the server responds with a timestamp. Otherwise, it orders the programs to cancel the acquisition and to wait for the next trigger pulse. Typically, about 5% of the shots are discarded by the server. To fully evaluate the performance of the instrument, the acquisition of four synchronized signals is required:

- Ion time-of-flight trace
- Ion velocity map image
- Electron velocity map image
- XUV intensity from photodiode

The ion TOF trace was obtained by decoupling the current from the back of the ion MCP and converting it into a voltage signal. The XUV photodiode generates a current, which is converted to a voltage signal by means of a transimpedance amplifier. These analog ion TOF and XUV photodiode voltage traces are subsequently converted into digital signals using a two-channel, 1-GHz sampling rate, analog-to-digital converter (Agilent Acquiris DP1400), which acquires 20,000 samples per laser shot in each of the channels, with a dynamic range of eight bits. The ion and electron VMI data are recorded with two one-megapixel Allied Vision Technology Pike F-145B cameras that have an 8 bit dynamic range and a maximum frame rate of 30 Hz. In terms of storage rate, this amounts to more than 2 MB of data per shot, or 20 MB/s.

As a benchmark molecule, we used N_2. Figure 6 shows simultaneously-acquired data from N_2, acquired using voltage ratios corresponding to Operation Mode 2(b), i.e., optimized for electron and ion VMI, but with absolute voltages adapted for a maximum electron kinetic energy of 30 eV. The data were recorded for 25,000 laser shots, corresponding to just above 40 minutes of acquisition time and amounting to ∼50 GB of data. The molecules were ionized using the harmonics 13–29 generated in argon, corresponding to photon energies between 20 and 45 eV, as displayed in Figure 5. The typical on-target pulse energy was ∼5 nJ, which corresponds to approximately 10^9 photons per pulse over the whole bandwidth and 10^8 photons per pulse and harmonic. The count rates were on the order of 500 particles detected per shot for the ions, as well as the electrons.

Considering that the maximum available photon energy is just above the double ionization threshold of N_2 (42.88 eV [50]), a number of electronic states in N_2 with ionization potential (IP) in the range can be accessed: $X^2\Sigma_g^+$, $A^2\Pi_u$, $B^2\Sigma_u^+$, $C^2\Sigma_u^+$, $F^2\Sigma_g^+$ and $H^2\Sigma_g^+$. The average ion mass spectrum in Figure 6d exhibits two main features, which were assigned to the N^+ and N_2^+ channels. While the former also contains a contribution coming from stable N_2^{2+} ions, only photons from the 29th harmonic or higher can contribute, and considering the low intensity at these photon energies (Figure 5), the contribution from this channel is expected to be negligible. The mass resolution was estimated to $m/\Delta m = 60$ for a mass of 28 u.

Figure 6b shows the photoion momentum distribution of all the ionic fragments that were generated in the interaction region, averaged over 25,000 shots. The anisotropy of the distribution, peaked in the vertical direction, is due to the fact that the cross-section for excitation to the dissociative states is higher for molecules aligned along the laser polarization direction. The faint horizontal ripple pattern in the images is a result of ions scattering on the mesh in the repeller electrode. In Figure 6e, the corresponding photoion kinetic energy is displayed. It reveals three main features: a peaked contribution shaded in blue, a broader feature shaded in green and another broad contribution almost spreading out to the edge of the detector shaded in orange. We attribute the strongest feature (shaded blue) to low kinetic energy N_2^+ ions and predissociation of the N_2^+ $C^2\Sigma_u^+$ state [51]. The contribution shaded in green has previously been assigned to dissociation from the $F^2\Sigma_g^+$ state, and the features in

the area shaded in orange are associated with dissociation from the highly-excited Rydberg-like states of N_2^+ and the H band [51–53].

Figure 6c,f shows the photoelectron momentum distribution and the photoelectron kinetic energy spectrum, respectively. From the photoelectron spectrum, it is apparent that the resolution of the spectrometer is limited by the bandwidth of the harmonics (∼0.5 eV) rather than by the electron imaging. Figure 6f contains the assigned contributions originating from the $X^2\Sigma_g^+$, $A^2\Pi_u$ and $B^2\Sigma_u^+$ states, after taking their respective branching ratios, cross-sections [54,55] and the relative XUV intensity at the photon energies contained in the XUV spectrum into account. The ratio of the contributions is displayed by a stacked bar plot, where each state has a specific color assigned. The much weaker contributions of the other cationic and dicationic states are not shown for clarity [53,54,56,57]. The signal at kinetic energies smaller than 1 eV can be assigned to highly excited inner valence states of N_2^+ and possibly the first electronic states of N_2^{2+} [52,53,57].

As mentioned earlier, in order to extract information about the correlation between the different single-shot datasets, it is important that the sets are acquired simultaneously and can be analyzed in a synchronized fashion. That this is indeed the case for the acquired dataset readily verified by studying the color-coded scatter plots in Figure 6g–i, indicating a high degree of correlation between the XUV intensity measured by the photodiode and the other three detector signals.

3.2. Covariance Analysis

Once the synchronized acquisition of data from all the detectors is established, covariance analysis can be applied to different variables to reveal more information about the underlying physical processes during and after the photoionization. As a proof-of-principle demonstration, we use covariance mapping to achieve post-acquisition mass selection of different ionic species. The aim is to extract the momentum distributions for individual ionic species from the average momentum distribution Figure 6b by calculating the covariance image with respect to the corresponding peak in the ion TOF spectrum shown in Figure 6a. For mass selection, temporal windows around the two features in the time-of-flight spectrum in Figure 6a were chosen. For this, the partial covariance [49], $\mathrm{pcov}(\mathbf{X}, \mathbf{Y})$, between every pixel in the ion velocity map image ($\mathbf{X}$) with the total signal in the studied channel in the time-of-flight spectrum ($\mathbf{Y}$) was calculated.

The resulting covariance maps are displayed in Figure 7a for the N_2^+ channel and in Figure 7b for the N^+ channel. As expected, the N_2^+ map (a) is dominated by the zero kinetic energy parent ions from ionization to the $X^2\Sigma_g^+$, $A^2\Pi_u$ and $B^2\Sigma_u^+$ states. The N^+ map (b) shows correlation both at low kinetic energies, previously attributed to the predissociation of the N_2^+ $C^2\Sigma_u^+$ state and, at higher kinetic energies, previously attributed to dissociation from the $F^2\Sigma_g^+$ state, highly excited Rydberg-like states of N_2^+ and the H band. Further, in order to compare it to the accumulated ion VMI data, the same inversion procedure was applied to the covariance maps. The results are shown side by side with the reproduced inverted data from Figure 6b in the left halves of Figure 7c for N_2^+ and Figure 7d for N^+, with the right halves being the inverted covariance maps. These results clearly show that mass selection via covariance is a viable method to extract correlated information about the products of photoionization using the proposed instrument.

A natural next step is to consider ion-electron covariance using this scheme. Consequently, the photoelectron covariance maps were calculated in an analogous way to the ion covariance maps shown in Figure 7a,b. Due to insufficient statistics, it was not possible to adequately invert the resulting covariance maps, and instead, the results of an angular integration of these are shown in Figure 8. Since, as shown in Figure 6f, the photoelectron spectrum primarily contains electrons from the $X^2\Sigma_g^+$, $A^2\Pi_u$ and $B^2\Sigma_u^+$ states that are all coupled to the N_2^+ channel, these completely dominate the covariance at photoelectron momenta between 1 and 2.6 yNs. While the individual peaks cannot be clearly resolved, partly due to a downsampling of the data for reasons of statistics, the contribution is stronger for the N_2^+ channel in this regime, as expected. However, at close to zero momentum, the contribution associated with the production of N^+ from dissociation is dominating, which is consistent with

our previous attribution of these low kinetic energy electrons to excitation of inner valence states of N_2^+. Although qualitative, these first ion-electron covariance results indicate the feasibility of using covariance analysis to extract channel-specific photoelectron data from experiments with high single-shot count rates using the double VMIS presented here.

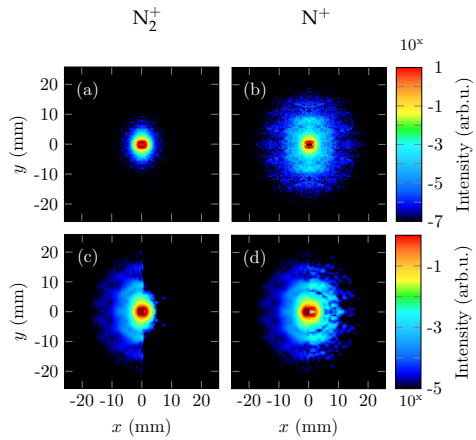

Figure 7. Results of ion-ion covariance analysis. (**a**,**b**) show covariance maps of the N_2^+ and the N^+ ion TOF fragments correlated with the ion VMI detector image, respectively. Furthermore, these maps were treated like raw VMI images and inverted. The results are displayed in the right halves of (**c**,**d**). For comparison the inverted image of the accumulated ion detector image from Figure 6b is reproduced in the left halves.

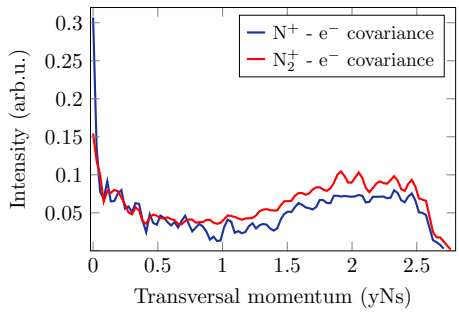

Figure 8. Results of ion-electron covariance analysis. Covariance between the photoelectron transversal momentum spectrum and the ion-TOF channels of N^+ (blue) and N_2^+ (red). Qualitatively, the N^+ channel shows stronger correlation with low momentum photoelectrons, whereas the N_2^+ channel exhibits a stronger correlation with photoelectrons at higher transversal momenta.

4. Conclusions and Outlook

In conclusion, we have reported on the design and performance of a velocity map imaging (VMI) spectrometer optimized for experiments using high-intensity extreme ultraviolet (XUV) sources such as laser-driven high-order harmonic generation (HHG) sources and free-electron lasers (FELs). The instrument is versatile and allows for combining photo-electron and -ion detection modes, such as ion time-of-flight (TOF), ion VMI and electron VMI, in different ways, depending on the required information and the process under study. The performance for the different detection modes was estimated using simulations, and first experimental results from an intense HHG source were presented

together with proof-of-principle application of covariance mapping to mass selection of photoions and extraction of channel-specific photoelectron spectra.

The analysis of the experimental results confirms that the acquired data contain information about the correlation between the products of the photoionization, and the first covariance mapping analysis demonstrates the feasibility of extracting such information, indicating that the suggested approach is viable for extracting feature-rich correlated information from future experiments using high-intensity XUV sources.

Author Contributions: Conceptualization: L.R. and P.J. Data curation: L.R., J.L. and S.M. Formal analysis: L.R., J.L., S.M. and P.J. Funding acquisition: P.J. Investigation: L.R., J.L., S.M., F.C., H.C.-A., B.O., J.P., H.W., P.R. and M.G. Project administration: P.J. Supervision: P.J.; Writing, original draft: L.R. and J.L. Writing, review and editing: L.R., J.L., S.M., F.C., H.C.-A., B.O., J.P., H.W., P.R., M.G. and P.J.

Funding: This research was supported by the Swedish Research Council, the Swedish Foundation for Strategic Research and the Crafoord Foundation. This project has received funding from the European Union's Horizon 2020 research and innovation program under the Marie Sklodowska-Curie Grant Agreement No. 641789 MEDEA.

Conflicts of Interest: The authors declare no conflict of interest. The founding sponsors had no role in the design of the study; in the collection, analyses or interpretation of data; in the writing of the manuscript; nor in the decision to publish the results.

References

1. Ferray, M.; L'Huillier, A.; Li, X.; Lompre, L.; Mainfray, G.; Manus, C. Multiple-harmonic conversion of 1064 nm radiation in rare gases. *J. Phys. B* **1988**, *21*, L31. [CrossRef]
2. Agostini, P.; DiMauro, L.F. The physics of attosecond light pulses. *Rep. Prog. Phys* **2004**, *67*, 813. [CrossRef]
3. McPherson, A.; Gibson, G.; Jara, H.; Johann, U.; Luk, T.S.; McIntyre, I.A.; Boyer, K.; Rhodes, C.K. Studies of multiphoton production of vacuum-ultraviolet radiation in the rare gases. *J. Opt. Soc. Am. B* **1987**, *4*, 595–601. [CrossRef]
4. Corkum, P. Plasma perspective on strong-field multiphoton ionization. *Phys. Rev. Lett.* **1993**, *71*, 1994. [CrossRef] [PubMed]
5. Schafer, K.J.; Yang, B.; DiMauro, L.F.; Kulander, K.C. Above threshold ionization beyond the high harmonic cutoff. *Phys. Rev. Lett.* **1993**, *70*, 1599. [CrossRef] [PubMed]
6. Ackermann, W.A.; Asova, G.; Ayvazyan, V.; Azima, A.; Baboi, N.; Bähr, J.; Balandin, V.; Beutner, B.; Brandt, A.; Bolzmann, A.; et al. Operation of a free-electron laser from the extreme ultraviolet to the water window. *Nat. Photonics* **2007**, *1*, 336. [CrossRef]
7. Emma, P.; Akre, R.; Arthur, J.; Bionta, R.; Bostedt, C.; Bozek, J.; Brachmann, A.; Bucksbaum, P.; Coffee, R.; Decker, F.J.; et al. First lasing and operation of an ångstrom-wavelength free-electron laser. *Nat. Photonics* **2010**, *4*, 641. [CrossRef]
8. Ishikawa, T.; Aoyagi, H.; Asaka, T.; Asano, Y.; Azumi, N.; Bizen, T.; Ego, H.; Fukami, K.; Fukui, T.; Furukawa, Y.; et al. A compact X-ray free-electron laser emitting in the sub-ångström region. *Nat. Photonics* **2012**, *6*, 540. [CrossRef]
9. McNeil, B.W.J.; Thompson, N.R. X-ray free-electron lasers. *Nat. Photonics* **2010**, *4*, 814. [CrossRef]
10. Glownia, J.M.; Cryan, J.; Andreasson, J.; Belkacem, A.; Berrah, N.; Blaga, C.I.; Bostedt, C.; Bozek, J.; DiMauro, L.F.; Fang, L.; et al. Time-resolved pump-probe experiments at the LCLS. *Opt. Express* **2010**, *18*, 17620–17630. [CrossRef] [PubMed]
11. Lépine, F.; Ivanov, M.Y.; Vrakking, M.J.J. Attosecond molecular dynamics: Fact or fiction? *Nat. Photonics* **2014**, *8*, 195. [CrossRef]
12. Krausz, F.; Ivanov, M. Attosecond physics. *Rev. Mod. Phys.* **2009**, *81*, 163–234. [CrossRef]
13. Sorokin, A.; Wellhöfer, M.; Bobashev, S.; Tiedtke, K.; Richter, M. X-ray-laser interaction with matter and the role of multiphoton ionization: Free-electron-laser studies on neon and helium. *Phys. Rev. A* **2007**, *75*, 051402. [CrossRef]
14. Berrah, N.; Bozek, J.; Costello, J.T.; Düsterer, S.; Fang, L.; Feldhaus, J.; Fukuzawa, H.; Hoener, M.; Jiang, Y.H.; Johnsson, P.; et al. Non-linear processes in the interaction of atoms and molecules with intense EUV and X-ray fields from SASE free electron lasers (FELs). *J. Mod. Opt.* **2010**, *57*, 1015–1040. [CrossRef]

15. Bucksbaum, P.H.; Coffee, R.; Berrah, N. The First Atomic and Molecular Experiments at the Linac Coherent Light Source X-Ray Free Electron Laser. In *Advances in Atomic, Molecular, and Optical Physics*; Academic Press: Cambridge, MA, USA, 2011; p. 239.
16. Fang, L.; Osipov, T.; Murphy, B.; Tarantelli, F.; Kukk, E.; Cryan, J.P.; Glownia, M.; Bucksbaum, P.H.; Coffee, R.N.; Chen, M.; et al. Multiphoton Ionization as a clock to Reveal Molecular Dynamics with Intense Short X-ray Free Electron Laser Pulses. *Phys. Rev. Lett.* **2012**, *109*, 263001. [CrossRef] [PubMed]
17. Gallagher-Jones, M.; Bessho, Y.; Kim, S.; Park, J.; Kim, S.; Nam, D.; Kim, C.; Kim, Y.; Miyashita, O.; Tama, F.; et al. Macromolecular structures probed by combining single-shot free-electron laser diffraction with synchrotron coherent X-ray imaging. *Nat. Commun.* **2014**, *5*, 3798. [CrossRef] [PubMed]
18. Seibert, M.M.; Ekeberg, T.; Maia, F.R.; Svenda, M.; Andreasson, J.; Jönsson, O.; Odić, D.; Iwan, B.; Rocker, A.; Westphal, D.; et al. Single mimivirus particles intercepted and imaged with an X-ray laser. *Nature* **2011**, *470*, 78–81. [CrossRef] [PubMed]
19. Neutze, R.; Wouts, R.; Van der Spoel, D.; Weckert, E.; Hajdu, J. Potential for biomolecular imaging with femtosecond X-ray pulses. *Nature* **2000**, *406*, 752–757. [CrossRef] [PubMed]
20. Ullrich, J.; Moshammer, R.; Dorn, A.; Dörner, R.; Schmidt, L.P.H.; Schmidt-Böcking, H. Recoil-ion and electron momentum spectroscopy: Reaction-microscopes. *Rep. Prog. Phys.* **2003**, *66*, 1463–1545. [CrossRef]
21. Eppink, A.T.J.B.; Parker, D.H. Velocity map imaging of ions and electrons using electrostatic lenses: Application in photoelectron and photofragment ion imaging of molecular oxygen. *Rev. Sci. Instrum.* **1997**, *68*, 3477–3484. [CrossRef]
22. Smith, L.M.; Keefer, D.R.; Sudharsanan, S. Abel inversion using transform techniques. *J. Quant. Spectrosc. Radiat. Transf.* **1988**, *39*, 367–373. [CrossRef]
23. Vrakking, M.J.J. An iterative procedure for the inversion of two-dimensional ion/photoelectron imaging experiments. *Rev. Sci. Instrum.* **2001**, *72*, 4084–4089. [CrossRef]
24. Eland, J.H.D. Improved resolution in fixed-wavelength photoelectron–photoion coincidence spectroscopy. *Rev. Sci. Instrum.* **1978**, *49*, 1688–1690. [CrossRef] [PubMed]
25. Bodi, A.; Hemberger, P.; Gerber, T.; Sztáray, B. A new double imaging velocity focusing coincidence experiment: i^2PEPICO. *Rev. Sci. Instrum.* **2012**, *83*, 083105. [CrossRef] [PubMed]
26. Sztáray, B.; Voronova, K.; Torma, K.G.; Covert, K.J.; Bodi, A.; Hemberger, P.; Gerber, T.; Osborn, D.L. CRF-PEPICO: Double velocity map imaging photoelectron photoion coincidence spectroscopy for reaction kinetics studies. *J. Chem. Phys.* **2017**, *147*, 013944. [CrossRef] [PubMed]
27. Garcia, G.A.; Soldi-Lose, H.; Nahon, L. A versatile electron-ion coincidence spectrometer for photoelectron momentum imaging and threshold spectroscopy on mass selected ions using synchrotron radiation. *Rev. Sci. Instrum.* **2009**, *80*, 023102. [CrossRef] [PubMed]
28. O'keeffe, P.; Bolognesi, P.; Coreno, M.; Moise, A.; Richter, R.; Cautero, G.; Stebel, L.; Sergo, R.; Pravica, L.; Ovcharenko, Y.; et al. A photoelectron velocity map imaging spectrometer for experiments combining synchrotron and laser radiations. *Rev. Sci. Instrum.* **2011**, *82*, 033109. [CrossRef] [PubMed]
29. Garcia, G.A.; Nahon, L. A refocusing modified velocity map imaging electron/ion spectrometer adapted to synchrotron radiation studies. *Rev. Sci. Instrum.* **2005**, *76*, 053302. [CrossRef]
30. Frasinski, L.J.; Codling, K.; Hatherly, P.A. Covariance Mapping: A Correlation Method Applied to Multiphoton Multiple Ionization. *Science* **1989**, *246*, 1029–1031. [CrossRef] [PubMed]
31. Frasinski, L.J.; Stankiewicz, M.; Hatherly, P.A.; Cross, G.M.; Codling, K.; Langley, A.J.; Shaikh, W. Molecular H_2 in intense laser fields probed by electron-electron, electron-ion, and ion-ion covariance techniques. *Phys. Rev. A* **1992**, *46*, R6789–R6792. [CrossRef] [PubMed]
32. Frasinski, L.J. Covariance mapping techniques. *J. Phys. B* **2016**, *49*, 152004. [CrossRef]
33. Kornilov, O.; Eckstein, M.; Rosenblatt, M.; Schulz, C.P.; Motomura, K.; Rouzée, A.; Klei, J.; Foucar, L.; Siano, M.; Lübcke, A.; et al. Coulomb explosion of diatomic molecules in intense XUV fields mapped by partial covariance. *J. Phys. B* **2013**, *46*, 164028. [CrossRef]
34. Boguslavskiy, A.E.; Mikosch, J.; Gijsbertsen, A.; Spanner, M.; Patchkovskii, S.; Gador, N.; Vrakking, M.J.J.; Stolow, A. The Multielectron Ionization Dynamics Underlying Attosecond Strong-Field Spectroscopies. *Science* **2012**, *335*, 1336–1340. [CrossRef] [PubMed]
35. Zhu, J.; Hill, W.T. Momentum and correlation spectra following intense-field dissociative ionization of H_2. *J. Opt. Soc. Am. B* **1997**, *14*, 2212–2220. [CrossRef]

36. Hansen, J.L.; Nielsen, J.H.; Madsen, C.B.; Lindhardt, A.T.; Johansson, M.P.; Skrydstrup, T.; Madsen, L.B.; Stapelfeldt, H. Control and femtosecond time-resolved imaging of torsion in a chiral molecule. *J. Chem. Phys.* **2012**, *136*, 204310. [CrossRef] [PubMed]
37. Slater, C.S.; Blake, S.; Brouard, M.; Lauer, A.; Vallance, C.; Bohun, C.S.; Christensen, L.; Nielsen, J.H.; Johansson, M.P.; Stapelfeldt, H. Coulomb-explosion imaging using a pixel-imaging mass-spectrometry camera. *Phys. Rev. A* **2015**, *91*, 053424. [CrossRef]
38. Pickering, J.D.; Amini, K.; Brouard, M.; Burt, M.; Bush, I.J.; Christensen, L.; Lauer, A.; Nielsen, J.H.; Slater, C.S.; Stapelfeldt, H. Communication: Three-fold covariance imaging of laser-induced Coulomb explosions. *J. Chem. Phys.* **2016**, *144*, 161105, doi:10.1063/1.4947551. [CrossRef] [PubMed]
39. Osipov, T.; Bostedt, C.; Castagna, J.C.; Ferguson, K.R.; Bucher, M.; Montero, S.C.; Swiggers, M.L.; Obaid, R.; Rolles, D.; et al. The LAMP instrument at the Linac Coherent Light Source free-electron laser. *Rev. Sci. Instrum.* **2018**, *89*, 035112. [CrossRef] [PubMed]
40. Johnsson, P.; Rouzée, A.; Siu, W.; Huismans, Y.; Lépine, F.; Marchenko, T.; Düsterer, S.; Tavella, F.; Stojanovic, N.; Redlin, H.; et al. Characterization of a two-color pump–probe setup at FLASH using a velocity map imaging spectrometer. *Opt. Lett.* **2010**, *35*, 4163–4165. [CrossRef] [PubMed]
41. Wiley, W.C.; McLaren, I.H. Time-of-Flight Mass Spectrometer with Improved Resolution. *Rev. Sci. Instrum.* **1955**, *26*, 1150. [CrossRef]
42. Manschwetus, B.; Rading, L.; Campi, F.; Maclot, S.; Coudert-Alteirac, H.; Lahl, J.; Wikmark, H.; Rudawski, P.; Heyl, C.M.; Farkas, B.; et al. Two-photon double ionization of neon using an intense attosecond pulse train. *Phys. Rev. A* **2016**, *93*, 061402. [CrossRef]
43. Coudert-Alteirac, H.; Dacasa, H.; Campi, F.; Kueny, E.; Farkas, B.; Brunner, F.; Maclot, S.; Manschwetus, B.; Wikmark, H.; Lahl, J.; et al. Micro-Focusing of Broadband High-Order Harmonic Radiation by a Double Toroidal Mirror. *Appl. Sci.* **2017**, *11*, 1159. [CrossRef]
44. Rosca-Pruna, F. Alignment of Diatomic Molecules Induced by Intense Laser Fields. Ph.D. Thesis, VU University of Amsterdam, Amsterdam, The Netherlands, 2001.
45. Dahl, D.A. Simion for the personal computer in reflection. *Int. J. Mass Spectrom.* **2000**, *200*, 3–25. [CrossRef]
46. Ghafur, O.; Siu, W.; Johnsson, P.; Kling, M.F.; Drescher, M.; Vrakking, M.J.J. A velocity map imaging detector with an integrated gas injection system. *Rev. Sci. Instrum.* **2009**, *80*, 033110. [CrossRef] [PubMed]
47. Even, U. Pulsed Supersonic Beams from High Pressure Source: Simulation Results and Experimental Measurements. *Adv. Chem.* **2014**, *2014*, 1–11. [CrossRef]
48. Even, U. The Even-Lavie valve as a source for high intensity supersonic beam. *EPJ Tech. Instrum.* **2015**, *2*, 17. [CrossRef]
49. Frasinski, L.J.; Giles, A.; Hatherly, P.; Posthumus, J.; Thompson, M.; Codling, K. Covariance mapping and triple coincidence techniques applied to multielectron dissociative ionization. *J. Electron Spectrosc. Relat. Phenom.* **1996**, *79*, 367–371. [CrossRef]
50. Hochlaf, M.; Hall, R.I.; Penent, F.; Kjeldsen, H.; Lablanquie, P.; Lavollée, M.; Eland, J.H.D. Threshold photoelectrons coincidence spectroscopy of N_2^{2+} and CO^{2+} ions. *Chem. Phys.* **1996**, *207*, 159–165. [CrossRef]
51. Lucchini, M.; Kim, K.; Calegari, F.; Kelkensberg, F.; Siu, W.; Sansone, G.; Vrakking, M.J.J.; Hochlaf, M.; Nisoli, M. Autoionization and ultrafast relaxation dynamics of highly excited states in N_2. *Phys. Rev. A* **2012**, *86*, 043404. [CrossRef]
52. Eckstein, M.; Yang, C.H.; Kubin, M.; Frasetto, F.; Poletto, L.; Ritze, H.H.; Vrakking, M.J.J.; Kornilov, O. Dynamics of N_2 Dissociation upon Inner-Valence Ionization by Wavelength-Selected XUV Pulses. *J. Phys. Chem. Lett.* **2015**, *6*, 419–425. [CrossRef] [PubMed]
53. Aoto, T.; Ito, K. Inner-valence states of N_2^+ and the dissociation dynamics studied by threshold photoelectron spectroscopy and configuration interaction calculation. *J. Chem. Phys.* **2006**, *124*, 234306. [CrossRef] [PubMed]
54. Plummer, E.W.; Gustafsson, T.; Gudat, W.; Eastman, D.E. Partial photoionization cross sections of N_2 and CO using synchrotron radiation. *Phys. Rev. A* **1977**, *15*, 2339–2355. [CrossRef]
55. Hammet, A.; Stoll, W.; Brion, C. Photoelectron branching ratios and partial ionization cross-sections for CO and N_2 in the energy range 18–50 eV. *J. Electron Spectrosc. Relat. Phenom.* **1976**, *8*, 367–376. [CrossRef]

56. Baltzer, P.; Larsson, M.; Karlsson, L.; Wannberg, B.; Carlsson-Göthe, M. Inner-valence states of N_2^+ studied by uv photoelectron spectroscopy and configuration-interaction calculations. *Phys. Rev. A* **1992**, *46*, 5545–5553. [CrossRef] [PubMed]
57. Ahmad, M.; Lablanquie, P.; Penent, F.; Lambourne, J.G.; Hall, R.I.; Eland, J.H.D. Structure and fragmentation dynamics of N_2^{2+} ions in double photoionization experiments. *J. Phys. B* **2006**, *39*, 3599. [CrossRef]

Printed by Media-Tryck, Lund 2021 NORDIC SWAN ECOLABEL 3041 0903

LUND UNIVERSITY
Faculty of Engineering, LTH
Department of Physics
Divison of Atomic Physics

ISBN: 978-91-8039-015-6 (print)
ISBN: 978-91-8039-014-9 (pdf)
ISSN: 0281-2762
Lund Reports on Atomic Physics, LRAP 576 (2021)